Petrogenesis of Hornblendite and Clinopyroxenite Cognate Xenoliths from the West Eifel Volcanic Field, Germany: A Textural Insight into Crystal and Melt Dynamics in an Intraplate Volcanic Setting

Zoë Matthews

Department of Earth Sciences

Royal Holloway, University of London

A thesis submitted to the University of London for the degree of Doctor of Philosophy

February 2022

Declaration

This thesis has been prepared on the basis of my own work. Where other source materials have been used, these have been acknowledged.

Word Count: 49,617

Student Name: Zoë Anne Matthews

Date: 23rd February 2022

Signature:

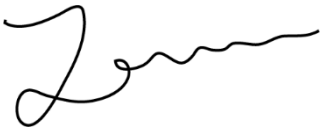

Abstract

Glass-bearing clinopyroxenite and hornblendite cognate xenoliths entrained in alkali basalts from the West Eifel Volcanic Field provide a snapshot of a semi-solidified mush that was rapidly quenched upon entrainment, preserving the melt distribution as interstitial glass. As such, they provide a unique opportunity to investigate the physical relationship between crystals and melt within a mush. At present, this relationship is poorly constrained and petrologists are largely reliant on using fully solidified plutonic rocks to interpret melt distribution and geometries in two-dimensions. Understanding where melt is distributed, and how magmatic processes act to influence this is integral in improving our understanding of sub-volcanic systems, with wider applicability to constraining the mechanisms that govern how melt is extracted from the crystal mush and erupted at the surface.

Quantitative textural analysis including crystal size distribution (CSD), spatial distribution pattern (SDP) and shape preferred orientation (SPO), as well as qualitative textural observations, are used in conjunction with supplementary geochemistry to constrain the petrogenetic history of four cognate xenoliths derived from the lower-crust to upper-mantle realm. Together, this data provides evidence for open system magmatic processes driving mineral dissolution and reactive crystallisation. Three-dimensional X-ray Computed Tomography is also utilised to visualise and quantify the geometry of the melt, now glass, which represents the porosity of the mush at the point of entrainment. This provides a valuable insight into how melt is stored within crystal mushes, without textural overprinting by secondary recrystallisation processes that are often pervasive in solidified plutons. Combining the two-dimensional textural data with the three-dimensional data identifies significant melt heterogeneity at a micro-scale, related to textural changes within the crystalline fraction acting to enhance melt migration. This not only provides an insight into melt distribution, but permits analysis of how the crystals and melt interact relative to one another in an active mush system. This work will contribute towards improving our understanding of crystal mushes and their significance in controlling volcanic eruptions.

Acknowledgements

Thank you to Christina Manning for primary supervision and to Hilary Downes for secondary supervision and provision of the samples. Additional thanks to Kevin D'Souza and Neil Holloway for technical support. My friends and family for support and motivation, and those who stepped up to help when things were particularly tough. Finally, Ryan. Thank you for everything, always and forever.

Table of contents

Digital appendices

1. Digital Appendix 1: Quantitative textural results
2. Digital Appendix 2: CT porosity data
3. Digital Appendix 3: LA-ICP-MS data
4. Digital Appendix 4: CT image files
5. Digital Appendix 5: CT videos

List of tables

List of Figures

List of Abbreviations

Abbreviation	Explanation
2D	Two-dimensional
3D	Three-dimensional
AF	Area fraction
AP	Apatite
CEVP	Central European Volcanic Province
CPX	Clinopyroxene
CSD	Crystal size distribution
CT	Computed tomography
EEVF	East Eifel Volcanic Field
ENSZD	Eifel North-South Zone Depression
GL	Glass
HBL	Hornblende
HEVF	Hocheifel Volcanic Field
LA-ICP-MS	Laser Ablation Inductively Coupled Plasma Mass Spectrometry
OL	Olivine
OP	Opaques
PC	Point count
PHL	Phlogopite
PL	Plagioclase
PNM	Pore Network Model
REE	Rare Earth Element
SD	Spatial distribution
SDF	Spatial distribution factor
WEVF	West Eifel Volcanic Field
WF	Westerwald Volcanic Field

Introduction

Chapter 1 presents an introduction to this thesis, providing an overview of the main themes that encompass and establish this research. Firstly, the main principles of textural analysis are described according to how igneous textures are classified, measured and then interpreted in the context of magmatic systems. Secondly, the concepts of primary, secondary and tertiary textures are outlined, with recognition of the difficulties associated with studying primary textures in fully solidified samples. From this, glass-bearing cognate xenoliths are introduced as semi-solidified products, with utility for examining the magmatic processes and crystal-melt geometries that are often obscured in solidified plutons. Hornblendite and clinopyroxenite xenoliths from the West Eifel Volcanic region of Germany constitute an example of these glass-bearing xenoliths and form the basis of this study. Finally, the aims and objectives of this research are presented alongside a thesis outline.

1 Introduction

The crystalline constituents of an igneous rock represent the cumulative product of the kinetic, mechanical and equilibration processes that sum to produce a solid rock from the progenitor magma (Higgins, 2006a). The enigmatic nature of magmatic systems means that these processes cannot be observed directly and it ensues that the detailed study of igneous rocks serves as the most astute means by which to study magmatic processes. These rocks provide a record of melt evolution: magmatic processes leave distinct textural and geochemical signatures that are preserved in the solid rock output. It is the decryption of these signatures that provides an insight into the petrogenetic evolution of an igneous product and permits the study of magmatic systems.

An igneous rock can be studied through its chemical and physical properties. The chemical properties of the rock manifest through the composition of the rock and its mineral phases, whilst the physical properties are expressed via the geometric arrangement of the solid (crystal), liquid (glass) and volatile (vesicle) phases of the rock. These physical properties are referred to as the texture of the rock, a term which encompasses a number of parameters including crystal shape, size (e.g. Cashman and Marsh, 1988; Marsh, 1988), alignment (e.g. Higgins, 1991; Meurer and Boudreau, 1998) and spatial distribution (Jerram et al., 1996). These parameters are a reflection of the solidification history of a magma, and provide a record of all of the processes that occurred during its formation (Higgins, 2011). Textural analysis aims to understand the relationship between these magmatic processes and their effects upon the three-dimensional configuration of the crystal populations within igneous rocks. Whilst compositional analyses are paramount in understanding the chemical evolution of a melt, textural studies provide an insight

into the physical processes that are fundamental in the fractionation and solidification of magmas. Such processes may only leave textural signatures (Higgins, 2011) and as such may be obscured with the application of geochemical techniques (Cashman and Blundy, 2013). Textural analyses are applicable across a broad array of igneous products including lava flows (Witter et al., 2016) and domes (Hammer et al., 2000), glass (Castro et al., 2002; Rust et al., 2003), scoria (Schaaf et al., 2005); ash particles (Taddeucci et al., 2004) and plutonic bodies ranging in composition from mafic (Holness et al., 2007a; Holness et al., 2007b; Holness et al., 2007c; Magee et al., 2010) to felsic (Ikeda et al., 2000; Weinberg et al., 2001; Johnson and Glazner, 2010; Higgins, 2017). With this wide applicability and the capacity to add quantitative constraints to otherwise enigmatic magmatic processes (Cashman and Marsh, 1988 Cashman, 1993; Higgins, 1996a), textural studies have continued to grow in potential and prevalence, particularly in instances where geochemical techniques cannot be used to reveal specific magmatic processes (e.g. Higgins, 2011). Textural studies therefore present the opportunity to complement and extend the geochemical and isotopic studies that currently dominate the petrology literature.

1.1 Studying igneous textures

The development of an igneous rock involves a combination of magmatic processes pertaining to crystal growth, solution, movement and deformation, which are recorded through changes in the rocks texture (Higgins, 2006a). In order to use textures as a tool to extract information about these processes, it is first important to establish the theories governing textural development and the methods by which to study textures observed in igneous rocks. Firstly, the processes that can act to generate igneous textures must be understood and classified in a framework

that defines their expected textural signatures. This provides a foundation from which to design a textural study, and has been well established through decades of petrological investigation (e.g. Higgins, 2006a). Secondly, these expected textures must be constrained by quantitative data. This requires a knowledge of the textural signatures left by specific magmatic processes, how these physically manifest in a crystal population, and which techniques are most appropriate for quantifying specific textural properties. Thirdly, the data must be analysed in a way that permits the textural development sequence to be established, within the context of the magmatic system. Whilst quantification aims to measure physical textural properties, the interpretation of this data aims to use the quantified textures as a way to constrain magmatic processes in an otherwise enigmatic product. These categories of classification, quantification and interpretation of igneous textures form the principles of textural analysis and together provide a broad framework through which to conduct a textural study.

1.1.1 Classification of igneous textures

Igneous textures may broadly be divided into three categories (Figure 1.1), encompassing the wide array of processes that can influence textural development. From the initial magma, undercooling drives kinetic processes that govern crystal nucleation and growth. These crystal populations may then be altered through mechanical processes. At the reduction of the kinetic driver, the crystals will begin to equilibrate to reduce the total energy of the system. These processes may occur sequentially, concurrently or intermittently until the magma reaches a closure temperature at which the final texture is 'frozen' in the solid rock output.

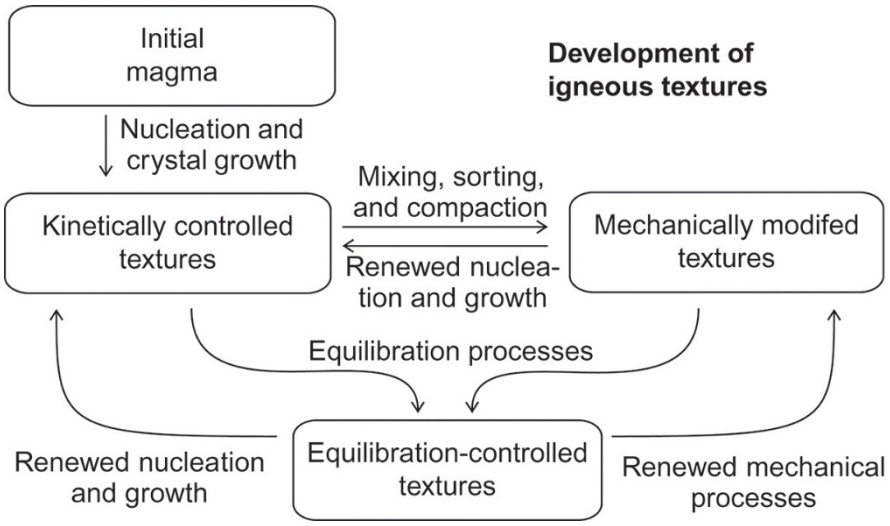

Figure 1.1 **–** Development of igneous textures. Kinetic, mechanical and equilibrium processes can occur and be renewed numerous times during crystallisation. From: Higgins, 2006a.

1.1.1.1 Kinetically controlled textures

Kinetic processes control the rate at which crystals will nucleate and grow, driven by the undercooling of the melt. For any mineral phase to crystallise from a melt, crystal nuclei must reach a critical threshold at which they are energetically stable (Swanson, 1977) and will continue to grow if it results in a reduction of energy from the system. Kinetic processes influence the development of texture as they govern the mobility and supply of materials to the crystal surface. This mobility, as measured by the diffusion coefficient, is strongly linked to the temperature of the system: higher temperatures dictate a more rapid diffusion rate and hence a faster rate of crystal growth. Crystal shape is then controlled by this growth rate and the mobility of the slowest crystal-forming material within the melt (Kirkpatrick, 1975). The number of crystal nuclei (nucleation density), growth rate and crystal shape of

each mineral phase are all important in governing the textures of the final rock; kinetic processes act to control how each of these factors will develop within a cooling magma.

1.1.1.2 Mechanically modified textures

After the generation and growth of a crystal population, mechanical processes can act to modify the kinetically induced textures. These processes may occur in a closed state (where there are no magmatic additions or magma removal from the system) or open state and reflect the dynamic nature of magmatic bodies. Mechanical processes, including compaction (e.g. Berger et al., 2017), crystal accumulation (e.g. Marsh, 1998) and magma mixing (Higgins, 1996b; Salisbury et al., 2008), act to influence the physical configuration of the crystal textures and modify grain morphologies. Any number of these processes may occur within a single melt, and often act to drive the renewal of kinetic processes (Maaløe, 2011). Mechanical textures are typically the simplest to isolate from a rock (Higgins, 2006a), though often act to obscure early kinetic textures.

1.1.1.3 Equilibrium textures

In any crystallising body of magma there exists a great disparity in the distribution of energy between the interior bonds of a crystal, the unsatisfied bonds at the crystal surface and the surrounding liquid (Higgins, 2011). Driven by the minimisation of interfacial energy, kinetic and mechanic textures will therefore evolve towards a state of equilibrium to result in a reduction in the total energy of the system (Higgins, 2011). Textural equilibrium occurs when the solid phase is in a state of chemical equilibrium with the liquid phase, meaning that the diffusion of energy between the fluid and solid phases favours the growth of crystals as opposed to the growth of the liquid filled pore spaces between them (Cheadle et

al., 2004). Whilst kinetic processes control the rate at which crystals nucleate and grow, and mechanical processes act to modify these kinetic textures, equilibration governs the final phase abundance and ultimately dictates the final rock texture (Higgins, 2006a).

The dynamic nature of magmatic systems means that igneous products represent a complex amalgamation of each of these types of textures. Unravelling the sequence of textural evolution is important for understanding the petrogenetic history of a rock, but is frequently complicated by the concurrence and renewal of magmatic processes. Textural analysis ultimately aims to produce quantitative links between these magmatic processes and rock textures, providing a structure for the petrogenetic interpretation of igneous rocks.

1.1.2 Quantification of igneous textures

The multiplicity of processes that can act to influence igneous textures therefore necessitates a quantitative framework by which to identify their occurrence and understand their effects upon the textures observed in a rock. Textures may be crudely studied through visual observations of crystal shape, size and contact relationships, however these qualitative observations cannot be used to constrain physical models of crystallisation and textural development (Merriam, 2004; Jerram and Higgins, 2007). Methods of quantitative textural analysis have therefore been developed for the purpose of identifying quantitative links between crystal textures and magmatic processes. This may be undertaken with either a two- or three-dimensional approach. Two-dimensional methods aim to quantify the textures sampled in thin section and mathematically extrapolate the data into 3D for the interpretation of the true rock texture (Cashman and Marsh, 1988; Higgins,

1998). This can be undertaken directly from the thin section, for example dihedral angles and grain boundary geometry can be measured with a universal stage (e.g. Kruhl and Peternell, 2002; Holness et al., 2005; Holness, 2006; Liebl et al., 2007). Most commonly, thin sections are digitised and measured with image analysis software. This data is then converted into a theoretical three-dimensional crystal population (Higgins, 1998). This incurs a number of limitations associated with the planar sectioning of a three-dimensional object (Figure 1.2), although statistical corrections are frequently applied to minimise the effects of these errors (Higgins, 2000). For example, When a crystal is cut to create a 2D section, the intersection plane rarely intersects the centre of each particle. This acts to distort the measured size of the crystal plane relative to the true intersection area of the 3D crystal. This effect, known as the cut section effect, results in a greater spread of measurements about the true modal size (Higgins, 2000). Additionally, the smallest crystals in a population are less likely to be cut along any line of intersection. This can act to exaggerate the abundance of larger crystals relative to small crystals. This is referred to as the intersection probability effect.

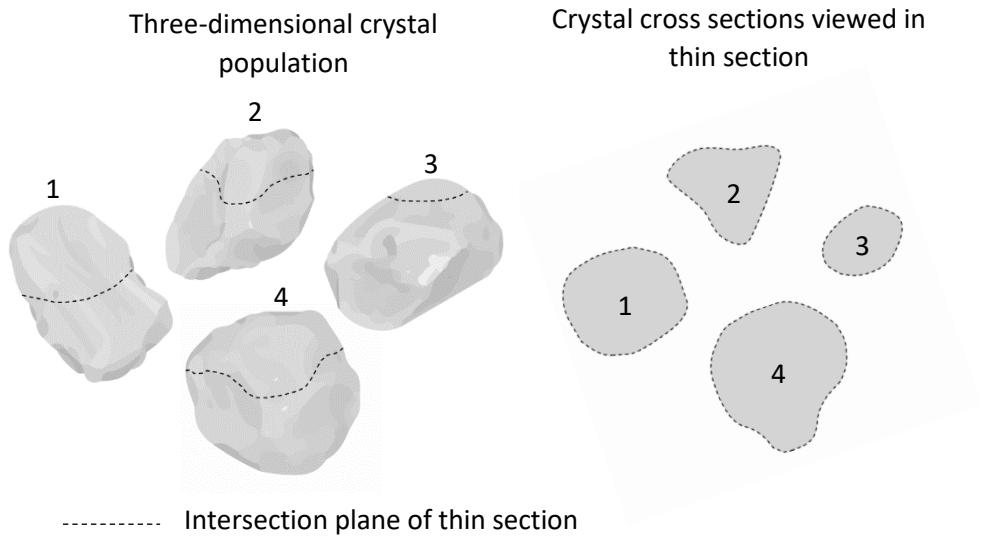

Figure 1.2 – Two-dimensional sectioning of a three-dimensional crystal population.

Three-dimensional techniques include serial sectioning (Bryon et al., 1995) or grinding (Mock and Jerram, 2005), tomography (e.g. Ketcham and Carlson, 2001) and, in instances where a crystal population is hosted in a transparent material, optical scanning (Castro et al., 2003). Rock textures are three-dimensional in nature and it is desirable that they are studied as such. However three-dimensional techniques are not appropriate for all rock types; selection of a two- or three-dimensional approach should be guided by the research aims, sample material and available resources.

Whether utilising a two- or three-dimensional approach, it is next important to quantify the rock textures with the application of quantitative textural techniques. Frequently used textural techniques include crystal size distribution (CSD) analysis (e.g. Higgins, 2000), spatial distribution factor (SDF) (e.g. Jerram et al., 1996) and alignment factor (AF) (e.g. Higgins, 1991). Less common techniques include the quantification of fractal geometry (Nkono et al., 2016), crystallographic preferred

orientation (Hasalova et al., 2011; Cheadle and Gee, 2017) and aggregation indices (Rudge et al., 2008). These techniques can be used to identify and constrain the kinetic, mechanical and equilibrium textures that are recorded in the rock.

1.1.2.1 An overview of Crystal Size Distribution Theory

Crystal size distribution analysis provides a measure of the distribution of crystal sizes within a defined crystal population, presented as a plot of crystal length against the natural logarithm of the population density (Marsh, 1988). This population density is related to the kinetic processes governing growth rate and nucleation, which are recorded by the X and Y axes of the CSD graph respectively. The time variation of nucleation and growth rates determine the CSD at any one point, hence CSDs can be used to constrain the kinetics of the crystallising magma with time. However, simple kinetic models for nucleation and growth are required to evaluate the relationship between igneous textures and CSD parameters.

CSD theory identifies two population models that represent the possible end member states for nucleation and growth regimes of magmatic systems. At one extreme, crystal nucleation and growth occur under an open-system steady-state regime, where there is a balance between the number of crystal that nucleate and grow within the magma and the loss or gain of crystals from the system (Marsh, 1988). Continuous crystallisation will result in a straight CSD if the nucleation and growth rates are constant (Figure 1.3 A). If the residence time remains constant but the nucleation density increases then the evolving CSDs will be parallel (Figure 1.3 B). If the nucleation density remains constant but the residence time increases, then the CSDs will rotate about a point on the Y-axis (Figure 1.3 C). This simplicity is not entirely representative of magmatic systems, and comagmatic CSDs

frequently deviate from log-linear, representing renewed nucleation events (Higgins, 2006a).

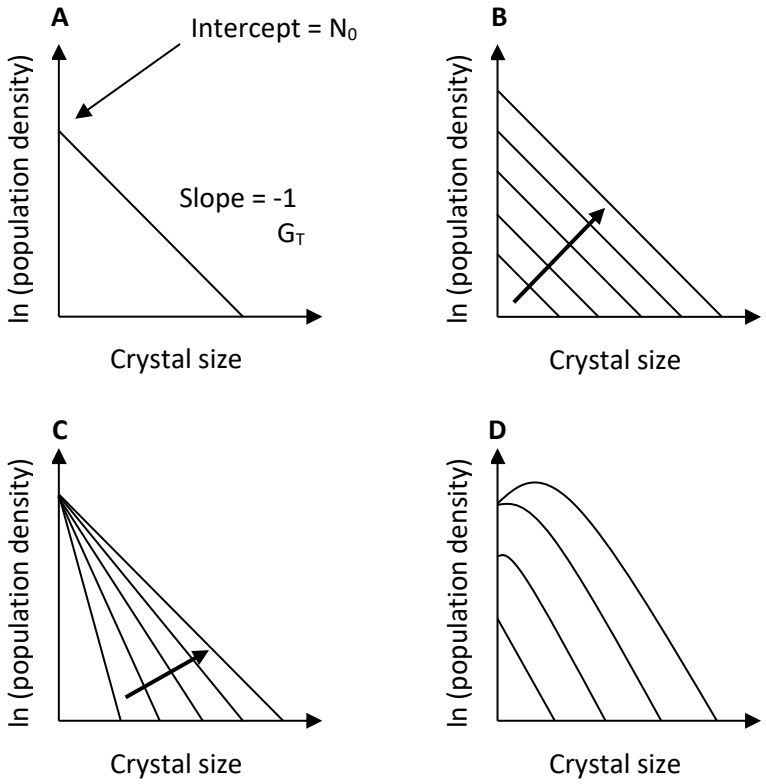

Figure 1.3 – Theoretical models of crystal size distribution in natural systems. **A)** Theoretical CSD for a steady-state open volcanic system, demonstrating kinetic parameters that can be derived from the CSD. **B)** If the residence time remains constant but the nucleation density increases then the evolving CSDs will be parallel. **C)** If the nucleation density remains constant but the residence time increases, then the CSDs will rotate about a point on the Y-axis. **D)** Theoretical CSD for a closed-system batch crystallisation model.

The other end member is a closed-system batch crystallisation model, where there is no input or output of crystals and the volume of available melt decreases with time. Straight CSDs are produced by exponentially increasing nucleation rate but maintaining a constant growth rate. This linearity is perturbed at crystal contents exceeding 50%, above which the decreased availability of melt causes the left hand side of the CSD to curve downwards (Figure 1.3 D). Comagmatic CSDs should be

parallel, but may form a fan at the right hand side of the CSD (e.g. Cashman and Marsh, 1988).

These population models form the basis of CSD theory, but represent the idealistic end members. As such, real world CSDs rarely conform to these models. Marsh (1998) examined a range of CSDs from a variety of igneous settings, concluding that none of them showed CSDs that were consistent with a true batch or open-system model. From this, they concluded that any CSD will express aspects of both the open-system and batch crystallisation models.

In the batch crystallisation model it is unclear whether the residence time is significant for the evolution of the CSD. For this reason, authors commonly cite the steady-state model when interpreting natural CSDs; the slope of the CSD can be used to derive the growth rate and residence time, even if the system is far from the continuous steady-state regime idealised by the log-linear population model. For this straight CSD, crystallised under continuous conditions, the slope can be expressed by:

$$slope = \frac{-1}{G\tau} \quad (2)$$

where G is growth rate and τ is residence time. The intercept is the nucleation density, expressed by:

$$intercept = \frac{J}{G} \quad (3)$$

where J is the nucleation rate. The slope and intercept of the CSD are ultimately controlled by the kinetic driver, which in turn is governed by variations in temperature and pressure. For example, decreasing the temperature will increase the nucleation density and cause the CSD to shift upwards without any effect upon

the slope. Increasing the growth rate will cause a change in the CSD slope, but will not affect the nucleation density (Marsh, 1998).

As crystallisation progresses, mechanical and equilibrium processes will modify the crystal textures from those established by kinetic processes. Many authors adopt the proposition of Marsh (1998) that unmodified kinetic textures produce straight, log-linear CSDs (e.g. O'Driscoll et al., 2007), which evolve into curved, kinked, humped or discontinuous CSDs in response to mechanical and equilibrium magmatic processes. Curved CSDs may arise from a number of magmatic processes including crystal accumulation (e.g. Neal et al., 2015; Fiedrich et al., 2017), compaction (e.g. Zieg and Marsh, 2012; Manoochehri and Scmidt, 2014), textural coarsening (e.g. Higgins, 1999; Higgins and Roberge, 2003) and mixing of crystal populations (e.g. Higgins and Roberge, 2007; Svetov et al., 2020; Lino and Vlach, 2021) (Figure 1.4).

The final CSD output records the summation of kinetic, mechanical and equilibrium magmatic processes that have occurred during the petrogenetic evolution of the igneous product. CSD analysis therefore aims to identify what these magmatic processes were from the distribution of crystal sizes measured in the rock. The wealth of information that can be derived from CSDs has established the technique as a highly valuable methodology for the interpretation of igneous textures, with a wide applicability including the study of deep Earth products (e.g. Armienti and Tarquini, 2002), crustal magma stores (e.g. Castro et al., 2013), magma transport (e.g. Del Gaudio et al., 2010), eruption triggers (e.g. Hammer et al., 1999; Ruprecht et al., 2012) and dynamics (e.g. Taddeucci et al., 2004), lava flows (e.g. Crisp et al., 1994) and even beyond Earth to Lunar and Martian products (e.g. Taylor et al., 2002; Day and Taylor, 2007; Filiberto et al., 2018).

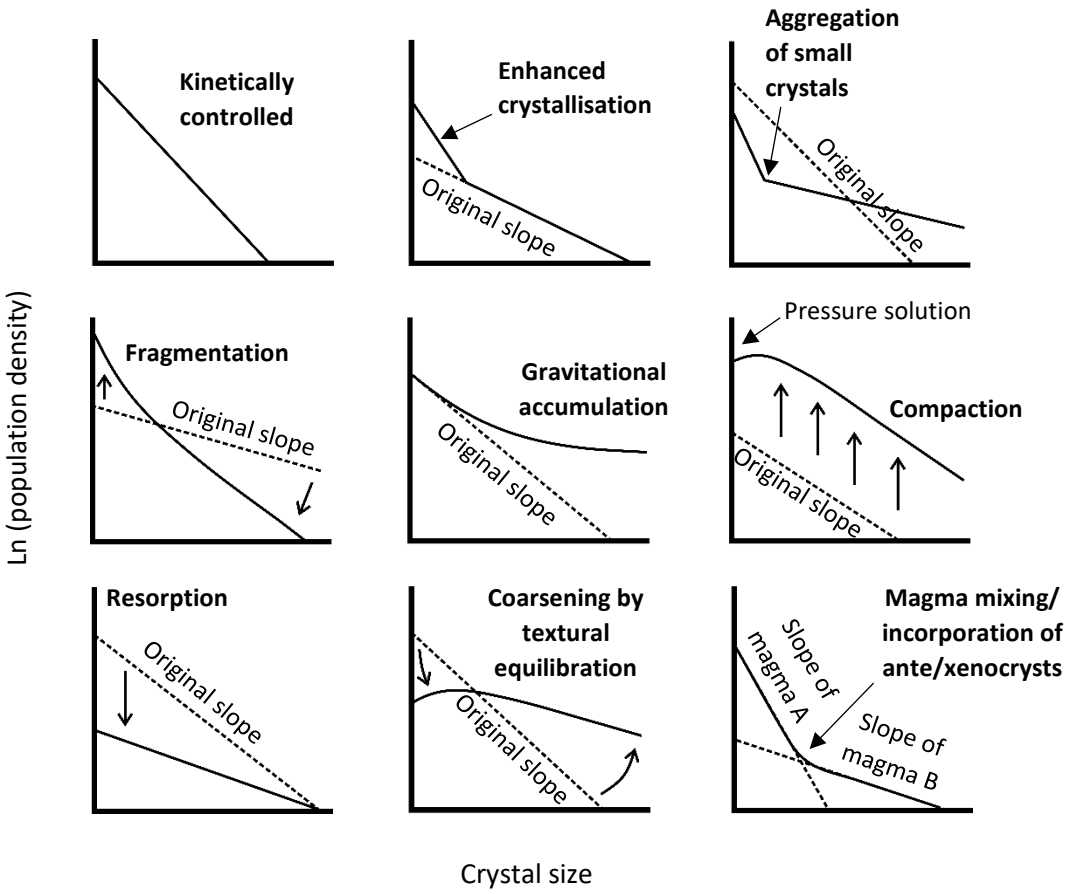

Figure 1.4 – Theoretical crystal size distribution plots, visualising how kinetic, mechanical and equilibrium processes manifest on a CSD. Dashed lines represent the original CSD, formed by kinetic processes. Solid lines represent the final CSD produced by a specific process. Redrawn and modified from van der Zwan et al. 2013, summarising information from Higgins, 2006a.

Crystal size distribution is the most commonly used technique for textural quantification of igneous rocks (Rannou and Caroff, 2010), but other textural parameters can also provide significant insight into magmatic processes. For example, crystal preferred orientation can be used to interpret cumulate processes including compaction (e.g. Garibaldi et al., 2018; Holness et al., 2020) and deformation (e.g. Friedrich et al., 2017) of a crystal mush, as well as magma chamber convection (Holness et al., 2020). The spatial distribution of crystals can

be used to interpret kinetic processes including crystal nucleation (Jerram et al., 2003), mechanical processes such as crystal accumulation, compaction (Jerram et al., 2003), flow and shear (Mock et al., 2003) and equilibrium processes that govern phase relationships (e.g. Saltzer et al., 2001). The application of these quantitative techniques, whether alone or in conjunction with one another provides an opportunity to gain significant insight into the multitude of magmatic processes that are recorded in igneous materials. Although geochemical studies dominate the literature, quantitative textural techniques have broadened the petrological tools needed to study magmatic products and systems.

1.1.3 Interpretation of igneous textures

An igneous rock represents a complex history of any number and sequence of magmatic processes, recorded in the texture. Quantitative techniques provide the tools needed to measure these textures; it is next important to consider how they can be used to aid with the interpretation of an igneous rock or system. That is, how to identify the occurrence of kinetic, mechanical and equilibrium processes in the rock textures and interpret their influence upon the petrogenetic evolution of the rock in question. This can be achieved through two approaches (Figure 1.5). The forward approach utilises an experimental approach; by defining an initial melt composition and stimulating crystallisation, it is possible to observe crystal growth within a laboratory setting. The growth of these experimental crystals may either be observed in-situ (Ni et al., 2014) or by quenching the melt at desired intervals (Donaldson, 1976). This provides a framework through which crystal textures can be related to experimental variables including composition, temperature, pressure and cooling rate (e.g. Welsch et al., 2013). By altering these variables, it is possible

to synthesise different igneous settings and processes including volcanic degassing (Hammer and Rutherford, 2002) and crystallisation at different depth intervals (e.g. Di Carlo et al., 2010).

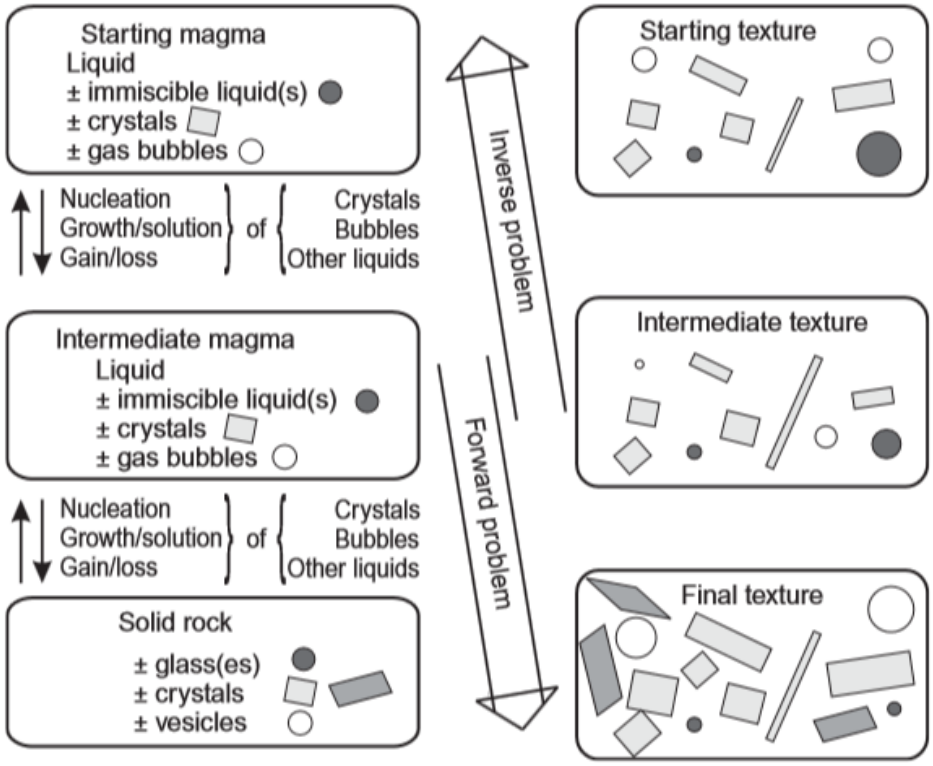

Figure 1.5 – Analysis of igneous textures using the inverse and forward approaches. The inverse problem is studied through detailed analyses of rock samples whilst the forward problem is investigated with experiments and modelling. From: Higgins, 2011.

This forward approach has been successful in determining crystallisation sequences (Diaz-Alvarado, 2017), phase relations (Scaillet and MacDonald, 2001), melt relations (Yaxley, 2000) and reaction sequences (Mitchell and Grove, 2016). However, it is difficult to directly relate these experimentally derived crystal populations to those observed in specific igneous samples (Higgins, 2011). As such this approach is typically used to improve understanding of crystallisation variables

that form the broader principles of magmatic evolution and petrogenetic interpretation (e.g. Ridolfi et al., 2010; Mollo et al., 2011; Welsch et al., 2013), thereby providing a framework for the interpretation of igneous samples.

Alternatively, and most commonly, the inverse approach is used to study the pre-existent textures that are contained in igneous rocks. These rocks represent the direct output of a magmatic system, and are the sum of all of the processes that occurred during its formation. In this approach, the textural data is used to aid the backwards interpretation of the textural development history recorded in the rock. However, the final texture captured in the rock may not preserve a record of all of the magmatic processes that have occurred during its solidification. The inverse approach therefore entails a degree of ambiguity regarding the extent to which the final rock texture provides a full or partial record of textural evolution. This is a persistent challenge in the interpretation of igneous rocks, and is particularly pervasive in the interpretation of slowly cooled plutonic bodies. Plutons represent the fully solidified end product of magma chamber evolution and whilst they yield an invaluable record of magma transport, storage and fractionation in the crust, they are frequently subjected to textural overprinting by secondary or even tertiary magmatic processes (e.g. McBirney, 2009). A full understanding of the solidification of plutonic bodies necessitates a complete picture of textural evolution and therefore requires that primary igneous textures are, to some extent, preserved in the final rock texture. In order to examine primary textures it is therefore important to be able to discriminate between primary, secondary and in some instances tertiary textures in igneous samples.

1.2 What is a primary igneous texture?

With the multiplicity of magmatic processes that can occur during crystallisation and textural development of an igneous product, it is important to clarify what is meant by a primary and secondary texture. A primary texture is one that forms as a result of crystal and melt interactions, driven by the kinetic processes discussed in Section 1.1.1.1. These textures occur as a function of nucleation density and crystal growth, driven by undercooling of the system (defined as the difference between the equilibrium liquidus temperature and ambient temperature). A secondary texture must then be defined as one which represents a modification of these primary textures, driven by non-kinetic processes. However, it is difficult to establish the point at which evolving primary textures can no longer be considered as representative of the kinetics of the system. Holness et al. (2018) visualise this problem as a spectrum between two end-member states. At one end of the spectrum lie crystal textures formed entirely by crystal nucleation and growth: primary igneous textures. Here the crystals assume growth-controlled shapes, commonly with planar faces, that will form an impingement texture during solidification (Elliott et al., 1997; Holness et al., 2005). At the other end are crystal textures controlled entirely by the minimisation of internal energies as the system evolves towards a state of equilibrium. The true end member at this end of the spectrum represents perfect equilibrium, which can be approached but never attained (Higgins, 2011). Textural equilibration acts to modify primary textures in either the solidus or the sub-solidus regime through diffusive mass transport during static recrystallization (e.g. Holness et al., 2018). This is exhibited in dihedral angle adjustment firstly at solid-solid-melt junctions (Holness et al., 2005) then at three-grain junctions (Holness et al., 2007a; Holness, 2010) towards a uniform mean angle

of 30° or 120° respectively (Holness, 2010). This adjustment develops an interface curvature that will also propagate from three-grain junctions until a constant mean curvature is reached (Holness and Siklos, 2000). Finally, crystal sizes will be altered through the solution of small crystals and growth of larger crystals through the process of textural coarsening (Higgins, 2011). Though it is likely that this process is only important for grains smaller than 10 microns in size (Cabane et al., 2001; 2005), the resultant effects upon grain shape act to further modify the crystal textures: dissolving grains tend to be more rounded, whilst the growing grains tend to be facetted (Holness et al., 2018). As a solidifying magma approaches this end of the spectrum it is clear that the crystal textures no longer represent the nucleation densities and growth rates governed by kinetic processes, and instead provide a record of recrystallisation and sub-solidus readjustment (Figure 1.6).

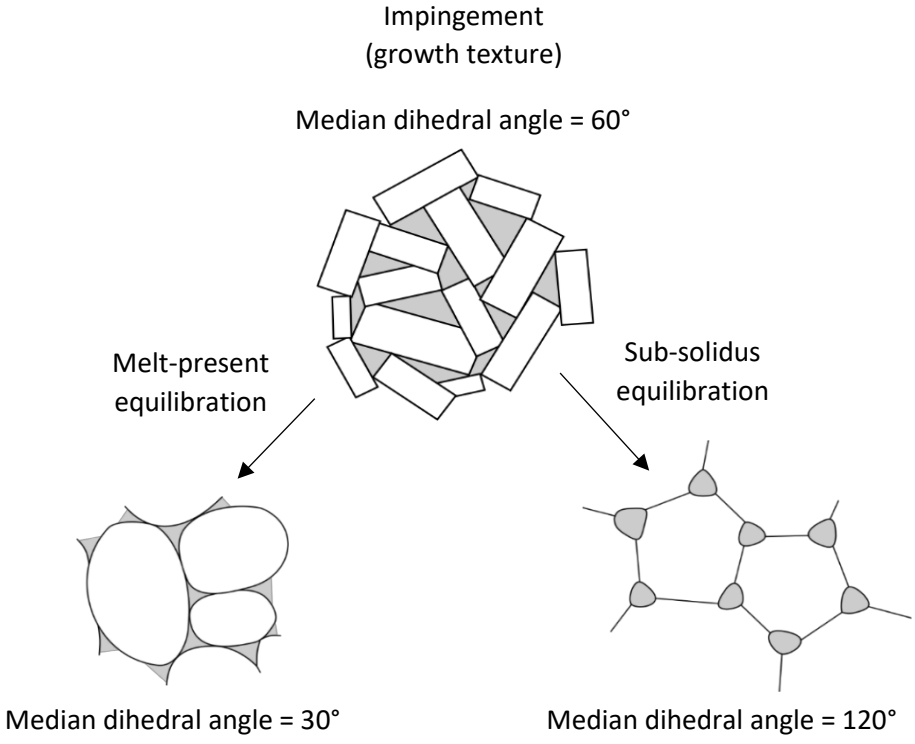

Figure 1.6 – Evolution of growth controlled textures towards melt-present and solid-state equilibrium textures, demonstrating how equilibrium may significantly modify the original kinetic texture. From: Holness et al., 2005.

In addition, at any point upon this spectrum, mechanical magmatic processes such as accumulation and compaction may occur to drive recrystallisation and obscure the primary kinetic textures (e.g. Meurer and Boudreau, 1998; Boorman et al., 2004) or indeed secondary equilibrium textures (e.g. Hier-Majumder and Kohlstedt, 2006). These processes are significant in the solidification of gabbroic (e.g. Irvine, 1980; Tegner et al., 2009; McKenzie, 2011; Schmidt et al., 2012) and granitic bodies (e.g. Pupier et al., 2008; Bea, 2010; Brown, 2013; Kruger and Kisters, 2016; Zhao et al., 2018) and impart their own textural signatures atop the primary kinetic textures (e.g. Gray et al., 2003; VanTongeren et al., 2015; Holness et al., 2017a). After solidification of a pluton, tertiary textures can be generated through regional deformation events (Burton-Johnson et al., 2019; Petford et al., 2020) or erosion by younger magmatic injections (Paterson et al., 2016; Pebane and Latypov, 2017; Loureiro et al., 2021), and can further obscure primary igneous textures, but are often identifiable as tertiary textures.

Distinction between a primary and secondary crystal texture is therefore a question of where on this spectrum does a primary texture no longer provide a significant record of nucleation and growth to allow interpretation of the kinetic crystallisation history? Igneous rocks contain the information needed to answer this question, but require a detailed knowledge about where they themselves fall on this spectrum. This necessitates a thorough understanding of how crystal textures evolve from a kinetic to equilibrium driven regime. The theoretical evolution of crystal textures in crystallising magmas is not unknown; experimental correlations to natural rock textures provide a framework of the contrast between textures formed through crystal growth and those formed through equilibrium processes (e.g. Brandeis et al., 1984; Solomatov and Stevenson, 1993; Cabane et al., 2001; 2005; Hersum and Marsh, 2006; Simakin and Bindeman, 2008). What is uncertain however, is the

degree to which a primary crystal texture can evolve towards a secondary texture before the rock no longer has the capacity to derive information pertaining to its early crystallisation history. Holness et al. (2007a) suggest that this can be quantified by a rock's 'textural maturity', whereby the value of the median dihedral angle can be used to measure the degree to which the rock has evolved towards textural equilibrium. Impingement textures formed by crystal growth express median dihedral angles of ~60° (±25°) and evolve towards ~120° (± 15°) as they approach equilibrium. Stratigraphic step-like changes of the median dihedral angle measured in the Skaergaard layered intrusion, Greenland, are suggested to provide a record of changes in the sub-solidus thermal history (Holness et al., 2005). Because changes in the dihedral angle involve mass migration by diffusion, Holness et al. (2005) therefore suggest that median dihedral angles provide a temporal indication of sub-solidus readjustment that can be used to constrain the textural maturity of a sample. However, McBirney et al. (2009) argue that this approach ignores the impacts of sub-solidus processes that occur independently from equilibrium processes (e.g. metasomatic alteration from hydrothermal fluids – McBirney and Creaser (2003)) that are conspicuous in field observations and therefore does not take into account the full complexity of the magmatic system. Dihedral angles may be a useful tool for indicating whether a rock has progressed towards equilibrium, but caution must be taken to consider how they themselves might have been altered (McBirney et al., 2009). This may help with the problem of placing a rock on the textural spectrum between primary and secondary, but does little to resolve the issue of reconstructing the primary textures that have been overprinted and obscured.

These issues are particularly problematic in the interpretation of plutonic rocks, which is frequently complicated by a debate over the extent to which the crystal

textures can be used to interpret early crystallisation dynamics, and whether a solidified pluton actually preserves any primary textures at all (McBirney, 2009; Glazner and Boudreau, 2011; Bartley, 2018; Dick et al., 2019). This latter point has led several authors to conclude that the extensive cooling history of plutonic magmas means that most plutonic rocks have undergone extensive recrystallisation and therefore no longer preserve their original primary textures (McBirney, 2009). Solidification timescales for plutonic bodies have been estimated in some examples to span several million years (Coleman et al., 2004; Matzel et al., 2006), though are more commonly estimated as several hundreds of thousands of years (Cawthorn and Walraven, 1998; Larsen and Tegner, 2006). Thermal modelling of these timescales suggests that a solidifying magma can maintain temperatures corresponding to amphibolite and greenschist metamorphic facies for protracted periods of time (McBirney, 2009; Zibra et al., 2014; Bartley et al., 2020), overprinting the primary magmatic textures through extensive recrystallisation. Textural observations in plutonic rocks that are akin to those in metamorphic rocks have led several authors to conclude that plutonic rocks are essentially metamorphic (Higgins, 1991; McBirney and Hunter, 1995; McBirney, 2009; Glazner and Boudreau, 2011) and that their crystal textures should be considered as such. Though other authors refute this suggestion (Holness et al., 2018), equilibrium textures are a common feature of mafic and felsic plutons, indicating that these rocks have, to some degree, undergone sub-solidus recrystallisation and textural modification. Whilst the wealth of information contained within plutonic rocks is invaluable for petrologists aiming to understand magmatic processes, careful consideration must therefore be taken over the extent to which the textures observed in the solidified output likely exhibit the full record of textural evolution.

This necessitates a thorough scrutiny of crystal textures, and should be undertaken on a case-by-case basis (Holness et al., 2018).

1.3 Studying plutonic textures

Despite the prevalence of secondary textural overprinting in plutonic rocks, it is important to analyse them as they provide a window into crustal magmatic processes, most significantly those that govern the formation of large volumes of eruptible melt. Because the sub-volcanic realm cannot be accessed directly, and magmatic processes cannot be observed in-situ, plutonic rocks provide the most direct method to investigate the sub-magmatic environment. However, this reliance on working with fully solidified end-products means that at present there are several knowledge gaps that remain in the study of plutonic rocks. Central to these uncertainties is the question of how melt is transported, stored and accumulated within magmatic systems, summarised by the so called 'crystal mush paradigm' (Cashman et al., 2017).

1.3.1 The crystal mush paradigm

One of the most fundamental questions in the field of volcanology relates to how melt is stored within magmatic systems, and how it is accumulated prior to eruption (e.g. Bachmann and Bergantz, 2004; 2008). In recent decades, the traditional view of magma being stored in a liquid-rich, sub-volcanic chamber has evolved towards a model of crustal magma reservoirs existing as vertically extensive mush columns (Marsh, 2004; Christopher et al., 2015; Cashman et al., 2017; Jackson et al., 2018; Sparks et al., 2019). A crystal mush is defined as a system of crystals and melt, where the crystals form a touching framework within which the melt is distributed (Cashman et al., 2017). A crystal mush may consist of smaller bodies of relatively

short-lived crystal-poor magma, but otherwise are considered to be liquid-poor, at or above the solidus (Cashman et al., 2017). This contrasts to the traditional magma chamber model, where crystallisation occurs at the margins of a crystal-poor magma reservoir via progressive inwards solidification at the chamber floor, walls and roof.

Geophysical imaging and thermal modelling provide evidence in support of the mush model, because there is no evidence that large volumes of melt exist in the crust today (e.g. Jaxybulatov et al., 2014; Ward et al., 2014; Comeau et al., 2015). However, textural and geochemical evidence provided in exposed layered intrusions such as Skaergaard, Bushveld and Rum reveal magmatic processes that necessitate a large volume of crystal-poor liquid (e.g. crystal accumulation, sorting and convection) (Irvine et al., 1998; Scoates et al., 2010). This textural evidence indicates that large magma chambers have existed at other times in geological history, juxtaposing the present day observations that support crystallisation in a more static mushy environment (e.g. Meurer and Boudreau, 1998; O'Drsicoll et al., 2007; O'Driscoll et al., 2008a). If crystal textures observed in plutonic rocks indicate a liquid-dominated regime, how then does this fit into the mush dominated model and why are these liquid-rich magma chambers so difficult to find in modern times?

There is an emerging consensus that the crystal mush model better explains the geophysical, geochemical, petrological and volcanic inconsistencies that arise from the classic magma chamber model. However, the main criticism of the crystal mush model is the uncertainty of how crystal-poor melt could be rapidly extracted from a crystal mush prior to eruption (e.g. Bachmann and Bergantz, 2004). Compaction is often considered to be the dominant mechanism for driving melt migration through mush systems (e.g. Germa et al., 2020; Carbotte et al., 2020; Ferrando et

al., 2021). However, this model is challenged by a widespread absence of textural evidence for compaction driven deformation in adcumulates that contain only minor fractions (<5%) of interstitial melt (e.g. Holness et al., 2017a). An alternative model cites reactive melt flow as a significant mechanism for controlling the migration and accumulation of melts within a mush (e.g. Solano et al., 2014; Hu and Jackson, 2020). Constraining the relative importance of these mechanisms is made particularly challenging because the geometry of melt distribution within crystal mushes is poorly understood (e.g. Cashman et al., 2017).

1.3.1.1 How can we study melt geometries in crystal mushes?

Because crystal mushes cannot be studied in-situ, the melt geometries of crystal mushes are commonly studied through computational modelling (e.g. Cheadle et al., 2004) or experimentally (e.g. Wark et al., 2003). These methods typically approach the problem in reverse by investigating how the pore spaces develop during melting, which may not produce the same textures developed during crystallisation (e.g. Holness et al., 2007d).Exposed plutonic rocks represent the final product of crystallisation, but represent a texturally evolved end member product of a solidified crystal mush. Crystal mush dynamics are governed by the relationship and interaction between the liquidus and solidus phases, however the prevalence of equilibrium driven textures in plutonic rocks suggests that their textures predominantly yield a record of sub-solidus textural evolution and therefore do not adequately represent an active crystal mush system. However, although crystal mushes are not eruptible in their entirety (Marsh, 1981), they may be sampled by ascending lavas and extruded at the surface (e.g. Holness et al., 2019). Fragments of crystalline material are commonly found in eruptive products, derived from depth within the volcanic plumbing system (e.g. Tait et al., 1989; Turbeville, 1992a;

Mattioli et al., 2003; Bachmann, 2010; Stock et al., 2012). These fragments are referred to in the literature by a number of names including crystalline enclaves (e.g. Holness et al., 2019), cognate nodules (Holness and Bunbury, 2006) and cognate xenoliths (Saadat et al., 2014). From herein they will be referred to as cognate xenoliths. These cognate xenoliths are particularly significant as they often yield significant quantities of glass (up to 45% (Holness and Bunbury, 2006)), indicating that they were only partially solidified upon entrainment (e.g. Leblanc et al., 1982). Such xenoliths have been found in erupted products from a range of volcanic settings including volcanic arcs (Martin et al., 2006a; Holness et al., 2007d), hot spots (Holness et al., 2019) and continental rift zones (Becker, 1977; Leblanc et al., 1982; Downes et al., 2004; Holness and Bunbury, 2006). These samples provide a unique opportunity to constrain the spatial and textural relationship between the crystal and melt phases prior to solidification and significant sub-solidus textural readjustment. Understanding this physical relationship between crystals and melt, including melt geometry and transport, is a critical area of ongoing research because it provides an important control on the volume and mobility of the eruptible melt fraction. This in turn is significant for understanding the so-called 'plutonic-volcanic connection' and the link between melt stored in the magmatic system and its eruptive potential.

1.3.2 Cognate xenoliths in the Eifel

Examples of cognate xenoliths in the literature are dominated by those that bare mineralogies which correspond to the dominant mineral assemblages commonly observed in mafic-ultramafic layered intrusions (plagioclase+olivine+ clinopyroxene) (e.g. Mattioli et al., 2003; Holness et al., 2007d; Klebesz et al., 2012; Holness et al., 2019). As such, crystal textures in these xenoliths are frequently

interpreted using the knowledge of textures associated with specific crystals in these intrusions, most frequently plagioclase and olivine (e.g. Holness et al., 2019). However, cognate xenoliths that are devoid of these common minerals are also recorded in the literature (e.g. Turbeville, 1992a; Holness and Bunbury, 2006). In particular, hornblende and clinopyroxene rich mafic xenoliths that are entrained by alkaline magmas tend to lack plagioclase, olivine and orthopyroxene. These xenoliths, termed hornblendites and clinopyroxenites, are nearly completely composed of amphibole and clinopyroxene (± phlogopite) and contain abundant interstitial glass (Downes et al., 2004). Examples of such samples have been identified in Israel (Mittlefehldt, 1984), Turkey (Holness and Bunbury, 2006), the United States of America (Best, 1975; Francis, 1976) and Germany (Becker, 1977; Downes et al., 2004). One thing that these locations have in common is that they have been associated with periods of continental extension and rifting (Richardson-Bunbury, 1996; Nelson and Tingey, 1997; Shaw et al., 2003; Chang et al., 2009; Tang et al., 2016). It is particularly challenging to study the relationship between magma plumbing systems and erupted products in rift zones (Holness and Bunbury, 2006), however cognate xenoliths provide direct access into these magmatic systems. Hornblendite and clinopyroxenite xenoliths from the West Eifel Volcanic region of Germany are of particular interest as previous geochemical work indicates that they were rapidly quenched upon entrainment and therefore preserve the chemical signatures of their crystallisation at depth (Downes et al., 2004). This is supported by qualitative observations of crystal textures which Downes et al. (2004) use as evidence that the glass represents trapped interstitial melt rather than being formed from melting of the minerals. Downes et al. (2004) primarily used these samples as a 'natural experimental charge' to study mineral/melt distribution coefficients in an alkaline magma. These results confirmed distribution coefficients

derived from experimental studies (LaTourette et al., 1995; Chazot et al., 1996; Vannucci et al., 1998), demonstrating the xenoliths usefulness as a record of magmatic processes. Becker (1977) conducted a geochemical investigation of similar hornblendite and clinopyroxenite xenoliths from the West Eifel and concluded that they represent comagmatic products of the alkali basalts in which they are entrained. From their geochemistry, both Becker (1977) and Downes et al. (2004) interpret the xenoliths to represent semi-solidified mush samples captured from depth within the sub-volcanic plumbing system. However, neither of these studies aimed to constrain specifically where in the plumbing system they were derived from nor to investigate the magmatic processes influencing crystallisation in that environment. Specifically, there have not been any detailed textural studies undertaken on these samples and as such their true potential has not yet been fully exploited. Indeed Downes et al. (2004) acknowledge the wide possibility of uses for these samples and recognise that the information recorded within them is of 'widespread significance'. This project therefore aims to conduct a thorough investigation of crystal and melt textures recorded in hornblendite and clinopyroxenite xenoliths entrained in alkali basalts from the West Eifel volcanic region of Germany. This is particularly significant as the mineralogy of these xenoliths differs to that of the plagioclase and olivine rich samples that dominate the literature and will therefore contribute toward broadening the understanding of crystal and melt dynamics in magmatic systems.

1.4 Aims and objectives

This thesis aims to conduct a quantitative textural investigation into the magmatic processes governing the petrogenesis of glass-bearing hornblendite and clinopyroxenite cognate xenoliths entrained in alkali basalts from the West Eifel Volcanic Field, Germany. Using a combination of two- and three-dimensional techniques, with supplementary geochemical analysis, this thesis aims to constrain textural signatures of magmatic processes significant for their petrogenesis, to visualise the melt geometries and to contribute towards the current understanding of the physical relationship between melt and crystals in sub-volcanic systems. This is significant for furthering our knowledge of the conditions that govern the eruptability of melt in different volcanic environments, with specific focus on a recently active intraplate volcanic setting.

This can be summarised by four research questions, which are answered by the following objectives:

1. **To what extent can the textures recorded in the xenoliths be considered representative of an in-situ crystal mush?**
    - Use qualitative thin section observations, including grain boundary morphology, crystal shape and glass distribution to examine whether processes related to entrainment and eruption of the xenoliths have modified the glass and crystal textures.

2. **What is the textural petrogenesis of the xenoliths?**
    - Utilise a combination of two-dimensional textural techniques including crystal size distribution (CSD), spatial distribution pattern (SDP) and shape preferred orientation (SPO) to quantify

the textures of essential mineral phases (clinopyroxene and hornblende ± phlogopite) within the xenoliths.

- Undertake supplementary geochemical analysis using Laser Ablation Inductively Coupled Plasma Mass Spectrometry (LA-ICP-MS) to analyse major and trace elements of clinopyroxene, hornblende, phlogopite and glass in situ from thin section.
- Analyse the quantitative textural data (with consideration to the geochemical data) to generate a petrogenetic model for the xenolith samples, identifying textural signatures for kinetic, mechanical and equilibrium magmatic process.
- From the petrogenetic model, consider whether the xenoliths provide a record of primary, secondary or tertiary magmatic textures.

3. **What do the crystal textures reveal about the magmatic environment in which they formed?**

   - Use the petrogenetic model to constrain the dynamics of the magmatic environment from where the xenoliths originated, with consideration to the wider magmatic regime of the West Eifel that is documented within the literature.

4. **What is the physical relationship between the crystal and melt phases within these samples?**

   - Undertake three-dimensional X-ray computed tomography (CT) scanning of the xenolith samples, with focus on the discrimination

and segmentation of the porosity fraction (glass + vesicles) from the crystal phases (all crystalline material).

- Quantify the porosity fraction by calculating the proportions of connected and disconnected porosity, and constructing pore network models to measure pore and throat geometries and connectivity.
- Visualise the geometry of the pore spaces in three-dimensions, rendered according to the distribution of connected and disconnected porosity.
- With consideration to the textural model of crystal petrogenesis, use the quantitative data and qualitative 3D data to examine the spatial geometry and connectivity of the pore spaces in relation to the crystal textures.
- From this, examine how the results of the 2D textural data and 3D melt visualisations could influence the mobility and transport of eruptible melt through the sub-volcanic system.

1.5 Thesis outline

These research aims are answered across nine chapters, a synopsis of which are provided below:

- **Chapter 2: Geological setting and literature review**

  An overview of the geological setting of the West Eifel region with focus on the magmatic and volcanic regime. A review of previous studies conducted on similar hornblendite and clinopyroxenite xenoliths, outlining the wider context of this research.

- **Chapter 3: Methodology**

  A summary of the methods used to investigate the research aims, grouped according to image acquisition technique. Two-dimensional techniques use digitised thin sections and digital image analysis to quantify crystal textures; three-dimensional X-ray computed tomography analyses the porosity fraction. LA-ICP-MS provides supplementary geochemical data.

- **Chapter 4: Optical petrography and mineralogy**

  Presentation of results from qualitative thin section observations, with additional geochemical data.

- **Chapter 5: Two-dimensional quantitative textural analysis**

  Results of the two-dimensional quantitative measurements of crystal textures including crystal size distribution, spatial distribution pattern and shape preferred orientation.

- **Chapter 6: Three-dimensional X-ray computed tomography**

  Results of the three-dimensional X-ray computed tomography analysis, focusing on the visualisation and quantification of pore spaces.

- **Chapter 7: Discussion and critical evaluation**

  Discussion of all of the results presented in chapters 4-6, structured according to each of the research aims, alongside a critical evaluation of results and methods.

- **Chapter 8: Points for future work**

  Based upon the discussion in Chapter 7, ideas for future work that could compliment or enhance the findings of this study.

- **Chapter 9: Conclusions**

  A summary of the key findings that answer each of the research aims.

Geological setting and literature review

This chapter describes the geological context of the Eifel Volcanic region, with focus on the Quaternary volcanism of the East and West Eifel Volcanic Fields. The regional tectonic setting is first outlined, followed by a description of the physical characteristics of the volcanic fields and eruptive products. Hypotheses for magma genesis in this region include hot spot activity and lithospheric extension; evidence that supports and challenges these theories is presented here to provide a broader context to the aims and discussions presented in this thesis. Lastly, a review of previous studies on texturally and compositionally similar cognate xenoliths in the West Eifel, and similar glass-bearing xenoliths from other volcanic locations, establishes the wider significance of this project and the value of these xenoliths.

2 Geological setting and literature review

2.1 Regional geology of the Eifel volcanic fields

The Eifel volcanic fields in western Germany represent the volcanic manifestation of intra-plate magmatism, temporally and spatially correlated to extensive rifting and lithospheric thinning during the late Alpine orogeny (Wilson and Downes, 1991; Zeyen et al., 1997; Regenauer-Lieb, 1998). Part of the Rhenish Massif, the Eifel volcanic zone is the most recent area of active volcanism at the westernmost tip of a 350 km intraplate volcanic belt that trends parallel to the Alpine collision belt in the northwestern area of the Central European Volcanic Province (CEVP) (Regenauer-Lieb, 1998) (Figure 2.1). Volcanism in the Rhenish Massif is largely confined to the northern Rhine Graben region (Figure 2.2) in a 50 km wide belt that extends from the Eifel in the west, to the Rhön-Heldberg area in the east (Wedepohl and Baumann, 1999). The 4-6 km thick Eifel basement belongs to the Rheno-Hercynian fold and thrust belt on the northern flank of the Middle European Variscan belt, consisting predominantly of Devonian slates, sandstones and limestones that were folded during the Hercynian orogeny (Illies et al., 1979). Regional uplift of the Rhenish Massif coincided with the onset of Tertiary volcanism (40 Ma), accelerating at 15 Ma and continuing to present day at a rate of ~1 mm/year (Kreemer et al., 2020). Xenoliths have sampled the entire crust, which consists of Devonian sediments (sandstones, siltstones, slates and limestones) (5 km depth), greenschist facies (metamorphosed from Devonian) (5-15 km depth), low (micaschists) to high (gneisses) grade amphibolite facies (15-~25/30 km depth) and a thin layer of granulite facies above the Moho (Voll, 1983), which lies at a depth between 29 and 34 km (Stosch et al., 2007).

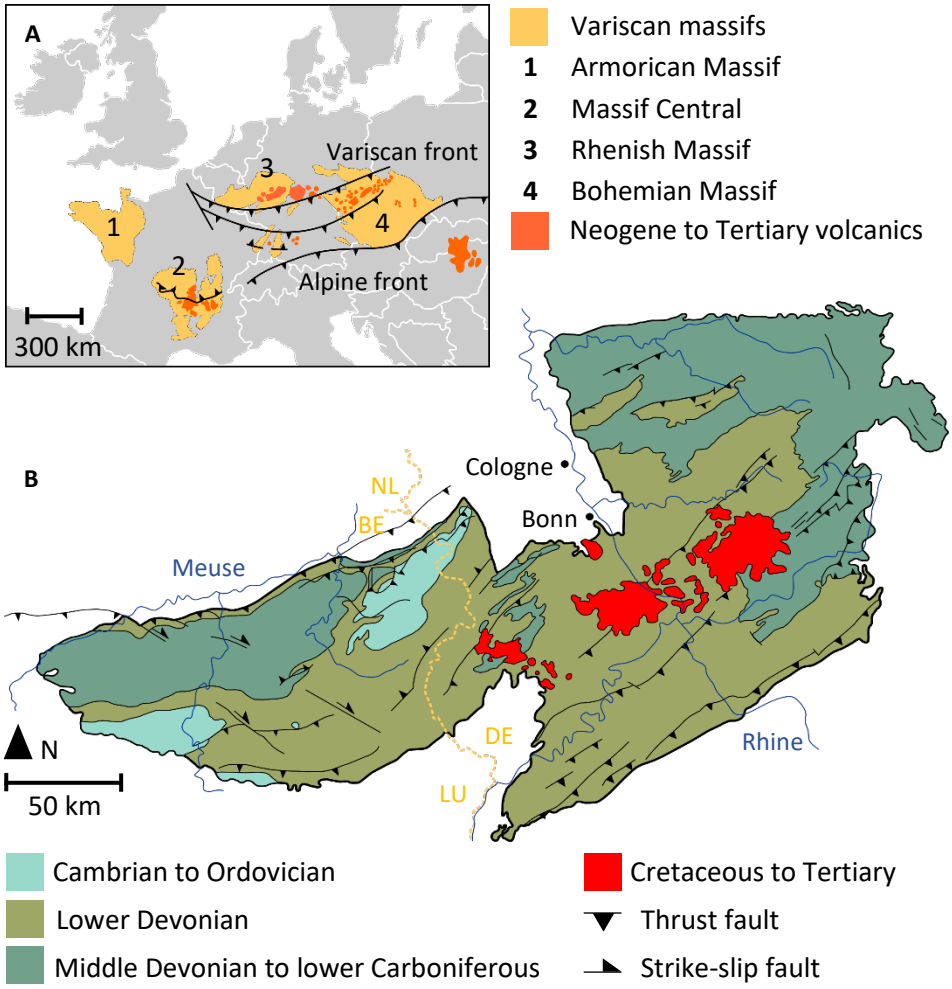

Figure 2.1 – Regional geology of the Rhenish Massif. **A)** Map of the Central European Volcanic Province (CEVP), highlighting the major Variscan massifs and Neogene to Tertiary volcanic districts. The Rhenish massif belongs to the Rheno-Hercynian fold and thrust belt, on the northern flank of the middle European Variscan front. **B)** Simplified geology of the Rhenish Massif, consisting predominantly of Devonian slates, sandstones and limestones. A: Redrawn and modified from Wilson and Downes (1991); B: Redrawn and modified from Barros et al. (2021), following Fielitz and Mansy (1999) and Meschede (2018), with additional information from Jansen (2019).

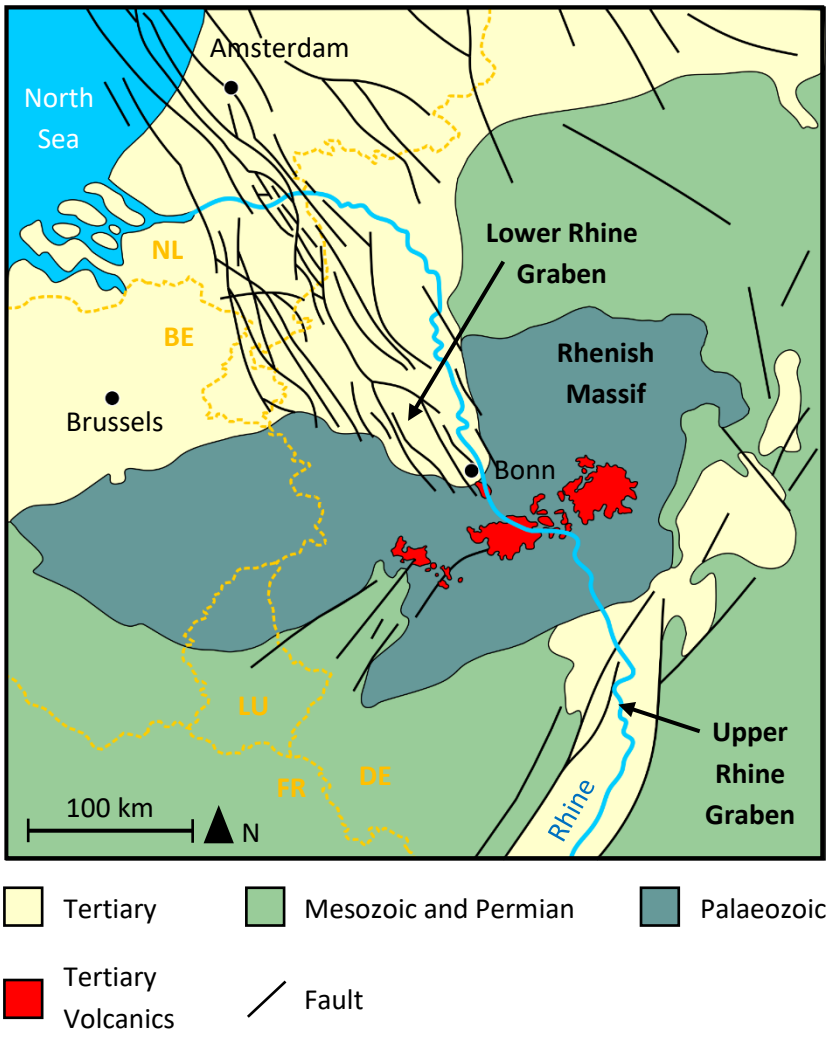

Figure 2.2 – Structural map of extension related faulting in the region of Rhenish Massif. Volcanism is largely confined to the lower Rhine graben, the northern portion of a ~50km wide rift system that is assumed to cut through the centre of the Palaeozoic Rhenish Massif. Redrawn and modified from Schäfer and Siehl (2002) and Schäfer et al. (2005), following Hager and Pruefert (1988), Zagwijn et al. (1985) and Vinken (1991).

2.2 Volcanic history

2.2.1 Tertiary volcanism

Volcanic activity in the Eifel region developed during the Tertiary period (~45 Ma) in the Hocheifel volcanic field (HEVF), the westernmost Tertiary volcanic field of the CEVP (Lippolt, 1983; Fekiacova et al., 2007) (Figure 2.3). Volcanism in the HEVF is divided into two periods of activity occurring between 44-39 and 37-35 Ma (Lippolt, 1983). Magmatic rocks are mainly basanites, nephelinites and alkali basalts with rare hawaiites, mugearites, benmoreites and trachytes (Jung et al., 2006), erupted from scoria cones and maars. Further east, the Westerwald volcanic field (WF) began eruptive activity ~30 Ma, forming scoria cones and maars between 30-20 Ma and again at 5.5 Ma (Haase et al., 2004). The greatest volumes of Tertiary magma were erupted between 19-9 Ma (Haase et al., 2004) from Vogelsberg stratovolcano which is located to the east of the WF (Bogaard and Wörner, 2003). This is the only stratovolcano in the Rhenish Massif, erupting 600 km^3 of basanites and alkali basalts, quartz tholeiites and limited quantities of evolved magmas ranging from hawaiite to trachyte (Bogaard and Wörner, 2003). Smaller Tertiary volcanic fields (Hessian, Rhön, Heldburg and Oberpfalz) are spatially and temporally related to the Westerwald volcanic field, but constitute smaller eruptive volumes (Mengel, 1990; Wedepohl et al., 1994; Jung and Hoernes, 2000).

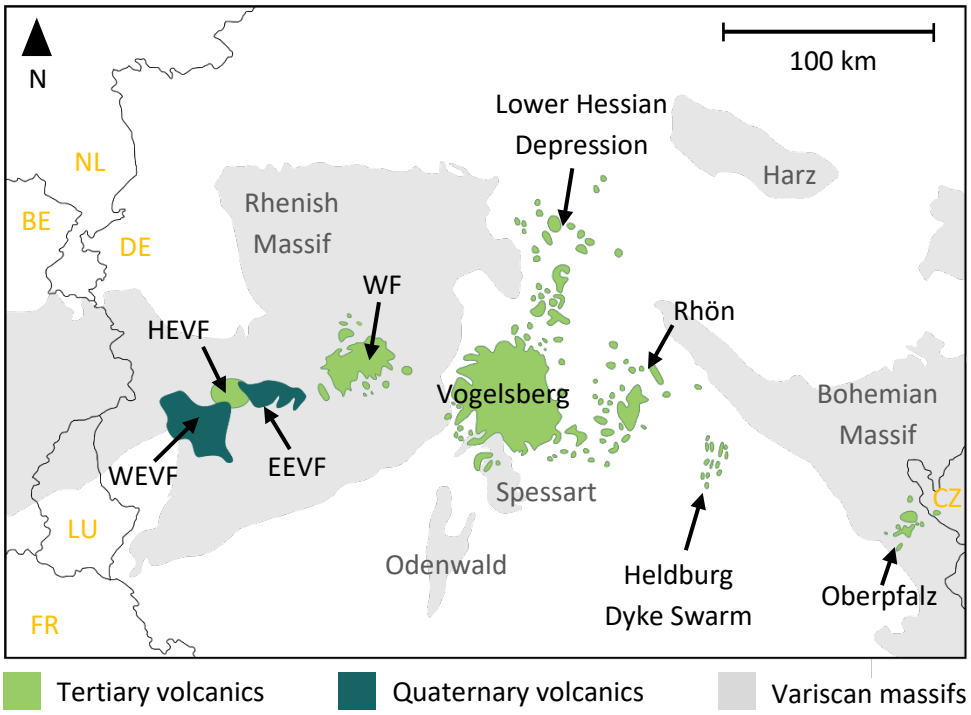

Figure 2.3 – Map of Tertiary volcanism in the region of the Rhenish Massif and Eifel fields. HEVF = Hocheifel volcanic field; WF = Westerwald volcanic field; WEVF = West Eifel volcanic field; EEVF = East Eifel volcanic field. Redrawn and modified from Büchner et al. (2015) with information from Megerle (2020).

2.2.2 Quaternary volcanism

The younger East and West Eifel Volcanic Fields formed during the Quaternary period, spatially separated from the older Hocheifel (Schmincke, 2007). The West Eifel covers an area between 500-600 km^2 (Illies et al., 1979), with ~240 mafic volcanic centres (6 maar lakes, 70 dry maar craters and 160 scoria cones) (Büchel and Mertes, 1982; Mertes, 1983; Büchel, 1994) (Figure 2.4). Eruptive activity began 700 ka and ceased ~11 ka, producing leucites, basanites and nephelinites (Mertes and Schminke, 1985) (Figure 2.5). The most recent volcanic event was the 11 ± 0.11 ka eruption of Ulmener Maar (Bräuer et al., 1999; Bräuer et al., 2000), though a high flux of magmatic gases can still be detected in the region today (Griesshaber

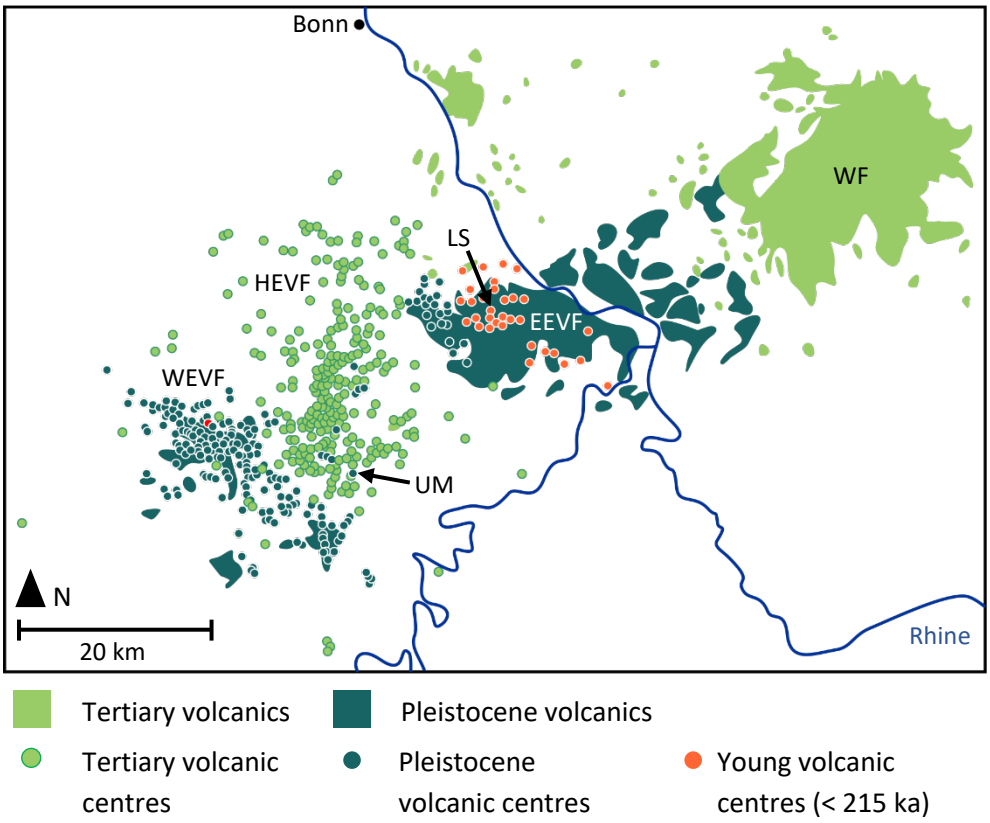

Figure 2.4 **–** Map showing the age and distribution of volcanic centres and deposits in the Eifel Volcanic region. Tertiary volcanic centres comprise the Hocheifel volcanic field, which is spatially and temporally separated from the Quaternary East and West Eifel volcanic fields, and the Westerwald volcanic field. Named volcanic centres indicate youngest eruption points: Ulmener Maar was the most recent eruptive event in the West Eifel volcanic field (11±0.11 ka)(Bräuer et al., 1999; Bräuer et al., 2000), Laacher See was the terminal eruptive event in the East Eifel (~12.9-13.1 ka)(Schmincke et al., 1999; Reinig et al., 2020). WEVF = West Eifel Volcanic Field; HEVF = Hocheifel Volcanic Field; EEVF = East Eifel Volcanic Field; WF = Westerwald Volcanic Field; UM = Ulmener Maar; LS = Laacher See. Redrawn and modified from Meschede and Warr (2019).

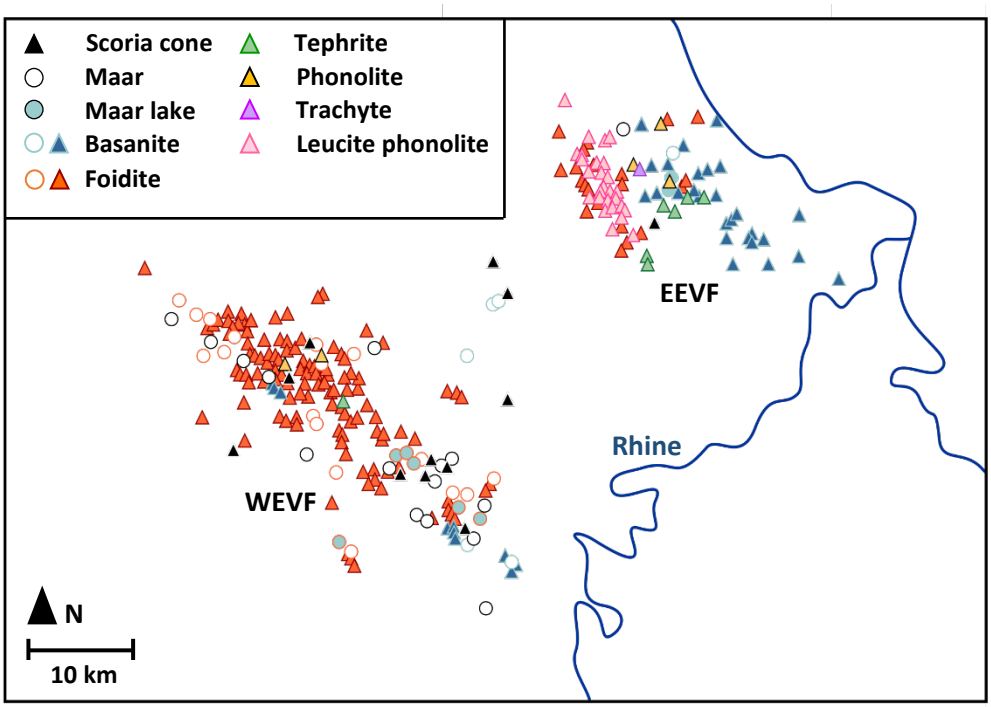

Figure 2.5 – Map of chemical composition of exposed volcanoes in the West and East Eifel Volcanic Fields. WEVF = West Eifel Volcanic Field; EEVF = East Eifel Volcanic Field. Redrawn and modified from Rausch et al. (2015), following Mertes and Schmincke (1985) and Schmincke (2007).

et al., 1992). The smaller East Eifel lies 60 km to the east, covering an area of around 400 km^2 that consists of ~100 scoria cones and maars, as well as three larger phonolitic centres including the Lacher See Volcano (Illies et al, 1979) (Figure 2.4). Volcanism began in the East Eifel ~460 ka and culminated with the ~12.9 ka plinian Laacher See eruption (Schmincke, 2007). This was the largest eruptive event in the Eifel fields, producing 6.3 km^3 of phonolitic magma and depositing volcanic material over an estimated area of 1300 km^2 (Schminke et al., 1999), impacting climate (Graf and Timmreck, 2001; Baldini et al., 2018), the environment (Baales et al., 2002; Riede and Kierdorf, 2020) and human settlement (Blong et al., 2018). Nephelinites, leucitites and basanites were erupted in the north west region of the East Eifel between ~460 - 430 ka, whilst basanites, intermediate (tephritic) and highly

differentiated (phonolitic) magmas were erupted in the south east between 400-13 ka (Illies et al., 1979; Jung et al., 2006) (Figure 2.5).

Between 700-10.8 ka it is estimated that ~300 eruptions occurred from 350 volcanic monogenetic centres in the East and West Eifel Volcanic fields (Schmincke, 2007). It is estimated that the West Eifel erupted around 1.5 km^3 of magma, whilst the East erupted around 10 km^3 (Schmincke et al., 1983). However, the volume of magma generated at depth is estimated to range between 70-100 km^3 (Wilson and Downes, 2006). Volcanic centres trend NW-SE in both the East and West fields and are typically spaced by <1 km in the centre of the fields and >1 km towards the margins (Illies et al., 1979). The volume of erupted material and the number of volcanoes increases towards the centre of each field, generally producing greater proportions of intermediate and differentiated products in the central volcanoes (Illies et al., 1979). The Eifel volcanic fields are the type locality for maar volcanism, however the properties of typical phreatomagmatic deposits are only identifiable in the East Eifel products (Schmincke, 2007; Rausch et al., 2015). Rausch et al. (2015) suggest that this indicates different eruption styles between maar volcanoes of the West and East volcanic fields. Cinder cones in both fields are up to 100 metres high (Schmincke et al., 1983) and were dominated by Strombolian and Hawaiian style eruptions, 10-30% of which have produced lava flows (Illies et al., 1979). Plinian eruptions occurred from three phonolitic calderas in the East Eifel, the Rieden (~450 ka), Wehr (~150 ka) and Laacher See (12.9 ka) (Dahm et al., 2020) that are 1.5-2.5 km in diameter (Schmincke et al., 1983). Abundant mantle and crustal xenoliths are common in volcanic deposits in both the West and East Eifel.

2.3 Source of magmatism

Volcanism in the East and West Eifel occurred in periodic phases of activity, separated by intervals of dormancy that correlate to records of climate and sea level change (Förster and Sirocko, 2015) as well as periods of increased tectonic uplift (Schmincke et al., 1983). This, in conjunction with evidence of a relatively thin crust (28-29 km) (Illies et al., 1979) and chemical signatures characteristic of a mantle source (Hegner et al., 1995; Wedepohl and Baumann, 1999; Haase et al., 2004; Buikin et al., 2005; Jung et al., 2005; Bräuer et al., 2013; Kreemer et al., 2020), suggests a clear relationship between mantle processes and volcanic activity (Schmincke et al., 1983). However, the exact nature of this relationship continues to be contested amongst authors. There are two main hypotheses presented in the literature. Firstly, intraplate volcanic activity in the Eifel region represents hot spot volcanism in response to a plume-like upwelling of lithospheric and asthenospheric mantle material (Granet et al., 1995; Ritter et al., 2001; Keyser et al., 2002; Montelli et al., 2006; Zhu et al., 2012). Specifically, the West and East Eifel Volcanic Fields occur above a 100 km wide low P-wave velocity anomaly that extends to a depth of ~410 km (Ritter et al., 2001; Keyser et al., 2002; Budweg et al., 2006; Zhu et al., 2012), though some studies have also identified a seismic anomaly deeper in the lower mantle (600 – 2000 km depth) (Goes et al., 1999; Grunewald et al., 2001). There is no apparent effect upon the 660 km discontinuity (Budweg et al., 2006) and as such it is unclear whether there is any physical connection between the shallower and deeper anomalies. A broader low velocity zone at ~50 km depth has been interpreted to represent the plume head (Mathar et al., 2006), though Dahm et al. (2020) argue that this zone does not exhibit the P- and S- wave anomaly trends associated with classic plume head models. Further evidence in support of the

plume hypothesis includes the exhalation of mantle helium in groundwater (Griesshaber et al., 1992), significant tectonic uplift centred in the Eifel region (Meyer and Stets, 1998) and isotopic and trace element signatures consistent with ocean island basalt (OIB) lavas (e.g. Wedepohl and Baumann, 1999; Bogaard and Wörner, 2003). Ritter et al. (2001) combine this evidence to suggest the existence of a 100 km wide deep mantle plume beneath the Eifel, centred ~50 km to the south of the West Eifel and 80 km southwest of the East Eifel volcanic fields, with excess temperatures of 150 – 200°C and a melt content of ~1-3% (Wüllner et al., 2006; Dahm et al., 2020). This plume activity is considered to be more broadly related to the presence of a wide plume-like upwelling in the lower mantle beneath central Europe (Goes et al., 1999), that feeds the volcanic regions of the Central European Volcanic Province via a series of smaller diapiric upwellings (Granet et al., 1995; Hoernle et al., 1995; Goes et al., 1999; Ritter et al., 2001; Wilson et al., 2001; Keyser et al., 2002).

However, the mantle plume hypothesis is contradicted by the pattern of surface volcanism. Firstly, the temporal pattern of volcanic activity recorded in the Eifel region is inconsistent with the age-progressive tracks that typically characterise hot spot magmatism (Lippolt, 1983). Volcanic centres are distributed along a NW-SE trend, contradictory to the modelled W-SW motion of the assumed mantle plume (Walker et al., 2007), and do not exhibit any spatiotemporal trend. Secondly, the volume of magma erupted at the surface is far smaller than that erupted at other established hot spot locations such as Iceland and Hawaii (White, 1993). A study by Marignier et al. (2020) utilised global tomography data to calculate the probability of a mantle plume's existence after transforming and reducing the signal to noise ratio in the seismic data. From this, they concluded that the existence of a mantle plume beneath Eifel was 'unlikely', with a probability between 32 and 46%. From

these observations, the mantle plume hypothesis can only be maintained with significant modification to current models and established concepts of hot spot volcanism.

The second hypothesis considers volcanism to represent the lithospheric response to large scale rifting caused by the Alpine collision. In this model, magma is generated through adiabatic melting in response to lithospheric extension and thinning that resulted in a localised upwelling of low-density asthenospheric mantle (Illies and Greiner, 1978; Sengör et al., 1978; Wilson and Downes, 1992; Meyer and Stets, 2002; Lustrino and Carminati, 2007). It is suggested that domal uplift in the Eifel region reflects this upwelling (Granet et al., 1995; Ritter et al., 2001; Wilson et al., 2001) and that volcanic centres and dykes trend in a direction consistent with the lithospheric stress field and extension (e.g. Regenauer-Lieb, 1998). The most significant criticism of this hypothesis is that the volume of magma estimated to have been produced at depth is considered to be too large to have been produced solely via lithospheric extension (Jung and Masberg, 1998; Bogaard and Wörner, 2003). However, the temporal correlation between Tertiary magmatism and changes to the intraplate stress field of Central Europe indicates some relationship between magmatism and tectonic processes (e.g. Pfänder et al., 2018).

Regardless of whether magma genesis represents lithospheric extension or hot spot activity, magmatism in the Rhenish Massif is considered to be a combined product of the interaction of upper mantle upwelling, tectonic stresses and pre-existent lithospheric structures developed during the Variscan orogeny (Dahm et al., 2020). Significantly, the continental crust in the Eifel region has a thickness of just ~30 km (Prodehl et al., 1992) which, combined with a dynamic tectonic history,

(Franke et al., 2017; Pfiffner, 2017) establishes a mantle and lithospheric regime that is particularly conducive for melt generation and volcanism (Dahm et al., 2020).

2.4 Xenoliths in the Eifel

Xenoliths brought to the surface by ascending magmas provide a valuable insight into sub-surface magmatic processes, particularly in regions where dissected magmatic intrusions are rare. A broad variety of xenolith types are abundant in the volcanic deposits of both the East and West Eifel volcanic fields, ranging from ultramafic mantle xenoliths, to ultramafic, mafic, intermediate, acid and metasedimentary crustal types (Downes, 1993). These xenoliths have inspired numerous studies, primarily focused on interpreting the chemistry and evolution of the mantle beneath the Eifel (e.g. Witt-Eickschen et al., 2003; Shaw et al., 2018; Rizzo et al., 2021), the structure of the Eifel crust (e.g. Voll, 1983; Mengel et al., 1991; Downes, 1993), and to understand the transportation and storage of magmas within this crust (e.g. Shaw, 2004; Dennis et al., 2013). Ultramafic xenoliths found in tuffs of maar-type volcanoes in the West Eifel volcanic field have been of particular focus in many of these studies. These xenoliths can be divided into two distinct suites, consisting of several recognised variants (Schminke, 2007). Firstly, mantle derived peridotitic xenoliths are common in the western part of the field (Shaw, 2004). These can be simply divided into a lherzolite and wehrlite series (Becker, 1977), with some additional examples of harzburgites and dunites (Schmincke, 2007) that together preserve evidence of multiple metasomatic events in the mantle (e.g. Edgar et al., 1989; Lloyd et al., 1991; Shaw, 1997; Witt-Eickschen et al., 1998; Shaw and Klügel, 2002; Mertz et al., 2015; Shaw et al., 2018; Rizzo et al., 2021). Secondly, glass-bearing clinopyroxenite, hornblendite and glimmerite (>90% phlogopite) xenoliths are found in both the western and eastern parts of the

volcanic field. These xenoliths exhibit cumulate textures and are generally interpreted to represent fragments that crystallised in the upper mantle or crust (e.g. Becker, 1977; Duda and Schmincke, 1985; Shaw and Eyzaguirre, 2000). Significantly, the West Eifel volcanic field is cross-cut by the eastern edge of a large graben structure, the Eifel North-South Zone Depression (ENSZD). Lavas erupted to the west of this cross-cutting edge yield xenoliths consisting of both mantle peridotite and cumulate textured hornblendite- clinopyroxenite-types, whilst lavas erupted on the east side only contain xenoliths of the latter type (Shaw et al., 2005). This project focuses on glass-bearing clinopyroxenite and hornblendites found in Neogene alkali basalt tuffs of maar-type volcanic centres.

2.4.1 Previous work: clinopyroxenite and hornblendite xenoliths in the West Eifel

Clinopyroxenite and hornblendite xenoliths are abundant in tuff deposits around maar-type cinder cone volcanoes in the West Eifel Volcanic Field (e.g. Becker, 1977). Numerous studies describe the petrography and chemical composition of these xenoliths, (e.g. Becker, 1977; Downes et al., 2004; Shaw, 2004; Shaw et al., 2005) with the common aim of better understanding the sub-surface magmatic regime in the Eifel region. This section provides a review of these studies, with focus on their key findings and contributions.

2.4.1.1 Origin of clinopyroxenite and hornblendite xenoliths

Previous studies maintain a particular focus upon determining the origin of these xenoliths. Specifically, variations between textural and compositional trends described by different authors have led some to suggest that they originated in the upper mantle (e.g. Lloyd and Bailey, 1975), whilst others propose a crustal origin

(e.g. Becker, 1977; Duda and Schmincke, 1985; Shaw, 2004). The former is supported by the presence of veins of similar amphibole-clinopyroxene-phlogopite rich material in upper mantle peridotite, which are sampled by wehrlite xenoliths (e.g. Ionov and Hofmann, 1995; Moine et al., 2001; Shaw et al., 2018). These veins, which are attributed to the infiltration of metasomatic fluids related to Quaternary volcanism (Witt-Eickschen et al., 1998), are thought to represent the final product of extensively metasomatised peridotite (e.g. Lloyd and Bailey, 1975), consistent with observations in mantle-derived ultramafic massifs and xenolith suites beyond the Eifel (e.g. Bodinier et al., 1987; Dawson, 2002; Fabries et al., 2000; Bodinier et al., 2004). Alternatively, Shaw and Klügel (2002) conclude that the geochemical composition of glasses preserved in these xenoliths is inconsistent with a metasomatic origin, and instead propose that they represent magmatic cumulates formed by the crystallisation of silicate melts along fractures within the lithospheric mantle (Witt-Eickschen et al., 1998; Witt-Eickschen and Kramm, 1998; Witt-Eickschen et al., 2003). Significant differences in their REE patterns compared to peridotite xenoliths are more consistent with amphibole and clinopyroxene megacrysts precipitated from basic melts (Irving and Frey, 1984), a result replicated by Downes et al. (2004). From this, Aoki and Kushiro (1968) and Duda and Schmincke (1985) conclude that they are not genetically related to peridotite xenolith suites. Trace element modelling indicates that the parental melts are primitive alkaline basalt melts, genetically related to the Quaternary volcanic rocks in the West Eifel area (Witt-Eickschen and Kramm, 1998). Significantly, Nd-Sr isotope compositions of clinopyroxenes cover the entire spectrum of Nd-Sr compositions observed for Eifel Cenozoic lavas (Witt-Eickschen and Kramm, 1998; Witt-Eickschen et al., 2003). In this model, the compositional variations recorded

between different xenoliths indicates that the magmas may have heterogeneously fractionated in localised regions of the upper mantle (Shaw and Eyzaguirre, 2000).

Alternatively, textural and geochemical evidence has led some authors to conclude that the xenoliths formed within the crust (e.g. Becker, 1977; Duda and Schmincke, 1985; Shaw, 2004). For example, Becker (1977) used Al isotope ratios to estimate that clinopyroxenites formed under shallow low-pressure conditions, likely less than 500 MPa (~15-20 km depth (Dahm et al., 2020)). Shaw (2004) estimates a depth range between 4-22 km, but acknowledges wide error ranges associated with the particular geobarometery technique. Geochemical similarities to clinopyroxene megacrysts formed in the lower crust may support a crustal origin (e.g. Aoki and Kushiro, 1968), although Shaw and Eyzaguirre (2000) identify a compositional relationship to megacrysts derived from the upper mantle. Nevertheless, prevalent cumulate textures, an absence of any significant deformation textures (Duda and Schmincke, 1985) and varied zonation trends within discrete xenoliths (Becker, 1977) are consistent with textures associated with crustal cumulates formed in low pressure mushy environments (e.g. Marsh, 1996; Shaw, 2004). Shaw (2004) suggests a particular affinity to the cumulate textures that are associated with magmatic solidification fronts typically found in fossilised magma chambers (e.g. Marsh, 1996; Bahl et al., 2001; Marsh, 2006; Holness et al., 2007c). This then raises the question of where, and for how long these cumulates were stored within the crust. Whilst some authors propose that these cumulates originated from a crustal dyke network (e.g. Duda and Schmincke, 1985), others advocate for larger sub-volcanic magma chambers (e.g. Shaw, 2004). Regardless of how they were stored in the crust, the xenoliths are interpreted as comagmatic products of a high-alkali basaltic melt (e.g. Becker, 1977), similar to the Cenozoic Eifel lavas (e.g. Aoki and Kushiro, 1968; Duda and Schmincke, 1985). Becker et al. (1977) constrain the

parental melt as an undersaturated nephelinitic magma, with a crystallisation history as follows: fo-rich olivine and chrome spinel appeared on the liquidus, followed by high-pressure clinopyroxene. As water was released from the melt, the liquidus moved towards lower temperatures and the olivine and clinopyroxene remelted. Phlogopite (which also became unstable) crystallised next, followed by low-pressure clinopyroxene and hornblende. Geochemical data indicates that discrete magma batches that stalled within the crust fractionated to varying degrees (e.g. Shaw, 2004), which some authors attribute to mechanical magma chamber processes (e.g. Duda and Schmincke, 1985).

2.4.1.2 Constraining volcanic dynamics

Xenoliths carried to the surface in volcanic eruptions provide a window into sub-surface magma storage and evolution in a system that is directly linked to active volcanism (e.g. Tollan et al., 2012; Perinelli et al., 2017; Cooper et al., 2019; Renzulli et al., 2021). As such, cumulate textured xenoliths found in the Eifel have also been used to better constrain the architecture of volcanic plumbing systems, as well as associated time-scales of magma emplacement and ascent that govern eruptive activity in the Eifel. For example, Shaw (2004) studied zoned crystals within cumulate textured clinopyroxenite xenoliths in order to calculate the time scales of magma ascent for three volcanic centres in the West Eifel. From this, they concluded that the development of the plumbing systems feeding the volcanoes occurred rapidly, with multiple magma batches infilling magma chambers no more than 4 years prior to eruption. Significantly, olivine and clinopyroxene crystals record emplacement events as little as 3 hours prior to eruption, corresponding to magmatic ascent rates between 3-15 km/hour, and establishing a link between eruptive events and sub-surface magma emplacement triggers. Inverse zoning

patterns described by Duda and Schmincke (1985) are attributed to polybaric crystallisation within a plumbing system comprised of multiple magma chambers, but acknowledge that the cumulates may have crystallised along the margins of a narrow dyke network (e.g. Irving, 1980). Shaw (2004) calculated a wide range of crystallisation depths for xenoliths erupted from a single eruption centre, which they suggest indicates that the volcanic plumbing system may either consist of multiple magma chambers or resemble a more vertically extensive mush column (e.g. Marsh, 1996). Shaw (2004) further utilises the xenoliths to approximate the rate of crystal accumulation in the sub-volcanic magma chamber, estimating a rate of between 45 and 160 cm/year. This rapid accumulation rate (compared to estimates by Hess, 1960 and Wager and Brown, 1967), suggests that the magma chamber systems were relatively short-lived (Shaw, 2004) and therefore fed monogenetic volcanoes. It is particularly challenging to study magma storage and transport in regions of intraplate extension (Holness and Bunbury, 2006), where monogenetic volcanoes are thought to be generated with the rapid development of short-lived magma transport pathways (e.g. Spera, 1984; Connor et al., 2000). These xenoliths provide an opportunity to better constrain the timescales and architecture of these pathways, however Shaw (2004) acknowledges that the number of detailed studies is insufficient to characterise magma transport across the Eifel fields.

2.4.1.3 Broader applicability

Downes et al. (2004) establish a wider significance in studying glass-bearing clinopyroxenite and hornblendite xenoliths from the Eifel region, exaggerating their potential in contributing more broadly towards the current understanding of alkaline magmatism. In particular, they regard the xenoliths as ‘natural

experimental charges' that present an opportunity to study mineral/melt distribution coefficients in alkali basaltic melts. Their results are generally consistent with distribution coefficients derived from experimental data (e.g. La Tourrette et al., 1995; Bottazzi et al., 1999; Tiepolo et al., 2001) which, with bulk rock compositions similar to those of typical intraplate alkali basalts (e.g. Wilson et al., 1995), demonstrates their usefulness for investigating trace element distributions in natural basaltic systems. Additionally, megacrysts of clinopyroxene, amphibole and phlogopite that commonly occur in alkaline basaltic lavas (e.g. Ho et al., 2003; Chen et al., 2009; Ashchepkov et al., 2011; Choi and Kim, 2012; Liu and Ying, 2019; Serre et al., 2020; Matusiak-Malek et al., 2021; Soukrati et al., 2021) show a geochemical similarity to the constituent minerals of the clinopyroxenite and hornblendite xenoliths erupted in the Eifel (Dobosi and Jenner, 1999; Shaw and Eyzaguirre, 2000; Downes et al., 2004). As such, Downes et al. (2004) and Shaw and Eyzaguirre (2000) consider their potential in explaining the origin of megacrysts in alkali basalts, which Downes et al. (2004) suggest may result from the disaggregation of similar melt-rich xenoliths. Downes et al. (2004) continue to state that these xenoliths are of 'widespread significance', with many possible uses. Notably, an absence of any detailed textural studies establishes a gap in the existing literature and signifies the opportunity to further utilise these samples.

2.5 Wider significance of clinopyroxenite and hornblendite xenoliths

Cumulate textured clinopyroxenite and hornblendite xenoliths are not unique to the Eifel region. Similar examples have been identified in the Middle East (Mittlefehldt, 1984; Holness and Bunbury, 2006; Eyuboglu et al., 2021), North America (Best, 1975; Francis, 1976), Europe (Dobosi et al., 2003; Downes et al., 2005; Bryant et al., 2007) Asia (Chandrasekharam and Vinod, 2000) and Africa (Chin, 2018). However, the Eifel samples are of particular importance as they contain ~10% interstitial glass (Downes et al., 2004) and thus were incompletely crystallised at the time of eruption. Holness et al. (2019) recognise the importance of such samples, which provide an insight into melt and crystal dynamics prior to any significant sub-solidus readjustment that is pervasive in exposed plutons (e.g. McBirney, 2009) (refer to Chapter one of this thesis for a more detailed review). These xenoliths are considered to provide a snapshot into cumulate processes operating in crustal magma stores (e.g. Hermes and Cornell, 1981; Giannetti and Luhr, 1990; Turbeville, 1992b; Mattioli et al., 2003), and as such have been utilised to better constrain the formation of orthocumulates, adcumulates and heteradcumulates that are widely recognised in plutonic bodies. In particular, they provide a valuable opportunity to constrain the geometry, distribution and movement of melt within magmatic systems that are directly linked to surface volcanism (e.g. Holness et al., 2007d). Efforts to gain an insight into pore geometries and connectivity in cumulates are typically experimental (e.g. Lupulescu and Watson, 1999; Wark et al., 2003) or computational (e.g. Cheadle et al., 2004; Bretagne et al., 2021) and hence require some simplification of the magmatic system, or rely on various assumptions about the inverse crystallisation process. It

is acknowledged that when limited to completely solidified plutonic samples, permeability and the distribution of melt remains poorly constrained (Bretagne et al., 2021). However, Holness et al. (2007d) recognise the potential of glass-bearing xenoliths in contributing towards this problem. By undertaking qualitative observations of glass distribution patterns in gabbroic cognate xenoliths entrained in lavas from Iceland, Santorini and Hawaii, they concluded that pore geometries are controlled by crystal growth rather than textural equilibration. Abundant glass along grain boundaries is interpreted as evidence of a highly interconnected liquid phase at high crystallinities (e.g. Meurer and Meurer, 2006), which alludes to a higher permeability than would be expected for a texturally mature cumulate (Cheadle et al., 2004). This provides a significant contribution to the understanding of melt distribution and connectivity in partially solidified mushes, however it is important to acknowledge that their methodology is entirely two-dimensional. Mattioli et al. (2003) studied a suite of glass-bearing mafic xenoliths associated with pyroclastic deposits of the Stromboli stratovolcano. From mineral and glass composition data they identified that the interstitial glass contained within the xenoliths is not genetically related to either the cumulus mineral assemblage or the host magma, but a compositionally distinct magma that completely infiltrated the crystal network. They conclude that the cumulus framework must have been sufficiently permeable to permit such effective infiltration, even in samples with glass contents <5%. This alludes to the presence of an interconnected liquid phase, but does not contribute any information about the three-dimensional geometry or movement of melt within the pore spaces. A persistent trend in the literature is the focus on the geochemical relationship between melt and crystals (e.g. Lissenberg et al., 2019; Sanfilippo et al., 2020; Maier et al., 2021; Renna et al., 2021), and the processes that control their chemical evolution. This project aims to better

understand the physical relationship between melt and crystals, with focus on the spatial relationship between the crystal phases and pore spaces.

It is important to constrain the distribution and behaviour of melt within incompletely solidified cumulates as the segregation of this melt from the cumulate framework can lead to the accumulation of potentially eruptible melt within the crust (e.g. Hildreth, 2004; Bachmann and Bergantz, 2004; 2008; Dufek and Bachmann, 2010; Deering et al., 2011). However, the physical mechanisms driving this separation remain uncertain (e.g. Holness et al., 2019). There is widespread evidence that melt extraction is a common process in volcanic episodes (e.g. Hildreth and Wilson, 2007; Dufek and Bachmann, 2010; Solano et al., 2012; Barboni and Schoene, 2014; Cashman and Giordano, 2014; Ellis et al., 2014; Wotzlaw et al., 2014; Christopher et al., 2015), however evidence for large scale melt accumulation is rarely found in dissected plutons (Coleman et al., 2012) and as such the relationship between plutonic and volcanic rocks remains ambiguous.

Glass-bearing, cumulate textured xenoliths provide a valuable tool to investigate this relationship; cognate xenoliths sample the plutonic realm and are entrained and then erupted via the sub-volcanic plumbing system, therefore allowing the plutonic-volcanic connection to be assessed directly (e.g. Lissenberg et al., 2019). This is particularly significant with the rapidly evolving mush paradigm (e.g. Cashman et al., 2017) (see Chapter one of this thesis for a review), for which melt distribution and extraction are predicted to differ from the traditional melt-rich magma chamber model (e.g. Hayes et al., 2015a; 2015b; Bédard, 2015; Lissenberg and Macleod, 2016). Regardless of the driving force behind melt segregation, the efficiency of melt migration in crystal mush systems is strongly dependent on the porosity and permeability of the mush, which are ultimately controlled by crystal

textures (Coogan et al., 2000). Therefore, the textural immaturity that is frequently recorded within glass-bearing cognate xenoliths (e.g. Holness et al., 2007d) provides a valuable opportunity to better constrain the influence of texture upon the relationship between crystals and melt in sub-volcanic environments. The Eifel samples present the opportunity to specifically investigate this relationship in the context of an intraplate setting. It is particularly significant to interrogate sub-volcanic dynamics in the Eifel region as recent evidence suggests that magma may be moving through the sub-Eifel crust (Hensch et al., 2019; Berberich et al., 2019). Patterns of deep low frequency earthquakes recorded in the Eifel are consistent with observations from other active volcanoes (e.g. Soosalu et al., 2009; Nichols et al., 2011; Shapiro et al., 2017), from which Berberich et al. (2019) conclude that volcanic activity in the Eifel region is currently dormant, but not extinct. Although Hensch et al. (2019) consider the volcanic hazard to be low, Leder et al. (2017) estimate that the risk from any eruption would be high due to a dense population and large damage potential in this region. Hensch et al. (2019) therefore suggest that the Eifel region should continue to be monitored, in conjunction with using the record provided within volcanic rocks and minerals to better understand the eruptive hazards in this region.

2.6 Summary

A summary of the key points from this chapter are provided in the following:

- The Eifel region belongs to the Rhenish Massif, a Variscan shield characterised by extensional tectonics, Tertiary-Quaternary intra-plate volcanism and ongoing uplift.
- Quaternary volcanism is concentrated in the West and East Eifel volcanic fields, which are the type locality for maar-type volcanism. Monogenetic

cinder cones and maar craters erupted alkaline magmas, temporally related to periods of increased tectonic uplift.

- Magmatism is attributed either to hot spot activity in association with a mantle plume structure, or adiabatic melting in response to lithospheric extension. Regardless of how magma is generated, the tectonic history of the region makes it particularly conducive for melt generation and volcanism.
- A broad variety of xenoliths sample the mantle and Eifel crust, which have inspired numerous studies. Glass-bearing clinopyroxenites and hornblendites found in tuffs of maar-type cinder cone volcanoes are of particular interest.
- Clinopyroxenite and hornblendite xenoliths may represent upper mantle or crustal cumulates, precipitated from primitive alkaline basalts and genetically related to Quaternary Eifel lavas.
- Previous studies have used them to constrain the architecture and magmatic timescales of volcanic plumbing systems in the West Eifel, revealing rapid rates of magmatic accumulation and ascent.
- More broadly, they have been used to investigate mineral/melt coefficients in alkali basalts and to investigate the origin of megacrysts that commonly occur in alkaline magmas.
- Previous studies of similar glass-bearing xenoliths from other locations recognise their potential in better constraining the relationship between melt and crystals prior to significant textural overprinting from equilibration processes. However, these studies are typically qualitative in nature and lack any three-dimensional insight.

- Glass-bearing clinopyroxenite and hornblendite xenoliths erupted in the West Eifel provide a valuable opportunity to further explore this relationship, contributing to the understanding of melt dynamics in an intra-plate setting that has the potential for future volcanic activity.

Methodology

This chapter summarises the methodologies used to investigate the research aims outlined in Chapter 1. Methods are grouped according to the image acquisition technique used to replicate the xenolith textures. Firstly, optical petrography using photo microscopy is utilised for qualitative descriptions of crystal and glass textures. Secondly, two-dimensional image analysis of digitised thin sections is used to quantify crystal textures including phase abundance, crystal size distribution (CSD), spatial distribution pattern (SDP) and shape preferred orientation (SPO). Thirdly, three-dimensional X-ray computed tomography (CT) is applied to analyse the non-crystalline constituents within the xenolith samples. Finally, supplementary geochemical analyses were undertaken using laser ablation inductively coupled plasma mass spectrometry (LA-ICP-MS). Potential methodological limitations are outlined alongside the steps taken to overcome them.

3 Methodology

3.1 Sampling rationale

Analysis was undertaken on four cognate xenoliths that were collected by H. Downes from Mertens Quarry in the Gemündener Maar complex within the West Eifel Volcanic province (Figure 3.1). It is presumed that the samples originated from the same eruptive centre, however the volcanic deposits from the Gemündener, Weinfelder and Schalkenmehrener Maars do overlap (Shaw, 2004). These four xenoliths comprise part of a larger suite of xenoliths described in Downes et al. (2004). They are herein referred to as M2, M4, M6 and M8 (Table 3.1). These four samples were selected as they provide a representation of the array of textures recorded in the xenolith suite and provided a large enough volume of material for the required textural analyses

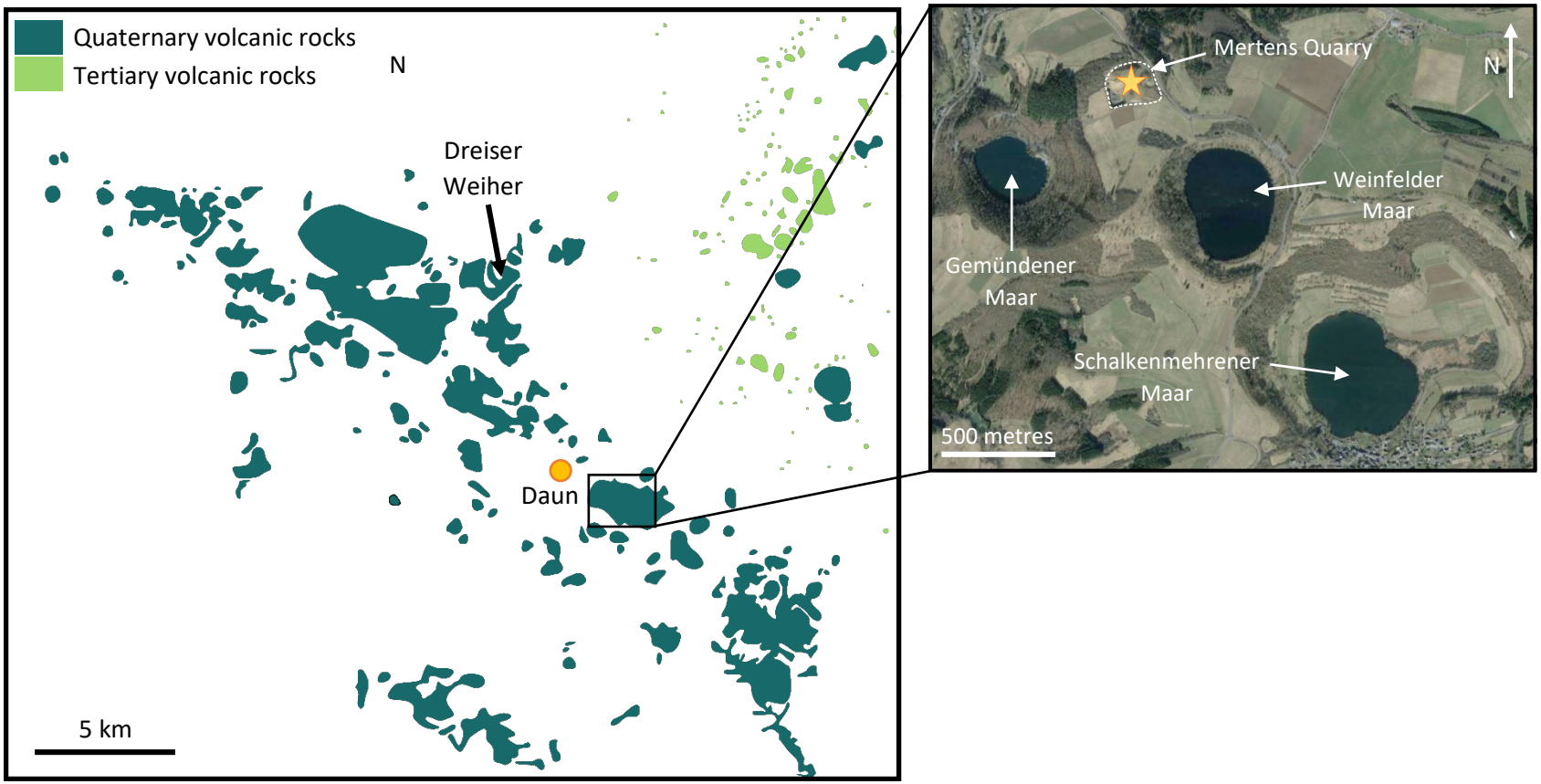

Figure 3.1 – Maps showing the sampling location of the xenoliths analysed in this study. *Left* – Geology of Quaternary and Tertiary volcanics in the West Eifel Volcanic Field. Redrawn and modified from Shaw et al. (2018) after Büchel (1994) and Shaw et al. (2010). Right – Satellite map showing Mertens Quarry (gold star), where the samples were collected, and nearby Maars. (Google Maps, 2022).

Sample number	Sample photograph	Sample dimensions
M2		15 x 15 x 12 cm
M4		10 x 10 x 12 cm
M6		8 x 9 x 10 cm
M8		20 x 16 x 18 cm

Table 3.1 – Xenolith samples selected for textural analysis, with photographs and dimensions (measured prior to cutting the sample).

3.2 Application of two- and three- dimensional methodologies

Igneous textures may be analysed in two-dimensions via thin section, or in three-dimensions via techniques such as serial sectioning or X-ray computed tomography. Although the texture of a rock is three-dimensional in nature, there are a number of criteria that the sample and study aims must satisfy in order to be a candidate for three-dimensional analysis (Figure 3.1). Because intrusive rocks often do not

satisfy these conditions (Figure 3.2), a two-dimensional approach is most frequently utilised within the literature. With this comes the limitations associated with viewing a three-dimensional object in one plane, which may introduce errors into the textural analysis (e.g. Jambon et al., 1992; Higgins, 2000; Shea et al., 2015). To compensate for this, mathematical corrections have been developed that aim to extrapolate the 2D data into a 3D output (e.g. Higgins, 2000). In this study, the crystal contents of the xenoliths do not satisfy the criteria for 3D analysis (Figure 3.3) and so are analysed from a two-dimensional perspective. However, the non-crystalline components (glass and vesicles) of these samples are suited for 3D analysis, providing the opportunity to integrate two- and three-dimensional methodologies. Crystal textures are therefore analysed in 2D, utilising thin sections, whilst glass textures are analysed in 3D through X-ray computed tomography.

Figure 3.2 (Overleaf) ▶ **–** Flowchart demonstrating the criteria that must be satisfied in order for an igneous sample to be suited for three-dimensional analysis. The orange path demonstrates the criteria for textural analysis of the crystal contents within the Eifel samples, which are most appropriately studied in thin section. It should be noted that this does not apply to the vesicle and glass fractions of the xenoliths, which are better suited for 3D analysis and described in Section 3.4.

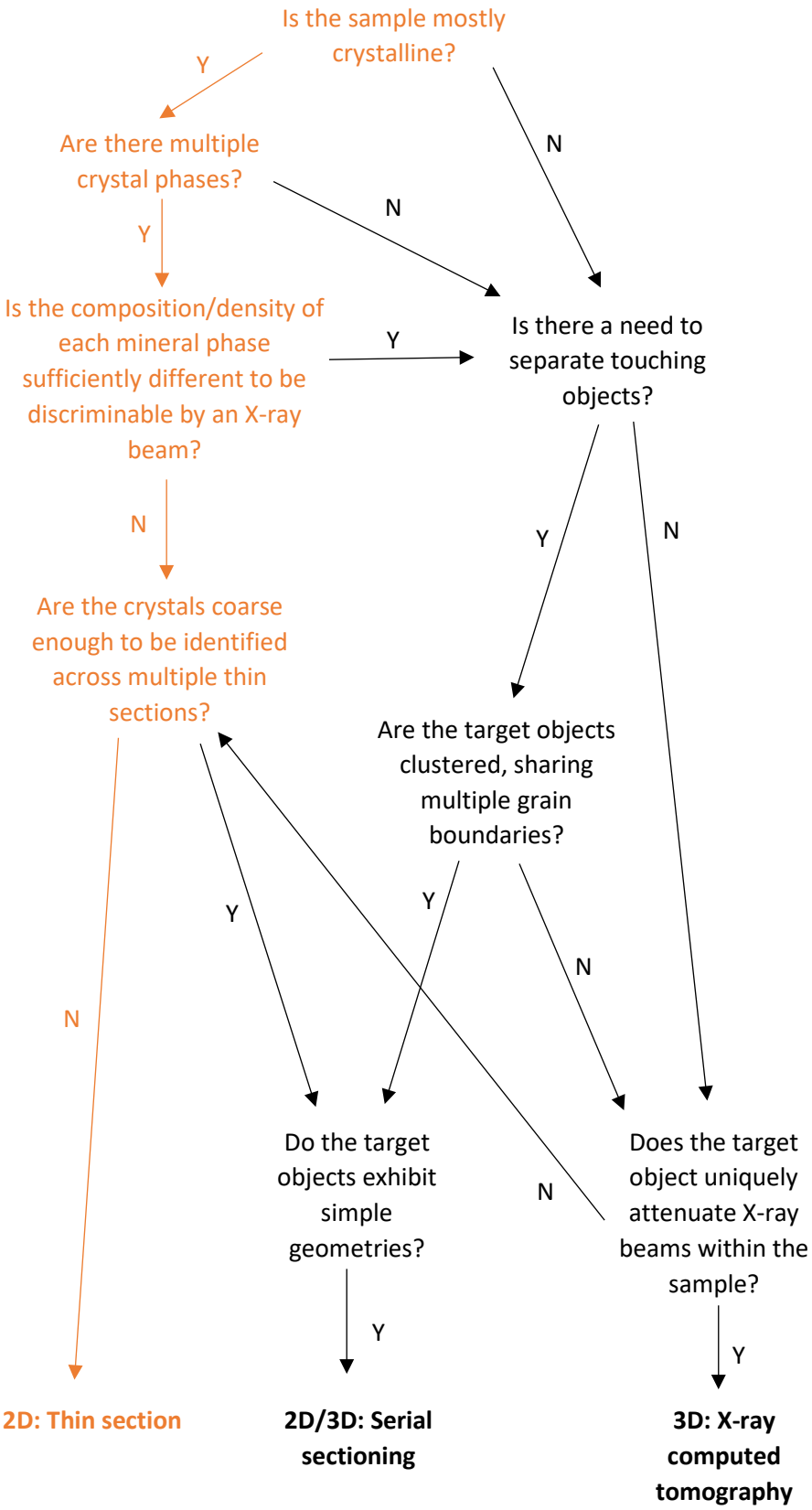

Figure 3.2 - ◄ Caption overleaf

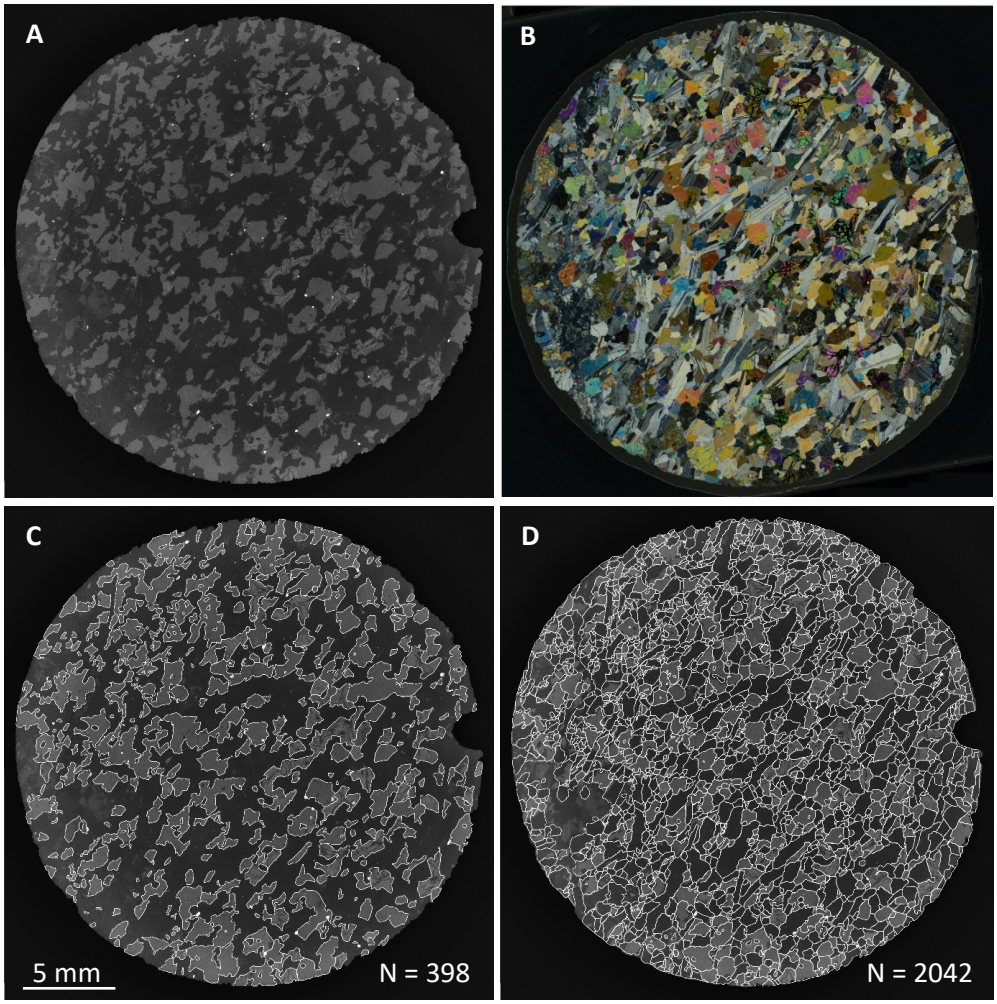

Figure 3.3 **–** Computed tomography (CT) images (**A**, **C**, **D**) alongside a correspondent thin section slice (**B**), photographed in cross-polarised light. The rock sample is a gabbro largely consisting of plagioclase, olivine and clinopyroxene. This sample demonstrates why predominantly crystalline samples (such as is represented by the Eifel samples) are unsuited for textural analysis using X-ray CT. **A)** Greyscale CT slice image. **B)** XPL photograph of a thin section, showing the equivalent plane visualised in the CT image. **C)** Visible crystal outlines traced onto the CT image, indicating that there are 398 individual objects in this image. **D)** Crystal boundaries traced from the thin section image in B, imposed onto the same CT slice in **C**. This reveals 2042 individual objects in the image. It is clear that the CT data is limited by its inability to separate touching crystals of the same mineral type and as such it does not provide a suitable dataset from which to analyse 3D crystal textures.

3.3 Two-dimensional analysis

3.3.1 Thin sectioning

Three thin sections were cut from each xenolith along an artificial X, Y and Z axis to sample any crystal orientation and fabric present in the rock (Figure 3.4). Three-dimensional fabrics can be challenging to sample in 2D, and at least three non-coplanar sections are required to sample orientation from two-dimensional sections (Launeau, 2004). The thin sections are 30 µm thick with a maximum area of 5 x 2 cm. The same thin sections were used for qualitative petrographic descriptions outlined in Section 3.3.2, the digital image analysis described in Section 3.3.3 and for supplementary geochemical analyses outlined in Section 3.5.

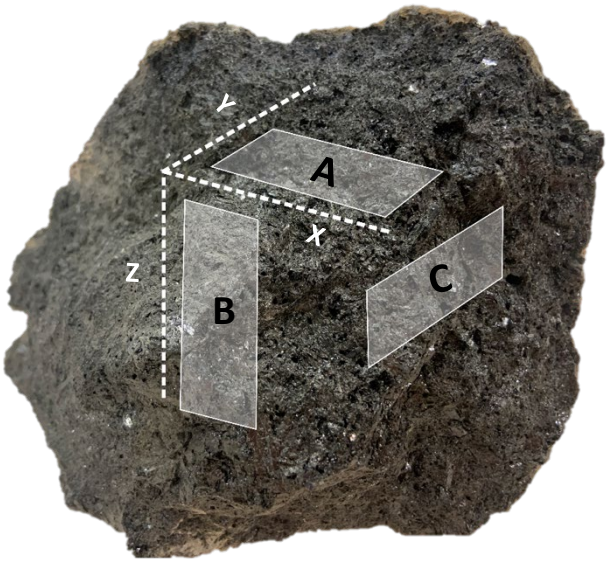

Figure 3.4 – Diagram demonstrating the relative orientation of thin sections cut from each sample. Because it is challenging to sample three-dimensional fabrics in two-dimensional thin sections, 3 thin sections were cut from each sample along an artificial X, Y and Z axis. Xenoliths are ex-situ in nature and so the thin sections are non-orientated and have no meaningful direction parameters.

3.3.2 Optical petrography

Qualitative descriptions of crystal and glass textures were undertaken using a binocular Nikon Microphot-FX microscope with 2, 4, 10 and 20 x objective lenses paired with a Nikon DS 5M camera. Descriptions of each thin section were generated from optical observations of textural features including grain boundary morphologies, glass distribution patterns and crystal shapes, which are challenging to quantitatively constrain using digital image analysis techniques. Photomicrographs were taken in plane- and cross-polarised light to record these features and to supplement the petrographic descriptions.

3.3.3 Quantitative textural analysis

The quantitative textural techniques described in this section were specifically used to quantify crystal textures. The methods used to constrain glass and vesicle textures are described in Section 3.4. Crystal textures were analysed using two-dimensional image analysis of digitised thin sections, utilising a combination of manual and automated analytical techniques.

3.3.3.1 Data acquisition

3.3.3.1.1 Manual digitisation

High-resolution (6016 x 4016p) whole-slide photographs were taken orthographically to the planar thin section surface in both plane and cross polarised light. With the aid of a petrographic microscope, crystal boundaries were manually traced atop the photographs using a stylus and graphics tablet in the graphic drawing software Adobe Illustrator CC2018. Any instances where the photograph was unclear (e.g. where minerals are photographed at extinction) were examined under a petrographic microscope before being drawn onto the image. All visible crystals were drawn, as well as boundaries of gas and liquid phases. However any

microlites in the glass were not traced, and examples where a crystal appeared to have been sectioned more than once (i.e. more than one optically continuous cross-section) were excluded from analysis. Each traced object was then classified to produce a digital slide map (Figure 3.5).

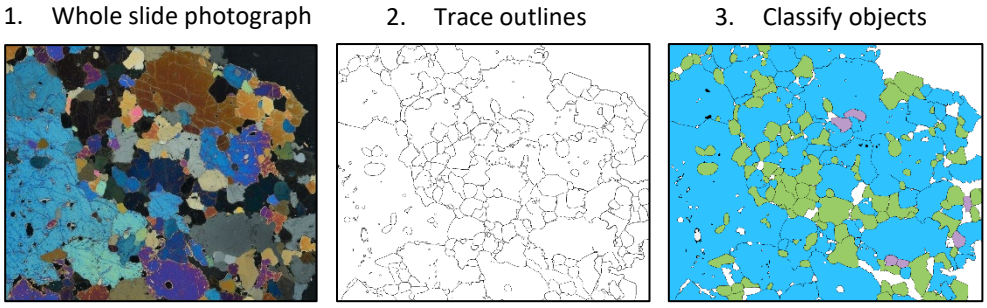

Figure 3.5 – Workflow summarising the manual digitisation process.

3.3.3.2 Data quantification

3.3.3.2.1 Phase abundance

A percentage area fraction of each identified mineral phase was measured by importing the digitised slide images into the digital image analysis software ImageJ and thresholding each phase by its assigned colour to produce a binary image. The percentage area occupied by each of the thresholded phases was used to calculate its total area fraction.

3.3.3.2.2 Crystal size distribution (CSD)

Crystal size distributions were calculated for essential mineral phases (hornblende + clinopyroxene) in each of the thin sections. Minerals present as accessory phases were excluded from the CSD analysis, unless the number density exceeded that of a more volumetrically abundant essential mineral phase. To calculate the CSD, binary images of the crystal populations were imported into ImageJ and used to

measure the long axis, short axis, area, perimeter and orientation of each crystal. The length and width of a crystal intersection can be defined in several ways; the exact definition used is not important but it must be consistent for all samples (Higgins, 2000). Here, these parameters were measured according to the best-fit ellipse (Figure 3.6).

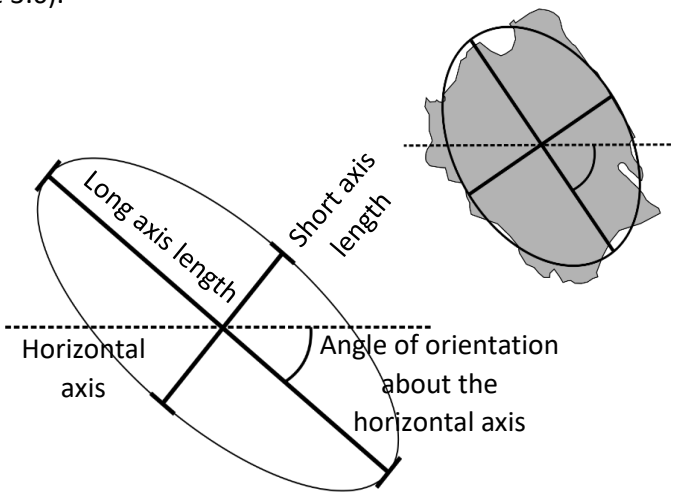

Figure 3.6 – Application of the best-fit ellipse used to measure two-dimensional crystal size parameters. To ensure a consistent methodology, all crystals were measured using this technique. The ellipse is fitted to the crystal outline based on its area, centroid and orientation.

Crystals truncated by the image boundary are not representative of their true size or shape and were excluded from the analysis. Although all visible crystals were traced and included in the digitised images, it is best practice to define a lower measurement limit based upon the resolution of the slide photograph being traced (e.g. Higgins, 2006a). This is because drawing inaccuracies will manifest the most in small crystals, leading to measurement artefacts in the CSD data. Following the recommendation of Higgins (2006a), 10 pixels was selected as the lower measurement threshold (70 µm). Crystals below this threshold are included in the CSDs to provide a representation of the whole crystal population, but are

highlighted on the CSD outputs to indicate potential measurement artefacts within particular size bins.

To calculate a three-dimensional CSD, the 2D shape data was imported into CSDCorrections v1.50, a programme specifically written for stereological conversion of crystal size data (Higgins, 2000). A CSD can be calculated if the sample meets the following criteria:

1. The sample size exceeds 250 crystals
2. A representative three-dimensional aspect ratio can be determined.

Although there is no universal minimum sample size required to calculate a CSD, Morgan and Jerram (2006) recommend that realistic CSDs cannot be produced from fewer than 250 crystals. To ensure that all of the CSDs exceeded this threshold, they were calculated by amalgamating all of the crystal shape data measured from the sample. Therefore, each CSD combines three thin sections, cut at different orientations. Three-dimensional aspect ratio was calculated using the Microsoft Excel macro CSDslice v5 (Morgan and Jerram, 2006). CSDslice produces a 3D aspect ratio (S:I:L) by comparing the 2D data to a database of 703 crystal habits to identify the best-fit shape curve. Using a linear regression, CSDslice then outputs the five closest-matching crystal habits and an R^2 value to measure how close the 2D data compares to the fitted regression line. An R^2 value >0.8 is considered representative of the true 3D crystal habit (Morgan and Jerram, 2006), which is then entered into the CSDCorrections interface.

Prior to calculating the CSD, CSDCorrections requires several pieces of information to be input by the user. The fabric and roundness of the crystal population was

estimated from the binarised images (block = 0; ellipsoid = 1). Crystal lengths were sorted into size bins with five bins per decade; this is considered the optimal number to avoid errors associated with having too few crystals in each size bin (Higgins, 2000; Higgins, 2006b). The total measured area was calculated as the sum of each of the three thin sections that were combined to produce the CSD.

The CSD output is a histogram, however the classic CSD plot is presented as a line graph for ease of interpretation (Higgins, 2000) that plots corrected crystal length against the natural logarithm of the population density (Marsh, 1988). There are three sources of error associated with the conversion of the 2D data into a three-dimensional population density. Two of these errors are associated with uncertainties in the probability parameters that are calculated for idealised crystal shapes and stereological conversion of 2D measurements to true 3D crystal lengths (Higgins, 2000). The third source of error is a counting error, which is taken as the square root of the number of crystals within each size interval. The uncertainties associated with quantifying the two probability errors mean that CSDCorrections only calculates the counting errors (Higgins, 2000). Error bars on the CSD data therefore only represent one of the three potential sources of error and should be considered as a minimum estimate. A summary of the steps taken to calculate the CSDs is provided in Figure 3.7.

1. Digitised slide image

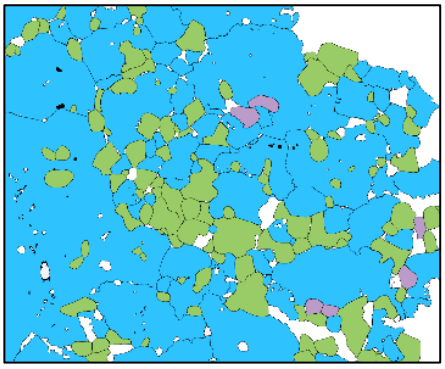

2. Binarise image, exclude truncated crystals

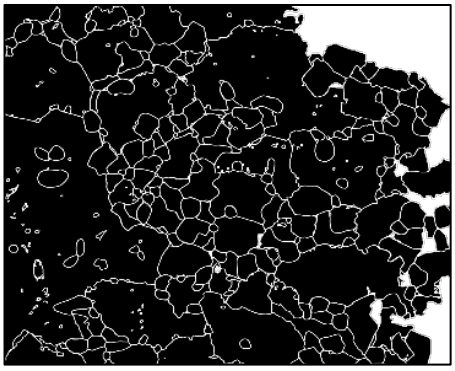

3. Quantify 2D shape parameters in ImageJ

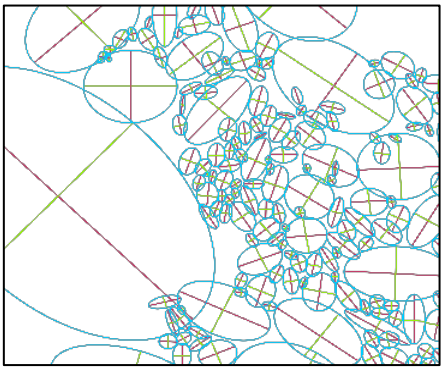

4. Calculate 3D aspect ratio in CSDSlice

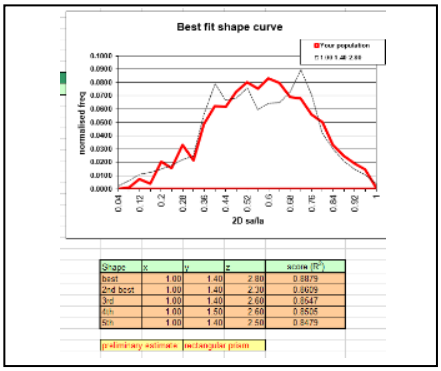

5. Input additional parameters (roundness, fabric etc)

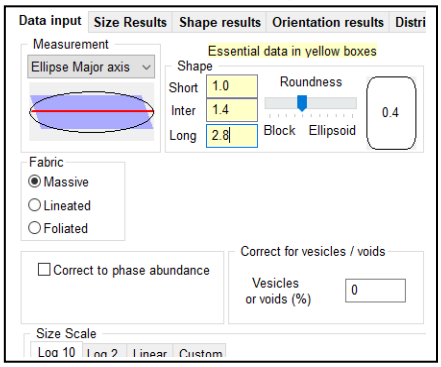

6. Calculate CSD

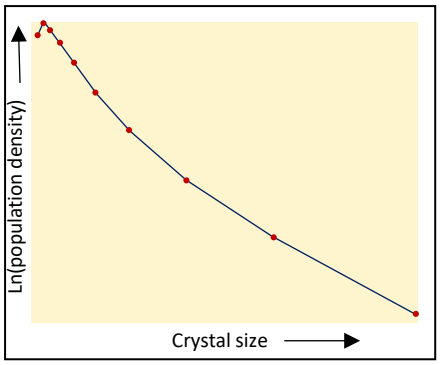

Figure 3.7 – Workflow summarising the steps taken to calculate a CSD. First, the digitised slide images are binarised and imported into ImageJ, which is used to calculate the long and short axis, area, perimeter and orientation of each crystal according to its best-fit ellipse. The 3D aspect ratio of the crystals are then calculated using CSDSlice and alongside estimates for crystal roundness, fabric, vesicularity, and desired number of bins per decade, input into CSDCorrections, to calculate the CSD.

3.3.3.2.3 Spatial distribution pattern (SDP)

Spatial distribution provides a measure of how clustered or random the distribution of crystals in a thin section are, and whether they form touching or non-touching frameworks (Jerram et al., 1996; Jerram et al., 2003; Mock et al., 2003). This provides an insight into the nucleation distribution of crystals (Jerram and Cheadle, 2000) as well as mechanical processes that act to influence the configuration and packing of crystals (Jerram et al., 1996; Jerram et al., 2003). The spatial distribution of the crystal populations were calculated following the methodology of Jerram et al. (1996), using the weighted centre point nearest neighbour method of Clark and Evans (1954). The spatial distribution factor is characterised by a parameter R, which represents a ratio of the mean nearest neighbour distance of a crystal population and the predicted mean nearest neighbour distance for a random distribution of points with the same population density (Jerram et al., 1996) and is given by:

$$R = \frac{r_A}{r_E} = \frac{\sqrt[2]{\rho}\sum r}{N} \quad (1)$$

where r_A is the mean nearest neighbour distance, r_E is the predicted nearest neighbour distance for a random distribution of points with the same population density, ρ is the density of crystals in the observed sample, r is the nearest neighbour distance of any particular crystal and N is the number of crystals measured. For a population of spherical objects, in a random distribution R =1, clustered points R <1 and for ordered points R >1 (Jerram et al., 1996) (Figure 3.8).

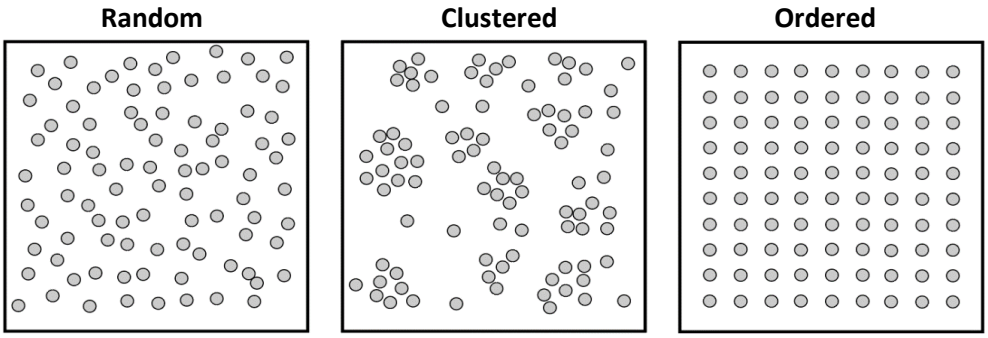

Figure 3.8 **-** Theoretical spatial distribution patterns for a population of monodisperse spheres. From: Higgins, 2006a.

3.2.3.2.4 Shape preferred orientation (SPO)

In the context of igneous textures, the term orientation typically encompasses two parameters: shape preferred orientation (SPO) and lattice preferred orientation (LPO). Here, orientation is used to refer to shape preferred orientation, which is a measure of the mean elongation direction of crystals. The software SPO 2003 (Launeau and Robin, 1996; Launeau and Cruden, 1998; Launeau, 2004) was used to calculate the shape preferred orientation of the digitised crystals using the of the crystal outline. Whereas ImageJ calculates the angle of orientation from the long axis of the best-fit ellipse, the inertia tensor method fits an orientation ellipse that has the same area and moment of inertia as the grain shape (Higgins, 1996b) (Figure 3.9). This gives an SPO which is weighted by the elongation of the crystal shape. To calculate a bulk SPO for the sample, the inertia tensor of all grains is used to calculate a bulk orientation ellipse, of which the contribution of each grain to the total orientation ellipse is weighted by its area (Launeau and Cruden, 1998) (Figure 3.10). From this, the coherence of the SPO was quantified by the ratio of the orientation ellipse axes (minor axis/major axis) (Higgins, 1996b). A sample with well aligned crystals will have an elongated orientation ellipse and hence a low ratio

value, whereas a sample with no preferred orientation will have a circular orientation ellipse and an axial ratio of one (Higgins, 1996b). As the xenoliths themselves are ex-situ and therefore not orientated, the SPO does not have any direction and is here used to quantify the preferred orientation of crystals relative to one another.

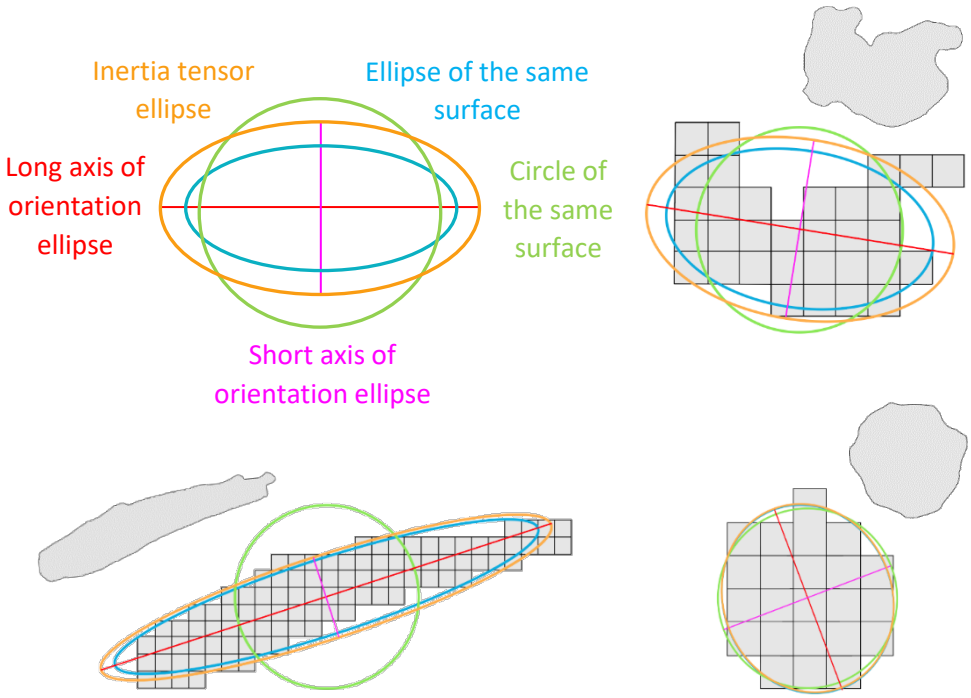

Figure 3.9 – Measurement of SPO for different grain shapes. Coloured ellipses demonstrate the ellipses used to calculate the SPO according to the shape of the crystal outline.

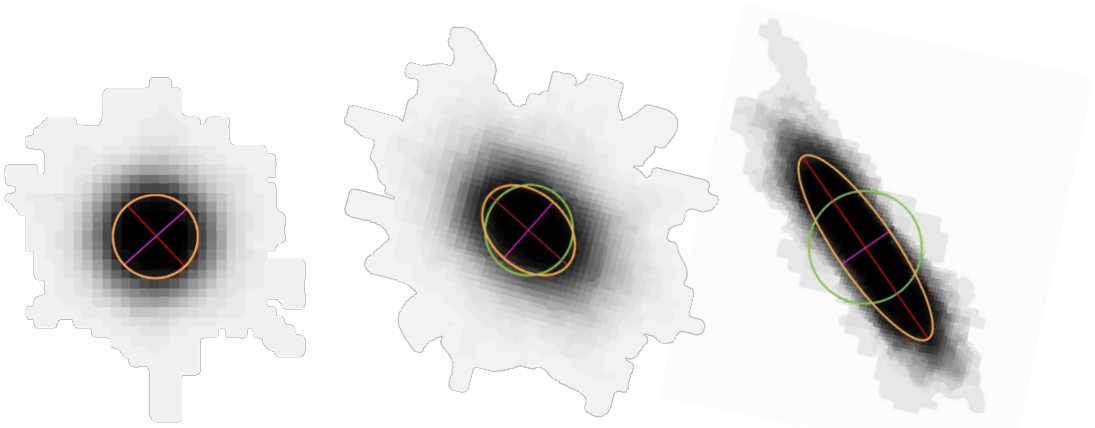

Minor axis = 1.45
Major axis = 1.46
Coherence = 0.98

Minor axis = 1.31
Major axis = 1.89
Coherence = 0.70

Minor axis = 0.68
Major axis = 2.60
Coherence = 0.26

Figure 3.10 – Measurement of a bulk SPO for a crystal population. Each crystal is divided by its area and the resulting shapes are stacked atop one another. This means that all grains have the same weight and their individual contributions to the bulk orientation ellipse are weighted by their area. The major and minor axis values are relative lengths and have no dimension. These values are used to calculate the coherence of the SPO: a coherence of 1 means that there is no shape preferred orientation, a value close to 0 means that the crystals are well aligned (Higgins, 1996b). Coloured ellipses represent the ellipses used in the SPO calculations, as described in Figure 3.9.

3.3.4 Potential limitations of two-dimensional analysis

It is widely acknowledged that working from 2D sections incurs a number of limitations associated with the planar viewing of a three-dimensional object. In particular, when a crystal population is intersected the 2D plane rarely dissects the centre of each crystal. Even in a homogenous population, the intersection surfaces will therefore exhibit a broad range of sizes around the modal value (Higgins, 2000). This is known as the cut section effect. In addition, the smallest crystals in a

polydisperse population are less likely to be intersected along any cut line. This acts to exaggerate the abundance of larger crystal sizes, distorting the true size distribution of the population (Higgins, 2000). This is referred to as the intersection probability effect. Potential limitations are also introduced from the assumption that all crystals in the sample have the same shape, which is unrealistic for magmatic systems (e.g. Lofgren, 1974). CSDCorrections is written to include mathematical corrections for the cut section and intersection probability effects, described in Higgins (2000), which aim to produce meaningful 3D CSDs from the two-dimensional data. All CSDs were calculated using CSDCorrections, and have therefore been corrected for these limitations. However, CSDCorrections does not account for potential variations in crystal shape, requiring one user determined 3D aspect ratio to perform the stereological conversions. To best overcome this limitation, CSDSlice was used to determine a 3D aspect ratio that best summarises the shape of the crystals within the CSD. Jaret et al. (2008) compared CSD methodologies and concluded that a method combining CSDSlice and CSDCorrections produces the most accurate estimation of 3D crystal shape and size distribution. By following this method, variations in crystal shape are incorporated into the 3D aspect ratio value used for the CSD calculations.

The main limitation of this methodology is that it is incredibly time consuming – in total over 2000 hours were spent completing the digitisations used in this thesis. This in turn limits the total number of samples that can be analysed. An alternative methodology is to utilise automatic image segmentation techniques (e.g. Bell et al., 2020). At present, there is no widely used automated technique that is appropriate for digitising polymineralic igneous rocks. Cone et al. (2020) undertook a comparison of automatic segmentation techniques versus manual tracing to

extract plagioclase crystal lengths and concluded that manual methods provide the most accurate assessment of crystal length, regardless of texture. Bell et al. (2020) utilised geochemical mapping as a semi-automated technique for crystal size distribution analysis, but found that this produced an upwards shift in CSD diagrams, caused by the inability to accurately separate touching grains of the same mineral phase. They concluded that manual methods remain superior for accurately segmenting polycrystalline igneous samples. It was therefore decided that the pay off between the number of samples that can be analysed versus the inaccuracies introduced with automated techniques was worthwhile, and a manual approach was utilised in this study.

3.4 Three-dimensional analysis

3.4.1 X-ray Computed Tomography (CT)

X-ray computed tomography (CT) is a non-destructive technique that can be used to visualise the internal structures of opaque geological samples. The sample is placed between an X-ray source and detector, and X-rays are variably attenuated as they pass through materials of differing atomic composition and density (Figure 3.11). Two-dimensional radiographs are acquired from different positions as the sample is rotated about its Z-axis, which are then stacked in a direction perpendicular to the axis of rotation to produce a three-dimensional image. The output is composed of three-dimensional pixels (voxels) which represent a 3D matrix of linear X-ray coefficient values (μ). The value of μ is a measure of X-ray absorption, and is a function of a material's atomic number, density and the X-ray energy used in the study. μ is represented as a greyscale value on the final tomographic output. Different greyscale values correspond to different rock

phases, permitting visualisation, classification and measurement of the 3D output and its constituents.

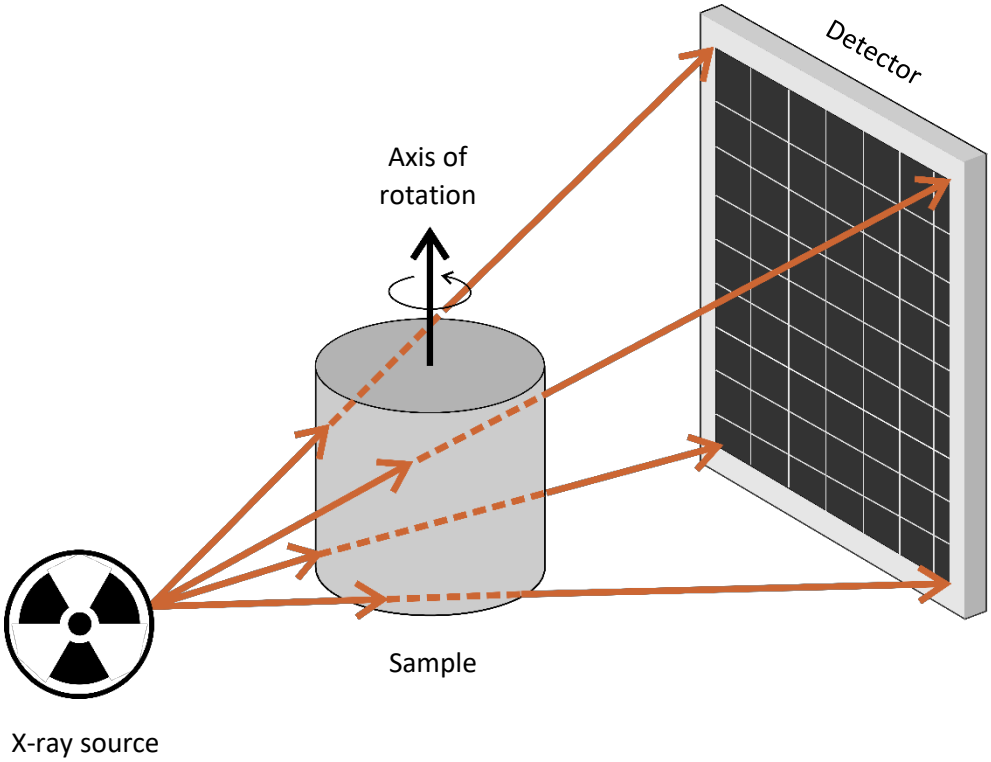

Figure 3.11 **–** Schematic representation of a typical CT setup. The sample is illuminated by a fan shaped beam of coplanar X-rays which are variably attenuated as they pass through the sample. The transmitted X-rays are measured and recorded by a detector system and recorded as a 2D radiograph. Redrawn and modified from Withers et al. (2021).

3.4.1.1 Sample preparation

The only essential sample preparation for CT scanning is to ensure that the sample will fit within the field of view and that it will remain stationary. Although it is not essential to sub-sample the rock volume, a cylindrical geometry will ensure equal penetration of the X-ray beam and reduce the influence of scan artefacts (e.g.

Ketcham and Carlson, 2001). Additionally, although the CT resolution is controlled by the intensity of the X-ray source and the size of the detector, it is ultimately constrained by the sample volume: smaller volumes yield higher voxel resolutions (Pamukcu and Gualda, 2010). This requires that the sub-volume size is large enough to be texturally representative of the sample, but small enough to achieve a voxel resolution that will include the smallest objects. Figure 3.12 shows the dimensions of the cored sub-volumes used in the CT analysis.

3.4.1.2 Data acquisition

CT images were obtained at the London Natural History Museum Imaging and Analysis Centre, using a Nikon Metrology HMX ST 225 micro-CT scanner. The scanner utilises polychromatic X-rays with a maximum accelerating voltage of 250 kV. A voltage of 140 kV was selected for these samples, chosen as sufficient to penetrate the sample volume and be recorded by the transmission target. This generated a voxel resolution of 10.27 μm^3. One image stack was produced for each sample, comprised of between 1012 and 1014 16-bit tiff images.

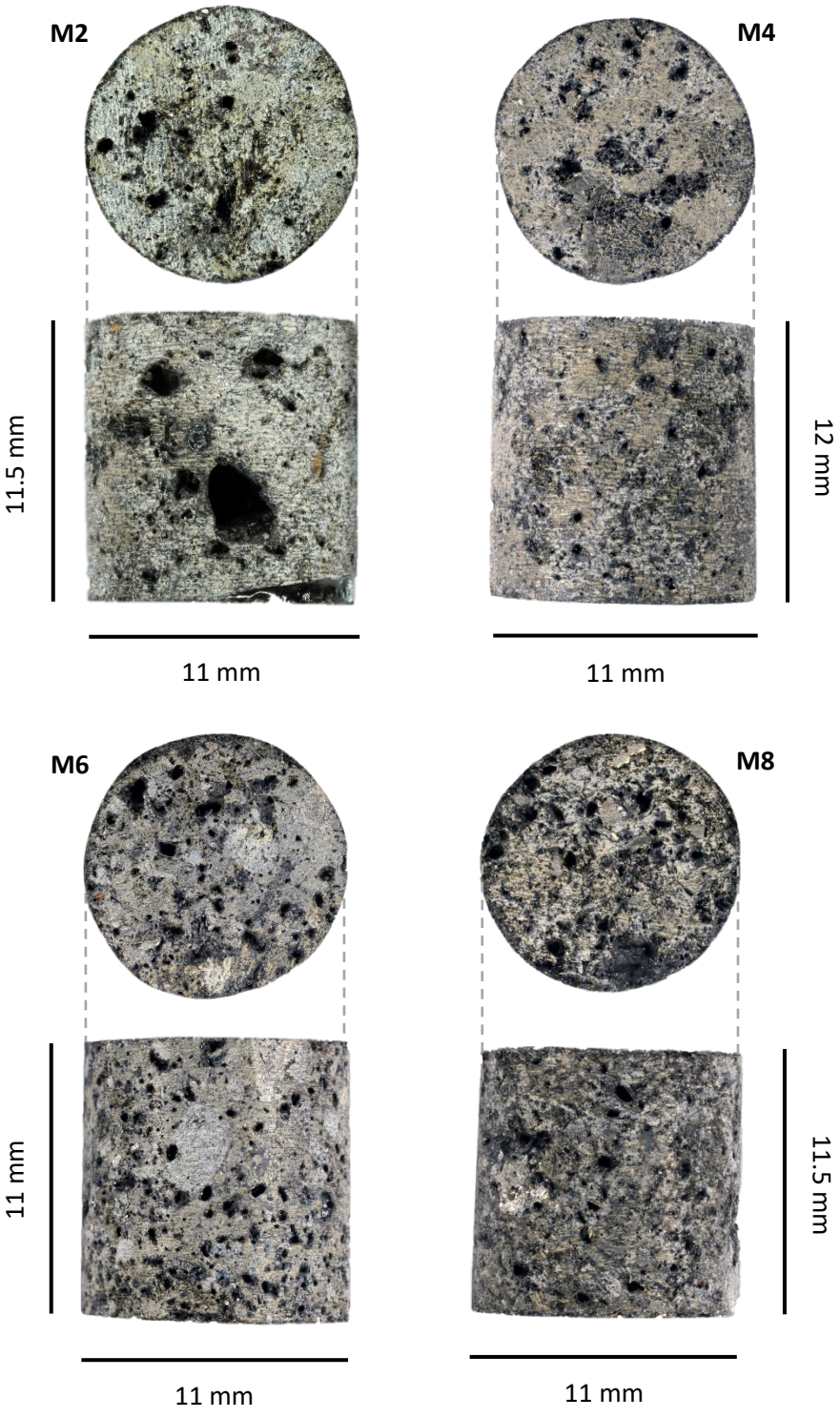

Figure 3.12 – Photographs of the cored xenolith sub-volumes.

3.4.1.3 Data processing

Data processing and quantitative analysis was predominantly undertaken using the commercial software package PerGeos version 1.7.0 (Thermo Fisher Scientific), designed specifically for digital rock analysis from CT data. Analysis was undertaken on a cuboidal sub-volume that was extracted from the centre of each sample. This removed exterior voxels and upper and lower slices that exhibited significant CT artefacts (e.g. beam-hardening).

3.4.1.3.1 Beam hardening

In samples M2 and M6 it was clear that the data output showed significant beam hardening – a common artefact that occurs as a consequence of using a polychromatic X-ray beam. This manifests on the CT output as an artificial darkening in the centre of the image. Beam hardening acts to make CT processing and segmentation more challenging by changing the greyscale value of a material depending on its position within an image. To minimise this effect, a beam hardening correction algorithm was applied within PerGeos. This correction applies a simple filter that computes the average radial greyscale intensity profile of the image stack, which is then smoothed with a Gaussian filter and normalised. All grey scale intensities in the image stack are then divided by the smoothed profile to perform a radial greyscale averaging.

3.4.1.3.2 Noise reduction

CT image noise manifests as an artificial change in pixel values in an otherwise homogenous region, resulting in the degradation of the visual information. This generates a grainy image texture and reduces image contrast. To reduce this effect, an anisotropic diffusion filter was first used to smooth pixels in the CT volume,

whilst preserving object edges. Using the default PerGeos parameters, the anisotropic diffusion filter reduces noise by comparing the value of each voxel with the value of its 6 neighbouring voxels. If the difference between the current voxel and the neighbour voxels is below the diffusion threshold then there is diffusion and pixel smoothing. Secondly, an iterative median filter was used to further attenuate noise by setting the pixel value to the median of the three-dimensional neighbourhood. This process was iterated 3 times within each sample. Figure 3.13 shows the outcome of this filtering process, resulting in an enhanced image quality and increased phase contrast. A summary of the data acquisition and processing parameters is provided in Table 3.2.

3.4.1.3.3 Segmentation

The CT image stacks were manually segmented according to the greyscale intensities of the sample components. Manual segmentation involves identifying the greyscale range that represents each phase. The assigned greyscale threshold is used to segment the image through each 2D slice, generating a 3D labelled volume. Three phases were segmented from the sub-volumes: glass, holes and crystals.

▶ ***Figure 3.13 (overleaf)*** **–** Results of the image filtering process. Zoomed images show the enhanced image quality produced by applying the anisotropic diffusion and iterative median filters. The grainy texture in the raw image is significantly reduced, meaning that the segmentation process is simplified.

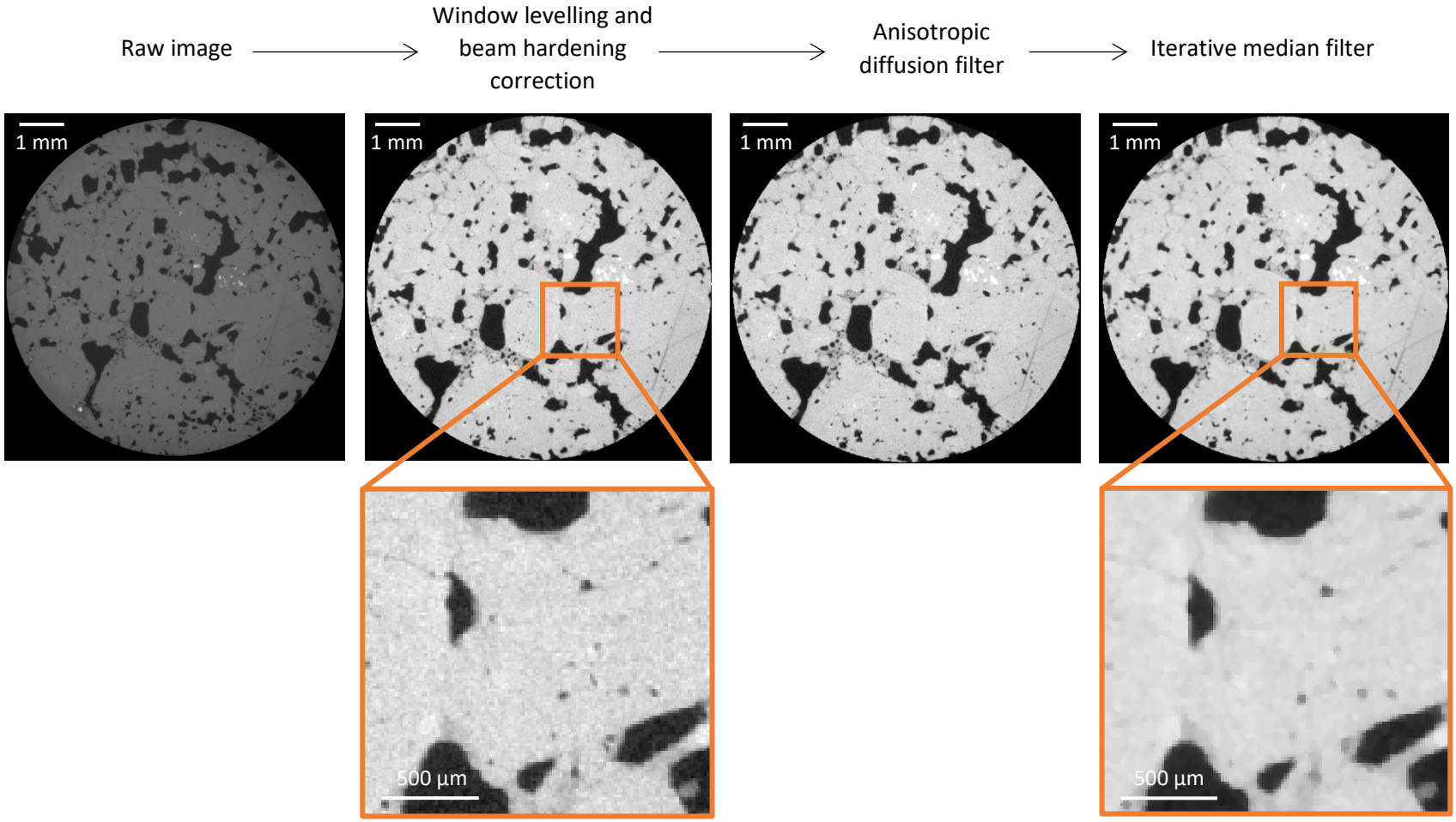

Figure 3.13 - ◄ Caption overleaf

Sample	Core dimensions (mm)	Cuboidal sub-volume dimensions (µm)	Voxel resolution (μm^3)	Filtering		
				Beam hardening correction	Anisotropic diffusion filter	Iterative median filter
M2	11 x 11.5	5135 x 5135 x 8216	10. 27	✓	✓	✓
M4	11 x 12	5340 x 5340 x 8216	10.27		✓	✓
M6	11 x 11	5340 x 5340 x 8216	10.27	✓	✓	✓
M8	11 x 11.5	5340 x 5340 x 8216	10.27		✓	✓

Table 3.2 – Summary of CT parameters used for the acquisition and processing of the xenolith sub-volumes

3.4.1.4 Data analysis

3.4.1.4.1 Porosity calculations

Porosity here refers to the fraction of the xenolith samples that was not solidified prior to entrainment and eruption, representing the melt fraction. As such, any segmented voxels labelled as glass or hole are considered to represent porosity. The PerGeos 'porosity' tool was used to calculate the total volume of porosity according to the sum of the segmented hole and glass phases. This establishes a binary segmentation, where any voxels assigned to the crystal phase were assumed to be impervious and any assigned to the glass and hole phases constitute porosity. It is important to remember that the resolution of the images defines a minimum threshold for identifiable porosity, meaning that any porosity below the resolution of the images is excluded (e.g. Thomson et al., 2019). To define the proportion of connected porosity, the PerGeos 'axis connectivity' tool was used to remove disconnected pore-phase voxels that do not belong to a connected pathway in any defined direction. Connected voxels were defined according to the most strict definition, specifying connectivity as six voxels with a shared face. This strict definition was selected to avoid an overestimation of connectivity. This tool was applied along the X, Y and Z orientations to identify a fully connected pore network in all directions, producing one value of connected porosity for each sample.

3.4.1.4.2 Pore network modelling

Pore network models (PNM) were constructed using the PNM extension in PerGeos, following a methodology described by Youssef et al. (2007) and utilised in a number of porosity studies (e.g. Thomson et al., 2018; 2019; 2020; Payton et al., 2021). This process is broken down into several steps (Figure 3.14). Firstly, a distance map of the pore space volume is created. Distances are measured inwards

from the solid crystal boundaries. Secondly, this distance map is eroded to form a one voxel thick skeleton that retains the original geometry of the pore network. Next, this skeleton is expanded to identify pores and throats. Regions of the skeleton that are one voxel thick are classified as throats, whereas a pore is identified as a point where two or more throats intersect to define a void space (Thomson et al., 2020). A number of geometric parameters can then be obtained from the PNM, described in Table 3.3. To provide a visual supplement to this quantitative data, the pore network models are also presented as ball and stick models, where the pores are scaled according to diameter and throats are scaled constantly.

▶ ***Figure 3.14 (overleaf)*** **–** Steps taken in the process of generating a pore network model in PerGeos. This network model is visualised as a ball and stick model. Balls (red spheres) represent pores, scaled according to the maximum radius of a sphere that would fit within the pore volume. Throats are represented by the sticks, which visualise the connectivity between pore spaces. See Thomson et al. 2018; 2019; 2020 and Payton et al. (2021) for more detailed descriptions of the PerGeos methodology.

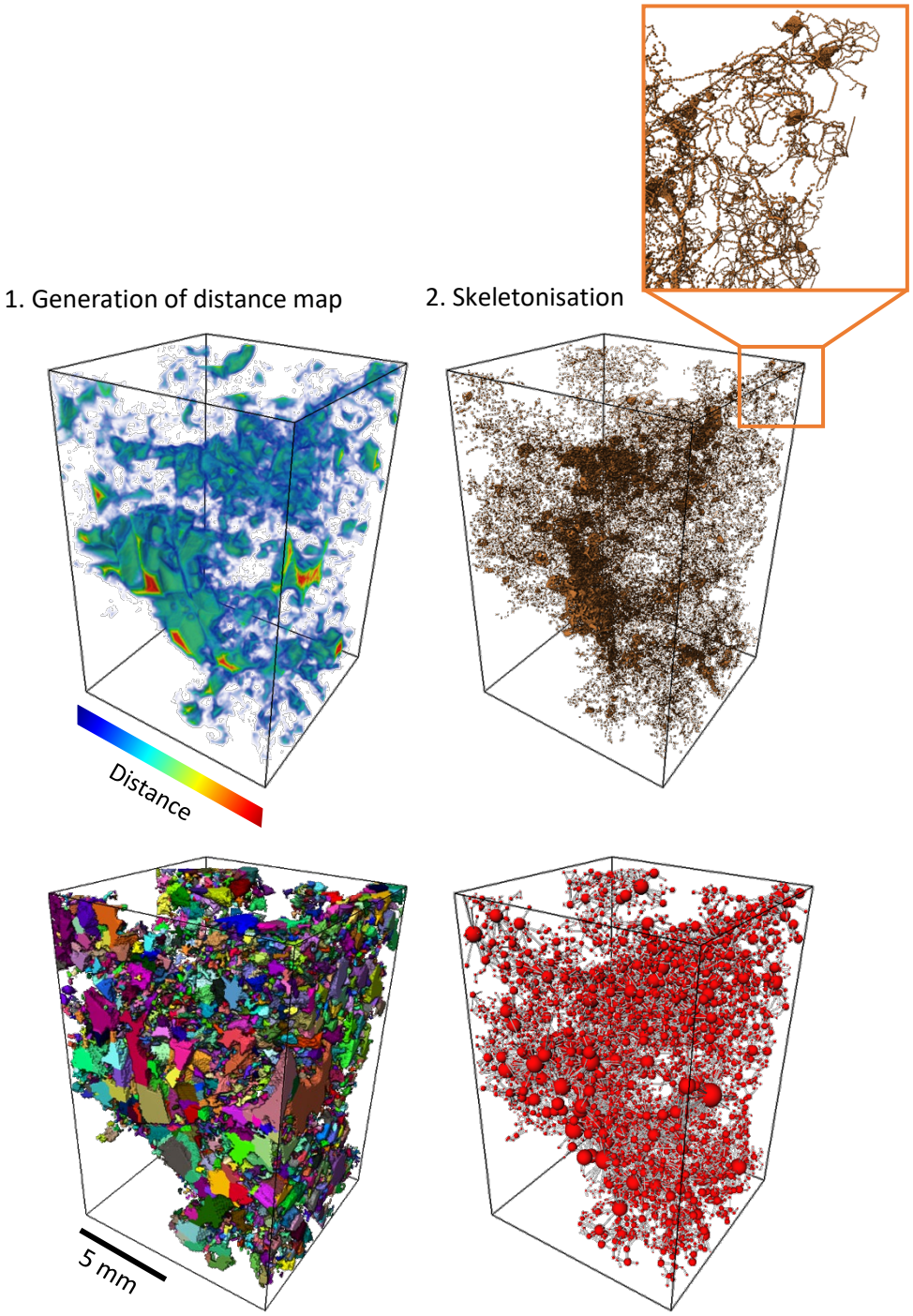

Figure 3.14 - ◄ Caption overleaf

Parameter	How it is calculated
Coordination number	The number of throats that intersect each pore. Coordination number defines the connectivity of the sample.
Equivalent radius (pores)	The one voxel thick skeleton is expanded to fit the boundary of the pore. From this, the equivalent radius is calculated as the maximum radius of a sphere that can fit within each pore.
Equivalent radius (throats)	The skeletonised throat is expanded to calculate the maximum radius of sphere that would fit within the throat.
Number density (pores and throats)	The number of pores or throats divided by the volume of the CT sub-volume.
Tortuosity	Geometrical tortuosity calculated as the ratio between the true length of a path and the straight line distance between the start and end points (see Fu et al., 2021). Computed using a pore centroid method integrated into PerGeos. A tortuosity value of 1 indicates a perfectly straight path, increasing values indicate more tortuous pathways.

Table 3.3 – Parameters that describe geometry of the pore network model and how they are calculated.

3.4.2 Potential limitations of three-dimensional analysis

The main limitation of the three-dimensional methodology is that X-ray attenuation occurs independently of crystallographic attenuation, meaning that CT images do not show grain boundaries and that individual crystals belonging to the same phase cannot be separated as discrete objects. Whilst the technique can provide a valuable insight into the three-dimensional relationship between phases with

contrasting chemistries and/or densities, it is not possible to use it to analyse the textural properties of individual mineral phases. Specifically, crystal size distributions cannot be measured accurately if a cluster of touching crystals cannot be correctly divided into separate crystals. The porosity fraction did not necessitate any object separation and could be analysed with this methodology, but the crystal fraction was unsuited for this technique. This therefore limited its application within these samples.

Another potential limitation of the CT data is that the voxel resolution is constrained by the volume of the material being analysed. This requires that the sub volume size is large enough to be texturally representative of the sample, but small enough to achieve a voxel resolution that will include the smallest objects. Because the CT core is essentially taken blindly from the sample, it was necessary to core a large enough volume to account for the largest crystals (in some instances exceeding 2 cm in length) being included within the core and occupying the majority of the volume. However, by increasing the field of view the resolution also decreases, meaning that small scale features may be present which are unresolvable at the necessary field of view. Consequently, regions of possible microporosity and pore connectivity may have been lost as they are smaller than the voxel resolution achieved for the necessary volume of material to be imaged. This has the potential to have significant impact on the overall measured connectivity of a particular study volume.

3.5 Geochemical analysis

Geochemical analysis was undertaken to supplement the textural observations and data, utilising Laser Ablation Inductively Coupled Plasma Mass Spectrometry (LA-ICP-MS). Major and trace element compositions in clinopyroxene, hornblende, phlogopite and glass were analysed in situ from thin sections using the LA-ICP-MS system at Royal Holloway University. The system couples a Resonetics 193nm ArF excimer laser coupled to an Agilent 8900 ICP-QQQ ICPMS. The LA-ICP-MS is tuned prior to analysis using a synthetic glass standard NIST612 to maximise the peak to background ratio across the mass range and achieve a $^{232}ThO/^{232}Th$ ratio of <0.2% and a $^{232}Th/^{238}U$ ratio >0.9. All minerals were analysed using the ablation parameters outlined in Table 3.4 and the acquisition parameters outlined in Table 3.5. Data was normalised using the chromium augite (NHM 164905) for major elements and NIST glass 612 (Jarosewich, 2002) for trace element concentrations. NIST 610 was also run as an external standard to check for short and long term drift. Data processing was undertaken using the method of Thirlwall et al. (unpublished) which utilises stoichiometric relationships to determine major element concentrations assuming totals of 100% for clinopyroxene and glass and 94% for hornblende and phlogopite to allow for water content.

ICPMS – Agilent 8900	
RF power	1280-1320 (optimised during tuning)
Carrier gas flow	~0.5 ml/min (optimised during tuning)
Coolant gas flow	15 l/min
Aux gas flow	1 l/min
Sampler/skimmer cones	Ni
Laser ablation system	
Energy density (fluence) on target	27 mj/cm^2
ThO+/Th+	<0.2%
He gas flow	850 ml/min
N2 gas flow	6 ml/min
Laser repetition rate	5Hz
Spot size	57 µm
Standards	NIST610 and 612, Cr Augite Cpx standard

Table 3.4 – ICPMS tuning and ablation parameters for mineral analysis

Isotope	Dwell time
^{7}Li	0.02
^{23}Na	0.01
^{25}Mg	0.01
^{27}Al	0.01
^{29}Si	0.01
^{39}K	0.02
^{44}Ca	0.01
^{45}Sc	0.01
^{49}Ti	0.01
^{51}V	0.01
^{53}Cr	0.01
^{55}Mn	0.01
^{57}Fe	0.01
^{60}Ni	0.01
^{85}Rb	0.02
^{88}Sr	0.02
^{89}Y	0.02
^{90}Zr	0.02
^{93}Nb	0.05
^{137}Ba	0.03
^{139}La	0.03
^{140}Ce	0.02
^{146}Nd	0.02
^{149}Sm	0.02
^{153}Eu	0.02
^{157}Gd	0.02
^{163}Dy	0.02
^{166}Er	0.02
^{172}Yb	0.02
^{178}Hf	0.05
^{208}Pb	0.02
^{232}Th	0.02
^{238}U	0.02

Table 3.5 **–** Data acquisition parameters for LA-ICP-MS mineral analysis.

3.6 Summary

A summary of the methodologies used in this thesis is provided in the following:

- Owing to the textural complexity of these samples, a combination of two- and three-dimensional techniques were used to quantify the crystal and melt textures. The crystal textures are most appropriately studied in thin section, utilising stereological corrections to derive 3D datasets. Because the melt textures did not necessitate any object separation, they were suited for 3D analysis using X-ray computed tomography (CT).
- Crystal textures were analysed qualitatively using a petrographic microscope, and then quantified by manually digitising thin sections for the application of digital image analysis techniques.
- Crystal size distributions were calculated using the software CSDCorrections, incorporating information about 3D crystal habit from the Excel macro CSDSlice. CSDs were calculated by amalgamating the crystal size data from three thin sections cut at different orientations within each sample, ensuring the sample size exceeded the recommended minimum of 250.
- Spatial distribution patterns were calculated using the methodology of Jerram et al. (1996), measured as the ratio of the mean nearest neighbour distance of a crystal population and the predicted mean nearest neighbour distance for a random distribution of points with the same population density.
- Shape preferred orientations were calculated using the software SPO 2003, which uses the inertia tensor of the crystal outline to give a directionless orientation parameter, weighted by the elongation of the crystal shape.

- The porosity fraction of the samples (glass + holes) was measured in three-dimensions using CT. The data was analysed by constructing pore network models in PerGeos, providing quantitative measures of connectivity and pore geometries.

Optical Petrography and Mineralogy

This chapter presents the results of the qualitative thin section analysis, focusing on textural characteristics and relationships that cannot be quantified with CSD, SDP or SPO analysis. These observations are supplemented by geochemical data, obtained through LA-ICP-MS. Together, these results describe the array of amphibole, clinopyroxene, accessory mineral and glass textures that characterise the xenolith samples.

4 Optical Petrography and Mineralogy

4.1 Hand specimen observations

The xenoliths comprise part of a larger sample suite, consisting of xenoliths that range in size between ~5-20 cm, and vary from sub-angular to rounded (Figure 4.1A). Rounding of the xenoliths likely reflects some degree of transport and erosion. The basaltic host material is sometimes preserved as a rim (~1 cm thick) around the xenolith material (Figure 4.1 B). In thin section, this host predominantly contains phenocrysts of rounded olivine and green-cored clinopyroxene, similar to those documented by Duda and Schmincke (1985).

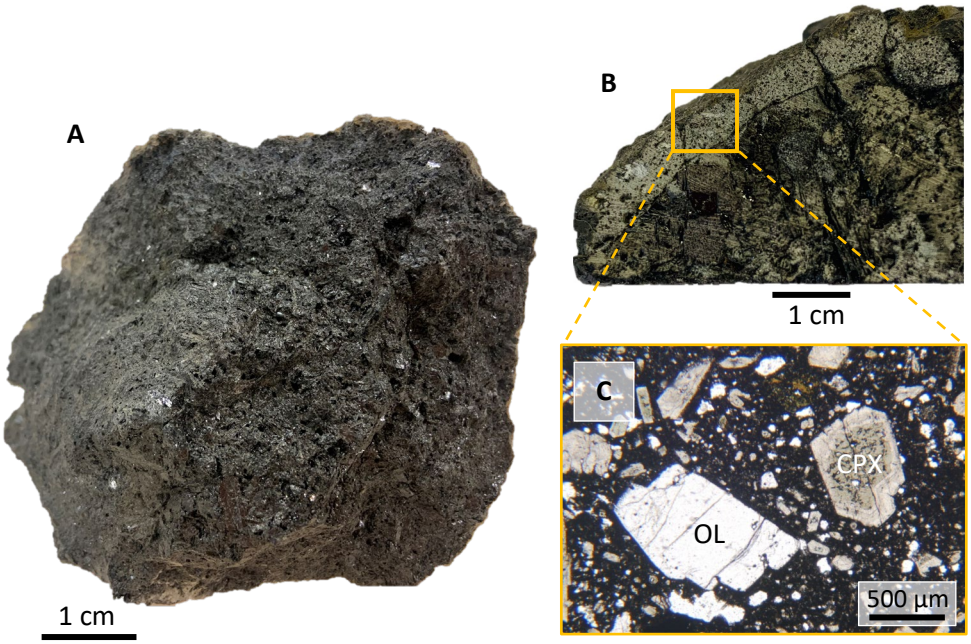

Figure 4.1 **–** Hand specimen photographs of sample M2. **A)** Photograph of the xenolith taken before any thin sectioning or coring. **B)** Photograph of the cut thin section, revealing the rim of host basalt that mantles the sample. **C)** Photomicrograph of the host basalt in thin section, taken in plane polarised light. Phenocrysts are rounded olivine and green, sieve cored clinopyroxene.

4.2 Thin section analysis

The four samples share the same general mineral assemblage (amphibole + clinopyroxene + phlogopite ± apatite ± olivine), and are characterised by the presence of interstitial glass. They have previously been termed clinopyroxenites and hornblendites and described as cumulates by Becker (1977) and Downes et al. (2004). Textural observations are supplemented with in situ geochemical data which is presented in Appendix 3.

4.2.1 Amphibole

Amphibole constitutes an essential mineral phase in all of the samples. The major element compositions of the amphiboles show that they are calcic amphiboles according to the criteria of Leake et al. (1997) ($Ca_B \geq 1$; $(Na+K)_A \geq 0.5$). When categorised according to this classification, they plot as titanium rich pargasites with Mg#s from 65.6-77.1 and titanium contents between 3.1-4.7 wt% TiO_2 (Figure 4.2). To fit with the nomenclature applied to the amphibole rich assemblages represented by these xenoliths, commonly referred to as 'hornblendites', the amphibole is more broadly referred to as hornblende throughout this study.

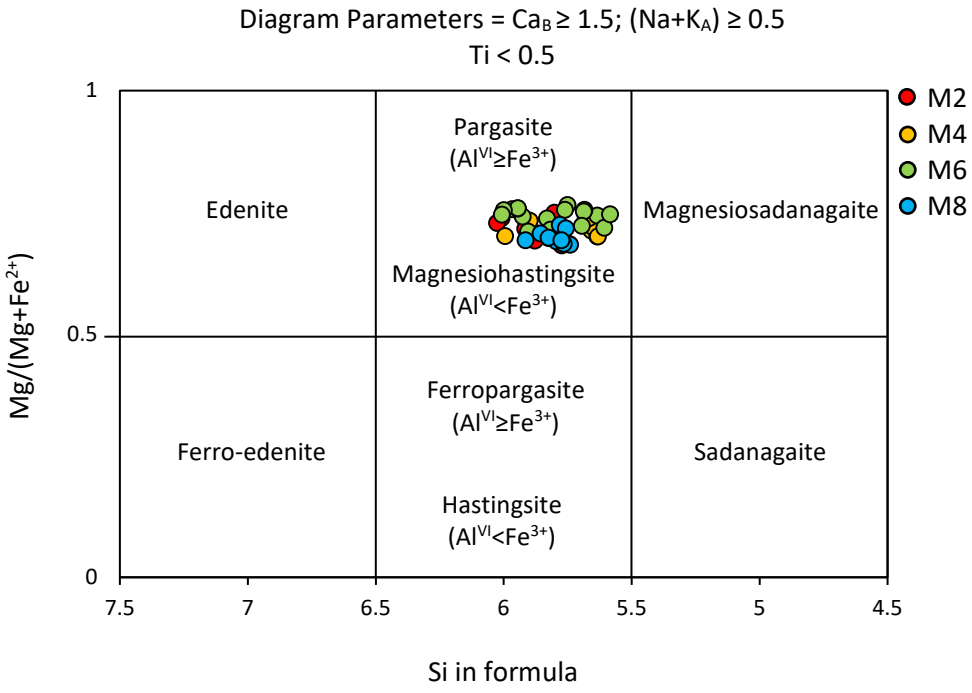

Figure 4.2 **–** Classification of amphiboles according to Leake et al. (1997). Formula units obtained according to Putirka (2016). Fe^{3+} calculated using an Excel spreadsheet from Putirka (2008), using the Fe^{3+}/Fe_{total} calculation of King et al. (2000).

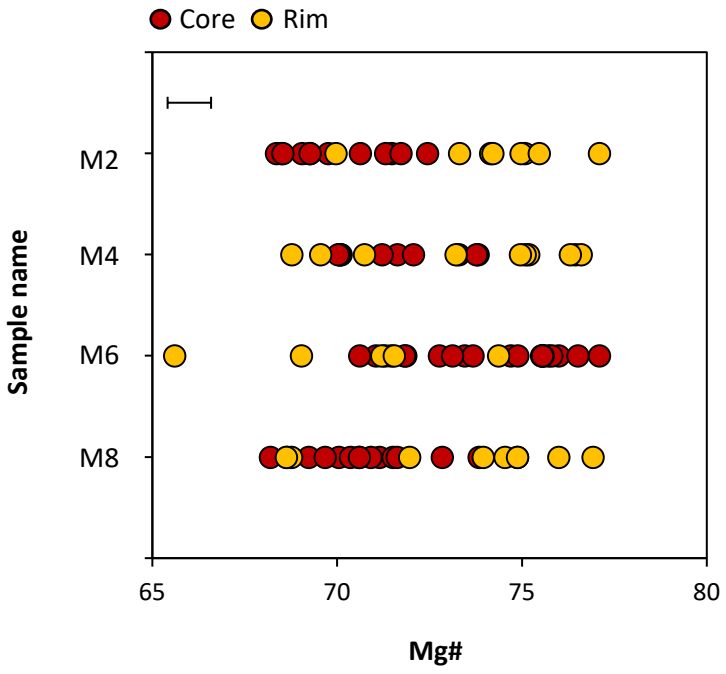

Figure 4.3 **–** Variation in amphibole Mg# between different samples. Red circles indicate core analyses, yellow circles are rim analyses. Mg#s show a range within samples, but overlap between samples. Error bar represents 2 standard deviations.

The hornblende exhibits a wide array of textures, both within and between samples. Significantly, the hornblendes do not appear to have a constant crystallisation sequence; textural differences identify early (non-poikilitic) (Figure 4.4A-B) and later (poikilitic) (Figure 4.4C-D) appearing hornblendes, but their compositions have overlapping Mg#s and major and trace element compositions (Figures 4.5 and 4.6). Representative mineral chemistries are provided in Tables 4.1 and 4.2.

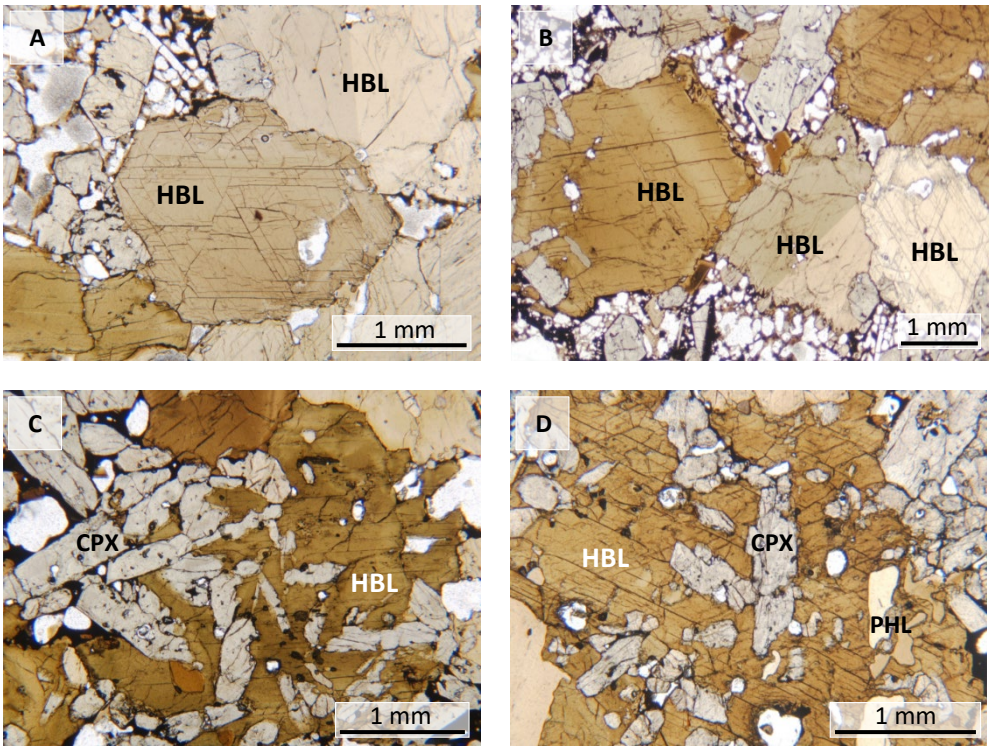

Figure 4.4 **–** Photomicrographs of non-poikilitic and poikilitic hornblende textures, taken in plane polarised light. **A and B)** Early forming (non-poikilitic) hornblende textures. The crystals are subhedral in habit and do not contain inclusions of other minerals. **C and D)** Later forming hornblende textures, characterised by poikilitic hornblende enclosing clinopyroxene and phlogopite chadocrysts.

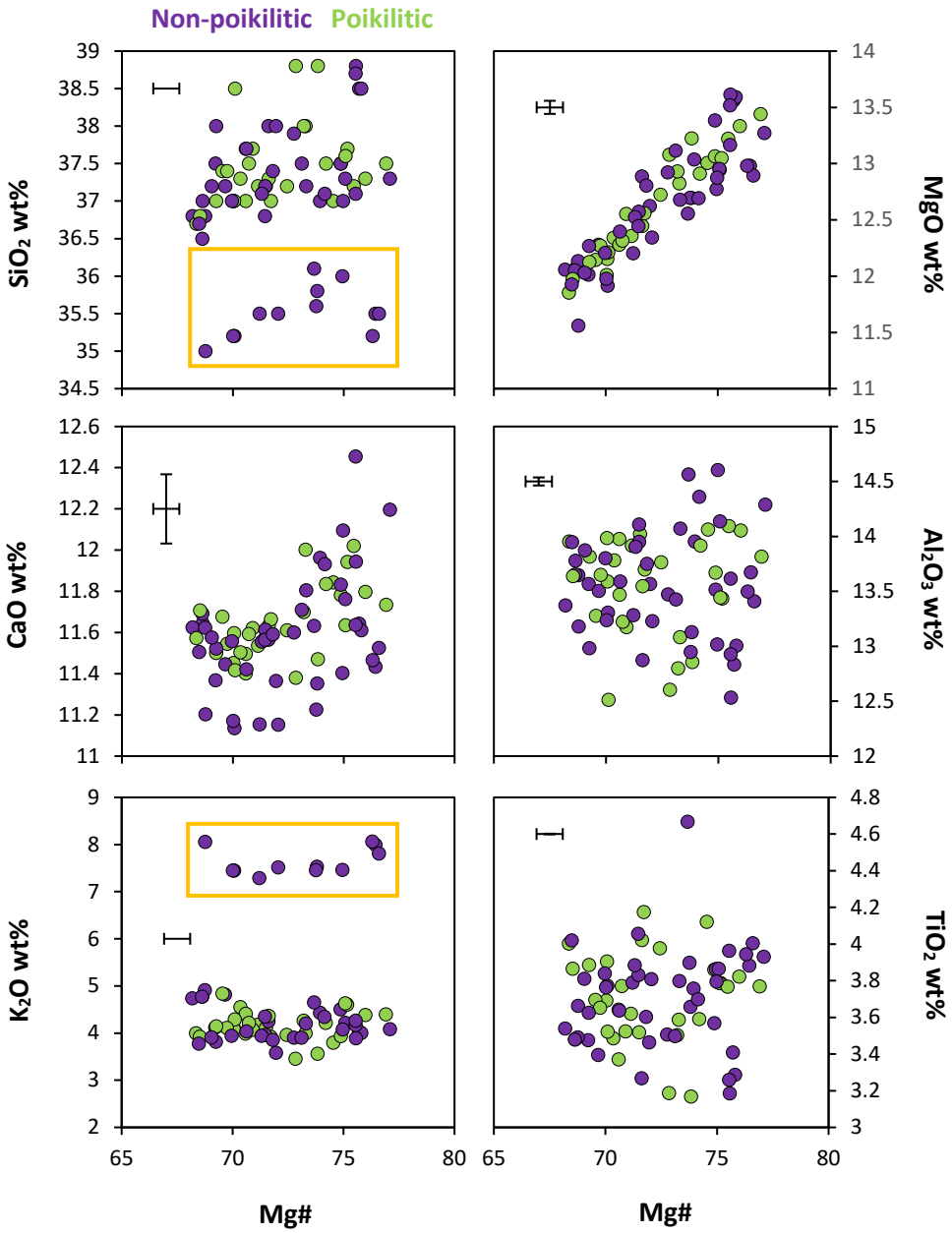

Figure 4.5 – Hornblende major element compositions, plotted according to textural classification. Major element compositions show an overlap despite the textural discrepancy between poikilitic and non-poikilitic crystals. The exception to this is highlighted by the yellow boxes, which represent the non-poikilitic hornblendes measured in sample M4. These crystals are enriched in K_2O and depleted in SiO_2 relative to hornblendes measured from the other samples. Error bars represent 2 standard deviations. Error bars for SiO_2, K_2O and TiO_2 are smaller than the data markers.

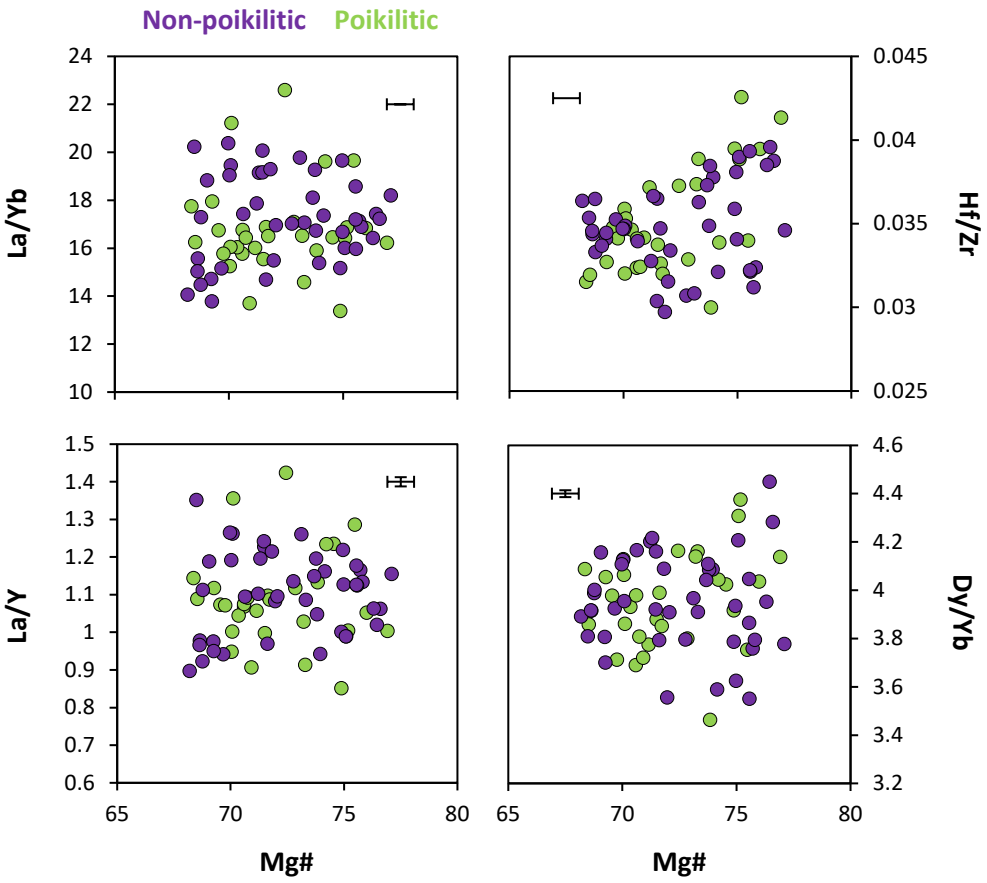

Figure 4.6 – Hornblende trace element ratios, plotted according to textural classification. Error bars represent 2 standard deviations.

	M2								M4							
	Non-poikilitic		Non-poikilitic		Poikilitic		Poikilitic		Non-poikilitic		Non-poikilitic		Poikilitic		Poikilitic	
	Core	Rim	Core	Rim	Core	Rim	Core	Rim	Core	Rim	Core	Rim	Core	Rim	Core	Rim
SiO_2	37.00	37.50	37.00	37.00	37.20	37.00	37.70	37.50	35.50	35.50	35.50	35.00	37.00	37.70	38.00	38.00
TiO_2	3.69	3.86	3.48	3.76	3.52	4.12	3.37	3.77	3.79	3.88	3.81	3.66	3.90	3.79	3.59	3.50
Al_2O_3	13.99	13.67	13.78	13.96	14.02	14.06	13.47	13.81	13.28	13.67	13.23	13.18	13.59	13.43	13.08	12.80
FeO	9.16	7.81	9.83	8.19	8.85	7.92	9.12	7.19	8.79	7.13	8.53	9.36	9.26	7.68	8.33	8.44
MnO	0.10	0.08	0.11	0.08	0.10	0.08	0.11	0.07	0.10	0.07	0.09	0.10	0.10	0.07	0.09	0.09
MgO	12.01	13.06	12.07	13.04	12.46	13.01	12.28	13.44	12.20	12.98	12.34	11.56	12.15	13.05	12.82	12.93
CaO	11.45	11.78	11.65	11.96	11.59	11.84	11.40	11.73	11.15	11.43	11.15	11.20	11.60	11.94	12.00	11.70
Na_2O	1.82	1.78	1.86	1.84	1.84	1.73	2.04	1.92	1.98	1.75	1.98	1.81	2.21	1.97	2.12	2.14
K_2O	4.13	3.94	4.78	4.43	4.11	3.80	4.41	4.40	7.29	8.00	7.51	8.06	4.08	4.60	4.00	4.26
Total	93.35	93.48	94.56	94.26	93.69	93.56	93.90	93.83	94.08	94.41	94.14	93.93	93.89	94.23	94.03	93.86
Mg#	70.04	74.88	68.64	73.95	71.50	74.54	70.59	76.91	71.21	76.44	72.06	68.77	70.06	75.17	73.29	73.21

	M6							M8							
	Non-poikilitic							Non-poikilitic		Non-poikilitic		Poikilitic		Poikilitic	
	Core	Rim	Core	Rim	Core	Core	Core	Core	Rim	Core	Rim	Core	Rim	Core	Rim
SiO_2	36.10	36.00	36.70	37.20	37.40	38.50	37.50	38.00	37.00	37.20	37.30	37.20	37.50	37.00	37.20
TiO_2	4.41	4.35	4.36	3.47	3.60	3.29	3.50	3.63	3.84	3.83	3.93	3.98	3.59	3.89	3.77
Al_2O_3	14.54	14.51	14.24	13.45	13.75	13.01	13.43	12.98	13.80	13.95	14.29	13.76	13.91	13.82	14.09
FeO	7.79	8.93	7.61	9.69	8.96	7.73	8.60	9.71	9.34	8.95	7.03	8.63	7.80	9.59	7.66
MnO	0.07	0.09	0.08	0.13	0.10	0.10	0.10	0.11	0.10	0.10	0.08	0.09	0.10	0.11	0.09
MgO	13.03	12.39	13.16	12.12	12.81	13.59	13.12	12.27	12.21	12.57	13.27	12.72	12.91	12.12	13.22
CaO	11.92	11.67	11.75	11.44	11.59	11.61	11.71	11.52	11.56	11.61	12.20	11.61	11.84	11.50	12.02
Na_2O	1.81	2.14	1.87	2.04	2.25	2.24	2.24	2.14	2.05	2.06	1.79	2.11	1.95	1.99	1.76
K_2O	4.48	4.10	4.56	4.61	3.86	4.00	3.90	3.82	3.95	3.96	4.09	3.97	4.22	4.15	4.22
Total	94.15	94.18	94.33	94.15	94.32	94.07	94.1	94.18	93.85	94.23	93.98	94.07	93.82	94.17	94.03
Mg#	74.88	71.20	75.52	69.03	71.81	75.80	73.11	69.25	69.96	71.47	77.09	72.44	74.21	69.26	75.46

Table 4.1 – Representative major element analyses (wt%) in poikilitic and non-poikilitic hornblende crystals measured by LA-ICP-MS. Results are reported to 2 decimal places. Raw data is presented in Digital Appendix 3.

	M2							
	Non-poikilitic		Non-poikilitic		Poikilitic		Poikilitic	
	Core	Rim	Core	Rim	Core	Rim	Core	Rim
Sr	827.53	959.17	834.83	953.39	939.43	1053.06	791.82	879.45
Y	13.90	15.59	14.02	14.64	15.65	17.09	14.36	14.71
Zr	113.70	137.86	113.82	118.07	124.41	153.63	136.52	123.91
Nb	30.79	40.57	38.39	36.65	39.56	38.56	43.85	33.35
Ba	747.63	973.44	763.44	879.24	778.80	1189.78	746.45	850.17
La	13.19	13.28	13.72	13.80	15.62	21.11	15.44	14.76
Ce	40.49	39.69	42.08	41.27	47.43	60.31	46.05	43.03
Nd	29.04	29.18	30.43	29.65	33.40	42.18	31.88	41.42
Sm	6.35	6.78	6.60	6.59	7.06	9.37	6.94	6.82
Eu	2.02	2.16	2.02	2.07	2.20	2.86	2.14	2.12
Gd	5.20	5.76	5.36	5.53	5.96	7.74	5.53	5.80
Dy	3.57	3.89	3.45	3.67	3.90	5.17	3.67	3.77
Er	1.30	1.52	1.32	1.37	1.47	1.92	1.39	1.33
Yb	0.86	0.99	0.88	0.90	1.01	1.28	0.92	0.91
Hf	4.08	5.44	3.91	4.46	4.20	7.81	4.66	5.12

	M4							
	Non-poikilitic		Non-poikilitic		Poikilitic		Poikilitic	
	Core	Rim	Core	Rim	Core	Rim	Core	Rim
Sr	778.54	870.46	762.99	802.48	816.37	868.58	785.15	798.63
Y	13.04	13.65	12.94	13.22	13.37	12.97	13.38	13.24
Zr	143.74	114.95	139.18	135.15	133.38	106.70	144.35	125.47
Nb	38.98	32.54	37.88	38.55	37.57	35.44	40.21	41.10
Ba	812.39	944.62	820.23	1030.81	749.93	958.82	740.56	790.59
La	14.37	13.92	14.18	14.71	13.40	13.03	12.23	13.62
Ce	42.64	41.32	41.90	44.00	39.98	39.30	37.30	40.64
Nd	29.21	29.29	28.60	30.38	28.27	28.82	26.93	28.81
Sm	6.43	6.71	6.27	6.48	6.30	6.45	6.16	6.47
Eu	1.98	2.03	1.93	2.02	1.89	1.98	1.91	1.95
Gd	5.26	5.64	5.02	5.29	5.31	5.23	5.17	5.28
Dy	3.38	3.55	3.27	3.40	3.39	3.38	3.49	3.41
Er	1.25	1.25	1.18	1.21	1.27	1.22	1.25	1.23
Yb	0.80	0.80	0.84	0.85	0.84	0.77	0.84	0.82
Hf	4.71	4.55	4.65	4.50	4.27	4.54	5.61	4.69

Table 4.2 (continued overleaf) ►

	M6 Non-poikilitic						
	Core	Rim	Core	Rim	Core	Core	Core
Sr	861.25	887.92	880.23	954.09	814.55	829.25	866.23
Y	14.34	16.48	14.70	16.32	16.24	16.29	16.62
Zr	129.04	163.57	129.29	148.25	164.05	142.80	164.64
Nb	33.14	45.09	37.73	60.21	50.20	68.04	54.47
Ba	850.81	602.77	828.36	861.92	450.73	684.48	498.04
La	14.27	18.73	15.95	18.86	19.73	18.47	20.95
Ce	41.73	54.19	45.71	55.61	57.40	53.96	59.30
Nd	29.71	36.75	31.82	36.86	37.71	35.51	38.36
Sm	6.82	7.80	6.96	7.58	7.82	7.53	8.11
Eu	2.05	2.38	2.12	2.30	2.33	2.28	2.37
Gd	5.60	6.48	5.66	6.09	6.36	6.08	6.39
Dy	3.63	4.32	3.83	3.98	4.18	4.15	4.20
Er	1.34	1.59	1.38	1.56	1.50	1.56	1.62
Yb	0.91	1.08	0.91	1.11	1.02	1.09	1.06
Hf	4.82	5.33	4.84	4.59	4.87	4.62	5.08

	M8							
	Non-poikilitic		Non-poikilitic		Poikilitic		Poikilitic	
	Core	Rim	Core	Rim	Core	Rim	Core	Rim
Sr	798.97	832.46	820.31	1542.19	878.57	1165.96	819.42	1505.93
Y	14.63	14.38	14.25	19.52	14.19	17.15	13.81	20.03
Zr	196.86	161.24	153.51	115.22	173.56	130.40	150.50	134.03
Nb	56.67	41.16	38.62	61.27	41.11	54.87	41.78	66.65
Ba	729.98	893.91	894.53	913.02	931.51	957.07	897.59	994.97
La	13.90	18.20	17.50	22.56	20.20	21.17	15.44	25.77
Ce	41.84	51.52	49.84	65.63	55.23	61.46	45.42	73.43
Nd	29.95	34.35	33.60	42.86	35.45	40.45	31.38	46.41
Sm	6.80	7.05	7.15	9.00	7.36	8.13	6.71	9.40
Eu	2.10	2.16	2.15	2.75	2.21	2.47	2.04	2.82
Gd	5.53	5.70	5.84	7.31	5.60	6.57	5.49	7.51
Dy	3.73	3.67	3.63	4.68	3.72	4.36	3.49	4.92
Er	1.39	1.33	1.37	1.85	1.34	1.61	1.29	1.90
Yb	1.01	0.89	0.87	1.24	0.89	1.08	0.86	1.31
Hf	6.78	5.59	5.60	3.99	6.47	4.42	4.92	4.55

Table 4.2 – Representative trace element compositions (ppm) in poikilitic and non-poikilitic hornblende crystals measured by LA-ICP-MS. Results are reported to 2 decimal places. Raw data is presented in Digital Appendix 3.

The non-poikilitic hornblendes are generally well-formed with a subhedral habit, but may exhibit irregular skeletal and finger like overgrowth rims when in contact with glass (Figure 4.7). In sample M2 they exhibit significant resorption textures including embayed outlines and glass-bearing cores (Figure 4.7C). The poikilitic hornblendes form an interlocking framework of oikocrysts that enclose anhedral rounded chadocrysts of clinopyroxene and phlogopite. Both types of texture yield crystals with a mixture of normal and reverse zoning trends, and frequently have rims with a higher Mg# than the respective core.

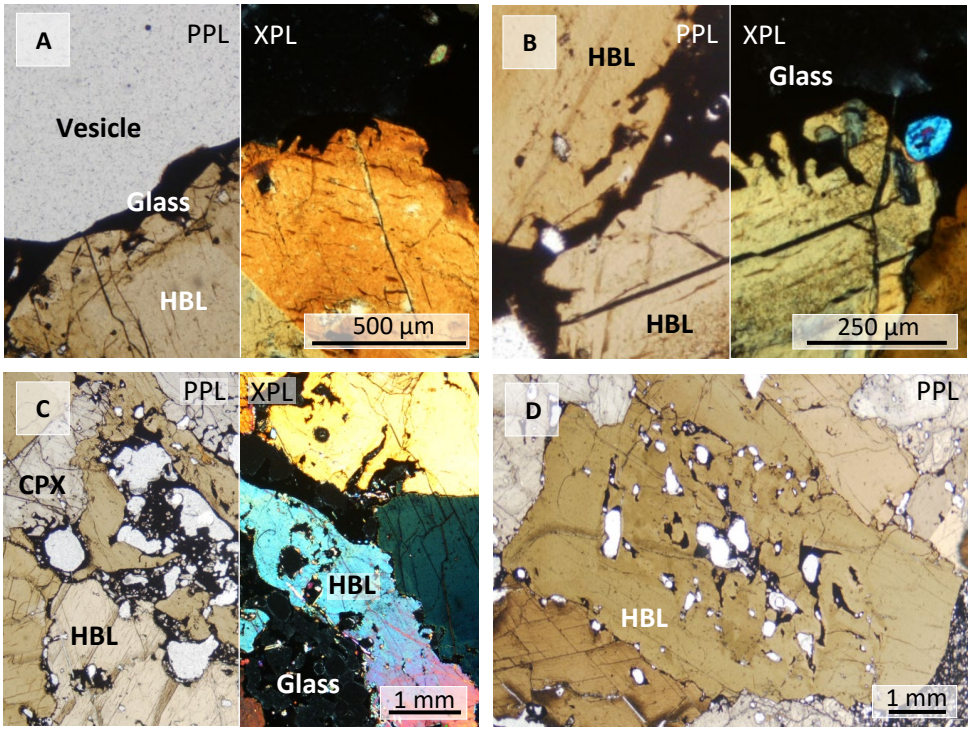

Figure 4.7 – Photomicrographs of overgrowth rims and resorption textures in hornblende crystals, taken in plane and cross polarised light. **A and B)** Skeletal and finger like overgrowths in contact with glass. **C and D)** Strongly resorbed hornblendes in sample M2.

Sample M6 provides an exception to this textural trend. The hornblende textures are relatively homogenous in size, forming a loosely-packed interlocking framework of subhedral-euhedral crystals (Figure 4.8). These crystals do not constitute the type of poikilitic texture described for the other samples, but often contain fine (<200 μm) inclusions of clinopyroxene. A few larger, anhedral hornblendes contrast to the fine-medium grained crystals that comprise the majority of the sample. These crystals exhibit disequilibrium textures and contain a greater number of mineral inclusions. Unlike the other samples, there is no clear textural sequence defined by poikilitic and non-poikilitic textures.

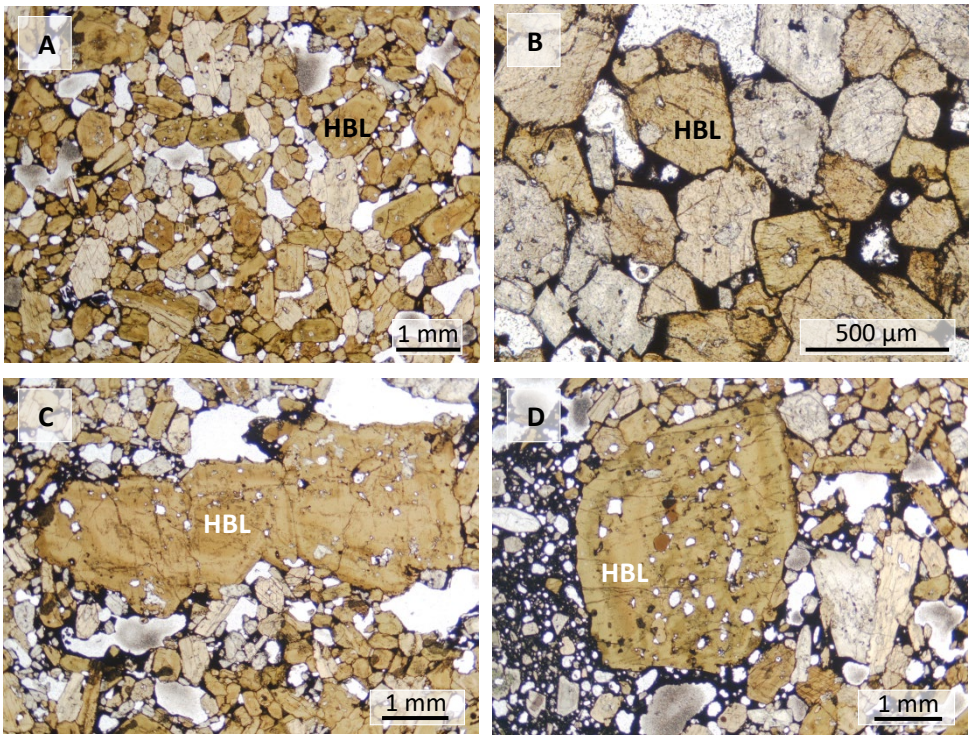

Figure 4.8 – Photomicrographs of hornblende textures in sample M6, taken in plane polarised light. **A and B)** Generally, the hornblendes form a loosely packed, interlocking framework of subhedral-euhedral grains, that are all similar in size. Crystal faces in contact with glass are euhedral, whilst HBL:HBL contacts are more irregular. The hornblendes do not form a poikilitic texture as in the other samples, but often contain fine inclusions of clinopyroxene. There is no clear textural sequence that would indicate the presence of earlier and later forming hornblendes. **C and D)** The hornblende framework is occasionally interrupted by the presence of coarse (>5 mm) hornblende crystals, that are subhedral-anhedral in shape with holey cores and inclusions of other mineral grains.

4.2.2 Clinopyroxene

As with hornblende, clinopyroxene is present as an essential mineral phase in all of the samples, at proportions ranging between 12.88% in sample M6 and 46.13% in sample M2. Clinopyroxenes are diopsides according to the wollastonite-enstatite-ferrosilite ternary classification scheme (Rock, 1990) (Figure 4.9). Because they have relatively high aluminium and titanium contents (~7.3 and ~2.5 wt%, respectively) they plot slightly above the diopside field, which is a typical pattern for pyroxenes in highly alkaline magmas (Bardintzeff et al., 2012). They yield Mg#s between 71.0-86.3 (Figure 4.10), which are generally higher than hornblendes within the same sample.

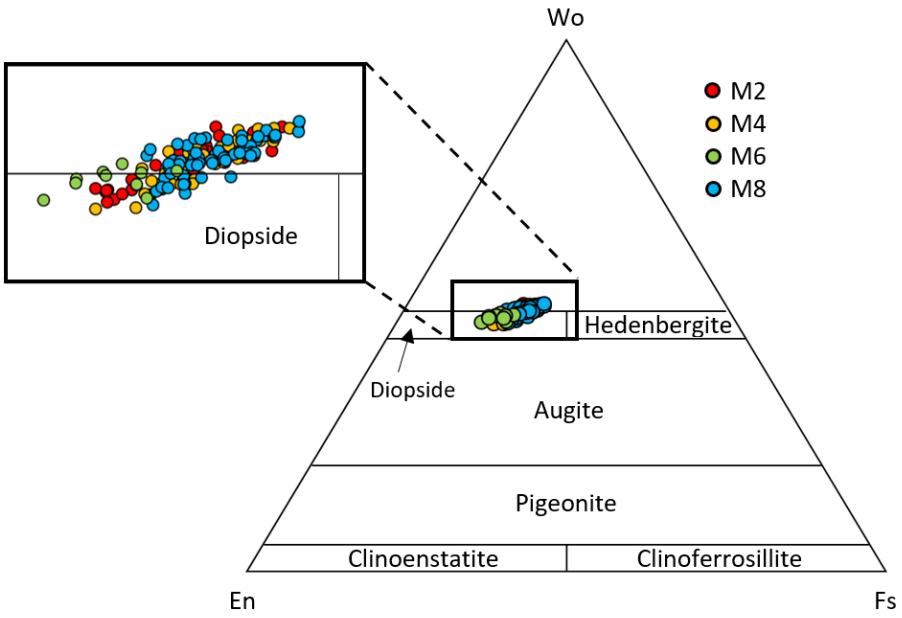

Figure 4.9 **–** Wo-En-Fs ternary plot, showing geochemical classification of clinopyroxenes. The clinopyroxenes plot as diopsides, but trend upwards above the diopside field, a phenomenon commonly reported in alkaline magmas.

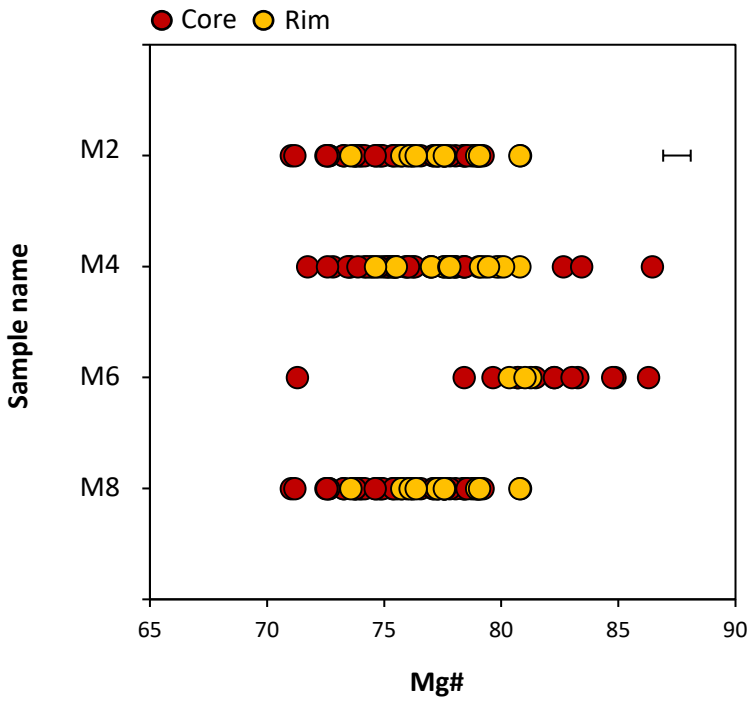

Figure 4.10 **-** Variation in clinopyroxene Mg# between different samples. Red circles indicate core analyses, yellow circles are rim analyses. Mg#s show a range within samples, but overlap between samples. However, the clinopyroxenes in sample M6 tend towards higher Mg#s than the other samples. Error bar represents 2 standard deviations.

Clinopyroxenes are either present as chadocrysts within poikilitic hornblende, or form high porosity frameworks within regions of glass. The former exhibit anhedral, rounded outlines, whereas the latter are well formed with euhedral crystal faces in contact with glass and anhedral mineral: mineral contacts (Figure 4.11A-B). The impingement of these crystals form planar sided pores that are occupied by glass and void spaces, constituting a diktytaxitic texture. In sample M2, the clinopyroxenes that are hosted in glass exhibit a wide array of crystal sizes (Figure 4.12). Coarser crystals (up to 15 mm in length) have corroded cores with a variety of visible zoning patterns. Finer crystals (<500 µm) occur in bands throughout the sample.

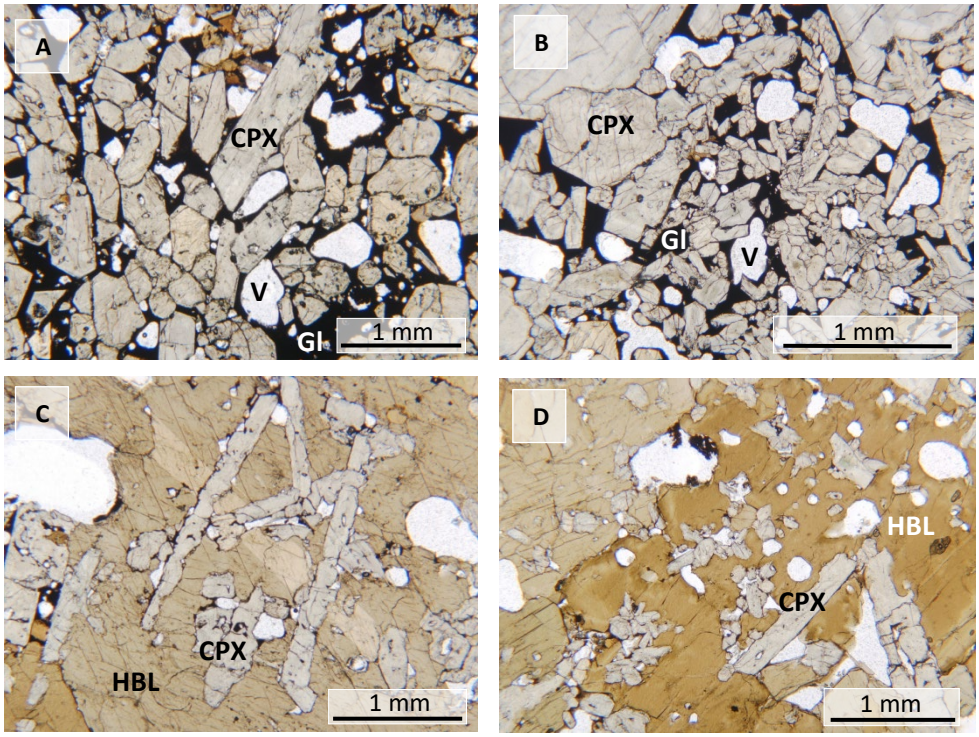

Figure 4.11 **–** Photomicrographs of clinopyroxene textures taken in plane polarised light. Gl = glass; V = vesicle. Clinopyroxenes can be divided into two textural groups. **A and B)** High porosity frameworks of clinopyroxene, with angular pore spaces infilled by black interstitial glass and void spaces. Crystal faces protruding into glass are planar and euhedral, whereas mineral: mineral faces are anhedral, frequently containing small pockets of glass. Clinopyroxene frameworks are mostly monomineralic in nature, but may yield small numbers of accessory phlogopite and apatite within glass filled pore spaces. **C and D)** Anhedral, rounded chadocrysts of clinopyroxene enclosed within hornblende oikocrysts. In some instances the chadocrysts appear to preserve a touching framework with angular pore spaces that are similar to those outside the oikocrysts. More commonly they are dispersed in clusters throughout the oikocrysts, with a clear textural difference to the framework forming crystals. These clinopyroxenes can be identified within samples M2, 4 and 8.

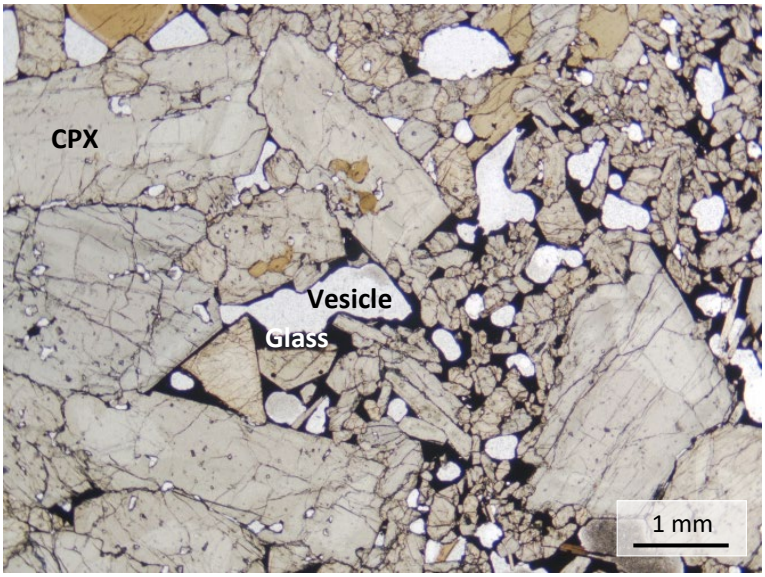

Figure 4.12 – Photomicrograph of clinopyroxene crystal textures in sample M2, taken in plane polarised light. Crystals that are not enclosed within hornblende oikocrysts form high porosity frameworks characterised by a juxtaposition of coarse (up to 15 mm) and fine (<500 µm) crystals. The coarser crystals frequently exhibit corroded cores and complex zoning patterns, but have euhedral crystal faces in contact with glass. The finer crystals occur in bands that form high porosity regions through the sample.

In sample M6, fine inclusions (<200 µm) of clinopyroxene are present within hornblende grains, but contrast to the poikilitic texture that characterises the other samples. If not enclosed, clinopyroxenes are dispersed throughout the hornblende framework, frequently exhibiting disequilibrium textures such as corroded cores and embayed outlines (Figure 4.13).

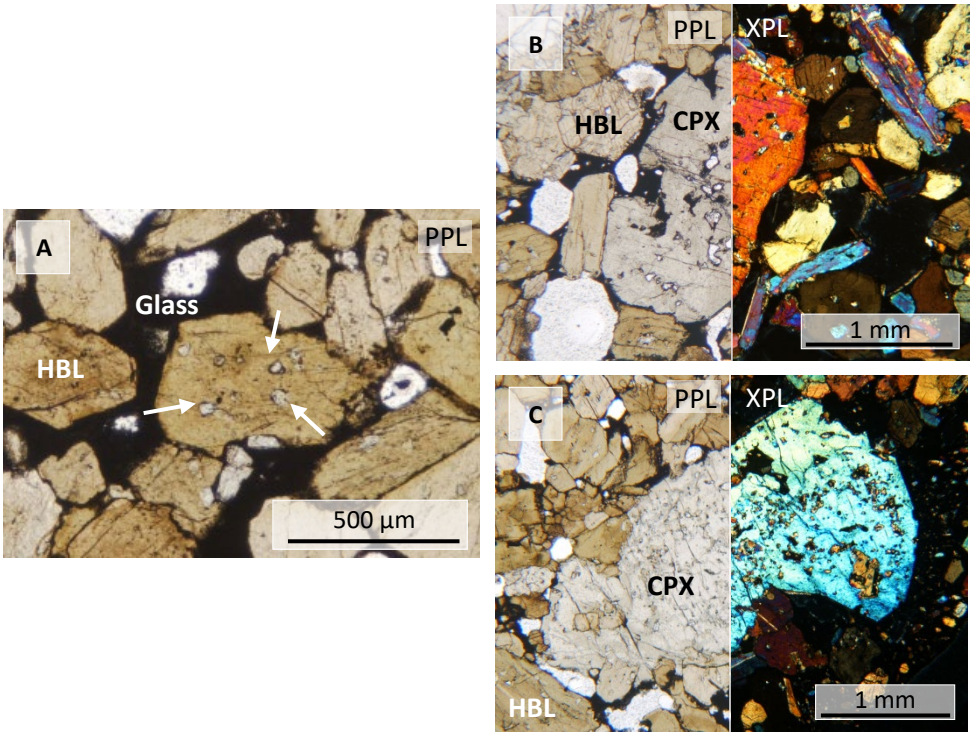

Figure 4.13 – Photomicrographs of clinopyroxene textures in sample M6, taken in plane and cross polarised light. **A)** Inclusions of clinopyroxene within hornblende grains contrast to the poikilitic textures observed within the other samples. **B and C)** Coarser (>1 mm) clinopyroxene crystals that are not included within hornblende grains frequently exhibit disequilibrium textures including rounded embayed outlines and sieve textured cores.

Texturally distinct clinopyroxenes (chadocrysts and non-chadocrysts) exhibit overlapping major element compositions and similar Mg#s (Figure 4.14), and therefore cannot be divided based upon their compositions. Normal and reverse zoning trends can be identified, and rims commonly have higher Mg#s than the respective core. Trace element compositions show a wide range within the same sample, with no particular trend between texturally distinct groups. There are no exsolution textures in chadocryst or non-chadocryst clinopyroxenes. Representative mineral chemistries are presented in Tables 4.3 and 4.4.

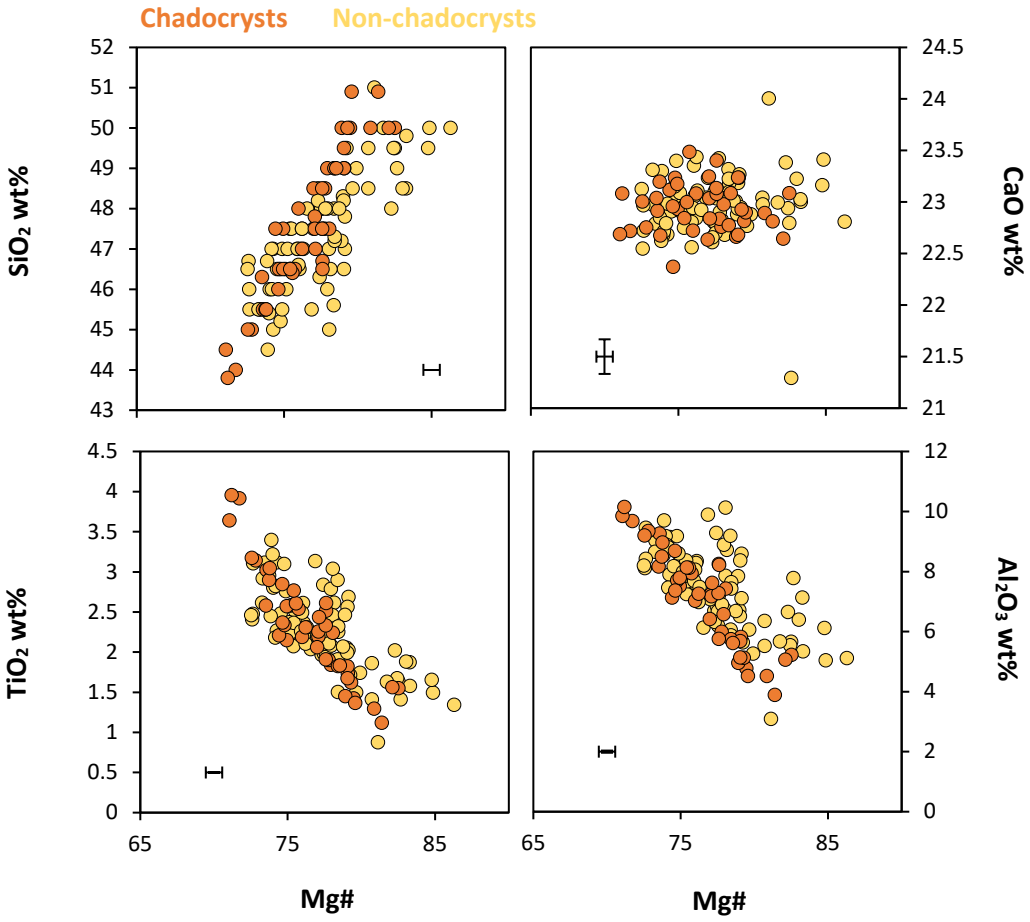

Figure 4.14 – Major element compositions of clinopyroxene crystals. Texturally distinct clinopyroxenes cannot be distinguished from their major element compositions. Major element compositions broadly overlap between samples, with similar Mg#s. Error bars represent 2 standard deviations. Errors for SiO_2, TiO_2 and Al_2O_3 are smaller than the data markers.

	M2								M4							
	Non-chadocryst				Chadocryst				Non-chadocryst		Non-chadocryst		Chadocryst			
	Core	Core	Core	Core	Core	Core	Core	Core	Core	Rim	Core	Rim	Core	Core	Core	Core
SiO_2	46.70	46.50	47.50	49.00	47.80	50.00	50.00	50.00	47.00	48.50	49.00	48.50	44.00	45.50	47.50	50.00
TiO_2	2.54	2.43	2.25	1.62	2.19	1.56	1.42	1.29	2.18	1.85	1.74	1.84	3.92	3.02	2.15	1.62
Al_2O_3	8.12	8.48	7.64	5.38	7.25	5.06	4.78	4.52	7.46	6.40	5.26	5.91	9.67	9.26	7.51	5.13
FeO	7.71	7.00	6.50	5.85	6.60	5.47	6.23	5.78	7.17	5.89	6.10	6.22	7.56	7.21	7.09	6.20
MnO	0.13	0.11	0.11	0.11	0.11	0.10	0.16	0.14	0.14	0.33	0.11	0.10	0.11	0.10	0.13	0.12
MgO	11.38	11.74	12.25	13.68	12.45	14.06	13.52	13.69	11.53	13.04	13.61	13.22	10.76	11.26	11.90	13.33
CaO	22.82	23.31	23.31	23.15	23.25	22.64	22.81	22.89	22.94	22.47	22.88	23.29	22.72	22.91	22.93	22.93
Na_2O	0.81	0.68	0.66	0.55	0.70	0.49	0.68	0.65	0.84	0.63	0.53	0.58	0.85	0.76	0.84	0.59
K_2O	0.01	0.00	0.00	0.00	0.00	0.00	0.00	0.00	0.04	0.02	0.00	0.01	0.00	0.01	0.17	0.00
Total	100.22	100.25	100.22	99.34	100.36	99.40	99.60	98.97	99.30	99.12	99.24	99.66	99.58	100.04	100.22	99.91
Mg#	72.47	74.94	77.05	80.66	77.07	82.10	79.46	80.84	74.15	79.79	79.91	79.11	71.72	73.56	74.94	79.29

	M6							M8							
	Non-chadocryst							Non-chadocryst		Non-chadocryst		Chadocryst			
	Core	Rim	Core	Rim	Core	Core	Core	Core	Rim	Core	Rim	Core	Core	Core	Core
SiO_2	47.00	47.50	48.50	49.50	49.00	48.00	50.00	47.20	47.00	46.00	46.30	44.50	49.50	46.40	45.50
TiO_2	2.10	1.70	2.51	1.61	1.50	2.02	1.34	2.46	2.36	2.80	2.74	3.64	1.67	2.61	2.90
Al_2O_3	9.28	6.04	8.67	5.76	5.87	6.65	5.11	7.85	8.70	8.89	8.55	9.85	5.14	8.12	8.49
FeO	4.95	5.71	8.32	5.60	6.38	5.21	4.21	6.07	5.45	7.18	6.35	7.78	6.44	6.99	7.28
MnO	0.07	0.11	0.15	0.11	0.14	0.08	0.08	0.09	0.08	0.11	0.09	0.12	0.13	0.10	0.11
MgO	12.88	13.08	11.58	13.62	12.99	13.56	14.83	12.71	12.87	11.47	12.33	10.71	13.63	12.12	11.45
CaO	22.50	22.60	24.26	23.08	23.23	23.38	22.81	23.01	22.95	22.71	23.01	22.69	22.68	23.00	23.20
Na_2O	0.63	0.62	0.88	0.63	0.75	0.46	0.45	0.59	0.45	0.76	0.59	0.86	0.60	0.66	0.73
K_2O	0.01	0.00	0.01	0.01	0.01	0.00	0.00	0.00	0.01	0.00	0.01	0.00	0.00	0.00	0.00
Total	99.43	97.36	104.88	99.92	99.86	99.37	98.83	99.97	99.87	99.93	99.97	100.15	99.79	99.98	99.66
Mg#	82.25	80.34	71.29	81.25	78.40	82.27	86.28	78.88	80.81	74.01	77.57	71.03	79.04	75.56	73.72

Table 4.3 **-** Representative major element analyses (wt%) in chadocryst and non-chadocryst clinopyroxene crystals measured by LA-ICP-MS. Results are reported to 2 decimal places. Raw data is presented in Digital Appendix 3.

	M2							
	Non-chadocrysts				Chadocrysts			
	Core	Core	Core	Core	Core	Core	Core	Core
Sr	262.68	248.27	238.12	220.81	232.54	164.54	238.06	248.15
Y	18.13	17.93	16.87	17.73	15.10	18.24	20.63	14.41
Zr	300.21	196.16	189.93	177.67	190.48	147.60	240.74	162.86
Nb	5.75	2.73	2.83	1.74	3.00	1.23	2.44	2.01
Ba	0.88	0.11	0.38	0.12	0.19	0.10	0.08	0.10
La	15.31	13.44	13.74	12.22	11.88	10.00	13.71	11.23
Ce	48.79	44.44	45.28	40.14	38.18	33.41	44.08	36.12
Nd	34.83	34.44	34.37	30.82	28.70	27.73	33.58	26.62
Sm	7.86	7.78	8.08	7.35	6.70	7.07	7.72	6.13
Eu	2.36	2.40	2.47	2.25	1.98	2.17	2.38	1.87
Gd	6.31	6.57	6.86	6.34	5.57	6.42	6.82	5.01
Dy	4.48	4.49	4.94	4.47	3.86	4.72	5.01	3.63
Er	1.80	1.78	1.99	1.76	1.47	1.84	2.10	1.45
Yb	1.41	1.24	1.33	1.21	1.07	1.25	1.66	1.11
Hf	9.05	7.21	8.49	6.83	7.06	6.49	8.60	5.47

	M4							
	Non-chadocrysts				Chadocrysts			
	Core	Rim	Core	Rim	Core	Core	Core	Core
Sr	422.21	428.57	168.86	187.22	229.31	219.46	337.75	187.14
Y	18.35	26.70	19.31	12.51	26.35	20.93	18.31	17.93
Zr	218.96	127.94	210.57	150.34	374.96	283.11	234.71	197.62
Nb	5.94	3.19	1.69	1.59	18.69	5.89	8.99	1.50
Ba	14.49	2.90	0.46	1.47	0.25	0.84	30.53	0.27
La	19.46	21.12	10.88	8.83	24.60	17.42	20.16	10.71
Ce	58.98	68.40	35.85	29.19	75.16	54.98	57.96	35.65
Nd	38.74	49.45	29.55	23.26	53.52	40.79	37.90	29.03
Sm	8.26	10.95	7.70	5.80	11.94	9.37	7.99	7.28
Eu	2.43	3.19	2.32	1.75	3.51	2.83	2.41	2.24
Gd	6.47	8.93	6.68	4.83	10.13	7.88	6.60	6.36
Dy	4.54	6.38	4.96	3.36	6.72	5.32	4.55	4.58
Er	1.80	2.69	1.94	1.25	2.62	2.13	1.80	1.80
Yb	1.44	2.09	1.37	0.86	1.89	1.49	1.42	1.22
Hf	7.29	5.11	8.59	5.61	11.86	10.03	7.56	7.74

Table 4.4 (continued overleaf) ▶

	M6						
	Non-chadocryst						
	Core	Rim	Core	Rim	Core	Core	Core
Sr	129.04	220.75	357.20	223.24	333.53	147.65	107.09
Y	13.57	16.11	18.29	14.80	17.19	14.07	11.17
Zr	86.37	159.10	250.10	146.42	171.32	131.27	65.57
Nb	1.19	2.00	4.18	1.92	2.55	1.27	0.61
Ba	1.18	0.42	0.41	1.59	0.98	0.14	0.30
La	7.22	12.18	16.47	12.21	16.19	8.54	5.25
Ce	23.72	39.14	52.32	39.02	51.30	28.43	17.83
Nd	20.13	29.10	36.56	28.53	34.90	23.46	15.80
Sm	5.37	6.67	8.10	6.54	7.63	5.92	4.49
Eu	1.66	1.99	2.37	1.97	2.29	1.77	1.33
Gd	4.82	5.84	6.53	5.33	6.12	5.15	4.01
Dy	3.51	4.06	4.55	3.78	4.26	3.74	2.95
Er	1.37	1.62	1.84	1.47	1.72	1.38	1.10
Yb	0.88	1.11	1.43	1.06	1.36	0.94	0.72
Hf	4.58	5.98	7.64	5.29	5.66	6.11	3.44

	M8							
	Non-chadocryst		Non-chadocryst		Chadocryst			
	Core	Rim	Core	Rim	Core	Core	Core	Core
Sr	211.92	244.89	213.40	220.86	252.69	179.75	211.43	230.55
Y	17.01	22.36	20.99	16.44	21.82	20.65	14.84	20.39
Zr	193.78	165.24	258.48	194.17	385.31	229.04	197.72	265.04
Nb	2.67	3.15	5.11	2.76	12.53	1.76	2.49	3.27
Ba	0.15	0.43	0.57	0.92	0.27	0.46	0.15	0.40
La	13.62	18.77	17.02	13.23	19.72	11.40	11.94	14.94
Ce	43.67	58.13	53.21	42.78	62.02	37.86	39.07	49.22
Nd	32.74	41.49	40.23	32.21	45.85	30.98	29.56	38.78
Sm	7.73	9.46	9.29	7.61	10.46	7.84	6.94	9.16
Eu	2.29	2.85	2.80	2.29	3.08	2.45	2.07	2.73
Gd	6.38	8.11	7.95	6.29	8.27	7.13	5.65	7.73
Dy	4.40	5.61	5.39	4.31	5.71	5.11	3.81	5.21
Er	1.67	2.14	2.01	1.59	2.15	2.06	1.44	2.02
Yb	1.09	1.54	1.42	1.07	1.54	1.46	1.01	1.41
Hf	7.77	6.51	9.14	7.95	12.50	9.12	7.88	9.67

Table 4.4 – Representative trace element compositions (ppm) in chadocryst and non-chadocryst clinopyroxene crystals measured by LA-ICP-MS. Results are reported to 2 decimal places. Raw data is presented in Digital Appendix 3.

4.2.3 Accessory minerals

4.2.3.1 Phlogopite

Phlogopite comprises an accessory phase in all of the samples, with proportions ranging between 2.16% and 6.88% in samples M8 and M4, but with a very limited presence in samples M2 and 6 (0.37% and 0.16% respectively). The phlogopites are highly aluminous (14.3-15.2 wt% Al_2O_3), with Mg#s between 73.6 and 80.8. Phlogopite occurs as anhedral chadocrysts within hornblende oikocrysts, or as subhedral crystals hosted in glass (Figure 4.15).

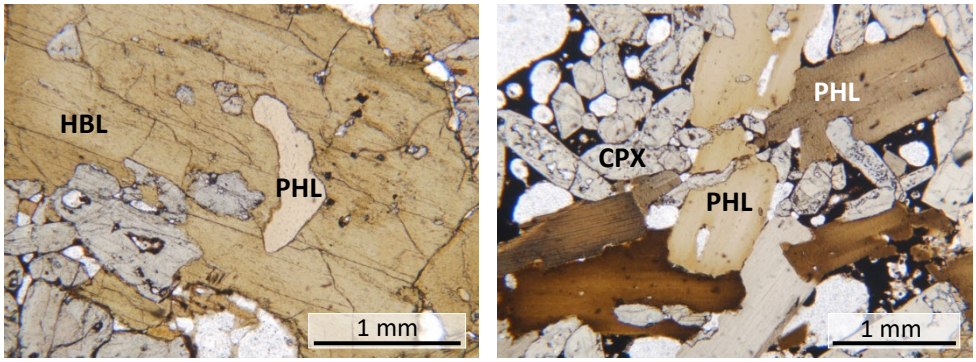

Figure 4.15 – Photomicrographs of phlogopite textures, taken in plane polarised light. Phlogopite crystals may be divided into two textural groups. Left – rounded, anhedral chadocrysts enclosed with hornblende. Right – Coarser (>3 mm) subhedral crystals hosted in glass.

4.2.3.2 Apatite

Apatite occurs as a minor accessory phase in all of the samples, excluding sample M2. Apatite crystals are hosted in glass, measuring up to 600 µm in length.

4.2.3.3 Olivine

Olivine is a minor accessory phase, contributing one or two crystals per sample. When identified in thin section, coarse (up to 5 mm) anhedral crystals are mantled by a reaction corona of phlogopite and pyroxene (Figure 4.16).

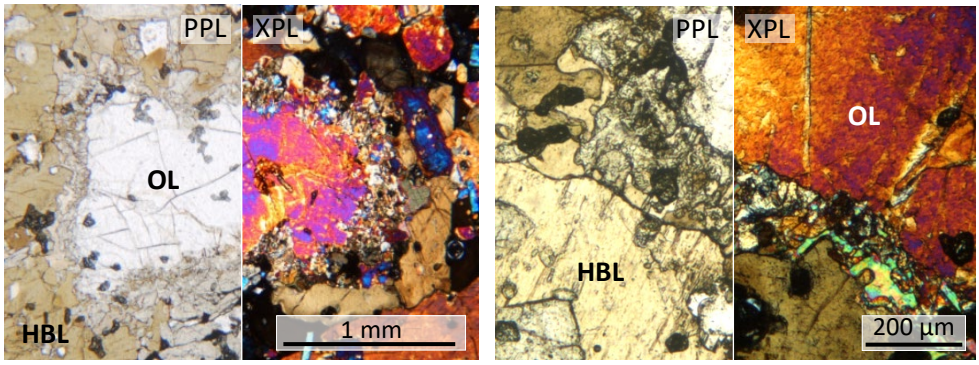

Figure 4.16 – Photomicrographs of accessory olivine, taken in plane and cross polarised light. Only one or two olivine crystals are identified within each sample, but consistently are mantled by reaction coronas of anhedral clinopyroxene and phlogopite. The olivine crystals are up to 5 mm in length, with anhedral habits.

4.2.4 Glass

A characteristic feature of these samples is that they contain interstitial glass that occupies the pore spaces between impinging crystals, and frequently forms films and pockets along grain boundaries. The glasses are foidite in composition (Figure 4.17); glass compositions do not vary much within a sample, but vary between samples. Mg#s range between 33.6 and 61.4. Compared to bulk rock measurements of the host basalt (obtained from Downes et al. (2004)), the glass within the xenoliths has greater Al_2O_3 and alkali contents, but are lower in MgO and CaO. Representative glass chemistries are presented in Tables 4.5 and 4.6.

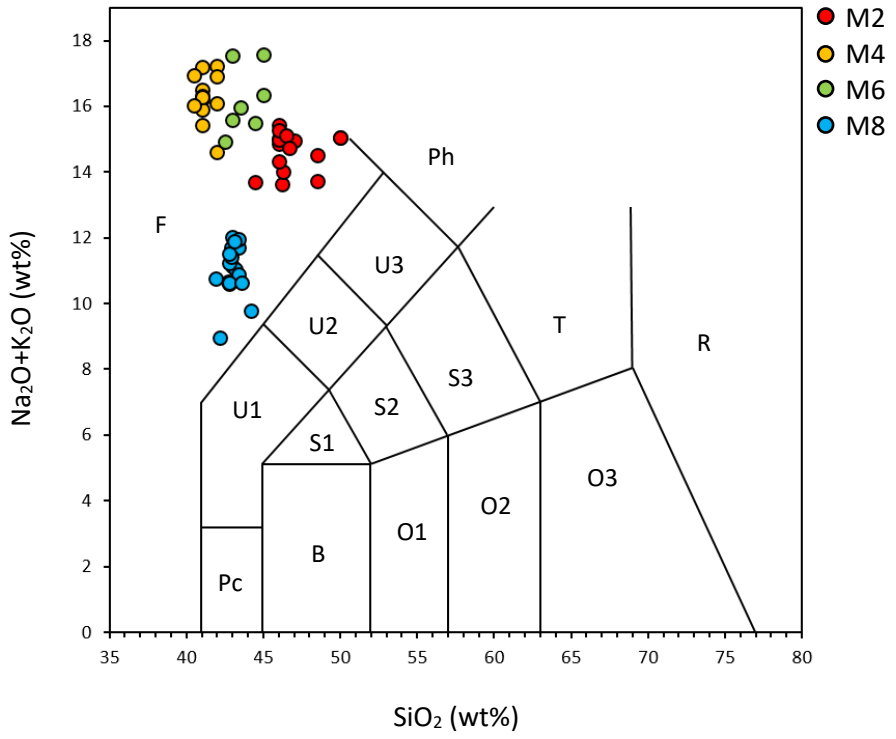

Figure 4.17 **-** Total alkali silica diagram showing the composition of interstitial glasses. Fields defined according to Le Maitre et al. (2002). B = Basalt; O1 = Basaltic andesite; O2 = Andesite; O3 = Dacite; R = rhyolite; T = Trachyte; Ph = Phonolite; S1 = Trachybasalt; S2 = Basaltic trachyandesite; S3 = Trachyandesite; Pc = Picrobasalt; U1 = Basanite; U2 = Phonotephrite; U3 = Tephriphonolite; F = Foidite. The glass from the xenoliths is foidite in composition, with high alkali contents. Glass composition are relatively homogenous within the same sample, but vary between samples.

The glass is vesiculated, representing the exsolution of a gas phase during eruption (Figure 4.18A). Quench microlites within the glass are distinguishable from the pre-eruptive mineral assemblage (Figure 4.18B). The brown-black glass is optically distinct from that of the host basalt, which forms a sharp contact with the xenolith (Figure 4.18C). Clinopyroxenes in contact with glass exhibit euhedral crystal faces, defining angular pore spaces with interstitial glass (Figure 4.18D).

	M2			M4			M6			M8		
SiO_2	44.50	46.00	46.00	40.50	41.00	42.00	43.00	45.00	44.50	42.90	44.20	43.00
TiO_2	1.92	2.05	1.95	2.21	2.25	2.45	1.78	1.52	2.12	2.18	2.22	1.97
Al_2O_3	17.73	17.28	18.16	17.44	17.59	17.52	17.08	18.25	16.98	18.21	16.96	18.72
FeO	10.59	8.92	8.65	10.17	8.81	8.77	9.46	7.81	8.94	9.53	9.18	9.35
MnO	0.27	0.21	0.20	0.33	0.31	0.29	0.32	0.24	0.25	0.33	0.29	0.33
MgO	3.02	2.78	2.95	3.32	3.31	4.14	3.49	3.32	6.25	3.55	4.51	3.15
CaO	7.77	6.94	6.90	8.90	8.86	9.92	8.51	8.11	11.23	11.51	12.68	12.18
Na_2O	6.03	6.50	6.09	6.54	6.78	5.73	6.51	6.94	6.83	7.65	6.15	6.70
K_2O	7.67	8.49	9.18	10.41	10.43	8.87	9.07	9.40	3.32	4.07	3.62	4.43
Total	99.50	99.17	100.09	99.82	99.35	99.68	99.22	100.59	100.44	99.93	99.80	99.83

Table 4.5 **-** Representative major element analyses of interstitial glass measured by LA-ICP-MS (wt%). Results are reported to 2 decimal places. Raw data is presented in Digital Appendix 3.

	M2			M4			M6			M8		
Sr	2249.97	1885.63	1958.30	2976.47	2851.68	2406.92	3310.85	2428.29	2458.40	3566.05	2730.77	3798.43
Y	27.53	25.48	24.29	35.81	32.99	30.79	34.42	27.22	33.77	43.57	42.72	49.84
Zr	241.85	251.34	253.21	263.18	262.11	266.71	262.53	253.59	238.57	298.01	328.99	279.66
Nb	215.90	176.42	189.45	234.80	218.46	199.88	206.32	193.16	207.33	323.72	270.27	339.95
Ba	1872.73	1725.86	1804.78	1752.80	1923.86	1120.17	2220.48	1916.87	1143.06	1662.04	1281.76	1979.83
La	169.87	151.33	155.44	1594.26	1742.74	1015.89	2015.17	1721.91	1035.41	1476.21	1139.66	1771.22
Ce	279.13	246.34	251.21	195.62	178.08	154.06	178.91	140.36	164.66	238.76	193.56	295.84
Nd	84.91	75.53	75.56	290.30	260.26	230.08	269.59	205.52	246.27	353.45	291.04	439.11
Sm	11.47	10.98	10.29	29.51	26.98	23.97	27.52	20.57	25.25	36.04	30.39	45.33
Eu	3.42	2.94	2.89	93.36	86.31	78.15	89.95	66.14	81.44	116.72	101.64	148.56
Gd	8.01	7.34	7.02	12.84	12.36	11.51	13.27	9.81	12.47	16.04	15.39	20.11
Dy	5.74	5.29	4.98	3.91	3.64	3.44	3.60	2.97	3.60	4.89	4.63	5.98
Er	2.68	2.49	2.41	10.09	9.66	9.04	9.75	7.22	8.81	13.00	11.99	15.58
Yb	2.54	2.17	2.21	7.76	7.12	6.93	6.92	5.27	6.72	9.58	9.74	11.32
Hf	4.17	4.98	4.82	3.66	3.36	3.04	2.90	2.37	3.01	4.44	4.28	4.84

Table 4.6– Representative trace element compositions (ppm) of interstitial glass measured by LA-ICP-MS. Results are reported to 2 decimal places. Raw data is presented in Digital Appendix 3.

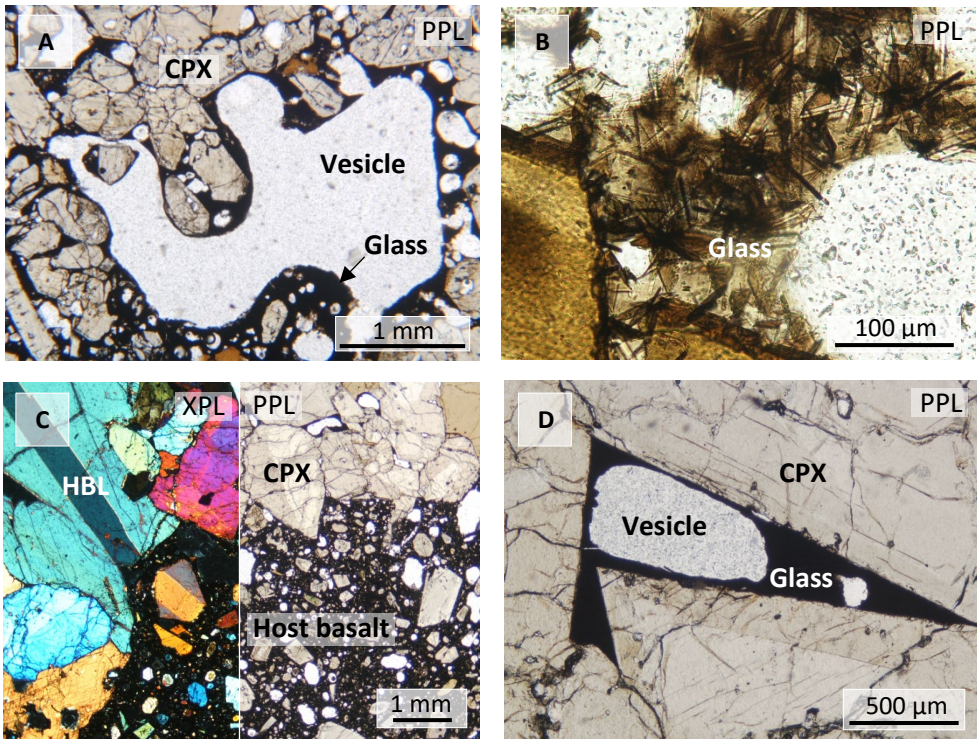

Figure 4.18 – Photomicrographs of glass textures, taken in plane and cross polarised light. **A)** The glass is widely vesiculated, photomicrograph shows a large (~3.5 mm), lobate vesicle within a crystal-poor pool of glass. **B)** Quench Microlites within the glass include apatite, sodalite and clinopyroxene (Downes et al., 2004). They can be clearly identified from the crystals that formed prior to quenching, exhibiting acicular and radial textures. **C)** Contact between the host basalt and the xenolith assemblage. The glass of the host basalt can be distinguished from that within the xenoliths and there is no evidence of mixing between the two. **D)** Angular pore formed by the impingement of planar sided clinopyroxene crystals. Glass occupies the acutely angled interstices within these pores, which together form concentrated regions of glass throughout the clinopyroxene frameworks.

Regions of vesiculated glass may be relatively crystal poor, or be occupied by clinopyroxene and accessory phlogopite and apatite. The glass is distributed throughout the sample, but is often concentrated around the clinopyroxene frameworks.

Many of the grain boundaries yield glass, either within isolated cusps or along the length of the boundary (Figure 4.19A-C). In sample M2 there are a few examples of serrated grain boundaries, in which recrystallisation appears to have occurred within trapped pockets of glass (Figure 4.19D-E). Glass-bearing grain boundaries are mostly un-vesiculated, but there are a few examples where the grain boundaries appear to have been pushed apart (Figure 4.19F). Such grain boundaries are limited, but are associated with broken crystals. Because of this it is likely that they are decompression features. A couple of arcuate, glass-free fractures traverse sample M8, which are also likely to be related to eruption.

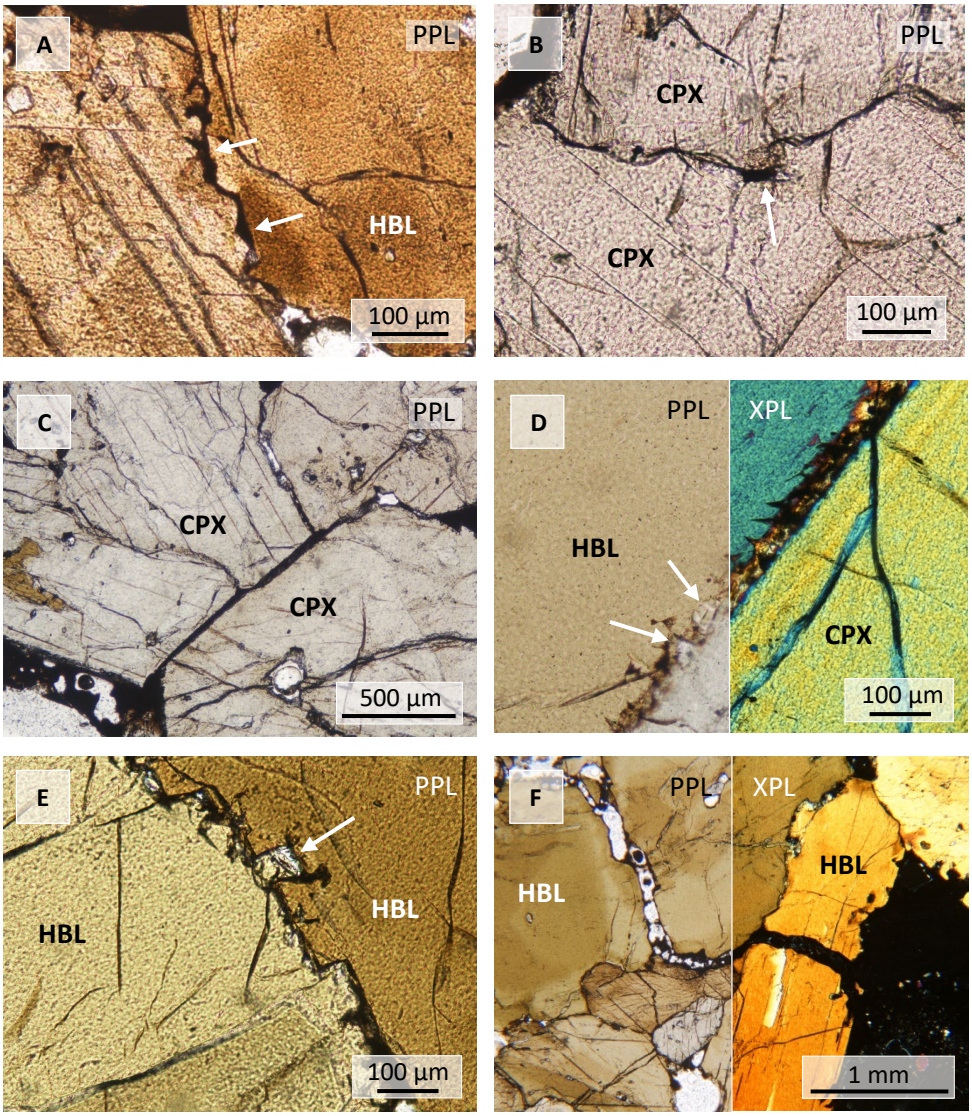

Figure 4.19 – Photomicrographs of glass-bearing grain boundaries, taken in plane and cross polarised light. **A and B)** Anhedral mineral: mineral boundaries, with cuspate pockets of glass, highlighted by white arrows **C)** Continuous film of glass between adjacent clinopyroxene crystals. **D and E)** Irregular, serrated grain boundaries; white arrows indicate recrystallisation within the glass. **F)** Vesiculated glass occupying a hornblende: hornblende boundary, and traversing a fractured hornblende crystal. The grain boundary looks as though it has been pushed apart, and therefore likely represents a decompression feature.

4.3 Summary

A summary of the key findings of this chapter are provided below:

- Amphiboles are titanium rich pargasites. In samples M2, 4 and 8 the hornblende has a discontinuous crystallisation sequence, defined by non-poikilitic and poikilitic crystals.
- In sample M6, homogenous hornblendes form an interlocking framework that contrasts to the poikilitic textures seen in the other samples.
- Clinopyroxenes are aluminium and titanium rich diopsides. In samples M2, 4 and 8 they can be divided into two textural groups: anhedral rounded chadocrysts within hornblende oikocrysts, and subhedral-euhedral crystals that form loosely packed frameworks in regions of glass.
- In sample M6, clinopyroxenes occur as fine inclusions within hornblende grains or as coarser, resorbed crystals dispersed throughout the hornblende framework.
- Accessory phlogopite, olivine and apatite occur throughout the samples. Phlogopite occurs as anhedral chadocrysts and as subhedral crystals hosted in glass. Olivine crystals are scarce, but exhibit reaction coronas of phlogopite and clinopyroxene.
- The samples are characterised by vesicular interstitial glass, which is foiditic in composition. This glass occupies the pore spaces between impinging clinopyroxenes and is present along grain boundaries.

Two-dimensional quantitative textural analysis

This Chapter presents the quantitative two-dimensional data, providing numerical constraints to the textural observations described in Chapter 4. Using digital image analysis of digitised thin sections, four textural parameters are presented to constrain information pertaining to both the solid crystalline and porosity fractions recorded within these samples. These results include phase abundances, crystal size distributions (CSD) (including 3D shape estimates), spatial distribution patterns (SDP) and shape preferred orientation (SPO).

5 Two-dimensional quantitative textural analysis

5.1 Phase abundance

Phase abundances measured in thin section yield varying abundances of hornblende (26.7-61.6%) and clinopyroxene (10.5-57.9%), with lesser amounts of accessory phlogopite (0.2-9.3%), apatite (0-0.2%) and olivine (0.1-3.1%) (Figure 5.1). The samples are mostly crystalline (74-88%) with lesser amounts of glass (3-14%) and holes (5-17%) that together comprise a porosity fraction. Differences in phase abundances measured between thin sections cut at different orientations indicate significant textural heterogeneity within each sample.

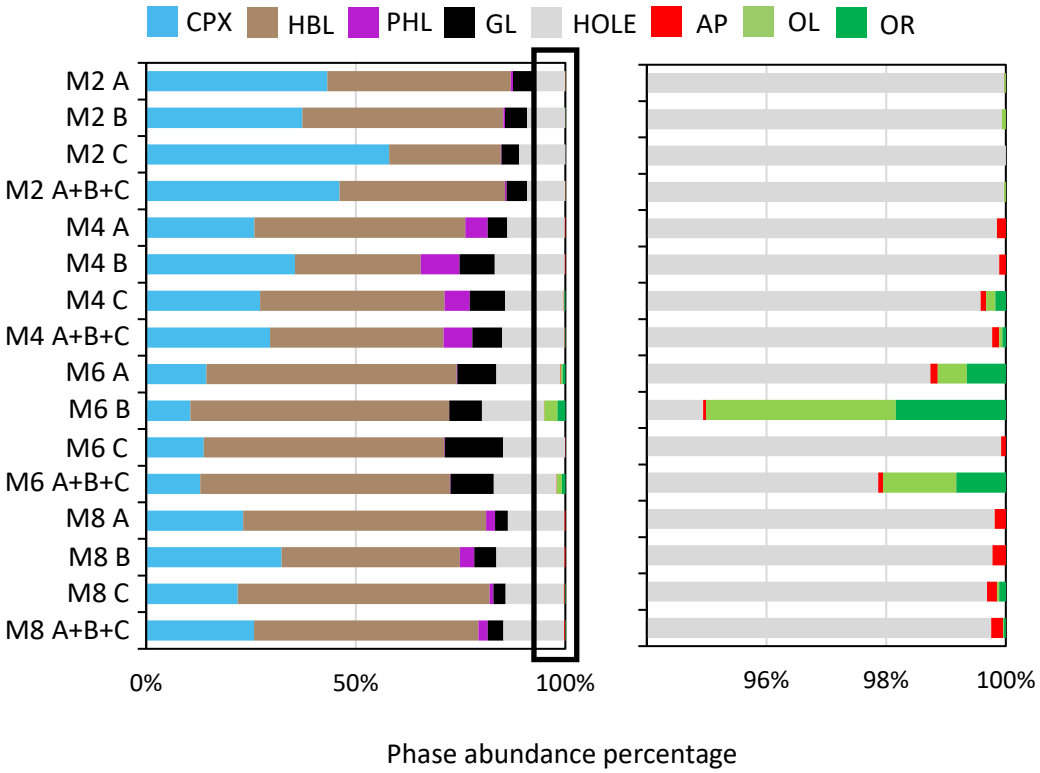

Figure 5.1 **–** Phase abundances calculated by area fraction analysis of the digitised slide images. OR refers to the reaction rims that mantle the olivine crystals. *Left* – Whole slide phase abundance for each thin section, along with an average calculated for each sample as the mean of the three sections. *Right* – Accessory phases zoomed in from the black box on the left hand figure.

Accessory phases exhibit greater variability between samples, most notably with the presence or absence of olivine. M6 exhibits the greatest olivine abundance by volume, but a low population density of just 1-2 crystals per thin section. M2 is the only sample devoid of accessory apatite, and compared to samples M4 and 8 contains only very minor quantities of PHL (<0.5%).

The relative proportions of crystalline and non-crystalline material are presented in Figure 5.2. Following Holness and Bunbury (2006), the different regions on this ternary plot can be used to describe the properties of the porosity fraction. The shaded regions can be used to constrain the three-dimensional connectivity and mobility of the gas and liquid phases through the crystal network. The white region denotes the crystallinity fraction at which the integrity of the crystal framework is sufficiently strong to survive eruption. In particular, the vesicles that occur throughout the glass phase can be described according to the gas percolation threshold (which marks the volume of gas bubbles at which there is sufficient connectivity to permit gas loss) and the bubble connectivity fraction (where the gas bubbles form a touching framework within the melt). Together, these parameters can be used to constrain the behaviour of the gas phase during decompression. Here, the proportions of gas bubbles preserved within the samples suggest that although the gas bubbles touch in in the melt, they do not exceed the critical percolation threshold (at approximately 30 vol% vesicles; Candela, 1991).

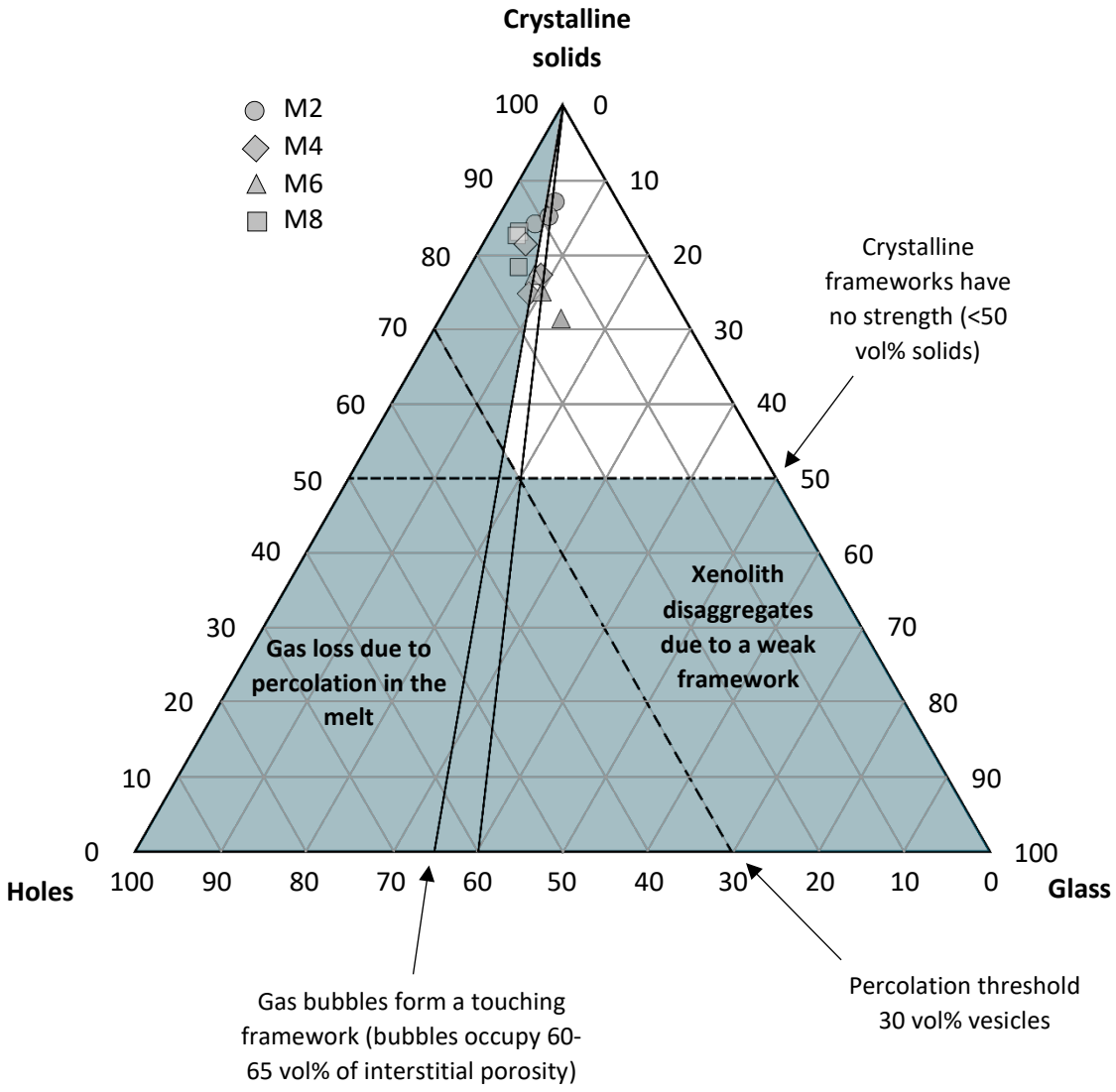

Figure 5.2 – Ternary plot showing the relative proportions of crystalline and non-crystalline (holes and glass) phases, after Holness and Bunbury (2006). Shaded regions indicate phase proportions that should result in disaggregation of the xenoliths during entrainment. These regions are marked by the gas percolation threshold (30 vol% holes – Candela, 1991), where spherical bubbles form a touching framework (when they occupy 60-65 vol% interstitial porosity – Eichelberger et al., 1986) and when crystalline frameworks have no strength (<50 vol% solids). These regions can be used to describe the properties of the porosity fraction; here the gas phase formed a touching framework, but was not sufficiently mobile to migrate through the crystal framework. To compare the 2D and 3D methodologies used in this thesis, this data is presented again in Chapter 6, alongside the phase abundances measured from the three-dimensional CT dataset.

5.2 Crystal size distribution analysis

Although crystal size distribution analysis aims to produce a three-dimensional estimate of crystal size using stereology techniques (e.g. Higgins, 2006a), it is included within this chapter as the input data is derived from 2D measurements. CSDs were calculated for clinopyroxene, hornblende and phlogopite, and are presented in the following sections.

5.2.1 Binarisation

The results of the digitisation and binarisation of the thin section photographs are provided in Figures 5.3-5.6. Each of the binarised slide images were then combined to produce one CSD per sample, hence amalgamating size data from three differently orientated section planes.

5.2.2 Three-dimensional crystal habit

Estimations of 3D crystal habit calculated by CSDSlice are presented in Table 5.1. The 3D crystal habit estimations for the HBL population in sample M2 and the PHL population in M8 are below the accepted R^2 value of 0.8. As both these populations exceed the minimum sample value, the low R^2 value likely indicates that there is some shape variability within the population that reduces the goodness of fit. The majority of the mineral populations are estimated as rectangular prisms, however populations with $R^2 < 0.8$ are estimated as acicular. Figure 5.7 shows the estimated three-dimensional aspect ratios for each of the amalgamated CSDs on a I/L versus S/I diagram (Zingg, 1935), which plot between equant and prolate.

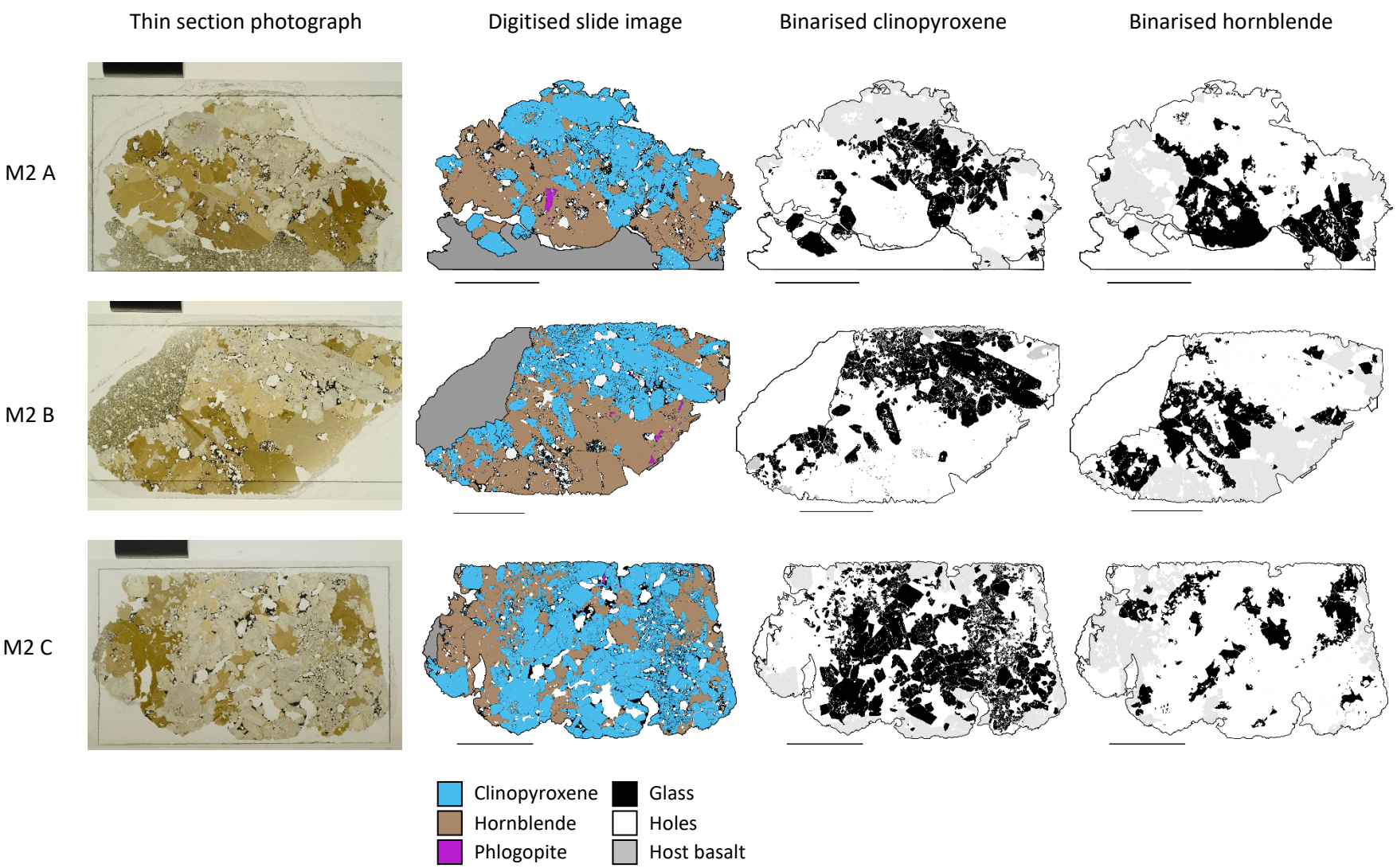

Figure 5.3 – Binarised images used to construct the CSDs for sample M2. All scale bars are 1 cm. Left-most column shows the original high resolution slide photograph. Coloured images are the complete digitised thin section. Binarised images show the mineral analysed for CSD in black, grey indicates crystals that were truncated from the image margin and excluded from the CSD.

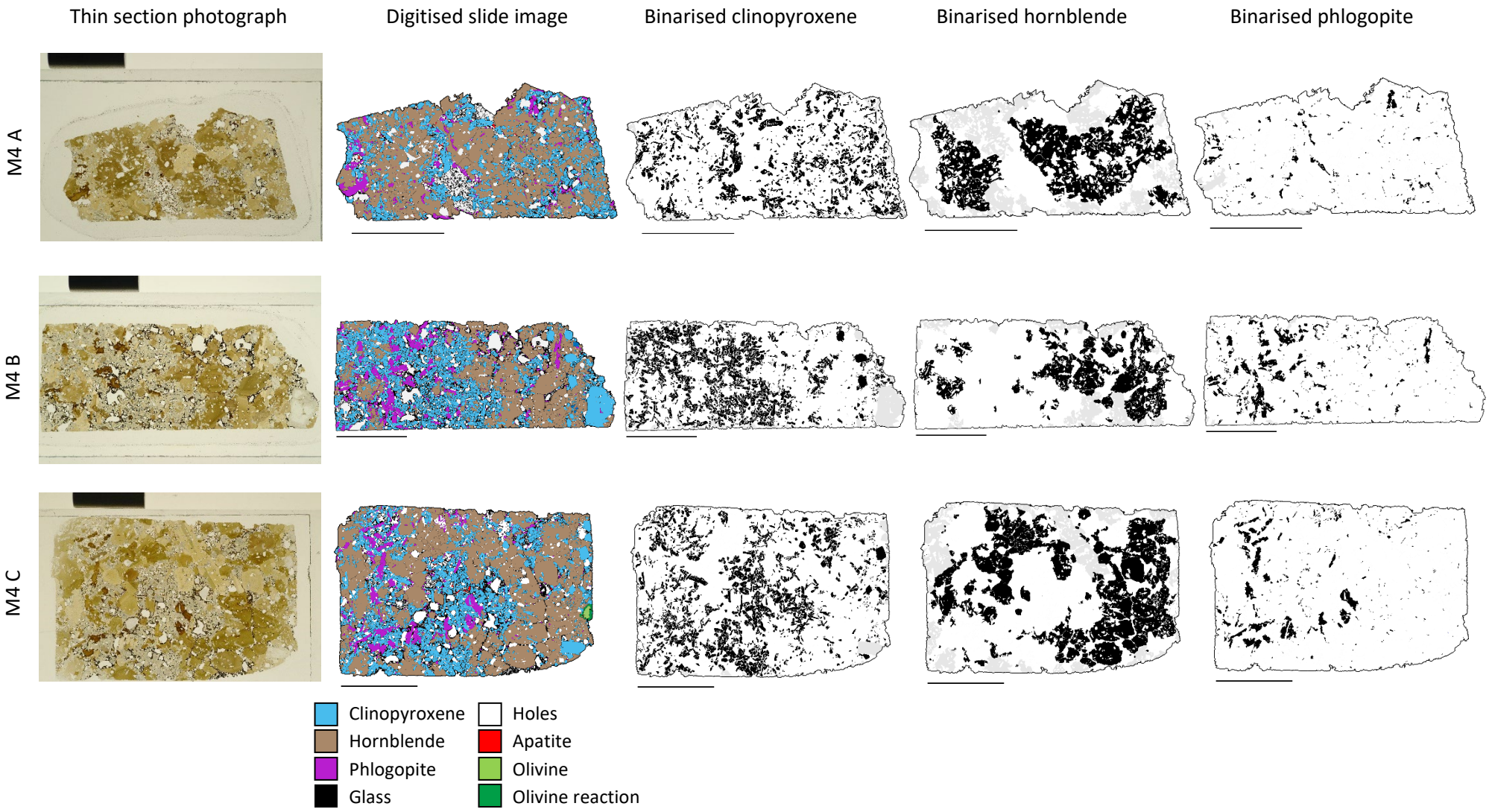

Figure 5.4 – Binarised images used to construct the CSDs for sample M4. All scale bars are 1 cm. Left-most column shows the original high resolution slide photograph. Coloured images are the complete digitised thin section. Binarised images show the mineral analysed for CSD in black, grey indicates crystals that were truncated from the image margin and excluded from the CSD.

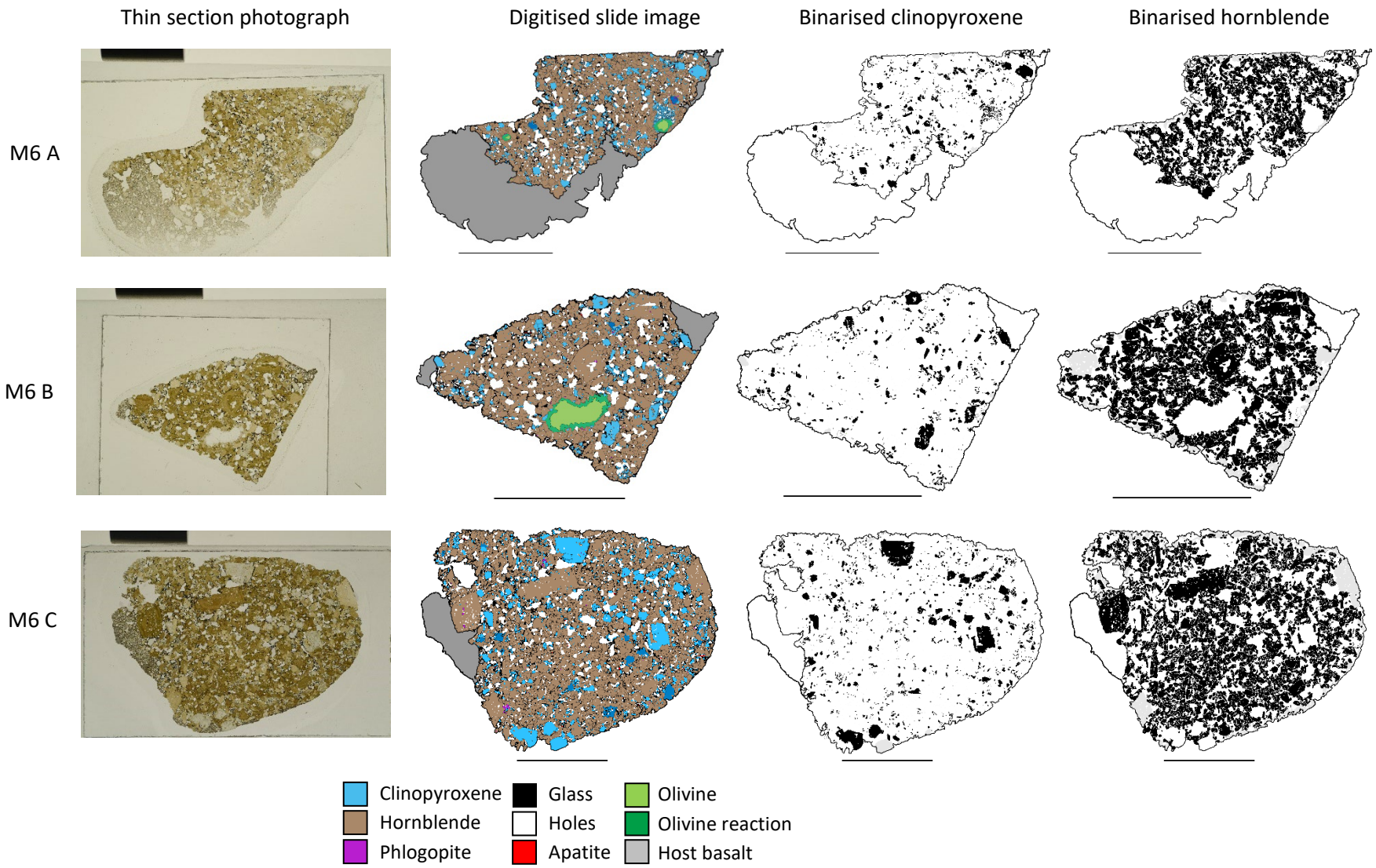

Figure 5.5 – Binarised images used to construct the CSDs for sample M6. All scale bars are 1 cm. Left-most column shows the original high resolution slide photograph. Coloured images are the complete digitised thin section. Binarised images show the mineral analysed for CSD in black, grey indicates crystals that were truncated from the image margin and excluded from the CSD.

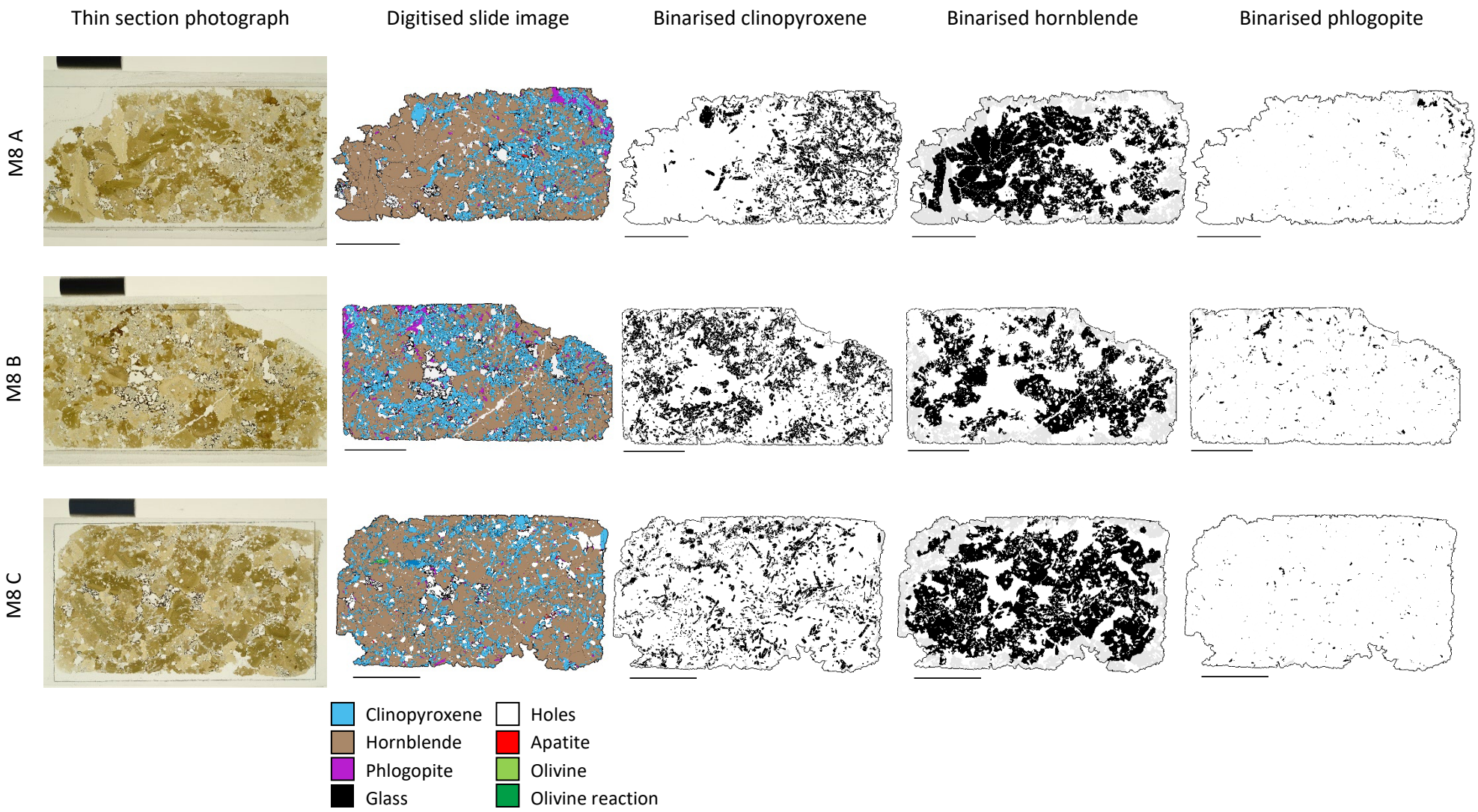

Figure 5.6 – Binarised images used to construct the CSDs for sample M8. All scale bars are 1 cm. Left-most column shows the original high resolution slide photograph. Coloured images are the complete digitised thin section. Binarised images show the mineral analysed for CSD in black, grey indicates crystals that were truncated from the image margin and excluded from the CSD.

Sample	Mineral	N	Estimated 3D aspect ratio			R^2	Shape estimate
			S	I	L		
M2	CPX	5397	1	1.25	2.1	0.88	Rectangular prism
	HBL	**186**	1	1.1	1.9	**0.71**	Rectangular prism
M4	CPX	6208	1	1.4	2.3	0.87	Rectangular prism
	HBL	459	1	1.25	1.8	0.92	Rectangular prism
	PHL	1337	1	1.6	3.6	0.84	Rectangular prism
M6	CPX	3690	1	1.25	1.9	0.9	Rectangular prism
	HBL	6777	1	1.2	1.7	0.9	Rectangular prism
M8	CPX	10121	1	1.4	2.3	0.85	Rectangular prism
	HBL	803	1	1.25	2.1	0.88	Rectangular prism
	PHL	1001	1	1.4	5	**0.75**	Acicular

Table 5.1 **–** Estimates of 3D aspect ratio, calculated using CSDSlice. Bold font denotes R^2 values below 0.8, or sample sizes below 250. Amalgamating the three thin sections into one CSD increases the sample size to above 250, excluding hornblende in sample M2. R^2 values below 0.8 likely indicate shape variability within the population that reduces the goodness of fit, rather than a function of small population sizes. Shape estimates are predominantly rectangular prism; populations estimated to be acicular in shape have R^2 values below 0.8.

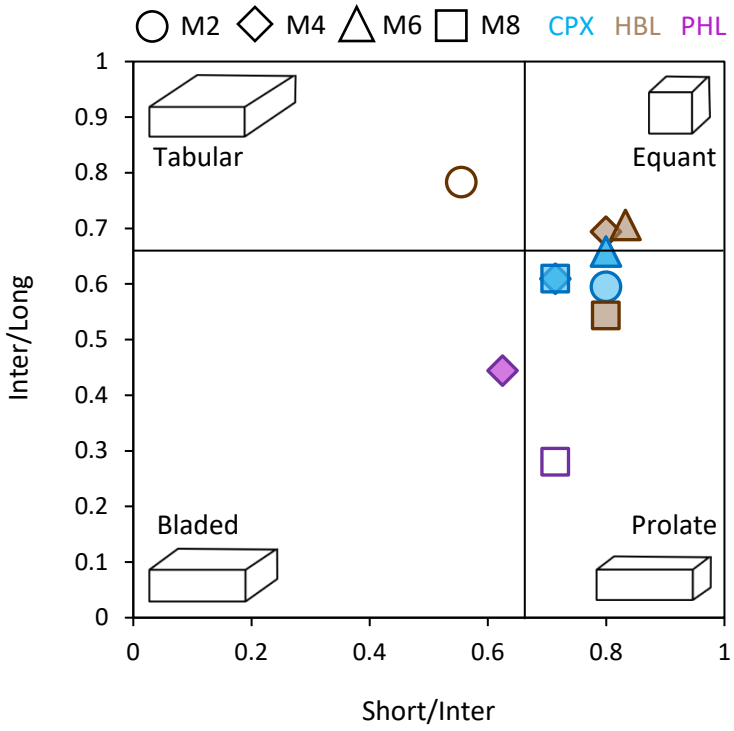

Figure 5.7 – I/L versus S/I diagram (after Zingg, 1935) of best fitting 3D aspect ratio estimates determined from CSDSlice. Filled markers indicate an R^2 value above 0.8, unfilled markers indicate an R^2 value below 0.8.

5.2.3 Crystal size distribution

5.2.3.1 Clinopyroxene

Clinopyroxene CSDs show a negative slope, with a concave upwards curvature (Figure 5.8). All traced crystals are included in the CSD, however grey markers indicate size bins occupied by crystals that fall below the recommended 10 pixel size threshold (<0.07 mm). It is common practice to exclude these crystals from analysis, however they have been included in the CSD as they represent a significant proportion of the total population (up to 8%) and to exclude them completely would obscure information about the nucleation and growth histories of the smallest crystal size fraction. However, interpretation of bins plotted in grey

should be undertaken with consideration that measurement artefacts may contribute towards the calculated population density.

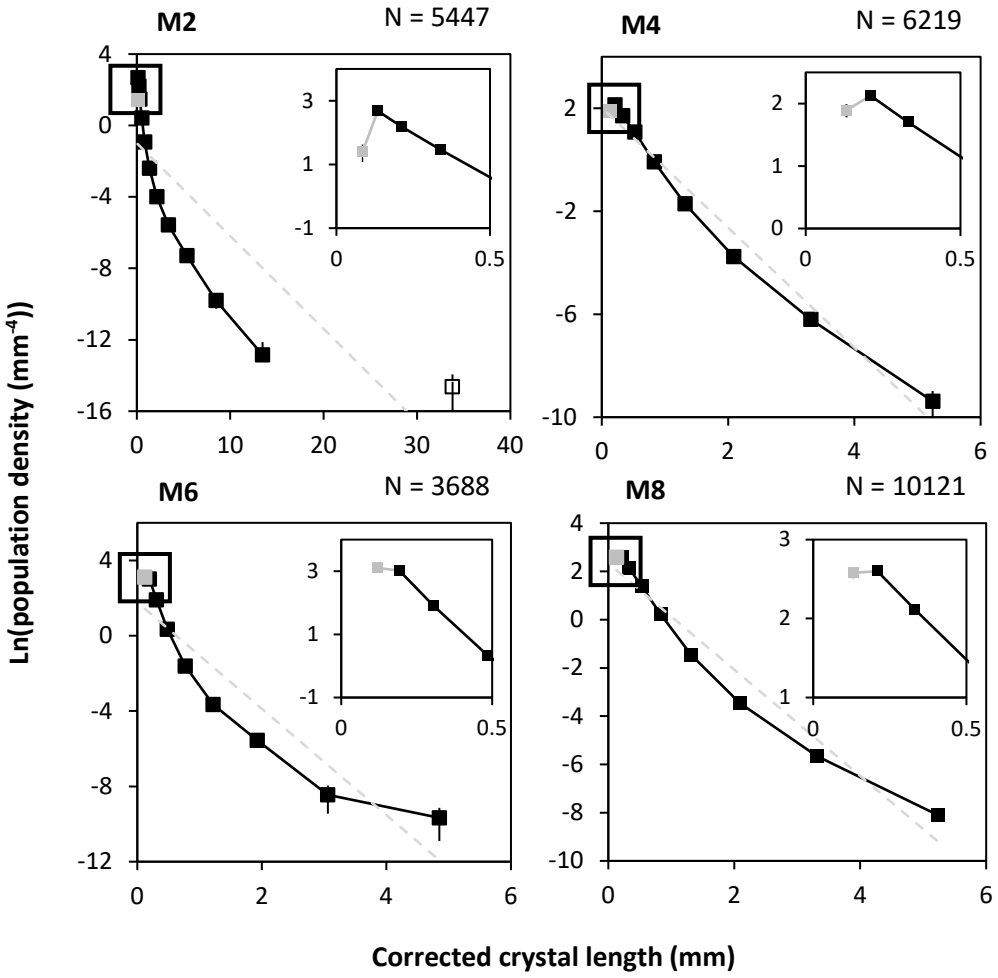

Figure 5.8 – Crystal size distribution graphs for clinopyroxene crystals. Inset is a magnification of the smallest crystals at the left hand side of the CSD. Grey dashed lines indicate the linear regression of the CSD, visualising their curvature and deviation from log-linear. Grey markers indicate size bins containing crystals that are smaller than ten pixels in length, which generate a downturn at the left hand of the CSD and causes positive regions of the CSD slope. Otherwise, all of the CSDs have a negative slope that forms a concave upwards curvature. Sample M2 exhibits a discontinuous CSD, however only one crystal occupies the discontinuous size bin. Error bars are a measure of counting errors, calculated according to the number of crystals within each size bin.

It is recommended that any future textural studies of these samples should utilise photographs taken at higher resolutions, to better resolve the population trend of these smallest crystals. Here, these crystals exhibit population densities that are lower than expected for a log-normal CSD, generating a downturn on the left hand side of the CSD. This downturn is greatest in samples M2 and M4, and produces more of a flattened peak in samples M6 and M8.

All CSDs fail the test for linearity ($Q<0.1$; Higgins, 2006b), however the upwards concavity of the CSDs can be approximated by two log-linear segments that describe the distribution of smaller crystals (represented by a steeper slope) and larger crystals (represented by a shallower slope). The size bin that marks the break in slope between these linear sections is consistent for samples M2, 4 and 8 (~2.09 mm), with similar slopes and Y-intercepts on the left hand side of this break (Figure 5.9). Larger crystals to the right hand side of this break exhibit a shallower slope that extends to the termination of the CSD. Together with the downturns observed for the smallest crystals, these CSDs can each be divided into three segments. M6 exhibits two clear kinks, as well as a flattened peak in the smallest size bin, and is better divided into four segments.

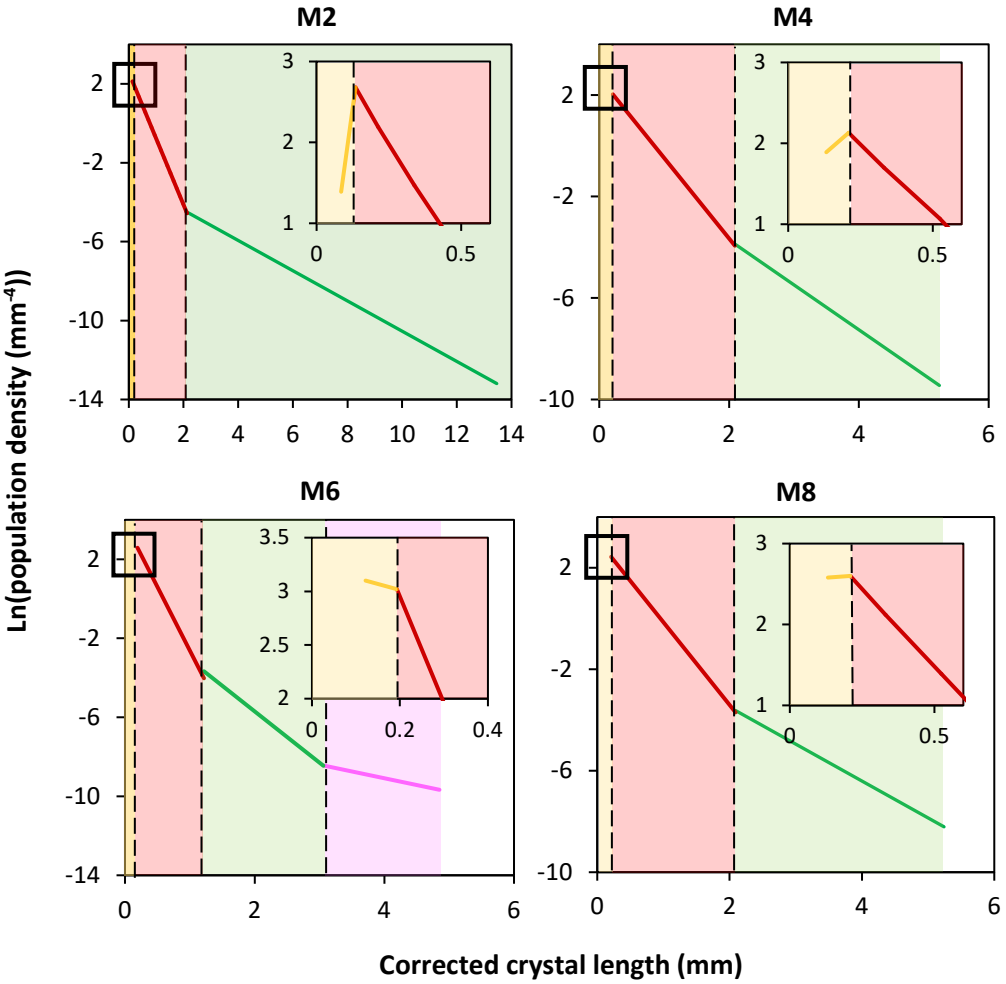

Figure 5.9 **–** Regression of log-linear segments of clinopyroxene CSDs, divided according to changes in slope**.** Dashed lines indicate the size bins that mark the breaks in slope that divide the CSD. For samples M2, 4 and 8 the CSD can be divided as follows. Firstly, the smallest crystals exhibit a downward trend in population density that cause the left hand portion of the CSD (<0.2 mm) to exhibit a positive slope (highlighted in inset image, shown in yellow). This region of the CSD is identified as a possible measurement artefact. Secondly, the steepest portions of the CSDs extend to an intermediate size fraction (red). Lastly, a change in slope occurs in the 2.09 mm size bin, from which the slopes diverge to form a fanned pattern (green). Sample M6 is better divided into four segments. The slope breaks (marked by the dashed line) do not correspond with that of the other samples and together produce a significant curvature.

To quantify the degree of curvature exhibited by these CSDs, Table 5.2 displays the regression statistics for the linear CSD portions that describe the steeper (S1) and shallower (S2) slope sections. Following Witter et al. (2016), curvature is calculated as the difference between slope values S1 and S2, where higher numbers indicate increased concavity.

Sample	Number of crystals	Intercept S1	Slope S1	Intercept S2	Slope S2	Curvature (S2-S1)
M2	5447	2.57	-3.35	-2.87	-0.76	2.59
M4	6219	2.69	-3.17	-0.17	-1.77	1.4
M6	3688	3.55	-4.33	-2.50	-1.51	2.82
M8	10121	3.11	-3.26	-0.59	-1.45	1.81

Table 5.2 – Regression statistics for log-linear portions of the CPX CSDs, summarised by a curvature value that describes the linear deviation of the CSD. S1 refers to the steepest portion of the CSD slope (drawn in red in Figure 5.9), S2 refers to the shallowest slope segment (shown in green). In samples M2, M4 and M8 this division occurs at 2.09 mm. Curvature is calculated as the difference between the slope values of S1 and S2. For Sample M6, which is comprised of three segments, curvature is calculated as the difference between the shallowest and steepest segments. The higher the number, the greater the degree of curvature. From this, samples M2 and M6 exhibit the greatest degree of concavity.

The crystals span a continuous size range in samples M4, M6 and M8 (maximum size bin = ~5 mm), whereas sample M2 has a discontinuous CSD. The continuous proportion of the CSD spans a wider size range than the other samples, occupying size bins up to 13.46 mm. Only one crystal occupies the largest, discontinuous size bin (33.8 mm). Discontinuous CSDs can appear from a scarcity of data and can be improved by acquiring more data or widening the size bin widths until each bin has

an adequate number of crystals in it (Higgins, 2006a). However, there is no reason why a CSD must be continuous, and in this instance it was considered best practice to maintain a constant recommended value of 5 bins per decade for all samples.

5.2.3.2 Hornblende

Hornblende CSDs exhibit a negative slope with a concave upwards curvature that is perturbed by variations in population density amongst the smallest crystal size bins (Figure 5.10). This results in portions of the CSD with a positive slope at crystal sizes <0.5 mm. Unlike the CPX data, these perturbations do not just occur within the size bins containing crystals below ten pixels in length. This reduces the likelihood that these trends represent a measurement artefact. These perturbations define one region of the CSD. In addition to this, the upwards curvature of the HBL CSDs can be divided into log-linear sections, approximated by a kink that marks a change in the slope. Each CSD can thus be divided into three segments (Figure 5.11). Firstly, crystals smaller than 0.5 mm show variations in population density that generate a positive slope. Secondly, the steepest portion of the CSD slope incorporates crystals up to the penultimate size bin. Thirdly, a kink in the largest size bin causes a decrease in slope. M2 is an exception to this; the shallowest slope segment incorporates multiple size bins. Unlike the CPX data, the size bins that mark the breaks in slope between these segments are different for every sample, with varied slope and intercept values (Table 5.3). The continuous portion of the CSDs each span a different crystal size range, and samples M4 and M6 produce discontinuous CSDs. The concavity of the CSDs is quantified by the curvature value, which also varies between the samples.

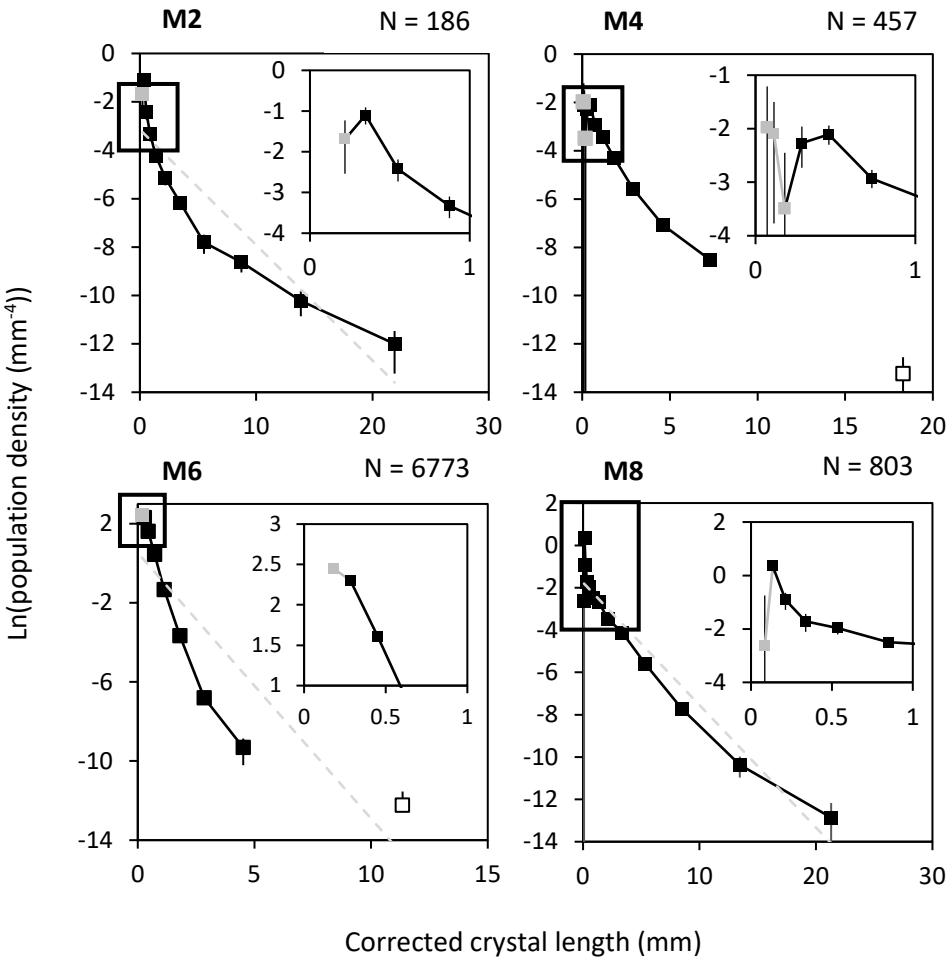

Figure 5.10 - Crystal size distribution graphs for hornblende crystals. Inset is a magnification of the smallest crystals at the left hand side of the CSD. Grey dashed lines indicate the linear regression of the CSD, visualising their curvature and deviation from log-linear. Grey markers indicate size bins containing crystals that are smaller than ten pixels in length. The population density of the smallest crystals fluctuates to generate portions of the CSD with a positive slope. Otherwise, the CSDs exhibit negative slopes that in their entirety form an upwards curvature. Samples M4 and M6 exhibit discontinuous CSDs; only one crystal occupies this size bin. Error bars are a measure of counting errors, calculated according to the number of crystals within each size bin.

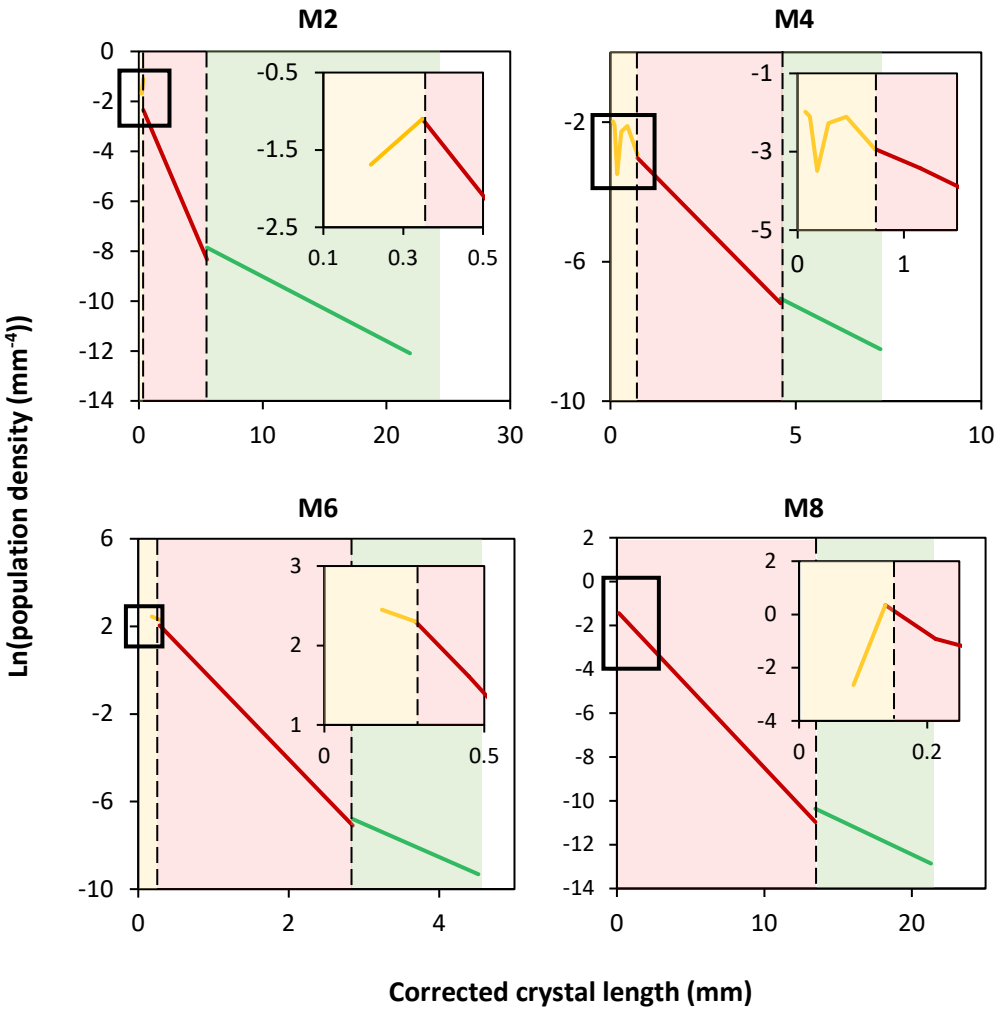

Figure 5.11 – Regression of log-linear segments of hornblende CSDs, divided according to changes in slope**.** Inset images show magnification of the smallest occupied size bins; to visualise the irregularity of sample M4 it has not been summarised by a linear regression model. Each CSD can be divided into three segments according to variations in slope. The smallest crystals (yellow) exhibit fluctuations in population density that generate regions of the CSD with a positive slope. The red section denotes the portion of the CSD that exhibits the steepest slope. The green section represents the shallowest slope. Excluding sample M2, the break in slope between these portions occurs at the largest occupied size bin.

Sample	Number of crystals	Intercept S1	Slope S1	Intercept S2	Slope S2	Curvature (S2-S1)
M2	186	-2.95	-0.61	-7.16	-0.22	0.39
M4	457	-2.24	-1.08	-4.59	-0.54	0.54
M6	6773	3.05	-3.56	-2.50	-1.51	2.05
M8	803	-1.34	-0.71	-6.07	-0.32	0.39

Table 5.3 – Regression statistics for log-linear portions of hornblende CSDs, summarised by a curvature value that describes the linear deviation of the CSD. S1 refers to the steepest portion of the CSD slope (shown in red in Figure 5.11), S2 refers to the shallowest slope (shown in green). Curvature is calculated as the difference between the slope values of S1 and S2.The higher the number, the greater the degree of curvature. All of the samples indicate some degree of concavity, although this varies between samples. Each of the concavity values are lower than for the correspondent CPX CSD.

5.2.3.3 Phlogopite

By its volumetric abundance (~<5%), phlogopite is categorised as an accessory phase within these samples. However, the number density of PHL crystals in samples M4 and M8 exceeds that of the essential HBL phase and a PHL CSD was therefore calculated for these samples. The resultant CSDs have a negative slope, with a concave curvature and downturn in the smallest occupied size bin (Figure 5.12). As with the CPX data, this downturn only occurs within the size bin that contains crystals below the measurement threshold, and it is possible that this represents a measurement artefact. The curvature of these CSDs can be divided into log-linear segments that approximate smaller and larger crystals. Together with the downturn that causes a positive slope, each PHL CSD can therefore be divided into three segments (Figure 5.13). The curvature of the CSDs is summarised in Table 5.4.

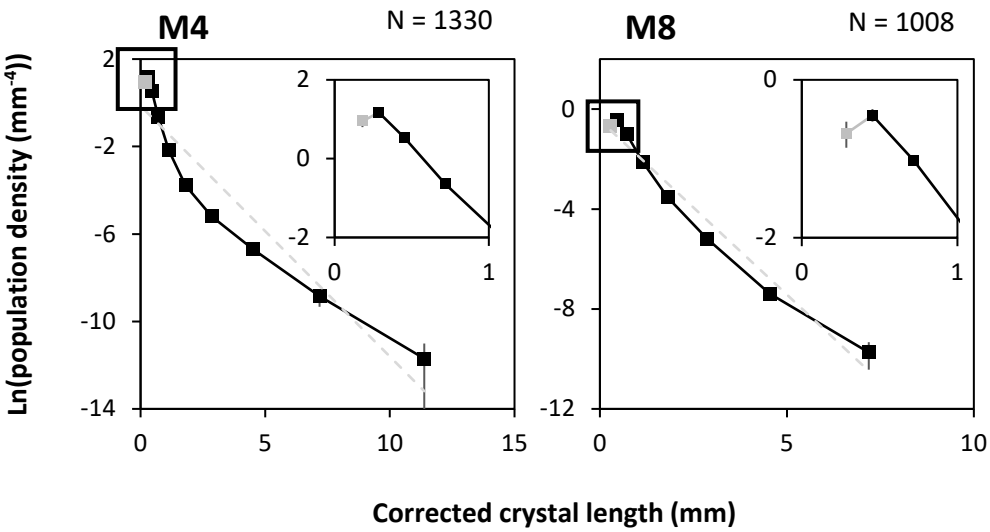

Figure 5.12 - Crystal size distribution graphs for phlogopite crystals. PHL crystals in samples M2 and 6 did not exceed the minimum required sample size of 250 and so realistic CSDs could not be calculated. Grey dashed lines indicate the linear regression of the CSD, visualising their curvature and deviation from log-linear. Inset graphs are a magnification of the smallest crystals at the left hand side of the CSD. Grey markers indicate size bins containing crystals that are smaller than ten pixels in length, which form a positive slope at the left hand of the CSD. Otherwise, both CSDs exhibit a negative slope with a concave upwards curvature. Error bars are a measure of counting errors, according to the number of crystals within each size bin.

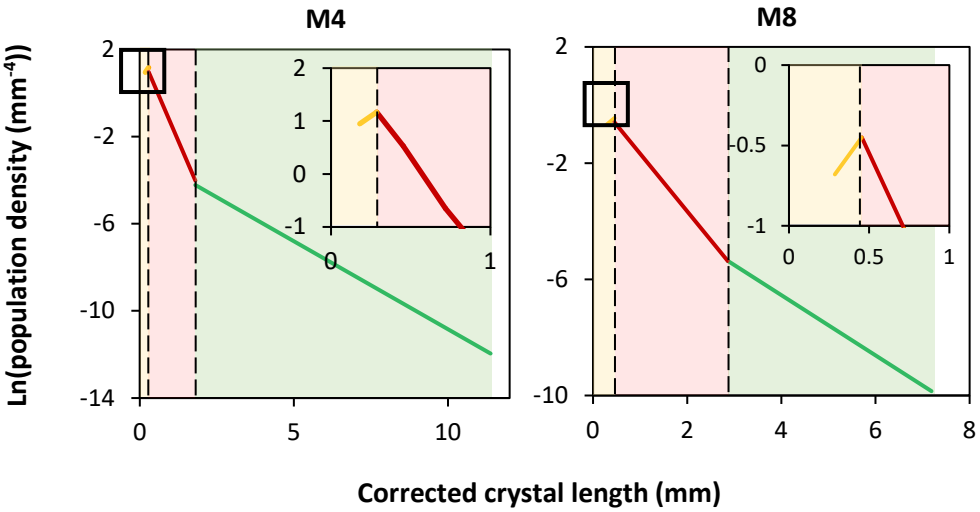

Figure 5.13 – Regression of log-linear segments of phlogopite CSDs, divided according to changes in slope**.** Inset images show magnification of the smallest occupied size bins. Each CSD can be divided into three segments according to variations in slope. The smallest crystals (yellow) exhibit a decrease in population density that generates a downward deflection at the left hand side of the CSD. The red section denotes the portion of the CSD that exhibits the steepest slope and the green section represents the shallowest slope portion. Although each CSD exhibits a variable size range, both can be divided according to these criteria.

Sample	Number of crystals	Intercept S1	Slope S1	Intercept S2	Slope S2	Curvature (S2-S1)
M4	1330	1.91	-3.29	-2.77	-0.81	2.48
M8	1008	0.31	-1.98	-2.40	-1.04	0.94

Table 5.4 – Regression statistics for log-linear portions of phlogopite CSDs, summarised by a curvature value that describes the linear deviation of the CSD. S1 refers to the steepest portion of the CSD slope (shown in red in Figure 5.13), S2 refers to the shallowest (shown in green). Curvature is calculated as the difference between the slope values of S1 and S2. The higher the number, the greater the degree of curvature. Here, the phlogopite crystals in sample M4 exhibit a greater concavity than those in sample M8.

5.2.3.4 Comagmatic CSDs

CSD studies generally focus on one mineral phase, providing an insight in to one component of the multiphase rock. This is a valuable approach when the samples are collected in-situ; CSDs of one mineral phase can be analysed to identify spatial variations that correspond to thermal or chemical trends in the igneous system (e.g. Cashman, 1993; Resmini and Marsh, 1995). There are comparatively few studies that analyse multiple comagmatic phases (e.g. Armienti et al., 1994; Higgins and Roberge, 2003). As the xenoliths are ex-situ in nature, they cannot be used in the aforementioned context and it is therefore valuable to compare multiple phases from the same rock in order to constrain the crystallisation history. To compare CSDs of different minerals, the crystal size is normalised to the maximum crystal size measured for each phase. This approach was utilised by Simakin and Bindeman (2008), and further investigated by Rannou and Caroff (2010). Recalculating the CSDs in this way does not significantly change the shape of the CSD, but allows the population distribution to be investigated between differently sized mineral phases (Simakin and Bindeman, 2008). This data can be visualised as a frequency plot of normalised crystal length (Figure 5.14). Comagmatic CSDs exhibit variations in population distribution that attest to varied crystallisation dynamics affecting each mineral phase. However all crystal populations are skewed towards the smallest crystal sizes, and the modal size class frequently overlaps for comagmatic CSDs. In sample M2 the HBL mode is shifted towards intermediate crystal sizes, and the population distribution does not overlap with comagmatic clinopyroxene.

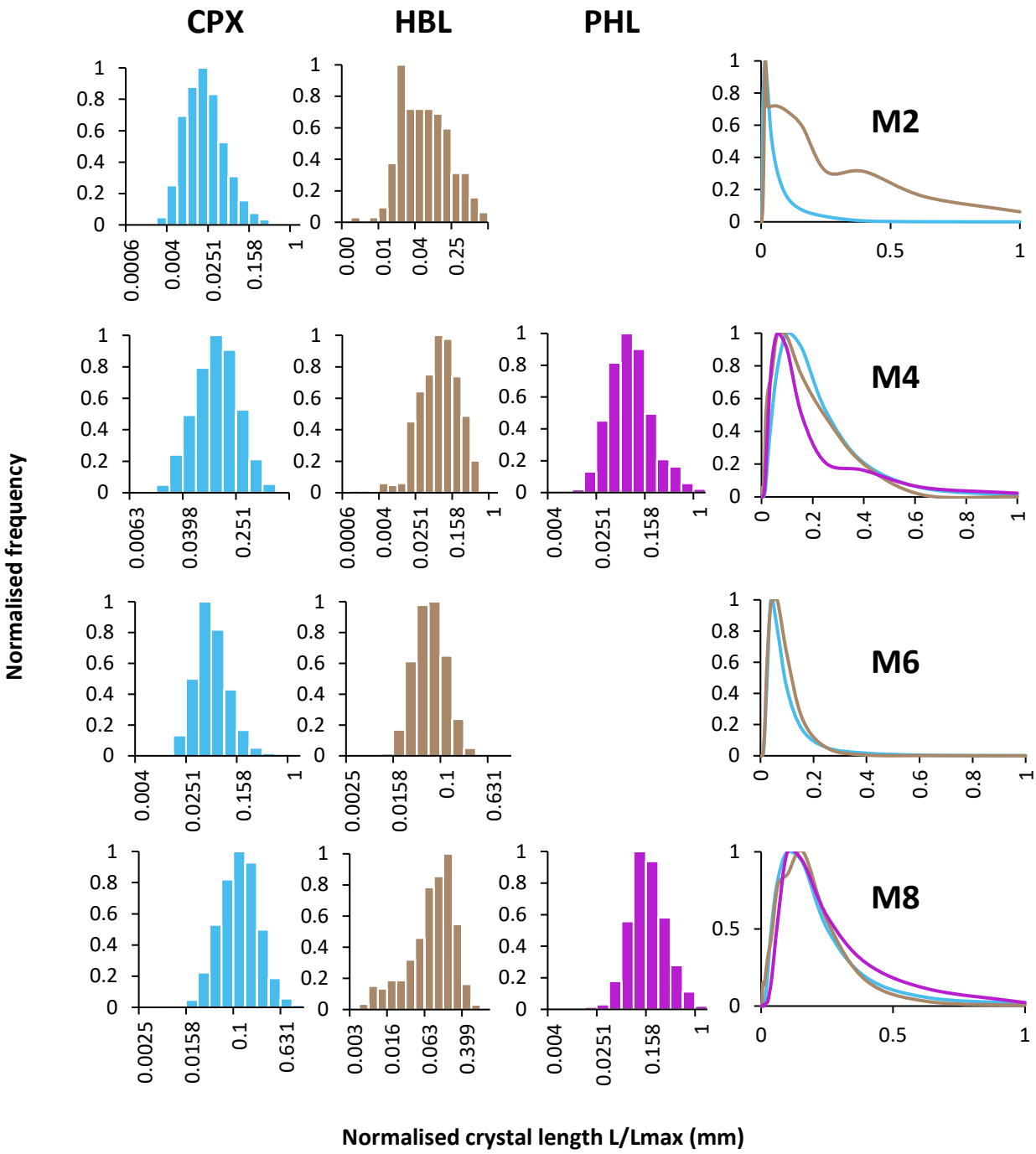

Figure 5.14 – Frequency plots of normalised crystal length, derived from the CSD data. Population distributions are compared in the right hand column, visualising the population differences between comagmatic mineral phases.

5.2.3.5 CSD summary

The results of the CSD analysis can be summarised as follows:

- The CSDs are characterised by a negative slope with a concave upwards curvature.
- The CSDs can be divided into three segments that represent breaks in the slope. Sample M6 provides an exception to this, because the clinopyroxene CSD is more appropriately divided into four segments.
- The smallest crystals exhibit population densities that are lower than expected for a log-normal CSD distribution, which generates positive regions of the CSD slope. It is possible that these downward deflections reflect the resolution limits of the methodology (10 pixels) as the smallest crystals are most likely to introduce measurement errors into the data set.
- The steepest portion of the CSD slope represents a continuous decrease in population density with increasing crystal size. This produces a log-linear segment of the CSD; the size range of crystals included in this segment vary between samples and mineral phase.
- A change in the slope defines a third segment of the CSD that is characterised by a shallower log-linear slope that extends to the largest measured crystal size. Combined with the steeper portion of the CSD, this generates the curvature that characterises all of the CSDs.

5.3 Shape preferred orientation (SPO)

Figure 5.15 shows a plot of the coherence of SPO against the average aspect ratio of the crystal populations. A coherence value of 1 indicates that there is no shape preferred orientation, whilst a value close to 0 means that the crystals are well aligned (Higgins, 1996b). Whereas the CSD data amalgamates the three sections cut from each sample, here they are plotted separately to ensure that any identified SPO trends are not obscured. Aspect ratios show little variation between samples, but are plotted to provide a shape context to the SPO data. All crystal populations in all samples have a coherence value close to 1, suggesting little to no shape preferred orientation. Coherence values vary between sections cut at different orientations, but do not indicate that any of the samples exhibit a preferred SPO on any particular sectioning plane. From this, it is considered unlikely that the crystal textures exhibit any significant fabric.

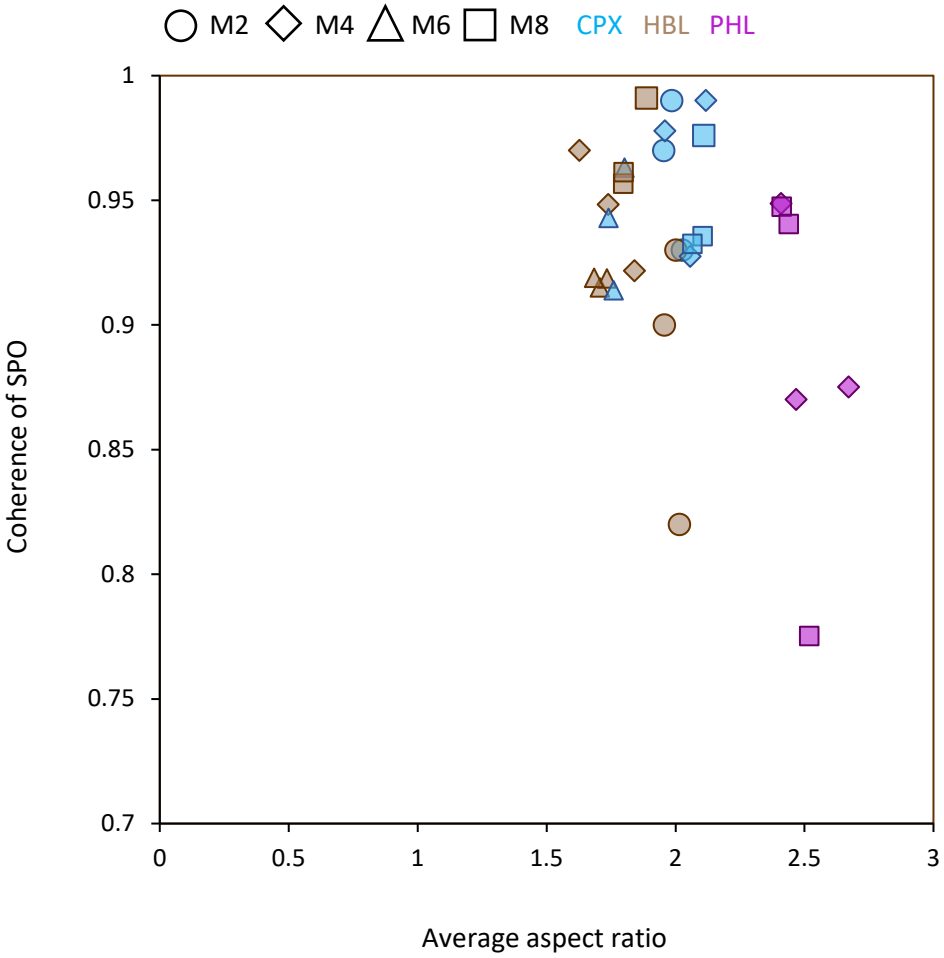

Figure 5.15 **–** Plot of coherence of shape preferred orientation versus the average aspect ratio measured in 2D. Coherence of SPO is a measure of the degree of alignment within a population, with no associated orientation direction. A value of 1 means there is no alignment, a value close to 0 means that there is a well-defined alignment. Aspect ratio is measured as the average ratio of the long and short axis of 2D crystal cross sections, as appropriated by the best fit ellipse.

5.4 Spatial distribution pattern (SDP)

Figure 5.16 shows a plot of the R-value (the ratio between the mean and predicted nearest neighbour distances) versus porosity (area% occupied by other phases), which defines the spatial distribution pattern (SDP). Shaded and non-shaded regions of the graph indicate touching and non-touching crystal frameworks, which can be further divided into clustered or ordered packing patterns by the random sphere distribution line (RDSL) (Jerram et al., 2003). Whereas the ternary plot in Figure 5.2 can be used to constrain three-dimensional connectivity of the porosity fraction, the SDP analysis can be used here to constrain the 3D packing of the solid crystalline framework, which in turn reflects the distribution of porosity (Jerram et al., 2003). Additionally SDP analysis can be used to indicate the occurrence of a number of magmatic processes. Trends for compaction, overgrowth, sorting and vesiculation (Jerram et al., 2003; Martin et al., 2006b) are shown by the labelled vectors. For all of the samples, both the CPX and HBL crystals each constitute a touching crystal framework, with a clustered packing trend. CPX crystals lie closer to the non-touching region, and show more packing variability between the different samples than is observed for the HBL crystals.

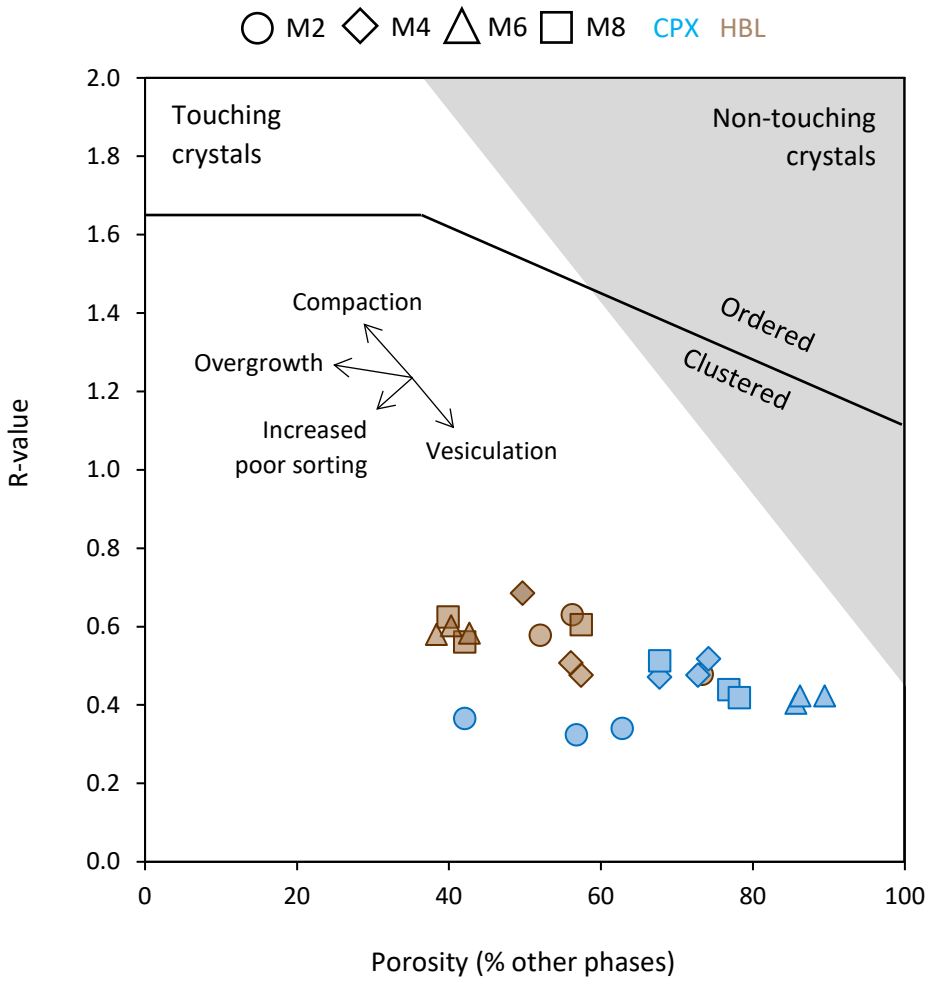

Figure 5.16 – Plot of porosity versus R-value to visualise the spatial distribution pattern of CPX and HBL crystals. The R-value is a parameter that quantifies the spatial distribution of a crystal population, quantified as the ratio of the mean nearest neighbour distance and the predicted nearest neighbour distance for a random population with the same population density. Percentage porosity describes the sum of all other phases excluded from the R-value calculation. The line separating ordered and clustered crystal represents the Random Sphere Distribution Line (RDSL) (Jerram et al., 2003). Trends for compaction, overgrowth and sorting are from Jerram et al. (2003), Vesiculation trend is from Martin et al. (2006b). In all samples, CPX and HBL crystals form a touching framework with a clustered, non-random packing trend.

5.5 Summary

All of the data used in this chapter is provided in Appendix 1. A summary of the main findings of this chapter are provided in the following:

- The crystalline contents of the samples are predominantly hornblende (26.7-61.6%) and clinopyroxene (10.5-57.9%), with accessory phlogopite (0.2-9.3%), olivine (0.1-3.1%) and apatite (0-0.2%). Thin sections cut through the same sample yield broad ranges in mineral abundance values, indicating that the samples are texturally heterogeneous.
- The porosity fraction of each sample can be quantified as the sum of the area occupied by glass and holes. This comprises between 12 and 26% of the samples.
- The connectivity of the gas phase is insufficient to exceed the critical percolation threshold, but the 2D data suggests that the gas bubbles form a touching framework. The total porosity fraction does not reach the threshold that exceeds the integrity of the crystal framework.
- The 3D crystal habit is consistently estimated as a rectangular prism, however some uncertainty in these estimates ($R^2 < 0.8$) suggests that there is some shape variability within crystal populations.
- Crystal size distributions for CPX, HBL and PHL crystals exhibit negative slopes characterised by a concave upwards curvature.
- These CSDs can be divided into three sections according to breaks in slope that separate log-linear segments.
- Downwards deflections at the smallest size fractions may indicate measurement artefacts rather than true population trends.

- There is no identifiable shape preferred orientation in any of the crystal populations.
- Spatial distribution patterns indicate that the 3D packing of clinopyroxene and hornblende crystals constitute a touching, clustered framework.

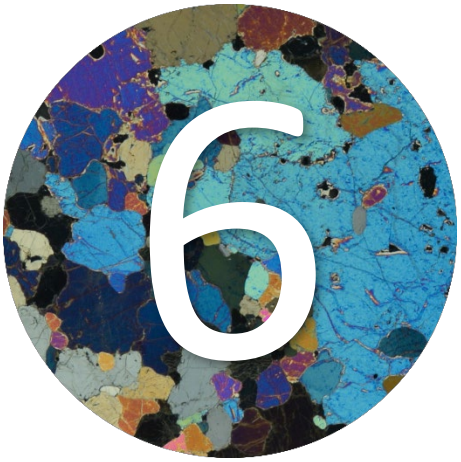

Three-dimensional X-ray Computed Tomography

Chapter 6 presents the results of the computed tomography (CT) data, with focus on the visualisation and quantification of the pore spaces that record melt distribution in the semi-solidified crystal framework. Pores (expressed as the sum of the non-crystalline components) are categorised into connected and disconnected networks using the commercial software PerGeos v 1.7.0. The geometries of these networks are analysed to constrain the distribution of the moveable and trapped melt fractions in these xenolith samples.

6 Three-dimensional X-ray Computed Tomography

6.1 Volume fraction

Following the filtering and segmentation processes outlined in Chapter 3, three phases were identified and segmented for each sample (Figure 6.1). The different mineralogies that comprise the total crystalline population (CPX + HBL + PHL ± AP± OL) cannot reliably be distinguished by their greyscale intensities and are combined into one segmented phase, referred to as 'crystalline solids'. Void spaces are easily discernible as the darkest greyscale phase and glass can be identified as an intermediate greyscale intensity. The volume fractions of crystalline solids, void spaces and glass are recorded in Table 6.1.

	Sample			
	M2	M4	M6	M8
Crystalline solids	80.37	82.21	73.14	85.59
Void	8.93	7.57	15.13	8.70
Glass	10.70	10.22	11.73	5.71

Table 6.1 – Volume fractions of segmented phases in the CT data.

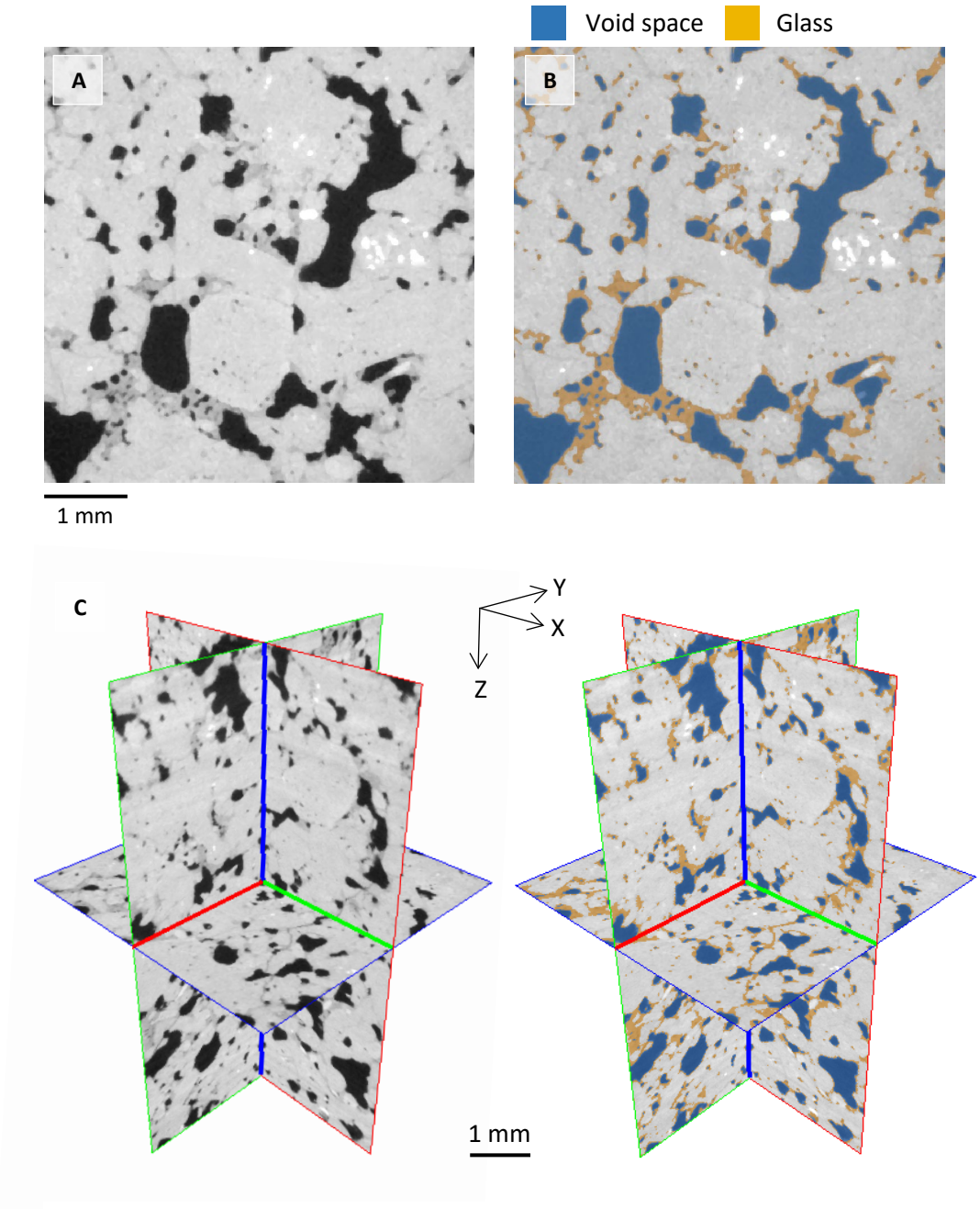

Figure 6.1 **–** Segmentation of CT images. **A)** Greyscale tiff image from sample M6, after filtering to reduce noise and image artefacts. The darkest areas represent void spaces, the darker grey represents glass and the lighter grey represents the crystal phase. The different mineralogies known to be present within this sample (essential CPX and HBL, accessory PHL, AP and OL) are indistinguishable from their greyscale values, however an accessory phase is more attenuating and appears as the brighter white patches. **B)** Same image as in **A**, showing segmentation of voids (blue) and glass (yellow). All crystals are combined into one phase: 'crystalline solids'. **C)** CT slices in the X, Y and Z planes, configured to show the internal structure of the sample. Right is unsegmented as in **A**, left is segmented as in **B**.

Figure 6.2 shows a ternary plot of the sum of the relative proportions of crystalline solids, holes and glass measured for each sample. Grey icons represent the same measurements obtained from the 2D area fraction analysis in Chapter 5, black icons are the measurements obtained from the 3D CT. The three-dimensional volume fractions plot in close proximity to those obtained from the 2D thin sections, however exhibit a greater fraction of glass than measured in 2D. This acts to shift the samples to the right hand side of the line that marks the bubble fraction that forms a connected framework (60-65 vol.% of interstitial porosity), suggesting that the bubbles are actually disconnected.

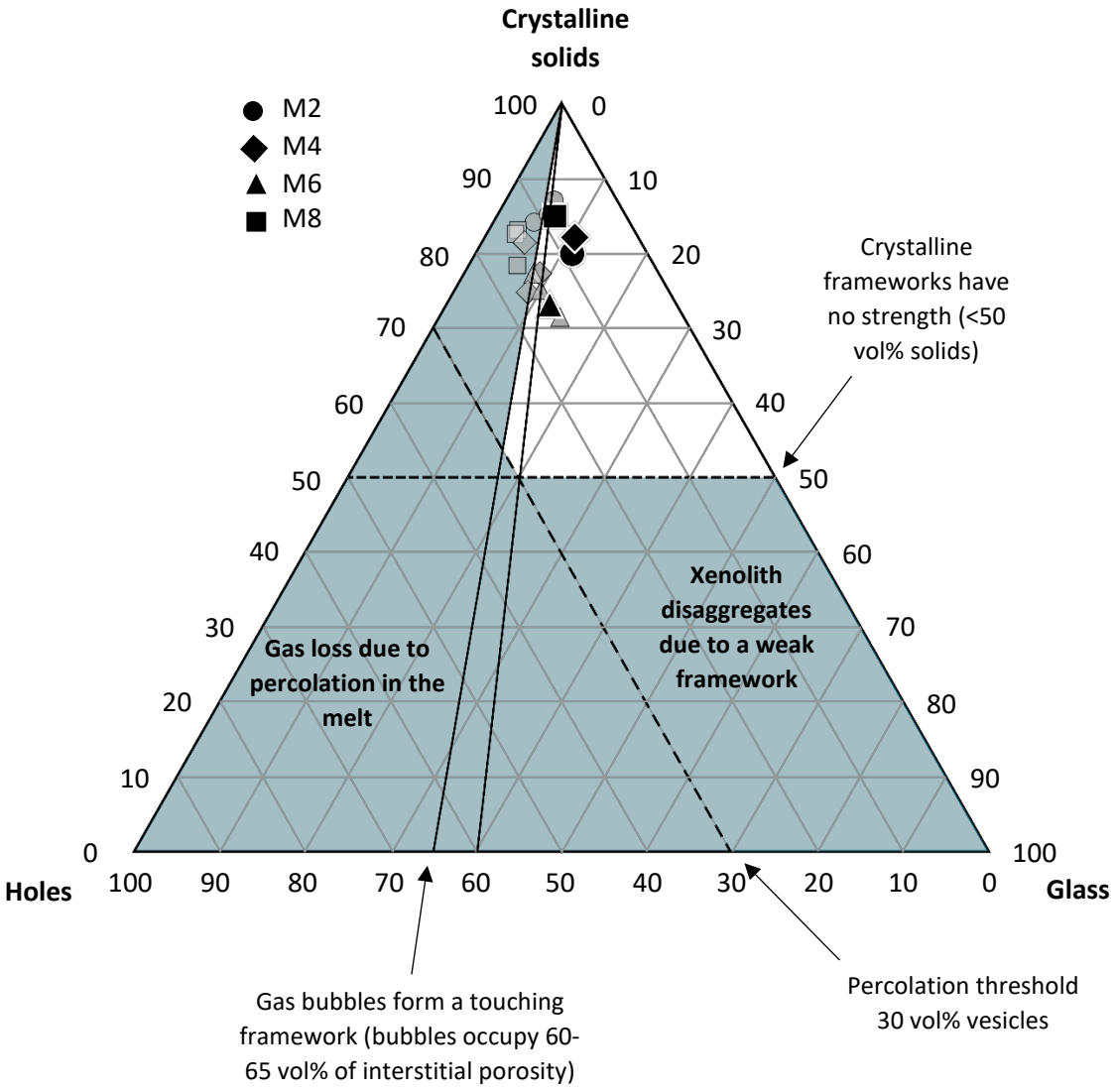

Figure 6.2 – Ternary plot showing the relative proportions of crystalline and non-crystalline (holes and glass) phases, after Holness and Bunbury (2006). Shaded regions indicate phase proportions that should result in disaggregation of the xenoliths during entrainment. These regions are marked by the gas percolation threshold (30 vol% holes – Candela, 1991), where spherical bubbles form a touching framework (when they occupy 60-65 vol% interstitial porosity – Eichelberger et al., 1986) and when crystalline frameworks have no strength (<50 vol% solids). Grey icons represent the measurements obtained from the 2D thin sections, black icons are the measurements obtained from 3D. The 3D data plots closely to the 2D data, but appears to shift towards a greater glass fraction. This results in the samples all plotting to the right hand side of the line that marks the bubble fraction at which bubbles form a connected framework, contrasting to the 2D data.

6.2 Porosity

As in Chapter 5 and following the work of Holness and Bunbury (2006), porosity herein refers to the sum of non-crystalline material (glass + holes), and is used as an analogue for melt distribution. Although the term porosity conventionally refers to just the void spaces, it is here used to refer to the fraction of the sub volumes that have not yet crystallised and are therefore occupied by potentially transportable melt. Figure 6.3 shows a graph of the total porosity measured for each sample, divided into connected and disconnected porosity.

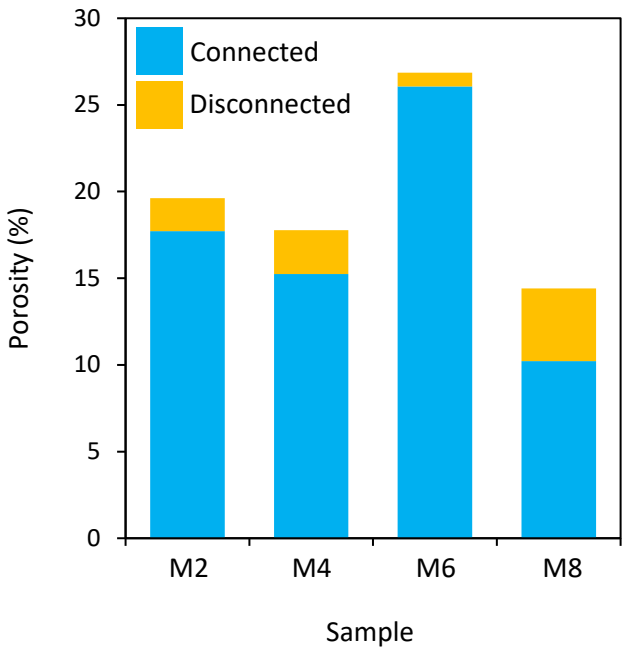

Figure 6.3 **–** Measurements of total porosity in each sample, divided into connected and disconnected porosity. Connected porosity is calculated through the X, Y and Z orientations to identify a fully connected pore network in all directions. This indicates that despite the high crystallinities measured in these samples (>73%), the melt fraction comprises a connected network with lesser volumes of trapped melt.

The samples show a range in the total measured porosity (14.4 – 26.9%), but are all characterised by a greater proportion of connected porosity which ranges between 70.9% of total porosity in M8 to 97.1% in M6. This indicates that the majority of pore spaces in these samples comprise a connected network, and that the melt phase is therefore well-connected through the crystal framework.

6.2.1 Pore geometries

The generation of pore network models provides a number of parameters that characterise pore geometries, derived from measurements of the pores and throats that constitute the model. Figure 6.4 shows a series of plots that depict the percentage of connected porosity versus measured geometries of the PNMs. It is clear that there is geometric variation between samples, however there is no significant correlation between the plotted parameters and the percentage of connected porosity. The greatest difference between samples manifests in the pore number density, which varies between 132.7 mm^{-3} in sample M8 and 354.7 mm^{-3} in sample M2. There is less variation in the throat number density, however M2 has a far greater density of throats than the other samples. This corresponds to the smallest average pore and throat radii of all of the samples. From this, the porosity in M2 can be described as consisting of a high-density network of volumetrically small pores with narrow throats. The sample also records the largest average coordination number and tortuosity values, however there is little variation between the samples. This indicates that the clear differences between pore and throat radius and number density do not significantly manifest in the connectivity and tortuosity of the samples, which vary between 2.05-3.34 and 1.83-2.78 respectively. This observation is of particular interest for sample M6, which exhibits the greatest proportion of connected porosity (26.07%) but no notable geometric

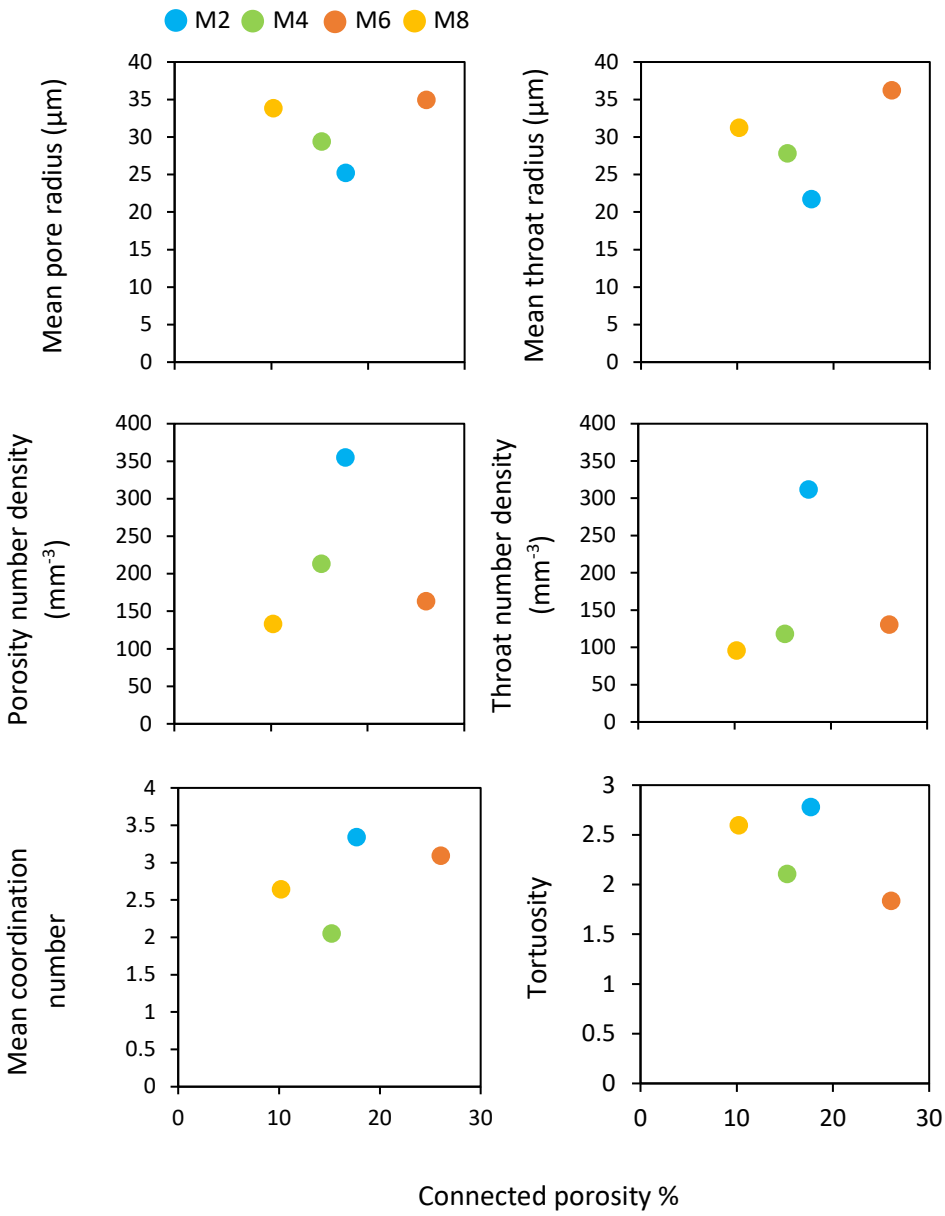

Figure 6.4 – Geometric properties of pores and throats versus the percentage of connected porosity in the CT volumes. From these plots it appears that there is no correlation between any of these geometric parameters and connected porosity, however it is clear that there is significant geometric variation between samples. Mean pore and throat radii and pore number density are calculated from disconnected + connected porosity. Throat number density and mean coordination number are calculated from only connected porosity.

characteristics that would attest to this. The pore and throat number densities in M6 lie between those of samples M4 and 8, and the average pore and throat radii are not significantly greater than that of the other samples. The pore geometries are further explored in Figure 6.5, which shows a series of histograms that display pore radii for disconnected and connected pore spaces.

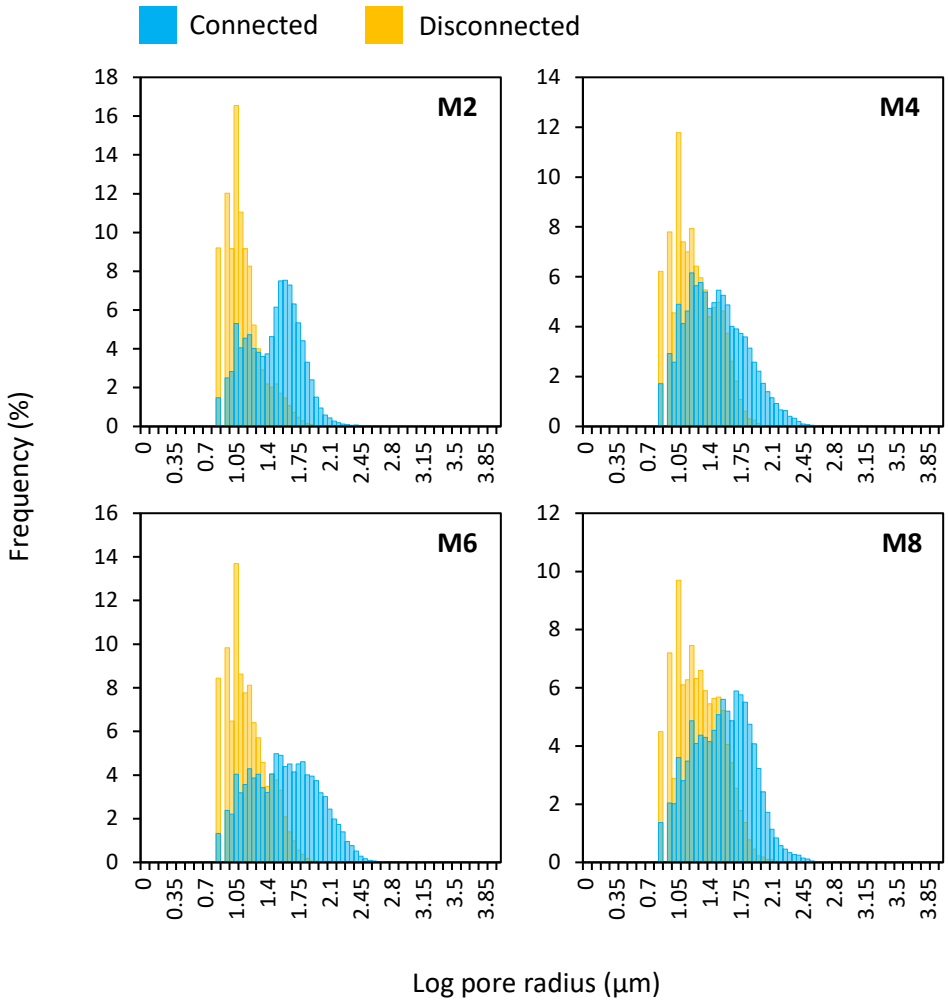

Figure 6.5 **–** Histograms showing the log distribution of connected and disconnected pore radii measured from the pore network models. Disconnected pores are characteristically smaller than the connected pores, however there is a significant overlap between the histogram peaks. Disconnected pores exhibit narrower peaks that are unimodal, whereas the connected pores show broader, frequently bimodal peaks.

For all samples, the disconnected pore spaces exhibit a peak at a smaller pore radius than the connected pores. These peaks are unimodal and are also narrower and characterised by a right hand skew towards smaller pore radii. This suggests that the disconnected pore spaces tend to be smaller than the connected pores, however there is a significant overlap between them caused by a high frequency of small connected pores with low coordination numbers (Figure 6.6).

► ***Figure 6.6 (overleaf)*** **–** Histograms showing the distribution of coordination numbers. A coordination number of zero indicates a pore with no throats connected to it that is therefore disconnected (shown in yellow). Blue bars indicate pores with at least one throat to connect it to another pore. For all samples, it is clear that there is a dominance of poorly connected pores with low coordination numbers. In sample M2 38.6% of connected pores have a coordination value of 1, M4 = 70.6%, M6 = 40.1% and M8 = 49.4%. The inset scatter plots show the average coordination number as a function of the log pore radius. For all samples there is a clear relationship between the size of the pore and the number of throats connected to it. This indicates that smaller pores are more likely to have fewer connections and therefore become disconnected. The high frequency of poorly connected pores, which characteristically exhibit small radii, explains the overlap between disconnected and connected histogram peaks in **Figure 6.5**.

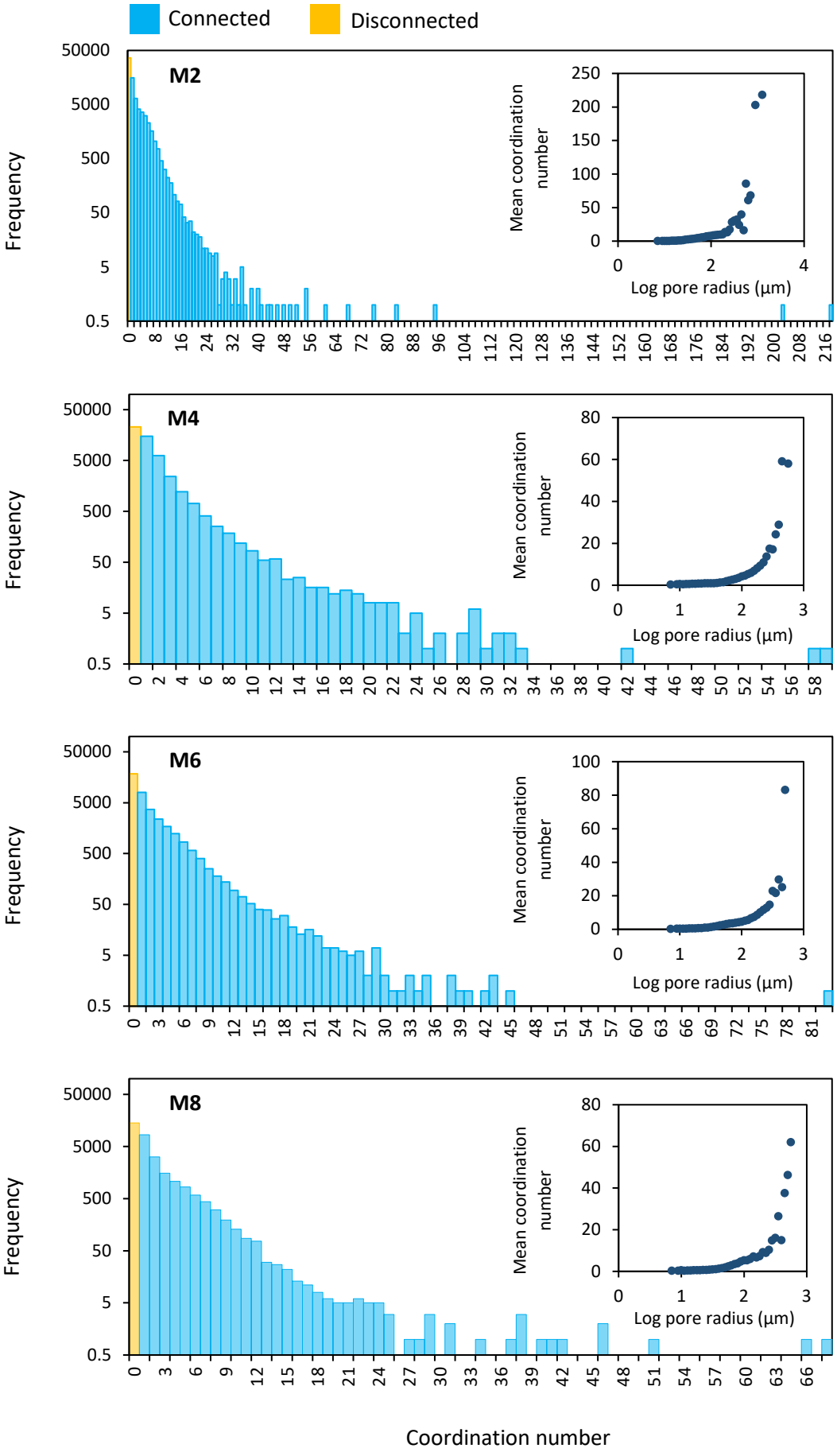

Figure 6.6 – ◄ Caption overleaf

6.2.2 Pore distribution

Quantitative measurements of pores and throats present an insight into the geometries of the segmented pore phase, but do not provide any spatial information. However, volume renderings of the segmented pore phase present the opportunity to visualise where this porosity is distributed relative to the crystal phase. Figure 6.7 shows a volume rendering for each sample, where everything rendered in 3D is porosity, and what appears as empty space is where a crystal would be. Blue indicates connected porosity, yellow indicates disconnected porosity. Porosity rendered in blue can therefore be considered to represent the melt fraction that is theoretically removable from the partially solidified mush, whereas porosity rendered in yellow represents the trapped melt fraction. From these visualisations, it is clear that the differences in pore geometries outlined in Section 6.2.1 translate into the spatial distribution of porosity within the samples. These differences most clearly manifest in the connected melt, which exhibits a range of distribution patterns including linear channels that mantle crystal boundaries and angular pools that reveal negative crystal shapes. These distributions are further explored in Section 6.2.2.2. Figure 6.8 depicts a slice-by-slice profile of porosity measured down the Z-axis of each sample. For all samples, porosity is heterogeneously distributed within the sub-volume, with peaks that define regions of greater or lesser porosity volumes. The relative proportions of connected and disconnected porosity also vary through the sub-volumes. The proportion of disconnected porosity is typically lower when there is a peak in the total porosity, and increases when the total porosity decreases. The proportion of connected porosity exceeds that of disconnected porosity in all samples, excluding the uppermost 2000 µm of sample M8. M6 exhibits the most homogenous porosity profile, characterised by a greater frequency of fluctuations but a lesser volume

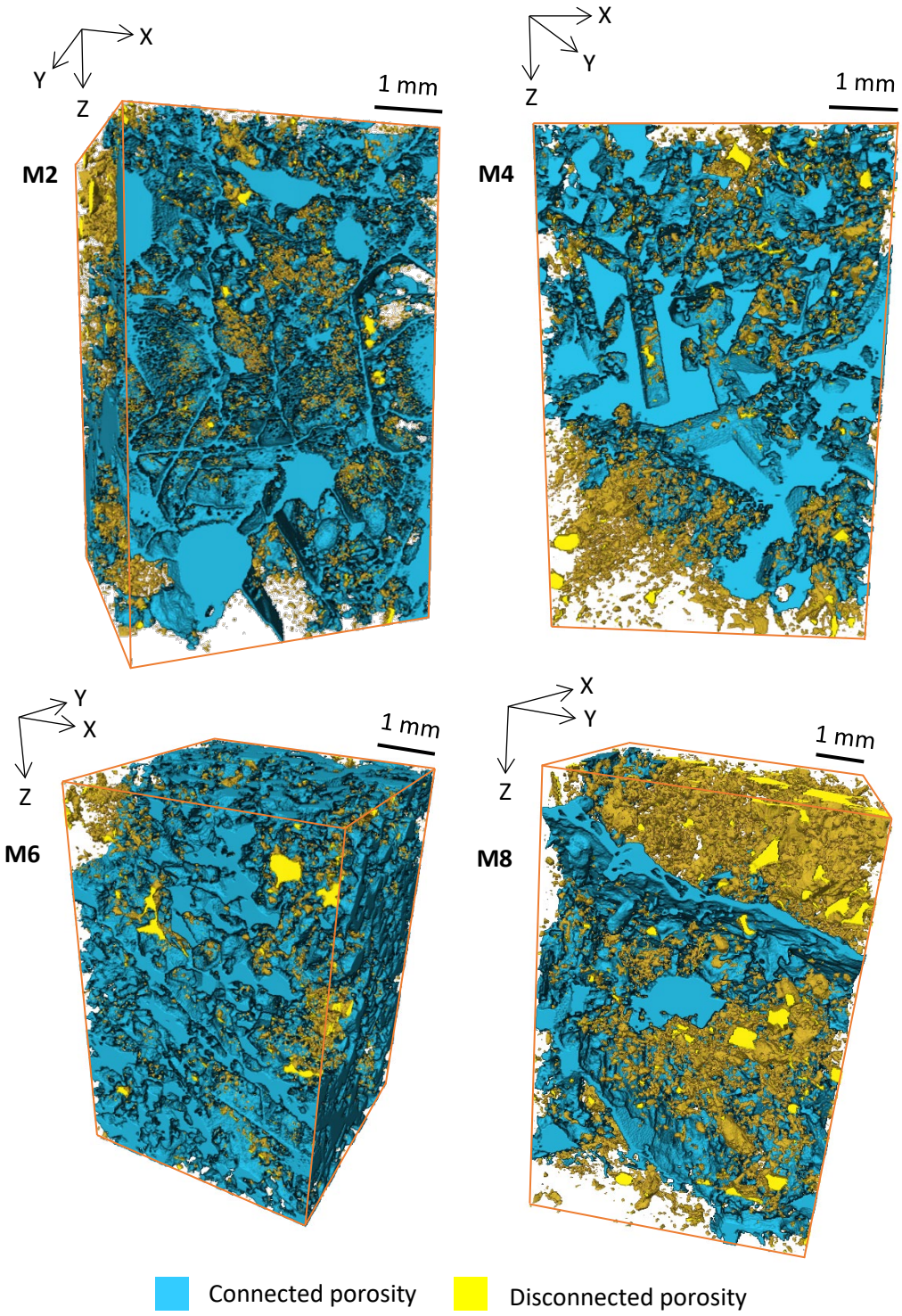

Figure 6.7 **–** Three-dimensional volume renderings of porosity. Everything rendered in 3D represents porosity (holes + glass), what looks like empty space is where the crystals would be. Blue indicates connected porosity, yellow indicates disconnected. It is clear that the porosity structures vary between samples, concordant with the geometric measurements displayed in **Figure 6.4**.

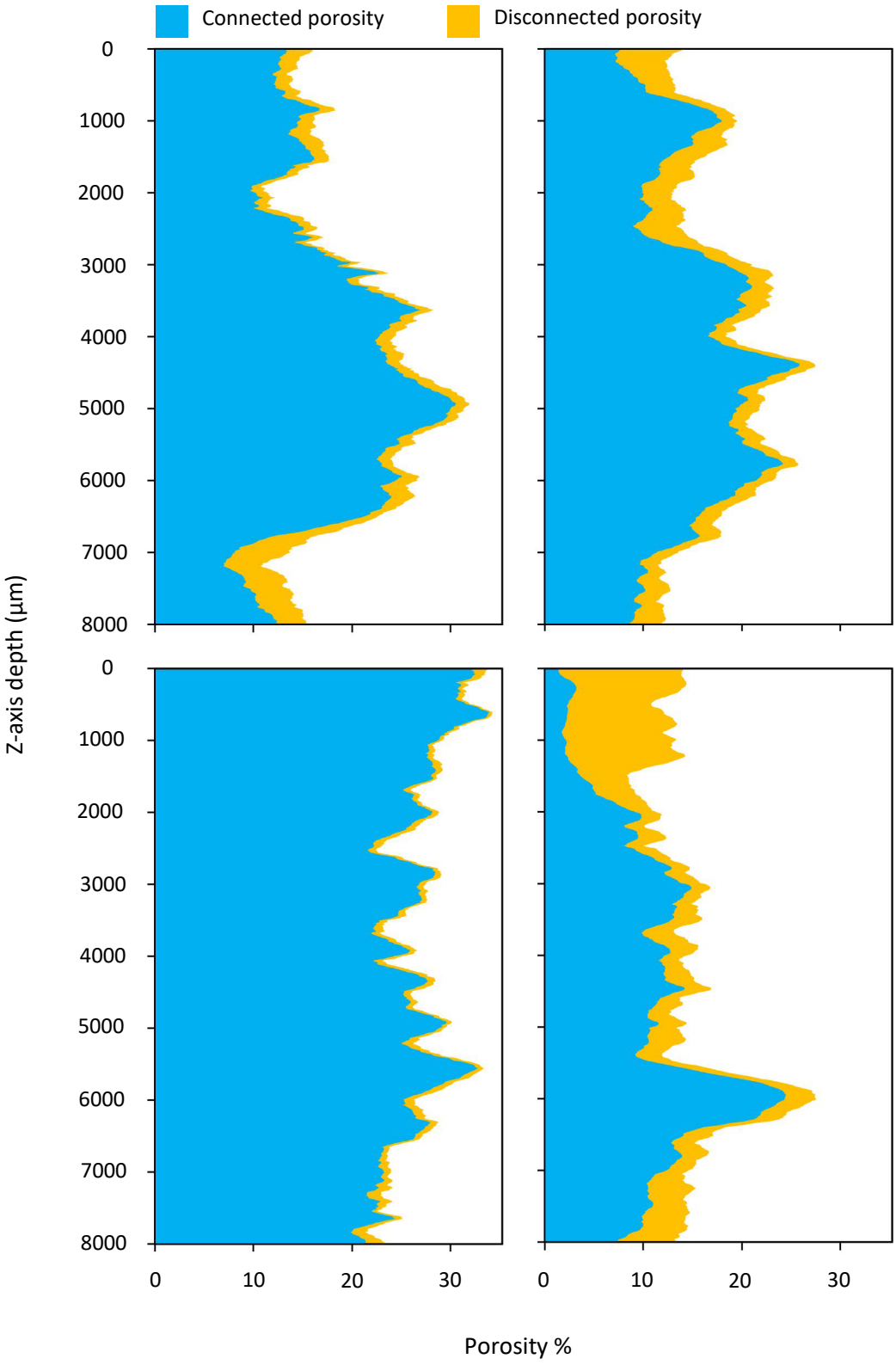

Figure 6.8 - Caption overleaf ▶

◀ ***Figure 6.8 (overleaf)*** **–** Porosity profiles measured down the Z-axis of each CT volume. Blue represents connected porosity, yellow represents disconnected. Porosity is calculated by the segmented area percentage of each CT image slice. From this, it is clear that porosity is heterogeneously distributed within the sub-volumes. However, the proportion of connected porosity continuously exceeds the proportion of disconnected porosity, excluding the top 2000 µm of sample M8. The proportion of disconnected porosity tends to increase in regions where the total porosity decreases. Sample M6 is the most homogenous, but still exhibits peaks and troughs of porosity along the Z-axis.

decrease between the peaks and troughs. Notably, the crystals in this sample are also the most texturally homogenous with a dominant hornblende framework and lesser volumes of clinopyroxene than is present in the other samples.

6.2.2.1 Disconnected porosity

Regions of disconnected porosity represent melt that is trapped within the crystal framework, significant for understanding the evolution of the crystallising mush system. From the three-dimensional renderings, 2 main observations can be made about the 3D distribution of disconnected melt relative to the solid crystalline material that dominates these samples.

6.2.2.1.1 Intracrystalline porosity

A significant proportion of the disconnected porosity observed in the 3D models is intracrystalline (Figure 5.9). This likely pertains to the resorption textures, specifically the glass-bearing and corroded crystal cores that are frequently observed in thin section. It is not possible to accurately segment and remove this disconnected intracrystalline porosity from the data set and it is possible that this

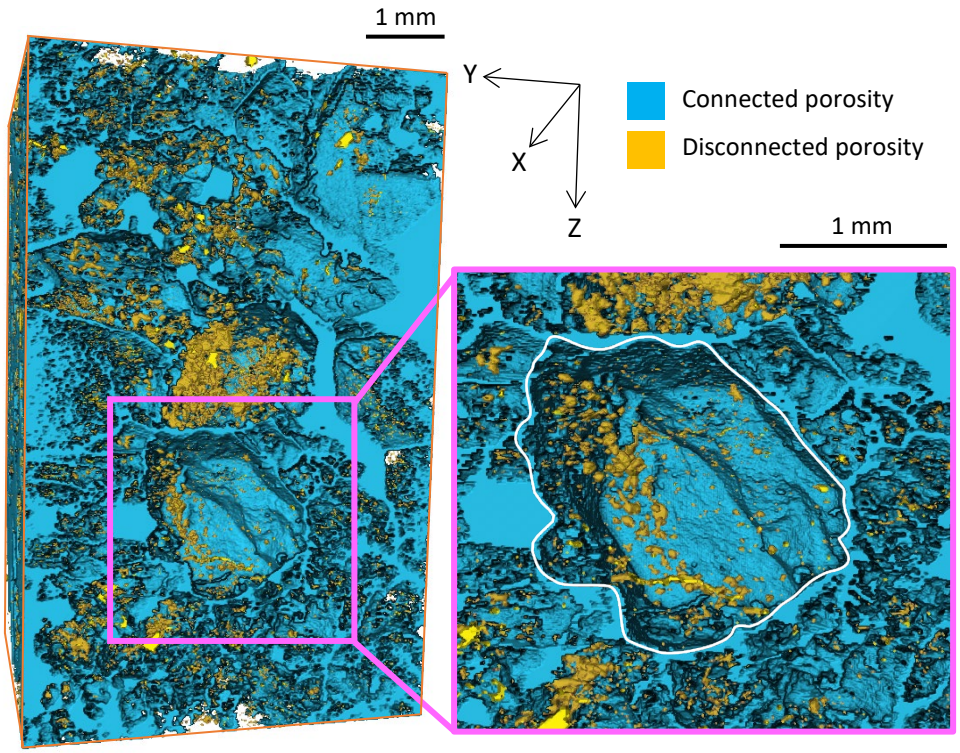

Figure 6.9 **–** Example of intracrystalline disconnected porosity. On the volume renderings it is possible to identify regions of disconnected porosity that occupy the negative spaces where crystals would be. The white line on the inset image (right) indicates the crystal boundary. Disconnected pores within this boundary are small and rounded, concordant with the observations of holey resorption textures observed in thin section (see Chapter 4).

provides a slight overestimation of the melt-bearing porosity network. This may provide one explanation for why the disconnected pore spaces are characteristically smaller than the connected pores. However, not all of the intracrystalline porosity is disconnected. In some instances it is possible to manually identify and segment individual crystals from the stacked CT slices. When configured within the sub-volume PNM, several examples of these individually segmented crystals contain connected porosity that contributes to the overall connected porosity of the sample (Figure 6.10). However, it is likely that not all of

this intracrystalline porosity traverses through the entire crystal and it is plausible that the high number of pores with low coordination numbers is attributable to dead end porosity channels within these resorbed, holey crystals.

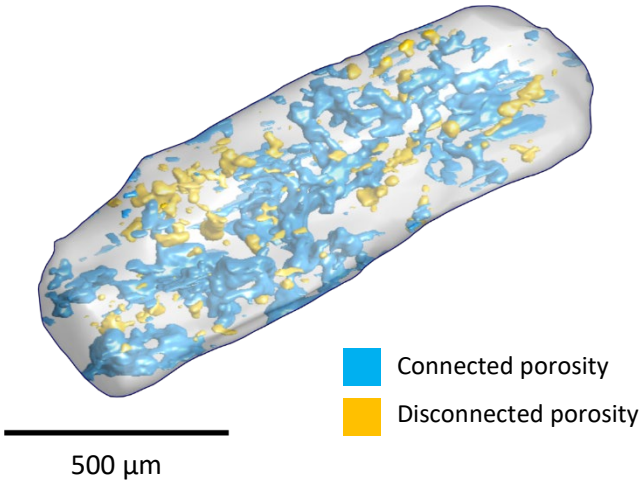

Figure 6.10 **–** Three-dimensional rendering of one segmented crystal, showing connected and disconnected intracrystalline porosity. The shape and size of the crystal suggests it is likely a clinopyroxene. There are a few examples of crystals in regions of low crystallinity that have traceable outlines on the CT images. By undertaking a manual slice-by-slice segmentation of these crystals, it is possible to render the individual crystal and configure it within the pore network model. Alongside the disconnected porosity identified in **Figure 6.9**, there is significant connected porosity within the crystal that contributes to the overall connected network of the sample. However, it is likely that not all of this connected intracrystalline porosity traverses through the entire crystal. This provides one explanation for the high frequency of dead end pores with coordination values of 1.

6.2.2.1.2 Intercrystalline porosity

Whilst it is apparent from the 3D renderings that a significant proportion of the disconnected porosity resides within crystal volumes, there are examples of disconnected porosity that attest to an intercrystalline distribution. In particular, elongate pockets of disconnected porosity form sheet-like structures that define crystal outlines (Figure 6.11).

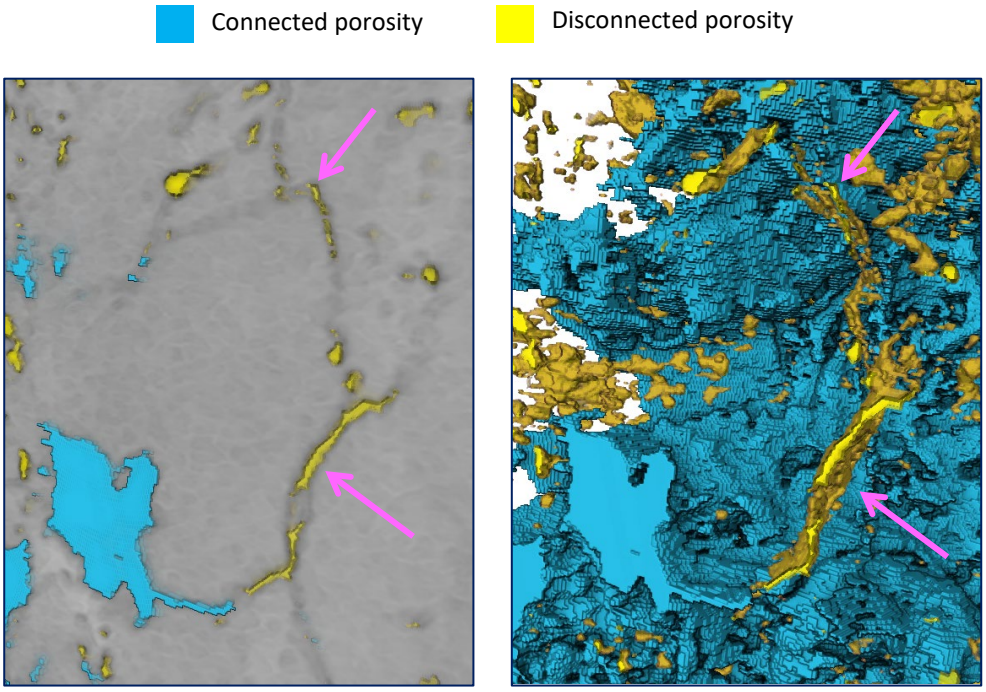

Figure 6.11 **–** Disconnected porosity confined to crystal boundaries. Left shows the solid crystalline material superimposed onto the 3D renderings of porosity, right shows the same image without the crystal material. From these images, the disconnected porosity appears to define crystal outlines that would otherwise be undeterminable from the CT data (highlighted by the pink arrows). Removing the crystal material from the rendering reveals the geometry of this disconnected porosity, which forms a sheet like structure around the negative crystal space. In conjunction with observations of glass bearing grain boundaries in thin section, these disconnected pores are interpreted to represent melt that is trapped along the boundary between touching crystals.

These structures yield greyscale values in the range assigned to glass, consistent with the pockets and films of glass that are identifiable along grain boundaries in thin section. In conjunction with these observations, these disconnected structures are therefore interpreted to represent trapped melt within the grain boundaries between adjacent crystals. The CT data therefore enhances the thin section observations by confirming that this melt is disconnected, and therefore trapped within the crystal framework. It is challenging to quantify how much of the disconnected porosity fraction is confined to grain boundaries, but examples of these structures are identifiable throughout the sub-volumes of each sample. Conversely, there are limited examples of disconnected pore spaces that represent interstitial porosity, which is identifiable by straight edged pores that record the angular interstices between impinging crystals. This suggests that the disconnected porosity fraction does not significantly contribute to the interstitial porosity that can be identified within these samples.

6.2.2.1.3 Influence of fracturing

It is important to comment on the apparent abundance of disconnected porosity presented in sample M8. Interpretation of this sample is complicated by the presence of two fractures that traverse the width of the sub volume (Figure 6.12). The majority of the connected porosity in this sample is in close spatial proximity to these fractures, whereas the majority of the disconnected porosity occurs around them, distinguishing them clearly on the 3D renderings. The PerGeos 'axis connectivity' tool is unable to ignore specified pathways and therefore the three-dimensional porosity in this sample is highly influenced by these fracture planes. As such, sample M8 is included in this chapter to provide some insight into the pore structure of each sample, but is described in less detail than the other samples.

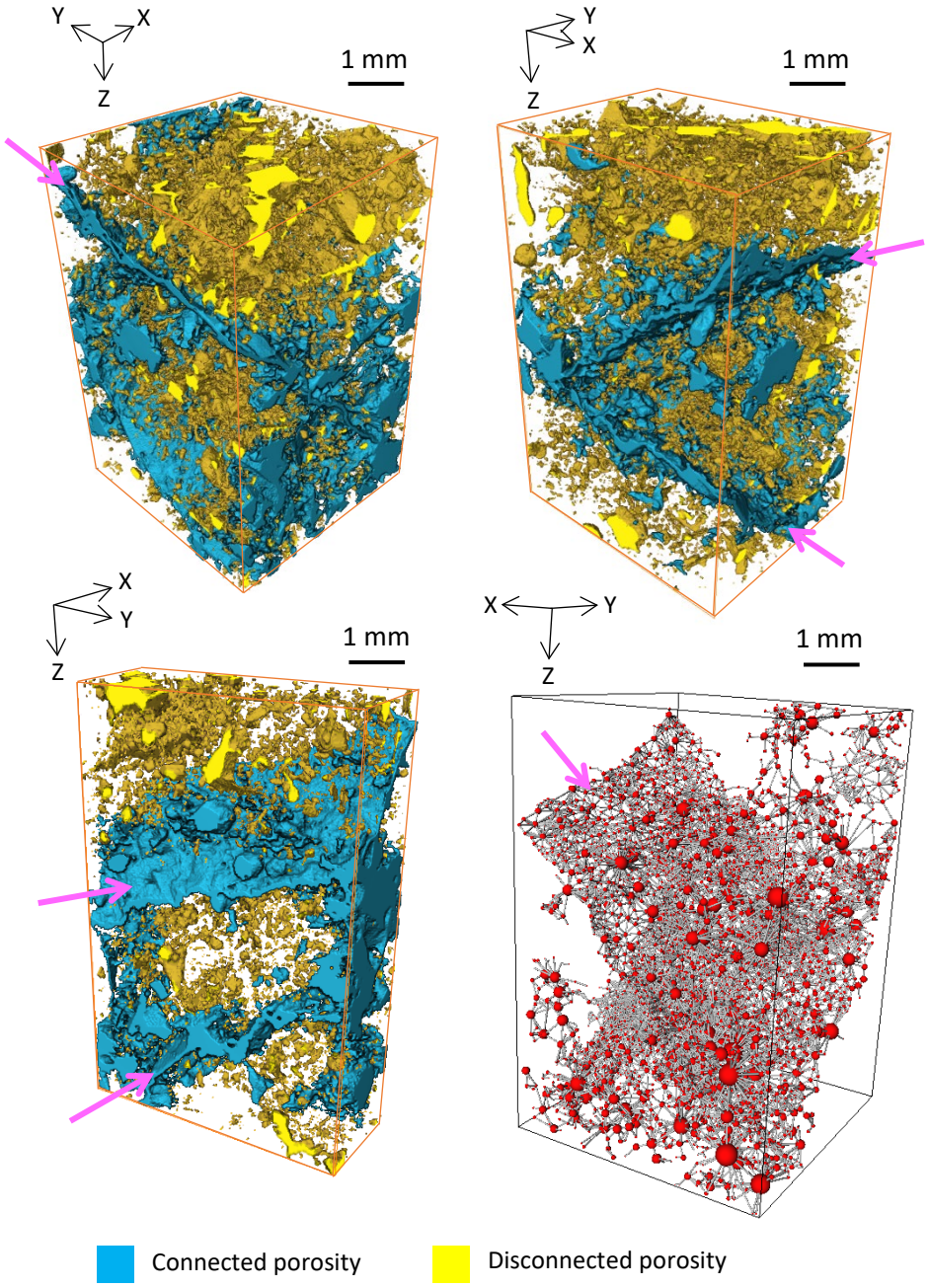

Figure 6.12 – Three-dimensional renderings and pore network model showing fractures in sample M8. Yellow shows disconnected and blue shows connected porosity. Red balls indicate pores and grey sticks indicate throats. Two crossing fracture planes can be clearly identified on the 3D renderings (highlighted by the pink arrows) that comprise the majority of the connected porosity network within the sample. Disconnected porosity dominates the spaces around these fracture planes, indicating that the connectivity measurements have been influenced by the presence of these fractures. As such, this sample is described in less detail, with acknowledgement of the limitations created by the fractures.

There are also two fine fractures in sample M6, however as the pattern of connected and disconnected porosity does not differ in regions close to the fracture planes it appears that they have not significantly influenced the connectivity calculations (Figure 6.13). Sample M6 is therefore examined in greater detail than sample M8, but with acknowledgment of the presence of these fractures.

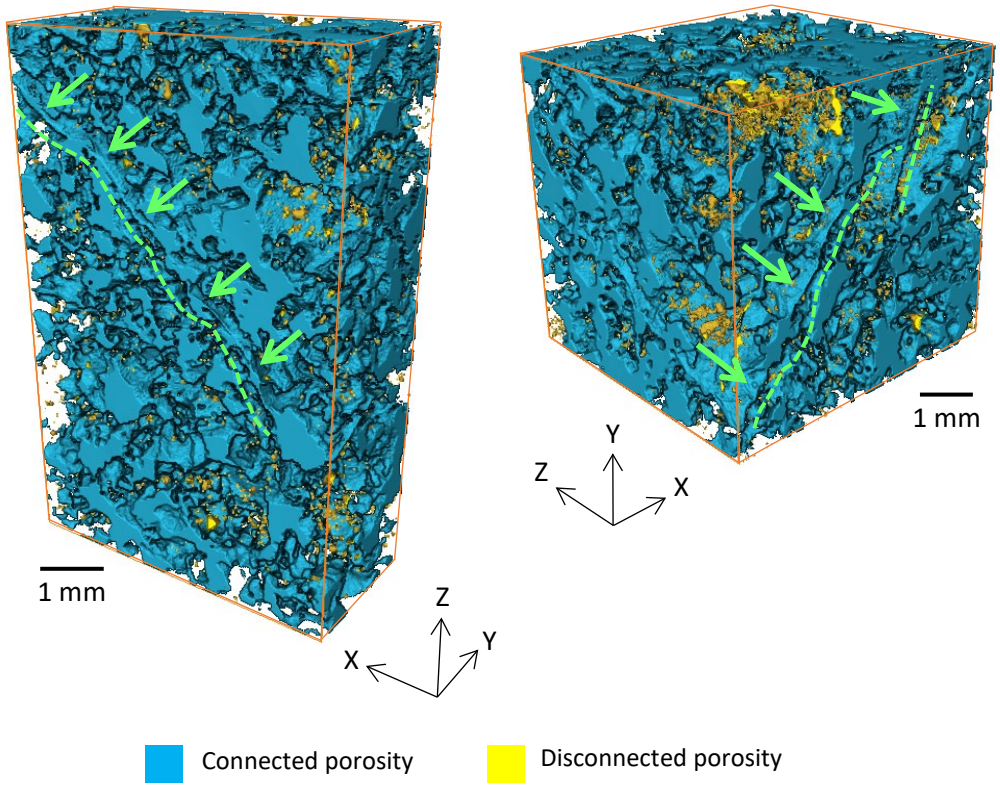

Figure 6.13 **–** Three-dimensional renderings highlighting fractures in sample M6. Dashed green lines and arrows indicate the location of the fractures through the sub-sample volume. Unlike the larger fractures that are present in sample M8, these fractures do not appear to influence the connectivity calculations. As such, this sample is analysed in greater detail than M8 but with consideration that the fractures may still exert an influence upon the data.

6.2.2.2 Connected porosity

Identifying the distribution of the connected porosity constrains the dispersal of potentially extractable melt from the crystal framework. From the three-dimensional renderings and pore network models, four main observations can be made about the 3D distribution of connected melt within these samples.

6.2.2.2.1 Grain boundaries

Planar sheets of melt are particularly prominent in sample M2, forming networks that outline crystal edges (Figure 6.14). In some instances, euhedral crystal faces can be clearly identified by the positioning of these sheet like structures (Figure 6.14B), which are obliquely orientated through the sample and sometimes show a curvature around rounded negative crystal spaces (Figure 6.14C). In conjunction with observations from thin section, these sheets are interpreted to represent continuous melt films along grain boundaries (Figure 6.15). This is consistent with the greyscale values of the voxels that comprise these structures, which measure within the range assigned to glass. Similar structures are observable to a lesser extent in sample M4, but are challenging to identify amongst the more prominent angular melt volumes. These grain boundary films clearly contrast to the pockets of disconnected grain boundary porosity described in Section 6.2.3.1.2, and are distinguishable from the fractures described in Section 6.2.3.1.3. Interestingly, the presence of these melt films does not appear to influence the overall connectivity of the sample. Although sample M2 exhibits the greatest tortuosity, indicative of a more sinuous and complex internal porosity structure, it has a mean coordination value close to that of the other samples. The geometry of these structures is clearly visualised by the pore network models, which show a sheet-like structure consisting

of a high density network of small pores and throats (Figure 6.16). This provides a likely explanation for the high number densities of pores and throats within this sample, alongside the small average radii of pores and throats measured in Figure 6.4.

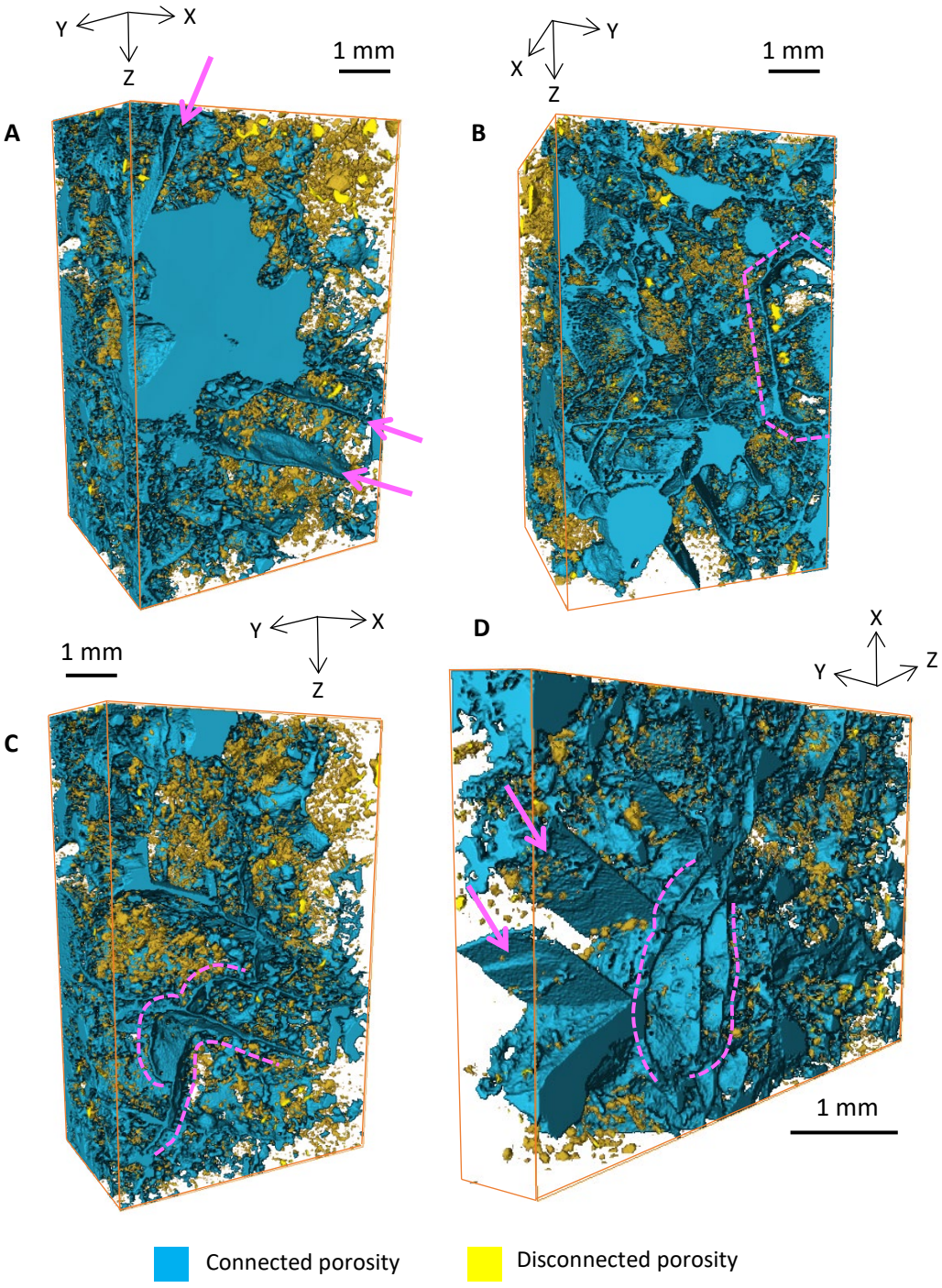

Figure 6.14 - Caption overleaf ▶

◄ ***Figure 6.14 (overleaf)*** **–** Three-dimensional renderings showing connected melt structures in sample M2. **A)** Pink arrows indicate linear, sheet-like structures that appear to outline crystal edges. **B)** In some instances these linear structures outline euhedral crystal faces, as marked by the pink dashed line. **C)** Alongside the linear structures, examples of curved structures outline rounded crystal spaces. **D)** Example of linear structures (arrows) in close proximity to a more rounded structure that appears to entirely surround the negative space that indicates a crystal. In conjunction with observations from thin section, these structures are interpreted to represent melt films along grain boundaries. They are distinguishable from the fractures described in Section 6.2.3.1.3 because they yield greyscale values in the range assigned to glass and outline crystal faces.

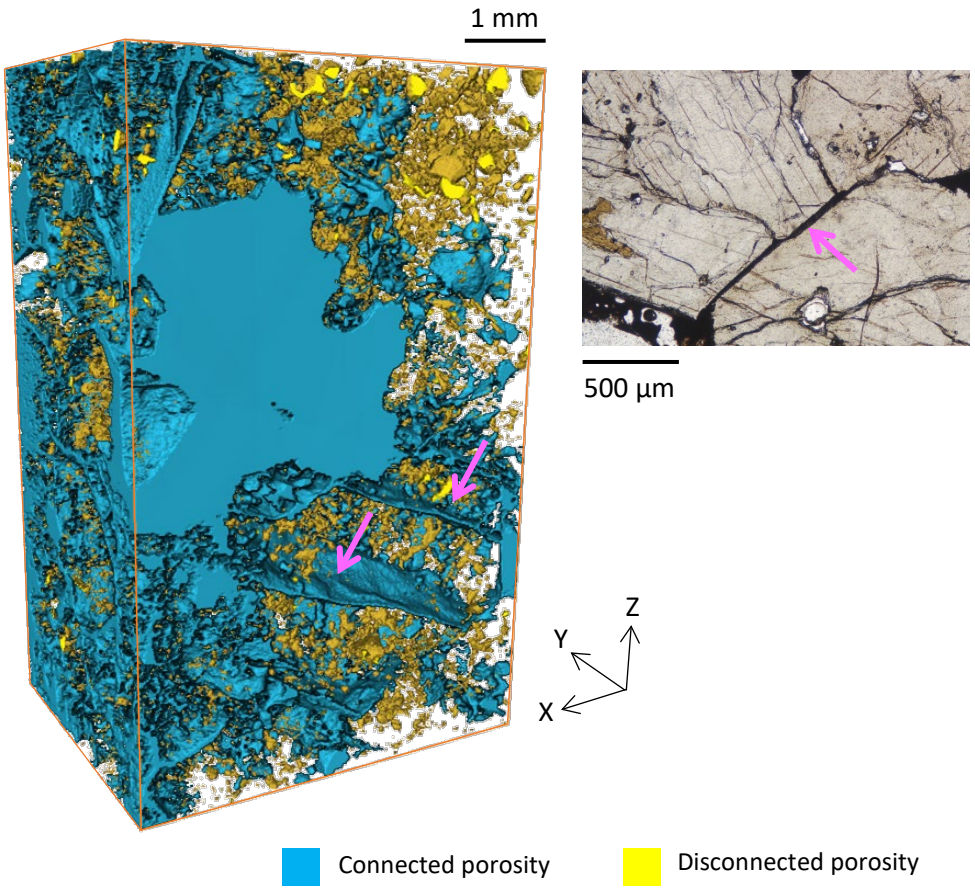

Figure 6.15 **–** Three-dimensional rendering of connected melt structures in sample M2 with a comparable structure photographed in thin section. Thin section observations of linear melt films between adjacent crystals aid the interpretation of the 3D structures, highlighted by the pink arrows.

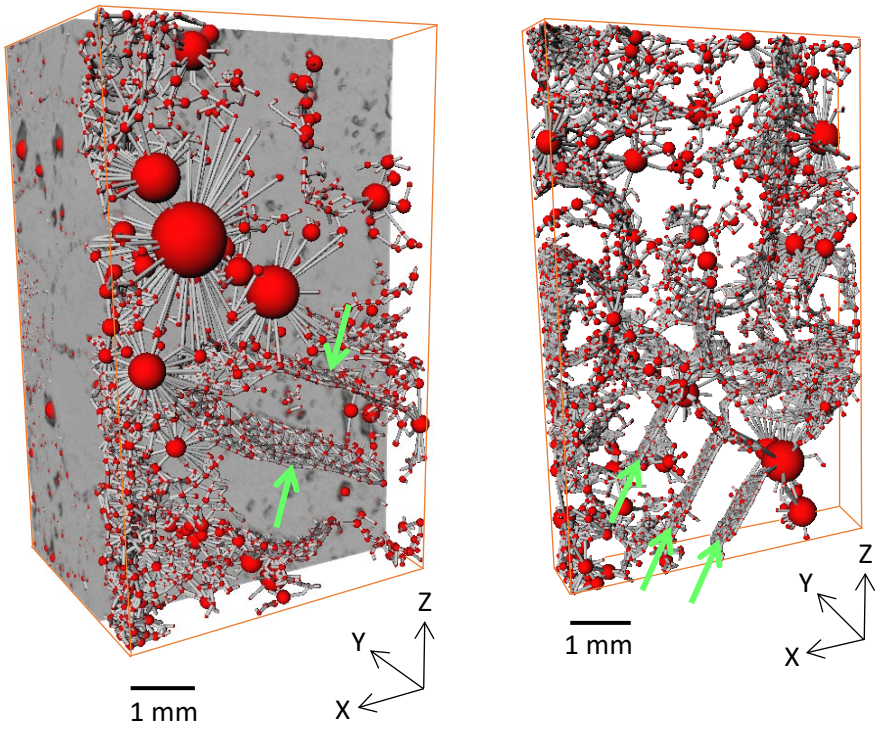

Figure 6.16 **–** Pore network models highlighting connected grain boundary structures in sample M2. Green arrows indicate the portions of the PNM that correspond to the features described in Section 6.2.2.2.1 and shown on the 3D renderings in **Figure 6.13**. Red balls represent pores, grey sticks represent throats. Solid grey material represents the crystalline material, which is included in the left hand figure to simplify the visualisation of the dense pore network. The structures consist of a high density network of well connected small pores and throats, that together form a flat, linear structure. These structures contrast to other regions of the PNM and likely contribute to the high number densities and small radii of pores and throats that characterise this sample.

6.2.2.2.2 Concentrated porosity pathways

The porosity profiles in Figure 6.8 show a clear heterogeneity in the distribution of connected porosity down the vertical axis of each sub-volume. In sample M4, this heterogeneity can be visualised in the PNM as a high porosity structure that traverses the diagonal of the sub-volume Z-axis (Figure 6.17). This channel of connected porosity occurs in a region of the sample characterised by loosely packed crystals that resemble the clinopyroxene frameworks identified in thin section (Figure 6.18). This melt therefore represents that contained within the interstitial pore spaces between these crystals, which in 3D is revealed to be connected and potentially extractable. Larger pools of melt comprise significant proportions of this connected region. These pools have angular boundaries that follow the planar crystal edges in contact with the melt and record the vertices at crystal-melt junctions (Figure 6.19). There are no comparable structures within the disconnected porosity fraction.

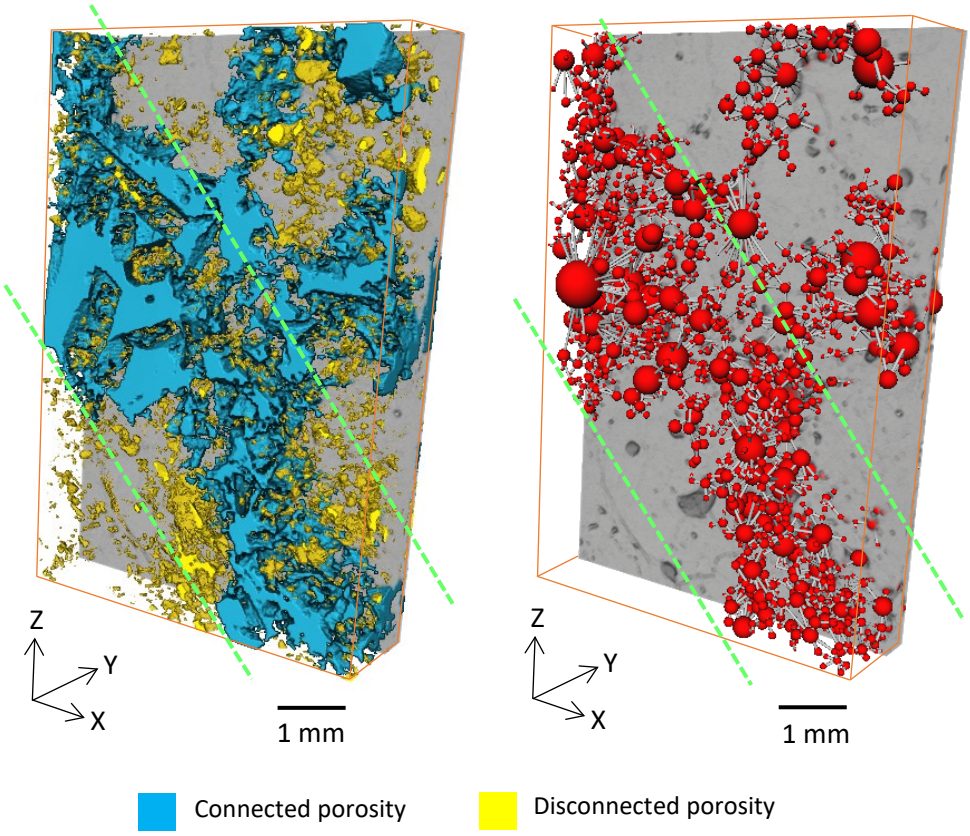

Figure 6.17 – Three-dimensional rendering and pore network model highlighting a concentrated region of porosity traversing the diagonal of the Z-axis in sample M4. Red balls indicate pores, grey sticks represent throats. Dashed green lines outline the trend of this high porosity region that is characterised by large pores of connected porosity that define negative crystal spaces.

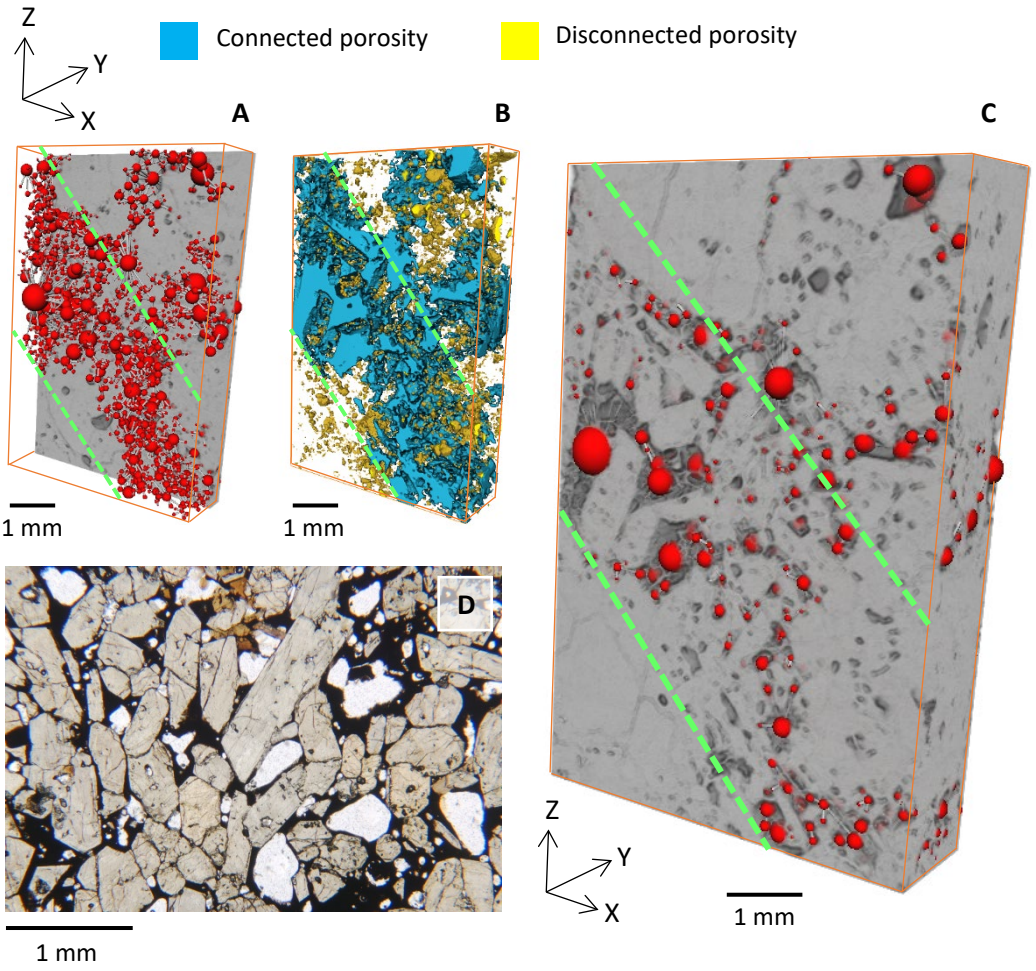

Figure 6.18 – Three-dimensional visualisations of a concentrated high-porosity region in sample M4, with a comparable region photographed in thin section. **A)** Pore network model extruded from the solid grey crystal phase, visualising the porosity network structure without any crystal context. **B)** Same as in A, but shown as a three-dimensional rendering of connected and disconnected porosity. Connected pore spaces reveal negative crystals. **C)** Pore network model shown in A, with the grey crystal phase superimposed over the top. This reveals the positioning of crystals relative to the pore spaces, visualising a three-dimensional texture comparable to the loosely packed crystal frameworks identifiable in thin section. **D)** Photomicrograph of aforementioned CPX framework taken in PPL. Of the varied crystal textures that can be identified in thin section, these loosely packed crystals yield a high-porosity framework that best fits the three-dimensional texture observed in C. From this, the concentrated porosity pathway that characterises sample M4 is attributed to the interstitial pore spaces between these CPX crystals.

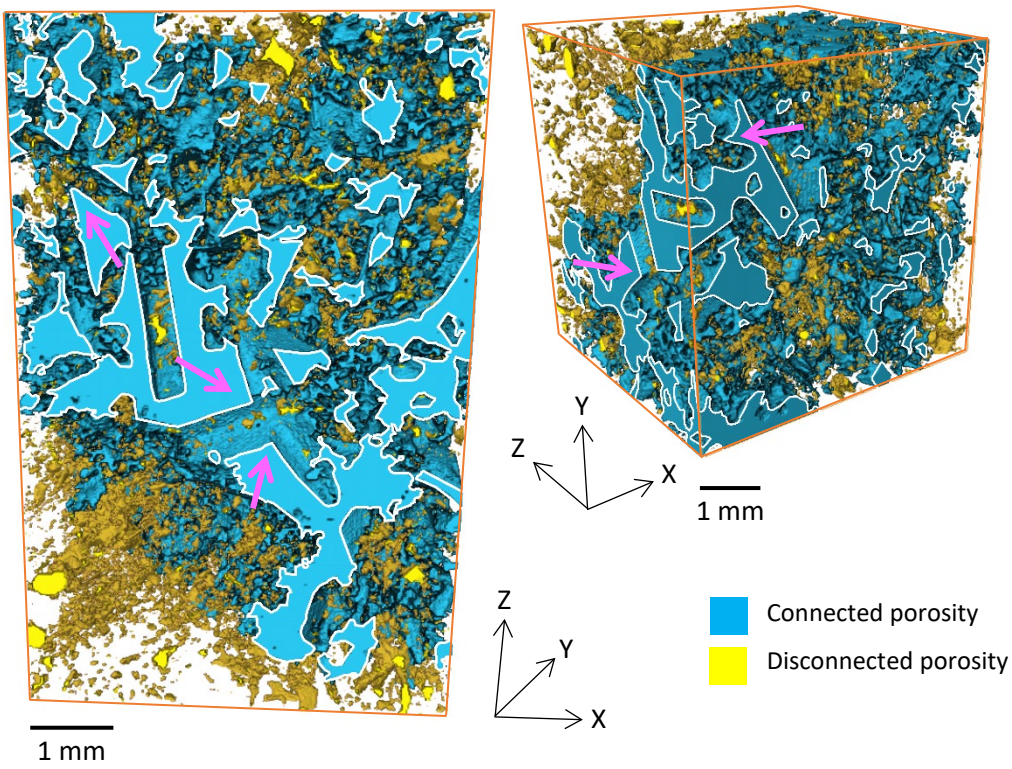

Figure 6.19 **–** Three-dimensional renderings of large, angular pore spaces in sample M4. White lines outline the cross-section of connected melt, which is characterised by angular boundaries that represent crystal faces in contact with the melt. Pink arrows show examples of vertices that record crystal-melt junctions, most of which yield acute angles in the melt fraction.

6.2.2.2.3 Heterogeneous melt structures

As already observed in Figure 6.8, the volume fraction of porosity varies through each of the sub-volumes. However, the 3D renderings and PNMs provide a further visual insight into the regions of greater and lesser porosity that are recorded in the Z-axis profiles. From these visualisations, it is clear that the structure and morphology of the pore spaces is itself heterogeneous within each sample. For example, the connected porosity in sample M2 consists of grain boundary films, angular melt in interstitial pore spaces and larger, well connected pools. The distribution of porosity is ultimately constrained by the crystal framework, and as

recorded in Chapters 4 and 5, the xenoliths are characterised by heterogeneous crystal textures. This appears to manifest in the pore spaces, resulting in the heterogeneity observed within each sample.

6.2.2.2.4 Connectivity

The graphs in Figure 6.6 show that a large proportion of the connected porosity is characterised by pores with low coordination numbers. A pore with a coordination number of one is considered to represent the dead end of a pathway whilst a coordination number of two represents a singular, non-branching pathway. In each sample, between 54.7 and 78.9% of connected pores have a coordination number lower than 2, of which between 38.6 and 70.6% have a coordination number of 1 and represent a dead end. This indicates that despite the high proportions of connected porosity within these samples (10.2 - 26.1%), the pore networks that comprise this porosity are relatively poorly connected. An abundance of dead ends and single pathways is significant for considering the permeability of the crystal framework and the ease at which melt could potentially be transported.

6.3 Potential limitations of 3D analysis

This three-dimensional dataset significantly contributes to the interpretation of the non-crystalline components of these samples. However, it is important to acknowledge the potential limitations associated with this data. Firstly, the resolution of the CT images provides a consistent threshold as to the minimum volume of an identifiable object. As such, any porosity below the image resolution (<5 voxels) is absent from the 3D data. Furthermore, in sample M2 there are regions of the three-dimensional rendering that show noise on the CT image has been

rendered as part of the porosity phase (Figure 6.20). These regions are clearly discernible and have not been described as a porosity feature in any of the previous sections.

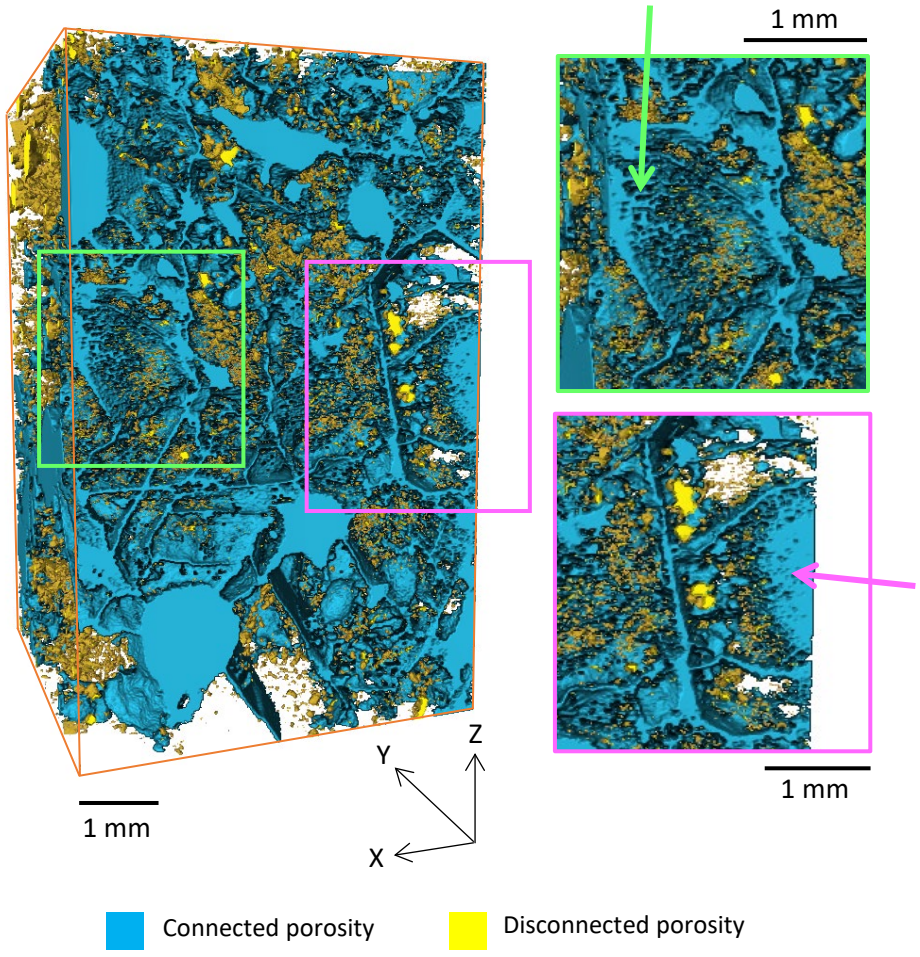

Figure 6.20 – Three-dimensional rendering of sample M2, highlighting regions of CT noise that have been incorporated into the 3D porosity fraction. This noise manifests as a pixelated region at the sub-volume margins, of which there is no correspondent feature in thin section. This noise may result in an overestimation of porosity in this sample, however it is clearly identifiable on the 3D renderings and so it has been ignored in the interpretation of porosity geometry and distribution.

Additionally, because of the known limitations of CT scanning it is not possible to identify individual touching crystals. Therefore, the only way to identify grain boundaries is instances where porosity clearly mantles crystal outlines (e.g. Figure 6.11). However, in some examples, linear porosity structures appear to traverse through the centre of crystals, constituting structures that appear to intersect one another at the cleavage angle of the minerals known to be present within these samples. Figure 6.21 demonstrates such an example, where linear porosity structures intersect at an approximate 120° angle and may therefore reflect the cleavage planes of a hornblende crystal. In this sample (M2), there are several example of strongly resorbed hornblende crystals and it is possible that these structures identified on the 3D data visualise melt that has percolated along the cleavage planes of a resorbed hornblende. However, without the capacity to identify grain boundaries, it is up to interpretation whether porosity structures represent grain boundary films (as suggested in Figure 6.14) or traverse through a crystal (Figure 6.21). This introduces some limitations into the CT data set, because it influences the interpretations of where melt is distributed relative to the crystal phase. To minimise this limitation, no attempt was made to quantify the relative proportions of the porosity pertaining to grain boundary structures versus interstitial melt versus intracrystalline porosity. Interpretations are instead made on a case-by-case basis, using information about crystal shapes and internal features observed in thin section.

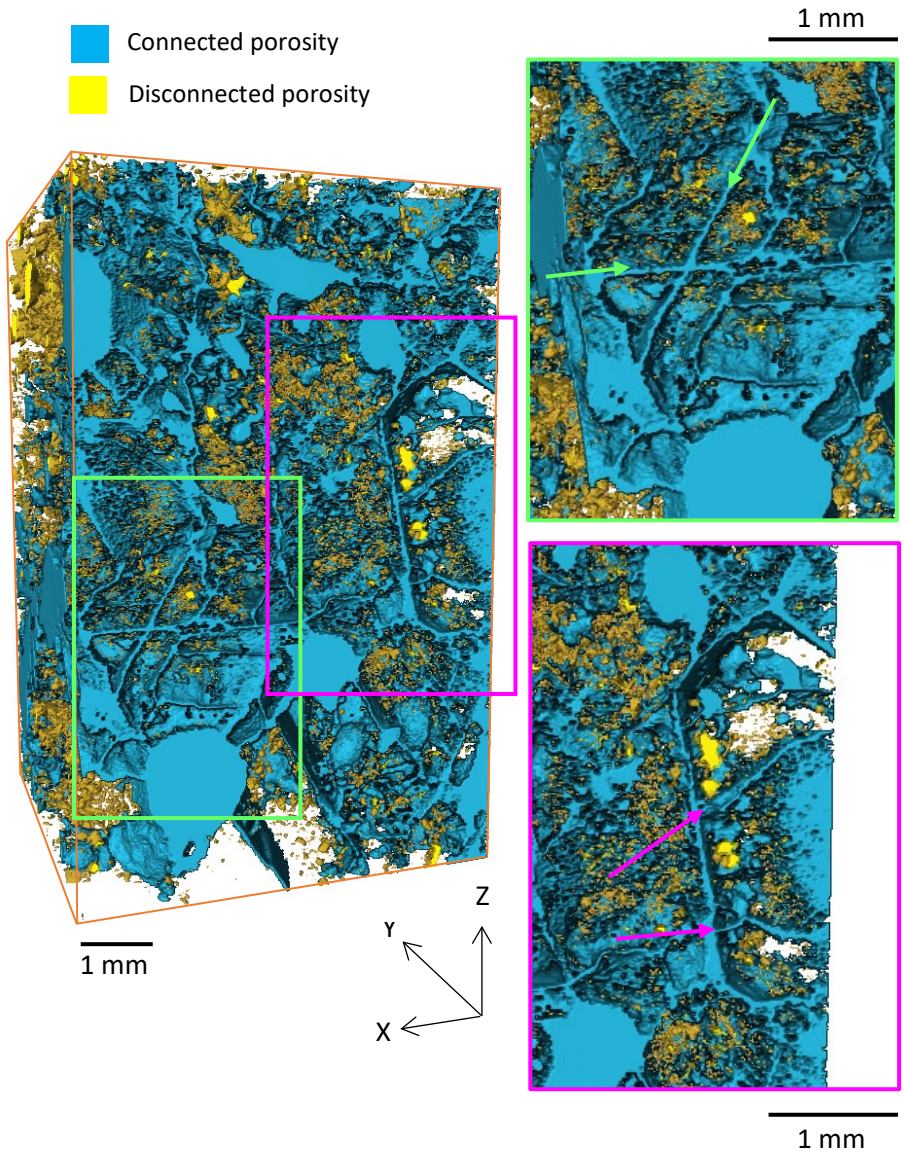

Figure 6.21 – Three-dimensional rendering of sample M2, highlighting porosity structures that are challenging to discriminate as grain boundary structures or intracrystalline porosity. Because the limitations of CT scanning mean that it is not possible to identify individual touching crystals, the only way to identify grain boundaries is instances where porosity clearly mantles crystal outlines. However there are several examples where porosity appear to traverse through a crystal, with a structure comparable to the melt films identified as grain boundary structures. Without the capacity to identify grain boundaries it is up to case-by-case interpretation as to whether porosity structures represent grain boundary films or are intracrystalline in nature.

6.4 Summary

A summary of the main points in this chapter are provided in the following:

- The CT data identifies a range in the total measured porosity between different samples (14.4-26.9%), of which between 70.9-97.1% is connected and potentially extractable.
- There is no correlation between geometric properties of the pore spaces and the total connected porosity.
- Disconnected porosity is concentrated along grain boundaries and also within the cores of resorbed crystals.
- Connected porosity is particularly heterogeneous; fine films along grain boundaries contrast to concentrated, channel like regions within clinopyroxene frameworks.
- Fractures in samples M6 and M8, and some CT noise introduce limitations into the CT dataset, but are easily discernible on the three-dimensional renderings.

Discussion and critical evaluation

This chapter provides a discussion of the results presented in Chapters 4-6, utilising the array of two- and three-dimensional textural data to interrogate the research aims outlined in Chapter 1. This discussion is structured into four sections. Firstly, the two-dimensional textures are scrutinised to evaluate whether eruption of the xenoliths may have modified the crystal and melt textures to a point rendering them unrepresentative of an in-situ crystal mush. Secondly, the two-dimensional data, with supplementary geochemistry, is analysed to determine the textural sequence and magmatic processes recorded in the xenoliths. From this, the magmatic environment is constrained, with wider consideration to the magmatic regime of the West Eifel. Finally, using the textural interpretations, the three-dimensional CT data is used to investigate the spatial relationship between the melt and crystal phases. Following this discussion, a critical evaluation of the methods and samples highlights potential limitations and points for future work.

7 Discussion and critical evaluation

This discussion aims to interrogate four main research questions, using the array of textural data provided in Chapters 4-6. Firstly, it is important to ascertain whether the entrainment and eruption of these xenoliths may alter their textures to mislead where the melt was distributed in situ. Secondly, if the melt distribution is deemed to be representative of that at depth, the textures must be scrutinised to constrain the dynamics of the magmatic environment in which they formed. This will provide a magmatic context to the samples, providing a better understanding of the processes affecting melt distribution within the mush. Finally, the physical relationship between melt and crystals will be discussed, with consideration to how the distribution of melt within the crystal framework is significant for the evolution and eruptability of the melt.

7.1 To what extent can the textures recorded in the xenoliths be considered representative of an in situ crystal mush?

The utility of these samples as representations of an in situ mush is largely dependent on whether the textures preserved within them are magmatic in nature; that is, whether the crystal and melt textures are representative of those formed prior to entrainment in the host magma. This section therefore aims to evaluate whether the textures recorded in the xenolith samples have been influenced by external (relating to entrainment and transport within the host magma) or internal (related to decompression driven vesiculation) forces that would modify their textures and render them unrepresentative of the in-situ mush.

7.1.1 Entrainment

Xenoliths are ex-situ in nature and it is therefore challenging to study the processes that lead to the incorporation of mush fragments within eruptible magmas. As such, the entrainment of cognate xenoliths is poorly understood (e.g. Holness et al., 2007d). From a thermodynamic perspective, the preservation of larger mush fragments, particularly those which maintain interstitial glass, requires that the density, temperature and viscosity contrasts between the crystal mush and replenishing magma were of sufficient magnitude to prevent significant deformation and break-up (Huppert et al., 1982; Sparks and Marshall, 1986; Snyder and Tait, 1995). In such a case, the crystal mush must have been sufficiently coherent, meaning that fracturing and fragmentation are favoured explanations for xenolith entrainment (Gurenko and Sobolev, 2006; Holness and Bunbury, 2006; Holness et al., 2007d; Holness et al., 2019). An absence of viscous or plastic deformation features in these study samples suggests that the mush was sufficiently rigid to resist shear by the surrounding magma (e.g. Blake and Fink, 2000). Because the xenoliths have a rounded shape (Figure 4.1), it is likely that some of the marginal material was lost after their initial entrainment. Martin et al. (2006b) suggest that mechanical processes can cause the attrition of peripheral crystals, resulting in a decrease in xenolith angularity. If the xenoliths are assumed to have behaved as a rigid solid, then this process will result in the gradual loss of material but should not alter the internal crystal textures.

7.1.1.1 Origin of interstitial glass

There are several ways in which the entrainment process could render the glass distribution unrepresentative of the melt at depth. Firstly, if the host magma that brought the xenoliths to the surface was sufficiently hot to trigger partial melting within the xenolith then the distribution of glass will no longer reflect pre-entrainment processes. However, the pore spaces occupied by the glass maintain angular interstices bounded by planar sided crystals, as observed in Figure 4.11. Because partial melting initiates within such interstitial pockets (Holness et al., 2013a), it is unlikely that the glass formed from melting of the minerals. Secondly, the host magma may enter into the xenolith during crystallisation and transport, potentially altering the melt-crystal textures. This scenario is rejected because contacts with the host magma are sharp (Figure 4.18) and the glass of the host is optically and chemically distinct from that of the xenolith (Section 4.2.4). Additionally, internal pressures exerted by gas bubbles expanding within the xenolith (recorded as vesicles in the glass), would likely prevent liquid from entering into the xenoliths at the same time (Holness et al., 2007d). Finally, the crystal framework may be disrupted by shear of the surrounding magma during entrainment, which can release the interstitial melt into the host magma (Martin et al., 2006b). However, because there is no evidence of viscous or plastic deformation the xenoliths are not considered to have been significantly disrupted by shear.

By excluding these alternative scenarios, the glass in these samples is interpreted to represent an in-situ melt that was quenched by rapid eruption. This is consistent with the conclusions of Downes et al. (2004) and Becker (1977), who have previously conducted chemical studies of these samples. This suggests that external

forces related to entrainment (melt infiltration, partial melting, deformation) have not acted to influence the distribution of glass preserved in these samples.

7.1.2 Decompression

7.1.2.1 Vesiculation

The abundance of vesicles within the glass (5.71 – 15.13 vol%) suggests that the melt exsolved a gas phase during ascent. During decompression of high-crystallinity magmas, gas bubbles that form within the crystal framework cause an increase in overpressure. If this overpressure exceeds the yield strength of the crystal framework then it will disrupt the framework through brittle failure (e.g. Okumura et al., 2019) and modify the porosity distribution by pushing apart the crystal framework (Holness et al., 2019). This will result in 'jigsaw fit' boundaries (e.g. Smith et al., 2008; Holness et al., 2019) where parallel-sided, vesicular melt films separate crystals that would otherwise fit together (Figure 7.1A). These features contrast to the geometries of pore spaces that represent pre-entrainment features, where non-parallel crystal margins prevent complete closure of the grain boundary, observed in Figure 7.1B (Holness et al., 2019).

'Jigsaw fit' type boundaries are only present along a few HBL:HBL boundaries in sample M8 (Figure 7.1A). Here, vesicular glass separates adjacent HBL crystals and occupies the regions between broken crystal fragments. This sample contains a few glass-free fractures (Figure 6.12), which likely represent a more extreme response to decompression. These grain boundaries are clearly distinguishable in thin section (e.g. Figure 7.1), and so should be disregarded when examining melt distribution. Otherwise, grain boundaries are non-parallel in nature, containing pockets of interstitial glass that reflect pre-entrainment porosity (Figure 7.1B). This suggests that the crystal framework was sufficiently strong to accommodate for vesicle

expansion, either by loss of gas, or by loss of interstitial melt (Holness and Bunbury, 2006). The former requires the formation of interconnected bubble chains, the latter results in glass-rich rinds at the xenolith-host contact (e.g. Bacon, 1986). It is likely that a combination of gas and melt loss occurred, because the CT analysis suggests that the vesicles do not exceed the gas percolation threshold of 30 vol% (Candela, 1991) (Figure 6.2), and the samples lack a substantial glassy margin (where the xenolith-host contact is preserved) (e.g. Figure 4.18). Although this suggests that some of the melt has been lost from the crystal framework, the preservation of pre-entrainment pore spaces means that melt distribution can be studied by analysing vesicles and glass together as a porosity fraction. The jigsaw-fit boundaries identified in sample M8 (Figure 7.1) are an exception to this, clearly representing a decompression feature.

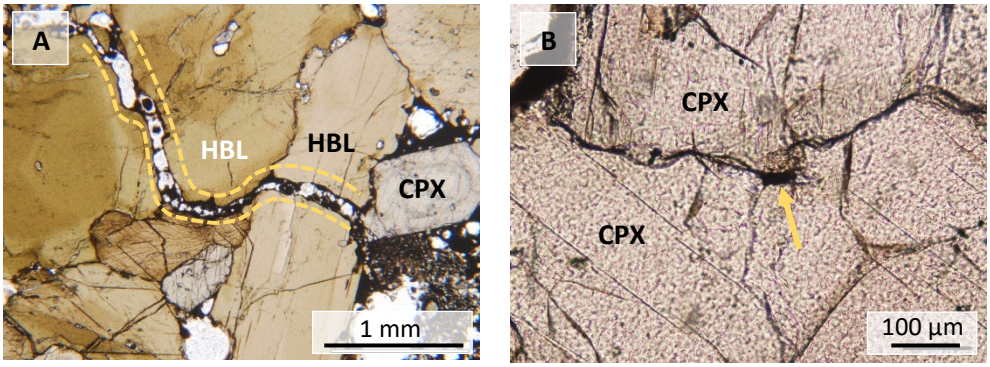

Figure 7.1 – Photomicrographs of grain boundary morphologies, taken in plane polarised light. **A)** Example of a 'jigsaw fit' boundary dividing adjacent hornblende crystals in sample M8. The boundary is parallel and occupied by vesicular glass that appears to have pushed the crystals apart from one another. This type of boundary is clearly distinguishable as a decompression feature. **B)** Example of a grain boundary preserving pre-entrainment porosity. The boundary is not parallel, a small pocket of unvesiculated glass (yellow arrow) prevents complete closure of the boundary.

7.1.2.2 Crystallisation

Crystallisation related to decompression is clearly distinguishable from earlier, pre-entrainment crystallisation. The impingement of CPX crystals forms straight-sided triangular pores that maintain acutely angled interstices, seen clearly in Figure 4.11. This suggests that crystallisation continued until entrainment and eruption. At this point, an absence of quench overgrowths across the study samples suggests that crystallisation of the pre-eruptive assemblage ceased, in favour of decompression driven nucleation and growth of microlite crystals in the glass (Figure 4.18). These microlites are clearly discernible from the crystals formed prior to decompression and have been excluded from any of the textural analysis. There is no relationship between crystal size and proximity to the contact with the host magma, precluding any influence of the host in governing the analysed crystal textures.

7.1.3 Do the xenoliths provide a representative sample of the crystal mush?

It is likely that the xenoliths studied here represent a region of mush with physical characteristics particularly conducive for survival. That is, the regions of the mush that were most easily fragmented to become entrained into the host magma, and sufficiently strong to avoid disaggregation during ascent (Holness and Bunbury, 2006; Holness et al., 2007d). Consequently, the xenoliths in this study are likely to be over-representative of particular mush regions that may comprise part of a more texturally heterogeneous system. The four samples analysed here do not provide a large enough sample size to constrain the properties that make these xenoliths particularly eruptible. However, it is likely that a combination of the high crystallinity fraction (>70%), relatively low interstitial melt content (<14%) and vesicularity (<15.1%) of these samples all contribute to their survival (Section 6.1).

Significantly, the samples all plot within the white region of the ternary diagram in Figure 6.2 (<20% glass; <30% holes; >50% crystals). This bears similarity with the results of Holness and Bunbury (2006) and Coombs et al. (2002), who analysed glass bearing xenoliths from the Kula Volcanic Province in Turkey and the Southwest Trident volcano in Alaska, respectively. All of their samples plotted within the same region of the ternary diagram, supporting the idea that mush samples, inclusive of those studied here, with these proportions of glass, voids and crystals are significantly more likely to survive eruption.

7.1.4 Implications for interpretation of the xenolith textures

The discussion presented above can be summarised as follows:

- The glass preserved within the study samples represents an in-situ melt that was quenched by rapid eruption.
- External forces such as melt infiltration and shear have not influenced the distribution of melt, however internal forces exerted by the expansion of a gas phase have modified the porosity along several HBL:HBL grain boundaries in sample M8.
- Some melt may have been lost from the xenoliths in order to accommodate for vesicle expansion. Because the majority of grain boundaries do not appear to have been affected by decompression, pre-entrainment melt distribution is recorded in the porosity fraction (glass + vesicles).
- Decompression induced nucleation and growth of microlites in the glass is distinguishable from earlier crystallisation of the pre-eruptive assemblage, which appears to have continued up until entrainment and eruption.

- The textures of these xenoliths are likely to be particularly conducive for xenolith survival, and it is likely that the samples comprise part of a more heterogeneous mush.

These interpretations suggest that the xenolith textures studied here predominantly provide a sample of in-situ, semi-solidified crystal mush. The exception to this is the jigsaw-fit boundaries identified in sample M8, and the associated glass-free fractures. Otherwise, the textures are interpreted to be magmatic in nature, pertaining to pre-entrainment processes. From this, these samples provide a valuable opportunity to investigate crystal and melt textures in a semi-solidified mush.

7.2 What is the textural petrogenesis of the xenoliths?

Chapter 1 introduces the classification of igneous textures into three categories, grouped according to the processes that govern their formation. Kinetic textures result from nucleation and growth processes, mechanically modified textures result from sorting and compaction, and equilibrium textures are driven by the minimisation of interfacial energy (Higgins, 2006a). Furthermore, a texture may be considered primary if it is formed by kinetic processes, and secondary if it has been modified by non-kinetic processes. This section therefore aims to interrogate the array of two-dimensional textural data reported in Chapter 5 to determine the crystallisation sequence recorded in these xenoliths. From this, the textures will be analysed to evaluate the extent to which they record primary textures that are often obscured in solidified plutonic rocks (e.g. Higgins, 1991; McBirney and Hunter, 1995; McBirney, 2009).

7.2.1 Establishing the textural sequence

The CSD results presented in Chapter 5 demonstrate that each of the CSDs exhibit a curvature that is best divided into 3 log-linear segments. According to the steady-state CSD model, this indicates that the crystal textures cannot be summarised by a single kinetic event. A persistent challenge in textural analyses is the ambiguity surrounding the completeness of the final texture recorded in the sample. That is, whether the final texture provides a full or partial record of textural evolution. However, because these samples are characterised by poikilitic textures they provide the opportunity to determine a textural sequence (e.g. Figure 4.4). Crystals inside and outside the oikocrysts can be considered a series of textural samples, linked by some combination of kinetic, mechanic or equilibration processes (Higgins and Roberge, 2003). This therefore provides the opportunity to scrutinise the textural evolution of the sample, constraining the sequence of magmatic processes recorded in the CSDs.

7.2.1.1 Early textures – chadocryst growth and dissolution

Chadocrysts of clinopyroxene and phlogopite are assumed to have formed prior to the hornblende crystals in which they are hosted, and are therefore interpreted to have crystallised early within the textural sequence. Poikilitic textures are most prevalent in samples M4 and M8, are less abundant in sample M2 and absent in sample M6. Therefore, interpretation of the earliest forming textures is undertaken using the abundant chadocrysts preserved in samples M4 and M8. These chadocrysts encompass a narrower range of crystal sizes (0.03- 1.50 mm) than the clinopyroxenes and phlogopites outside of the chadocrysts (0.03- 4.04 mm), but are characterised by rounded and embayed outlines indicative of disequilibrium and dissolution, as observed in Figure 4.11. Because of this, they only provide a partial

record of the earliest texture, but give an insight into magmatic processes occurring early in the crystallisation sequence. The simplest interpretation of the chadocryst clinopyroxene textures is as follows:

Firstly, the nucleation and growth of clinopyroxene formed the earliest crystal texture, now partially preserved within the hornblende oikocrysts. Because an unknown volume of crystal material has been lost, it is not possible to quantify the degree of crystallinity reached in this initial period of CPX nucleation and growth (e.g. Higgins, 1998). However, in some areas the chadocrysts preserve the remnants of triangular pore structures that reflect the impingement textures observed outside of the oikocrysts in samples M2, M4 and M8 (Figure 7.2). This suggests that the crystallinity was sufficiently high to form a touching crystal framework, which typically occurs at crystallinities in excess of 20% (Jerram et al., 2003). The chadocrysts do not exhibit any preferred orientation, suggesting that processes such as compaction or flow of magmatic currents were not active at this time (e.g. Higgins, 1998). The chadocrysts then became unstable and experienced a period of dissolution. The shape of the CSD produced by the chadocrysts (Figure 7.3 A) suggests that there was likely only one dissolution event, because repeated cycles of dissolution and growth produce a strongly humped CSD (Simakin and Bindemann, 2008) (e.g. Figure 7.3). This dissolution event was captured by the growth of the hornblende oikocrysts, which inhibited any further dissolution and preserved the remaining CPX.

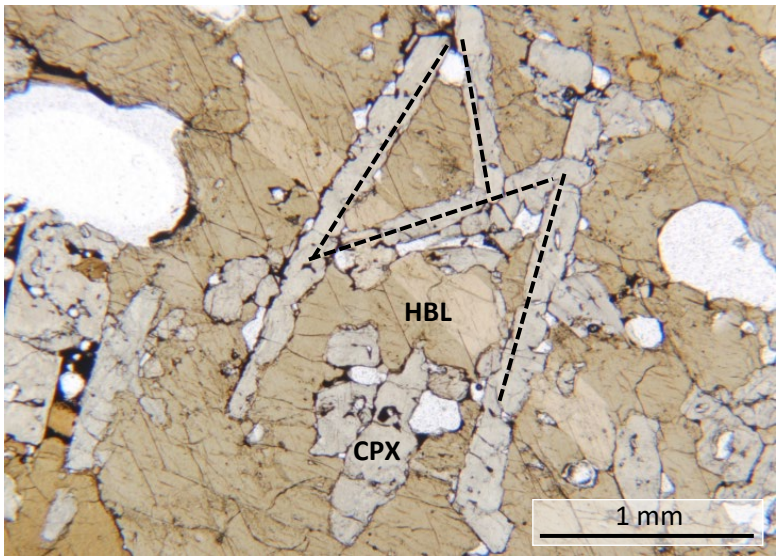

Figure 7.2 – Photomicrograph of clinopyroxene chadocrysts, demonstrating the earliest forming crystal textures. Photomicrograph is taken from sample M8 in plane polarised light. The chadocrysts are anhedral, with rounded outlines that attest to disequilibrium and dissolution. Dashed lines demonstrate remnants of a triangular pore structure. This suggests that these clinopyroxenes may have reached crystallinities that formed a touching crystal framework. It is plausible that growth of the oikocrysts may have pushed the clinopyroxenes out of their initial position, in which case these triangular pore spaces may be deceptive of the original texture. However, if this were the case then the margins of the oikocrysts would be particularly chadocryst-rich (e.g. Higgins and Roberge, 2003), which is not the case. Therefore, the chadocrysts are considered to preserve the remnants of the earliest texture.

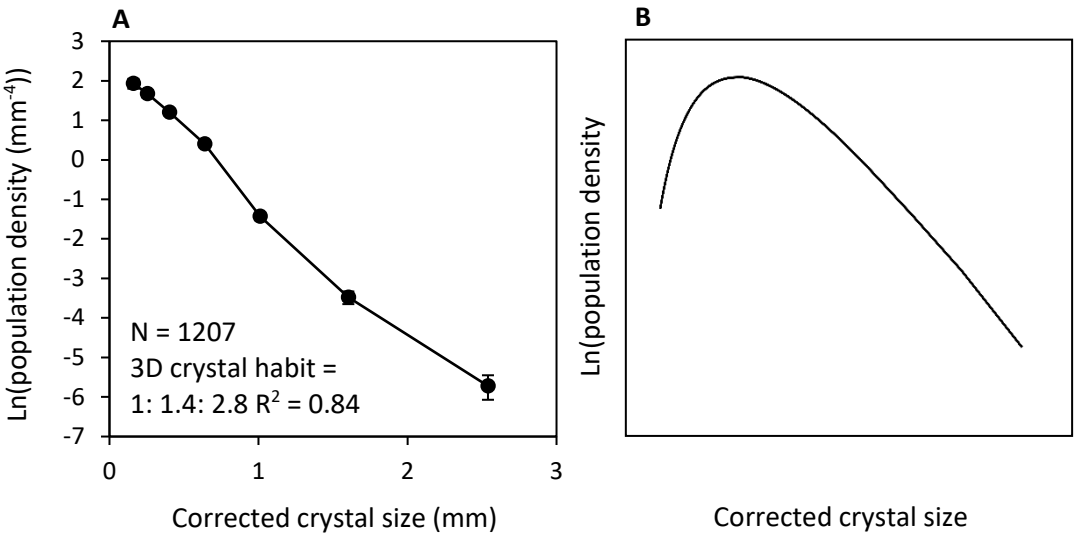

Figure 7.3 **–** Crystal size distribution calculated from clinopyroxene chadocrysts. **A)** Plot showing crystal size distribution of clinopyroxene chadocrysts in sample M4. For consistency, a chadocryst was considered as a crystal entirely enclosed by one optically continuous oikocryst. The CSD exhibits several kinks but maintains a negative slope across all size fractions. **B)** Theoretical crystal size distribution for a crystal population experiencing multiple dissolution/ reprecipitation events, following Simakin and Bindemann (2008). Because the chadocryst CSD does not exhibit this humped profile it is interpreted that the chadocrysts only experienced one period of dissolution prior to being captured by the oikocrysts.

Because of the low number of phlogopite chadocrysts within any of the samples, it is not possible to derive as much information about their original textures. From the information that is preserved within the oikocrysts, it is likely that there were fewer phlogopite crystals and that they crystallised after the clinopyroxene. Because resorbed phlogopites are enclosed within the same oikocrysts as the clinopyroxene chadocrysts (e.g. Figure 4.15), they likely became unstable alongside the clinopyroxene.

Resorption textures are a common feature in pyroxenes from a multitude of igneous rocks (e.g. Humphreys et al., 2006; Streck, 2008; Neumann, 2019; Lormand et al., 2021), are typical of disequilibrium conditions and are commonly cited to indicate open system processes such as magma recharge and mixing (e.g. Svetov et al., 2020; Palummo et al., 2021; Liu et al., 2022). It is likely that the resorption textures exhibited by the chadocrysts (Figure 4.11) record an influx of melt, driving the dissolution of early forming clinopyroxenes and phlogopites. Following the steady-state CSD model, this would affect the original CSD by modifying the slope. Because dissolution rate is inversely proportional to crystal size (Simakin and Bindemann, 2008; Noiriel et al., 2020), the smallest crystals will be lost more readily and the CSD slope will become less steep (Figure 7.3) (e.g. Higgins, 2002; Zieg and Lofgren, 2006; Magee et al., 2010; Neal et al., 2015). Alternatively, it is plausible that crystal dissolution was driven by textural coarsening (e.g. Higgins and Roberge, 2003). However, CSDs produced from the clinopyroxene chadocrysts (Figure 7.3) do not exhibit the humped profile that is characteristic of coarsened crystal populations (e.g. Higgins 2006a, Higgins, 2011). Additionally, crystals outside of the oikocrysts are frequently mantled by rims with higher Mg#s (reported in Section 4.2). This provides chemical evidence for open system processes (albeit later in the textural sequence) which appear to have been significant throughout crystallisation.

7.2.1.2 Oikocryst textures – a product of crystal-melt reaction?

The textural affinity between hornblende oikocrysts and resorbed clinopyroxene chadocrysts raises the question of whether the chadocrysts may have been consumed at the expense of the poikilitic hornblende as described by Higgins and Roberge (2003), Barnes et al. (2016), Kaufmann et al. (2018) and Barnes et al. (2021). The textural relationship between chadocrysts and oikocrysts is similar to a texture documented by Cooper et al. (2016), who proposed that the oikocrysts formed according to the reaction: clinopyroxene (± phlogopite) + melt = peritectic hornblende (Blatter et al., 2017). The formation of amphibole by melt-clinopyroxene reaction is well documented in the literature (e.g. Coltorti et al., 2004; Smith, 2014; Cooper et al., 2016), and may form an important mechanism for the generation of such amphibole rich assemblages as are observed in the study samples investigated here (e.g. Debari et al., 1987; Neal, 1988; Coltorti et al., 2004; Beard et al., 2004; Smith et al., 2014). Across the study samples, oikocrysts with Mg#s that overlap with the chadocrysts (Figures 4.3 and 4.10), relatively low trace element contents and wide ranges of incompatible element concentrations (documented in Appendix 3) may provide chemical evidence for this reaction as stated by Cooper et al. (2016) and Klaver et al. (2016). From a textural perspective, it is conceivable that the early formed clinopyroxene and phlogopite was partially replaced by a reaction with infiltrating melts, resulting in the oikocryst rich texture observed in samples M4 and M8. From a chemical perspective, whole rock geochemistry would better constrain this relationship (e.g. Davidson, 2007; Zhou et al., 2020).

Sample M6 provides the most amphibole rich assemblage and is lacking in poikilitic textures that characterise the other samples. Therefore it is plausible that this

sample may represent a more complete example of this clinopyroxene replacement. The texture of this sample is characterised by an interlocking hornblende framework, comprised of subhedral-euhedral crystals with a narrow size distribution, similar to that reported by Daczko et al. (2016). Clinopyroxenes associated with these textures are anhedral and frequently exhibit disequilibrium textures, or are contained as fine (<500 μm) anhedral inclusions (Figure 4.13). This texture may be attributed to near complete reaction-replacement of pre-existing pyroxenes, which would establish the rock as an 'imposter cumulate' (Daczko et al., 2016). Alternative explanations for such an amphibole rich assemblage include the possibility that amphibole was simply the dominant phase on the liquidus (e.g. Holness and Bunbury, 2006), oscillatory nucleation about a binary eutectic (e.g. Hort et al., 1993) or via mechanical sorting processes (Zhou et al., 2020). However, because the Cr contents of the clinopyroxenes analysed in this sample are as much as ten times higher than in the other samples, coupled with higher Mg#s (> 80) (reported in Appendix 3), this sample may simply represent a deeper region that was more prone to reaction with an infiltrating melt.

7.2.1.3 Addition of exogenous crystals

The textural sequence defined by the poikilitic relationship between clinopyroxene, phlogopite and hornblende is complicated by the presence of well-formed, subhedral hornblende crystals that do not contain any chadocrysts (Figure 4.4). From an entirely textural perspective, the non-poikilitic hornblendes appear to have formed prior to the poikilitic hornblendes. Chemically, in sample M4 the non-poikilitic hornblendes are characterised by greater concentrations of potassium (~7 wt% K_2O) and lower concentrations of SiO_2 (~35 wt%) than the poikilitic hornblendes (~4 wt% K_2O; ~38 wt% SiO_2). Further examination of the major

element compositions reveals a variation in the pressure sensitive components of the two hornblende populations, potentially indicating that textural discrepancies could be attributable to crystallisation at different pressures (e.g. Kiss et al., 2014; Cooper et al., 2016; Mandler and Grove, 2016). Specifically, although the total Al_2O_3 content of amphibole is dependent on melt composition and temperature, Al^{VI} content is significantly pressure dependent (e.g. Blundy and Holland, 1990; Putirka, 2016). The poikilitic hornblendes exhibit greater coordination of Al^{VI} (Figure 7.4), which under experimental conditions is typically diagnostic of crystallisation at lower pressures (e.g. Pichavant and Macdonald, 2007; Klaver et al., 2017). Conversely, the non-poikilitic hornblendes exhibit increased contents of K-, and decreased Si- (Figure 7.4), which is characteristic of amphiboles formed under higher pressure conditions (e.g. Konzett et al., 1997; Lisboa et al., 2020). Together, this suggests that the non-poikilitic hornblendes may have been formed under higher pressure conditions than the later-forming oikocrysts.

This interpretation is made with some caution, because variations in Al-content of amphiboles cannot always be attributed to crystallisation at different pressures (Kiss et al., 2014). Independent of pressure, variations in oxygen fugacity, melt water content and chemistry may also influence this Al-content in hornblende (e.g. Scaillet and Evans, 1999; Anderson and Smith, 1995; Kiss et al., 2014). Notably, although sample M8 demonstrates the same textural distinction between poikilitic and non-poikilitic hornblendes, there is an overlap in their major element chemistries. Therefore, the hornblendes can be distinguished texturally, but not chemically. From the chemical data alone, they do not give the same evidence as in sample M4 for formation at different pressure conditions.

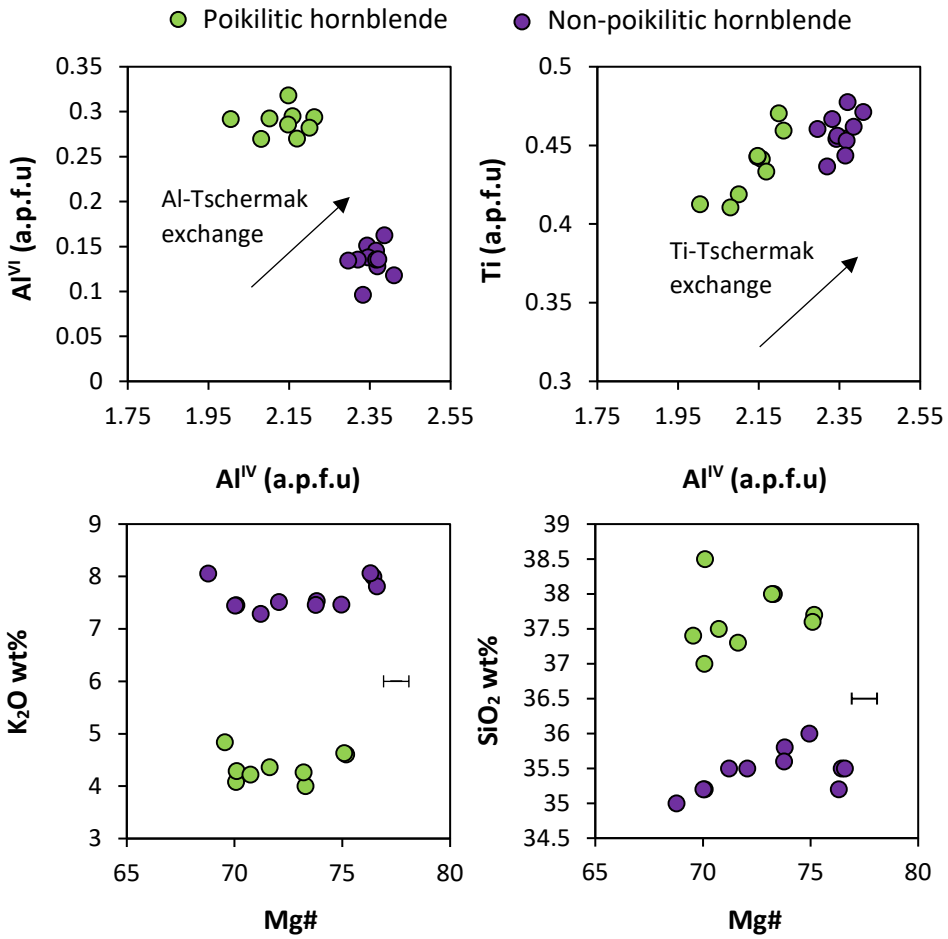

Figure 7.4 – Pressure and temperature sensitive hornblende components, plotted for poikilitic and non-poikilitic crystals in sample M4. Poikilitic and non-poikilitic hornblendes exhibit a correlation between Al^{IV} and Ti that indicates the role of temperature sensitive Ti-Tschermak exchange. Although they don't exhibit the correlation indicative of pressure sensitive Al-Tschermak exchange, relative changes in octahedral and tetrahedral Al coordination can suggest formation under different PT conditions (Cooper et al., 2016). Here, the poikilitic amphiboles have a greater coordination of Al^{VI}, which under experimental conditions is typically diagnostic of crystallisation at lower pressures (e.g. Pichavant and MacDonald, 2007; Klaver et al., 2017). Coupled with differences in K_2O and SiO_2 wt%, which may vary with pressure and temperature, the major element chemistries suggest that the non-poikilitic amphiboles may have formed at higher PTs than the poikilitic amphibole. This interpretation is made with some caution, because factors other than pressure and temperature can influence the Al-content in hornblendes (e.g. Kiss et al., 2014). Error bars represent 2 standard deviations, Y-error bars are smaller than the data marker.

However, because of the uncertainties surrounding pressure sensitive hornblende components, it is conceivable that other magmatic variables may exert a stronger influence over their major element compositions, masking chemical evidence of a higher pressure origin.

Because PT values obtained using amphibole-only barometers have been shown to have large uncertainties (e.g. Erdmann et al., 2014; Putirka, 2016; Molina et al., 2021), absolute PT values have not been calculated for these samples. However, the relationship between clinopyroxene composition and pressure is better constrained (e.g. Putirka, 2008), and so major element chemistries can provide an estimate of crystallisation depth without the need to derive absolute PT values (e.g. Shaw and Eyzaguirre, 2000; Ashchepkov and André, 2002; Zhang et al., 2018; Neave and Maclennan, 2020). In clinopyroxene, the coordination of Al- is closely related to pressure and temperature (Morimoto, 1988): Al- tends to enter into the octahedral site at higher pressures, and into the tetrahedral site at higher temperatures (Thomson, 1974). From this, relative proportions of tetrahedral and octahedral Al- can be used to provide an estimate of crystallisation depth, without the need to calculate equilibrium liquid compositions (e.g. Putirka, 2008). On an Al^{VI}-Al^{IV} discrimination diagram (Figure 7.5 A) (Aoiki and Shiba, 1964), all of the clinopyroxenes measured in each sample (including both chadocrysts and non-chadocrysts) plot in the granulite facies regime, indicating that they formed under high pressure and temperature conditions consistent with the lower crust or upper mantle. These results agree with those of Becker (1977) who conducted an earlier study on these samples. The poikilitic relationship with hornblende entails that hornblende oikocrysts likely formed under similar pressures.

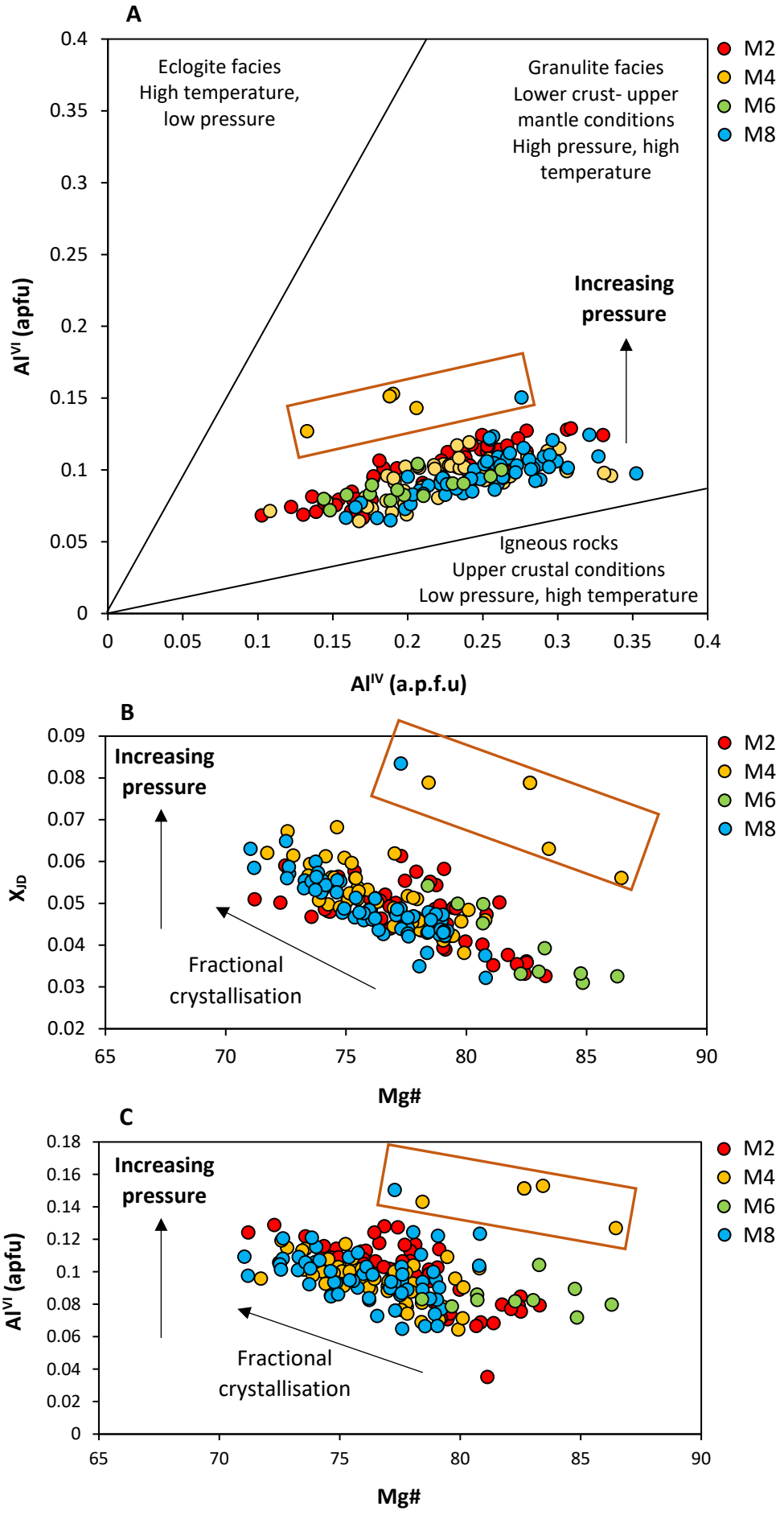

Figure 7.5 (Caption overleaf) ▶

◄ ***Figure 7.5 (Overleaf)*** **–** Pressure sensitive clinopyroxene components. **A)** Composition of clinopyroxenes according to the Al^{VI}-Al^{IV} discrimination diagram of Aoki and Shiba (1964), indicating that the clinopyroxene formed under lower curst or upper mantle conditions. The orange box highlights clinopyroxenes that plot further away from the igneous realm of the diagram. **B)** Plot of Mg# versus jadeite component for clinopyroxenes measured in all four samples. The orange box highlights the same crystals as in A, suggesting that they are slightly enriched in jadeite component compared to clinopyroxenes with similar Mg#s. **C)** Plot of Mg# versus pressure sensitive Al^{VI} for clinopyroxenes measured in all four samples. Orange box highlights the same crystals as in A and B. Although there is less of a separation than for the jadeite component, the highlighted crystals exhibit slightly elevated Al^{VI} coordination than clinopyroxenes with similar Mg#s. Together, the major element chemistry suggests that these crystals may have formed under higher pressure conditions, suggesting that the samples comprise a complex clinopyroxene population containing crystals formed at different pressure conditions.

Several clinopyroxenes (all outside the oikocrysts) also appear to have formed under higher pressure conditions. These crystals are somewhat enriched in jadeite component (X_{JD} = ~0.08) and octahedral Al- (Al^{VI}= 0.16), with high concentrations of Cr (Figure 7.5 B). These clinopyroxenes plot closer to the upper pressure field, but still yield depth estimates in the lower-crust upper-mantle realm (Figure 7.5 C). These crystals are not identified in every sample, however because a spot analysis technique was used it is likely that there are more of these crystals than have been identified through this geochemical analysis. It is conceivable that the non-poikilitic hornblendes crystallised at similar depths, comprising a crystal cargo from deeper in the magmatic system.

According to these findings, clinopyroxene and hornblende crystals comprise varied populations that include crystals that likely formed under different pressure conditions. This assemblage could therefore potentially contain xenocrysts, antecrysts or a mixture of these components (e.g. Ubide et al., 2014). The crystals that are interpreted to have formed under higher pressure conditions have subhedral-euhedral crystal habits, are mostly lacking in resorption features and have similar REE profiles to the crystals that appear to have formed at shallower pressures (Figure 7.6). This indicates that they originated from within the magmatic system, and are best described as antecrysts. Additionally these antecrysts exhibit greater concentrations of compatible Cr, and lesser concentrations of incompatible Zr, Hf and Y than the clinopyroxenes inferred to have formed under shallower pressure conditions (both chadocrysts and non-chadocrysts) (Figure 7.6). Coupled with higher Mg#s in the high pressure clinopyroxenes, this suggests they formed from a more primitive melt. Limited olivine crystals (1-2 per section) mantled by reaction coronas of clinopyroxene and phlogopite may represent xenocrysts, suggesting further diversity within the crystal cargo. The antecrysts could be recycled from earlier accumulation or could have crystallised on ascent as precursors to the mush assemblage. Because all of the identified clinopyroxene antecrysts are outside of the oikocrysts, it is likely that they were incorporated at a point that would negate the latter of these scenarios.

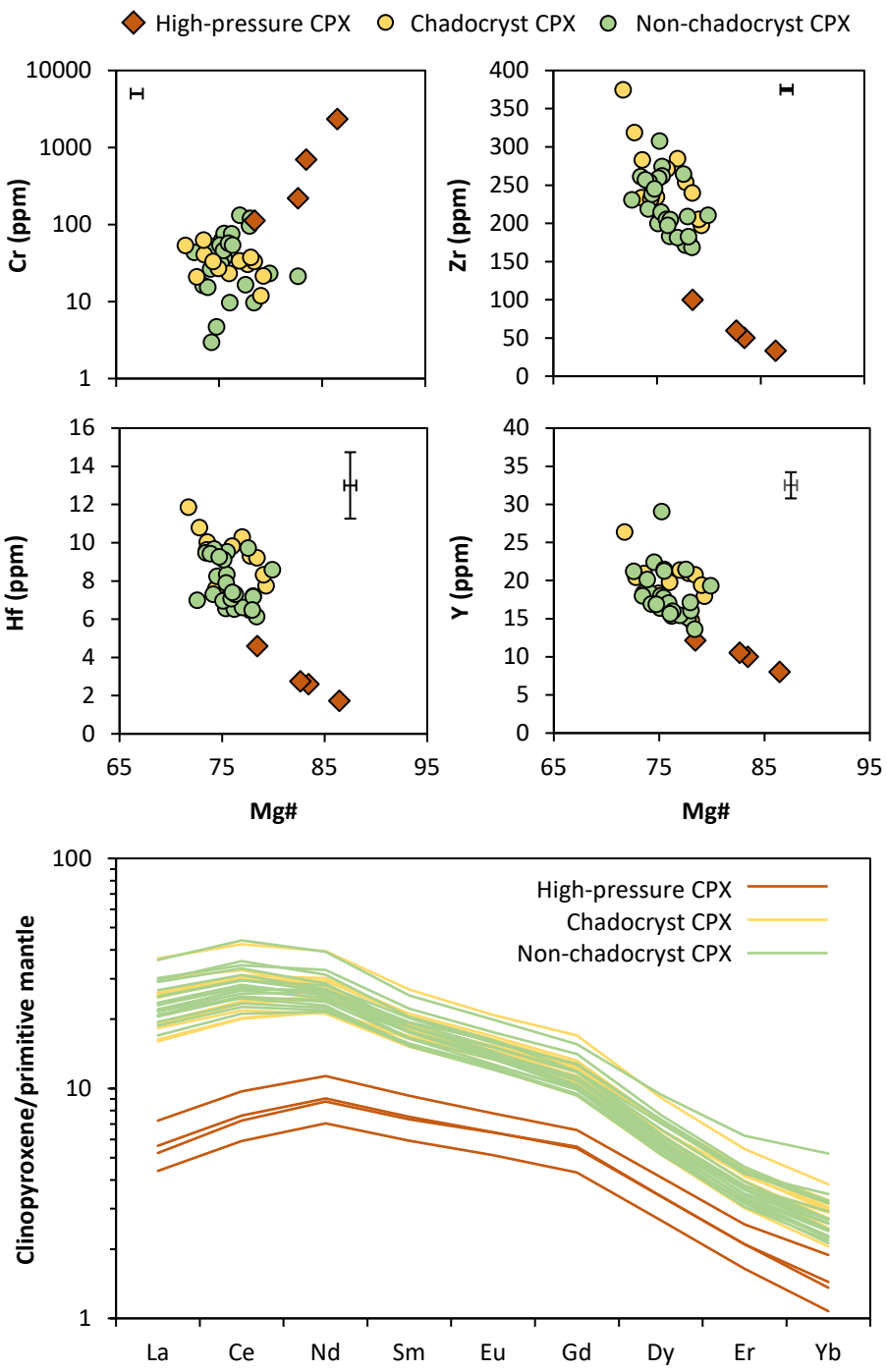

Figure 7.6 – Caption overleaf ▶

◄ ***Figure 7.6 (Caption overleaf)*** **–** Trace element composition of clinopyroxenes. The clinopyroxenes interpreted to have formed under higher pressures exhibit greater concentrations of compatible Cr, and lesser concentrations of incompatible Zr, Hf and Y than the clinopyroxenes inferred to have formed under shallower pressure conditions (both chadocrysts and non-chadocrysts). Coupled with higher Mg#s in the high pressure clinopyroxenes, this suggests they formed from a more primitive melt. REE compositions follow a similar pattern (normalised mantle values from Sun and McDonough, 1989), indicating that they are best described as antecrysts. Error bars represent 2 standard deviations; Cr and Zr errors are smaller than the data marker.

The incorporation of antecrysts will result in a kinked CSD, where a break in slope signifies different crystal populations (e.g. van der Zwan et al., 2013; Svetov et al., 2020). The antecrysts that have been identified yield crystal sizes that tend towards the right-hand termination of the CSD, and therefore likely contribute to the increase in population density seen in the largest size fractions (Section 5.2.3). Because the antecrysts are best identified by compositional trends, it is likely that there are a greater number of antecrysts in these samples than have been identified by using a spot analysis technique.

7.2.1.4 Late crystallisation – enhanced nucleation of clinopyroxenes

Clinopyroxenes outside of the oikocrysts are interpreted to represent the latest forming textures. Hosted in glass, frameworks of loosely packed clinopyroxene are almost monomineralic, with only minor amounts of accessory phlogopite and apatite in glass filled pore spaces (Figure 4.11). The crystallisation of one mineral phase at high population densities suggests that at this point, nucleation was promoted over growth. Enhanced nucleation, producing clinopyroxenes with relatively primitive compositions (Mg#s and major element chemistries overlapping

with earlier forming chadocryst populations (Figure 4.14)), coupled with irregular hornblende overgrowths in contact with glass (Figure 4.7), suggests that these latest textures may also be attributable to open system processes. Enhanced crystallisation necessitates an increase in the kinetic driver, which can be facilitated by the influx of compositionally distinct melts (e.g. Hort, 1998; Ni et al., 2014). With textural and geochemical evidence that melts were percolating through the system up until the latest stages of crystallisation, it is conceivable that these clinopyroxenes represent enhanced nucleation in response to the late-stage infiltration of a clinopyroxene saturated melt. According to the open system CSD model, this enhanced crystallisation of clinopyroxene would increase the intercept of the CSD, further modifying the original slope. In sample M2 it appears that this late clinopyroxene crystallisation was followed by a period of renewed hornblende growth, demonstrated in Figure 7.7. This late reappearance of hornblende is only identified within this sample, suggesting that melt percolating through this region of the mush was potentially more hydrous than that in samples M4 and M8. This demonstrates the heterogeneity of the mush and the melts percolating through it, which is captured by the textural variations recorded between each of the samples.

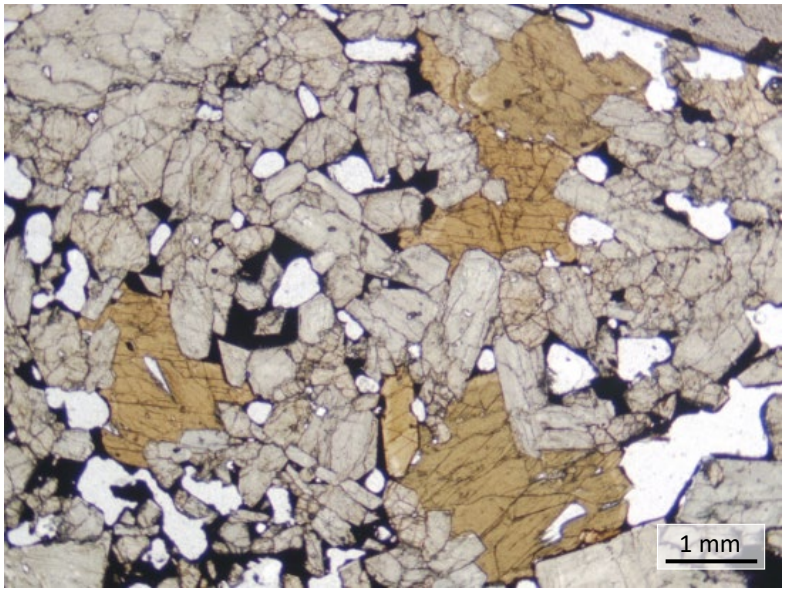

Figure 7.7 **–** Late reappearance of hornblende in sample M2, taken in plane polarised light. In sample M2 there are examples of renewed hornblende growth; according to the textural relationship with the late forming clinopyroxene frameworks (the hornblende is interstitial to the clinopyroxene) this hornblende must have formed after the clinopyroxene. This late forming hornblende is only identified in sample M2, suggesting that the melt percolating through this region of the mush was sufficiently hydrous to facilitate renewed hornblende crystallisation. This not only demonstrates the textural heterogeneity of the mush, but also compositional heterogeneity in the melts percolating through it.

7.2.1.5 Quenching and entrainment

As outlined in Section 7.1, crystallisation associated with decompression is clearly distinguishable to pre-entrainment crystallisation. Clinopyroxene crystals in contact with glass form straight-sided triangular pores (Figure 4.18) that suggest crystallisation continued up until entrainment and eruption. Vesiculation of the glass within these pore spaces constitute a diktytaxitic texture (Figure 4.11), indicating that solidification occurred in response to quench crystallisation by rapid entrainment and eruption (Downes et al., 2004). The chemistry of the glass

preserved within the xenoliths is compositionally distinct from that of the host basalt (Downes et al., 2004). Therefore, the late percolating melts related to crystallisation of texturally late forming clinopyroxene are not considered to be related to the melt that ultimately transported the xenoliths to the surface.

7.2.2 Petrogenetic model for the formation of the xenoliths

From the interpretations discussed above, the following model is proposed to describe the textural petrogenesis of the sample suite analysed in this study:

- The nucleation and growth of clinopyroxene formed the earliest texture, followed by phlogopite. Clinopyroxene may have reached sufficient crystallinities to form a touching framework. Although some of the textural information has been lost, there is no evidence to suggest that mechanical processes (that would generate alignment in the chadocrysts) or equilibrium processes (that would cause a left-hand downturn in the chadocryst CSDs) were significant during the formation of this earliest texture. Therefore, it is assumed that the earliest CSDs were straight, reflecting a kinetic texture.
- An influx of melt caused the early clinopyroxenes and phlogopites to become unstable and dissolve. The clinopyroxene and phlogopite CSDs flatten as resorption reduces the slope.
- The growth of hornblende oikocrysts (which appear to have formed via a peritectic reaction with the clinopyroxene and melt) captured the dissolving clinopyroxenes and phlogopites, partially preserving the earliest texture. The hornblende CSD starts to develop, rotating about the Y-axis as the residence time increases and the oikocrysts continue to grow. The clinopyroxene and phlogopite CSDs are temporarily frozen as the crystals

are captured in the hornblende oikocrysts. Sample M6 may represent a more complete example of this reaction. In order to form hornblende at the expense of clinopyroxene, this melt is inferred to have been relatively hydrous and more primitive in composition.

- Hornblende and clinopyroxene antecrysts entrained from deeper regions of the magmatic system were incorporated into the crystal assemblage. It is challenging to constrain exactly when they were incorporated, but because all identified antecrysts are outside of the oikocrysts they were likely incorporated after oikocryst growth. The inclusion of these antecrysts kinks the slope of those CSDs, flattening the right-hand portion of the slope.
- Enhanced nucleation of clinopyroxene formed high porosity frameworks in regions of glass between the hornblende antecrysts and oikocrysts. Phlogopite and apatite crystals constitute an accessory phase within these frameworks. Because these frameworks are almost entirely comprised of clinopyroxene, they may represent the system's response to the influx of a clinopyroxene saturated melt, suggesting open system processes were significant throughout crystallisation of the xenoliths. This represents a separate nucleation event to that which formed the earliest texture, kinking the CSD slope by steepening the left-hand side of the CSD.
- In samples M4 and M8, hornblende rims in contact with glass exhibit irregular overgrowths that further demonstrate the importance of open system processes at later stages of crystallisation. In sample M2, interstitial hornblende hosted within the late forming clinopyroxene frameworks indicates the late crystallisation of hornblende in this sample.

- Because the host basalt and xenolith glass are compositionally distinct, the latest injection of melt recorded within these samples is not considered to be related to the event that ultimately quenched and transported these samples.
- Finally, the xenoliths are rapidly quenched as they are captured and erupted at the surface. Because the xenoliths did not disaggregate during entrainment, it is likely that there was a significant viscosity, temperature and density contrast between the mush comprising the xenolith and the melt that finally transported them to the surface. Decompression induces vesiculation and the nucleation and growth of microlites. The CSDs of the pre-eruptive assemblage are frozen.

This model is summarised in Figures 7.8 and 7.9, detailing the inferred evolution of the CSD. The textural history of the xenoliths does not recognise a magmatic process that would generate the downturn recognised in the smallest size bins. Therefore, regions of positive slope identified in Chapter 5 are assumed to represent measurement artefacts, introduced from measurement inaccuracies in the smallest crystals.

▶ ***Figure 7.8 (Overleaf)*** **–** Model for the petrogenesis of the crystal textures. Cartoons illustrate the textural sequence; CSD schematics detail evolution of the clinopyroxene, hornblende and phlogopite CSDs.

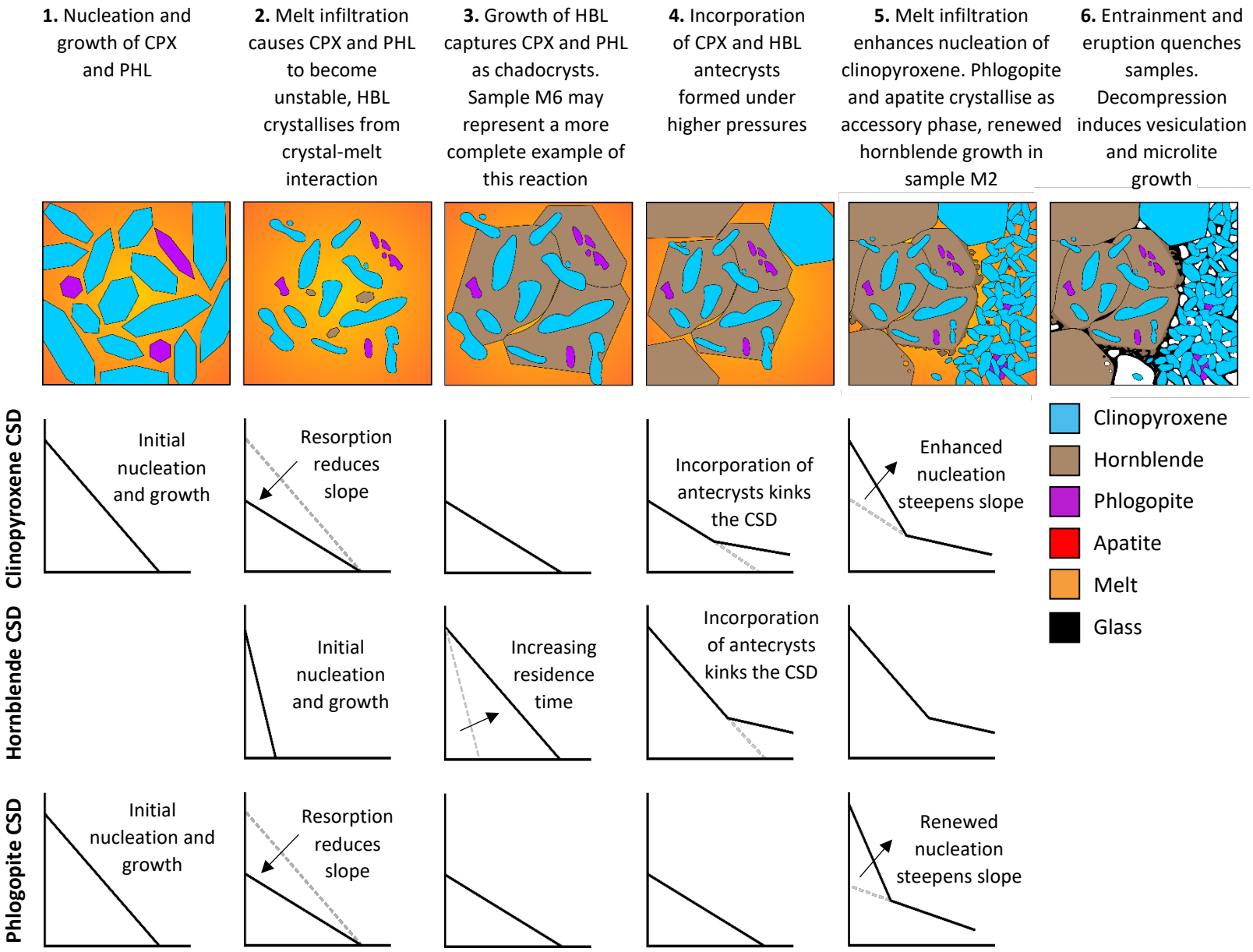

Figure 7.8 (Caption overleaf) ◀

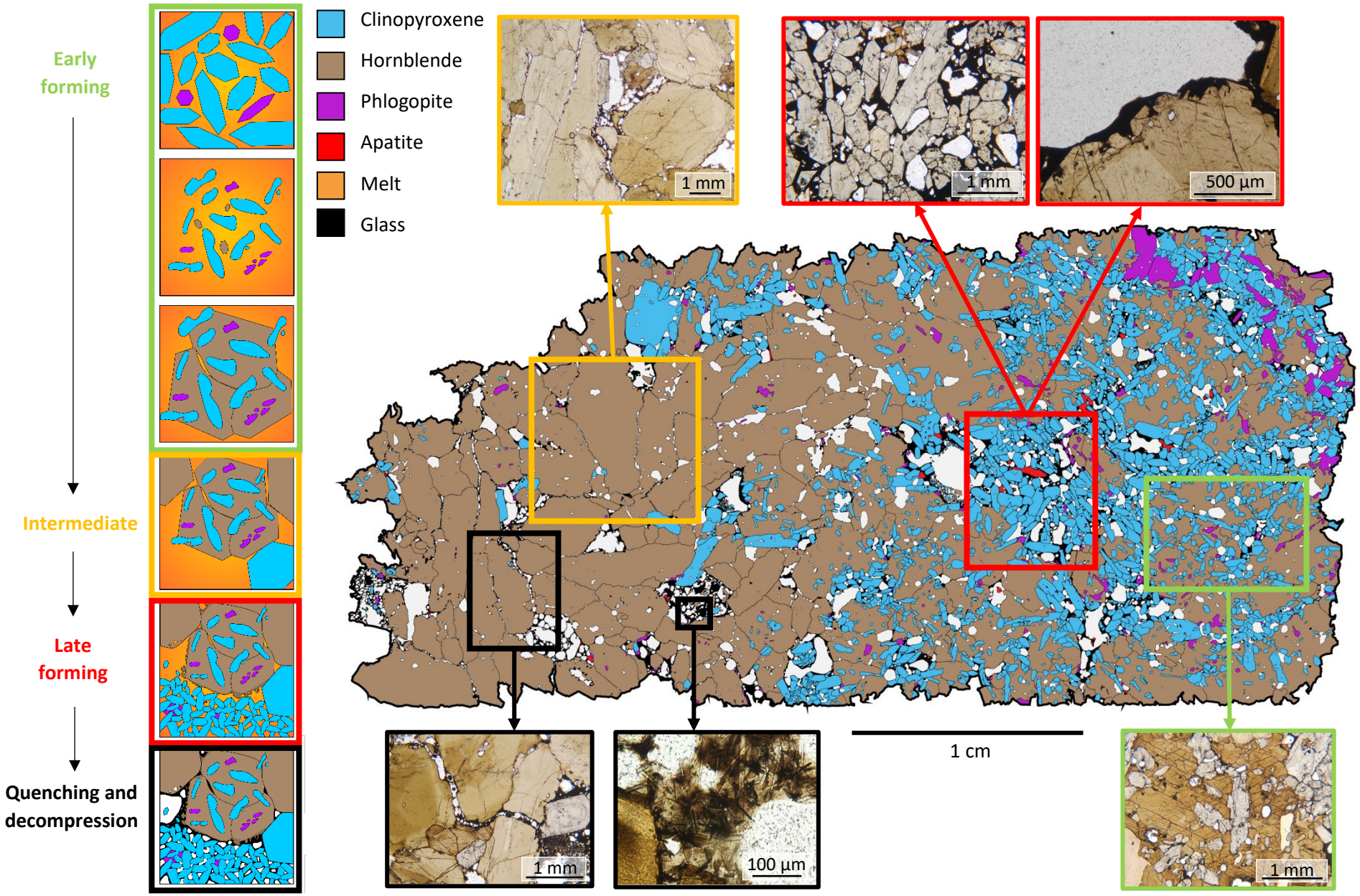

Figure 7.9 (Caption overleaf) ▶

◄ ***Figure 7.9 (Overleaf)*** **–** Petrogenesis of the crystal textures, with photomicrographs demonstrating textural evidence for each stage of the petrogenetic model. Digitised thin section is sample M8 A. Early forming textures (green) are represented by chadocrysts of clinopyroxene and phlogopite within hornblende oikocrysts. Intermediate textures (yellow) are crystals inferred to represent antecrysts, incorporated into the assemblage after the initial formation of poikilitic hornblende. Late forming textures (red) include the frameworks of clinopyroxene hosted in glass and irregular overgrowths on hornblendes in contact with glass. Textures related to entrainment and eruption (black) include 'jigsaw fit' boundaries (only identified in this thin section) and vesicles and microlites in glass.

7.2.3 Are these textures primary?

Adopting the criteria outlined in Chapter one of this thesis, a texture produced entirely by kinetic processes would be primary, and any modification by non-kinetic (mechanical and equilibrium) processes would constitute a secondary texture. However, the broad spectrum of textures observed in igneous samples entail that there is some ambiguity regarding the extent to which a kinetic texture can be modified before it is truly a secondary texture. Holness et al. (2017a) acknowledge the wide number of magmatic processes that can impact the textural evolution of a sample, and further break down the classification of igneous textures into primary, secondary and tertiary according to the following criteria:

Primary texture: A kinetic texture formed in-situ during crystal nucleation and growth or during the mechanical accumulation of crystals by gravitational settling.

Secondary texture: A texture that forms after initial crystal accumulation, by mechanical processes such as slumping or rearrangement by magmatic currents. This occurs at crystallinities around the transition between suspended flow and a solid state.

Tertiary texture: A texture formed entirely by the recrystallisation of a low porosity mush, through compaction or equilibration processes.

In this context, Holness et al. (2017a) use the term recrystallisation to refer to the formation of new crystals through grain boundary generation and migration (e.g. Doherty et al., 1997).

Using these more detailed criteria, the following evidence suggests that the crystal textures are not secondary in nature. Firstly, the crystals show no shape preferred orientation (Figure 5.15) (in early or later forming crystals) that would attest to mechanical rearrangement (e.g. Paterson et al., 1998; Holness et al., 2019; Mock et al., 2021). The spatial distribution pattern analysis, reported in Section 5.4, suggests that all of the samples are poorly sorted, with a clustered packing trend. Conversely, in samples reworked by mechanical processes, the SDP plots toward an ordered framework with greater degrees of sorting (Jerram et al., 2003). Crystal-crystal boundaries are ubiquitously irregular, with small pockets of glass between touching crystals (e.g. Figure 4.19, Figure 6.11). A similar texture was identified by Holness et al. (2007d), attributed to in-situ growth and impingement within a static environment. Finally, the wide range of crystal sizes expressed in the CSDs is consistent with a static regime, because mechanical reworking of crystals commonly results in a uni-modal grain size as a consequence of hydrodynamic sorting (e.g. Holness et al., 2019). The curvatures expressed by the CSDs are not considered to reflect mechanical rearrangement because it is commonly only the largest size bin that breaks the CSD slope. This is atypical of CSDs produced through gravitational or hydrodynamic rearrangement (e.g. Marsh, 1998; Higgins, 2002).

The crystal textures also do not suggest that compaction or equilibration have caused recrystallisation to form tertiary textures within the samples. Evidence that these samples have not been affected significantly by compaction processes include an absence of any shape preferred orientation (Figure 5.15) (e.g. Miranda et al., 2016; Holness et al., 2017a; Yao et al., 2019), unimodal crystal size distribution (figure 5.14) (e.g. Satsukawa et al., 2013; Vukmanovic and Holness, 2018), lack of intra-crystalline deformation features (e.g. Holness et al., 2017a) and a clustered packing trend characterised by very low R values (Figure 5.16) (Jerram

et al., 1996). There are limited examples of recrystallisation occurring in the study samples within glass-bearing, serrated grain boundaries that could be considered as evidence for some degree of deformation (Figure 4.19) (e.g. Bollinger et al., 2018; Yao et al., 2019; Fazio et al., 2020). However, serrated grain boundaries may also occur in response to open-system processes (e.g. Holness et al., 2011) which, considering the strong textural evidence for repeated melt influx and absence of any other compaction textures, is considered a better explanation for these boundary morphologies. Evidence negating that they have experienced recrystallisation through equilibration is visible in the acutely angled interstices between impinging clinopyroxenes; the corners of the pore spaces are not rounded, and the pores maintain a straight sided morphology (Figure 4.18). Together, this suggests that crystallisation processes, rather than equilibration processes, were significant up until the sample was quenched and crystallisation ceased. It is possible that earlier textures may have been subject to some textural equilibration (e.g. Higgins and Roberge, 2003), however the chadocrysts that are interpreted to represent the earliest texture do not yield a CSD slope consistent with a texturally equilibrated crystal population.

Together, the textural evidence leads to the conclusion that the xenoliths yield primary crystal textures. This means that the distribution of melt and crystals in these samples can be considered to record the spatial and textural relationship between the solid and melt phases, without any overprinting by sub-solidus textural readjustment. This is significant because the fully solidified record provided in plutonic rocks is frequently overprinted by significant textural readjustments that misrepresent the true melt geometries. Two notable exceptions to this are the jigsaw fit boundaries identified in sample M8 (Figure 7.1), and the glass-free fractures traversing samples M8 and M6 (Figures 6.12 and 6.13), all formed as

decompression features. Otherwise, these samples provide an example of mush material that was abruptly solidified at a point where the melt was able to migrate through the pore spaces. Significantly, thermomechanical models indicate that the optimal crystallinity for melt extraction occurs in the range of 50-70 vol% crystals (Bachmann and Bergantz, 2004; Dufek and Bachmann, 2010; Gelmen et al., 2014). Although the average crystallinity of these samples is around 80 vol%, the CT data reveals that the melt fraction is highly connected (15.24-26.07% connected porosity) and therefore able to permeate through the samples (Section 6.2, Figure 6.3). Therefore, they provide a valuable contribution towards understanding where and how melt is able to move through crystal mushes.

Although the aforementioned textural criteria classifies the sample textures as primary, the interpretations discussed above suggest that open system processes including the entrainment of antecrysts and dissolution of early textures have together contributed to the curvature that characterises these CSDs. This implies that the CSDs provide a record of several nucleation and growth events, which manifest in a complex textural sequence. Crystals that have undergone at least one cycle of dissolution and overgrowth yield time breaks at the boundary between the resorption surface and overgrowth rim (e.g. Cashman, 2020). Therefore, these crystals cannot be used to determine a realistic residence time or growth rate from the CSD (e.g. Cashman, 2020). This in turn limits the kinetic information that can be derived from the CSD. Additionally, conventional CSD theory suggests the largest crystals in a CSD should be the oldest because they must have nucleated first and grown for the longest time (Eberl et al., 2002). The chadocryst textures preserved here challenge this, because they record the earliest clinopyroxene textures but do not contribute the largest crystals. Therefore, although the crystals constitute a

primary texture, the kinetic information that can be derived from this texture is still in part limited by open system dynamics.

7.3 What do the crystal textures reveal about the magmatic environment in which they formed?

The textures recorded within these xenoliths provide evidence for open system processes such as disequilibrium (recorded in resorption textures), the inclusion of crystal cargos (evidenced from higher pressure antecrysts) and percolating reactive melts (indicated by the textural affinity between resorbed chadocrysts and oikocryst amphibole) (Figure 7.10). Percolating melts are inferred to be relatively hydrous (facilitating the crystallisation of hornblende at the expense of earlier forming clinopyroxene) and relatively primitive in nature (resulting in reverse zoning trends and rims with higher Mg#s than cores). They could represent accumulated melts percolating upwards through the mush (e.g. Khazan, 2010; Petford et al., 2020), or recharge melts added into the system (e.g. Sliwinski et al., 2017; Sato et al., 2017; Nebel et al., 2020). Determining the origin of these melts would require a more complete picture of the wider system, and detailed geochemical analyses that are beyond the textural scope of this study. The latter is particularly significant because recharges of hotter melt can thermally sustain the magmatic system, with implications for the longevity of eruptive potential (e.g. Wilcock et al., 2012).

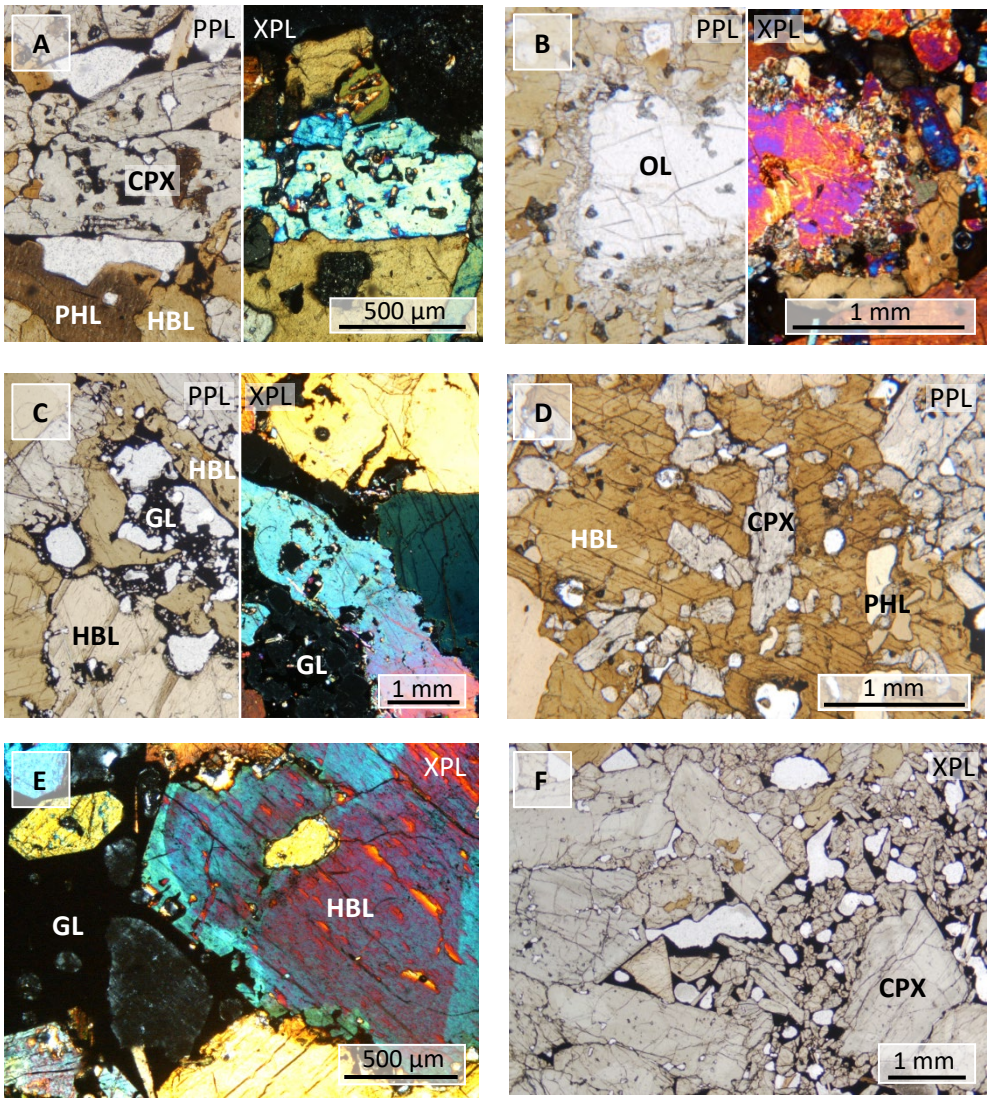

Figure 7.10 **–** Photomicrographs demonstrating textural evidence for an open system, taken in plane and cross polarised light. **A)** Sieve texture in a clinopyroxene crystal, partly enclosed by a hornblende oikocryst. **B)** Olivine crystal mantled by a reaction corona of clinopyroxene and phlogopite. Because these crystals are so few in number they were not analysed in detail within this study, but are inferred to represent exogenous crystals included within the assemblage. **C)** Strongly resorbed hornblende crystal in contact with glass. **D)** Anhedral chadocrysts enclosed in hornblende. **E)** Hornblende crystal with rounded core and irregular overgrowth in contact with glass. **F)** Region of glass occupied almost entirely by small clinopyroxene crystals, indicative of enhanced nucleation.

Estimates of crystallisation depth derived from Al-in clinopyroxene suggest that these samples crystallised at lower-crust to upper-mantle pressures (Figure 7.7). The absence of plagioclase in any of these samples further supports a high pressure origin (e.g. Green and Hibberson, 1970). Considering the wider magmatic setting of the West Eifel, where alkaline magmas are interpreted to be transported within a network of dyke-like conduits that traverse the lithosphere (e.g. Duda and Schmincke, 1985), it is plausible that these xenoliths represent fragments of mush crystallised within these conduits. An alternative scenario is that the xenoliths crystallised within a deep melt reservoir. However, an absence of textural features diagnostic of a liquid-rich reservoir (e.g. lack of deformation or gravitational sorting (Holness et al., 2019)) makes the conduit setting more reasonable. In this case, reactive percolating melts may be related to those responsible for the formation of metasomatic veins in the Eifel mantle (e.g. Shaw et al., 2018).

7.4 What is the physical relationship between the crystal and melt phases within the xenoliths?

The study samples examined here are considered to be suitable for the evaluation of melt distribution within an incompletely solidified crystal mush for the following reasons:

1. The textural evidence does not suggest that the samples were sufficiently impacted by sub-solidus recrystallisation.
2. The textures indicate that crystallisation was occurring up until the point of quenching and eruption, indicating interaction between the melt and crystal phases up until this point.

3. The melt fraction recorded within the xenoliths is well-connected, and therefore records the mush at a point when the melt was potentially extractable.

The samples in this study therefore provide a valuable opportunity to investigate melt distribution within a partially solidified crystal mush, contributing towards the understanding of where and how melt migrates through a mush system.

7.4.1 Melt migration

The migration of melt through a crystal mush occurs on a spectrum between two end-member models: porous flow and channelised flow. Porous flow occurs along grain boundaries in densely packed regions and is widely recognised as a mechanism for redistributing incompatible elements and facilitating the dissolution and recrystallisation of secondary mineral phases (e.g. Lissenberg and Dick, 2008; Renna and Tribuzio, 2011; Hayes et al., 2015a; 2015b; Lissenberg and MacLeod, 2016). Examples of porous flow through crystal mushes are widely documented within the literature, but largely maintain a geochemical focus (e.g. Lissenberg and MacLeod, 2016; Sanfilippo et al., 2020). Where textures are explored within such studies, they are mainly analysed from the crystal perspective of providing additional evidence for reactive porous flow, rather than for constraining the geometries of the melt phase itself (e.g. Sanfilippo and Tribuzio, 2013; Lissenberg and MacLeod, 2016; Leuthold et al., 2018; Lissenberg et al., 2019). On the other end of the spectrum, channelised flow is caused by the flow of accumulated pore melt within focused channels (Sleep, 1974), and may be responsible for the more rapid and direct transfer of melts through the crystal mush (e.g. Hepworth et al., 2018).

The main observation that can be made about the porosity distribution within these samples is how heterogeneously it is distributed within a relatively small volume (Figure 6.8). Fine films follow grain boundaries (e.g. Figure 6.14), forming interconnected networks that attest to porous flow. Within the same sample, high porosity regions occupy the angular pore spaces between impinged crystals (Figure 6.18), manifesting in concentrated melt pathways that are more akin to channelised flow structures. As well as connected porosity, disconnected pockets of melt decorate grain boundaries (Figure 6.11) and the cores of partially resorbed crystals (Figures 6.9 and 6.10). Together, the CT data reveals significant heterogeneity on a scale less than 1 cubic centimetre. This heterogeneity provides the opportunity to compare regions of relatively high porosity with regions of relatively low porosity, visualising where the melt may be distributed in mushes that have undergone varying degrees of solidification. On the basis of the melt geometries observed within these samples, the following interpretations can be made about the distribution of melt within the crystal mush.

7.4.2 Melt-bearing grain boundaries

Firstly, the widespread occurrence of melt along grain boundaries significantly contributes to the overall connectivity of the melt network. From melting experiments and computational modelling, the critical melt fraction at which a mafic mush forms a connected network is estimated to be around 2 vol% melt (e.g. Faul, 1999; Solano et al., 2014). Although the total melt fraction within these samples far exceeds 2 vol% (between 14.4 and 19.63 vol%), regions of the pore network confined within grain boundaries provide an insight into the melt geometries of mushes closer to this critical threshold. Specifically, work from solidified mafic intrusions suggests that grain boundaries may yield melt even at

late stages of crystallisation (e.g. Morse and Nolan, 1984; Stripp et al., 2006; Holness et al., 2007d; Roelosfe et al., 2009; Humphreys, 2009). These studies typically adopt a geochemical approach, identifying chemical signatures that allude to the presence of a late-stage liquid (e.g. Morse and Nolan, 1984). The dataset studied here supports and visualises such grain boundary porosity, which is pervasive within all of the CT volumes and clearly constitutes a connected pathway (e.g. Figure 6.14), even through tightly packed impinging crystals. This is significant because grain boundary transport facilitates reactive melt flow, resulting in re-crystallisation and metasomatism along grain boundaries (e.g. Hayes et al., 2015a; 2015b) or promoting late-stage partial melting of the mush (e.g. Jackson et al., 2018). This in turn may play a significant role in influencing the chemistry of the melt fraction, or in rejuvenating and remobilising the crystal mush (e.g. Jackson et al., 2018; Spera and Bohrson, 2018) even at relatively low porosities.

7.4.3 Channelised porosity

From outcrop observations and numerical modelling, effective melt migration is inferred to occur within high-permeability channel-like structures within sub-volcanic mushes, at scales on the order of tens to hundreds of metres (e.g. Tait and Jaupart, 1992; Bouilhol et al., 2015). Meurer and Claeson (2002) and Meurer and Meurer (2006) identified concentrated regions of interstitial liquid within fully solidified cumulates, which Holness et al. (2007d) suggest may represent centimetre scale analogues of these channel features. These features were interpreted to have formed in the latest stages of solidification, when compaction concentrated the melt into channelised pathways.

The CT data visualises similar structures, comprised of channel-like regions of relatively large, well-connected pore spaces (e.g. Figure 6.17). Whereas Meurer and

Claeson (2002) and Meurer and Meurer (2006) rely on apatite distribution and trace element mapping to demonstrate these channels, this data contributes a three-dimensional visualisation of such porosity. However, the crystal textures do not indicate that they were significantly influenced by compaction processes, and thus it is unlikely that these channels formed in the way postulated by Meurer and Meurer (2006). Alternatively, Meurer and Cleason (2002) suggest that melt may become increasingly channelised as it is forced around impermeable regions of the mush. From the textural sequence inferred in Section 7.2.3, it is plausible that the interlocking hornblende oikocrysts may have acted as a region of low permeability, focusing the flow of melt around them. This is evidenced by the abundance of small, disconnected pore spaces (Figure 6.6) that frequently occur along grain boundaries (Figure 6.11). When such grain boundary porosity is viewed in thin section, it comprises irregular shaped cusps and pockets of glass that are akin to the impingement structures described by Holness et al., 2007d. This so-called 'impingement porosity' is interpreted to form via the occlusion of the pore spaces between growing crystals, that traps the melt within the grain boundary. The CT data in this study visualises these impingement pores (Figure 6.11), which in 3D are revealed to mostly comprise disconnected porosity. In thin section, the oikocrysts exhibit an interlocking framework, with only minor amounts of glass between grain boundaries. From the CT and thin section data it is suggested that these oikocryst-rich textures are relatively impermeable, and may have acted to focus the melt around them. Coupled with textural evidence that the oikocrysts formed at the expense of earlier forming clinopyroxene, this channelisation may have been exacerbated by these earlier crystal-melt reactions (e.g. Keleman et al., 1995; Daczko et al., 2016) (Figure 7.11).

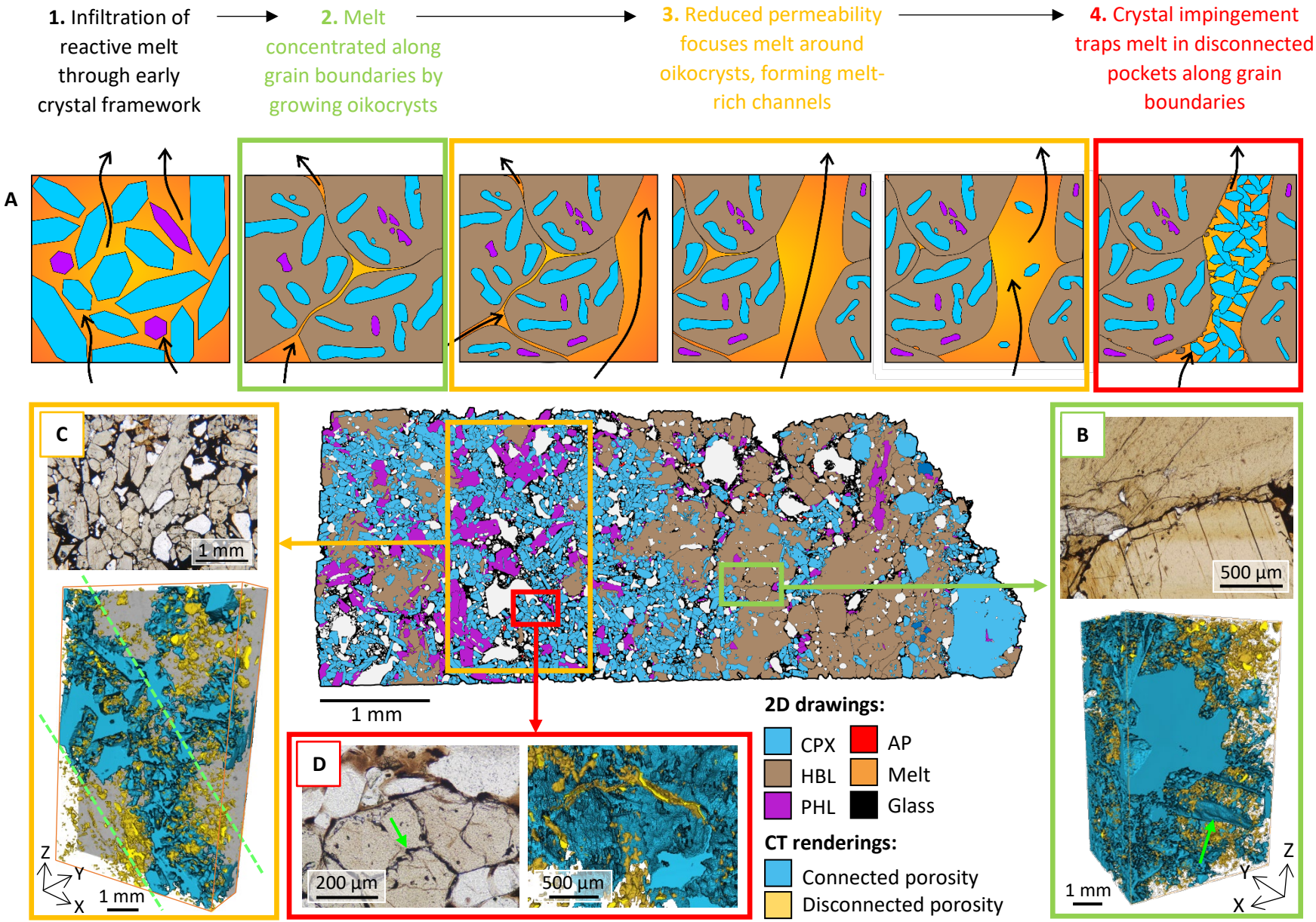

Figure 7.11 (Caption overleaf) ▶

◀ ***Figure 7.11 (Overleaf)*** **–** Model for the evolution of melt geometries, with evidence from thin section and CT scanning. Digitised thin section drawing is sample M4 B. **A)** Cartoon depicting the evolution of channelised melt flow. After the oikocryst hornblende forms, occlusion of grain boundaries concentrates melt along the grain boundary, reducing permeability (**B**). As oikocrysts further impinge on one another, they form an impermeable texture that focuses melt around the oikocrysts. Melt become increasingly channelised, forming bands of high permeability between the oikocrysts (**C**). Finally, nucleation and growth of clinopyroxenes within these channels impinge on one another, trapping melt between grain boundaries (**C**).

It is conceivable that influxes of melt, leading to mineral dissolution and crystallisation, also facilitated extended connectivity of the pore network for prolonged periods of time, retaining permeability. This presents a feedback loop where percolating melts drive chemical and textural changes to the mush that in turn enhance melt migration (e.g. Kelemen et al., 1995).

From this, the 3D melt geometries are considered to record an organised flow regime, where reactive flow processes (resulting in the early crystallisation of poikilitic amphibole) ultimately act to concentrate the melt into focused channels. The chemical consequences of reactive flow manifest in the early crystallisation of hornblende, which may affect the composition of the melt by introducing amphibole into the system earlier than through perfect fractional crystallisation. However, once these amphiboles are sufficiently impermeable to concentrate melt channelised flow structures around them, melt compositions may be largely unchanged as melt migrates rapidly through the channel (e.g. Kelemen et al., 1995). Indeed, glass compositions measured within these regions are fairly homogenous in composition, providing further evidence for high permeability and rapid melt migration.

7.4.4 Do crystal textures influence melt connectivity?

Previous studies that have aimed to study melt connectivity of crystal mushes suggest that permeability is only weakly dependent on crystal texture at porosities greater than 20 vol% melt (Cheadle et al., 2004). The results presented here demonstrate that the pore and throat geometries (measured by the mean radius), pore connectivity (measured by the coordination number) and tortuosity do not correlate with the overall volume of connected porosity (Figure 6.4). These factors are ultimately controlled by the crystal textures, which at the crystallinities recorded in these samples (73.14-85.59%) appear to agree with the results of Cheadle et al. (2004). However, these results also appear to indicate that melt connectivity is at least in part controlled by crystal textures, because interlocking oikocrysts appear to generate regions of low permeability that focus the melt into channels. Therefore, the physical relationship between the melt and crystal textures can be summarised by the heterogeneity of the melt distribution, which is ultimately governed by a feedback loop between melt percolation and textural evolution.

7.4.5 Wider significance and implications

The main implication of these findings is that melt is heterogeneously stored within crystal mushes, on a micro-scale on the order of millimetres-centimetres. Heterogeneities at this scale may manifest significantly at the larger scale, providing a challenge to those aiming to calculate the melt capacity within sub-volcanic crystal mushes (e.g. Paulatto et al., 2012; Flinders et al., 2018; Paulatto et al., 2019). For example, Paulatto et al. (2019) estimate eruptible melt fractions stored beneath the Souferière Hills Volcano to be in the range of 3-13%, depending on the melt geometry. Such uncertainties have significant implications for evaluating the

volcanic risk imposed by this system. Holness et al. (2007d) envision a textural distinction between samples in which the melt is largely concentrated along grain boundaries, and those in which melt is contained within larger interstitial pore spaces. Specifically, they suggest that highly porous mushes are formed by the impingement of fine-medium crystals, which confines the melt within planar-sided tetrahedral pores. On the other hand, low porosity mushes are formed via extensive in situ crystallisation of coarse crystals, where porosity is concentrated along grain boundaries. The samples discussed here add a level of complexity to this interpretation, because high and low porosity textures are found together within the same sample. Therefore, it is unlikely that a melt system can be defined as either one or the other, giving rise to the need to consider a more complex intermediate state. Studies aiming to model permeability within crystal mushes (e.g. Cheadle et al., 2004) may therefore benefit from incorporating these findings.

Channelised flow structures are widely reported as a process by which to rapidly extract melt from the mantle (e.g. Peč et al., 2017; Rees Jones and Katz, 2018) through channels on the scale of several centimetres to several hundreds of metres in width (Spiegelman et al., 2001). Here, the xenoliths appear to record a similar structure occurring on a millimetre scale. The recent paradigm shift towards vertically extensive mushy zones necessitates that melt is able to effectively migrate and accumulate through the mush, forming large volumes of eruptible melt (e.g. Lundstrom and Glazner, 2016). These results suggest that the mechanisms for melt accumulation may be significant down to the crystal-scale, suggesting that micro-scale melt processes may contribute towards the accumulation of eruptible melts.

In the absence of textural evidence for compaction, coupled with textural evidence for melt-crystal reaction, these samples are interpreted to provide an example of melt migration related to reactive flow processes. Because it is unknown from where in the wider magmatic system these samples originate, it is possible that influxes of melt are expelled from compaction at depth and have percolated upwards through the mushy zone that is sampled by these xenoliths. At this point, where compaction appears to have little influence on the crystal and melt textures, reactive flow mechanisms (perhaps exacerbated by changes in the melt chemistry during migration) appear to influence melt accumulation and distribution. Without wider knowledge of the magmatic system, it is challenging to constrain the relative influence of compaction and reactive flow processes in driving melt migration. Nevertheless, these xenoliths demonstrate that melt may be accumulated within regions of the mush that are not directly undergoing compaction, challenging studies that promote compaction as the main driver for melt migration.

Finally, there is widespread evidence that erupted lavas frequently contain fragments of material previously stored within a crystal mush, necessitating that crystal mushes may be reactivated and incorporated into eruptions (e.g. Holness et al., 2007d; Cooper and Reid, 2008; Salaün et al., 2010; Costa et al., 2010; Schmitt et al., 2011; Passmore et al., 2012; Neave et al., 2017). Despite this evidence, the physical mush conditions that facilitate remobilisation are relatively poorly understood (e.g. Burgisser and Bergantz, 2011; Cooper and Kent, 2014). Because these studies typically rely on chemistry to estimate the porosity of the mush prior to disaggregation (e.g. Passmore et al., 2012), the melt geometries preserved within the samples discussed here may be used to inform dynamical modelling of mush rejuvenation. Specifically, mush rejuvenation models cite the importance of melt recharge (e.g. Passmore et al., 2012; Neave et al., 2014; 2017). With textural

evidence for reactive melt influx, and melt distributions inferred to be at least in part controlled by melt-crystal reactions, it is conceivable that these samples provide a valuable snapshot of a mush that could be prone to rejuvenation.

7.5 Critical evaluation

7.5.1 Spatial context

The interpretation of the results presented within this thesis demonstrate the value of these samples in providing a textural record of crystal-melt dynamics that might otherwise be lost or modified in fully solidified plutons that are prone to sub-solidus readjustment (e.g. Higgins, 1991; McBirney and Hunter, 1995; McBirney, 2009; Glazner and Boudreau, 2011). Nevertheless, there is a trade-off between this benefit and limitations imposed by the ex-situ nature of the xenoliths. That is, unlike solidified plutons that preserve spatial information, the xenoliths have no spatial context and therefore cannot be uniquely associated with a specific position in the magmatic system.

Studies of fully solidified plutons frequently benefit from the ability to scrutinise how crystal textures vary with stratigraphic height and distance from the margin of the magmatic body (e.g. Holness et al., 2013b; Namur et al., 2013; Leuthold et al., 2014; Wilson et al., 2017; Holness et al., 2020; Latypov et al., 2020; Berthod et al., 2020; Pedersen et al., 2021). There is a clear advantage to studying magmatic textures in-situ. For example, Magee et al. (2010) utilised crystal size distributions to track the solidification history of the Lilloise intrusion, Greenland. By quantifying the evolution of the CSDs with stratigraphic height, they were able to constrain the spatial extent of post cumulus deformation and pinpoint the timing of these events relative to the arrival of each mineral phase. Holness et al. (2007a) studied changes in dihedral angle in the lower zones of the Skaergaard layered series, identifying

spatial variations in dihedral angle related to convection and cooling rates. Both of these studies necessitated analysis on a spatial scale far greater than that provided within the individual xenoliths analysed in this study. The main implication of this is that the samples analysed in this study each provide a snapshot of one particular region of the magmatic system. Without information about how the samples are positioned relative to one another, it is challenging to derive any information about the wider dynamics of the system. For example, if the samples originated fairly close to one another then it might imply that reactive flow pathways were localised in particular regions of the sub-volcanic system. If they originated from different regions of the mush then it might imply that reactive flow was a very widespread process. Answering these questions would contribute to the current uncertainties about the spatial scales of melt migration and accumulation.

Additionally, the petrogenetic model presented in Section 7.2.3 summarises the key textural features observed across each of the samples analysed in this study. However, the samples exhibit a greater degree of textural heterogeneity between one another than is outlined by this model. For example, some of the hornblende crystals in sample M2 exhibit pervasive resorption textures that are not observed within any of the other samples (Figure 4.7), and interstitial hornblende has crystallised late in the textural sequence. Whilst the model provides a summary of the textural sequence presented by the four samples, significant for constraining the petrogenetic history, there are more detailed textural variations between each xenolith that cannot be summarised in one model. This demonstrates textural heterogeneities that represent more localised magmatic processes within the system. However, without any spatial information it is challenging to constrain the scales at which the crystal and melt textures exhibit these variations.

This problem could in part be resolved if the sample size is increased beyond the four samples analysed within this study. The incredibly time consuming nature of manual textural analysis manifests in a pay off between the number of samples and the level of detail at which they can be analysed. By increasing the number of samples, there is potential to better constrain the relative positions of the samples. For example, Zieg and Marsh (2002) demonstrate that within an intrusion, the slope and intercept of a CSD will vary systematically with distance from the margin, correspondent with cooling rate (Figure 7.12). The CSDs can therefore be related to the position of the sample with respect to the margin. From this, CSDs from a suite of comagmatic samples can be used to determine their relative positions within the magmatic body. Similarly, Holness (2016) suggests that dihedral angles have the potential to constrain the size of a magmatic body from which ex-situ plutonic fragments originated. Together, these studies suggest that further analyses on a greater number of samples could potentially contribute the spatial information that is lacking from these four samples.

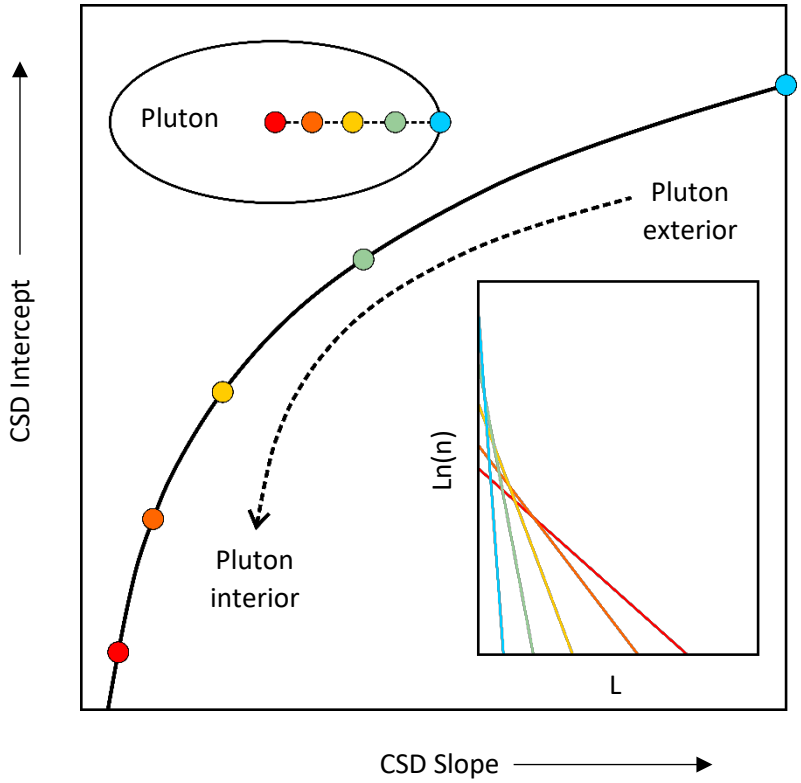

Figure 7.12 **–** Variation of CSD intercept and slope with distance from the margin of an intrusion, after Zieg and Marsh (2002). With enough samples, the intercept and slope values can be used to relate the position of individual samples with respect to the margin. Redrawn and modified from Zieg and Marsh (2002).

7.5.2 Eruption bias

In Section 7.1.3 it is acknowledged that the suite of xenoliths erupted from this centre may not be entirely representative of the wider mush system, if the crystal and melt textures were particularly conducive to survive entrainment and eruption. Although the crystal textures within these samples do not yield any evidence for compaction, it cannot be ruled out that compaction was occurring elsewhere within the system. The nature of compaction entails that the mush volume is significantly

reduced, and it is conceivable that any compacted regions of mush were not in a favourable position to be entrained and carried to the surface. This presents a challenge when trying to build a wider picture of the processes governing the migration of melt within this system. There is little that can be done to overcome this problem, but increasing the number of samples in the way described in Section 7.5.1 could identify broader trends between groups of samples that may together build a picture of variations within the system.

7.5.3 Methodological limitations

As previously acknowledged, the main limitation of the methodologies used in this study is that they are incredibly time consuming and therefore limit the number of samples that can be analysed. Otherwise, the methodology is limited by the image resolution obtained in both the 2D and 3D analysis. In the 2D analysis, this manifests in a significant proportion of crystals that fall below the recommended measurement threshold of 10 pixels. These crystals constitute a downturn in the smallest size fractions of the CSD, which is inferred to represent a measurement artefact rather than a true population trend (Figure 7.13). To overcome this limitation, slide photographs could be taken and traced at multiple resolutions, following the methodology of Gualda (2006). By combining higher and lower resolution images, they were able to measure the smallest crystals in the sample with increased accuracy at high resolution and improve uncertainties on the larger size ranges by analysing a greater area at a lower resolution. In adopting this methodology, they were able to avoid the trade off between sample area and spatial resolution. A similar approach could be adopted to improve the resolution limits of the CT data, where regions of microporosity and pore connectivity might be obscured if they are smaller than the voxel resolution. However, it would be

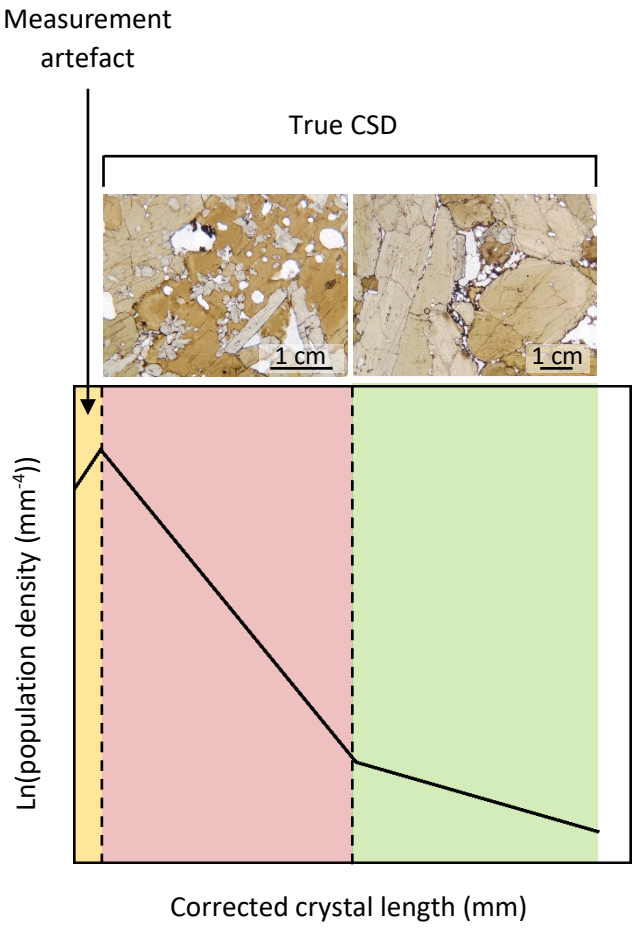

Figure 7.13 **–** Division of CSDs into log-linear sections, recognising methodological limitations. When the CSDs are divided according to breaks in slope between log-linear segments (as identified in Chapter 5), there is no magmatic process identified in the textural model that accounts for the downturn at the smallest size bin. Because these downturns contain size bins occupied by crystals smaller than ten pixels in length, they are therefore attributed to measurement artefacts. These crystals were initially included in the CSDs because as much as 8% of the total number of crystals fell under this measurement threshold. However, it is clear that the photographs were taken at an insufficient resolution to permit accurate tracing of these crystals. Therefore, future work may benefit from utilising a multi-resolution approach that would allow the smallest crystals to be traced at higher resolutions, and larger crystals to be traced at lower resolutions.

more challenging to do so because the CT core volumes are essentially taken blind. It is possible that as the core size is decreased to improve the voxel resolution, the volume is increasingly occupied by crystals rather than pore spaces.

7.6 Summary

The key findings of this discussion are summarised as follows:

- Entrainment and decompression of the xenoliths has not significantly altered their original textures, excluding limited examples of grain boundaries and fractures caused by decompression.
- The textural sequence can be identified by studying the relationship between different textures, facilitated by the presence of poikilitic hornblende.
- The crystal textures are primary in nature, recording open system magmatic processes that drive crystal dissolution, reactive crystallisation and renewed growth. High pressure antecrysts contribute to the crystal cargo, further evidencing open system behaviours. Each of these processes are recorded by the CSDs, causing them to deviate from log-linear and limiting the kinetic information that can be derived from the slope.
- Melt is heterogeneously distributed throughout the samples, at the millimetre scale. Melt is distributed on grain boundaries, visualising the late stage porosity that is inferred to be significant for late stage solidification of cumulate rocks. Crystal textures also concentrate the melt into regions of high permeability, without the need for compaction and deformation.
- Together, the melt and crystal textures provide evidence that melt migration and accumulation processes may be related in a feedback loop,

where earlier melt-crystal reactions act to enhance and maintain permeability.

- These results contribute to the current uncertainties surrounding the geometry of melt within crystal mushes, and suggest that mechanisms controlling melt distribution may be significant down to the scale of individual crystals.

Points for future work

Chapter 8 outlines ideas for future work that could compliment or enhance the findings of this study. These include adapting the methodology to answer some of the questions that could not be resolved in the scope of this project, and ideas to broaden the application of these samples beyond interpretation of this magmatic system.

8 Points for future work

The findings of this study demonstrate significant potential for future analyses of these samples, extending beyond the scope of this work. To expand upon these findings and to further utilise these samples, suggestions for future work are provided within this chapter.

8.1 Compositional CSDs

A key magmatic process affecting the CSDs in this study is the dissolution of earlier forming crystals, driven by periodic influxes of melt, which is interpreted to contribute to the curvatures recorded in the CSDs. One limitation of these CSDs is that resorption events recorded in crystal cores could be masked by later overgrowths, which would then generate a time break between the core-rim boundary. This means that individual crystals could record separate nucleation and growth histories that are obscured by producing the CSD from the crystal outline. Using this methodology, it is challenging to derive information pertaining to nucleation and growth kinetics.

A recent advancement in CSD analysis aims to combine chemical information with textural information, utilising compositional imaging techniques to pull apart growth events that are better represented as separate CSDs (e.g. Morgan et al., 2007; Cashman, 2020). For example, Cashman (2020) used compositional maps made from BSE images to separate cores and rims of plagioclase crystals in a lava sample from Mt St Helens. From this they were able to calculate separate CSDs from core and rim thicknesses, better constraining variations in growth rate that would otherwise be obscured using conventional CSD methods (Figure 8.1).

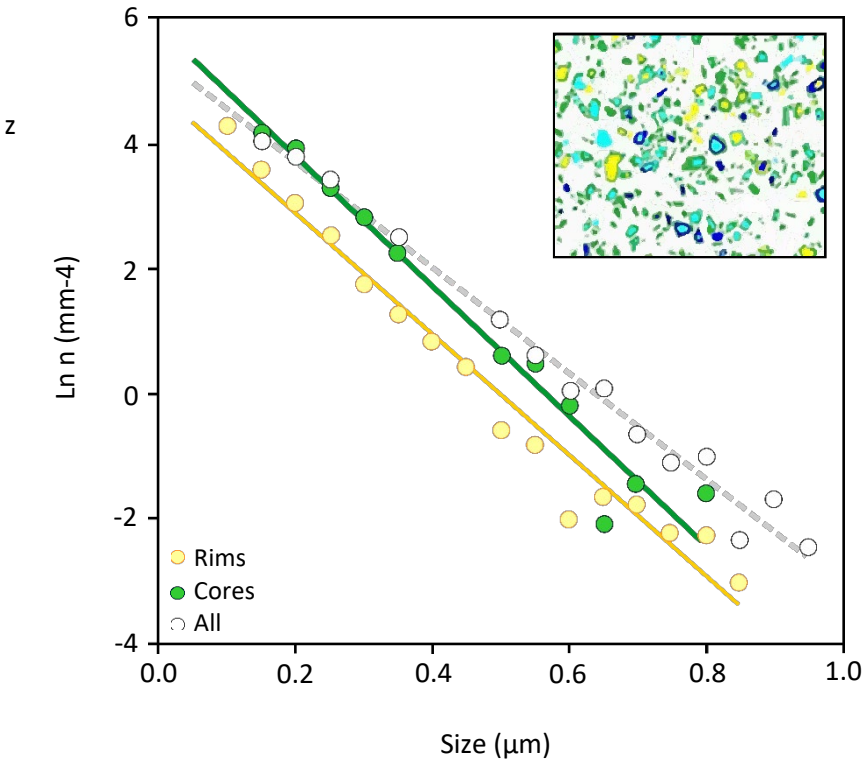

Figure 8.1 – Example of a compositional CSD of a Mount St Helens lava sample, from Cashman (2020). Using BSE maps, Cashman (2020) divided plagioclase crystals into compositionally distinct core and rim components, which each yield different growth rates and storage times from the CSD. Redrawn and modified from Cashman, 2020.

In the Eifel xenoliths, the earliest texture has been partially preserved by the growth of hornblende oikocrysts. However, because an unknown volume of crystal material was lost at this time, it is challenging to use the textures alone to specifically pinpoint the timescales associated with melt influx events. Future work on these samples may benefit from the application of compositional CSD techniques, which may act to pull apart the growth events recorded within individual crystals.

8.2 Automated techniques

The main methodological limitation of this study is the small number of samples that could be analysed. This in turn means that it is challenging to construct the architecture of the magmatic system, and constrain the spatial extent of the processes inferred to be occurring within the individual xenolith samples. In line with the methodologies required to construct compositional CSDs, future work may benefit from utilising more automated imaging techniques. At present, automated methods are largely limited to chemical mapping techniques (e.g. Neave et al., 2017; Willis et al., 2017; Hornby et al., 2019; Bell et al., 2020; Shulz et al., 2020), which require additional processing to separate touching crystals of the same mineral phase. These approaches are often considered to be less accurate than manual techniques (e.g. Bell et al., 2020; Cone et al., 2020) but enable a far greater number of samples to be analysed. Application of geochemical mapping techniques may also further compliment the textural interpretations made in this work. Alternatively, ongoing efforts to develop advanced deep-learning algorithms capable of detecting grain boundaries in thin section may provide a fast and accurate methodology in the future (e.g. Tang et al., 2020; Koh et al., 2021; Saxena et al., 2021). This remains an ongoing area of study with the potential to provide an invaluable contribution to textural analyses.

8.3 Permeability modelling

Effective models for melt migration and extraction are essential for understanding how melt is accumulated and erupted. Any model of melt extraction requires a knowledge of mush permeability, which can exert significant control on the eruptive potential and volcanic hazards (e.g. Cassidy et al., 2018). Because permeability calculations depend heavily on detailed representations of pore

geometries, knowledge of crystal mush permeability is currently poorly constrained (e.g. Bretagne et al., 2021).

Modelling of melt fraction and mush behaviour are currently undertaken on the assumption that melt filled pore spaces can be represented by simple geometric shapes (e.g. Bretagne et al., 2021). The results of this study demonstrate that the geometries and connectivity of such pores are of far greater complexity and significant heterogeneity, which may limit the utility of models that assume simple and homogenous pore spaces (e.g. Paulatto et al., 2012). Future work may benefit not only from the geometric and spatial information derived from this study, but may utilise these samples to directly model permeability (Figure 8.2). This would offer the opportunity to derive permeability measurements that overcome the need to rely on simplified crystal and melt geometries. Furthermore, undertaking permeability analyses on these samples presents the opportunity to contribute towards the definition of a percolation threshold (e.g. Vasseur et al., 2020) that defines the minimum melt fraction required to enable melt connectivity. Previous work has calculated connectivity thresholds for mafic and silicic mushes (e.g. Cheadle et al., 2004), but with reliance on simplified computational models or two-dimensional thin section analysis.

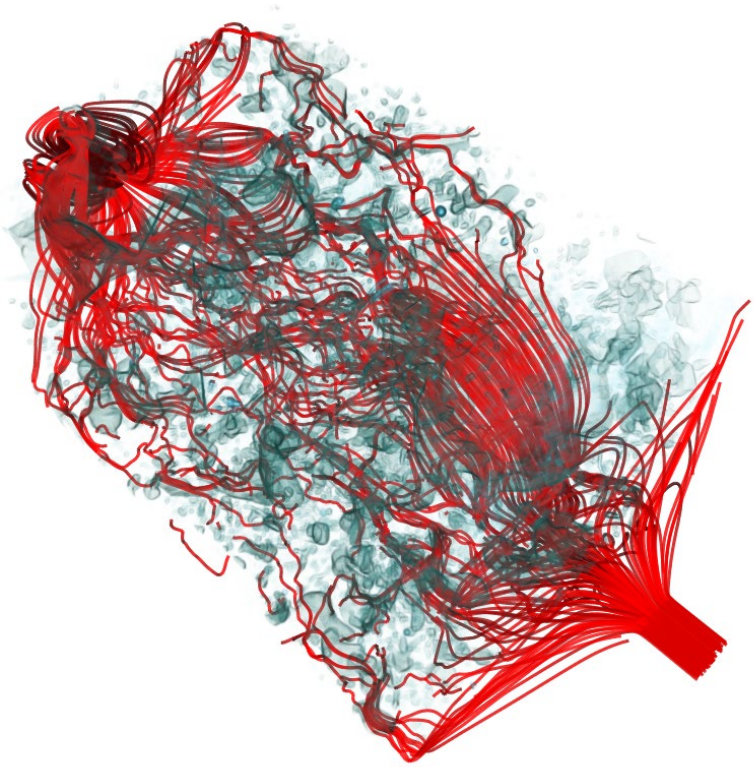

Figure 8.2 **–** Fluid velocity streamlines (red) calculated using a numerical simulation of Stokes flow, from which permeability can be calculated. An opaque representation of the surrounding solid crystal phase is shown in blue. This simulation was performed on sample M4 using the commercial software package PerGeos as a proof of concept that these samples can be used for permeability modelling.

These findings may contribute towards better understanding how mush heterogeneities on the micro-scale could manifest at the macro scale, a scale significant for evaluating eruption dynamics and volcanic hazards.

Conclusions

This chapter provides a summary of the key findings that answer each of the research aims outlined in Chapter 1.

9 Conclusions

The clinopyroxenite and hornblendite xenoliths analysed in this study are interpreted to represent samples of a crystal mush that record the petrogenetic evolution of an open magmatic system. In particular, melt infiltration driving mineral dissolution and peritectic crystallisation can be identified from qualitative and quantitative measurements of crystal textures, which acts to influence the geometry of the melt distribution at a crystal-size scale. These samples contribute a valuable example of a semi-solidified mush that was rapidly quenched upon entrainment, capturing the melt distribution of a mush derived from the lower-crust or upper-mantle. This provides a record of primary magmatic textures and melt geometries, both of which are challenging to analyse in fully solidified rocks that have experienced extensive sub-solidus recrystallisation. This is significant for bettering the current understanding of how melt is stored within crystal mushes, and how it migrates and accumulates prior to eruption. Specifically, the findings of this study demonstrate that melt geometries are heterogeneous at a micro-scale and in this instance are governed by a feedback loop where percolating melts drive textural changes to the mush that in turn enhance melt migration. These findings contribute a three-dimensional reconstruction of a crystal mush sample with a highly connected and therefore potentially extractable melt fraction.

9.1 Summary of key findings

This study aimed to investigate four research questions, using a combination of two- and three-dimensional textural techniques as a tool to quantify crystal and melt textures in four glass-bearing xenoliths collected from the West Eifel. The key findings are summarised below.

The first research question aimed to investigate the extent to which the sample textures are representative of an in-situ crystal mush. The glass preserved within the samples is interpreted to represent an in-situ melt that was quenched by rapid eruption. 'Jigsaw fit' boundaries along HBL:HBL boundaries in sample M8, as well as glass-free fractures traversing samples M6 and M8, represent decompression features. Crystallisation related to decompression manifests as microlites in the glass, which are clearly discriminable from the pre-entrainment assemblage. Therefore, the main finding of this research aim is that the entrainment and eruption of the xenoliths has not significantly modified their magmatic textures; they therefore provide a sample of in-situ, semi-solidified crystal mush.

The second research question aimed to constrain the textural petrogenesis of the xenoliths. The presence of poikilitic hornblende enclosing chadocrysts of clinopyroxene and phlogopite defined a textural sequence recording the early, intermediate and late forming textures. Most significantly, pervasive resorption textures attest to periodic melt infiltrations, driving the peritectic crystallisation of hornblende at the expense of the early mineral assemblage. There is no textural evidence of secondary or tertiary magmatic processes and the crystal-melt textures recorded in these samples are therefore interpreted to be primary in nature, preserving the geometric relationship between the solid and melt phases.

The third research question aimed to constrain the magmatic environment in which the xenoliths formed. Using the petrogenetic model and the magmatic processes identified throughout the textural sequence, the magmatic environment is interpreted as an open system characterised by the infiltration of hydrous melts. Crude estimates of crystallisation depth using Al- in clinopyroxene suggest that the xenoliths crystallised within the lower-crust or upper-mantle. Because there is no

textural evidence that suggests they formed within a liquid-rich melt reservoir, it is likely that they represent mush samples crystallised within a conduit setting, akin to the dyke-like conduits that are commonly invoked to traverse the lithosphere beneath the West Eifel.

The final research question aimed to constrain the physical relationship between the crystal and melt phases recorded within the xenoliths. Three-dimensional analysis of the melt phase demonstrated that the melt is heterogeneously distributed within the crystal network, on a microscale on the order of millimetres-centimetres. This includes melt distributed along grain boundaries that forms an interconnected network of relatively low permeability, and concentrated channel-like structures of high permeability. This is inferred to record an organised flow regime, in part controlled by the crystal textures.

Overall, this study demonstrates that glass-bearing xenoliths have significant potential to contribute to the current knowledge gap surrounding the physical relationship between melt and crystals in mush systems. Combined two- and three-dimensional textural analysis of such samples could be applied to glass-bearing xenoliths collected from volcanic centres in a variety of magmatic settings, building a more complete picture of crystal mush textures and the link to eruptive dynamics.

9.2 Significance for intraplate volcanism

The findings of this study are particularly significant because the xenolith samples provide a snapshot of a crystal mush that is directly associated with volcanic activity. At present, the so-called 'plutonic-volcanic connection' remains an ongoing challenge in volcanology (e.g. Bachmann et al., 2007; Glazner et al., 2015; Watts et al., 2016). These xenoliths contribute a sample of crystalline material from the depths of a volcanic plumbing system, providing the opportunity to examine a

crystal mush frozen at the point where the melt may either be removed and erupted at the surface, or solidify to form a pluton. It is particularly challenging to examine this connection in intraplate volcanic settings, where monogenetic volcanoes are thought to be generated by the rapid development of short-lived magma transport pathways that erupt single batches of magma (e.g. Spera, 1984; Connor et al., 2000). The textural evidence for open system processes within this magmatic setting is particularly significant because influxes of melts not only introduce mineral phases into the assemblage earlier than through fractional crystallisation, but also can thermally sustain the system for longer periods of time. Evidence for melt infiltrations throughout the crystallisation history of these samples, enhancing permeability, indicates a dynamic magmatic regime within an example of a monogenetic plumbing system. Significantly, the entrainment of mushy material inferred to be derived from a conduit-like environment indicates that transport pathways associated with monogenetic volcanism may in fact be used multiple times.

9.3 Significance of textural analysis

Finally, the findings of this study demonstrate the usefulness of textural analysis, a tool that is conventionally overlooked in favour of geochemical studies. This study shows that textural analysis can provide a valuable insight into both crystal and melt petrogenesis, generating large volumes of data at relatively low costs. Approaching these samples from a textural perspective contributes an insight into their physical parameters, including melt and crystal geometries, which are challenging to quantify using geochemistry alone.

List of references

- Anderson, J.L. and Smith, D.R. (1995) The effects of temperature and fO_2 on the Al-in-hornblende barometer, American Mineralogist, **80** (5-6): 549-559
- Aoki, K. and Shiba, I. (1964) Clinopyroxenes from alkaline rocks of Japan, American Mineralogist, **49**: 1199-1223
- Aoki, K.-I. and Kushiro, I. (1968) Some clinopyroxenes from ultramafic inclusions in Dreiser Weiher, Eifel, Contributions to Mineralogy and Petrology, **18**: 326-337
- Armienti, P. and Tarquini, S. (2002) Power law olivine crystal size distributions in lithospheric mantle xenoliths, Lithos, **65** (3-4): 273-285
- Armienti, P.; Pareschi, M.T.; Innocenti, F. and Pompilio, M. (1994) Effects of magma storage and ascent on the kinetics of crystal growth, Contributions to Mineralogy and Petrology, **115**: 402-414
- Ashchepkov, I. and André, L. (2002) Pyroxenite xenoliths in picrite basalts (Vitim Plateau): origin and differentiation of mantle melts, Russian Geology and Geophysics, **43** (4): 343-363

- Ashchepkov, I.V.; Andre, L.; Downes, H. and Belyatsly, B.A. (2011) Pyroxenites and megacrysts from Vitim picrate-basalts (Russia): polybaric fractionation of rising melts in the mantle? Journal of Asian Earth Sciences, **42** (1-2): 14-37
- Baales, M.; Joris, O.; Street, M.; Bittman, F.; Weninger, B. and Wiethold, J. (2002) Impact of the late glacial eruption of the Laacher See volcano, Central Rhineland, Germany, Quaternary Research, **58** (3): 273-288
- Bachmann, O. (2010) The petrologic evolution and pre-eruptive conditions of the rhyolitic Kos Plateau Tuff (Aegean arc), Central European Journal of Geosciences, **2** (3): 270-305
- Bachmann, O. and Bergantz, G.W. (2004) On the origin of crystal-poor rhyolites: extracted from batholithic crystal mushes, Journal of Petrology, **45** (8): 1565-1582
- Bachmann, O. and Bergantz, G.W. (2008) Rhyolites ad their source mushes across tectonic settings, Journal of Petrology, **49**: 2277-2285
- Bachmann, O. and Huber, C. (2019) The inner workings of crustal distillation columns; the physical mechanisms and rates controlling phase separation in silicic magma reservoirs, Journal of Petrology, **60** (1): 3-18
- Bachmann, O.; Miller, C.F. and de Silva, S.L. (2007) The volcanic-plutonic connection as a stage for understanding crustal magmatism, Journal of Volcanology and Geothermal Research, **167** (1-4): 1-23
- Bacon, C.R. (1986) Inclusions of mafic magma in intermediate and silicic volcanic rocks, Journal of Geophysical Research, **91**: 6091-6112
- Bahl, C.A.; Miller, C.F.; Miller, J.S. and Faulds, J.E. (2001) Construction of a pluton: evidence from an exposed cross section of the Searchlight pluton, Eldorado Mountains, Nevada, Geological Society of America Bulletin, **113** (9): 1213-1228
- Baker, D.R.; Polacci, M. and LaRue, A. (2011) A study on the reproducibility of counting vesicles in volcanic rocks, Geosphere, **7**: 70-78
- Baldini, J.U.L.; Brown, R.J. and Mawdsley, N. (2018) Evaluating the link between the sulphur-rich Laacher See volcanic eruption and the Younger Dryas climate anomaly, Climate of the past, **14** (7): 969-990

- Barboni, M. and Schoene, B. (2014) Short eruption window revealed by absolute crystal growth rates in a granitic magma, Nature Geosciences, **7**: 524-528
- Bardintzeff, J.M.; Deniel, C.; Guillou, H.; Platevoet, B.; Télouk, P. and Oun, K.M. (2012) Miocene to recent alkaline volcanism between Al Haruj and Waw an Namous (southern Libya) International Journal of Earth Sciences, **101**: 1047-1063
- Barnes, S.J.; Latypov, R.; Chistyakova, S.; Godel, B. and Schoneveld, L.E. (2021) Idiomorphic oikocrysts of clinopyroxene produced by a peritectic reaction within a solidification front of the Bushveld Complex, Contributions to Mineralogy and Petrology, **176**: 5
- Barnes, S.J.; Mole. D.R.; Le Vaillant, M.; Campbell, M.J.; Verrall, M.R.; Roberts, M.P. and Evans, N.J. (2016) Poikilitic textures, heteradcumulates and zoned orthopyroxenes in the Ntaka ultramafic complex, Tanzania: implications for crystallization mechanisms of oikocrysts, Journal of Petrology, **57** (6): 1171-1198
- Barros, R.; Defourny, A.; Collignon, A.; Jobe, P.; Dassargues, A.; Piessens, K. and Welkenhuysen, K. (2021) A review of the geology and origin of CO2 in mineral water springs in east Belgium, Geologica Belgica, **24** (1-2): 17-31
- Bartley, J.M.; Glazner, A.F. and Coleman, D.S. (2018) Dike intrusion and deformation during growth of the half dome pluton, Yosemite National Park, California, Geosphere, **14** (3): 1283-1297
- Bartley, J.M.; Glazner, A.F.; Stearns, M.A. and Coleman, D.S. (2020) The granite aqueduct and autometamorphism of plutons, Geosciences, **10** (4): 136
- Bea, F. (2010) Crystallization dynamics of granite magma chambers in the absence of regional stress: Multiphysics modelling with natural examples, Journal of Petrology, **51** (7): 1541-1569
- Beard, J.S.; Ragland, P.C. and Rushmer, T. (2004) Hydration crystallization reactions between anhydrous minerals and hydrous melt to yield amphibole and biotite in igneous rocks: description and implications, The Journal of Geology, **112** (5): 617-621

- Becker, H.J. (1977) Pyroxenites and hornblendites from the maar-type volcanoes of the West Eifel, Federal Republic of Germany, Contributions to Mineralogy and Petrology, **65**: 45-52
- Bédard, J. (2015) Ophiolitic magma chamber processes, a perspective from the Canadian Appalachians, In: Charlier, B.; Namur, O.; Latypov, R. and Tegner, C. (eds) Layered Intrusions, Springer Geology, Springer, Dordrecht: 693-732
- Bell, S.K.; Joy, K.H.; Pernet-Fisher, J.F. and Hartley, M.E. (2020) QEMSCAN as a method of semi-automated crystal size distribution analysis: Insights from Apollo 15 Mare basalts, Journal of Petrology, **61** (4): egaa047
- Berberich, G.M.; Berberich, M.B.; Ellison, A.M. and Wöhler, C. (2019) First identification of periodic degassing rhythms in three mineral springs of the East Eifel Volcanic Field (EEVF, Germany), Geosciences, **9** (4)
- Berger, J.; Lo, K.; Diot, H.; Triantafyllou, A.; Plissart, G. and Femenias, O. (2017) Deformation-driven differentiation during in-situ crystallization of the 2.7 Ga Iguilid Mafic intrusion (West African Craton, Mauritania), Journal of Petrology, **58** (4): 819-840
- Berthod, C.; Michon, L.; Famin, V.; Welsch, B.; Bachelery, P. and Bascou, J. (2020) Layered gabbros and peridotites from Piton des Neiges volcano, La Reunion Island, Journal of Volcanology and Geothermal Research, **405** (1): 107039
- Best, M.G. (1975) Amphibole-bearing cumulate inclusions, Grand Canyon, Arizona and their bearing on silica-undersaturated hydrous magmas in the upper mantle, Journal of Petrology, **16** (1): 212-236
- Blake, S. and Fink, J.H. (2000) On the deformation and freezing of enclaves during magma mixing, Journal of Volcanology and Geothermal Research, **95**: 1-8
- Blatter, D.L.; Sisson, T.W. and Hankins, W.B. (2017) Voluminous arc dacites as amphibole reaction-boundary liquids, Contributions to Mineralogy and Petrology, **172**: 27
- Blong, R.J.; Riede, F. and Chen, Q. (2018) A fuzzy logic methodology for assessing the resilience of past communities to tephra fall: a Laacher See eruption 13,000 year BP case, Volcanica, **1** (1): 63-84

- Blundy, J.D. and Holland, T.J.B. (1990) Calcic amphibole equilibria and a new amphibole-plagioclase geothermometer, Contributions to Mineralogy and Petrology, **104**: 208-224
- Bodinier, J.-L.; Fabriès, J.; Lorand, J. –P.; Dostal, J. and Dupuy, C. (1987) Petrogenesis of amphibole pyroxenite veins from the Lherz and Freychinede ultramafic bodies (Ariège French Pyrenees), Bulletin de Minéralogie, **110**: 345-358
- Bodinier, J.-L.; Menzies, M.A.; Shimizu, N.; Frey, F.A. and McPherson, A. (2004) Silicate, hydrous and carbonate metasomatism at Lherz, France: contemporaneous derivatives of silicate melt-harzburgite reaction, Journal of Petrology, **45**: 299-320
- Bogaard, P.J.F. and Wörner, G. (2003) Petrogenesis of basanitic to tholeiitic volcanic rocks from the Miocene Vogelsberg, Central Germany, Journal of Petrology, **44** (3): 569-602
- Bollinger, C.; Nzogang, B.C.; Mussi, A.; Bouquerel, J.; Molodov, D.A. and Cordier, P. (2018) Microstructural evidence for grain boundary migration and dynamic recrystallization in experimentally deformed forsterite aggregates, Minerals, **9** (1): 17
- Boorman, S.; Boudreau, A. and Kruger, F.J. (2004) The lower zone-critical zone transition of the Bushveld complex: A quantitative textural study, Journal of Petrology, **45** (6): 1209-1235
- Bottazzi, P.; Tiepolo, M.; Vannucci, R.; Zanetti, A.; Brumm, R.; Foley, S.R. and Oberti, R. (1999) Distinct site preferences for heavy and light REE in amphibole and the prediction of $^{Amph/L}D_{REE}$, Contributions to Mineralogy and Petrology, **137**: 36-45
- Bouilhol, P.; Schmidt, M.W. and Burg, J.P. (2015) Magma transfer and evolution in channels within the arc crust: the pyroxenitic feeder pipes of Sapat (Kohistan, Pakistan), Journal of Petrology, **56** (7): 1309-1342
- Brandeis, G.; Jaupart, C. and Allegre, C.J. (1984) Nucleation, crystal-growth and the thermal regime of cooling magmas, Journal of Geophysical Research, **89** (12): 161-177
- Bräuer, A.; Andres, C.; Günter, C.; Litt, T.; Stebich, M. and Negendank, J.F.W. (1999) High resolution sediment and vegetation response to the Younger

Dryas climate change in varved lake sediments from Meerfelder Maar, Germany, Quaternary Science Reviews, **18**: 321-329

- Bräuer, A.; Endres, C.; Zolitschka, B. and Negendank, J.F.W. (2000) AMS radio-carbon and varve chronology from the annually laminated sediment record of Lake Meerfelder Maar, Germany, Radiocarbon, **42**: 355-368
- Bräuer, K.; Kampf, H.; Niedermann, S. and Strauch, G. (2013) Indications for the existence of different magmatic reservoirs beneath the Eifel area (Germany): A multi-isotope (C, N, He, Ne, Ar) approach, Chemical Geology, **356**: 193-208
- Bretagne, E.; Wadsworth, F.B.; Dobson, K.J.; Vasseur, J. and Coumans, J.P. (2021) The permeability of magma mush assembled from anisotropic tabular crystals, EGU General Assembly 2021, Abstract #16010
- Brown, M. (2013) Granite: From genesis to emplacement, Geological Society of America Bulletin, **125** (7-8): 1079-1113
- Bryant, J.A.; Yogodzinski, G.M. and Churikova, T.G. (2007) Melt-mantle interactions beneath the Kamchatka arc: evidence from ultramafic xenoliths from Shiveluch volcano, Geochemsitry Geophysics Geosystems, **8** (4)
- Bryon, D.N.; Atherton, M.P. and Hunter, R.H. (1995) The interpretation of granitic textures from serial thin sectioning, image-analysis and 3-dimensional reconstruction, Mineralogical magazine, **59** (395): 203-211
- Büchel, G. (1994) Vulkanologische Karte der West- und Hocheifel 1:50,000, Koblenz. (Hrsg) Landesvermessungsamt, Rheinland-Pfalz
- Büchel, G. and Mertes, H. (1982) Die Eruptionszentrum des Westeifeler Vulkanfeldes, Zeitschrift der Deutschen Geologischen Gesellschaft, **133**: 409-429
- Büchner, J.; Tietz, O.; Viereck, L.; Suhr, P. and Abratis, M. (2015) Volcanology, geochemistry and age of the Lausitz Volcanic Field, International Journal of Earth Sciences, **104**: 2057-2083
- Budweg, M.; Bock, G. and Weber, M. (2006) The Eifel plume – imaged with converted seismic waves, Geophysical Journal International, **166** (2): 579-589
- Buikin, A.; Trieloff, M.; Hopp, J.; Althaus, T.; Korochantseva, E.; Schwarz, W.H. and Altherr, R. (2005) Noble gas isotopes suggest deep mantle plume

source of late Cenozoic mafic alkaline volcanism in Europe, Earth and Planetary Science Letters, **230** (1-2): 143-162

- Burgisser, A. and Bergantz, G.W. (2011) A rapid mechanism to remobilize and homogenize highly crystalline magma bodies, Nature, **471** (7337): 212
- Burton-Johnson, A.; Macpherson, C.G.; Muraszko, J.R.; Harrison, R.J. and Jordan, T.A. (2019) Tectonic strain recorded by magnetic fabrics (AMS) in plutons, including Mt Kinabalu, Borneo: A tool to explore past tectonic regimes and syn-magmatic deformation, Journal of Structural Geology, **119**: 50-60
- Cabane, H.; Laporte, D. and Provost, A. (2001) Experimental investigation of the kinetics of Ostwald ripening of quartz in silicic melts, Contributions to Mineralogy and Petrology, **142** (3): 361-373
- Cabane, H.; Laporte, D. and Provost, A. (2005) An experimental study of Ostwald ripening of olivine and plagioclase in silicate melts: Implications for the growth and size of crystals in magmas, Contributions to Mineralogy and Petrology, **150** (1): 37-53
- Candela, P.A. (1991) Physics of aqueous phase evolution in plutonic environments, American Mineralogist, **76**: 1081-1091
- Carbotte, S.M.; Arnulf, A.; Spiegelman, M.; Lee, M.; Harding, A.; Kent, G.; Canales, J.P. and Nedimovic, M. (2020) Stacked sills forming a deep melt-mush feeder conduit beneath Axial Seamount, Geology, **48** (7): 693-697
- Cashman, K. and Blundy, J. (2013) Petrological cannibalism: the chemical and textural consequences of incremental magma body growth, Contributions to Mineralogy and Petrology, **166**: 703-729
- Cashman, K.V. (1993) Relationship between plagioclase crystallization and cooling rate in basaltic melts, Contributions to Mineralogy and Petrology, **113**: 126-142
- Cashman, K.V. (2020) Crystal size distribution (CSD) analysis of volcanic samples: advances and challenges, Frontiers in Earth Sciences, **8**: 291
- Cashman, K.V. and Giordano, G. (2014) Calderas and magma reservoirs, Journal of Volcanology and Geothermal Research, **288**: 28-45
- Cashman, K.V. and Marsh, B.D. (1988) Crystal size distribution (CSD) in rocks and the kinetics and dynamics of crystallization II: Makaopuhi lava lake, Contributions to Mineralogy and Petrology, **99**: 292-305

- Cashman, K.V.; Sparks, R.S.J. and Blundy, J. (2017) Vertically extensive and unstable crystal mushes: a unifying view of igneous processes associated with volcanoes, Science, **355** (6331)
- Cassidy, M.; Manga, M.; Cashman, K. and Bachmann, O. (2018) Controls on explosive-effusive volcanic eruption styles, Nature Communications, **9**: 2839
- Castro, J.; Manga, M. and Cashman, K. (2002) Dynamics of obsidian flows inferred from microstructures: insights from microlite preferred orientations, Earth and Planetary Science Letters, **199** (1-2): 211-226
- Castro, J.M., Cashman, K.V. and Manga M. (2003) A technique for measuring 3D crystal-size distributions of prismatic microlites in obsidian, American Mineralogist, **88** (8-9): 1230-1240
- Castro, J.M.; Schipper, C.I.; Mueller, S.P.; Militzer, A.S.; Amigo, A.; Parajes, C.S. and Jacob, D. (2013) Storage and eruption of near-liquidus rhyolite magma at Cordon Caulle, Chile, Bulletin of Volcanology, **75** (702): 1-17
- Cawthorn, R.G. and Walraven, F. (1998) Emplacement and crystallization time for the Bushveld Complex, Journal of Petrology, **39** (9): 1669-1687
- Chandrasekharam, D. and Vinod, K.C. (2000) Clinopyroxenite xenoliths from the Deccan trap lavas of Kutch and Mumbai, Current Science, **78** (5): 607-610
- Chang, M.J.; Feeley, T.C. and Deraps, M.R. (2009) Petrogenesis of basaltic volcanic rocks from the Pribilof Islands, Alaska, by melting of metasomatically enriched depleted lithosphere, crystallization differentiation, and magma mixing, Journal of Petrology, **50** (12): 2249-2286
- Chazot, G.; Menzies, M. and Harte, B. (1996) Determination of partition coefficients between apatite, clinopyroxene, amphibole, and melt in natural spinel peridotites from Yemen: implications for wet melting of the lithospheric mantle, Geochimica et Cosmochimica Acta, **60** (3): 423-437
- Cheadle, M.J. and Gee, J.S. (2017) Quantitative textural insights into the formation of gabbro in mafic intrusions, Elements, **13** (6): 409-414
- Cheadle, M.J.; Elliott, M.T. and McKenzie, D. (2004) Percolation threshold and permeability of crystallizing igneous rocks: the importance of textural equilibrium, Geology, **32** (9): 757-760

- Chen, X.M.; Chen, L.H. and Xu, X.S. (2009) Study on the genesis of clinopyroxene megacrysts in the Cenozoic alkali basalt at Changle, Shadong Province, Acta Petrologica Sinica, **25** (5): 1105-1116
- Chin, E.J. (2018) Deep crustal cumulates reflect patterns of continental rift volcanism beneath Tanzania, Contributions to Mineralogy and Petrology, **173** (10)
- Choi, S.H. and Kim, N.K. (2012) Petrogenesis of anhydrous clinopyroxenite xenoliths and clinopyroxene megacrysts in alkali basalts from the Ganseong area of South Korea, Island Arc, **21** (2): 101-117
- Christopher, T.E.; Blundy, J.; Cashman, K.; Cole, P.; Edmonds, M.; Smith, P.J.; Sparks, R.S.J. and Stinton, A. (2015) Crustal-scale degassing due to magma system destabilization and magma-gas decoupling at Soufrière Hills Volcano, Montserrat, Geochemistry Geophysics Geosystems, **16** (9): 2797-2811
- Clark, P.J. and Evans, F.C. (1954) Distance to nearest neighbour as a measure of spatial relationships in populations, Ecology, **35**, (4): 445-453
- Coleman, D.S.; Bartley, J.M.; Glazner, A.F. and Pardue, M.J. (2012) Is chemical zonation in plutonic rocks driven by changes in source magma composition or shallow-crustal differentiation? Geosphere, **8**: 1568-1587
- Coleman, D.S.; Gray, W. and Glazner, A.F. (2004) Rethinking the emplacement and evolution of zoned plutons: Geochronologic evidence for incremental assembly of the Tuolumne Intrusive Suite, California, Geology, **32** (5): 433-436
- Coltorti, M.; Beccaluva, L.; Bonadiman, C.; Faccini, B.; Ntaflos, T. and Siena, F. (2004) Amphibole genesis via metasomatic reaction with clinopyroxene in mantle xenoliths from Victoria Land, Antarctica, Lithos, **75** (1): 115-139
- Comeau, M.J.; Unsworth, M.J.; Ticona, F. and Sunagua, M. (2015) Magnetotelluric images of magma distribution beneath Volcan Uturuncu, Bolivia: Implications for magma dynamics, Geology, **43** (3): 243-246
- Cone, K.A.; Wendlandt, R.F.; Pfaff,K. and Orlandini, O.F. (2020) Texture constraints on crystal size distribution methodology: An application to the Laki fissure eruption, American Mineralogist, **105** (5): 585-598
- Connor, C.B.; Stamatakos, J.A. and Ferrill, D.A. (2000) Geological factors controlling patterns of small-volume basaltic volcanisms: application to a

volcanic hazards assessment at Yucca Mountain, Journal of Geophysical Research, **105**: 417-432

- Coogan, L.A.; Saunders, A.D.; Kemptn, P.D. and Norry, M.J. (2000) Evidence from oceanic gabbros for porous melt migration within a crystal mush beneath the Mid-Atlantic ridge, Geochemistry, Geophysics, Geosystems, **1** (9)
- Coombs, M.L.; Eichelberger, J.C. and Rutherford, M.J. (2002) Experimental and textural constraints on mafic nodule formation in volcanic rocks, Journal of Volcanology and Geothermal Research, **119**: 125-144
- Cooper, G.F.; Blundy, J.D.; Macpherson, C.G.; Humphreys, M.C.S and Davidson, J.P. (2019) Evidence from plutonic xenoliths for magma differentiation, mixing and storage in a volatile-rich crystal mush beneath St. Eustatius, Lesser Antilles, Contributions to Mineralogy and Petrology, **174** (5)
- Cooper, G.F.; Davidson, J.P. and Blundy, J.D. (2016) Plutonic xenoliths from Martinique, Lesser Antilles: evidence for open system processes and reactive melt flow in island arc crust, Contributions to Mineralogy and Petrology, **171** (87)
- Cooper, K.M. and Kent, A.J.R. (2014) Rapid remobilization of magmatic crystals kept in cold storage, Nature, **506** (7489): 480
- Cooper, K.M. and Reid, M.R. (2008) Uranium-series crystal ages, Reviews in Mineralogy and Geochemistry, **69**: 479-544
- Costa, F.; Coogan, L.A. and Chakraborty, S. (2010) The timescales of magma mixing and mingling involving primitive melts and melt-mush interaction at mid-ocean ridges, Contributions to Mineralogy and Petrology, 159 (3): 371-387
- Crisp, J.; Cashman, K.V.; Bonini, J.A.; Hougen, S.B. and Pieri, D.C. (1994) Crystallization history of the 1984 Mauna Loa lava flow, Journal of Geophysical Research – Solid Earth, **99** (B4): 7177-7198
- Daczko, N.R.; Piazolo, S.; Meek, U.; Stuart, C.A. and Elliott, V. (2016) Hornblendite delineates zones of mass transfer through the lower crust, Scientific Reports, **6**: 31369
- Dahm, T.; Stiller, M.; Mechie, J.; Heimann, S.; Hensch, M.; Woith, H.; Schmidt, B.; Gabriel, G. and Weber, M. (2020) Seismological and

geophysical signatures of the deep crustal magma systems of the Cenozoic volcanic fields beneath the Eifel, Germany, Geochemistry, Geophysics, Geosystems, **21** (9)

- Davidson, J.; Turner, S.; Handley, H.; MacPherson, C. and Dosseto, A. (2007) Amphibole ''sponge'' in arc crust? Geology, **35** (9): 787-790
- Dawson, J.B. (2002) Metasomatism and partial melting in upper-mantle peridotite xenoliths from the Lashaine volcano, northern Tanzania, Journal of Petrology, **43**: 1749-1777
- Dawson, J.B. (2009) The Neogene-Recent volcanic rocks, The Gregory Rift Valley and Neogene-Recent volcanoes of Northern Tanzania, Geological Society of London Memoirs, **33** (1): Chapter 7
- Day, J.M.D. and Taylor, L.A. (2007) On the structure of mare basalt lava flows from textural analysis of the LaPaz Icefield and Northwest Africa 032 lunar meteorites, Meteoritics & Planetary Sciences, **42** (1): 3-17
- Debari, S.; Mahlburg Kay, S. and Kay, R.W. (1987) Ultramafic xenoliths from Adagdak Volcano, Adak, Aleutian Islands, Alaska, deformed igneous cumulates from the Moho of an island arc, The Journal of Geology, **95** (3): 329-341
- Deering, C.D.; Bachmann, O.; Dufek, J. and Gravley, D.M. (2011) Rift-related transition from andesite to rhyolite volcanism in the Taupo volcanic zone (New Zealand) controlled by crystal-melt dynamics in mush zones with variable mineral assemblages, Journal of Petrology, **52**: 2243-2263
- Del Gaudio, P.; Mollo,, S.; Ventura, G.; Iezzi, G.; Taddeucci, J and Cavallo, A. (2010) Cooling rate-induced differentiation in anhydrous and hydrous basalts at 500 MPa: Implications for the storage and transport of magmas in dikes, Chemical Geology, **270** (1-4): 164-178
- Dellino, P.; Mele, D.; Bonasia, R.; Braia, G.; Volpe, L.L. and Sulpizio, R. (2005) The analysis of the influence of pumice shape on its terminal velocity, Geophysical Research Letters, **32** (21)
- Dennis, C.M.M.; Demouchy, S. and Shaw, C.S. (2013) Evidence of dehydration in peridotites from Eifel volcanic field and estimates of the rate of magma ascent, Journal of Volcanology and Geothermal Research, **258**: 85-99

- Di Carlo, I.; Rotolo, S.G.; Scaillet, B.; Buccheri, V. and Pichavant, M. (2010) Phase equilibrium constraints on pre-eruptive conditions of recent felsic volcanism at Pantelleria Island, Italy, Journal of Petrology, **51** (11): 2245-2276
- Di Salvo, S.; Avanzinelli, R.; Isaia, R.; Zanetti, A.; Druitt, T. and Francalanci, L. (2020) Crystal-mush reactivation by magma recharge: Evidence from the Campanian Ignimbrite activity, Campi Flegrei volcanic field, Italy, Lithos, **376-377**: 105780
- Diaz-Alvarado, J. (2017) Experimental early crystallization of K-feldspar in granitic systems. Implications on the origin of magmatic fabrics in granitic rocks, Geologica Acta, **15** (4): 261-281
- Dick, H.J.B.; Kvassnes, A.J.S.; Robinson, P.T.; MacLeod, C.J. and Kinoshita, H. (2019) The Atlantis Bank gabbro massif, southwest Indian ridge, Progress in Earth and Planetary Science, **6** (64)
- Dobosi, G. and Jenner, G.A. (1999) Petrological implications of trace element variation in clinopyroxene megacrysts from the Nograd volcanic province, north Hungary: a study by laser ablation microprobe-inductively coupled plasma-mass spectrometry, Lithos, **46**: 731-749
- Dobosi, G.; Downes, H.; Embey-Isztin, A. and Jenner, G.A. (2003) Origin of megacrysts and pyroxenite xenoliths from the Pliocene alkali basalts of the Pannonian Basin (Hungary), Neues Jahrbuch fur Mineralogie-Abhandlungen, **178** (3): 217-237
- Doherty, R.D.; Hughes, D.A.; Humphreys, F.J.; Jonas, J.J.; Juul Jensen, D.; Kassner, M.E.; King, W.E.; McNelley, T.R.; McQueen, H.J. and Rollett, A.D. (1997) Current issues in recrystallisation: a review, Materials Science and Engineering, **A 238**: 219-274
- Donaldson, C.H. (1976) An experimental investigation of olivine morphology, Contributions to Mineralogy and petrology, **57**: 187-213
- Downes, H. (1993) The nature of the lower continental crust of Europe: Petrological and geochemical evidence from xenoliths, Physics of the Earth and Planetary interiors, **79** (1-2): 195-218
- Downes, H.; Balaganskaya, E.; Beard, A.; Liferovich, R. and Demaiffe, D. (2005) Petrogenetic processes in the ultramafic, alkaline and carbonatitic magmatism in the Kola alkaline province: a review, Lithos, **85** (1-4): 48-75

- Downes, H.; Beard, A. and Hinton, R. (2004) Natural experimental charges: an ion-microprobe study of trace element distribution coefficients in glass-rich hornblendite and clinopyroxenite xenoliths, Lithos, **75** (1-2): 1-17
- Duda, A. and Schmincke, H.-U. (1985) Polybaric differentiation of alkali basalt magmas: evidence from green-core clinopyroxenes (Eifel, FRG), Contributions to Mineralogy and Petrology, **91**: 340-353
- Dufek, J. and Bachmann, O. (2010) Quantum magmatism: magmatic compositional gaps generated by melt-crystal dynamics, Geology, **38**: 687-690
- Eberl, D.D.; Kile, D.E. and Drits, V.A. (2002) On geological interpretations of crystal size distribution: constant vs. proportionate growth, American Mineralogist, **87** (8-9): 1235-1241
- Edgar, A.D.; Lloyd, F.E.; Forsyth, D.M. and Barnett, R.L. (1989) Origin of glass in upper mantle xenoliths from the quaternary volcanics of Gees, West Eifel, Germany, Contributions to Mineralogy and Petrology, **103**: 277-286
- Eichelberger, J.C.; Carrigan, C.R.; Westrich, H.R. and Price, R.H. (1986) Non-explosive silicic volcanism, Nature, **323**: 598-602
- Elliott, M.T.; Cheadle, M.J. and Jerram, D.A. (1997) On the identification of textural equilibrium in rocks using dihedral angle measurements, Geology, **25** (4): 355-358
- Ellis, B.S.; Bachmann O. and Wolff, J.A. (2014) Cumulate fragments in silicic ignimbrites: the case of the Snake River Plain, Geology, **42**: 431-434
- Erdmann, S.; Martel, C.; Pichavant, M. and Kushnir, A. (2014) Amphibole as an archivist of magmatic crystallization conditions: problems, potential, and implications for inferring magma storage prior to the paroxysmal 2010 eruption of Mount Merapi, Indonesia, Contributions to Mineralogy and Petrology, **167**: 1016
- Eyuboglu, Y.; Dudas, F.O.; Zhu, D.C.; Liu, Z.; Chatterjee, N.; Akbulut, K.; Zhang, L.L. and Li, S.M. (2021) Xenoliths in late Cretaceous to Early Paleocene adakites of the Eastern Pontides Orogenic Belt, NE Turkey, Lithos, **398**: 106265
- Fabries, J.; Lorand, J.P. and Guiraud, M. (2000) Petrogenesis of the amphibole-rich veins from the Lherz orogenic lherzolite massif (Eastern Pyrenees, France): a case study for the origin of orthopyroxene-bearing

amphibole pyroxenites in the lithospheric mantle, Contributions to Mineralogy and Petrology, **140**: 383-403

- Faul, U. (1997) Permeability of partially molten upper mantle rocks from experiments and percolation theory, Journal of Geophysical Research, **102** (B5): 10299- 10311
- Fazio, E.; Fiannacca, P.; Russo, D. and Cirrincione, R. (2020) Submagmatic to solid-state deformation microstructures recorded in cooling granitoids during exhumation of late-Variscan crust in North-Eastern Sicily, Geosciences, **10**: 311
- Fekiacova, Z.; Mertz, D.F. and Hofmann A.W. (2007) Geodynamic setting of the tertiary Hocheifel volcanism (Germany), Part II: Geochemistry and Sr, Nd and Pb isotopic compositions, In: Ritter J.R.R., Christensen U.R. (eds) Mantle Plumes. Springer, Berlin, Heidelber
- Ferrando, C.; Basch, V.; Ildefonse, B.; Deans, J.; Sanfilippo, A.; Barou, F. and France, L. (2021) Role of compaction in melt extraction and accumulation at a slow spreading centre: microstructures of olivine gabbros from the Atlantis Bank (IODP Hole U1473A, SWIR), Tectonophysics, **815**: 229001
- Fiedrich, A.M.; Bachmann, O.; Ulmer, P.; Deering, C.D.; Kunze, K. and Leuthold, J. (2017) Mineralogical, geochemical, and textural indicators of crystal accumulation in the Adamello batholith (Northern Italy), American Mineralogist, **102** (12): 2467-2483
- Fielitz, W. and Mansy, J.L. (1999) Pre- and synorogenic burial metamorphism in the Ardenne and neighbouring areas (Rhenohercynian zone, central European Variscides), Tectonophysics, **309** (1-4): 227-256
- Filiberto, J.; Gross, J.; Udry, A.; Trela, J.; Wittmann, A.; Cannon, K.M.; Penniston-Dorland, S.; Ash, R.; Hamilton, V.E.; Meado, A.L.; Carpenter, P.; Jolliff, B. and Ferre, E.C. (2018) Shergottite Northwest Africa 6963: A pyroxene-cumulate Martian Gabbro, Journal of Geophysical Research – Planets, **123** (7): 1823-1841
- Flinders, A.F.; Shelley, D.R.; Dawson, P.B.; Hill, D.P.; Tripoli, B. and Shen, Y. (2018) Seismic evidence for significant melt beneath the Long Valley Caldera, California, USA, Geology, **46** (9): 799-802

- Förster, M. and Sirocko, F. (2015) The eruption history of the quaternary Eifel volcanic fields: Implications from the ELSA-Tephra-Stack, EGU General Assembly 2015, Abstract #11287, Vienna, AT
- Francis, D.M. (1976) Amphibole pyroxenite xenoliths: cumulate or replacement phenomena from the upper mantle Nunivak Island, Alaska, Contributions to Mineralogy and Petrology, **58**: 51-61
- Franke, W.; Cocks, L.R.M. and Torsvik, T.H. (2017) The Palaeozoic Variscan oceans revised, Gondwana Research, **48**: 257-284
- Friedrich, A.M.; Bachmamann, O.; Ulmer, P.; Deering, C.D.; Kunze, K. and Leuthold, J. (2017) Mineralogical, geochemical and textural indicators of crystal accumulation in the Adamello Batholith (Northern Italy), American Mineralogist, **102** (12): 2467-2483
- Fu, J.; Thomas, H.R. and Li, C. (2021) Tortuosity of porous media: Image analysis and physical simulation, Earth-Science Reviews, **212**: 103439
- Garibaldi, N.; Tikoff, B.; Schaen, A.J. and Singer, B.S. (2018) Interpreting granitic fabrics in terms of rhyolitic melt segregation, accumulation, and escape via tectonic filter pressing in the Huemul Pluton, Chile, Journal of Geophysical Research – Solid Earth, **123** (10): 8548-8567
- Gelmen, S.E.; Deering, C.D.; Bachmann, O.; Huber, C. and Gutierrez, F.J. (2014) Identifying the crystal graveyards remaining after large silicic eruptions, Earth and Planetary Science Letters, **403**: 299-306
- Germa, A.; Koebli, D.; Wetmore, P.; Atlas, Z.; Arias, A.; Savov, I.P.; Diez, M.; Greaves, V. and Gallant, E. (2020) Crystallization and segregation of syenite in shallow mafic sills: insights from the San Rafael subvolcanic field, Utah, Journal of Petrology, **61** (9)
- Giannetti, B. and Luhr, J.F. (1990) Phlogopite-clinopyroxenite nodules from high-K magmas, Roccamonfina Volcano, Italy: evidence for a low-pressure metasomatic origin, Earth and Planetary Science Letters, **101**: 402-424
- Glazner, A.F. and Boudreau, A. (2011) Metamorphism of thought about igneous rock textures, International Geology Review, **54** (3-4): 327-329
- Glazner, A.F.; Coleman, D. and Mills, R.D. (2015) The volcanic-plutonic connection, Physical Geology of Shallow Magmatic Systems, in: Breitkreuz, C. and Rocchi, S. (eds.) Physical Geology of Shallow Magmatic Systems, Advances in Volcanology (An Official Book Series of the International

Association of Volcanology and Chemistry of the Earth's Interior). Springer, Cham: 61-82

- Goes, S.; Spakman, W. and Bijwaard, H. (1999) A lower mantle source for Central European volcanism, Science, **286**: 1928-1931
- Google Maps (2022) *Daun Maars,* Available at: https://www.google.co.uk/maps/@50.1711781,6.8454217,15z/data=!5m1!1e4 (Accessed 21/8/22)
- Graf, H.F. and Timmreck, C. (2001) A general climate model simulation of the aerosol radiative effects of the Laacher See eruption (10,900 BC), Journal of Geophysical Research – Atmospheres, **106** (D14): 14747-14756
- Granet, M.; Wilson, M. and Achauer, U. (1995) Imaging a mantle plume beneath the French Massif Central, Earth and Planetary Science Letters, **136**: 281-296
- Gray, N.H.; Philpotts, A.R. and Dickson, L.D. (2003) Quantitative measures of textural anisotropy resulting from magmatic compaction illustrated by a sample from the Palisades sill, New Jersey, Journal of Volcanology and Geothermal Research, **121** (3-4): 293-312
- Green, D.H. and Hibberson, W. (1970) The instability of plagioclase in peridotite at high pressure, Lithos, **3** (3): 209-221
- Griesshaber, E.; O'Nions, R.K. and Oxburgh, E.R. (1992) Helium and carbon isotope systematics in crustal fluids from the Eifel, the Rhine Graben and Black Forest, F.R.G., Chemical Geology, **99**: 213-235
- Grunewald, S.; Weber, M. and Kind, R. (2001) The upper mantle under Central Europe: indications for the Eifel plume, Geophysics Journal International, **147** (3): 590-601
- Gualda, G.A.R. (2006) Crystal size distributions derived from 3D datasets: sample size versus uncertainties, Journal of Petrology, **47** (6): 1245-1254
- Gurenko, A.A. and Sobolev, A.V. (2006) Crust-primitive magma interaction beneath neovolcanic rift zone of Iceland recorded in gabbro xenoliths from Midfell, SW Iceland, Contributions to Mineralogy and Petrology, **151** (495)
- Haase, K. M.; Goldschmidt, B. and Garbe-Schönberg, C.-D. (2004) Petrogenesis of Tertiary continental intra-plate lavas from the Westerwald region, Germany, Journal of Petrology, **45** (5): 883-905

- Hager, H. and Pruefert, J. (1988) Tertiär, in: Hilden, H.D. (ed.): Geologie am Niederrhein, Geologisches Landesamt Nordrhein-Westfalen (Krefeld): 4th ed: 32-40
- Hammer, J.E. and Rutherford, M.J. (2002) An experimental study of the kinetics of decompression-induced crystallization in silicic melt, Journal of Geophysical Research – Solid Earth, **107** (B1): ECV 8-1-ECV 8-24
- Hammer, J.E.; Cashman, K.V. and Voight, B. (2000) Magmatic processes revealed by textural and compositional trends in Merapi dome lavas, Journal of Volcanology and Geothermal Research, **100** (1-4): 165-192
- Hammer, J.E.; Cashman, K.V.; Hoblitt, R.P. and Newman, S. (1999) Degassing and microlite crystallization during pre-climactic events of the 1991 eruption of Mt. Pinatubo, Philippines, Bulletin of Volcanology, **60** (5): 355-380
- Hasalova, P.; Weinberg, R.F. and Macrae, C. (2011) Microstructural evidence for magma confluence and reusage of magma pathways: implications for magma hybridization, Karakoram Shear Zone in NW India, Journal of Metamorphic Geology, **29** (8): 875-900
- Hayes, B.; Bedard, J.H. and Lissenberg, C.J. (2015a) Olivine slurry replenishment and the development of igneous layering in a Franklin Sill, Victoria Island, Arctic Canada, Journal of Petrology, **56** (1): 83-112
- Hayes, B.; Lissenberg, C.J.; Bedard, J.H. and Beard, C. (2015b) The geochemical effects of olivine slurry replenishment and dolostone assimilation in the plumbing system of the Franklin Large Igneous Province, Victoria Island, Arctic Canada, Contributions to Mineralogy and Petrology, **169** (2)
- Hegner, E.; Walter, H.J. and Satir, M. (1995) Pb-Sr-Nd isotopic compositions and trace element geochemistry of megacrysts and melilitites from the Tertiary Urach volcanic field: Source composition of small volume melts under SW Germany, Contributions to Mineralogy and Petrology, **122** (3): 322-335
- Hensch, M.; Dahm, T.; Ritter, J.; Heimann, S.; Schmidt, B.; Stange, S. and Lehmann, K. (2019) Deep low-frequency earthquakes reveal ongoing magmatic recharge beneath Laacher See Volcano (Eifel, Germany), Geophysical Journal International, **216** (3): 2025-2036

- Hepworth, L.N.; O'Driscoll, B.; Gertisser, R.; Daly, J.S. and Emeleus, C.H. (2018) Linking in situ crystallization and magma replenishment via sill intrusion in the Rum western layered intrusion, NW Scotland, Journal of Petrology**, 59** (8): 1605-1642
- Hermes, O. and Cornell, W.C. (1981) Quenched crystal mush and associated magma compositions as indicated by intercumulus glasses from Mt. Vesuvius, Italy, Journal of Volcanology and Geothermal Research, **9** (2-3): 133-149
- Hersum, T.G. and Marsh, B.D. (2006) Igneous microstructures from kinetic models of crystallisation, Journal of Volcanology and Geothermal Research, **154** (1-2): 34-47
- Hess, H.H. (1960) Stillwater igneous complex, Montana: a quantitative mineralogical study, Memoirs of the Geological Society of America, **80**: 230
- Hier-Majumder, S. and Kohlstedt, D.L. (2006) Role of dynamic grain boundary wetting in fluid circulation beneath volcanic arcs, Geophysical Research Letters, **33** (8)
- Higgins, M.D. (1991) The origin of laminated and massive anorthosite, Sept Iles layered intrusion, Quebec, Canada, Contributions to Mineralogy and Petrology, **106**: 340-354
- Higgins, M.D. (1996a) Magma dynamics beneath Kameni volcano, Thera, Greece, as revealed by crystal size and shape measurements, Journal of Volcanology and Geothermal Research, **70** (1-2): 37-48
- Higgins, M.D. (1996b) Crystal size distributions and other quantitative textural measurements in lavas and tuff from Egmont volcano (Mt Taranaki), New Zealand, Bulletin of Volcanology, **58** (2-3): 194-204
- Higgins, M.D. (1998) Origin of anorthosite by textural coarsening: quantitative measurements of natural sequence of textural development, Journal of Petrology, **39** (7): 1307-1323
- Higgins, M.D. (1999) Origin of megacrysts in granitoids by textural coarsening: a crystal size distribution (CSD) study of microcline in the Cathedral Peak Granodiorite, Sierra Nevada, California, Geological Society of London, Special Publications, **168**: 207-219
- Higgins, M.D. (2000) Measurement of crystal size distributions, American Mineralogist, **85** (9): 1105-1116

- Higgins, M.D. (2002) A crystal size-distribution study of the Kiglapait layered mafic intrusion, Labrador, Canada: evidence for textural coarsening, Contributions to Mineralogy and Petrology, **144**: 314-330
- Higgins, M.D. (2006a) Quantitative textural measurements in igneous and metamorphic petrology, 1st ed. Cambridge: Cambridge University Press
- Higgins, M.D. (2006b) Verification of ideal semi-logarithmic, lognormal or fractal crystal size distributions from 2D datasets, Journal of Volcanology and Geothermal Research, **154** (1-2): 8-16
- Higgins, M.D. (2011) Textural coarsening in igneous rocks, International Geology Review, **53** (3-4): 354-376
- Higgins, M.D. (2017) Quantitative investigation of felsic rock textures using cathodoluminescence images and other techniques, Lithos, **277**: 259-268
- Higgins, M.D. and Roberge, J. (2003) Crystal size distribution of plagioclase and amphibole from Soufrière Hills Volcano, Montserrat: Evidence for dynamic crystallization-textural coarsening cycles, Journal of Petrology, **44** (8): 1401-1411
- Higgins, M.D. and Roberge, J. (2007) Three magmatic components in the 1973 eruption of Eldfell volcano, Iceland: Evidence from plagioclase crystal size distribution (CSD) and geochemistry, Journal of Volcanology and Geothermal Research, **161** (3): 247-260
- Hildreth, W. (2004) Volcanological perspectives on Long Valley, Mammoth Mountain , and Mono Craters: several contiguous but discrete systems, Journal of Volcanology and Geothermal Research, **136**: 169-198
- Hildreth, W. and Wilson, C.J.N. (2007) Compositional zoning of the Bishop tuff, Journal of Petrology, **48**: 951-999
- Ho, K.S.; Chen, J.C.; Lo, C.H. and Zhao, H.L. (2003) Ar-40-Ar-39 dating and geochemical characteristics of late Cenozoic basaltic rocks from the Zhejiang-Fujian region, SE China: eruption ages, magma evolution and petrogenesis, Chemical Geology, **197** (1-4): 287-318
- Hoernle, K.; Zhang, Y.S. and Graham, D. (1995) Seismic and geochemical evidence for large-scale mantle upwelling beneath the Eastern Atlantic and Western and Central-Europe, Nature, **374** (6517):34-39
- Holness, M.B. (2006) Melt-solid dihedral angles of common minerals in natural rocks, Journal of Petrology, **47** (4): 791-800

- Holness, M.B. (2007b) Textural immaturity of cumulates as an indicator of magma chamber processes: infiltration and crystal accumulation in the Rum eastern layered intrusion, Journal of the geological Society, **164** (3): 529-539
- Holness, M.B. (2010) Decoding dihedral angles in melt-bearing and solidified rocks, Journal of the Virtual Explorer, **35** (2)
- Holness, M.B. (2016) Dihedral angles as a diagnostic tool for interpreting the cooling history of mafic rocks, American Geophysical Union, Fall Meeting 2016, San Francisco, Abstract# V31D-01
- Holness, M.B. and Bunbury, J.M. (2006) Insights into continental rift-related magma chambers: cognate nodules from the Kula Volcanic Province, Western Turkey, Journal of Volcanology and Geothermal Research, **153** (3-4): 241-261
- Holness, M.B. and Siklos, S.T.C. (2000) The rates and extent of textural equilibration in high-temperature fluid-bearing systems, Chemical Geology, **162** (2): 137-153
- Holness, M.B.; Anderson, A.T.; Martin, V.M.; Maclennan, J.; Passmore, E. and Schwindinger, K. (2007d) Textures in partially solidified crystalline nodules: a window into the pore structure of slowly cooled mafic intrusions, Journal of Petrology, **48** (7): 1243-1264
- Holness, M.B.; Cheadle, M.J. and McKenzie, D. (2005) On the use of changes in dihedral angle to decode late-stage textural evolution in cumulates, Journal of petrology, **46** (8): 1565-1583
- Holness, M.B.; Clemens, J.D. and Vernon, R.H. (2018) How deceptive are microstructures in granitic rocks? Answers from integrated physical theory, phase equilibrium, and direct observations, Contributions to Mineralogy and Petrology, **173** (62)
- Holness, M.B.; Morris, C.; Vukmanovic, Z. and Morgan, D.J. (2020) Insights into magma chamber processes from the relationship between fabric and grain shape in troctolitic cumulates, Frontiers in Earth Science, **8**: 352
- Holness, M.B.; Namur, O. and Cawthorn, R.G. (2013b) Disequilibrium dihedral angles in layered intrusions: a microstructural record of fractionation, Journal of Petrology, **54** (10): 2067-2093

- Holness, M.B.; Nielsen, T.F.D. and Tegner, C. (2007a) Textural maturity of cumulates: a record of chamber filling, liquidus assemblage, cooling rate and large-scale convection in mafic layered intrusions, Journal of Petrology, **48** (1): 141-157
- Holness, M.B.; Richardson, C. and Andersen, J. (2013a) The campsite dykes: a window into the early post-solidification history of the Skaergaard intrusion, East Greenland, Lithos, **180-183**: 134-149
- Holness, M.B.; Stock, M.J. and Geist, D. (2019) Magma chambers versus mush zones: constraining the architecture of sub-volcanic plumbing systems from microstructural analysis of crystalline enclaves, Philosophical transactions of the Royal Society A – Mathematical Physical and Engineering Sciences, **377** (2319)
- Holness, M.B.; Stripp, G.; Humphreys, M.C.S.; Veksler, I.V.; Nielsen, T.F.D. and Tegner, C. (2011) Silicate liquid immiscibility within the crystal mush: late stage magmatic microstructures in the Skaergaard Intrusion, East Greenland, **52** (1): 175-222
- Holness, M.B.; Tegner, C.; Nielsen, T.F.D.; Stripp, G. and Morse, S.A. (2007c) A textural record of solidification and cooling in the Skaergaard intrusion, East Greenland, Journal of Petrology, **48** (12): 2359-2377
- Holness, M.B.; Vukmanovic, Z. and Mariani, E. (2017a) Assessing the role of compaction in the formation of adcumulates: a microstructural perspective, Journal of Petrology, **58** (4): 643-673
- Hornby, A.J.; Lavallée, Y.; Kendrick, J.E.; Rollinson, G.; Butcher, A.R.; Clesham, S.; Kueppers, U.; Cimarelli, C. and Chigna, G. (2019) Phase partitioning during fragmentation revealed by QEMSCAN particle mineralogical analysis of volcanic ash, Scientific Reports, **9**: 126
- Hort, M. (1998) Abrupt changes in magma liquidus temperature because of volatile loss or magma mixing: effects on nucleation, crystal growth and thermal history of the magma, Journal of Petrology, **39** (5): 1063-1076
- Hort, M.; Marsh, B.D. and Spohn, T. (1993) Igneous layering through oscillatory nucleation and crystal settling in well-mixed magmas, Contributions to Mineralogy and Petrology, **114**: 425-440

- Hu, H. and Jackson, M. (2020) Compaction versus reactive flow: how does melt fraction change in crustal mush reservoirs? EGU General Assembly 2020, Abstract #5715
- Humphreys, M.C.S. (2009) Chemical evolution of intercumulus liquid, as recorded in plagioclase overgrowth rims from the Skaergaard intrusion, Journal of Petrology, **50** (1): 127-145
- Humphreys, M.C.S.; Blundy, J.D. and Sparks, R.S.J. (2006) Magma evolution and open-system processes at Shiveluch Volcano: insights from phenocryst zoning, Journal of Petrology, **47** (12): 2303-2334
- Huppert, H.E.; Turner, J.S. and Sparks, R.S.J. (1982) Replenished magma chambers: effects of compositional zonation on input rates, Earth and Planetary Science Letters, **57**: 345-357
- Ikeda, S.; Nakano, T. and Nakashima, Y. (2000) Three-dimensional study on the interconnection and shape of crystals in a graphic granite by X-ray CT and image analysis, Mineralogical Magazine, **64** (5): 945-959
- Illies, J. H.; Prodehl, C.; Schmincke, H.-U. and Semmel, A. (1979) The Quaternary uplift of the Rhenish shield in Germany, Tectonophysics, **61** (1-3): 197-225
- Illies, J.H. and Greiner, G. (1978) Rhinegraben and the Alpine system, Geological Society of America Bulletin, **89**: 770-782
- Ionov, D.A. and Hofmann, A.W. (1995) Nb-Ta-rich mantle amphiboles and micas: implications for subduction-related metasomatic trace element fractionations, Earth and Planetary Science Letters, **131**: 341-356
- Irvine, T.N. (1980) Magmatic infiltration metasomatism, double diffusive fractional crystallisation and adcumulus growth in the Muskox Intrusion and other layered intrusions. In: Haargraves R.B. (ed.) Physics of Magmatic Processes. Princeton, N.J: Princeton University Press, 325-383
- Irvine, T.N.; Anderson, J.C.O. and Brooks, C.K. (1998) Included blocks (and blocks within blocks) in the Skaergaard intrusion: geologic relations and the origins of rhythmic modally graded layers, Geological Society of America Bulletin, **110** (11): 1398-1447
- Irving, A.J. (1980) Petrology and geochemistry of composite ultramafic xenoliths in alkali basalts and implications for magmatic processes within the mantle, American Journal of Science, **280-A**: 389-426

- Irving, A.J. and Frey, F.A. (1984) Trace element abundances in megacrysts and their host basalts: constraints on partition coefficients and megacryst genesis, Geochimica et Cosmochimica Acta, **48**: 1201-1221
- Jackson, M.D.; Blundy, J. and Sparks, R.S.J. (2018) Chemical differentiation, cold storage and remobilization of magma in the Earth's crust, Nature, **564**: 405-409
- Jambon, A.; Lussiez, P.; Clocchiatti, R.; Weisz, J.; Hernandez, J. (1992) Olivine growth rates in a tholeiitic basalt: an experimental study of melt inclusions in plagioclase, Chemical Geology, **96** (3-4): 277-287
- Jansen, U. (2019) Pragian-Emsian brachiopods from the Rhenish Massif (Germany): new data on evolution and biostratigraphy, Rivista Italiana di Paleontologia e Stratigrafia, **125** (3): 735-759
- Jaret, S.J.; Mayne, R.G. and McSween, H.Y. (2008) Demystifying crystal size distribution (CSD): a comparison of methodologies using eucrite meteorites, 39th Lunar and Planetary Science Conference, Abstract #1391, Houston, TX: Lunar and Planetary Institute
- Jarosewich, E. (2002) Smithsonian microbeam standards, Journal of Research of the National Institute of Standards and Technology, **107** (6): 681-685
- Jaxybulatov, K.; Shapiro, N.M.; Koulakov, I.; Mordret, A.; Landes, M. and Sens-Schonfelder, C. (2014) A large magmatic sill complex beneath the Toba caldera, Science, **346** (6209): 617-619
- Jerram, D.A. and Cheadle, M.J. (2000) On the cluster analysis of grains and crystals in rocks, American Mineralogist, **85** (1): 47-67
- Jerram, D.A. and Higgins, M.D. (2007) 3D analysis of rock textures: quantifying igneous microstructures, Elements, **3** (4): 239-245
- Jerram, D.A.; Cheadle, M.J. and Philpotts, A.R. (2003) Quantifying the building blocks of igneous rocks: are clustered crystal frameworks the foundation? Journal of Petrology, **44** (11): 2033-2051
- Jerram, D.A.; Cheadle, M.J.; Hunter, R.H. and Elliott, M.T. (1996) The spatial distribution of grains and crystals in rocks, Contributions to Mineralogy and Petrology, **125**: 60-74

- Johnson, B.R. and Glazner, A.F. (2010) Formation of K-feldspar megacrysts in granodioritic plutons by thermal cycling and late-stage textural coarsening, Contributions to Mineralogy and Petrology, **159**: 599-619
- Jung, C.; Jung, S.; Hoffer, E. and Berndt, J. (2006) Petrogenesis of tertiary mafic alkaline magmas in the Hocheifel, Germany, Journal of Petrology, **47** (8); 1637-1671
- Jung, S. and Hoernes, S. (2000) The major- and trace-element and isotope (Sr, Nd, O) geochemistry of Cenozoic alkaline rift-type volcanic rocks from the Rhön area (central Germany): petrology, mantle source characteristics and implications for asthenosphere-lithosphere interactions, Journal of Volcanology and Geothermal Research, **99**: 27-53
- Jung, S.; and Masberg, P. (1998) Major- and trace- element systematics and isotope geochemistry of Cenozoic mafic volcanic rocks from the Vogelsberg (central Germany) – Constraints on the origin of continental alkaline and tholeiitic basalts and their mantle sources, Journal of Volcanology and Geothermal Research, **86** (1-4): 151-177
- Jung, S.; Pfänder, J.A.; Brügmann, G. and Stracke, A. (2005) Sources of primitive alkaline volcanic rocks from the Central European Volcanic Province (Rhön, Germany) inferred from HF, Os and Pb isotopes, Contributions to Mineralogy and Petrology, **150**: 546-559
- Kaufmann, F.E.D.; Vukmanovic, Z.; Holness, M.B. and Hecht, L. (2018) Orthopyroxene oikocrysts in the MG1 chromitite layer of the Bushveld Complex: implications for cumulate formation and recrystallisation, Contributions and Mineralogy and Petrology, **173**: 17
- Kelemen, P.B.; Whitehead, J.A.; Aharonov, E. and Jordahl, K.A. (1995) Experiments on flow focusing in soluble porous media, with applications to melt extraction from the mantle, Journal of Geophysical Research, **100** (B1): 475-496
- Ketcham, R.A. (2005) Computational methods for quantitative analysis of three-dimensional features in geological specimens, Geosphere, **1**: 32-41
- Ketcham, R.A. and Carlson, W.D. (2001) Acquisition, optimization and interpretation of X-ray computed tomographic imagery: applications to the geosciences, Computers and Geosciences, **27** (4): 381-400

- Keyser, M.; Ritter, J.R.R. and Jordan, M. (2002) 3D shear-wave velocity structure of the Eifel plume, Germany, Earth and Planetary Science Letters, **203**: 59-82
- Khazan, Y. (2010) Melt segregation and matrix compaction: the mush continuity equation, compaction/segregation time, implications, Geophysical Journal International, **183**: 601-610
- King, P.L.; Hervig, R.L.; Holloway, J.R.; Delaney, J.S. and Dyar, M.D. (2000) Partitioning of Fe^{3+}/Fe_{total} between amphibole and basanitic melt as a function of oxygen fugacity, Earth and Planetary Science Letters, **178**: 97-112
- Kirkpatrick, R.J. (1975) Crystal growth from the melt: a review, American Mineralogist, **60**: 798-814
- Kiss, B.; Harangi, S.; Ntaflos, T.; Mason, P.R.D. and Pál-Molnár, E. (2014) Amphibole perspective to unravel pre-eruptive processes and conditions in volcanic plumbing systems beneath intermediate arc volcanoes: a case study from Ciomadul volcano (SE Carpathians), Contributions to Mineralogy and Petrology, **167**: 986
- Klaver, M.; Matveev, S.; Berndt, J.; Lissenberg, C.J. and Vroon, P.Z. (2017) A mineral and cumulate perspective to magma differentiation at Nisyros volcano, Aegean arc, Contributions to Mineralogy and Petrology, **172**: 95
- Klebesz, R.; Bodnar, R.J.; De Vivo, B.; Torok, K.; Lima, A. and Petrosino, P. (2012) Composition and origin of nodules from the ~20 ka Pomici di Base (PB) – Sarno eruption of Mt. Somma – Vesuvius, Italy, Central European Journal of Geosciences, **4** (2): 324-337
- Koh, E.J.Y.; Amini, E.; McLachlan, G.J. and Beaton, N. (2021) Utilising convolutional neural networks to perform fast automated modal mineralogy analysis for thin-section optical microscopy, Minerals Engineering, **173** (1): 107230
- Konzett, J.; Sweeney, R.J.; Thompson, A.B. and Ulmer, P. (1997) Potassium amphibole stability in the upper mantle: an experimental study in a peralkaline KNCMASH system to 8.5 GPa, Journal of Petrology, **38** (5): 537-568

- Kreemer, C.; Blewitt, G. and Davis, P.M. (2020) Geodetic evidence for a buoyant mantle plume beneath the Eifel volcanic area, NW Europe, Geophysical Journal International, **222** (92): 1316-1332
- Kruger, T. and Kisters, A. (2016) Magma accumulation and segregation during regional-scale folding: The Holland's dome granite injection complex, Damara belt, Namibia, Journal of Structural Geology, **89**: 1-18
- Kruhl, J.H. and Peternell, M. (2002) The equilibration of high-angle grain boundaries in dynamically recrystallized quartz: the effect of crystallography and temperature, Journal of Structural Geology, **24** (6-7): 1125-1137
- Larsen, R.B. and Tegner, C. (2006) Pressure conditions for the solidification of the Skaergaard intrusion: Eruption of East Greenland flood basalts in less than 300,000 years, Lithos, **92** (1-2): 181-197
- LaRue, A.; Baker, D.R.; Polacci, M.; Allard, P. and Sondini, N. (2013) Can vesicle size distributions assess eruption intensity during volcanic activity? Solid Earth, **4** (2): 373-380
- LaTourette, T.; Hervig, R.L. and Holloway, J.R. (1995) Trace-element partitioning between amphibole, phlogopite, and basanite melt, Earth and Planetary Science Letters, **135** (1-4): 13-30
- Latypov, R.M.; Chistyakova, S.Y.; Namur, O. and Barnes, S. (2020) Dynamics of evolving magma chambers: textural and chemical evolution of cumulates at the arrival of new liquidus phases, Earth Science Reviews, **210**: 103388
- Launeau, P. (2004) Evidence of magmatic flow by 2-D image analysis of 3-D shape preferred orientation distributions, Bulletin de la Societe Geologique de France, **175** (4): 331-350
- Launeau, P. and Cruden, A.R. (1998) Magmatic fabric acquisition mechanisms in a syenite: Results of combined anisotropy of magnetic susceptibility and image analysis study, Journal of Geophysical Research – Solid Earth, **103** (B3): 5067-5089
- Launeau, P. and Robin, P.Y.F (1996) Fabric analysis using the intercept method, Tectonophysics, **267** (1-4): 91-119
- Le Maitre, R.; Streckeisen, A.; Zanettin, B.; Le Bas, M.; Bonin, B. and Bateman, P. (2002) Igneous Rocks: A classification and glossary of terms:

recommendations of the International Union of Geological Sciences Subcommission on the Systematics of Igneous Rocks, (2nd ed.), Cambridge: Cambridge University Press

- Leake, B.E.; Woolley, A.R.; Arps, C.E.S.; Birch, W.D.; Gilbert, M.C.; Grice, J.D.; Hawthorne, F.C.; Kato, A.; Kisch, H.J.; Krivovichev, V.G.; Linthout, K.; Laird, J.; Mandarino, J.A.; Maresch, W.V.; Nickel, E.H.; Rock, N.M.S.; Schumacher, J.C.; Smith, D.C.; Stephenson, N.C.N.; Ungaretti, L.; Whittaker, E.J.W. and Youzhi, G. (1997) Nomenclature of amphiboles; report of the Subcommittee on Amphiboles of the International Mineralogical Association, Commission on new minerals and mineral names, American Mineralogist, **82** (2): 1019-1037
- Leblanc, M., Dautria, J.M. and Girod, M. (1982) Magnesian ilmenite xenoliths in a basanite from Tahalra, Ahaggar (Southern Algeria), Contributions to Mineralogy and Petrology, **79**: 347-354
- Leder, J.; Wenzel, F.; Daniell, J.E. and Gottschämmer, E. (2017) Loss of residential buildings in the event of a re-awakening of the Laacher See Volcano (Germany), Journal of Volcanology and Geothermal Research, **337**: 111-123
- Leuthold, J.; Blundy, J.D.; Holness, M.B. and Sides, R. (2014) Successive episodes of reactive liquid flow through a layered intrusion (Unit 9, Rum Eastern layered intrusion, Scotland), Contributions to Mineralogy and Petrology, **168**: 1021
- Leuthold, J.; Lissenberg, C.J.; O'Driscoll, B.; Karakas, O.; Falloon, T.; Klimentyeva, D.N. and Ulmer, P. (2018) Partial melting of lower oceanic crust gabbro: constraints from poikilitic clinopyroxene primocrysts, Frontiers in Earth Sciences, **6**: 15
- Liebl, C.; Kuntcheva, B.; Kruhl, J.H. and Kunze, K. (2007) Crystallographic orientations of quartz grain-boundary segments formed during dynamic recrystallization and subsequent annealing, European Journal of Mineralogy, **19** (5): 735-744
- Lino, L.M. and Vlach, S.R.F (2021) Textural and geochemical evidence for multiple, sheet-like magma pulses in the Limeira Intrusion, Parana Magmatic Province, Brazil, Journal of Petrology, **62** (3)

- Lippolt, H.J. (1983) Distribution of volcanic activity in space and time, in Fuchs et al. (eds.) Plateau Uplift, Springer Berlin: 112-120
- Lisboa, V.A.C.; Conceição, H.; Rosa, M.L.S.; Marques, G.T.; Lamarão, C.N. and Lima, A.L.R. (2020) Amphibole crystallization conditions as record of interaction between ultrapotassic enclaves and monzonitic magmas in the Glória Norte Stock, south of Borborema province, Brazilian Journal of Geology, **50** (2)
- Lissenberg, C.J. and Dick, H.J.B. (2008) Melt-rick reaction in the lower oceanic crust and its implication for the genesis of mid-ocean ridge basalts, Earth and Planetary Science Letters, **271**: 311-325
- Lissenberg, C.J. and Macleod, C.J. (2016) A reactive porous flow control on mid-ocean ridge magmatic evolution, Journal of Petrology, **57** (11-12): 2195-2219
- Lissenberg, C.J.; MacLeod, C.J. and Bennett, E.N. (2019) Consequences of a crystal mush-dominated magma plumbing system: a mid-ocean ridge perspective, Philosophical Transactions of the Royal Society A, **377** (213)
- Liu, S-Q.; Zheng, Y-C.; Hou, Z-Q. and Shen, Y. (2022) Multi-stage crustal magma reservoirs of ultrapotassic rocks recorded by zoned clinopyroxene, Journal of Asian Earth Science, **226**: 105072
- Liu, Y.D.; Ying, J.F. (2020) Origin of clinopyroxene megacrysts in volcanic rocks from the North China Craton: a comparison study with megacrysts worldwide, International Geology Review, **62** (15): 1845-1861
- Lloyd, F.E. and Bailey, D.K. (1975) Light element metasomatism of the continental mantle: the evidence and the consequence, In: Ahrens, L.H.; Dawson, J.B.; Duncan, A.R. and Erlank, A.J. (eds) Physics and Chemistry of the Earth, **9**, Permagon, Oxford: 389-416
- Lloyd, F.E.; Edgar, A.D.; Forsyth, D.M. and Barnett, R.L. (1991) The paragenesis of upper-mantle xenoliths from the Quaternary volcanics south-east of Gees, West Eifel, Germany, Mineralogical Magazine, **55**: 95-122
- Lofgren, G. (1974) An experimental study of plagioclase crystal morphology; isothermal crystallization, American Journal of Science, **274** (3): 243-273

- Lormand, C.; Zellmer, G.F.; Sakamoto, N.; Ubide, T.; Kilgour, G.; Yurimoto, H.; Palmer, A.; Németh, K.; Iizuka, Y. and Moebis, A. (2021) Shallow magmatic processes revealed by cryptic microantecrysts: a case study from the Taupo volcanic zone, Contributions to Mineralogy and Petrology, **176**: 97
- Loureiro, P.O.; Koester, E.; Weinberg, R.F.; Lenz, C.; Porcher, C.C.; Ramos, R.C.; Vieira, D.T.; Bastos, V.A.; Knijnik, D. and Primentel, M.M. (2021) Recycling and hybridization of incremental episodes of magma intrusions: Pinheiro Machado Complex, South eastern Dom Feliciano Belt, Brazil Paula, Journal of South American Earth Sciences, **105**: 102922
- Lundstrom, C.C. and Glazner, A.F. (2016) Silicic magmatism and the volcanic-plutonic connection, Elements, **12** (2): 91-96
- Lupulescu, A. and Watson, E.B. (1999) Low melt fraction connectivity of granitic and tonalitic melts in a mafic crustal rock at 800°C and 1 GPa, Contributions to Mineralogy and Petrology, **134**: 202-216
- Lustrino, M. and Carminati, E. (2007) Phantom plumes in Europe and the circum-Mediterranean region, in Special Paper 430: Plates, Plumes and Planetary Processes, Foulger, G.R. and Judy, D.M., **430**: 723-745
- Maaløe, S. (2011) Olivine phenocryst growth in Hawaiian tholeiites: evidence for supercooling, Journal of Petrology, **52** (7-8): 1579-1589
- Magee, C.; O'Driscoll, B. and Chambers, A.D. (2010) Crystallization and textural evolution of a closed-system magma chamber: insights from a crystal size distribution study of the Lilloise layered intrusion, East Greenland, Geological Magazine, **147** (3): 363-379
- Maier, W.D.; Barnes, S.-J.; Muir, D.; Savard, D.; Lahaye, Y. and Smith, W.D. (2021) Formation of Bushveld anorthosite by reactive porous flow, Contributions to Mineralogy and Petrology, **176**: 3
- Mandler, B.E. and Grove, T.L. (2016) Controls on the stability and composition of amphibole in the Earth's mantle, Contributions to Mineralogy and Petrology, **171**: 68
- Manoochehri, S and Schmidt, M.W. (2014) Settling and compaction of chromite cumulates employing a centrifuging piston cylinder and application to layered mafic intrusions, Contributions to Mineralogy and Petrology, **168**: 1091

- Marignier, A.; Ferreira, A.M.G. and Kitching, T. (2020) The probability of mantle plumes in global tomographic models, Geochemistry, Geophysics, Geosystems, **21** (9)
- Marsh, B. (2004) A magmatic mush column Rosetta stone: the McMurdo Dry Valleys of Antarctica, Eos Transactions American Geophysical Union, **85** (47): 497-502
- Marsh, B.D. (1998) On the interpretation of crystal size distributions in magmatic systems, Journal of Petrology, **39** (4): 553-599
- Marsh, B.D. (1981) On the crystallinity, probability of occurrence and rheology of lava and magma, Contributions to Mineralogy and Petrology, **78** (1): 85-98
- Marsh, B.D. (1988) Crystal size distribution (CSD) in rocks and the kinetics and dynamics of crystallization. I. Theory, Contributions to Mineralogy and Petrology, **99**: 277-291
- Marsh, B.D. (1996) Solidification fronts and magmatic evolution, Mineralogical Magazine, **60**: 5-40
- Marsh, B.D. (2006) Dynamics of magmatic systems, Elements, **2** (5): 287-292
- Martin, V.M.; Holness, M.B. and Pyle, D.M. (2006a) Textural analysis of magmatic enclaves from the Kameni Islands, Santorini, Greece, Journal of Volcanology and Geothermal Research, **154** (1-2): 89-102
- Martin, V.M.; Pyle, D.M. and Holness, M.B. (2006b) The role of crystal frameworks in the preservation of enclaves during magma mixing, Earth and Planetary Science Letters, **248** (3-4): 787-799
- Mathar, J.P.; Ritter, J.R.R. and Friedrich, W. (2006) Surface waves image the top of the Eifel plume, Geophysical Journal International, **164**: 377-382
- Mattioli, M.; Serri, G.; Salvioli-Mariani, E.; Renzulli, A.; Holm, P.M.; Santi, P. and Venturelli, G. (2003) Sub-volcanic infiltration and syn-eruptive quenching of liquids in cumulate wall-rocks: the example of the gabbroic nodules of Stromboli (Aeolian Islands, Italy), Mineralogy and Petrology, **78** (3-4): 201-230
- Matusiak-Malek, M.; Puziewicz, J.; Ntaflos, T.; Woodland, A.; Uever-Thiele, L.; Buchner, J.; Gregoire, M. and Aulbach, S. (2021) Variable origin of clinopyroxene megacrysts carried by Cenozoic volcanic rocks from the

eastern limb of Central European Volcanic Province (SE Germany and SW Poland), Lithos, **382**: 105936

- Matzel, J.E.P.; Bowring, S.A. and Miller, R.B. (2006) Time scales of pluton construction at differing crustal levels: examples from the Mount Stuart and Tenpeak intrusions, North Cascades, Washington, Geological Society of America Bulletin, **118** (11-12): 1412-1430
- McBirney, A.R. (2009) Factors governing the textural development of Skaergaard gabbros: A review, Lithos, **111** (1-2): 1-5
- McBirney, A.R. and Creaser, R.A. (2003) The Skaergaard Layered Series, Part VII. Sr and Nd isotopes, Journal of Petrology, **44** (4): 757-771
- McBirney, A.R. and Hunter, R.H. (1995) The cumulate paradigm reconsidered, The Journal of Geology, **103** (1): 114-122
- McBirney, A.R.; Boudreau, A.E. and Marsh, B.D. (2009) Comments on: 'Textural maturity of cumulates: a record of chamber filling, liquidus assemblage, cooling rate and large-scale convection in mafic layered intrusions' and 'A textural record of solidification and cooling in the Skaergaard intrusion, East Greenland', Journal of Petrology, **50** (1): 93-95
- McKenzie, D. (2011) Compaction and crystallization in magma chambers: towards a model of the Skaergaard Intrusion, Journal of Petrology, **52** (5): 905-930
- Mengel, K. (1990) Crustal xenoliths from Tertiary volcanics of the Northern Hessian Depression, Contributions to Mineralogy and Petrology, **104**: 8-26
- Mengel, K.; Sachs, P.M.; Stosch, H.G.; Wörner, G. and Loock, G. (1991) Crustal xenoliths from Cenozoic volcanic fields of West Germany: implications for structure and composition of the continental crust, Tectonophysics, **195**: 271-289
- Merriam, D.F. (2004) The quantification of geology: from abacus to Pentium: A chronicle of people, places and phenomena, Earth-Science Reviews, **67** (1-2): 55-89
- Mertes, H. (1983) Aufbau und Genese des Westeifeler Vulkanfeldes, Bochumer geologische und geotechnische Arbeiten, **9**: 1-1415
- Mertes, H. and Schmincke, H.-U. (1985) Mafic potassic lavas of the Quaternary West Eifel volcanic field, Contributions to Mineralogy and petrology, **89**: 330-345

- Mertz, D.F.; Löhnertz, W.; Nomade, S.; Periera, A.; Prelević, D. and Renne, P.R. (2015) Temporal-spatial evolution of low-SiO2 volcanism in Pleistocene West Eifel volcanic field (West Germany) and relationship to upwelling asthenosphere, Journal of Geodynamics, **88**: 59-79
- Meschede, M. (2018) Deutschland im späten Paläozoikum, In Geologie Deutschlands, 2nd edition. Springer Spektrum, Berlin: 61-101
- Meschede, M. and Warr, L.N. (2019) Tertiary and Quaternary volcanism, In: The geology of Germany, Regional Geology Reviews, Springer, Cham.
- Meurer, W. and Boudreau, A. (1998) Compaction of igneous cumulates part II: compaction and the development of igneous foliations, Journal of Geology, **106** (3): 293-304
- Meurer, W.P. and Claeson, D.T. (2002) Evolution of crystallizing interstitial liquid in an arc-related cumulate determined by LA-ICP-MS mapping of a large amphibole oikocryst, Journal of Petrology, **43** (4): 607-629
- Meurer, W.P. and Meurer, M.E.S. (2006) Using apatite to dispel the 'trapped liquid' concept and to understand the loss of interstitial liquid by compaction in mafic cumulates: an example from the Stillwater Complex, Montano, Contributions to Mineralogy and Petrology, **151**: 187-201
- Meyer, W. and Stets, J. (1998) Junge tektonik im Reinischen Schieferbirge und ihre quantifizierung, Zeitschrift der Deutschen Geologischen Gesellschaft, **149** (3): 359-379
- Meyer, W. and Stets, J. (2002) Pleistocene to recent tectonics in the Rhenish Massif (Germany), Netherlands Journal of Geosciences – Geologie en Mijnbouw, **81** (2): 217-221
- Miranda, E.A.; Hirth, G. and John, B.E. (2016) Microstructural evidence for the transition from dislocation creep to dislocation-accommodated grain boundary sliding in naturally deformed plagioclase, Journal of Structural Geology, **92**: 30-45
- Mitchell, A.L. and Grove, T.L. (2016) Experiments on melt-rock reaction in the shallow mantle wedge, Contributions to Mineralogy and Petrology, **171** (107)
- Mittlefehldt, D.W. (1984) Genesis of clinopyroxene-amphibole xenoliths from Birket Ram: trace element and petrologic constraints, Contributions to Mineralogy and Petrology, **88**: 280-287

- Mock, A. and Jerram, D.A. (2005) Crystal Size Distributions (CSD) in three dimensions: insights from the 3D reconstruction of a highly porphyritic rhyolite, Journal of Petrology, **46** (8): 1525-1541
- Mock, A.; Jerram, D.A. and Breitkreuz, C. (2003) Using quantitative textural analysis to understand the emplacement of shallow-level rhyolitic laccoliths – A case study from the Halle Volcanic Complex, Germany, Journal of Petrology, **44** (5): 833-849
- Mock, D.; Neave, D.A.; Müller, S.; Garbe-Schönberg, D.; Namur, O.; Ildefonse, B. and Koepke, J. (2021) Formation of igneous layering in the lower oceanic crust from the Samail Ophiolite, Sultanate of Oman, Journal of Geophysical Research: Solid Earth, American Geophysical Union
- Moine, B.N.; Gregoire, M.; O'Reilly, S.Y.; Sheppard, S.M.F. and Cottin, J.Y. (2001) High field strength element fractionation in the upper mantle: evidence from amphibole-rich composite mantle xenoliths from the Kerguelen Islands (Indian Ocean), Journal of Petrology, **42**: 2145-2167
- Molina, J.F.; Cambeses, A.; Moreno, J.A.; Morales, I.; Lázaro, C.; Montero, P. and Bea, F. (2021) A cautionary note on amphibole geobarometry, Environmental Sciences Proceedings, **6**: 17
- Mollo, S.; Putirka, K.; Iezzi, G.; Del Guadio, P. and Scarlato, P. (2011) Plagioclase-melt distribution (dis)equilibrium due to cooling dynamics: Implications for thermobarometry, barometry and hygrometry, Lithos, **125** (1-2): 221-235
- Montelli, R.; Nolet, G.; Dahlen, F.A. and Masters, G. (2006) A catalogue of deep mantle plumes: new results from finite-frequency tomography, Geochemistry Geophysics Geosystems, **7** (11)
- Morgan, D.J. and Jerram, D.A. (2006) On estimating crystal shape for crystal size distribution analysis, Journal of Volcanology and Geothermal Research, **154** (1-2): 1-7
- Morgan, D.J.; Jerram, D.A.; Chertkoff, D.G.; Davidson, J.P.; Pearson, D.G. Kronz, A. and Nowell, G.M. (2007) Combining CSD and isotopic microanalysis: magma supply and mixing processes at Stromboli volcano, Aeolian Islands, Italy, Earth and Planetary Science Letters, **260** (3-4): 419-431

- Morimoto, N. (1988) Nomenclature of Pyroxenes, Mineralogy and Petrology, **39**: 55-76
- Morse, S.A. and Nolan, K.M. (1984) Origin of strongly reversed rims on plagioclase in cumulates, Earth and Planetary Science Letters, **68**: 485-498
- Namur, O.; Humphreys, M.C.S. and Holness, M.B. (2013) Lateral reactive infiltration in a vertical gabbroic crystal mush, Skaergaard intrusion, East Greenland, Journal of Petrology, **54** (5): 985-1016
- Neal, C.R. (1988) The origin and composition of metasomatic fluids and amphiboles beneath Malaita, Solomon Islands, Journal of Petrology, **29** (1): 149-179
- Neal, C.R.; Donohue, P.; Fagan, A.L.; O'Sullivan, K.; Oshrin, J. and Roberts, S. (2015) Distinguishing between basalts produced by endogenic volcanism and impact processes: a non-destructive method using quantitative petrography of lunar basaltic samples, Geochimica et Cosmochimica Acta, **148**: 62-80
- Neave, D.A. and Maclennan, J. (2020) Clinopyroxene dissolution records rapid magma ascent, Frontiers in Earth Sciences, **8**: 188
- Neave, D.A.; Buisman, I. and MacLennan, J. (2017) Continuous mush disaggregation during the long-lasting Laki fissure eruption, Iceland, American Mineralogist, **102** (10): 2007-2021
- Neave, D.A.; Maclennan, J.; Hartley, M.E.; Edmonds, M. and Thordarson, T. (2014) Crystal storage and transfer in basaltic systems: the Skuggafjöll eruption, Iceland, Journal of Petrology, **55**: 2311-2346
- Nebel, O.; Sossi, P.A.; Ivanic, T.J.; Bénard, A.; Gardiner, N.J.; Langford, R.L. and Arculus, R.J. (2020) Incremental growth of layered mafic-ultramafic intrusions through melt replenishment into a crystal mush zone traced by Fe-Hf isotope systematics, Frontiers in Earth Science, **8**: 2
- Nelson, S.T. and Tingey, D.G. (1997) Time-transgressive and extension-related basaltic volcanism in southwest Utah and vicinity, Geological Society of America Bulletin, **109** (10): 1249-1265
- Neumann, E.-R. (2019) Origin and evolution of the early magmatism in the Oslo Rift (Southeast Norway): evidence from multiple generations of clinopyroxene, Lithos, **340-341**: 139-151

- Ni, H.; Keppler, H.; Walte, N.; Schiavi, F.; Chen, Y.; Masotta, M. and Li, Z. (2014) In situ observation of crystal growth in a basalt melt and the development of crystal size distribution in igneous rocks, Contributions to Mineralogy and Petrology, **167** (5): 1003-1519
- Nichols, M.L.; Malone, S.D.; Moran, S.C.; Thelan, W.A. and Vidale, J.E. (2011) Deep long-period earthquakes beneath Washington and Oregon volcanoes, Journal of Volcanology and Geothermal Research, **200** (3): 116-128
- Nkono, C.; Femenias, O.; Lesne, A.; Mercier, J.C.; Ngounouno, F.Y. and Demaiffe, D. (2016) Relationship between the fractal dimension of orthopyroxene distribution and the temperature in mantle xenoliths, Geological Journal, **51** (5): 748-759
- Noiriel, C.; Oursin, M. and Daval, D. (2020) Examination of crystal dissolution in 3D: a way to reconcile dissolution rates in the laboratory? Geochimica et Cosmochimica Acta, **273**: 1-25
- O'Driscoll, B.; Donaldson, C.; Troll, V.R.; Jerram, D.A. and Emeleus, H. (2007) An origin for harrisitic and granular olivine in the Rum layered suite, NW Scotland: a crystal size distribution study, Journal of Petrology, **48** (2): 253-270
- O'Driscoll, B.; Stevenson, C.T.; Troll, V.R. (2008) Mineral lamination development in layered gabbros of the British Palaeogene Igneous Province: A combined anisotropy of magnetic susceptibility, quantitative textural and mineral chemistry study, Journal of Petrology, **49** (6): 1187-1221
- Okumura, S.; de Silva, S.L.; Nakamura, M. and Sasaki, O. (2019) Caldera-forming eruptions of mushy magma modulated by feedbacks between ascent rate, gas retention/loss and bubble/crystal framework interaction, Scientific Reports, **9**: 15845
- Palummo, F.; Mollo, S.; Petrone, C.M.; Ellis, B.D.; De Astis, G.; Scarlato, P. and Bachmann, O. (2021) Decoding multiple zoning patterns in clinopyroxene phenocrysts at Volcano Island: a record of dynamic crystallization through interconnected reservoirs, Lithos, **406-407**: 106517

- Pamukcu, A.S. and Gualda, G.A.R. (2010) Quantitative 3D petrography using X-ray tomography 2: Combining information at various resolutions, Geosphere, **6** (6): 775-781
- Passmore, E.; Maclennan, J.; Fitton, J.G. and Thordarson, T. (2012) Mush disaggregation in basaltic magma chambers: evidence from the AD 1783 Laki eruption, Journal of Petrology, **53**: 2593-2623
- Paterson, S.; Memeti, V.; Mundil, R. and Zak, J. (2016) Repeated, multiscale, magmatic erosion and recycling in an upper-crustal pluton: Implications for magma chamber dynamics and magma volume estimates, American Mineralogist, **101** (9-10): 2176-2198
- Paterson, S.R.; Fowler Jr, T.K.; Schmidt, K.L.; Schmidt, K.L.; Yoshinobu, A.S.; Yuan, E.S. and Miller, R.B. (1998) Interpreting magmatic fabric patterns in plutons, Lithos, **44**: 53-82
- Paulatto, M.; Annen, C.J.; Henstock, T.J.; Kiddle, E.J.; Minshull, T.A.; Sparks, R.S.J. and Voight, B. (2012) Magma chamber properties from integrated seismic tomography and thermal modelling at Montserrat, Geochemistry, Geophysics, Geosystems, **13** (1)
- Paulatto, M.; Moorkamp, M.; Hautmann, S.; Hooft, E.; Morgan, J.V.; Sparks, R.S.J. (2019) Vertically extensive magma reservoir revealed from joint inversion and quantitative interpretation of seismic and gravity data, Journal of Geophysical Research, Solid Earth, **124** (11): 11170-11191
- Payton, R.L.; Fellgett, M. Clark, B.L.; Chiarella, D.; Kingdon, A. and Hier-Majumder, S. (2021) Pore-scale assessment of subsurface carbon storage potential: implications for the UK Geoenergy Observatories project, Petroleum Geoscience, **27** (2)
- Pebane, M. and Latypov, R. (2017) The significance of magmatic erosion for bifurcation of UG1 chromitite layers in the Bushveld Complex, Ore Geology Reviews, **90**: 65-93
- Peč, M.; Holtzmann, B.K.; Zimmerman, M.E. and Kohlstedt, D.L. (2017) Reaction infiltration instabilities in mantle rocks: an experimental investigation, Journal of Petrology, **58** (5): 979-1003
- Pedersen, J.M.; Ulrich, T.; Whitehouse, M.J.; Kent, A.J.R. and Tegner, C. (2021) The volatile and trace element composition of apatite in the

Skaergaard intrusion, East Greenland, Contributions to Mineralogy and Petrology, **176**: 102

- Perinelli, C.; Gaeta, M. and Armienti, P. (2017) Cumulate xenoliths from Mt. Overlord, northern Victoria Land, Antarctica: a window into high pressure storage and differentiation of mantle-derived basalts, Lithos, **268**: 225-239
- Petford, N., Koenders, M.A. and Clemens, J.D. (2020) Igneous differentiation by deformation, Contributions to Mineralogy and Petrology, **175** (45)
- Pfänder, J.A.; Jung, S.; Klügel, A.; Münker, C.; Romer, R.L.; Sperner, B. and Rohrmüller, J. (2018) Recurrent local melting of metasomatized lithospheric mantle in response to continental rifting: constraints from basanites and nephelinites/melilitites from SE Germany, Journal of Petrology, **59** (40): 667-694
- Pfiffner, O. A. (2017) Thick-skinned and thin-skinned tectonics: A global perspective, Geosciences, **7** (3): 71
- Pichavant, M. and Macdonald, R. (2007) Crystallization of primitive basaltic magmas at crustal pressures and genesis of the calc-alkaline igneous suite: experimental evidence from St Vincent, Lesser Antilles arc, Contributions to Mineralogy and Petrology, **154**: 535-558
- Prodehl, C.; Mueller, S.; Glahn, A.; Gutscher, M. and Haak, V. (1992) Lithospheric cross sections of the European Cenozoic rift system, Tectonophysics, **208**: 113-138
- Pupier, E.; Barbey, P.; Toplis, M.J. and Bussy, F. (2008) Igneous layering, fractional crystallisation and growth of granitic plutons: the Dolbel batholith in SW Niger, Journal of Petrology, **49** (6): 1043-1068
- Putirka, K. (2016) Amphibole thermometers and barometers for igneous systems and some implications for eruption mechanisms of felsic magmas at arc volcanoes, American Mineralogist, **101** (4): 841-858
- Putirka, K.D. (2008) Thermometers and barometers for volcanic systems, Reviews in Mineralogy and Geochemistry, **69** (1): 61-120
- Rannou, E. and Caroff, M. (2010) Crystal size distribution in magmatic rocks: proposition of a synthetic theoretical model, Journal of Petrology, **51** (5): 1087-1098

- Rausch, J.; Grobéty, B. and Vonlanthen, P. (2015) Eifel maars: Quantitative shape characterization of juvenile ash particles (Eifel Volcanic Field, Germany), Journal of Volcanology and Geothermal Research, **291**: 86-100
- Rees Jones, D. and Katz, R. (2018) Reaction-infiltration instability in a compacting porous medium, Journal of Fluid Mechanics, **852**: 5-36
- Regenauer-Lieb, K. (1998) Dilatant plasticity applied to Alpine collision: ductile void growth in the intraplate area beneath the Eifel volcanic field, Journal of Geodynamics, **27**: 1-21
- Reinig, F.; Cherubini, P.; Engels, S.; Esper, J.; Guidobaldi, G.; Jöris, O.; Lane, C.; Nievergelt, D.; Oppenheimer, C.; Park, C.; Pfanz, H.; Riede, F.; Schmincke, H-.U.; Street, M.; Wacker, L. and Büntgen, U. (2020) Towards a dendrochronologically refined date of the Laacher See eruption around 13,000 years ago, Quaternary Science Reviews, **229**: 106128
- Renna, M.R. and Tribuzio, R. (2011) Olivine-rich troctolites from Ligurian ophiolites (Italy): evidence for impregnation of replacive mantle conduits by MORB-like melts, Journal of Petrology, **52**: 1763-1790
- Renna, M.R.; Armandola, S.; Becker, H.; Sanfilippo, A.; Tribuzio, R. and Wang, Z.C. (2021) Fractionation of highly siderophile and chalcogen elements in the lower oceanic crust: insights from the troctolites of the Alpine-Apennine Jurassic ophiolites, Lithos, **380**: 105873
- Renzulli, A.; Taussi, M.; Brink, F.J.; Del Moro, S. and Henley, R.W. (2021) Sulphide globules in a porcellanite-buchite composite xenolith from Stromboli volcano (Aeolian Islands, Southern Italy): products of open-system igneous pyrometamorphism, Minerals, **11** (6)
- Resmini, R.G. and Marsh, B.D. (1995) Steady-state volcanism, paleoeffusion rates, and magma system volume inferred from plagioclase crystal size distributions in mafic lavas: Dome Mountain, Nevada, Journal of Volcanology and Geothermal Research, **68** (4): 273-296
- Richardson-Bunbury, J.M. (1996) The Kula Volcanic Field, western Turkey: the development of a Holocene alkali basalt province and the adjacent normal-faulting graben, Geological Magazine, **133** (3): 275-283
- Ridolfi, F.; Renzulli, A. and Puerini, M. (2010) Stability and chemical equilibrium of amphibole in calc-alkaline magmas: an overview, new

thermobarometric formulations and application to subduction-related volcanoes, Contributions to Mineralogy and Petrology, **160** (1): 45-66

- Riede, F. and Kierdorf, U. (2020) The eruption of the Laacher See volcano (similar to 13,000 years BP) and possible fluoride poisoning amongst contemporaneous wildlife and human foragers- Outline of a hypothesis and the way to test it, International Journal of Osteoarchaeology, **30** (6): 855-871
- Ritter, J.R.R.; Jordan, M.; Christensen, U.R. and Achauer, U. (2001) A mantle plume below the Eifel volcanic fields, Germany, Earth and Planetary Science Letters, **186**: 7-14
- Rizzo, A.L.; Faccini, B.; Casetta, F.; Faccincani, L.; Ntaflos, T.; Italiano, F. and Coltorti, M. (2021) Melting and metasomatism in West Eifel and Siebengebirge sub-continental lithospheric mantle: evidence from concentrations of volatiles in fluid inclusions and petrology of ultramafic xenoliths, Chemical Geology, **581**: 120400
- Rock, N.M.S. (1990) The International Mineralogical Association (INA/CNMMN) pyroxene nomenclature scheme: computerization and its consequences, Mineralogy and Petrology, **43** (2): 99-119
- Roelofse, F.; Ashwal, L.D.; Pinedra-Vargas, C. and Przybyłowicz, W.J. (2009) Enigmatic textures developed along plagioclase-augite grain boundaries at the base of the Main Zone, Northern Limb, Bushveld complex – evidence for late stage melt infiltration into a nearly solidified crystal mush, South African Journal of Geology, **112** (1): 39-46
- Rudge, J.F.; Holness, M.B. and Smith, G.C. (2008) Quantitative textural analysis of packing of elongate crystals, Contributions to Mineralogy and Petrology, **156**: 413-429
- Ruprecht, P.; Bergantz, G.W.; Cooper, K.M. and Hildreth, W. (2012) The crustal magma storage system of Volcan Quizapu, Chile, and the effects of magma mixing on magma diversity, Journal of Petrology, **53** (4): 801-840
- Rust, A.C.; Manga, M. And Cashman, K.V. (2003) Determining flow type, shear rate and shear stress in magmas from bubble shapes and orientations, Journal of Volcanology and Geothermal Research, **122** (1-2) 111-132

- Saadat, S.; Stern, C.R. and Moradian, A. (2014) Petrochemistry of ultrapotassic tephrites and associated plutonic xenoliths with carbonatite affinities from the late Quaternary Qa'le Hasan Ali maars, central Iran, Journal of Asian Earth Sciences, **89**: 108-122
- Salaün, A.; Villemant, B.; Semet, M.P. and Staudacher, T. (2010) Cannibalism of olivine-rich cumulate xenoliths during the 1998 eruption of Piton de la Fournaise (La Réunion hotspot): implications for the generation of magma diversity, Journal of Volcanology and Geothermal Research, **198**: 187-204
- Salisbury, M.J.; Bohrson, W.A.; Clynne, M.A.; Ramos, F.C. and Hoskin, P. (2008) Multiple plagioclase crystal populations identified by crystal size distribution and in situ chemical data: implications for timescales of magma chamber processes associated with the 1915 eruption of Lassen Peak, CA, Journal of Petrology, **49** (10): 1755-1780
- Saltzer, R.L.; Chatterjee, N. and Grove, T.L. (2001) The spatial distribution of garnets and pyroxenes in mantle peridotites: pressure-temperature history of peridotites and Kaapvaal Craton, Journal of Petrology, **42** (12): 2215-2229
- Sanfilippo, A. and Tribuzio, R. (2013) Origin of olivine-rich troctolites from the oceanic lithosphere: a comparison between the Alpine Jurassic ophiolites and modern slow spreading ridges, Ofiolitti, **38**: 89-99
- Sanfilippo, A.; MacLeod, C.J.; Tribuzio, R.; Lissenberg, C.J. and Zanetti, A. (2020) Early-stage melt-rock reaction in a cooling crystal mush beneath a slow-spreading mid-ocean ridge (IODP Hole U1473A, Atlantis Bank, southwest Indian Ridge, Frontiers in Earth Sciences, **8**: 473
- Sato, H.; Holtz, F.; Botcharnikov, R.E. and Nakada, S. (2017) Intermittent generation of mafic enclaves in the 1991-1995 dacite of Unzen volcano recorded in mineral chemistry, Contributions to Mineralogy and Petrology, **172**: 22
- Satsukawa, T.; Ildefonse, B.; Mainprice, D.; Morales, L.; Michibayashi, K. and Barou, F. (2013) A database of plagioclase crystal preferred orientations (CPO) and microstructures – implications for CPO origin, strength, symmetry and seismic anisotropy in gabbroic rocks, Solid Earth, **4**: 511

- Saxena, N.; Day-Stirrat, R.J.; Hows, A. and Hofmann, R. (2021) Application of deep learning for semantic segmentation of sandstone thin sections, Computers and Geosciences, **152**: 104778
- Scaillet, B. and Evans, B.W. (1999) The 15 June 1991 eruption of Mount Pinatubo. I. Phase equilibria ad pre-eruption P-T-fO_2-fH_2O conditions of dacite magma, Journal of Petrology, **40** (3): 381-411
- Scaillet, B. and Macdonald, R. (2001) Phase relations of peralkaline silicic magmas and petrogenetic implications, Journal of Petrology, **42** (4): 825-845
- Schaaf, P.; Stimac, J.; Siebe, C. And Macias, J.L. (2005) Geochemical evidence for mantle origin and crustal processes in volcanic rocks from Popocatepetl and surrounding monogenetic volcanoes, central Mexico, Journal of Petrology, **46** (6): 1243-1282
- Schäfer, A. and Siehl, A. (2002) Preface: Rift tectonics and syngenetic sedimentation – the Cenozoic lower Rhine Basin and related structures, Netherlands Journal of Geosciences, **81** (2): 145-147
- Schäfer, A.; Utescher, T.; Klett, M. and Valdivia-Manchego, M. (2005) The Cenozoic lower Rhine Basin – rifting, sedimentation, and cyclic stratigraphy, International Journal of Earth Sciences, **94**: 621-639
- Schmidt, M.W.; Forien, M.; Solferino, G. and Bagdassarov, N. (2012) Settling and compaction of olivine and basaltic magmas: an experimental study on the time scales of cumulate formation, Contributions to Mineralogy and Petrology, **164**: 959-976
- Schmincke, H. -U.; Lorenz, V. and Seck, H.A. (1983) The Quaternary Eifel Volcanic Fields, In: Fuchs K., K.; Gehlen, K.; Mälzer, H. and Semmel, A. (eds) Plateau Uplift. Springer, Berlin, Heidelberg
- Schmincke, H.U. (2007) The Quaternary Volcanic Fields of the East and West Eifel (Germany) In: Ritter, J.R.R., Christensen, U.R. (eds) Mantle Plumes, Springer, Berlin, Heidelberg
- Schmincke, H.U.; Park, C. and Harms, E. (1999) Evolution and environmental impacts of the eruption of Laacher See Volcano (Germany) 12,900 a BP, Quaternary International, **61**: 61-72
- Schmitt, A.K. (2011) Uranium series accessory crystal dating of magmatic processes, Annual Reviews in Earth and Planetary Science, **39**: 321-349

- Schulz, B.; Sandmann, D. and Gilbricht, S. (2020) SEM-based automated mineralogy and its application in geo- and material sciences, Minerals, **10** (11): 1004
- Scoates, J.S.; Lindsley, D.H. and Frost, B.R. (2010) Magmatic and structural evolution of an anorthositic magma chamber: the Poe Mountain intrusion, Laramie anorthosite complex, Wyoming, Canadian Mineralogist, **48** (4): 851-885
- Sengör, A.M.C.; Burke, K. and Dewey, J.F. (1978) Rifts at high angles to orogenic belts: tests for their origin and the upper Rhine Graben as an example, American Journal of Science, **278**: 24-40
- Serre, S.H.; van der Meer, G.H.A.; Waight, T.E.; Scott, J.M.; Munker, C.; Thomsen, T.B. and le Roux, P.J. (2020) Petrogenesis of amphibole megacrysts in lamprophyric intraplate magmatism in southern New Zealand, New Zealand Journal of Geology and Geophysics, **63** (4): 489-509
- Shapiro, N.M.; Droznin, D.V.; Senyukov, S.L.; Gusev, A.A.; Gordeev, E.I. (2017) Deep and shallow long-period volcanic seismicity linked by fluid-pressure transfer, Nature Geoscience, **10**: 442-446
- Shaw, C.S.J. (1997) Origin of sulphide blebs in variably metasomatised mantle xenoliths, Quaternary West Eifel volcanic field, Germany, Canadian Mineralogist, **35**: 1453-1463
- Shaw, C.S.J. (2004) The temporal evolution of three magmatic systems in the West Eifel volcanic field, Germany, Journal of Volcanology and Geothermal Research, **131** (1-3): 213-240
- Shaw, C.S.J. and Eyzaguirre, J. (2000) Origin of megacrysts in the mafic alkaline lavas of the West Eifel volcanic field, Germany, Lithos, **50** (1-3): 75-95
- Shaw, C.S.J. and Klügel, A. (2002) The pressure and temperature conditions and timing of glass formation in mantle-derived xenoliths from Baarley, West Eifel, Germany: the case for amphibole breakdown, lava infiltration and mineral-melt reaction, Mineralogy and Petrology, **72**: 163-187
- Shaw, C.S.J.; Eyzaguirre, J.; Fryer, B. and Gagnon, J. (2005) Regional variations in the mineralogy of metasomatic assemblages in mantle xenoliths from the West Eifel Volcanic Field, Germany, Journal of Petrology, **46**: 945-972

- Shaw, C.S.J.; Woodland, A.B.; Hopp, J. and Trenholm, N.D. (2010) Structure and Evolution of the Rockeskyllerkopf Volcanic Complex, West Eifel Volcanic Field, Germany, Bulletin of Volcanology, **72** (8): 971-990
- Shaw, C.S.J.; Lebert, B.S. and Woodland, A.B. (2018) Thermodynamic modelling of mantle-melt interaction evidenced by veined Wehrlite xenoliths from the Rockeskyllerkopf volcanic complex, West Eifel Volcanic Field, Germany, Journal of Petrology, **59** (1): 59-86
- Shaw, J.E.; Baker, J.A.; Menzies, M.A.; Thirlwall, M.F. and Ibrahim, K.M. (2003) Petrogenesis of the largest intraplate volcanic field on the Arabian plate (Jordan): a mixed lithosphere-asthenosphere source activated by lithospheric extension, Journal of Petrology, **44** (9): 1657-1679
- Shea, T.; Costa, F.; Krimer, D. and Hammer, J.E. (2015) Accuracy of timescales retrieved from diffusion modelling in olivine: a 3D perspective, American Mineralogist, **100**: 2026-2042
- Simakin, A.G. and Bindeman, I.N. (2008) Evolution of crystal sizes in the series of dissolution and precipitation events in open magma systems, Journal of Volcanology and Geothermal Research, **177** (4): 997-1010
- Sleep, N.H. (1974) Segregation of magma from a mostly crystalline mush, Geological Society of America Bulletin, **85**: 1225-1232
- Sliwinski, J.T.; Bachmann, O.; Dungan, M.A.; Huber, C.; Deering, C.D.; Lipman, P.W.; Martin, L.H.J. and Liebske, C. (2017) Rapid pre-eruptive thermal rejuvenation in a large silicic magma body: the case of the Masonic Park Tuff, Southern Rocky Mountain volcanic field, CO, USA, Contributions to Mineralogy and Petrology, **172**: 30
- Smith, D.J. (2014) Clinopyroxene precursors to amphibole sponge in arc crust, Nature Communications, **5**: 4329
- Smith, G.C.; Holness, M.B. and Bunbury, J.M. (2008) Interstitial magmatic scapolite in glass-bearing crystalline nodules from the Kula Volcanic Province, Western Turkey, Mineralogical Magazine, **72** (6): 1243-1259
- Snyder, D. and Tait, S. (1995) Replenishment of magma chambers: comparison of fluid mechanic experiments with field relations, Contributions to Mineralogy and Petrology, **122**: 230-240
- Solano, J.M.S.; Jackson, M.D.; Sparks, R.S.J. and Blundy, J. (2014) Evolution of major and trace element composition during melt migration through

crystalline mush: implications for chemical differentiation in the crust, American Journal of Science, **314** (5): 895-939

- Solano, J.M.S.; Jackson, M.D.; Sparks, R.S.J.; Blundy, J.D. and Annen, C. (2012) Melt segregation in deep crustal hot zones: a mechanism for chemical differentiation, crustal assimilation and the formation of evolved magmas, Journal of Petrology, **53**: 1999-2026
- Solomatov, V.S. and Stevenson, D.J. (1993) Kinetics of crystal-growth in a terrestrial magma ocean, Journal of Geophysical Research Letters – Planets, **98** (E3): 5407-5418
- Soosalu, H.; Key, J.; White, R.S.; Knox, C.; Einarsson, P. and Jakobsdóttir, S.S. (2009) Lower-crustal earthquakes caused by magma movement beneath Askja volcano on the north Iceland rift, Bulletin of Volcanology, **72** (1): 55-62
- Soukrati, A.; Youbi, N.; Grégoire, M.; Berger, J.; Boumehdi, M.A.; Ibhi, A. and Chaham, K.R. (2021) Pyroxenite xenoliths and clinopyroxene megacrysts from the Cenozoic Jbel Saghro volcanic field (Anti-Atlas, Morocco): Petrography, mineral chemistry and equilibration conditions, Geochemistry, **81** (1)
- Sparks, R.S.J. and Marshall, L.A. (1986) Thermal and mechanical constraints on mixing between mafic and silicic magmas, Journal of Volcanology and Geothermal Research, **29**: 99-124
- Sparks, R.S.J.; Annen, C.; Blundy, J.D.; Cashman, K.V.; Rust, A.C. and Jackson, M.D. (2019) Formation and dynamics of magma reservoirs, Philosophical transactions of the Royal Society A – Mathematical Physical and Engineering Sciences, **377**, (2319)
- Spera, F.J. (1984) Carbon dioxide in petrogenesis III: role of volatiles in the ascent of alkaline magma with special reference to xenolith bearing mafic magmas, Contributions to Mineralogy and petrology, **88**: 217-232
- Spera, F.J. and Bohrson, W.A. (2018) Rejuvenation of crustal magma mush: a tale of multiply nested processes and timescales, American Journal of Science, **318**: 90-140
- Spiegelman, M.; Keleman, P.B. and Aharonov, A. (2001) Causes and consequences of flow organization during melt transport: the reaction

infiltration instability in compactible media, Journal of Geophysical Research Atmospheres, **106** (B2): 2061-2078

- Stock, M.J.; Taylor, R.N. and Gernon, T.M. (2012) Triggering of major eruptions recorded by actively forming cumulates, Scientific Reports, **2** (731)
- Stosch, H. – G.; Schmucher, A. and Reys, C. (2007) The nature and geological history of the deep crust under the Eifel, Germany, Terra Nova, **4** (1): 53-62
- Streck, M.J. (2008) Mineral textures and zoning as evidence for open system processes, Reviews in Mineralogy and Geochemistry, **69**: 595-622
- Stripp, G.; Holness, M. and Veksler, I. (2006) Enigmatic late-stage textures in mafic cumulates: Skaergaard intrusion, East Greenland, American Geophysical Union, Fall Meeting, Abstract# V51B-1672, San Francisco, USA
- Sun, S.S. and McDonough, W.F. (1989) Chemical and isotopic systematics of oceanic basalts: implications for mantle composition and processes, Geological Society Special Publications, **42**: 313-345
- Svetov, S.A.; Chazhengina, S.Y. and Stepanova, A.V. (2020) Geochemistry and texture of clinopyroxene phenocrysts from Paleoproterozoic picrobasalt, Karelian Craton, Fennoscandian Shield: records of magma mixing processes, Minerals, **10** (5)
- Swanson, S.E. (1977) Relation of nucleation and crystal-growth rate to the development of granitic textures, American Mineralogist, **62** (9-10): 966-978
- Taddeucci, J.; Pompilio, M. And Scarlato, P. (2004) Conduit processes during the July-August 2001 explosive activity of Mt. Etna (Italy): inferences from glass chemistry and crystal size distribution of ash particles, Journal of Volcanology and Geothermal Research, **137** (1-3): 33-54
- Tait, S. and Jaupart, C. (1992) Compositional convection in a reactive crystalline mush and melt differentiation, Journal of Geophysical Research, **97**: 6735-6756
- Tait, S.R.; Worner, G.; Vandenbogaard, P. and Schminke, H.U. (1989) Cumulate nodules as evidence for convective fractionation in a phonolite magma chamber, Journal of Volcanology and Geothermal Research, **37** (1): 21-37

- Tang, C.N.; Bao, C.Y.; Li, S.Z. and Xia, K.W. (2016) A stress-rifting origin of Grand Canyon, Science Bulletin, **61**, (6): 495-504
- Tang, D.G.; Milliken, K.L. and Spikes, K.T. (2020) Machine learning for point counting and segmentation of arenite in thin section, Marine and Petroleum Geology, **120**: 104518
- Taylor, L.A.; Nazarov, M.A.; Shearer, C.K.; McSween, H.Y.; Cahill, J.; Neal, C.R.; Ivanova, M.A.; Baruskova, L.D.; Lentz, R.C.; Clayton, R.N. and Mayeda, T.K. (2002) Martian meteorite Dhofar 019: A new shergottite, Meteoritics & Planetary Sciences, **37** (8): 1107-1128
- Tegner, C.; Thy, P.; Holness, M.B.; Jakobsen, J.K. and Lesher, C.E. (2009) Differentiation and compaction in the Skaergaard intrusion, Journal of Petrology, **50** (5): 813-840
- Thomson Jr, J.B. (1947) Role of aluminium in the rock-forming silicates, Geological Society of America Bulletin, **58** (12): 1232
- Thomson, P.-R.; Aituar-Zhakupova, A. and Hier-Majumder, S. (2018) Image segmentation and analysis of pore network geometry in two natural sandstones, Frontiers in Earth Science, **6** (58): 1-14
- Thomson, P.-R.; Hazel, A. and Hier-Majumder, S. (2019) The influence of microporous cements on the pore network geometry of natural sedimentary rocks, Frontiers in Earth Science, **7** (48): 1-14
- Thomson, R.-R.; Jefferd, M.; Clark, B.L. Chiarella, D.; Mitchell, T.M. and Hier-Majumder, S. (2020) Pore network analysis of Brae Formation sandstone, North Sea, Marine and Petroleum Geology, **122**: 104614
- Tiepolo, M.; Bottazzi, P.; Foley, S.; Oberti, R.; Vannucci, R. and Zanetti, A. (2001) Fractionation of Nb and Ta from Zr and Hf at mantle depths: the role of titanian pargasite and kaersutite, Journal of Petrology, **42**: 221-232
- Tollan, P.M.E.; Bindeman, I. and Blundy, J.D. (2012) Cumulate xenoliths from St. Vincent, Lesser Antilles island arc: a window into upper crustal differentiation of mantle derived basalts, Contributions to Mineralogy and Petrology, **163**: 189-208
- Turbeville, B.N. (1992a) Relationships between chamber margin accumulates and pore liquids – evidence from arrested in situ processes in ejecta, Latera Caldera, Italy, Contributions to Mineralogy and Petrology, **110** (4): 429-441

- Turbeville, B.N. (1992b) Sidewall differentiation in an alkali magma chamber: evidence from syenite xenoliths in tuffs of the Latera caldera, Italy, Geological Magazine, **130**: 453-470
- Ubide, T.; Galé, C.; Larrea, P.; Arranz, E. and Lago, M. (2014) Antecrysts and their effect on rock compositions: the Cretaceous lamprophyre suite in the Catalonian Coastal Ranges (NE Spain) Lithos, **206-207**: 214-233
- Van der Zwan, F.M.; Chadwick, J.P. and Troll, V.R. (2013) Textural history of recent basaltic-andesites and plutonic inclusions from Merapi volcano, Contributions to Mineralogy and Petrology, **166** (1): 43-63
- Vannucci, R.; Bottazzi, P.; Wulff-Pedersen, E. and Neumann, E.R. (1998) Partitioning of REE, Y, Sr, Zr and Ti between clinopyroxene and silicate melts in the mantle under La Palma (Canary Islands): implications for the nature of the metasomatic agent, Earth and Planetary Science Letters, **158** (1-2): 39-51
- VanTongeren, J.A.; Hirth, G. and Kelemen, P.B. (2015) Constraint on the accretion of the gabbroic lower oceanic crust from plagioclase lattice preferred orientation in the Samail ophiolite, Earth and Planetary Science Letters, **427**: 249-261
- Vasseur, J.; Wadsworth, F.B. and Dingwell, D.B. (2020) Permeability of polydisperse magma foam, Geology, **48** (6): 536-540
- Vinken, R. (1991) The Northwest European Tertiary basin, results of the international geological correlation programme, project No. 124, Geologisches Jahrbuch, **A 100**: 508
- Voll, G. (1983) Crustal xenoliths and their evidence for crustal structure underneath the Eifel Volcanic District, In: Fuchs K., K.; Gehlen, K.; Mälzer, H. and Semmel, A. (eds) Plateau Uplift. Springer, Berlin, Heidelberg
- Voltolini, M.; Zandomeneghi, D.; Mancini, L. and Polacci, M. (2011) Texture analysis of volcanic rock samples: Quantitative study of crystals and vesicles shape preferred orientation from X-ray microtomography data, Journal of Volcanology and Geothermal Research, **202**: 83-95
- Vukmanovic, Z. and Holness, M. (2018) Syn-magmatic deformation of the Upper-zone anorthosites of the Bushveld Complex, South Africa, EGU General Assembly 2018, 6503, Vienna, AT

- Wadell, H. (1933) Sphericity and roundness of rock particles, The Journal of Geology, **41** (3): 310-331
- Wager, L.R. and Brown, C.M. (1967) Layered igneous complexes, Oliver and Boyd, Edinburgh: 588
- Walker, K.T.; Bokelmann, G. H. R.; Klemperer, S.L.; Bock, G. and the Eifel Team (2007) Seismic anisotropy in the asthenosphere beneath the Eifel, In: J.R.R. Ritter and U.R. Christiensen (Eds.), Mantle Plumes – A multidisciplinary Approach: 493-464; Heidelberg: Springer Verlag.
- Ward, K.M.; Zandt, G.; Beck, S.L.; Christensen, D.H. and McFarlin, H. (2014) Seismic imaging of the magmatic underpinnings beneath the Altiplano-Puna volcanic complex from the joint inversion of surface wave dispersion and receiver functions, Earth and Planetary Science Letters, **404**: 43-53
- Wark, D.A.; Williams, C.A.; Watson, E.B. and Price, J.D. (2003) Reassessment of pore shapes in microstructurally equilibrated rocks, with implications for permeability of the upper mantle, Journal of Geophysical Research, **108** (B1)
- Watts, K.E.; John, D.A.; Colgan, J.P.; Henry, C.D.; Bindeman, I.N. and Schmitt, A.K. (2016) Probing the volcanic-plutonic connection and the genesis of crystal-rich rhyolite in a deeply dissected supervolcano in the Nevada Great Basin: source of the Late Eocene Caetano Tuff, Journal of Petrology, **57** (8): 1599-1644
- Wedepohl, K.H. and Baumann, A. (1999) Central European Cenozoic plume volcanism with OIB characteristics and indications of a lower mantle source, Contributions to Mineralogy and Petrology, **136**: 225-239
- Weinberg, R.F.; Sial, A.N. and Pessoa, R.R. (2001) Magma flow within the Tavares pluton, northeastern Brazil: compositional and thermal convection, Geological Society of America Bulletin, **113** (4): 508-520
- Welsch, B.; Faure, F.; Famin, V.; Baronnet, A. and Bachelery, P. (2013) Dendritic crystallization: a single process for all the textures of olivine in basalts?, Journal of Petrology, **54** (3): 539-574
- White, R.S. (1993) Melt production rates in mantle plumes, Philosophical Transaction of the Royal Society of London, **342**: 137-153
- Wilcock, J.; Goff, F.; Minarik, W.G. and Stix, J. (2012) Magmatic recharge during the formation and resurgence of the Valles Caldera, New Mexico,

USA: Evidence from Quartz Compositional zoning and Geothermometry, Journal of Petrology, **54** (4): 635-664

- Willis, K.V.; Srogi, L.; Lutz, T.; Monson, F.C. and Pollock, M. (2017) Phase composition maps integrate mineral compositions with rock textures from the micro-meter to the thin section scale, Computers and Geosciences, **109**: 162-177
- Wilson, A.H.; Zeh, A. and Gerdes, A. (2017) In situ Sr isotopes in plagioclase and trace element systematics in the lowest part of the Eastern Bushveld complex: dynamic processes in an evolving magma chamber, Journal of Petrology, **58** (2): 327-359
- Wilson, M. and Downes, H. (1991) Tertiary-Quaternary extension related alkaline magmatism in Western and Central Europe, Journal of Petrology, **32**: 811-849
- Wilson, M. and Downes, H. (1992) Mafic alkaline magmatism associated with the European Cenozoic rift system, Tectonophysics, **208**: 173-182
- Wilson, M. and Downes, H. (2006) Tertiary-Quaternary intra-plate magmatism in Europe and its relationship to mantle dynamics, In: Gee, D.G. and Stephenson, R. (eds.) European lithosphere dynamics. Geological Society of London Memoir 32. London: Geological Society of London
- Wilson, M.; Downes, H. and Cebria, J. –M. (1995) Contrasting fractionation trends in coexisting continental alkaline magma series Cantal, Massif Central, France, Journal of Petrology, **36**: 1729-1753
- Wilson, M.; Patterson, R.; Ernst, R. and Buchan, K. (2001) Intra-plate magmatism related to hot fingers in the upper mantle: evidence from the Tertiary-Quaternary volcanic province of western and central Europe, Mantle Plumes: their identification through time, Geological Society of America, Special Papers, **352**: 37-58
- Withers, P.J.; Bouman, C.; Carmignato, S.; Cnudde, V.; Grimaldi, D.; Hagen, C.K.; Maire, E.; Manley, M.; Plessis, A.D. and Stock, S.R. (2021) X-ray computed tomography, Nature Reviews Methods Primers, **1**: 18
- Witt-Eickschen, G. and Kramm, U. (1998) Evidence for the multiple stage evolution of the subcontinental lithospheric mantle beneath the Eifel (Germany) from pyroxenite and composite pyroxenite/peridotite xenoliths, Contributions to Mineralogy and Petrology, **131**: 258-272

- Witt-Eickschen, G.; Kaminsky, W.; Kramm, U. and Harte, B. (1998) The nature of young vein metasomatism in the lithosphere of the West Eifel (Germany): geochemical and isotopic constraints from the composite mantle xenoliths from the Meerfelder Maar, Journal of Petrology, **39**: 155-185
- Witt-Eickshen, G.; Seck, H.A.; Mezeger, K.; Eggins, S.M. and Altherr, R. (2003) Lithospheric mantle evolution beneath the Eifel (Germany): Constraints from Sr-Nd-Pb isotopes and trace element abundances in spinel peridtites and pyroxenite xenoliths, Journal of Petrology, **44** (6): 1077-1095
- Witter, M.; Furman, T.; LaFemina, P. And Feineman, M. (2016) Understanding magmatic processes at Telica volcano, Nicaragua: crystal size distribution and textural analysis, American Mineralogist, **101** (5): 1052-1060
- Wotzlaw, J.; Bindemann, I.N.; Watts, K.E.; Schmitt, A.K.; Caricchi, L. and Schaltegger, U. (2014) Linking rapid magma reservoir assembly and eruption trigger mechanisms at evolved Yellowstone-type supervolcanoes, Geology, 42: 807-810
- Wüllner, U.; Christensen, U. and Jordan, M. (2006) Joint geodynamical and seismic modelling of the Eifel plume, Geophysical Journal International, **165**: 357-372
- Yao, Z.; Qin, K.; Wang, Q. and Xue, S. (2019) Weak B-type olivine fabric induced by fast compaction of crystal mush in a crustal magma reservoir, Journal of Geophysical Research: Solid Earth, **124** (4): 3530-3556
- Yaxley, G.M. (2000) Experimental study of the phase and melting relations of homogenous basalt plus peridotite mixtures and implications for the petrogenesis of flood basalts, Contributions to Mineralogy and Petrology, **139**: 326-338
- Yoshinobu, A.S.; Wolak, J.M.; Paterson, S.R.; Pignotta, G.A. and Anderson, H.S. (2009) Determining relative magma and host rock xenolith rheology during magmatic fabric formation in plutons: examples from the middle and upper crust, Geosphere, **5** (3): 270-285
- Youssef, S.; Rosenberg, E.; Gland, N.; Kenter, J. Skalinski, M. and Vizika, O. (2007) High resolution CT and pore-network models to assess petrophysical

properties of homogenous and heterogeneous carbonates, Paper SPE-111427 presented at the SPE/EAGE Reservoir Characterization and Simulation Conference, 28–31 October, 2007, Abu Dhabi, UAE

- Zagwijn W.H.; Beets, D.J.; van den Berg, M.; van Montfrans, H.M. and van Rooijen, P. (1985) Atlas van Nederland in 20 delen, Deel 13 – Geologie Stichting Wetenschappelijke Atlas van Nederland, Staatsuitgeverij (s'Gravenhage): 23
- Zeyen, H.; Volker, F.; Wehrle, V.; Fuchs, K.; Sobolev, S.V. and Altherr, R. (1997) Styles of continental rifting: crust-mantle detachment and mantle plumes, Tectonophysics, **278**: 329-352
- Zhang, Y.; Yu, K. and Qian, H. (2018) LA-ICP-MS analysis of clinopyroxenes in basaltic pyroclastic rocks from the Xisha Islands, northwestern South China Sea, Minerals, **8** (12): 575
- Zhao, K.; Xu, X.S. and Erdmann, E. (2018) Thermodynamic modelling for an incrementally fractionated granite magma system: Implications for the origin of igneous charnockite, Earth and Planetary Science Letters, **499**: 230-242
- Zhou, J-S.; Yang, Z-S.; Hou, Z-G. and Wang, Q. (2020) Amphibole-rich cumulate xenoliths in the Zhazhalong intrusive suite, Gangdese arc: implications for the role of amphibole fractionation during magma evolution, American Mineralogist, **105** (2): 262-275
- Zhu, H.J.; Bozdag, E.; Peter D. and Tromp, J. (2012) Structure of the European upper mantle revealed by adjoint tomography, Nature Geoscience, **5** (7): 493-498
- Zibra, I.; Smithies, R.H.; Wingate, M.T.D. and Kirkland, C.L. (2014) Incremental pluton emplacement during inclined transpression, Tectonophysics, **623**: 100-122
- Zieg, M.J. and Lofgren, G.E. (2006) An experimental investigation of texture evolution during continuous cooling, Journal of Volcanology and Geothermal Research, **154** (1-2): 74-88
- Zieg, M.J. and Marsh, B.D. (2002) Crystal size distributions and scaling laws in the quantification of igneous textures, Journal of Petrology, **43** (1): 85-101

- Zieg, M.J. and Marsh, B.D. (2012) Multiple reinjections and crystal-mush compaction in the Beacon sill, McMurdo Dry Valleys, Antarctica, Journal of Petrology, **53** (12): 2567-2591
- Zingg, T. (1935) Beitrag zur Schotteranalyse. – Schweizeriscke Mineralogische und Petrologische Mitteilungen, **15**: 39-140

Appendix A: Limitations of X-ray computed tomography (CT) for textural analysis of crystalline igneous samples

---

Appendix A presents a pilot study undertaken prior to the data collection presented in the main body of this thesis. This study aimed to investigate whether the limitations associated with analysing crystal textures in 3D were offset by the advantages of viewing and measuring them as true three-dimensional objects. Textural reproductions conducted in 2D (thin section digitisation and image analysis) and 3D (X-ray computed tomography) were compared according to three textural criteria. From this, it was determined that two-dimensional techniques would be the most appropriate methodology by which to quantify the crystal textures within the main body of work.

A Limitations of X-ray tomography for textural analysis of crystalline igneous samples

A.1 Introduction

In a geological sample, textural data can be obtained through either a two- or three-dimensional methodology. The former aims to extrapolate textures from two-dimensional cross sections, whilst the latter aims to reproduce the textures directly in a 3D format using techniques such as serial sectioning (e.g. Bryon et al., 1995) and X-ray computed tomography (CT) (e.g. Ketcham and Carlson, 2001). Both of these approaches present advantages and limitations, which manifest differently for particular sample types and research aims. At present, textural studies of igneous rocks most commonly utilise 2D optical microscopy techniques: different phases can be identified by their optical properties and adjacent crystals of the same mineral phase can be distinguished by differences in the orientation of the crystal lattice. The resolution is controlled by both the pixel size (as governed by the quality of the camera used to image the thin section) and the thickness of the thin section (commonly 30 µm) (Higgins, 2006). However, the advantages of optical microscopy are impeded by its two-dimensional capacity. For example, sectioning artefacts introduce the need to rely on stereological corrections, which can introduce errors into the textural data (e.g. Berger et al., 2011). Additionally, complex textures may be inappropriately sampled by a planar section, providing cross sections that are unrepresentative of the true three-dimensional geometry (e.g. Krimer and Costa, 2017). Three-dimensional analytical methods have therefore gained popularity as an alternative approach, particularly with the continued optimisation of instruments specifically for geological application (e.g. Carlson et al., 2000). Techniques such as CT provide the opportunity to visualise

igneous textures in their true geometries and positions. However, it is a well known limitation that 3D methods cannot identify grain boundaries and as such 3D techniques are often considered unsuitable for rocks with high crystal contents. Therefore, both two- and three-dimensional techniques have limitations that may inhibit their application for textural analysis. This pilot study was undertaken to conduct an evaluation of two- and three-dimensional methods and to compare their suitability for conducting textural analysis of a holocrystalline gabbro sample. This evaluation aimed to produce two digital reproductions of the same rock sample, one made using a two-dimensional approach (digitised thin sections), and the other a three-dimensional approach (X-ray computed tomography). These were then compared in the context of the following criteria:

1) Each mineral phase can be identified
2) Adjacent crystals of the same mineral phase can be distinguished
3) The output does not introduce any significant errors that may impact the textural interpretation of the sample

A medium grained gabbro was chosen as the material for this study, consisting predominantly of plagioclase, clinopyroxene and olivine. This sample was selected at is texturally homogenous, allowing for comparisons between thin sections and CT volumes cut from the rock.

A.2 Methods

A.2.1 Three-dimensional X-ray computed tomography (CT)

X-ray computed tomography (CT) is a non-destructive technique that can be used to visualise the internal structures of opaque geological samples. The sample is placed between an X-ray source and detector, and X-rays are variably attenuated as they pass through materials of differing atomic composition and density (Figure A.1). Two-dimensional radiographs are acquired from different positions as the sample is rotated about its Z-axis, which are then stacked in a direction perpendicular to the axis of rotation to produce a three-dimensional image. The output is composed of three-dimensional pixels (voxels) which represent a 3D matrix of linear X-ray coefficient values (μ). The value of μ is a measure of X-ray absorption, and is a function of a material's atomic number, density and the X-ray energy used in the study. μ is represented as a greyscale value on the final tomographic output. Different greyscale values correspond to different rock phases, permitting visualisation, classification and measurement of the 3D output and its constituents.

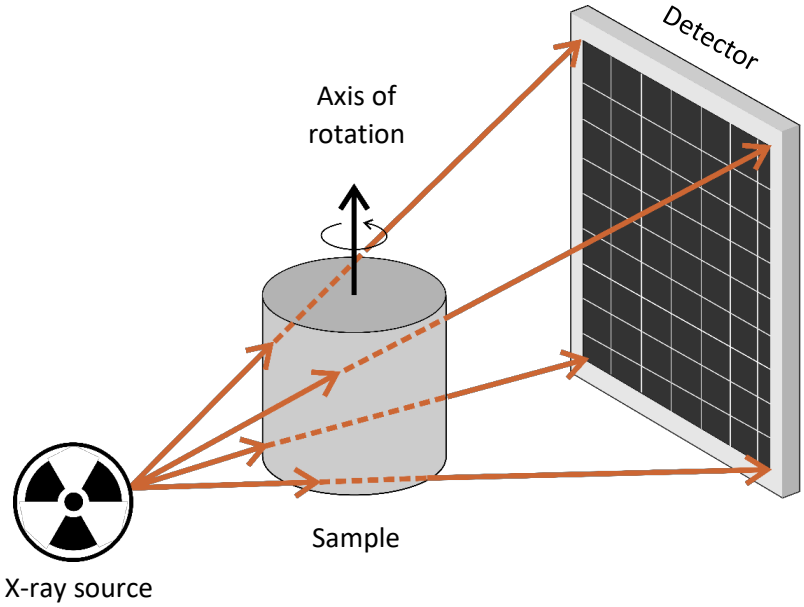

Figure A.1 **–** Schematic representation of a typical CT setup. The sample is illuminated by a fan shaped beam of coplanar X-rays which are variably attenuated as they pass through the sample. The transmitted X-rays are measured and recorded by a detector system and recorded as a 2D radiograph. Redrawn and modified from Withers et al. (2021).

A.2.2 Two-dimensional thin section analysis

Whereas 3D analysis aims to visualise rock textures in their true three-dimensional geometry, 2D analysis aims to take planar samples through a rock and extrapolate cross-sectional data into a three-dimensional population. This is achieved by tracing grain boundaries atop high-resolution slide photographs or scans and using image analysis software to automatically extract the desired textural parameters. This textural data is then mathematically corrected to convert the 2D shape data into 3D, factoring in known limitations of 2D sampling such as the cut section and intersection probability effects (Higgins, 2000).

A.2.3 Sampling

Because samples are rotated about the Z-axis during CT acquisition, the full scan view is a cylinder and therefore the most efficient sample geometry is also a cylinder. Cylinders are isotropic in the scan plane and will therefore ensure equal absorption and penetration of the X-ray beam, reducing the influence of scan artefacts (e.g. Ketcham and Carlson, 2001). Therefore, sampling aimed to identify a cylindrical volume that could be scanned using CT, and then cut to produce thin sections through the same material. To constrain a cylindrical volume that was equally suited for CT and thin section analysis, it was necessary to scrutinise the sample textures to identify a volume with a diameter that was representative of the crystal size distribution in 2D, but small enough to permit sufficient penetration of X-ray beams in 3D.

A.2.3.1 Two-dimensional area analysis

Prior to coring the cylindrical sub-volume, four thin sections (measuring 5 x 7.5 cm) were cut from the sample at different orientations (0°, 45°, 90° and 135° - relative to one another) (Figure A.2).

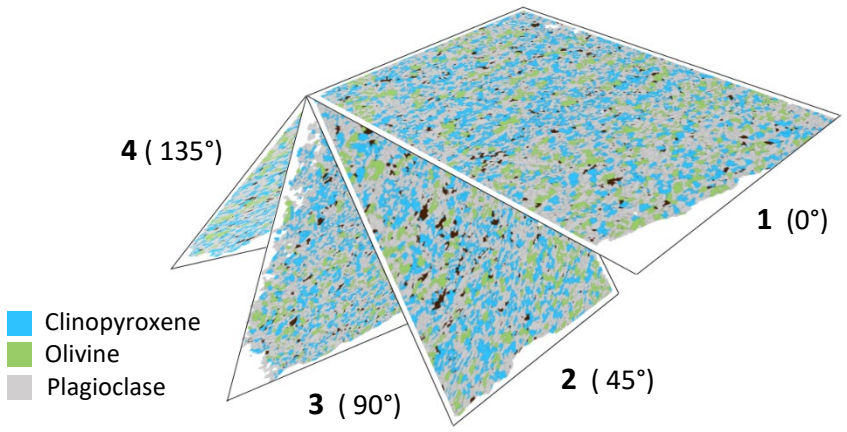

Figure A.2 – Spatial relationship between the thin sections cut from the gabbro sample.

These thin sections were used to investigate the approximate 2D area required to construct a realistic crystal size distribution (CSD). To do this, each of the four sections were digitised by tracing crystal outlines atop high resolution photographs (Figure A.3). A petrographic microscope was used to assist with the digitisations, clarifying instances where mineralogy or grain boundaries were unclear from the photograph. In total 37,326 crystals were identified and traced, in a period of 497 hours.

From these thin sections, 80 random points were selected and a circular sub-sample area (reflecting the cylindrical CT volume) was drawn around each point, varying between 1- 2.5 cm in diameter (Figure A.4). Crystals included within each circular sub-sample area were used to calculate a CSD, using CSDSlice (Morgan and Jerram, 2006) and CSDCorrections v1.50 (Higgins, 2000) to create a stereologically corrected CSD. These CSDs were then compared to a CSD created from the entire thin section area (Figures A.5- A.8). From this, a circular area with a diameter of 2.5 cm was selected as the most representative sub-sample area. This diameter was selected because it yielded the greatest proportion (60%) of CSDs that spanned the crystal size range measured from the whole slide CSD. In comparison, only 42% of the CSDs measured from the 2 cm diameter areas encompassed the full range of crystal sizes. Additionally, a sample size of 250 crystals is often cited as the minimum number of crystals required to produce a realistic CSD (Morgan and Jerram, 2006). The 2.5 cm sample areas also provided the greatest number of CSDs that exceeded 250 crystals.

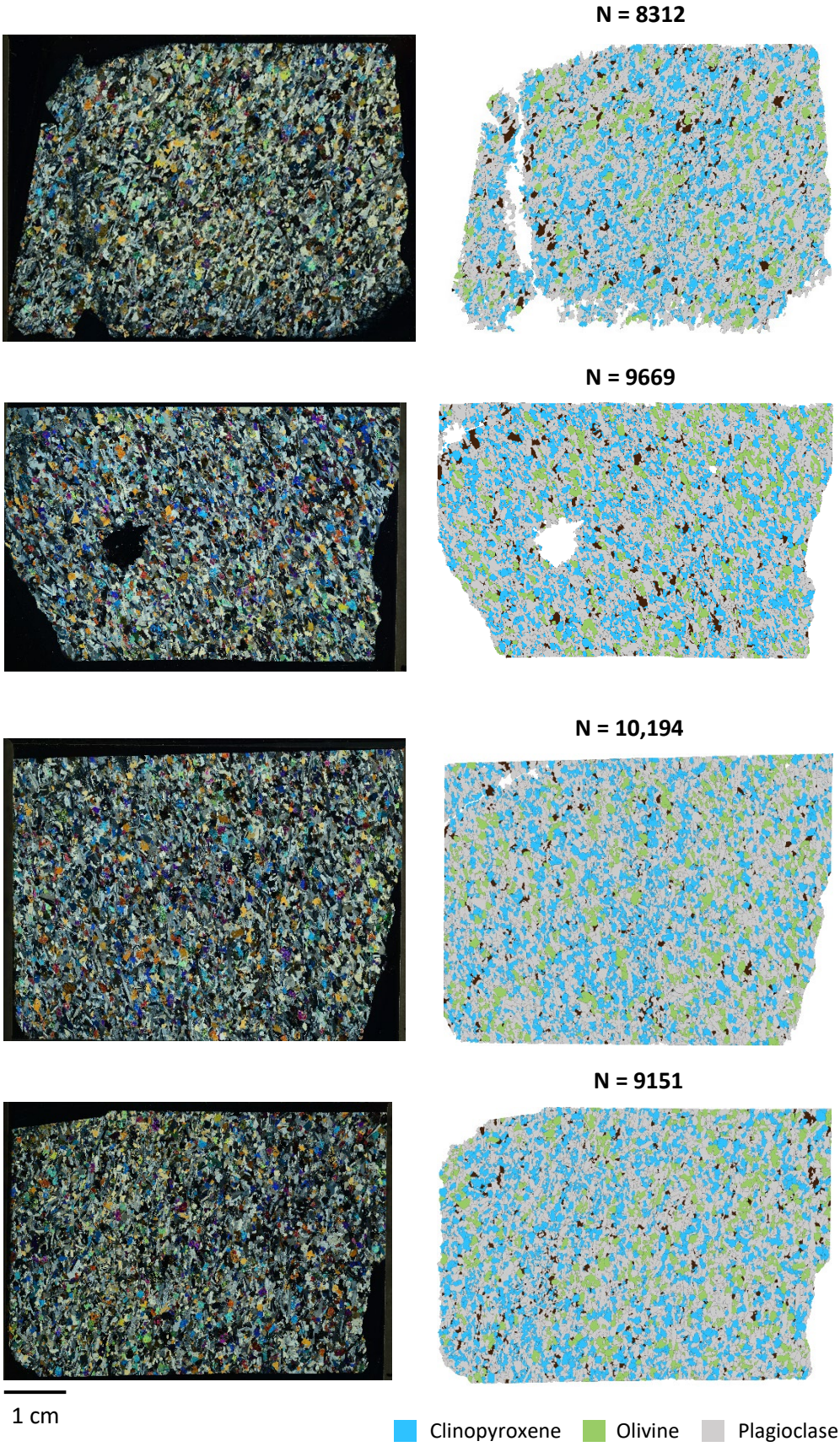

Figure A.3 **–** Thin section photographs taken in cross-polarised light (left), alongside digitisations completed by tracing crystal outlines atop the photos (right).

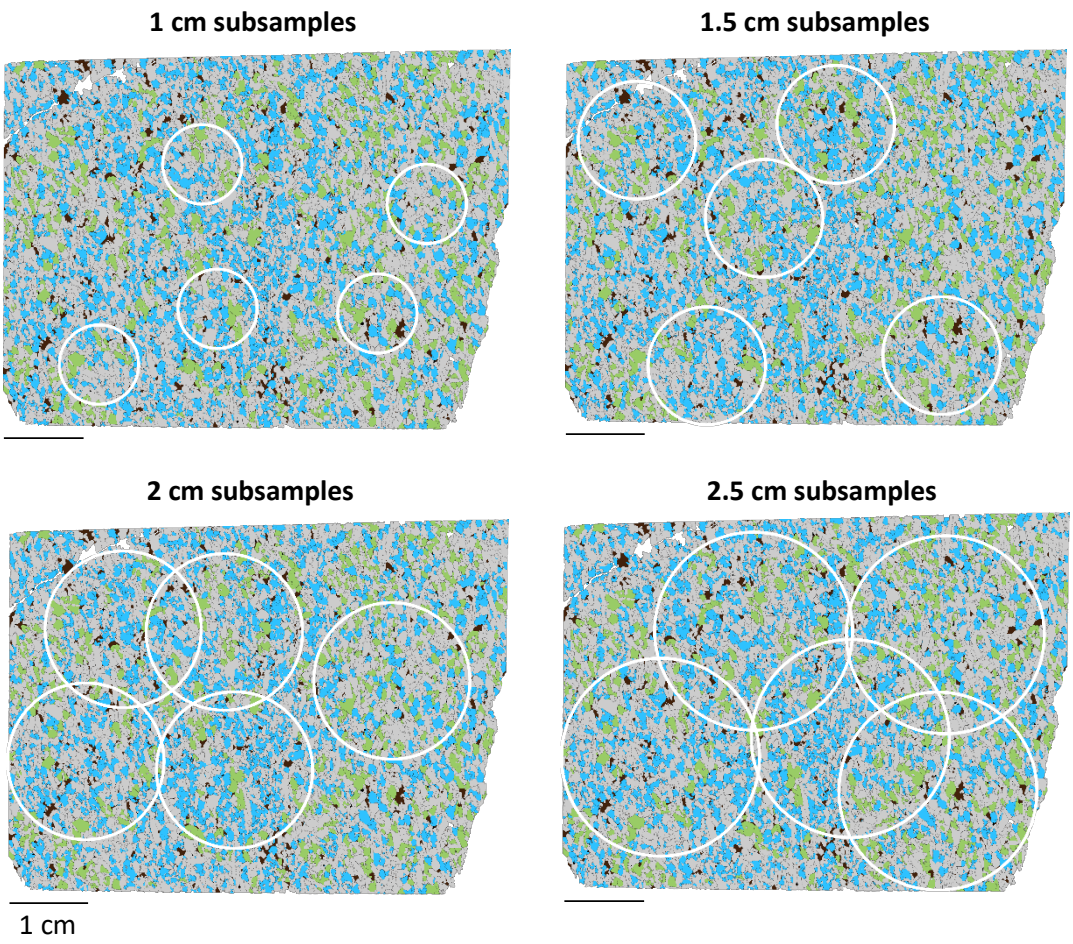

Figure A.4 – Sub-sample areas for 20 random points in thin section 3. Distance in cm refers to the diameter of the circle.

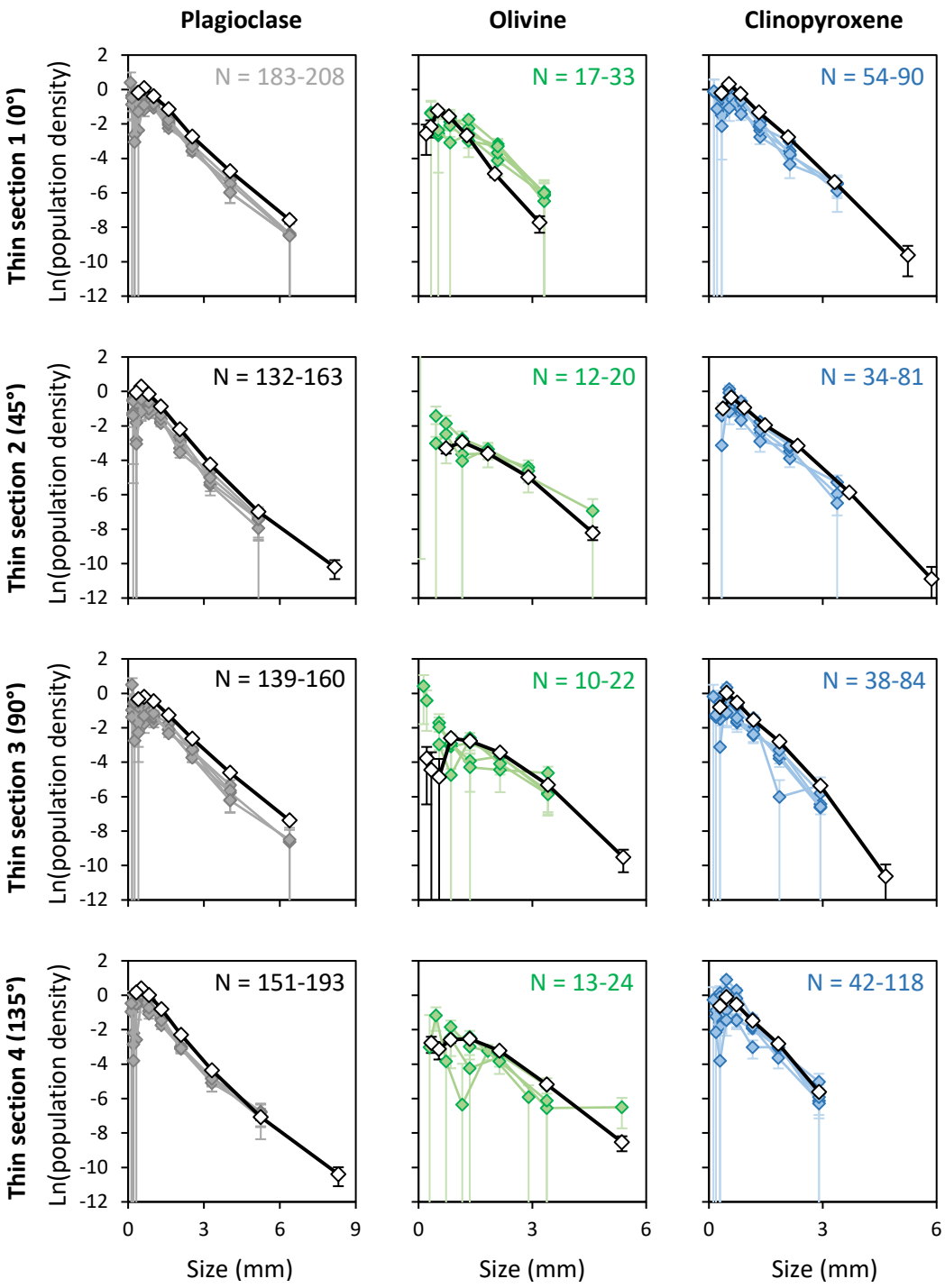

Figure A.5 – Crystal size distribution graphs produced from circular sub-sample areas with a 1 cm diameter. Grey, green and blue coloured lines represent the sub-sample CSDs, black lines are whole slide CSDs. N refers to the range of the number of crystals in the sub-sample CSDs. It is recommended that a CSD should not be constructed from fewer than 250 crystals.

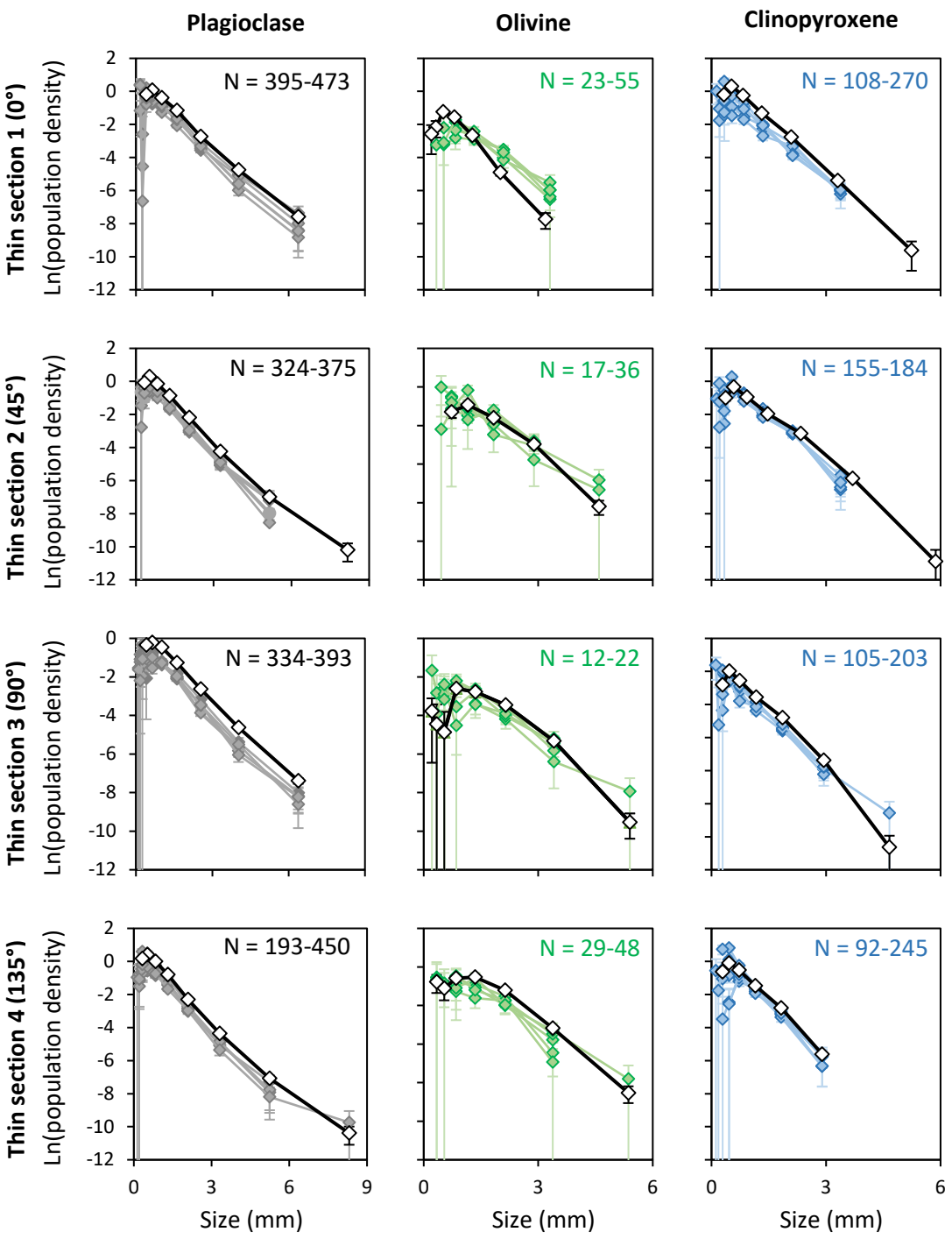

Figure A.6 – Crystal size distribution graphs produced from circular sub-sample areas with a 1.5 cm diameter. Grey, green and blue coloured lines represent the sub-sample CSDs, black lines are whole slide CSDs. N refers to the range of the number of crystals in the sub-sample CSDs. It is recommended that a CSD should not be constructed from fewer than 250 crystals.

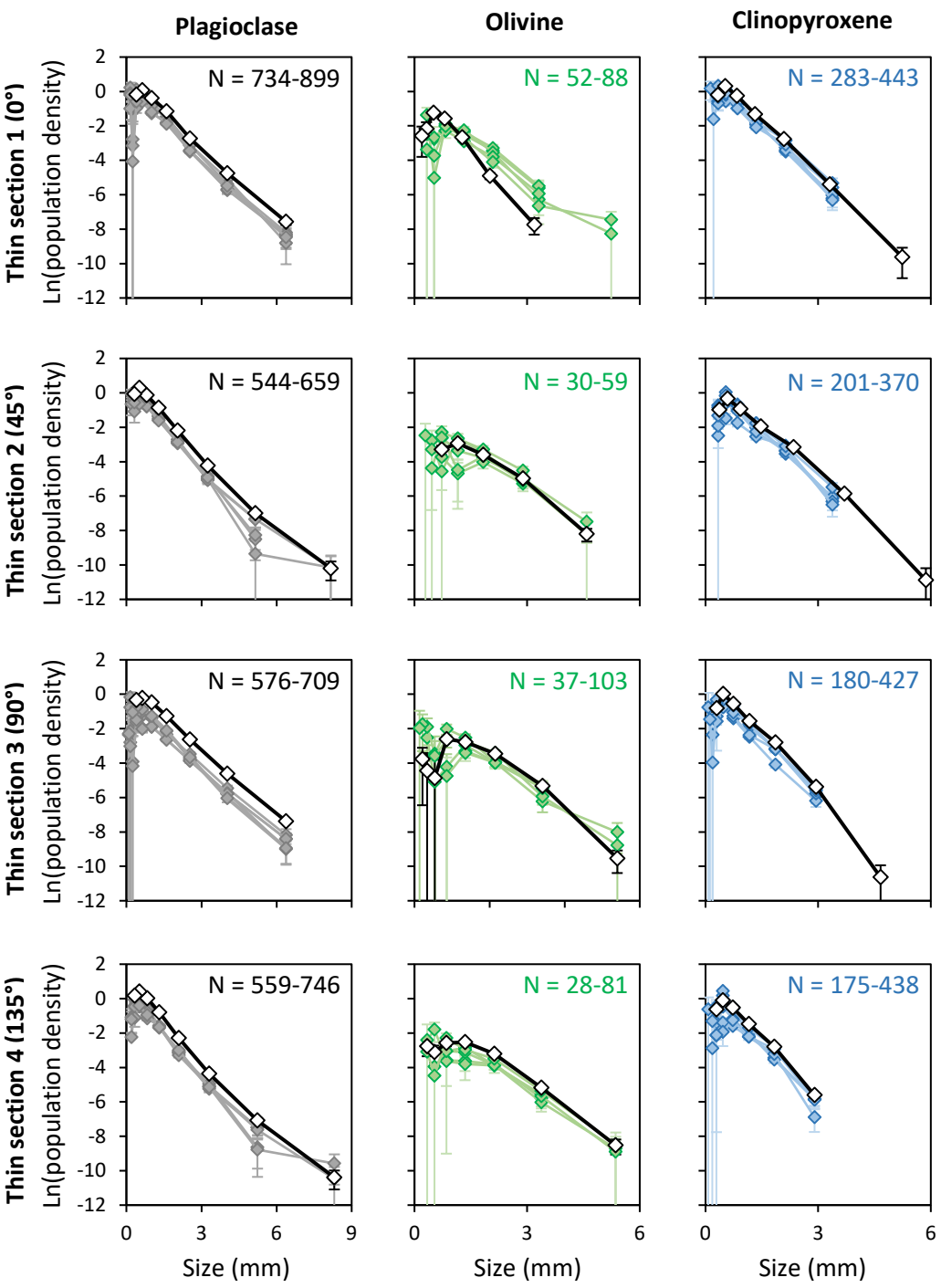

Figure A.7 – Crystal size distribution graphs produced from circular sub-sample areas with a 2 cm diameter. Grey, green and blue coloured lines represent the sub-sample CSDs, black lines are whole slide CSDs. N refers to the range of the number of crystals in the sub-sample CSDs. It is recommended that a CSD should not be constructed from fewer than 250 crystals.

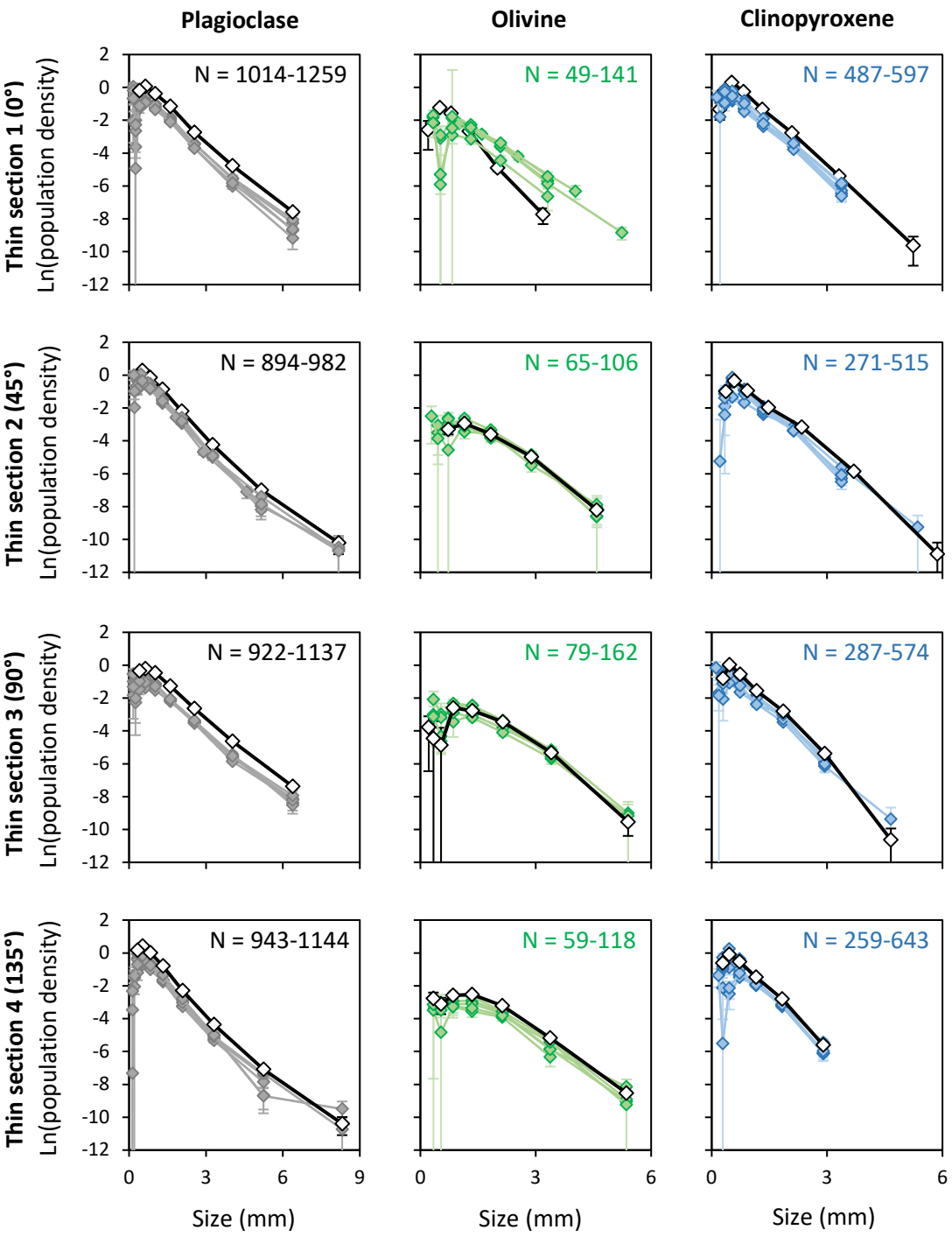

Figure A.8 – Crystal size distribution graphs produced from circular sub-sample areas with a 2.5 cm diameter. Grey, green and blue coloured lines represent the sub-sample CSDs, black lines are whole slide CSDs. N refers to the range of the number of crystals in the sub-sample CSDs. It is recommended that a CSD should not be constructed from fewer than 250 crystals.

A.2.3.2 CT experiment design

Owing to the possible variations in sample size, shape and composition there are no defined and fixed instrumental parameters for CT scanning. Unique to every study, the volume of the sample material will govern the experimental parameters required to penetrate through the volume, at a voltage that permits discrimination of the sample components. The 2D area analysis suggested that a cylindrical volume with a diameter of 2.5 cm provided the most representative sample area. Figure A.9 shows a plot of the expected X-ray survival percentage through a cylindrical sub-volume of this diameter. To do this, An% (plagioclase), Fo% (olivine) and Di% (clinopyroxene) determined using LA-ICP-MS on individual mineral grains were used to input solid solution compositions into MuCalc (Hanna and Ketcham, 2017). MuCalc is a Microsoft Excel workbook that uses X-ray coefficients for individual atomic species (obtained from the experimentally derived online XCOM database (Berger et al., 2010), and collates them into mass X-ray coefficients for a wide array of minerals. X-ray survival is calculated using Lambert-Beer's law:

$$\frac{I}{I_0} = \exp(-\mu x) \times 100$$

where I is the final x-ray intensity, I_0 is the initial X-ray intensity, μ is the linear attenuation coefficient (calculated from the compositional data) and x is the length of material through which the X-ray passes (input by the user as a distance in mm) (Hanna and Ketcham, 2017). In a non-homogenous sample, this equation must be solved for each mineral and its proportionate linear occurrence (Hanna and Ketcham, 2017):

$$\frac{I}{I_0} = \exp[\Sigma(-\mu_i x_i)] \text{ x } 100$$

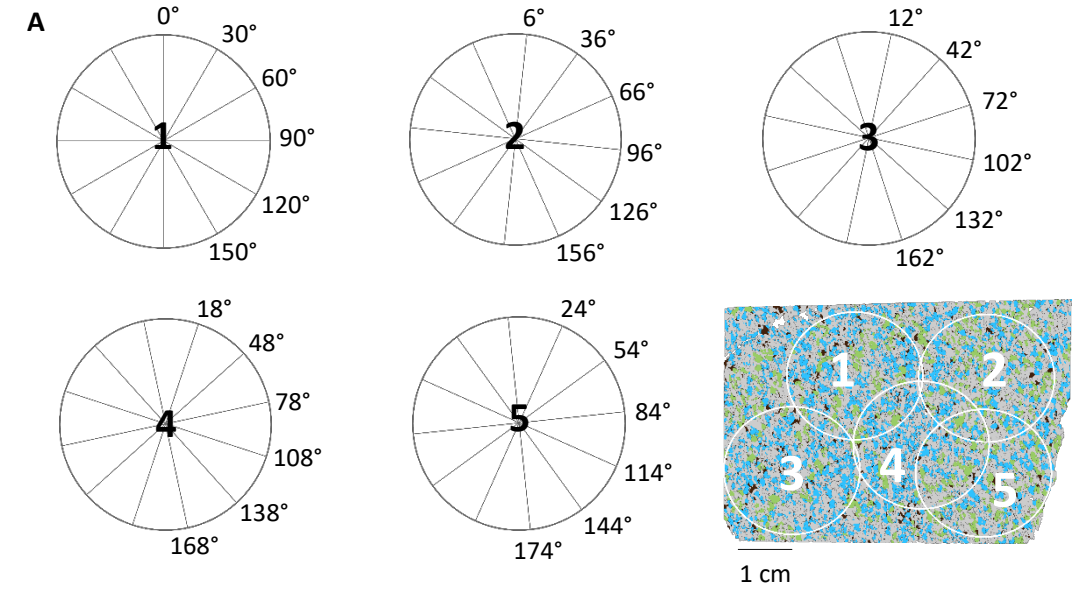

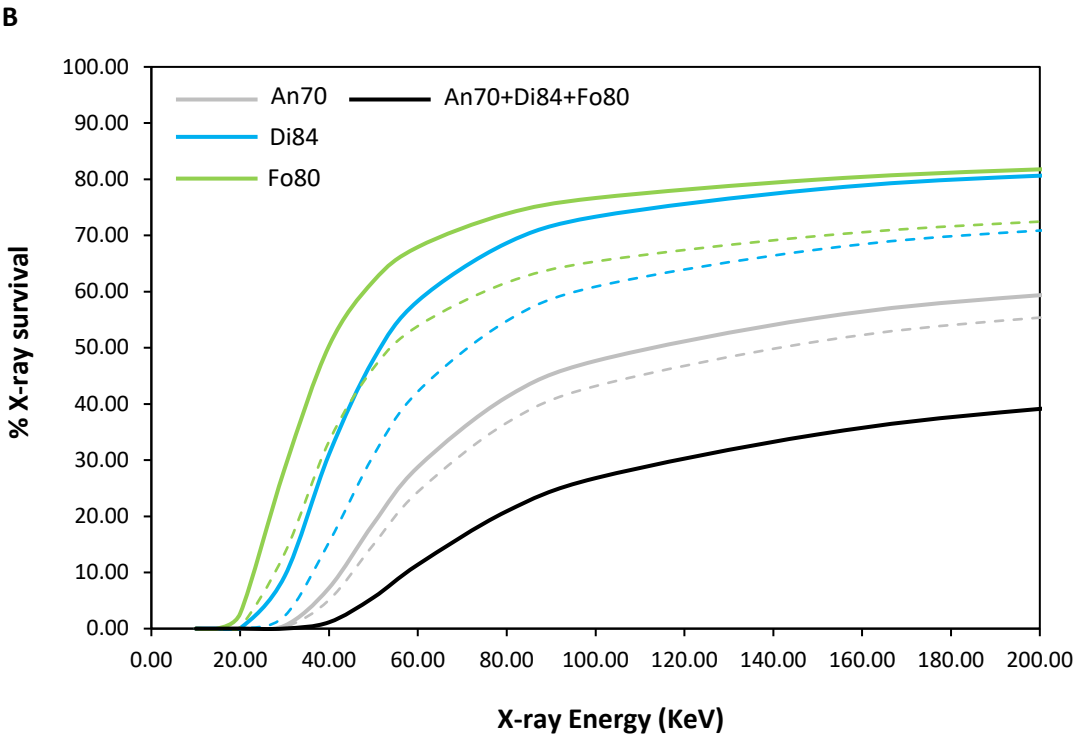

Figure A.9 (caption overleaf) ▶

◄ ***Figure A.9 (overleaf)*** **–** Calculation of X-ray photon survival through a 2.5 cm diameter sample volume. **A)** Transects used to calculate the total distances of plagioclase, clinopyroxene and olivine along straight-line paths through 2.5 cm cross sections. The equation for X-ray survival must be solved for each mineral in a non-homogenous sample, proportionate to its linear distance along the X-ray path. To estimate these length values, transects were drawn through the same circular sample areas used for the CSD analysis in Section A.2.3.1. 6 transects were drawn through each circular area, at 30° intervals and offset by 6° between each sub-sample area. This provided a total of 30 transects at different orientations for each of the four thin sections, with a total of 120 transects across all four thin sections. For each transect, the cumulative distances of plagioclase, clinopyroxene and olivine were measured in the digital image analysis software ImageJ. These distances, alongside mineral compositions determined from LA-ICP-MS, were input into the Excel Workbook MuCalc (Hanna and Ketcham, 2017). The average thickness values for plagioclase (An70%), clinopyroxene (Di84%) and olivine (Fo80%) were 15, 5 and 5 mm respectively. **B)** Graph depicting the expected percentage of X-ray survival at voltages between 10 and 200 KeV. Solid lines represent the average thickness measured from the transect data, dashed lines represent the maximum thickness measured in the transect data. The black line represents the cumulative thickness of each of the three minerals, providing an estimate of X-ray survival through a 2.5 cm X-ray path. X-ray survival was calculated using MuCalc, which uses Lambert-Beer's law to estimate the percentage of X-ray photons that will penetrate the sample and be recorded by the detector to form a CT image. These results suggest that a voltage of at least 80 KeV is required to attain a survival percentage greater than 20% (a minimum estimate of acceptable survival) (Stock, 2009).

Although there is no defined acceptable X-ray survival percentage (minimum estimates exceed >20%) (Stock, 2009), a higher percentage of X-ray survival will improve the signal to noise ratio and generate a better CT output (Verdun et al., 2015). Because the linear attenuation coefficients do not significantly vary from one another over the same energy spectrum (Figure A.10), it was not essential to image at a specific voltage. Therefore, the most important factor when deciding an appropriate study volume was X-ray survival and image quality. Personal communications with CT technicians led to the conclusion that 2.5 cm (the most appropriate diameter for the 2D analysis) would be an appropriate sample diameter, provided the sample was analysed at a voltage greater than 80 KeV.

The final sub-volume was a cylindrical core with an equal diameter and height of 2.5 cm (Figure A.11).

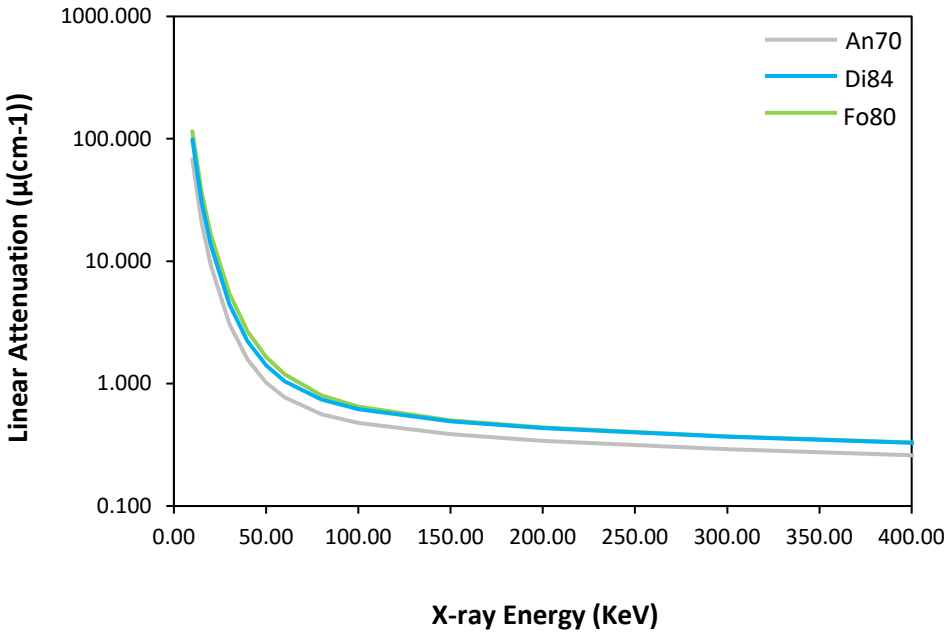

Figure A.10 **–** Plot of the linear attenuation of plagioclase (An 70%), clinopyroxene (Di 84%) and Olivine (Fo 80%) across an X-ray energy spectrum of 10-400 KeV. Solid solution compositions were derived using LA-ICP-MS; linear attenuation coefficients were calculated using MuCalc (Hanna and Ketcham, 2017). Olivine and clinopyroxene are closely attenuating across all X-ray energies, at a maximum discrimination of just 16.392 μ(cm-1) at 10 KeV. However, laboratory CT machines typically utilise a polychromatic beam that features a broad spectrum of energies up to the maximum energy of the incident electrons. This means that the true attenuation variability between sample components will vary as a function of the mean X-ray energy of the polychromatic beam. Therefore, it is unlikely that such closely attenuating minerals would be discriminable at any voltage (personal communication). Therefore, the sample could be analysed at any voltage high enough to penetrate through the sample volume.

Figure A.11 – Sub-volume used for the CT and thin section analysis.

A.2.3.3 Data acquisition

CT scanning was undertaken at the University of Texas high-resolution X-ray computed tomography facility (UTCT), Jackson School of Geosciences, the University of Texas at Austin using a North Star Imaging (NSI) scanner. This hardware uses a Fein Focus FXE High Power transmission source with an aluminium filter and a Perkin Elmer 16 inch 2048 x 2048 detector, generating polychromatic X-rays with an energy range between 70 and 225 kV. A voltage of 150 KV sampled a voxel size of 14.7 µm. A full 360° rotation was used to collect 3000 projections. A filtered back projection algorithm was used to reconstruct the projections into a stack of 1811 16-bit tiff images.

After the CT was completed, the same volume was sequentially sectioned at regular intervals along its Z-axis. The thickness of the cutting blade and the precision of the laser guiding the cutting intervals, permitted a sectioning interval of 1800 µm and provided 6 thin sections (Figure A.12). These thin sections were photographed in both PPL and XPL and digitised by tracing atop the crystal boundaries in a graphic drawing software. A petrographic microscope was used in conjunction with the

photographs to check mineral classification and ensure appropriate tracing around plagioclase twins. The resolution is controlled by both the pixel size of the photographs (14 μm/pixel) and the thickness of the thin section (30 μm). In total, 13,968 crystals were identified and traced in a period of 314 hours. In coarser samples it is often possible to identify continuous crystals between sections, and interpolate the connection between them (e.g. Mock and Jerram, 2005; Garapić et al., 2013). However, this was not possible for the serial sections obtained from this sample as 95% of the crystals have a long axis measurement smaller than the sectioning interval. The final 2D textural reproduction is therefore presented as a stack of images that are spatially related, but texturally discontinuous.

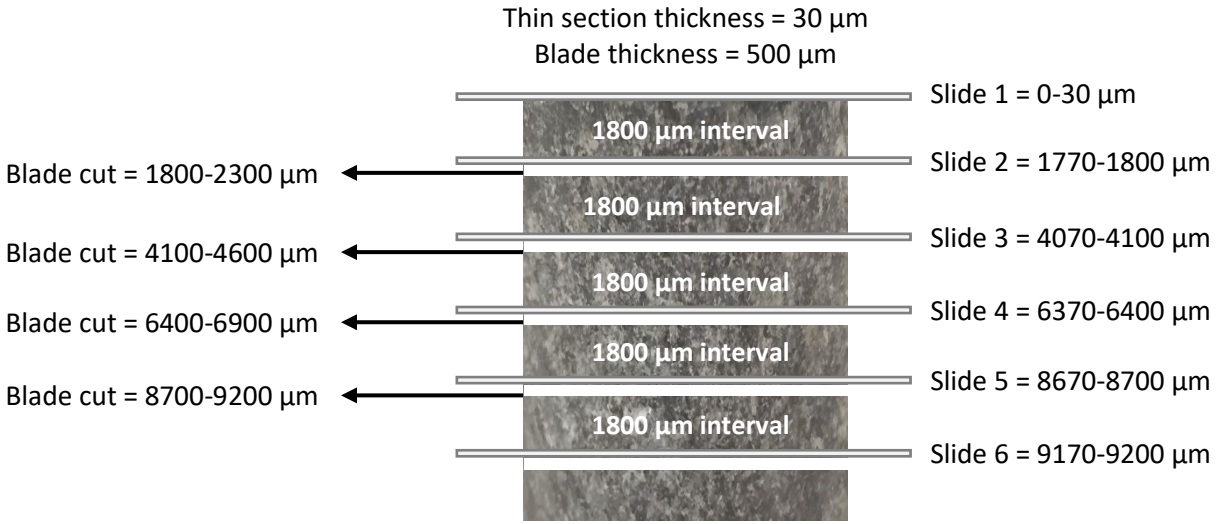

Figure A.12 – Sampling locations of thin sections through the core volume also used for CT analysis. A constant sampling interval of 1800 µm was used, with a 500 µm blade and 30 µm thin section thickness.

A.3 Results

The two-dimensional reproduction is shown in Figure A.13. The model consists of six digitised crystal maps, stacked atop one another to reconstruct their spatial relationship relative to the original cylindrical core. Because crystals are identified and classified during data acquisition, there is no need for additional processing after assembly of the model.

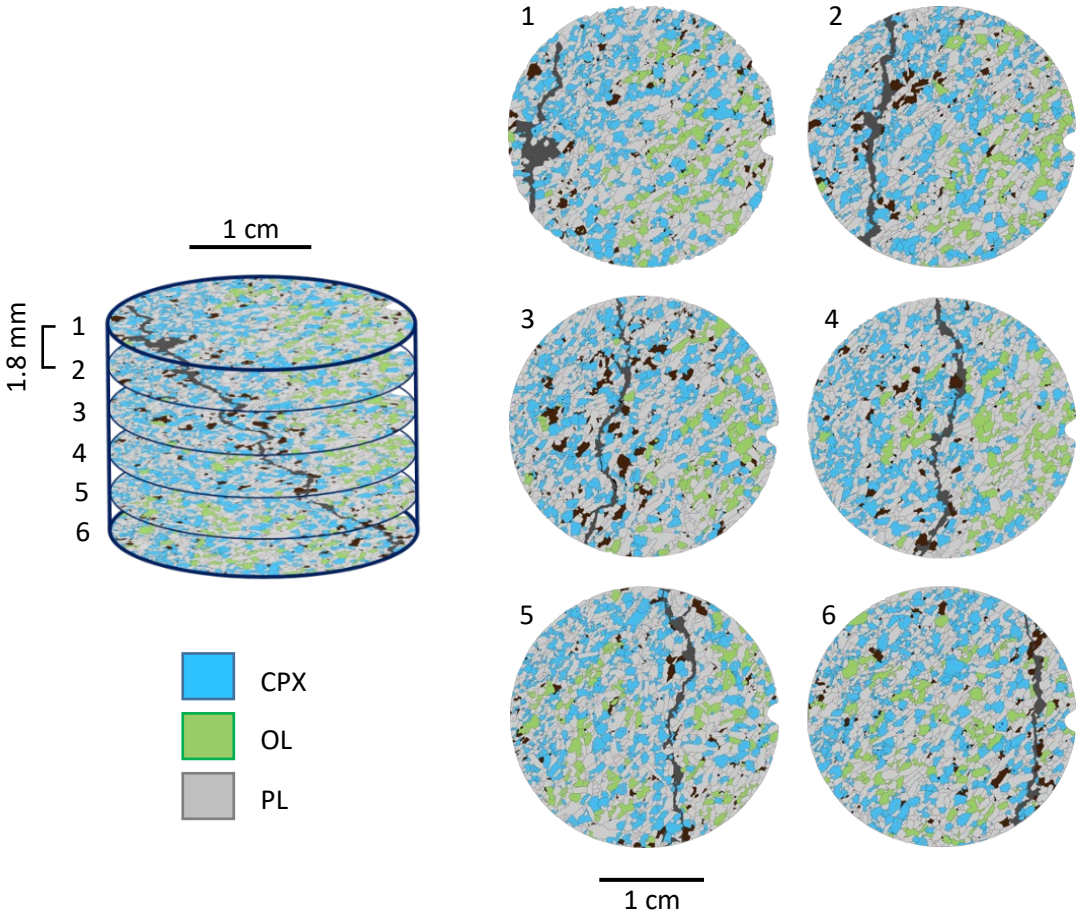

Figure A.13 **–** Two-dimensional reproduction of crystal textures. Thin sections are cut at a 1.8 mm interval down the vertical z-axis of the core. As it was not possible to interpolate crystal connections between the sections, each section is spatially related, but texturally discontinuous. The notch on the left hand side of the digitised thin sections was cut prior to sectioning to allow the thin sections to be aligned during reconstruction and analysis.

CT acquisition provides a stack of greyscale images that can be assembled into a three-dimensional volume. Figure A.14 depicts a three-dimensional rendering of the CT data, without any additional image processing. The data is visualised in the open access software Dragonfly 2020.1 (Object Research Systems).

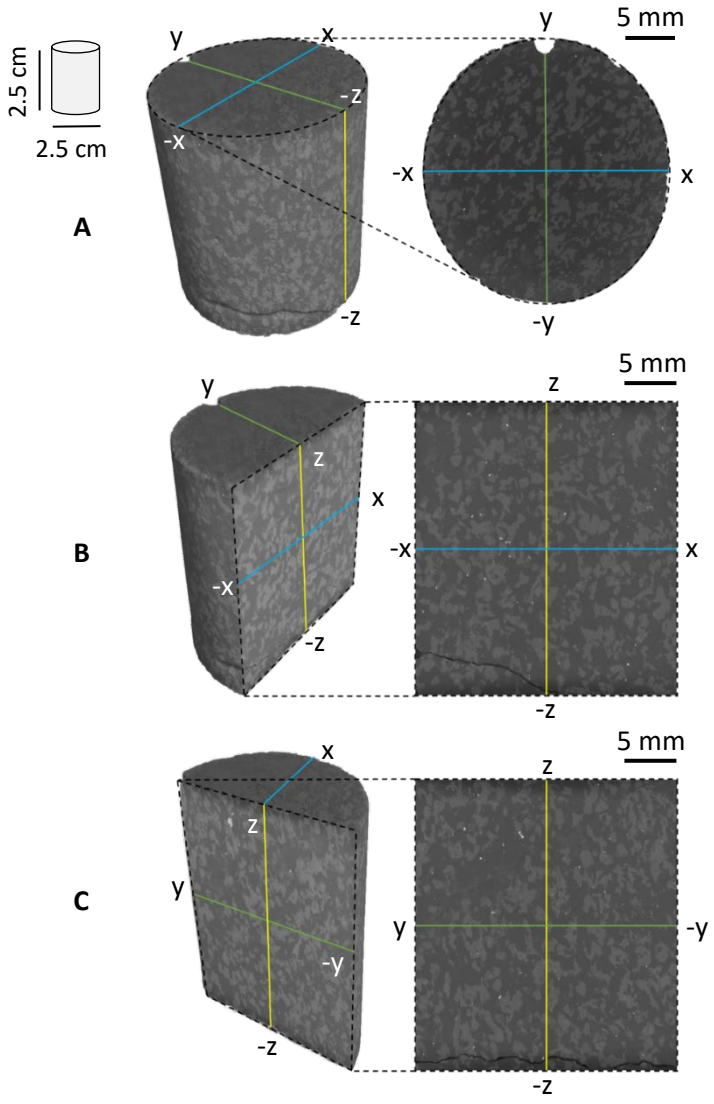

Figure A.14 – Three dimensional rendering of the CT data. ***A)*** Rendering of complete scan volume with parallel view down the vertical z-axis showing projection in X Y plane. ***B)*** Orthogonal projection of rendered volume on the X Z plane. ***C)*** Orthogonal projection of rendered volume on the Y Z plane. 2D cross section images can be extracted from these projections, providing slice images that are orthogonal to the imaging geometry (orthoslices).

However, from initial observations of the CT data it was clear that further image processing would be necessary. Firstly, the output showed significant beam hardening - a common CT artefact that occurs as a consequence of using a polychromatic X-ray beam. This manifests on the CT output as an artificial darkening of the centre of the image, caused by a reduction in the effective attenuation coefficient of the sample materials in response to changes in the mean X-ray energy passing through the sample. Beam hardening therefore acts to make CT processing and segmentation more complicated by changing the greyscale value of a material depending on its position within an image. Figure A.15 demonstrates the extent of beam hardening in the gabbro sample, showing a clear decrease in the average greyscale values in the centre of the image.

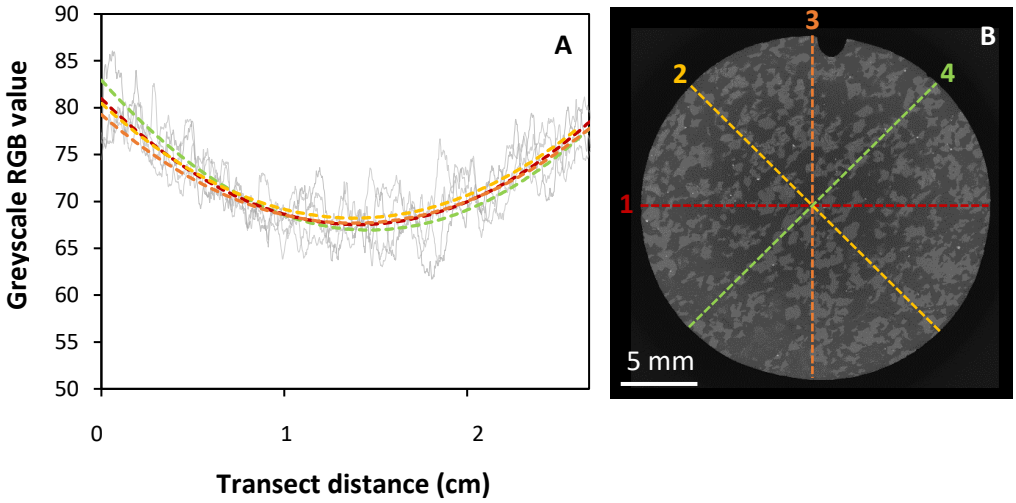

Figure A.15 – A) Transects of average greyscale vales across the CT data. Grey lines are the measured values, coloured lines are fitted trend lines, corresponding to the transects drawn in ***B.*** The transects show a clear cupped profile, demonstrating the extent of the artificial darkening in the centre of the image introduced by beam hardening.

A beam hardening correction was applied using the commercial software PerGeos 1.7.0. PerGeos corrects for beam hardening by applying a simple filter that computes the average radial greyscale intensity profile of the image stack, which is then smoothed with a gaussian filter and normalised. All grey scale intensities in the image stack are then divided by the smoothed profile to perform a radial greyscale averaging. The results of the beam hardening correction are shown in Figure A.16.

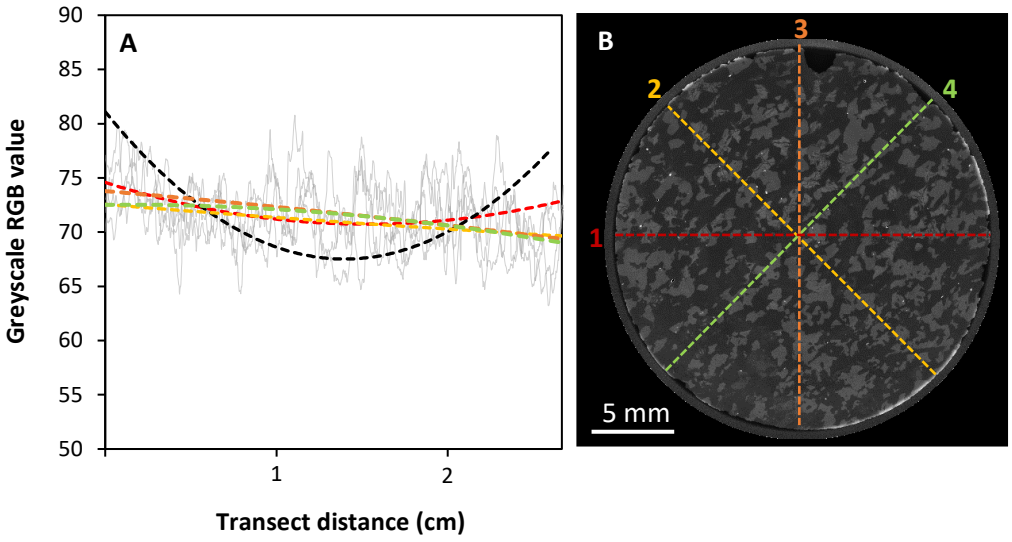

Figure A.16 – A) Transects of average greyscale values across the CT data (positioning shown in ***B***). Coloured lines are trend lines fitted for transects measured after correcting for beam hardening, black line is the averaged greyscale profile measured before beam hardening. The greyscale transects have been significantly flattened, but are not completely uniform. This could be an artefact of the correction method used, or simply a reflection of variations in the materials through which the transect is passing.

In addition, anisotropic diffusion filtering (10 iterations) was applied in ImageJ to reduce image noise whilst preserving edges and boundary lines. Image contrast was enhanced by applying the histogram equalisation function as a means to increase contrast without affecting the structure of the information contained within the image. The results of this filtering are shown in Figure A.17.

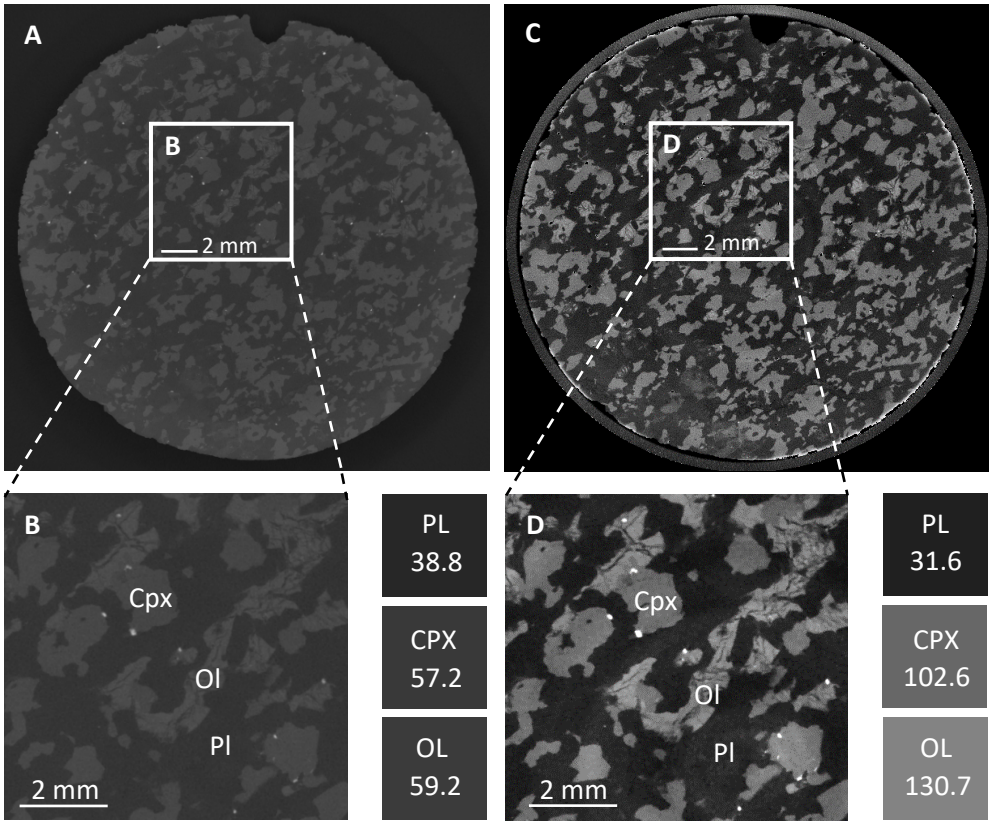

Figure A.17 – A) CT slice image before any image processing or artefact correction. ***B)*** Magnification of greyscale image, highlighting poor discrimination between cpx, ol and pl and their correspondent average greyscale values. ***C)*** The same image as in ***A***, after correction for beam hardening, anisotropic diffusion filtering and histogram equalisation. ***D)*** Magnification of ***C***, showing the improvement in mineral discrimination compared to the original tiff images in ***A*** and ***B***. Most notably, the improvement in the greyscale difference between cpx and ol.

A.4 Discussion

In order to evaluate the two- and three-dimensional models, this discussion compares each model in the context of the criteria outlined in Section A.1. These criteria were selected as essential for the undertaking of quantitative textural analysis including crystal size distribution and spatial distribution analysis.

A.4.1 Each mineral phase can be identified

Each of the mineral phases can be simply identified in 2D by their optical properties. During digitisation, traced crystal outlines are classified to provide a crystal map that visualises each mineral phase (see Figure A.13). The 2D reconstruction therefore satisfies this criteria. In contrast, it is challenging to identify each of the mineral phases in the CT dataset. As expected from the modelled linear attenuation coefficients in Figure A.10, the CT image files show poor greyscale discrimination between clinopyroxene and olivine crystals, but a clear greyscale difference between these phases and plagioclase. However, independent of its greyscale values, olivine can be identified in the CT by the presence of thick alteration lines within the olivine crystals (Figure A.18).

To classify each mineral phase through the CT volume, the CT image sequence was imported into Dragonfly 2020.1. Dragonfly is a 3D image processing and visualisation software, designed specifically for segmentation, analysis and quantification of CT data. For a CT volume where each mineral phase is variably attenuated, the greyscale values can be used to automatically segment the volume by identifying voxels within the greyscale ranges assigned to each mineral phase.

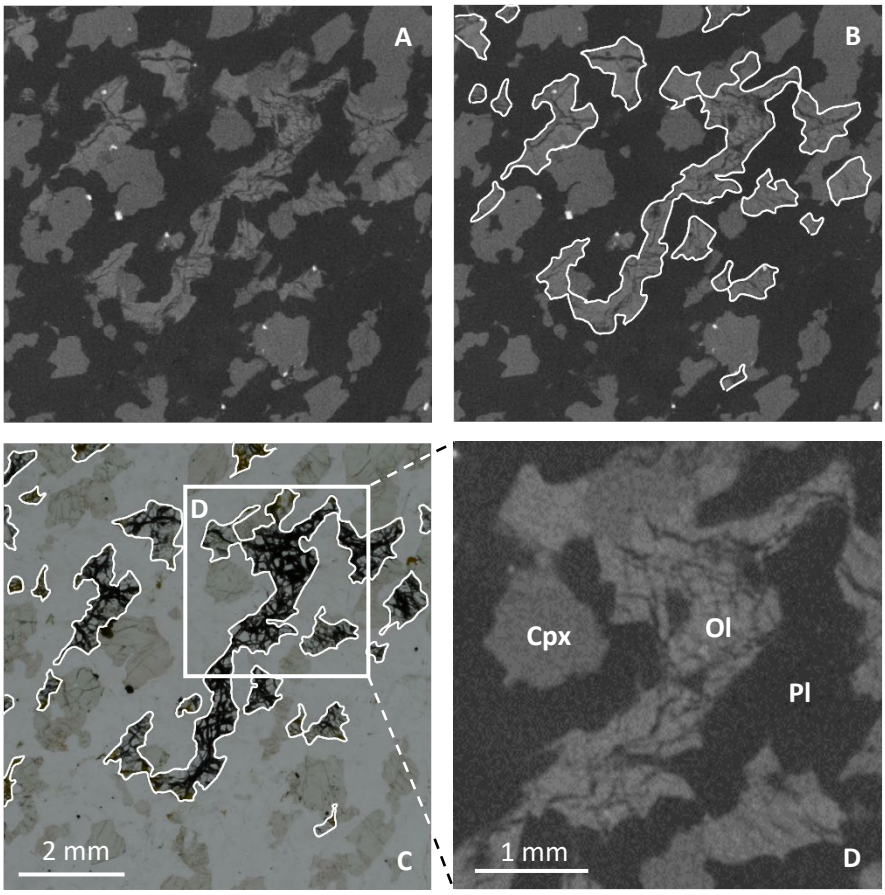

Figure A.18 – A) Greyscale tiff image (slice 20 of 1811) containing pl, ol and cpx. ***B)*** Olivine crystals drawn onto this diagram, using olivine alteration to dictate separation of OL and CPX. ***C)*** Photomicrograph taken in PPL of a thin section cut along the same plane as the CT image in ***A***, demonstrating the distribution of olivine crystals (outlined in white) and the correspondence to the segmentation drawn in ***B***. ***D)*** Magnification of CT data relative to its positioning in the photomicrograph, labelling the Pl, Ol and Cpx to demonstrate their qualitative distinctions.

Dragonfly contains several automated segmentation tools that are designed to provide the user with the opportunity to select a segmentation technique that best suits their dataset. However, exploration of these segmentation tools, including the built-in machine and deep learning functions, led to no successful result.

Consequently, segmentation had to be conducted manually for each CT slice. Using the Dragonfly paintbrush tool to trace around object boundaries, each segmented area was then assigned to a three-dimensional region of interest (ROI) volume corresponding to either clinopyroxene, olivine or plagioclase. Due to the time consuming nature of this process (1 CT slice = > 6 hours work), the CT volume had to be subsampled to provide a more realistic processing volume. However, even when subsampled to ~16% of the original CT slice area, only 150 CT slices (equivalent to 2.2mm in the vertical z-axis) were segmented in a time period of 100 hours. This gave a processed CT volume of 226.2 mm^2, just 7.7% of the original CT volume (Figure A.19). This is a clear disadvantage of the methodology, undermining the work undertaken to determine the most representative CT volume. The results of this segmentation are shown in Figure A.20.

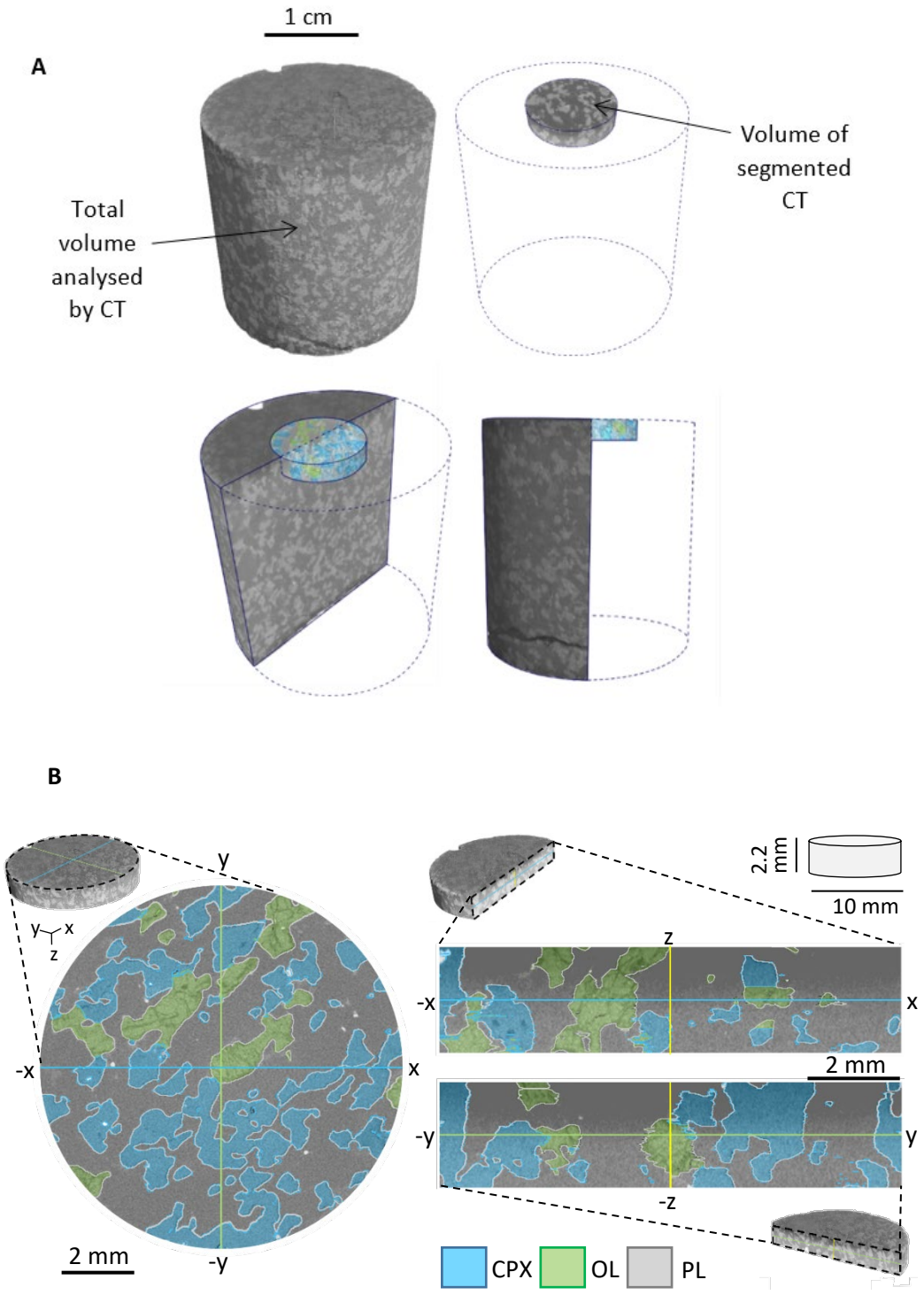

Figure A.19 – A) Comparison of total CT volume with the volume that was segmented in a time period of 100 hours. This volume represents 7.7% of the original CT volume. ***B)*** Segmentation of the CT data. Segmentation was undertaken slice by slice on the circular X Y projection, which built up a 3D image along the X Z and Y Z planes.

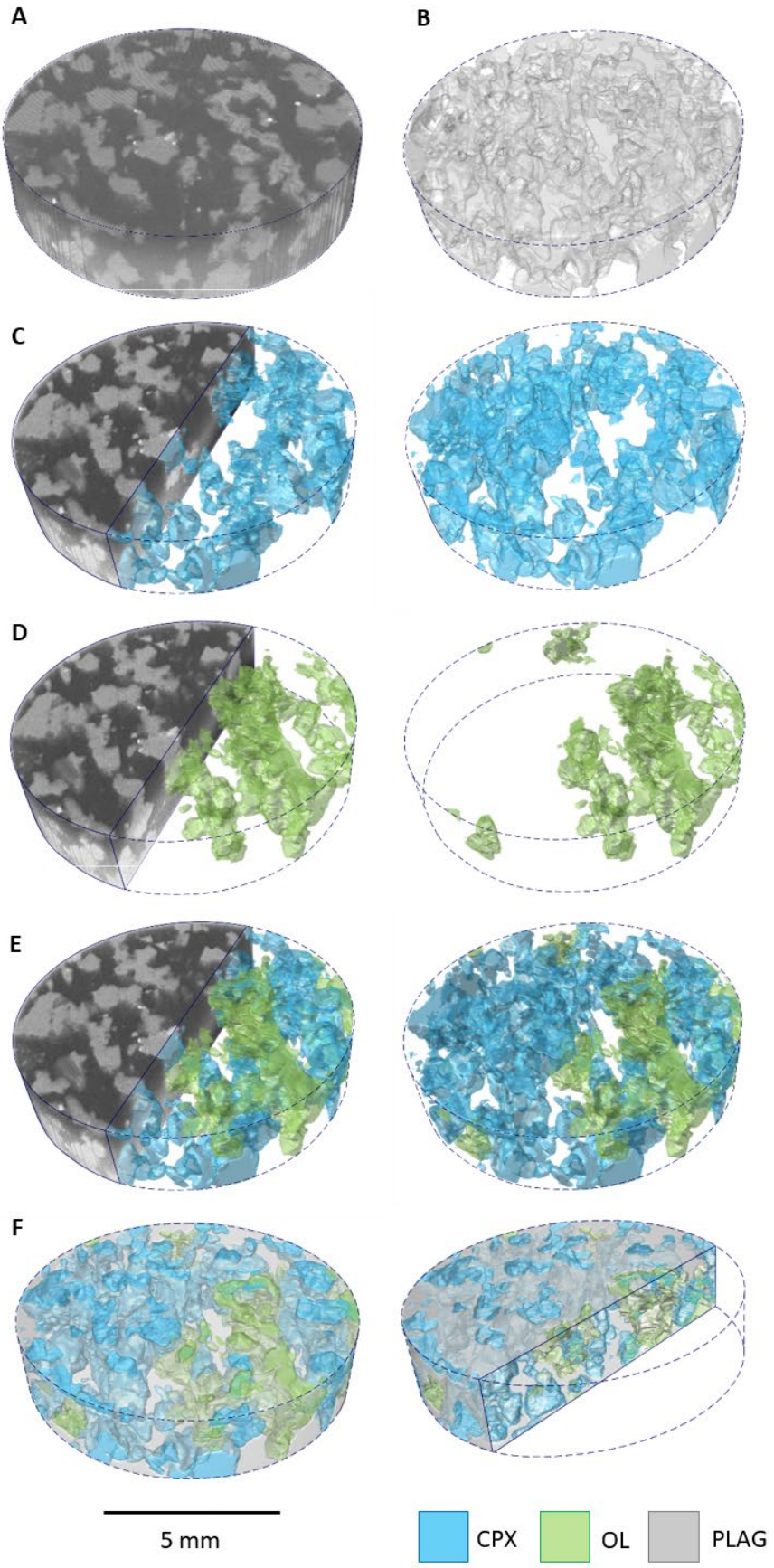

Figure A.20 (Caption overleaf) ▶

◀ ***Figure A.20 (overleaf)*** **–** Three-dimensional reproduction of crystal textures in the gabbro sample. ***A)*** Volume rendering prior to segmentation. ***B)*** Segmented plagioclase. ***C)*** Segmented clinopyroxene. ***D)*** Segmented olivine. ***E)*** Segmented olivine and clinopyroxene, demonstrating spatial relationship between the two phases. ***F)*** Segmented plagioclase, clinopyroxene and olivine, cut away shows cross section of segmented data. All 3D renderings were constructed from a contour mesh sampled every 1 voxel in the X, Y and Z axes and smoothed with a laplacian smoothing algorithm.

However, further inspection of the VOIs revealed a lot of segmentation errors that were introduced by human misinterpretation of the data. Because clinopyroxene and olivine exhibited an overlap in their greyscale values, segmentation was completed by using the aforementioned olivine alteration to guide the separation of these mineral phases. It is clear from the segmented orthoslices in Figure A.21 that there are instances where crystals have been misidentified, suggesting that this technique was not accurate enough to correctly segment the data. Therefore, although each mineral phase can crudely be identified in the CT data, it cannot be segmented accurately enough for further textural analysis.

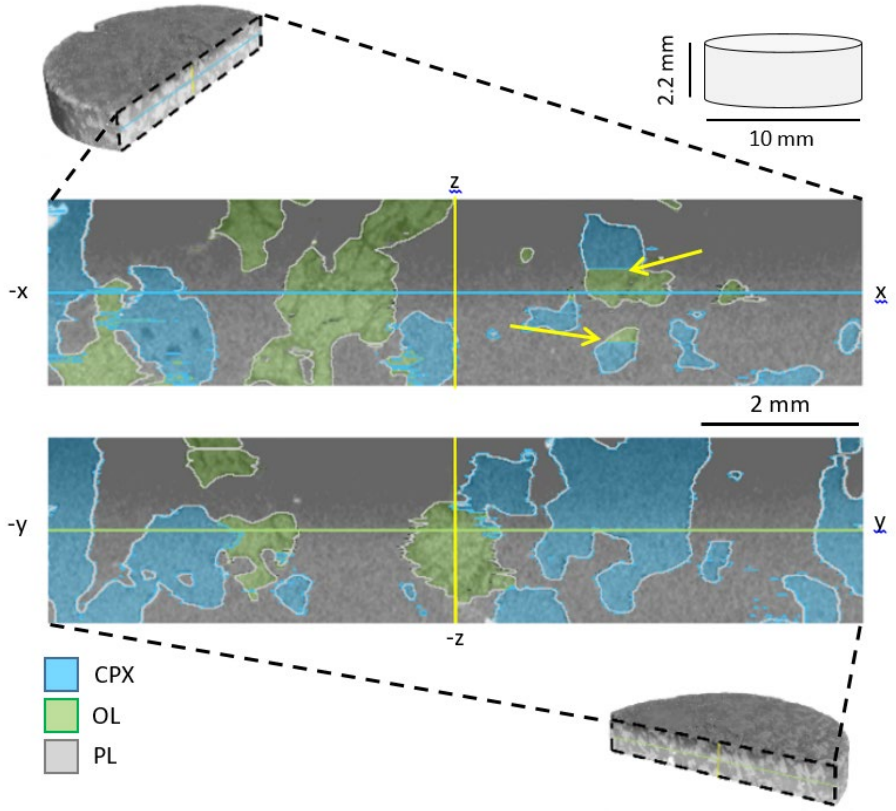

Figure A.21 **–** Segmentation of clinopyroxene and olivine crystals, demonstrating errors and misclassification between CT slices. Orthoslices show a cross section in the Z-X and Z-Y plane. Because the segmentation was undertaken slice by slice on the circular X-Y projection, it is clear that there are examples where the operator initially started classifying an object as one mineral type, then further down the image stack changed their opinion and classified it as another. The yellow arrows demonstrate instances where segmentation abruptly changes to another mineral, suggesting a classification error.

A.4.2 Adjacent crystals of the same mineral phase can be distinguished

To distinguish touching crystals of the same mineral phase requires that the grain boundaries are identifiable on the digital model. In 2D, grain boundaries can be easily identified in thin section, and traced to produce the digital crystal maps that comprise the two-dimensional model. By using a microscope in conjunction with the slide photographs, any instances where the grain boundary is unclear (e.g. minerals photographed at extinction, complex twinning patterns) can be checked and drawn onto the image. This produces an output where individual crystals can be separated as discrete objects, even if the crystal is in contact with another crystal of the same mineralogy.

Conversely, an important characteristic of X-rays is that their attenuation occurs independently of crystallographic orientation. This means that the output image will not identify any grain boundaries. To examine how the absence of grain boundaries manifests within the CT data, Figure A.22 depicts a comparison between crystal outlines identified in one of the thin sections, compared to the correspondent CT slice. By imposing the crystal boundaries drawn from thin section atop the equivalent CT slices, it is apparent that the absence of grain boundaries means that the 3D data does not appropriately identify individual crystals (Table A.1). Therefore, the CT data constitutes a phase map rather than a crystal map.

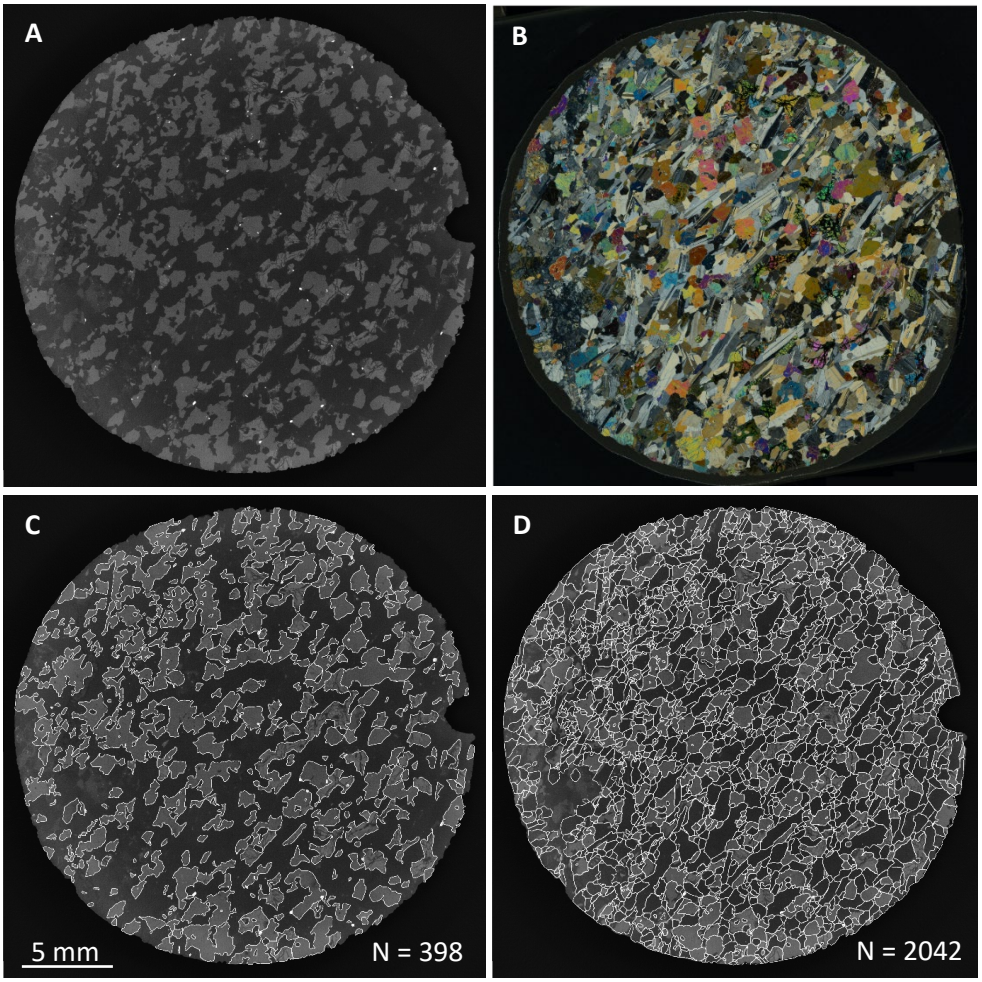

Figure A.22 – A) Greyscale CT slice image ***B)*** XPL Photomicrograph of thin section 1. By ensuring a constant sectioning interval it is possible to match the thin sections to the correspondent CT slice image. This thin section therefore represents the same data as provided in ***A. C)*** Segmented boundaries traced onto the CT image, showing boundaries between cpx, ol and pl. This yields 398 segmented objects. ***D)*** Crystal boundaries drawn from tracing atop B, imposed atop the CT slice. This yields 2042 segmented objects.

	Number of segmented objects	
Thin section number	CT	Thin Section
1	398	2042
2	398	2166
3	365	2005
4	417	2204
5	422	2105
6	384	2149

Table A.1 **–** Number of segmented objects identified in the CT data, compared to the number of segmented areas identified in the correspondent thin section.

However, because the need to separate touching objects is a pervasive challenge within geoscientific CT, there have been numerous attempts to develop a methodology that approaches object separation from a mathematical perspective (e.g. Leonti et al., 2020; Balcewicz et al., 2021). To further investigate whether touching crystals could be separated in this manner, the 3D dataset was analysed with a methodology used by Fei and Narsilio (2020) and Payton et al. (2021) that utilises a watershed algorithm to split up a segmented ROI into individual components (Beucher and Meyer, 2018). This methodology was shown by Payton et al. (2021) to provide effective grain segmentation for sandstones. The watershed algorithm works by treating the 3D object as a topographic map, from which seed points are placed within topographic lows and then flooded to identify barriers between individual objects (Sun et al., 2019). The algorithm utilises the greyscale values on the CT data, therefore olivine and clinopyroxene could not be analysed separately and are treated together as one phase. The results of this segmentation are shown in Figure A.23, with comparison to the equivalent area on the two dimensional digitisation. The three-dimensional results of this segmentation are

visualised in Figure A.24. The 2D data identifies a total of 1267 crystals whereas the watershed segmentation only identifies 944 in the same area. The difference between the two techniques can be further examined by plotting the centre points of each identified crystal. Figure A.25 not only demonstrates the difference in the number of crystals identified by each technique, but visualises spatial differences between the two datasets. From this, it was determined that segmentation of the 3D CT dataset did not provide an accurate representation of the sample textures. Therefore, the 3D data does not satisfy the criteria to distinguish adjacent crystals of the same mineralogy.

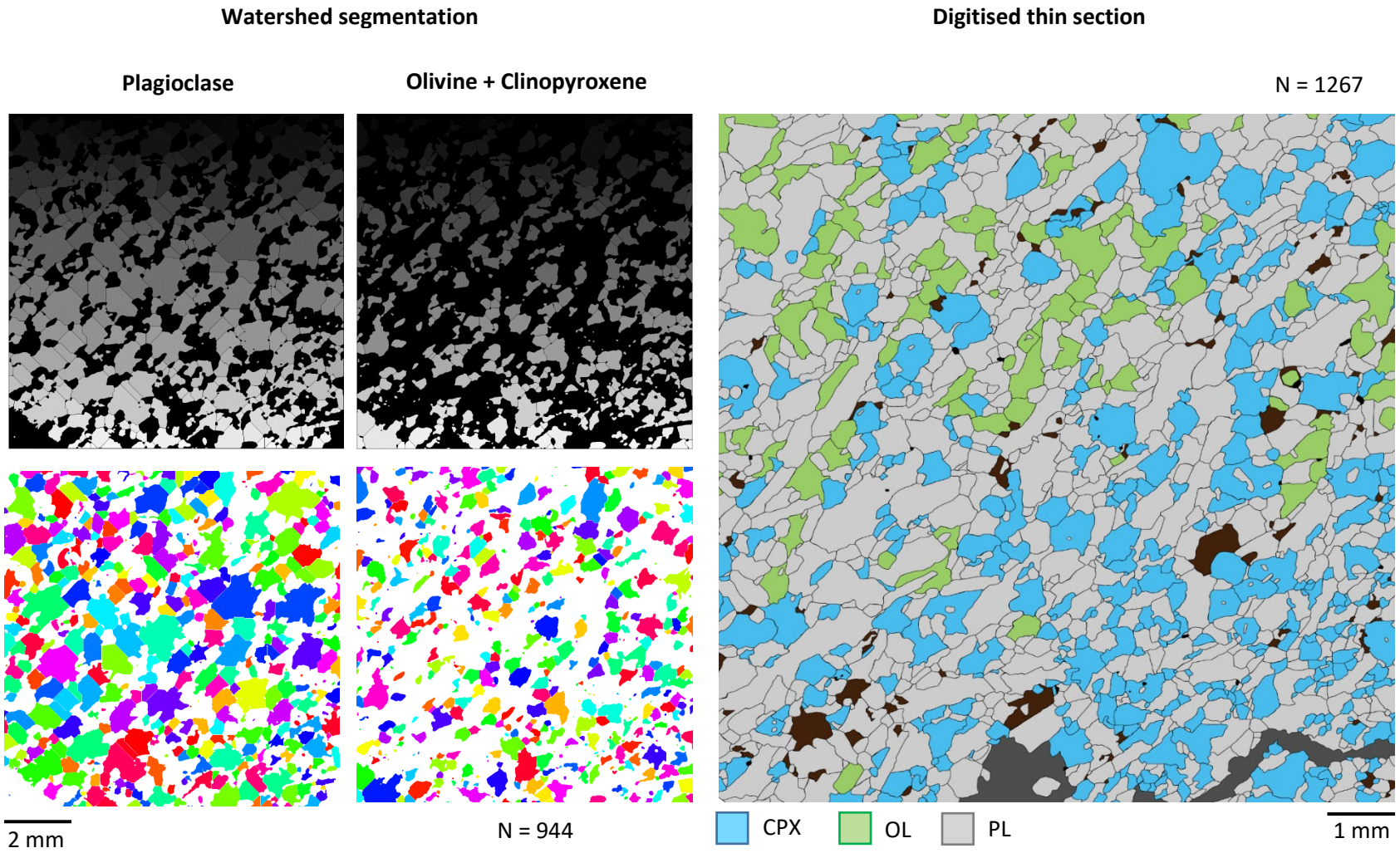

Figure A.23 **-** Results of the watershed segmentation (left), compared to the equivalent area in the two-dimensional model (right). Right - From the watershed segmentation process, each segmented object is assigned a unique greyscale value that can then be visualised on a random colour spectrum. Because the algorithm uses the CT greyscale values, it was not possible to segment olivine and clinopyroxene as separate phases. The watershed algorithm identified 944 crystals, whereas the 2D model 1267 in the same area.

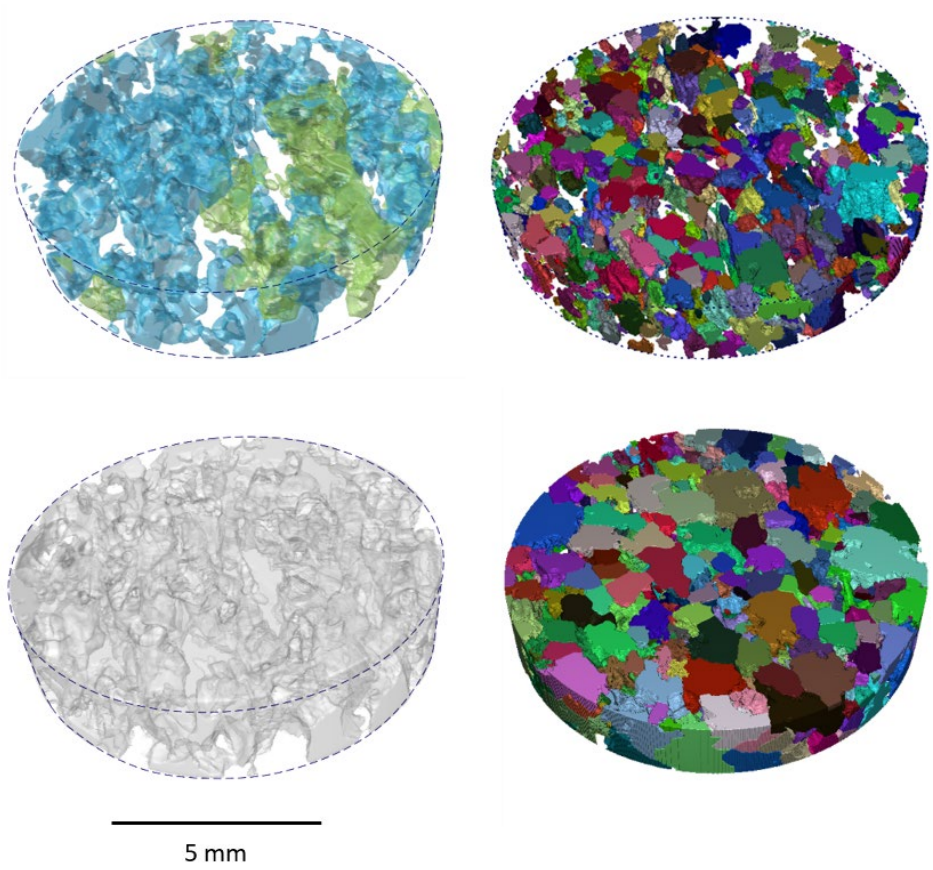

Figure A.24 – Three-dimensional visualisation of the watershed segmentation. Images in the left hand column are the results of the manual phase segmentation. Blue = clinopyroxene; green = olivine; grey = plagioclase. Images on the right are the same volume, segmented using the watershed algorithm. Each identified crystal is assigned a random colour to better visualise discrete objects.

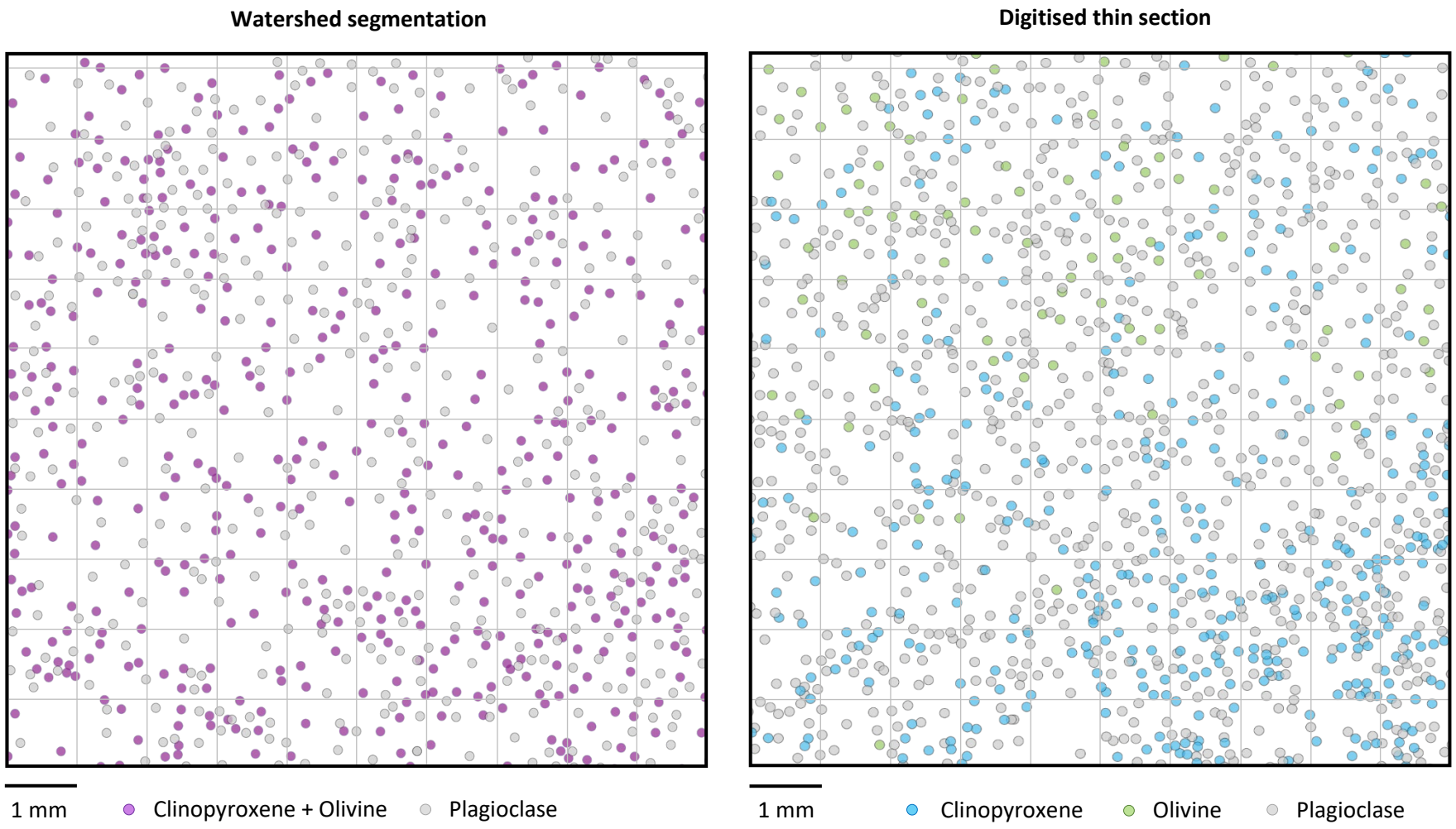

Figure A.25 – Centre points of segmented crystals identified by the watershed algorithm (left) and from the 2D digitised thin section (right). In the left hand image it was not possible to separate clinopyroxene and olivine and so they are colour coded as one phase. The spatial distribution of the centre points visualises the differences in the number and placement of crystals identified by the two techniques.

A.4.3 The output does not introduce any significant errors that may impact the textural interpretation of the sample

The limitations of the CT data discussed in Sections A.4.1 and A.4.2 demonstrate that the 3D dataset does not allow for accurate discrimination and segmentation of the crystal textures. Specifically, olivine and clinopyroxene cannot be identified correctly from the greyscale slices, and grain boundaries cannot be accurately determined if between two crystals of the same mineral type. This firstly manifests in mineralogical misclassification, which will over or under estimate the prevalence and spatial distribution of each mineral phase. Secondly, inaccurate grain boundary placement will not only influence the number of crystals assigned to each mineral phase, but will provide incorrect measurements of crystal size and shape. Because all of these parameters are essential for textural analysis, it is clear that any textural data derived from the CT will be unrepresentative of the true crystal textures.

It is widely acknowledged that working from 2D sections incurs a number of limitations associated with the planar viewing of a three-dimensional object. Specifically, when a crystal population is intersected, the 2D plane rarely dissects the centre of each crystal. Even in a monodisperse population, the intersection surfaces will exhibit a broad range around the modal value (Higgins, 2000). This is known as the cut section effect. Additionally, the smallest crystals in a polydisperse population are less likely to be intersected along any cut line. This acts to exaggerate the true size distribution of the population (Higgins, 2000). This is referred to as the intersection probability effect. However, stereological corrections have been written specifically to overcome these limitations and generate a three-dimensional population model. The programme CSDCorrections (Higgins, 2000) is specifically written to correct for both the cut section and

intersection probability effects, built on a modification of the Saltikov correction (Saltikov, 1967) which aims to calculate the true crystal length from the intersection length. By utilising this software, errors in the data are mathematically corrected to produce a meaningful and realistic crystal size distribution. Error bars on the CSD represent counting errors, taken as the square root of the number of crystals within each size bin, providing a quantitative measure of errors in the textural data. Therefore, although the two-dimensional nature of thin sections does introduce some errors, it can be mathematically corrected to provide realistic textural data.

To visualise the limitations of the textural data derived from the 3D dataset, Figure A.26 depicts a crystal size distribution calculated from the CT data alongside a crystal size distribution calculated from the 2D data. The former is constructed following the watershed segmentation outlined in Section A.4.2, using the maximum feret diameter of the segmented three-dimensional crystals. The latter is calculated from all six thin sections, using CSDCorrections. Because the CT data cannot discriminate olivine and clinopyroxene it was not possible to calculate a CSD for these phases, therefore the CSDs in Figure A.26 are for plagioclase crystals. From a 3D volume of 2.3 cm^3, the watershed algorithm identified 4107 plagioclase crystals, excluding those which are truncated by the boundary of the 3D volume. From the six thin sections that sample an area of 33.46 cm^2, a total of 7513 plagioclase crystals were identified, again excluding any crystals truncated by the thin section boundary.

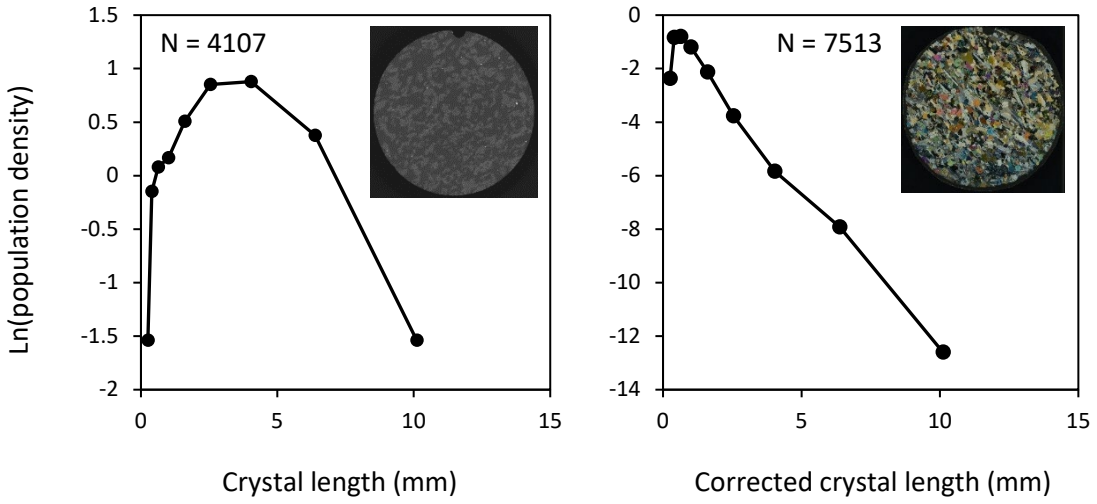

Figure A.26 – Crystal size distribution graphs for plagioclase crystals calculated from the three-dimensional CT data (left) and the two-dimensional thin section data (right). The left hand CSD was calculated following crystal segmentation using a watershed algorithm described in Fei and Narsilio (2020) and Payton et al. (2021). This algorithm identified 4107 plagioclase crystals (excluding any that were truncated by the boundary of the analysis volume), from which crystal length was measured as the maximum feret diameter. The right hand CSD was calculated by importing two-dimensional crystal cross-section measurements into CSDCorrections (Higgins, 2000), which mathematically converts the data into a 3D population. A total of 7513 plagioclase crystals were identified across 6 thin sections, which were amalgamated into one CSD. Crystal lengths were binned at the same intervals for each CSD. Although both CSDs span the same crystal size range, it is clear that the CSD constructed from the CT data exhibits a slope that significantly deviates from the log-normal slope that is theorised for most CSD models. Although it is not unrealistic for a CSD to exhibit such a convex profile (e.g. Simakin and Bindeman, 2008), the known limitations of the CT data provide an explanation for this CSD trend. Specifically, the absence of grain boundaries means that it likely that the smallest crystals have been incorrectly combined with another grain. This downturn on the CSD further visualises the inaccuracies of the watershed segmentation algorithm.

Although the two CSDs span a comparable size range, the CSD constructed from the CT data exhibits a slope that significantly deviates from that expected of a log-normal distribution. This can be explained by the known limitations of the CT data. The absence of grain boundaries means that the watershed algorithm appears to have incorrectly combined the smallest crystals with another grain. As such, the population density of smaller crystals is significantly reduced and the CSD exhibits a convex profile.

In contrast, the 2D CSD was constructed with mathematical corrections for known sources of error, using a data input that satisfies the previously stated textural criteria. This technique is widely used and considered by many authors to provide realistic crystal size distributions. Therefore, of the two models the two-dimensional data is considered to provide the most accurate representation of the sample textures, with steps taken to reduce the associated errors.

A.4.4 Future work

The results of this study suggest that at present, X-ray computed tomography is limited in its capacity to analyse highly crystalline samples. Because these limitations manifest significantly within the textural data, it is therefore more appropriate to utilise a two-dimensional methodology for such samples. However, the excellent 3D visualisations and results obtained for pumices (e.g. Castro et al., 2012; Andrews et al., 2014; Jones and Manga, 2016), meteorites (e.g. Lindgren et al., 2015; McCubbin et al., 2019; Zubov et al., 2021; Zhang et al., 2021) and for highly attenuating phases in mantle xenoliths (e.g. Bhanot et al., 2020; Chatzaras et al., 2021) demonstrate that in some instances, CT can provide valuable textural data for igneous products.

The specific limitations identified in this study remain a focus of ongoing development in geological CT research. X-rays are variably attenuated according to a materials composition and density, hence silicate minerals commonly overlap in CT outputs. In some instances, it is possible to scan a material at two X-ray energies above and below the absorption edge energy of certain abundant elements, which are subtracted from one another to produce a map of the materials containing these elements (e.g. Ikeda et al., 2004; Ketcham and Koberl, 2013; Mayo et al., 2015; Sittner et al., 2021). However, this technique requires careful calibration using materials of known composition and density, a sample containing minerals that vary sufficiently in composition of the targeted element (Sittner et al., 2021) and the capacity to undertake multiple scans on one sample, which is most successful with a monochromatic beam source (Tsuchiyama et al., 2013) using synchrotron radiation (e.g. Ikeda et al., 2004). Application of this technique is beyond the scope of this pilot study; conventional CT studies typically sample at one X-ray energy, which may be constrained by performing multiple scans to optimise the image output (e.g. Pamucku and Gualda, 2010) or prior to scanning using compositional data (e.g. Boone et al., 2011). The grain-boundary challenge also remains an ongoing area of research, with continued efforts to improve image segmentation (e.g. Fei and Narsilio, 2020). For some samples where the crystals are sub-spherical in shape it is possible to separate individual crystals by peeling them down to a nucleation point from which they can be rebuilt and quantified (Proussevitch and Sahagian, 2001; Ketcham, 2005). From this, three-dimensional crystal size distributions can be produced that plot within error of those produced by crushing and extracting individual crystals from the same sample (Gualda and Rivers, 2006). However, for samples in which the crystals exhibit more complex

geometries or are tightly clustered, there is still no definitive method by which to accurately identify grain boundaries.

A.5 Conclusions

The results of this pilot study indicate that two-dimensional methods provide the most accurate means by which to analyse the crystal textures of highly-crystalline samples with closely attenuating mineralogies. Regardless of the known limitations associated with studying a three-dimensional object as a two-dimensional cross section, this technique provides a more accurate representation of the sample textures that can currently be obtained by three-dimensional X-ray computed tomography. Therefore, a two-dimensional approach is recommended for analysis of crystal textures within the Eifel xenoliths that comprise the main body of this thesis.

A.6 References

- Andrews, B.J. and Manga, M. (2014) Thermal and rheological controls on the formation of mafic enclaves or banded pumice, Contributions to Mineralogy and Petrology, **167** (1): 961
- Balcewicz, M.; Siegert, M.; Gurris, M.; Ruf, M.; Krach, D.; Steeb, H. and Saenger, E.H. (2021) Digital rock physics: a geological driven workflow for the segmentation of anisotropic Ruhr sandstone, Frontiers in Earth Science, **9**
- Berger, A.; Herwegh, M.; Schwarz, J-O. and Putlitz, B. (2011) Quantitative analysis of crystal/grain sizes and their distributions in 2D and 3D, Journal of Structural Geology, **33**: 1751-1763
- Berger, M.J.; Hubbell, J.H.; Seltzer, S.M.; Chang, J.; Coursey, J.S.; Sukmar, R.; Zucker, D.S. and Olsen, K. (2010) XCOM: Photon Cross Section Database (version 1.5), National Institute of Standards and Technology (NIST), Online Access: http://physics.nist.gov/xcomw

- Beucher, S. and Meyer, F. (2018) The morphological approach to segmentation: the watershed transformation, In: Mathematical morphology in image processing, 1st edition, CRC Press: 433-481
- Bhanot, K.K.; Downes, H.; Petrone, C.M.; Humphreys-Williams, E. and Clark, B. (2020) Micro-CT investigation of garnet-spinel clusters in mantle peridotite xenoliths, Lithos, **352**: 105250
- Boone, M.; Dewanckele, J.; Boone, M.; Cnudde, V.; Silversmit, G.; Van Ranst, E.; Jacobs, P.; Vincze, L. and Van Hoorebeke, L. (2011) Three-dimensional phase separation and identification in granite, Geosphere, **7**: 79-86
- Bryon, D.N.; Atherton, M.P. and Hunter, R.H. (1995) The interpretation of granitic textures from serial thin sectioning, image-analysis and 3-dimensional reconstruction, Mineralogical Magazine, **59** (395): 203-211
- Carlson, W.D.; Denison, C. and Ketcham, R.A. (2000) High-resolution X-ray computed tomography as a tool for visualisation and quantitative analysis of igneous textures in three dimensions, Visual Geosciences, **4**: 1-14
- Castro, J.M.; Burgisser, A.; Schipper, C.I. and Mancini, S. (2012) Mechanisms of bubble coalescence in silicic magmas, Bulletin of Volcanology, **74** (10): 2339-2352
- Chatzaras, V.; Lusk, A.D.J.; Chapman, T.; Aldanmaz, E.; Davis, J.R. and Tikoff, B. (2021) Transpressional deformation in the lithospheric mantle beneath the North Anatolian fault zone, Tectonophysics, **815**: 228989
- Fei, W. and Narsilio, G.A. (2020) Impact of three-dimensional sphericity and roundness on coordination number, Journal of Geotechnical and Geoenvironmental Engineering, **146** (12): 06020025
- Garapić, G.; Faul, U.H. and Brisson, E. (2013) High-resolution imaging of the melt distribution in partially molten upper mantle rocks: evidence for wetted two-grain boundaries, Geochemistry, Geophysics, Geosystems, **14**: 556-566
- Gualda, G.A.R. and Rivers, M. (2006) Quantitative 3D petrography using X-ray tomography: application to Bishop Tuff pumice clasts, Journal of Volcanology and Geothermal Research, **154**: 48-62

- Hanna, R. D. and Ketcham, R. (2017) X-ray computed tomography of planetary materials: A primer and review of recent studies, Chemie de Erde – Geochemsitry, **77** (4): 547-572
- Higgins, M.D. (2000) Measurements of crystal size distributions, American Mineralogist, **85**: 1105-1116
- Higgins, M.D. (2006) Quantitative textural measurements in igneous and metamorphic petrology, 1st ed. Cambridge: Cambridge University Press
- Ikeda, S.; Nakano, T.; Tsuchiyama, A.; Uesugi, K.; Suzuki, Y.; Nakamura, K.; Nakashima, Y. and Yoshida, H. (2004) Nondestructive three-dimensional element concentration mapping of a Cs doped partially molten granite by X-ray computed tomography using synchrotron radiation, American Mineralogist, **89**: 1304-1313
- Jones, T.J.; McNamara, K.; Eychenne, J.; Rust, A.C.; Cashman, K.V.; Scheu, B. and Edwards, R. (2016) Primary and Secondary fragmentation of crystal-bearing intermediate magma, Journal of Volcanology and Geothermal Research, **327**: 70-83
- Ketcham, R. (2005) Three-dimensional textural measurements using high-resolution X-ray computed tomography, Journal of Structural Geology, **27** (7): 1217-1228
- Ketcham, R.A. and Carlson, W.D. (2001) Acquisition, optimization and interpretation of X-ray computed tomographic imagery: applications to the geosciences, Computers and Geosciences, vol. 27, 381-400
- Ketcham, R.A. and Koeberl, C. (2013) New textural evidence on the origin of carbonado diamond: an example of 3D petrography using X-ray computed tomography, Geosphere, **9**: 1336-1347
- Krimer, D. and Costa, F. (2017) Evaluation of the effects of 3D diffusion, crystal geometry, and initial conditions on retrieved time-scales from Fe-Mg zoning in natural orientated orthopyroxene crystals, Geochimica et Cosmochimica Act, **196**: 271-288
- Leonti, A.; Fonesca, J.; Valova, I.; Beemer, R.; Cannistraro, D.; Pilskaln, C.; DeFlorio, D. and Kelly, G. (2020) Optimized 3D segmentation algorithm for shelly sand images, Proceedings of the 6th World Congress on Electrical

Engineering and Computer Systems and Science (EECSS'20) 13-15 August 2020, Virtual Conference

- Lindgren, P.; Hanna, R.D.; Dobson, K.J.; Tomkinson, T. and Lee, M.R. (2015) The paradox between low shock-stage and evidence for compaction in CM carbonaceous chondrites explained by multiple low-intensity impacts, Geochimica et Cosmochimica Acta, **148**: 159-178
- Mayo, S.; Josh, M.; Nesterets, Y.; Esteban, L.; Pervukhina, M.; Clennell, M.B.; Maksimenko, A. and Hall, C. (2015) Quantitative micro-porosity characterization using synchrotron micro-CT and xenon K-edge subtraction in sandstones, carbonates, shales and coal, Fuel, **154**: 167-173
- McCubbin, F.M.; Herd, C.D.K.; Yada, T.; Hutzler, A.; Calaway, M.J.; Allton, J.H.; Corrigan. C.M.; Fries, M.D.; Harrington, A.D.; McCoy, T.J.; Mitchell, J.L.; Regberg, A.B.; Righter, K.; Snead, C.J.; Tait, K.T.; Zolensky, M.E. and Zeigler, R.A. (2019) Advanced curation of astromaterials for planetary science, Space Science Reviews, **215**: 8
- Mock, A. and Jerram, D.A. (2005) Crystal Size Distributions (CSD) in three dimensions: insights from the 3D reconstruction of a highly porphyritic rhyolite, Journal of Petrology, **46**: 1525-1541
- Morgan, D.J. and Jerram, D.A. (2006) On estimating crystal shape for crystal size distribution analysis, Journal of Volcanic and Geothermal Research, **154**: 1-7
- Pamukcu, A.S. and Gualda, G.A.R. (2010) Quantitative 3D petrography using X-ray tomography 2: Combining information at various resolutions, Geosphere, **6**: 775-781
- Payton, R.L.; Chiarella, D. and Kingdon, A. (2021) The influence of grain shape and size on the relationship between porosity and permeability in sandstone, Preprint
- Proussevitch, A.A. and Sahagian, D.L. (2001) Recognition and separation of discrete objects within complex 3D voxelized structures, Computers and Geosciences, **27** (4): 441-454
- Saltikov, S.A. (1967) The determination of the size distribution of particles in an opaque material from a measurement of the size distributions of their

sections. In H. Elias, Ed. Proceedings of the Second International Congress for Stereology, Springer-Verlag, Berlin: 163–173

- Simakin, A.G. and Bindeman, I.N. (2008) Evolution and crystal sizes in the series of dissolution and precipitation events in open magma systems, Journal of Volcanology and Geothermal Research, **177**: 997-1010
- Sittner, J.; Godinho, J.R.A.; Renno, A.D.; Cnudde, V.; Boone, M.; De Scryver, T.; Van Loo, D.; Merkulova, M.; Roine, A. and Liipo, J. (2021) Spectral X-ray computed micro-tomography: 3-dimensional chemical imaging, X-ray spectrometry, **50**: 92-105
- Stock, S.R. (2009) Microcomputed tomography: Methodology and applications, Boca Raton, Florida, CRC Press: 348-349
- Sun, Q.; Zheng, J. and Li, C. (2019) Improved watershed analysis for segmenting contacting particles of coarse granular soils in volumetric images, Powder Technology, **356**: 295-303
- Tsuchiyama, A.; Nakano, T.; Uesugi, K.; Uesugi, M.; Takeuchi, A.; Suzuki, Y.; Noguchi, R.; Matsumoto, T.; matsuno, J.; Nagano, T.; Imai, Y.; Nakamura, T.; Ogami, T.; Noguchi, T.; Abe, M.; Yada, T and Fujimura, A. (2013) Analytical dual-energy microtomography: A new method for obtaining three-dimensional mineral phase images and its application to Hayabusa samples, Geochimica et Cosmochimica Acta, **116**: 5-16
- Verdun, F.R.; Racine, D.; Ott, J.G.; Tapiovaara, K.J.; Toroi, P.; Bochud, F.O.; Veldkamp, W.J.H.; Schegerer, A.; Bouwman, R.W.; Hernandez Giron, I.; Marshall, N.W. and Edyvean, S. (2015) Image quality in CT: From physical measurements to model observers, Physica Medica, **31**: 823-843
- Withers, P.J.; Bouman, C.; Carmignato, S.; Cnudde, V.; Grimaldi, D.; Hagen, C.K.; Maire, E.; Manley, M.; Plessis, A.D. and Stock, S.R. (2021) X-ray computed tomography, Nature Reviews Methods Primers, **1**: 18
- Zhang, M.M.; Clark, B.; King, A.J.; Russell, S.S. and Lin, Y.T. (2021) Shape and porosity of refractory inclusions in CV3 chondrites: a micro-computed tomography (μCT) study, Meteoritics and Planetary Science, **56** (3): 500-514
- Zubov, A.A.; Shumilova, T.G.; Zhuravlev, A.V. and Isaenko, S.I. (2021) X-ray computed tomography of diamondiferous impact suevitic breccia and

clast-poor melt rock from the Kara astrobleme (Pay-Khoy, Russia), American Mineralogist, **106** (11): 1860-1870

Appendix B: Impacts of human error on manual digitisation of crystal textures

---

Appendix B presents a short study undertaken prior to the data collection presented in the main body of this thesis. This study aimed to investigate the extent to which human errors manifest within the digitisation process, and whether the pay off between a manual methodology and the total number of samples that can be analysed was worthwhile. In a repeat error test where the same thin section was digitised three times, statistical testing suggested that the impacts of human error did not cause a significant variation between textural datasets derived from each of the repeats. Therefore, manual methods produce accurate replications of igneous textures and are utilised over faster, less accurate automated methodologies in the main body of this work.

B Impacts of human error on manual digitisation of crystal textures

B.1 Introduction

In recent years there have been many advancements in automated imaging techniques, mainly utilising geochemical mapping to generate digital thin section maps (e.g. Neave et al., 2014; 2017; Bell et al., 2020). This approach achieves good results for volcanic samples with a low crystal density, but is less successful when applied to plutonic samples (e.g. Cone et al., 2020). For a non-geochemical approach (i.e. – utilising thin section photographs), any automatic mapping method needs to consider a multitude of optical properties. For example, colour, pleochroism, birefringence, opacity, isotropy, extinction angles, twinning, zoning, cleavage and fractures (Aligholi et al., 2015) may all influence how an automated method identifies different mineral types and places grain boundaries. The complexity of this problem means that there is no widely used automated technique; published examples typically require vast training and reference databases (Rubo et al., 2019; Tang et al., 2020), are computationally demanding (Izadi et al., 2020), necessitate significant user input (Mingireanov Filho et al., 2013; Asmussen et al., 2015;) and are frequently limited in application to monomineralic samples (Heilbronner et al., 2000; Obara, 2007; Li et al., 2008),or segmentation of void spaces (Borazjani et al., 2016; Dong et al. 2019; Rubo et al., 2019). When compared to manual segmentations, the accuracy of automated techniques are consistently poorer (Cone et al., 2020). Cone et al. (2020) undertook a comparison of automatic segmentation techniques versus manual tracing to extract plagioclase crystal lengths and concluded that manual methods provide the most accurate assessment of crystal length, regardless of texture. Bell et al. (2020) utilised

geochemical mapping as a semi-automated technique for crystal size distribution analysis, but found that this produced an upwards shift in CSD diagrams, caused by the inability to accurately separate touching grains of the same mineral phase. They concluded that manual methods remain superior for accurately segmenting polymineralic igneous samples. However, manual methods are incredibly time consuming and therefore limit the total number of samples that can be analysed. As such, there is a pay off between the number of samples and the accuracy with which they can be studied. This short study aims to investigate whether human errors associated with manually digitising thin section photographs are significant enough to warrant the use of a faster automated technique, regardless of the known inaccuracies associated with both geochemical and photography based methods.

B.2 Methods

Potential sources of human error in thin section digitisation include misidentification of minerals, drawing errors (not drawing the true crystal boundary) and misclassification of drawn crystal outlines (labelling it as a different mineral to what it was identified as). In order to identify the significance of human error in this research, a repeat error test was undertaken on a thin section of a gabbro sample from Ardnamurchan, Scotland. This sample was selected as it contains abundant plagioclase (~78% from point count data). Plagioclase is a particularly challenging mineral to digitise as its first order birefringence colours and twinning patterns can make it challenging to identify crystal outlines.

One thin section was cut from the gabbro sample and photographed at a resolution of 6016 x 4016 pixels (Figure B.1).

Figure B.1 **–** Photograph of the gabbro section, taken in cross-polarised light.

The sample was then digitised by tracing crystal outlines atop the photograph using a graphics tablet in the graphic drawing software Adobe Illustrator CC 2018. A petrographic microscope was used to clarify instances where the photograph was unclear, for example where minerals are photographed at extinction. Traced crystals were classified by mineralogy to produce a digital crystal map. This process was repeated three times, leaving one month between each digitisation to avoid 'remembering' the sample and influencing the repeat. The same author completed all of these digitisations, which are presented in Figure B.2.

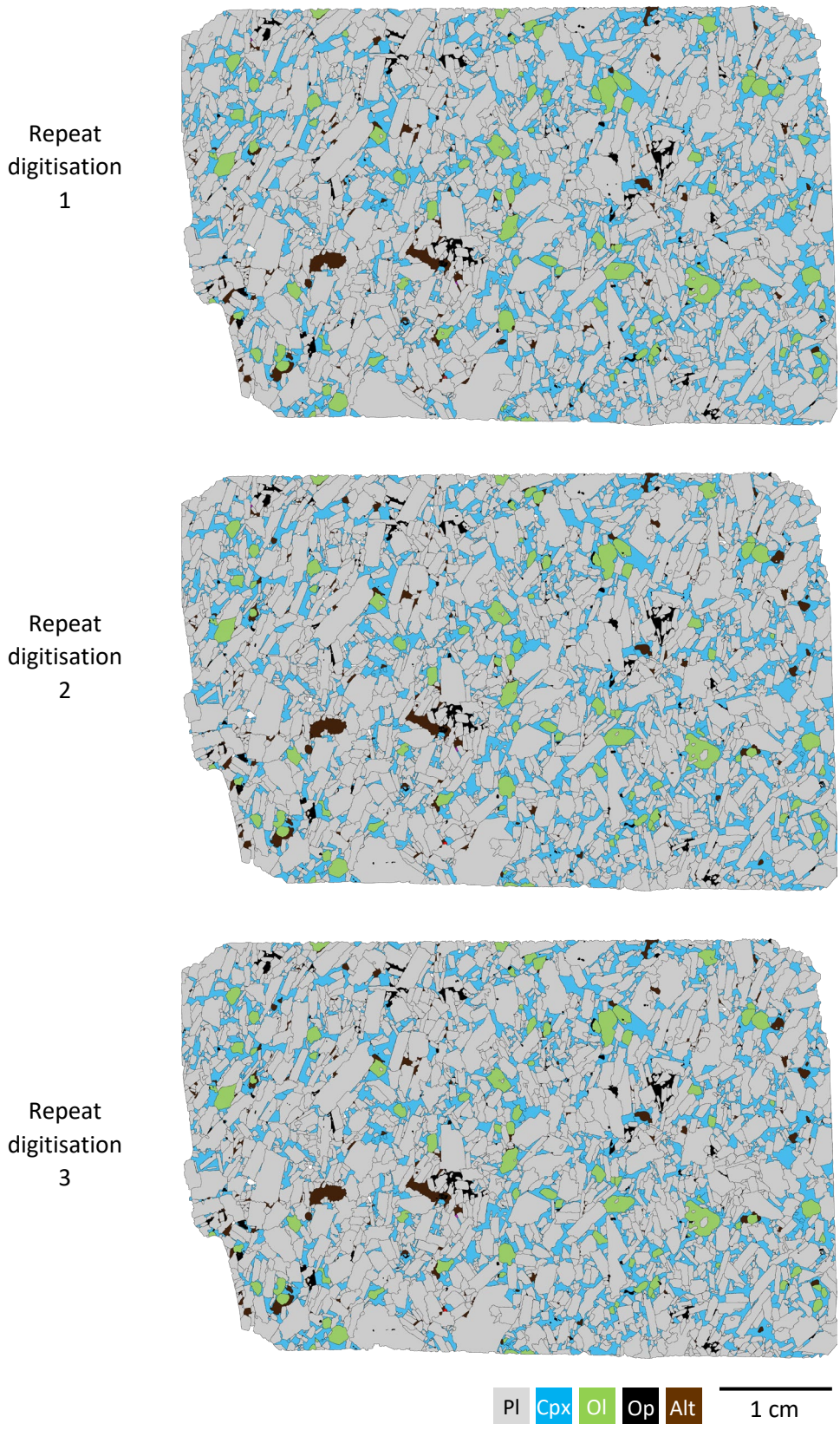

Figure B.2 – Results of the repeat digitisations, completed by the same author conducting the same methodology. A time interval of one month was elapsed between digitisations. Pl = plagioclase; Cpx = clinopyroxene; Ol = olivine; Op = opaque; Alt = alteration

B.3 Results

Quantitative parameters including the total crystal count and the area fraction occupied by each mineral phase indicates that there is some variation between each of the digitised samples, which have been introduced by human error (Figure B.3). To understand how these errors manifests in the textural data, a single factor ANOVA test was undertaken on long axis measurements of the plagioclase and olivine crystals, and the area of plagioclase, olivine and clinopyroxene crystals for each of the repeats. The clinopyroxene in the sample is mostly interstitial, meaning that the long axis cannot be appropriately measured, and it was therefore excluded from the length analysis. In an ANOVA test, the ratio of the inter-group variability to the within-group variability follows an F-distribution when the null hypothesis is true. Here the null hypothesis is that there is no significant difference in the distribution of the datasets. All of the ANOVA tests returned F-values that were less than the F-critical value, and the null hypothesis is therefore accepted as true (Figure B.4). From this, it appears that differences between the repeat digitisations do not manifest significantly within the textural data. This is visualised in Figure B.5, which plots a crystal size distribution graph for plagioclase crystals in each of the repeat digitisations. The CSDs exhibit a small degree of variation in linear regression statistics, causing minor differences in the slope and intercept values, but plot closely atop one another and within the error bar range. Olivine CSDs show much greater variation (Figure B.6), but because they are constructed from fewer than 250 crystals (the recommended minimum sample size for a realistic CSD; Mock and Jerram, 2006), it is likely that sample size, rather than human error, is generating this variation.

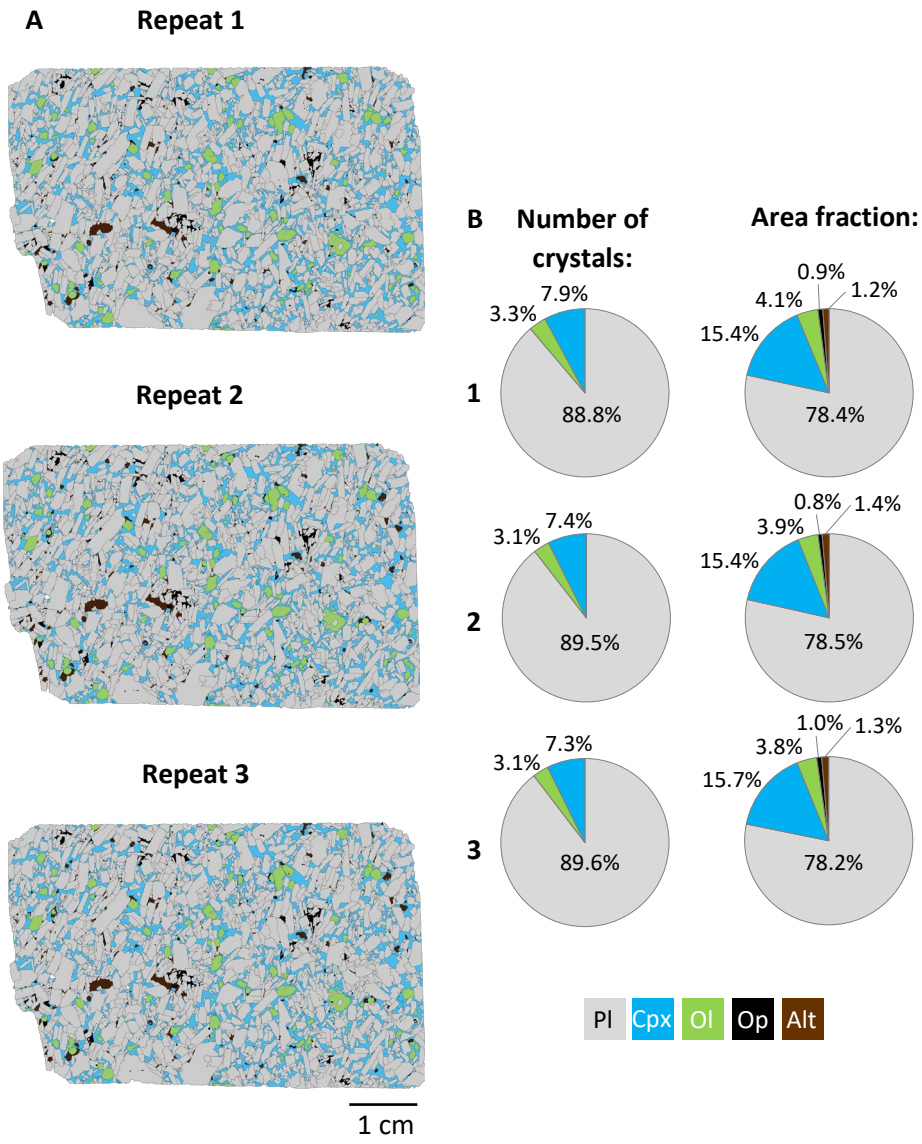

***Figure B.3* – A)** Digitised thin section maps from the three repeat digitisations. Pl = plagioclase, Cpx = clinopyroxene, Ol = olivine, Op = opaques, Alt = alteration. **B)** Percentage of the number of plagioclase, clinopyroxene and olivine in each of the three repeats (opaques and alteration are excluded as crystal boundaries cannot easily be distinguished and counted as separate objects) and the area fraction occupied by each phase in the repeat digitisations.

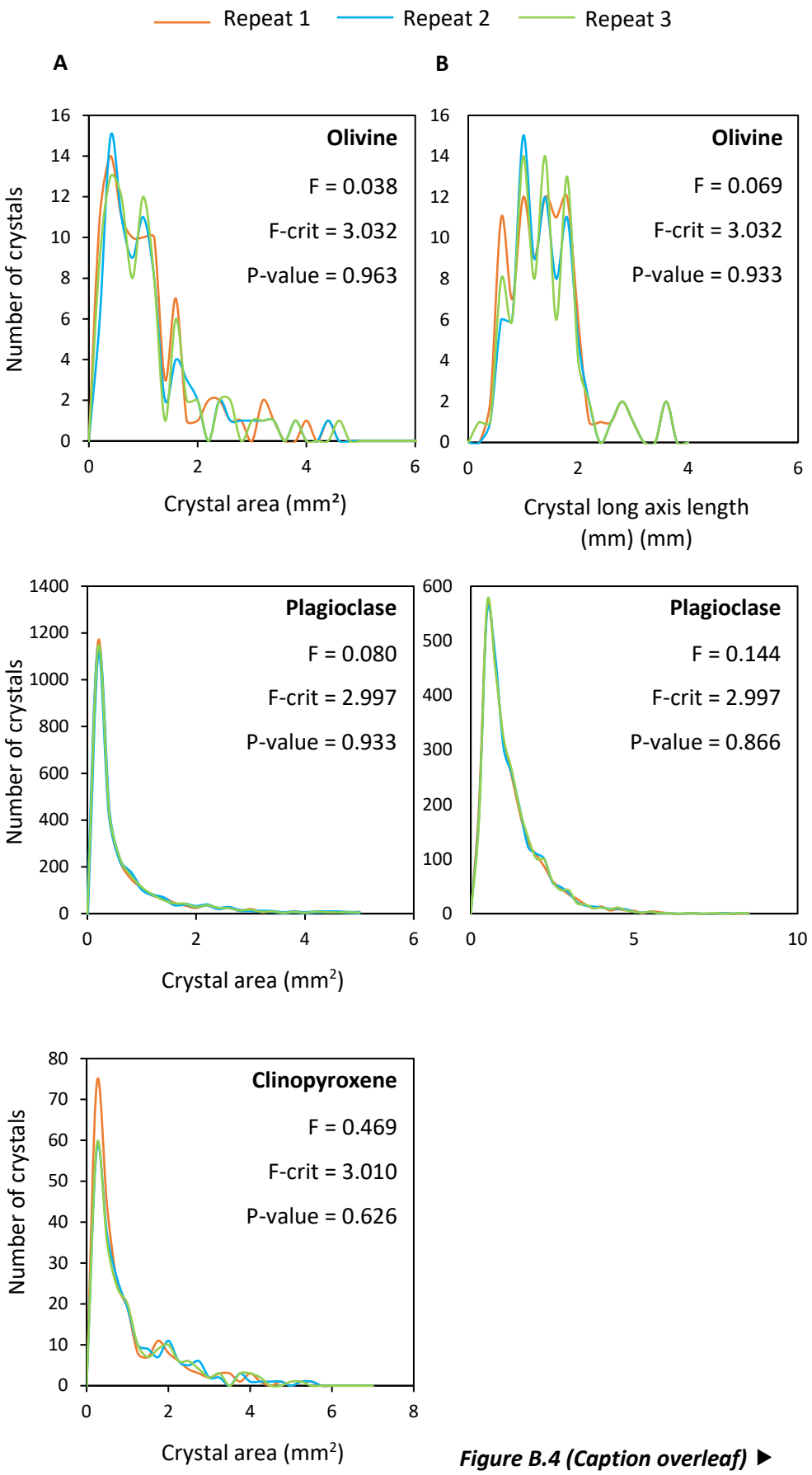

Figure B.4 (Caption overleaf) ▶

◀ ***Figure B.4 (Overleaf) –*** Graphical results of the ANOVA tests undertaken on the repeat sample digitisations. **A)** Distributions of crystal long axis lengths measured for plagioclase and olivine crystals in each of the repeats. For both datasets, the F-value is less than the F-critical value and the null hypothesis is accepted as true. The olivine crystal lengths appear to show greater variability, but still follow the same distribution. This is likely due to the smaller numbers of olivine crystals (87-96 per slide) compared to plagioclase (2533-2549 per slide). **B)** Distributions of crystal areas measured for plagioclase, olivine and clinopyroxene crystals in each of the repeats. In each of the ANOVA tests, the null hypothesis is accepted as true. For all of the ANOVA tests undertaken, the F-distribution indicates that there is no significant variability between the textural data outputs from the repeat digitisations.

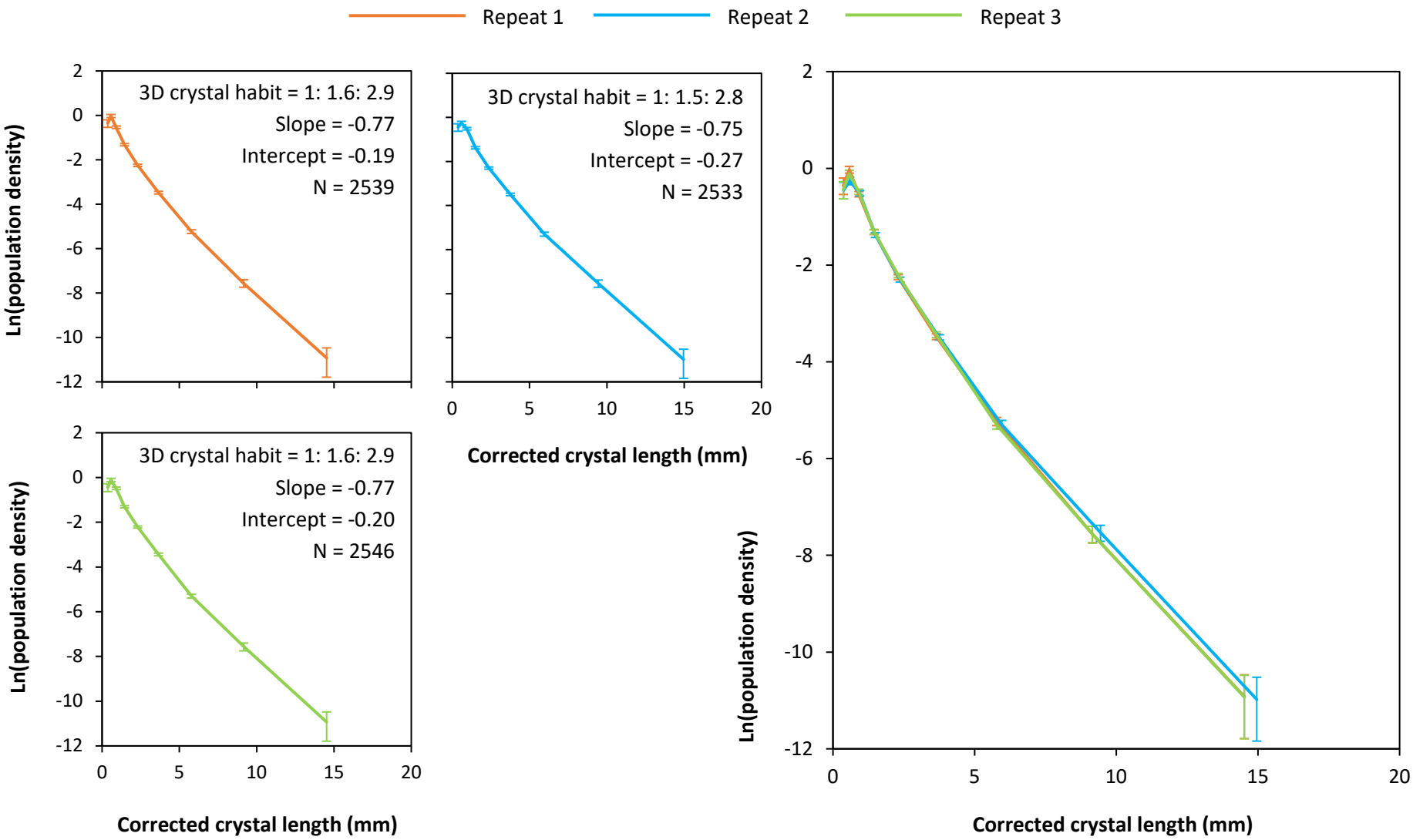

Figure B.5 (caption overleaf) ▶

◄ ***Figure B.5 (overleaf) –*** Crystal size distribution graphs for plagioclase crystals calculated from each of the three repeat digitisations. Crystal size distributions were constructed using CSDSlice to estimate three-dimensional crystal habit (Mock and Jerram, 2006) and CSDCorrections to produce a stereologically corrected CSD (Higgins, 2000). Linear regression statistics are recorded in the individual CSDs. Slope and intercept values show slight variation, but overall the CSDs plot within error of one another.

► ***Figure B.6 (overleaf) -*** Crystal size distribution graphs for olivine crystals calculated from each of the three repeat digitisations. Crystal size distributions were constructed using CSDSlice to estimate three-dimensional crystal habit (Mock and Jerram, 2006) and CSDCorrections to produce a stereologically corrected CSD (Higgins, 2000). Each repeat generates a unique olivine CSD, resulting in varied slope and intercept values. However, it is recommended that a minimum of 250 crystals are required to produce a realistic CSD (Mock and Jerram, 2006). Because the number of olivine crystals in each CSD are below this threshold, it is likely that the differences between these CSDs are exacerbated by the low sample number.

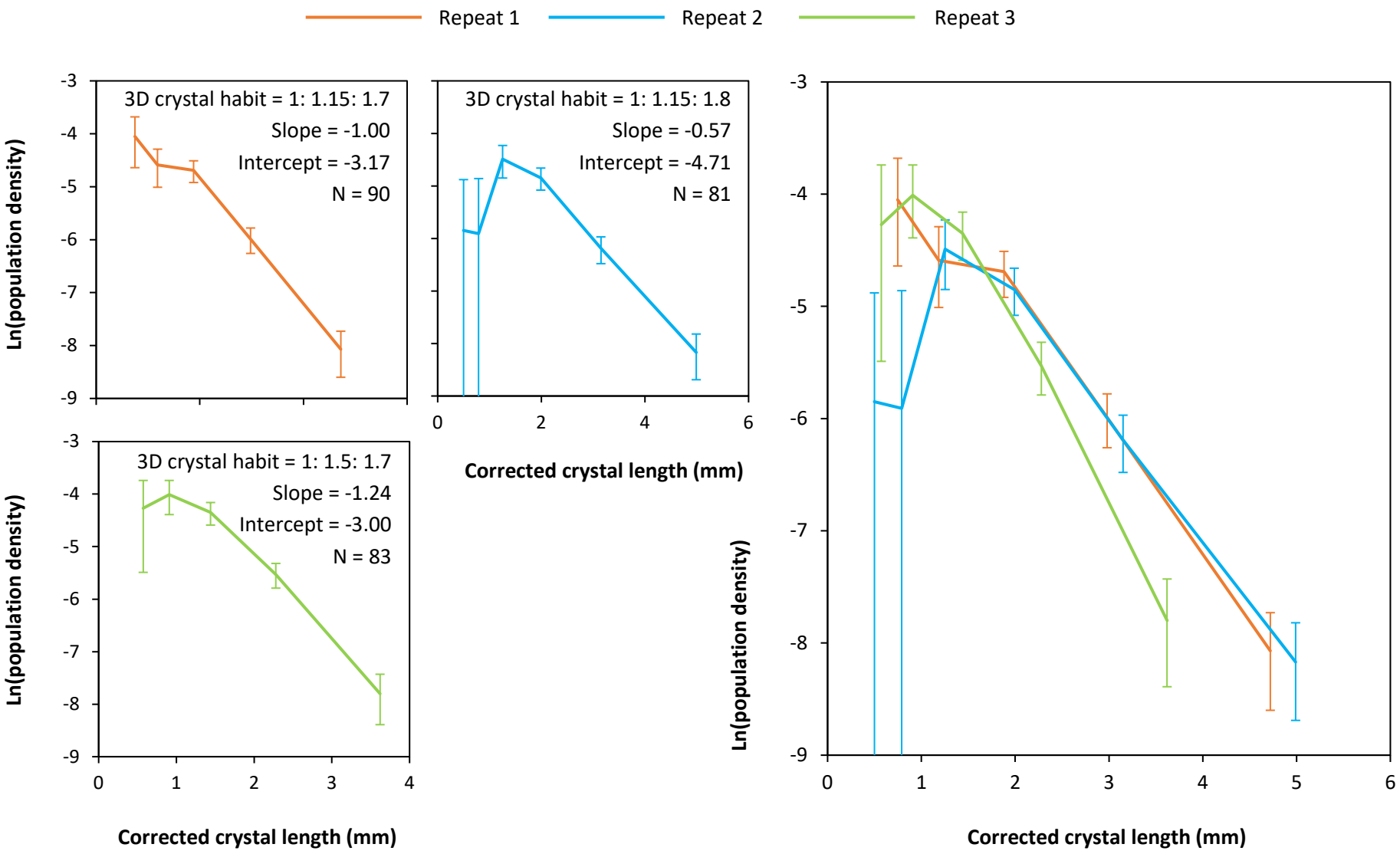

◀ ***Figure B.6 (Caption overleaf)***

B.4 Discussion and conclusions

The results of this error test suggest that the repeat digitisations do include some human error, either by misidentification of minerals or through drawing inaccuracies. However, ANOVA tests indicate that there is no significant variation between textural data derived from each of the repeats. Therefore, even though the manual technique is much slower and limits the number of samples that can be analysed, these results suggest that the degree of error is minimal and therefore does not significantly impact the textural data. Although these results were not directly compared to an automated approach, Cone et al. (2020) undertook such a comparison and concluded that manual methods are always more accurate than automated techniques. Because textural analysis aims to obtain accurate quantitative measurements of crystal textures it was therefore decided that a manual methodology was most appropriate for the main body of this thesis, regardless of the pay off with the number of samples that can then be analysed.

However, it is important to acknowledge that these results are unique to the author who completed the repeat digitisations, upon these specific samples. It is likely that factors such as experience and equipment might influence the drawing accuracy of other users, who may introduce fewer or more errors into the digitisations. Therefore, the results of this study cannot be used to derive an error value applicable beyond this study.

B.5 References

- Aligholi, S.; Khajavi, R. and Razmara, M. (2015) Automated mineral identification algorithm using optical properties of crystals, Computers and Geosciences, **85**: 175-183
- Asmussen, P.; Conrad, O.; Gunther, A.; Kirsch, M. and Riller, U. (2015) Semi-automatic segmentation of petrographic thin section images using a "seeded-region growing algorithm" with an application to characterize weathered subarkose sandstone, Computers & Geosciences, **83**: 89-99
- Bell, S.K.; Joy, K.H.; Pernet-Fisher, J.F. and Hartley, M.E. (2020) QEMSCAN as a method of semi-automated crystal size distribution analysis: Insights from Apollo 15 Mare basalts, Journal of Petrology, **61** (4)
- Borazjani, O.; Ghiasi-Freez, J.; Hatampour, A. (2016) Two intelligent pattern recognition models for automatic identification of textural and pore space characteristics of the carbonate reservoir rocks using thin section images, Journal of Natural Gas Science and Engineering, **35**: 944-955
- Cone, K.A.; Wendlandt, R.F.; Pfaff,K. and Orlandini, O.F. (2020) Texture constraints on crystal size distribution methodology: An application to the Laki fissure eruption, American Mineralogist, **5**: 585-598
- Dong, S.Q.; Zeng, L.B.; Xu, C.S.; Dowd, P.; Gao, Z.Y.; Mao, Z. and Wang, A. (2019) A novel method for extracting information on pores from cast thin-section images, Computers & Geosciences, **130**: 69-83
- Heilbronner, R. (2000) Automatic grain boundary detection and grain size analysis using polarization micrographs or orientation images, Journal of Structural Geology, **22**: 969-981
- Izadi, H.; Sadri, J.; Hormozzade, F. and Fattahpour, V. (2020) Altered mineral segmentation in thin sections using an incremental-dynamic clustering algorithm, Engineering Applications of Artificial Intelligence, **90**
- Li, Y.K.; Onasch, C.M and Guo, Y. (2008) GIS-based detection of grain boundaries, Journal of Structural Geology, **30**: 431-443
- Mingireanov Filho, I; Spina, T.V.; Falcao, A.X. and Vidal, A.C. (2013) Segmentation of sandstone thin section images with separation of touching grains using optimum path forest operators, Computers & Geosciences, **62**: 241-242

- Neave, D.; Buisman, I. and Maclennan, J. (2017) Continuous mush disaggregation during the long-lasting Laki fissure eruption, American Mineralogist, **102**: 2007-2021
- Neave, D.; Maclennan, J.; Hartley, M.; Edmonds, M. and Thordarson, T. (2014) Crystal storage and transfer in basaltic systems: the Skuggafjoll eruption, Journal of Petrology, **55**: 2311-2346
- Obara, B. (2007) A new algorithm using image colour system transformation for rock grain segmentation, Mineralogy and Petrology, **91**: 271-285
- Rubo, R.A.; Carneiro, C.D.; Michelon, M.F. and Gioria, R.D. (2019) Digital petrography: Mineralogy and porosity identification using machine learning algorithms in petrographic thin section images, Journal of Petroleum Science and Engineering, **183:** 106382
- Tang, D.G.; Milliken, K.L and Spikes, K.T. (2020) Machine learning for point counting and segmentation of arenite in thin section, Marine and Petroleum Geology, **120:** 104518

Appendix C: Digitised thin section images

Appendix C contains all of the digitised slide images used for the textural analysis presented in Chapter 5. This includes the coloured thin section drawing, the binarised images used to calculated CSDs, the coordinate points used to measure SDF and maps that visualise shape preferred orientation.

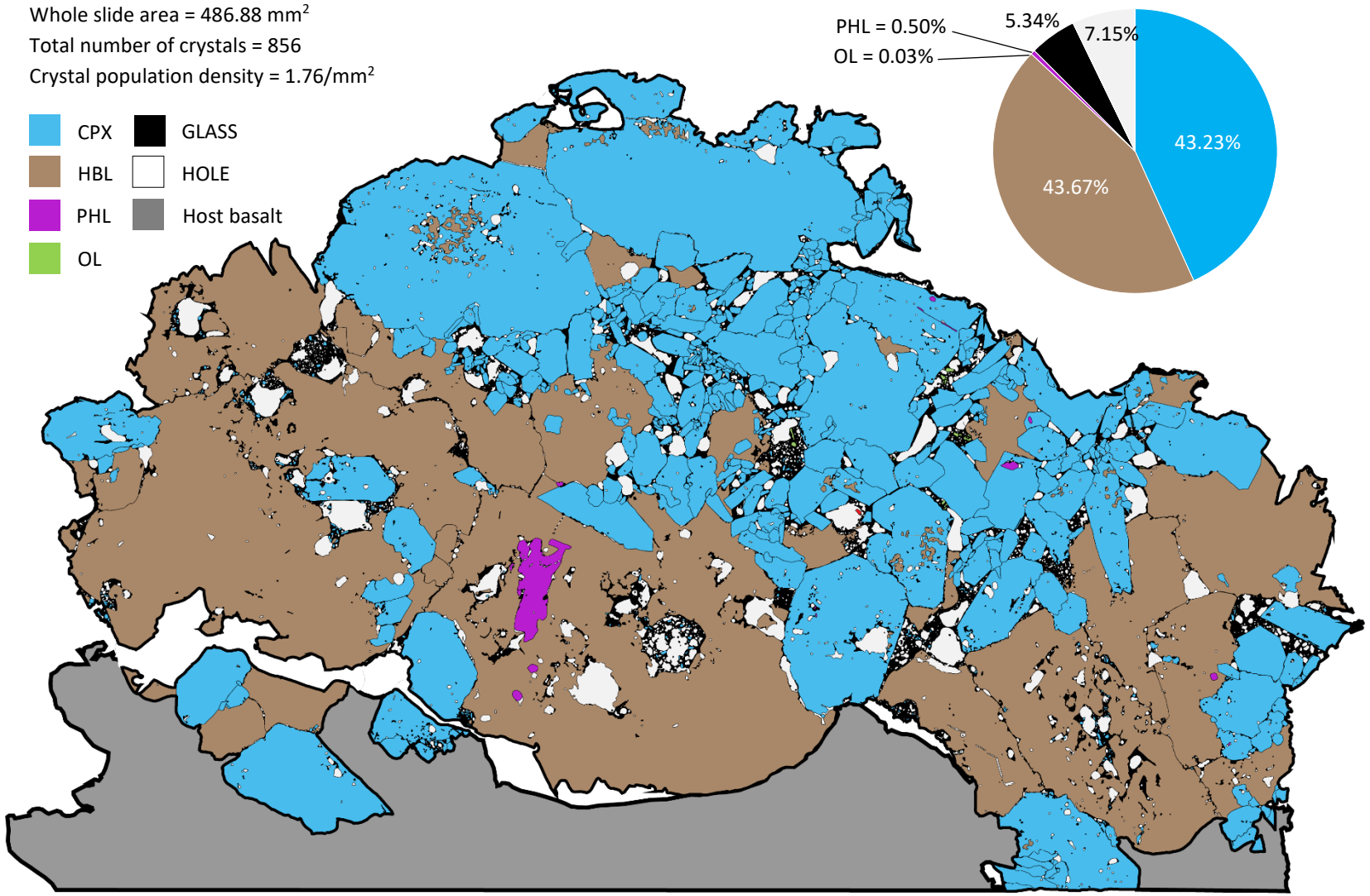

Figure C.1 – Digitised thin section image of sample M2 A. Inset pie chart visualises the area fraction of sample components.

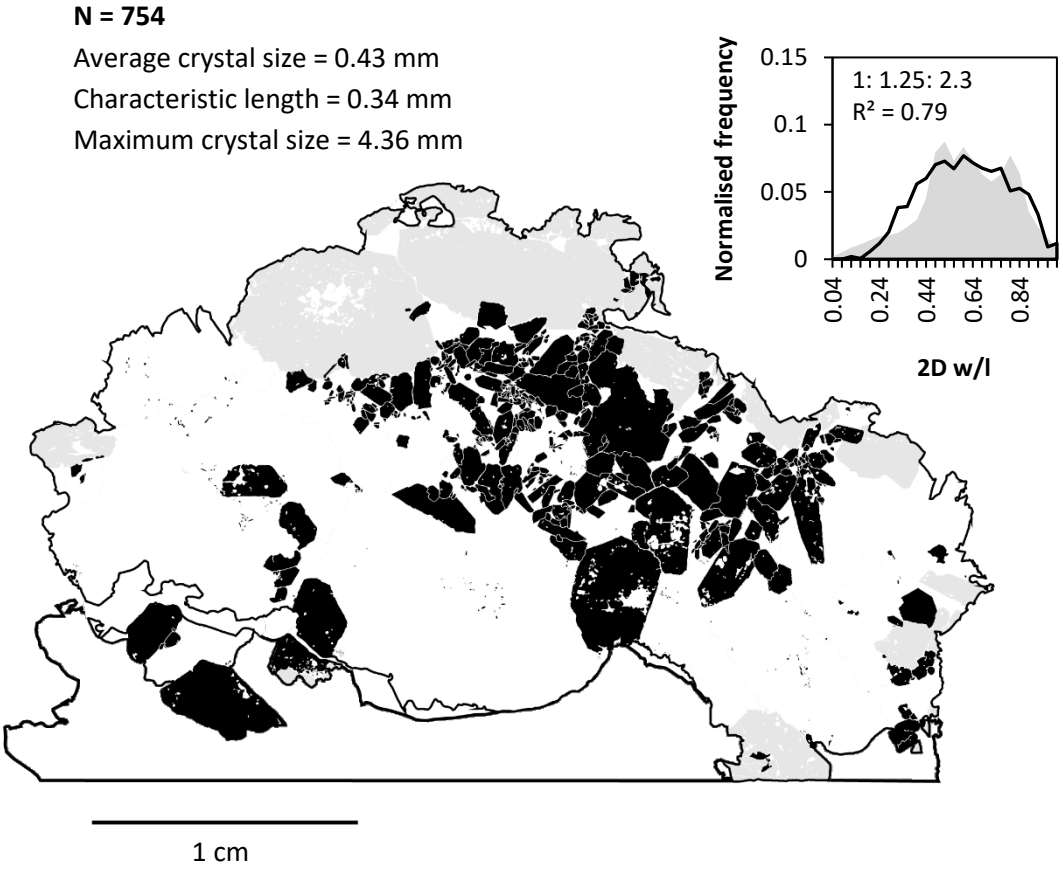

Figure C.2 – Binarised image used to calculate clinopyroxene CSDs in sample M2 A. Grey crystals indicate those truncated by the boundary of the thin section and thus excluded from analysis. Inset histogram visualises the aspect ratio distribution of the measured population (black line), against that of the best fitting shape estimate (grey area).

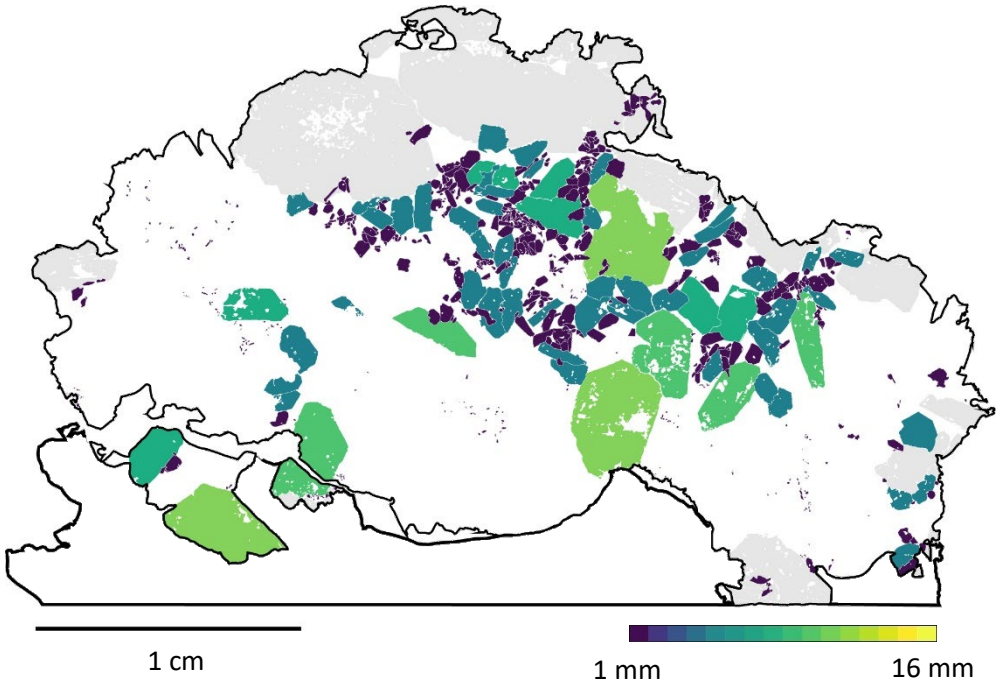

Figure C.3 – Visualisation of clinopyroxene crystal sizes in sample M2 A. Crystals are scaled according to their long axis length, measured by the two-dimensional best-fit ellipse. Grey crystals indicate truncated by the boundary of the thin section and thus excluded from analysis.

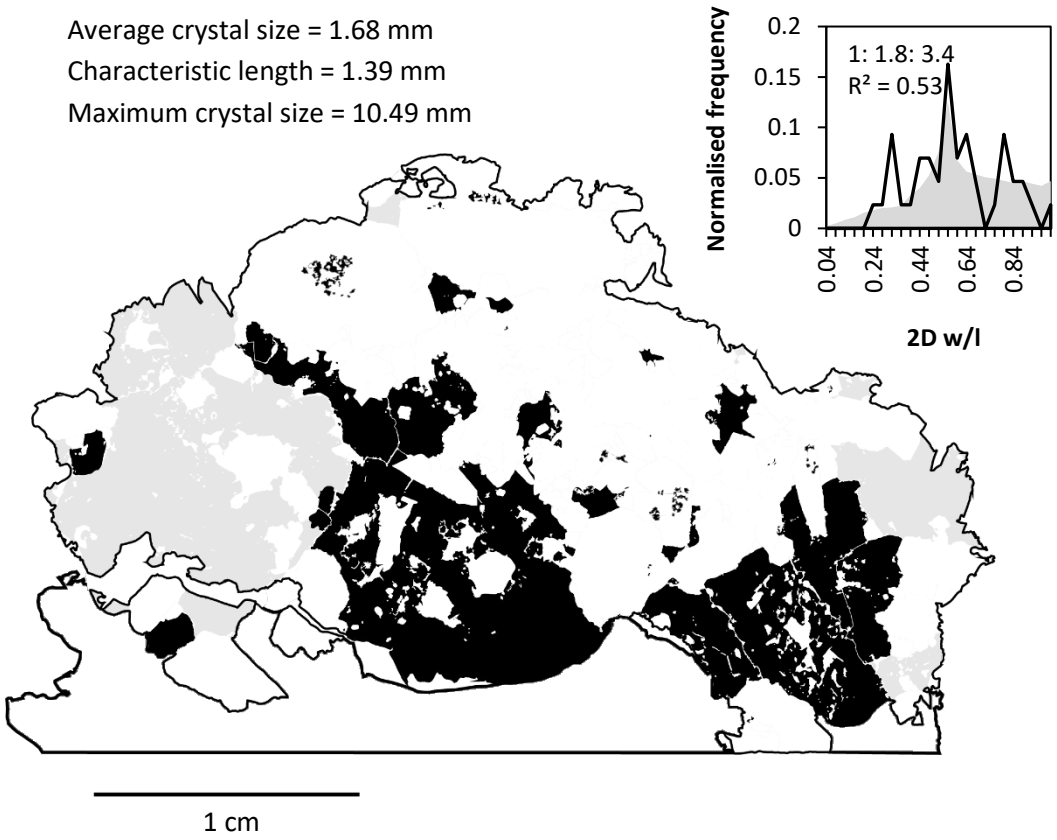

Figure C.4 – Binarised image used to calculate hornblende CSDs in sample M2 A. Grey crystals indicate those truncated by the boundary of the thin section and thus excluded from analysis. Inset histogram visualises the aspect ratio distribution of the measured population (black line), against that of the best fitting shape estimate (grey area).

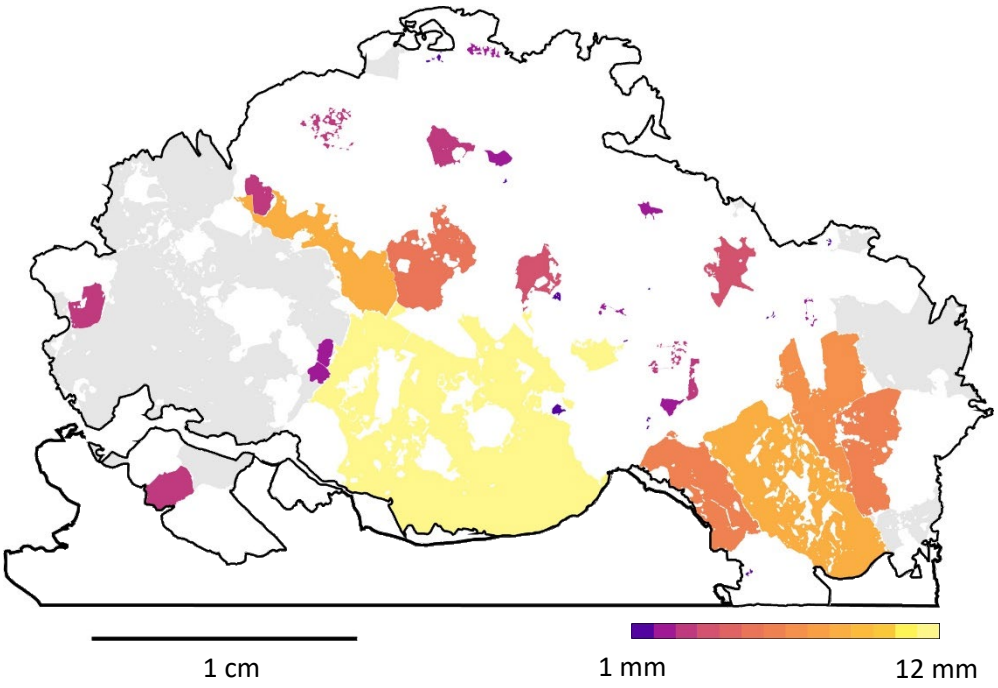

Figure C.5 – Visualisation of hornblende crystal sizes in sample M2 A. Crystals are scaled according to their long axis length, measured by the two-dimensional best-fit ellipse. Grey crystals indicate truncated by the boundary of the thin section and thus excluded from analysis.

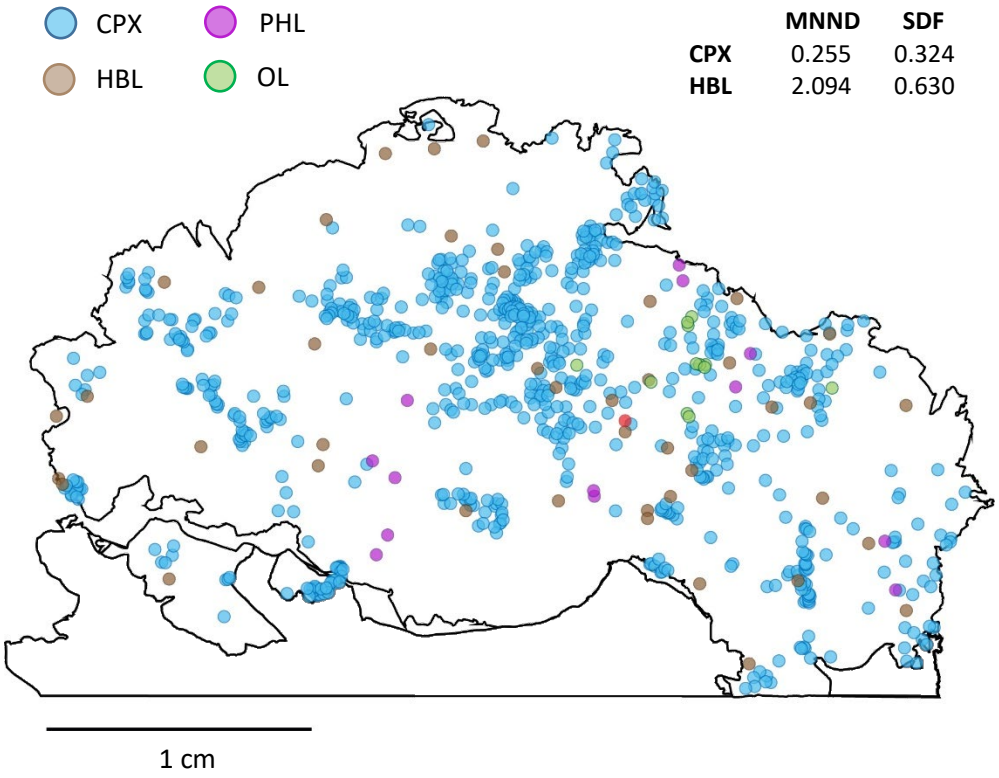

Figure C.6 – Coordinate points used to calculate nearest neighbour distances (in mm) for spatial distribution calculations in sample M2 A. Coordinates represent the weighted centre point of each identified crystal.

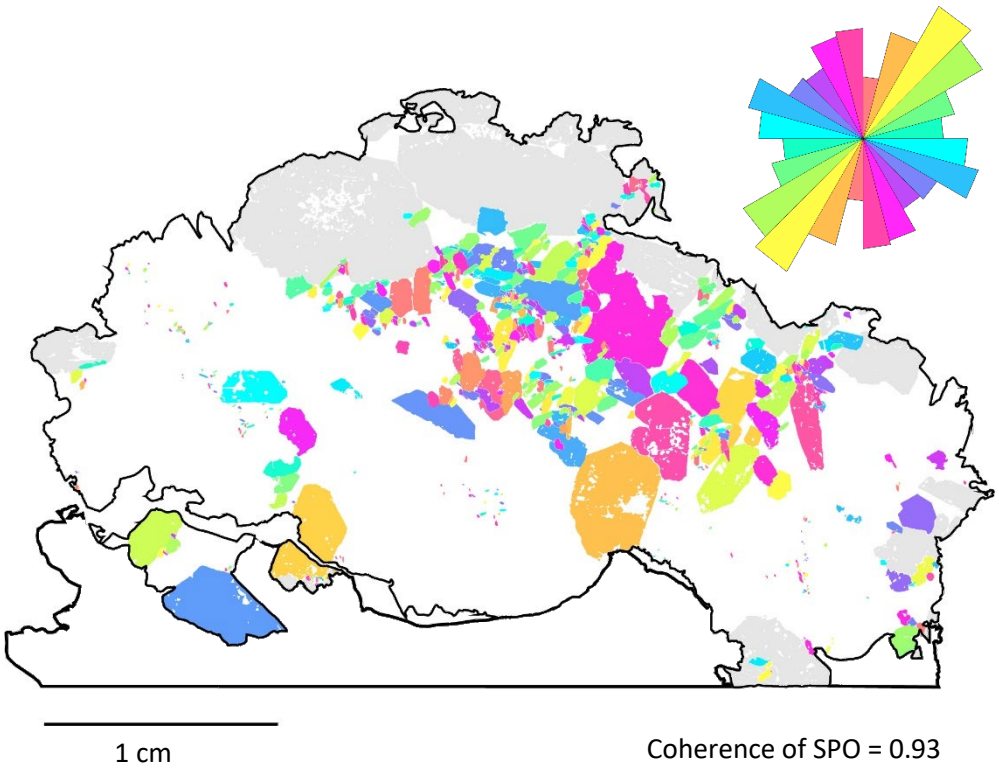

Figure C.7 – Visualisation of shape preferred orientation for clinopyroxene crystals in sample M2 A. Because the xenoliths are ex-situ they are unorientated, meaning that they have no significant direction.

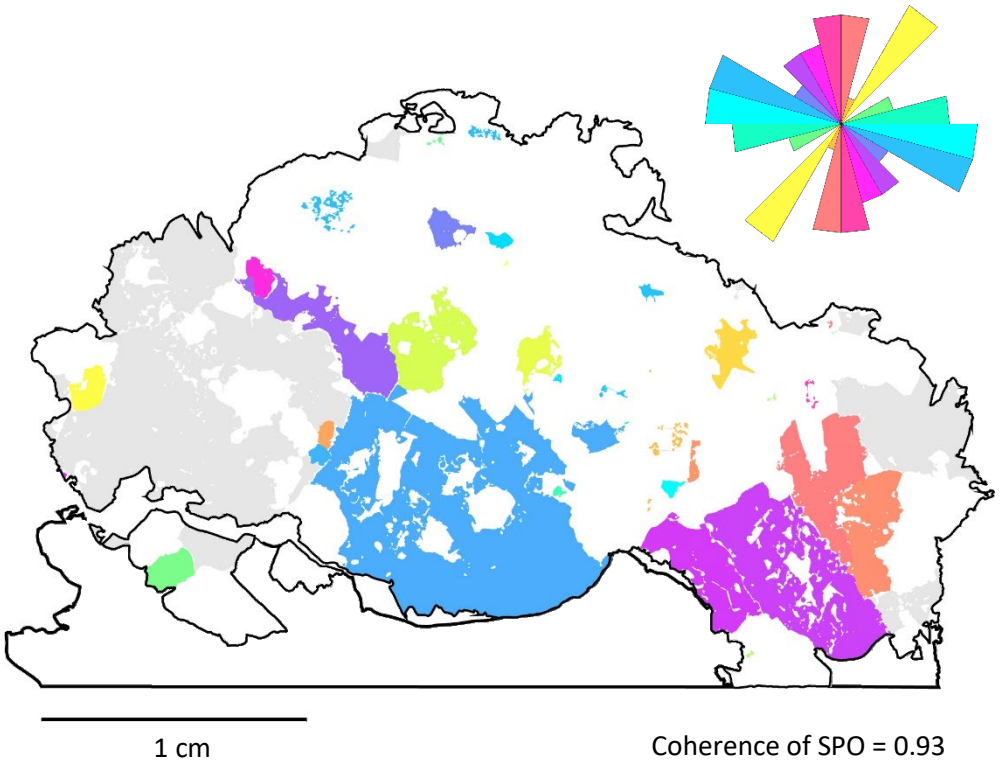

Figure C.8 – Visualisation of shape preferred orientation for hornblende crystals in sample M2 A. Because the xenoliths are ex-situ they are unorientated, meaning that they have no significant direction.

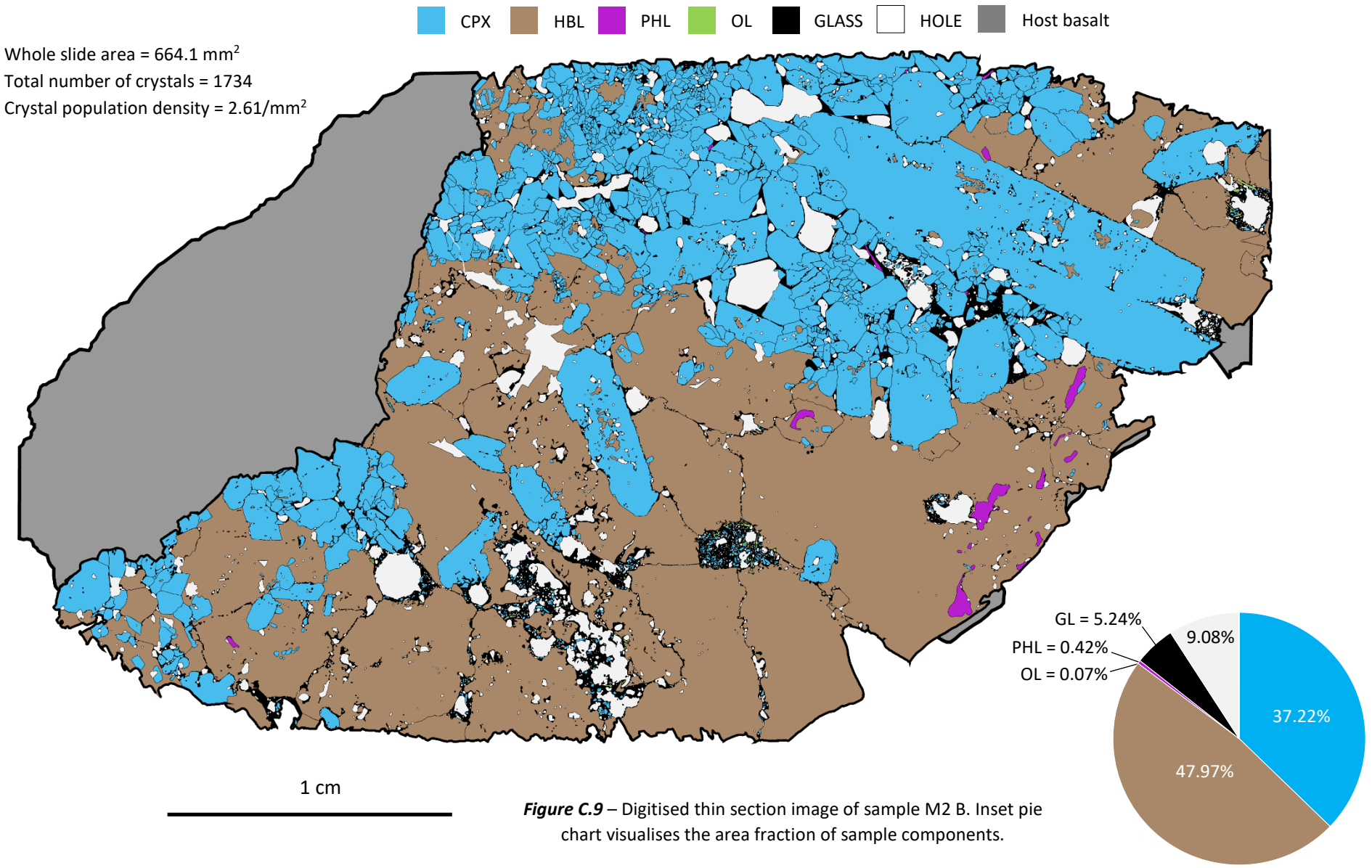

Figure C.9 – Digitised thin section image of sample M2 B. Inset pie chart visualises the area fraction of sample components.

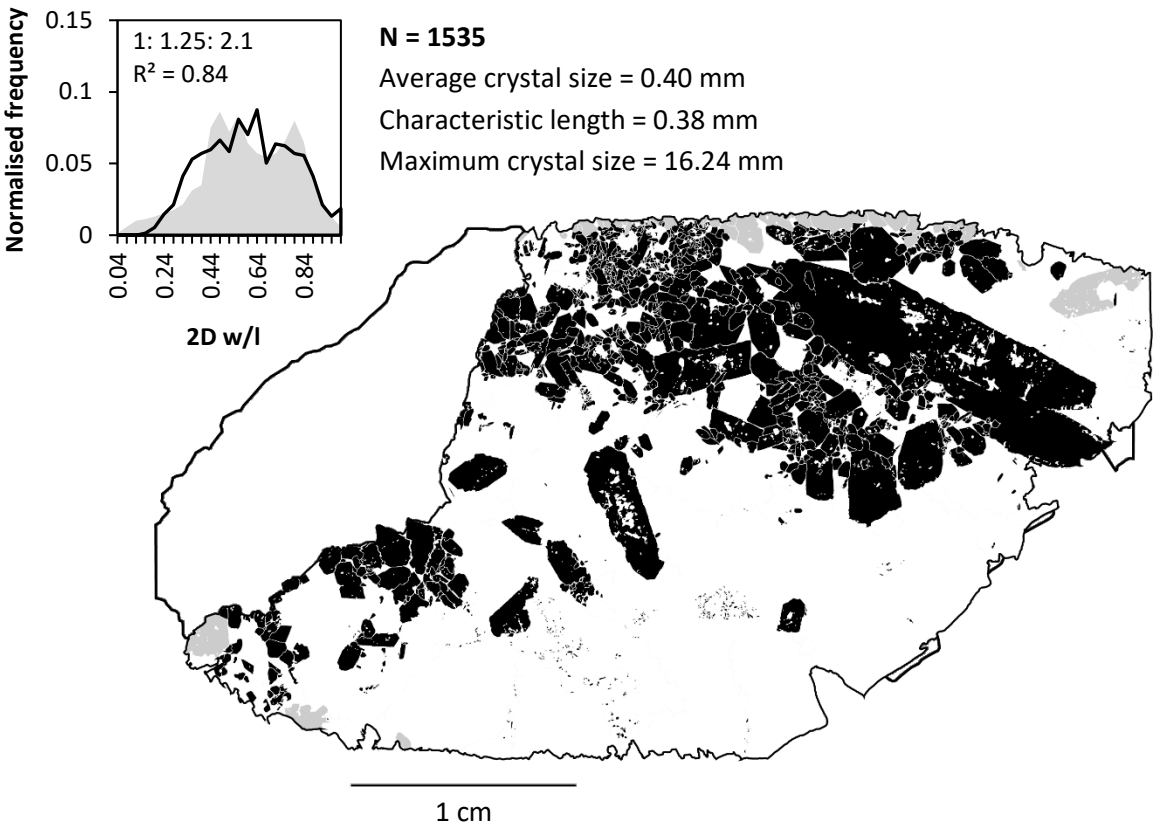

Figure C.10 – Binarised image used to calculate clinopyroxene CSDs in sample M2 B. Grey crystals indicate those truncated by the boundary of the thin section and thus excluded from analysis. Inset histogram visualises the aspect ratio distribution of the measured population (black line), against that of the best fitting shape estimate (grey area).

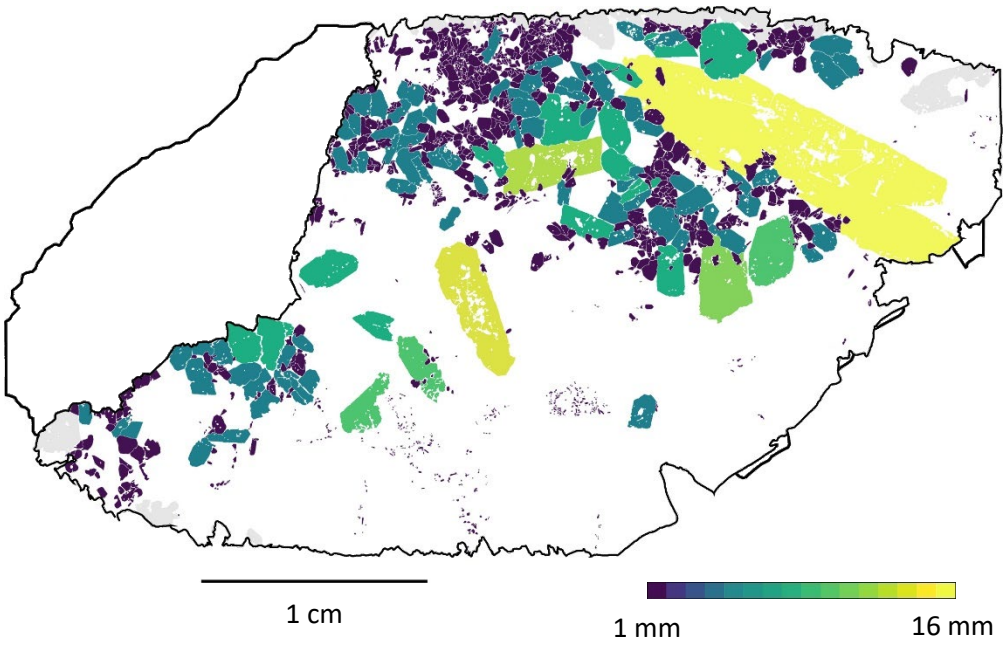

Figure C.11 – Visualisation of clinopyroxene crystal sizes in sample M2 B. Crystals are scaled according to their long axis length, measured by the two-dimensional best-fit ellipse. Grey crystals indicate truncated by the boundary of the thin section and thus excluded from analysis.

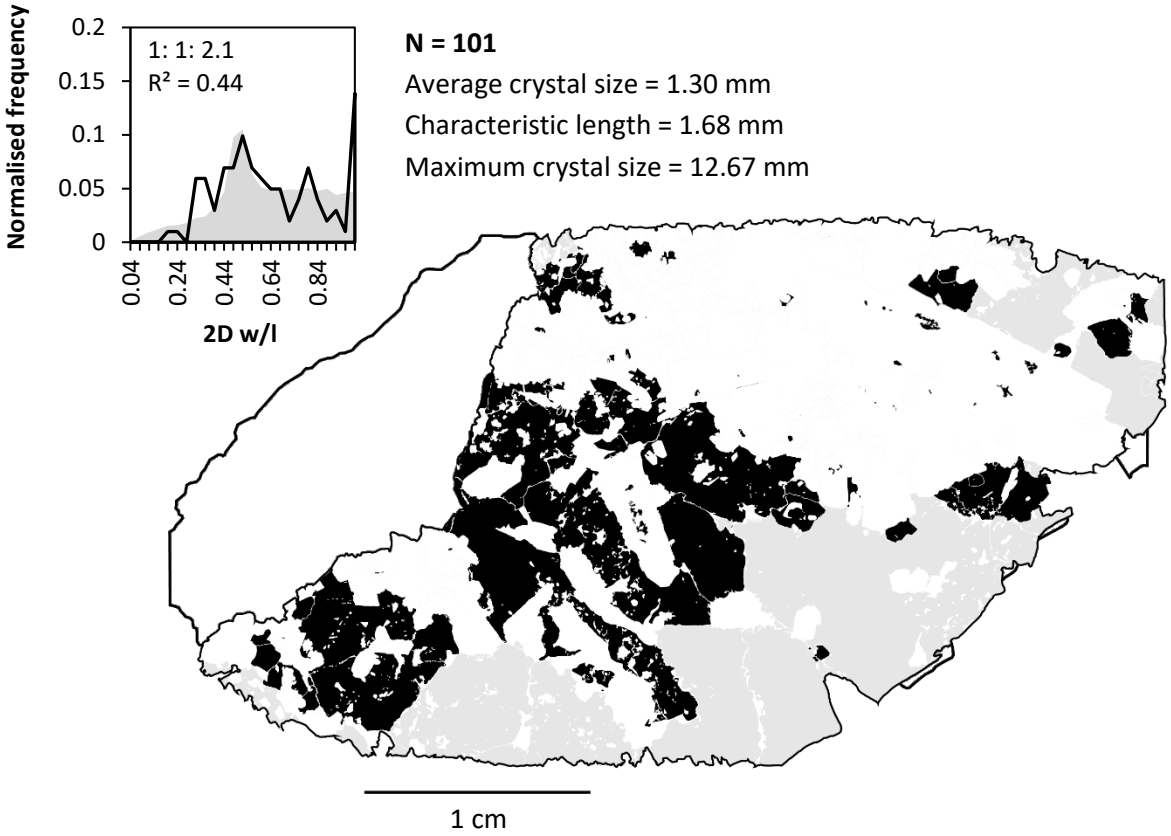

Figure C.12 – Binarised image used to calculate hornblende CSDs in sample M2 B. Grey crystals indicate those truncated by the boundary of the thin section and thus excluded from analysis. Inset histogram visualises the aspect ratio distribution of the measured population (black line), against that of the best fitting shape estimate (grey area).

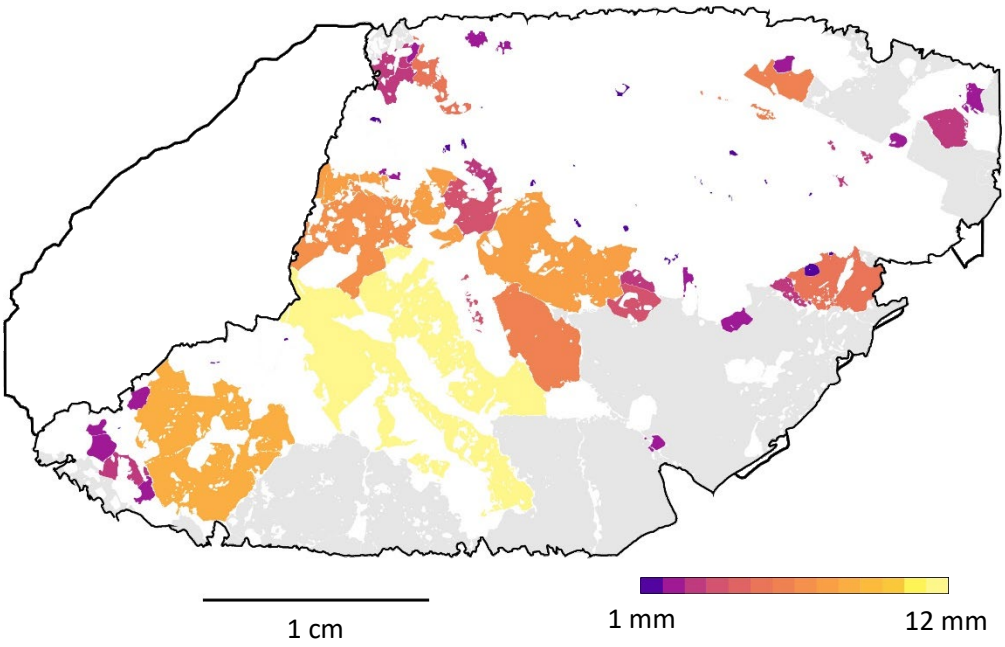

Figure C.13 – Visualisation of hornblende crystal sizes in sample M2 B. Crystals are scaled according to their long axis length, measured by the two-dimensional best-fit ellipse. Grey crystals indicate truncated by the boundary of the thin section and thus excluded from analysis.

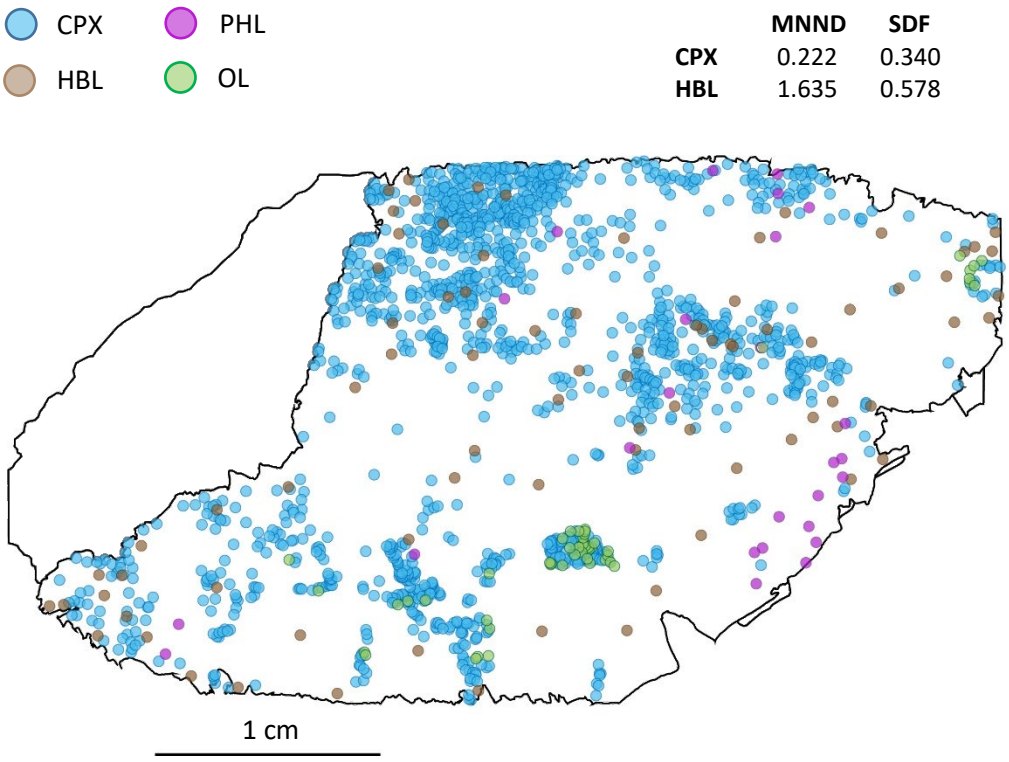

Figure C.14 – Coordinate points used to calculate nearest neighbour distances (in mm) for spatial distribution calculations in sample M2 B. Coordinates represent the weighted centre point of each identified crystal.

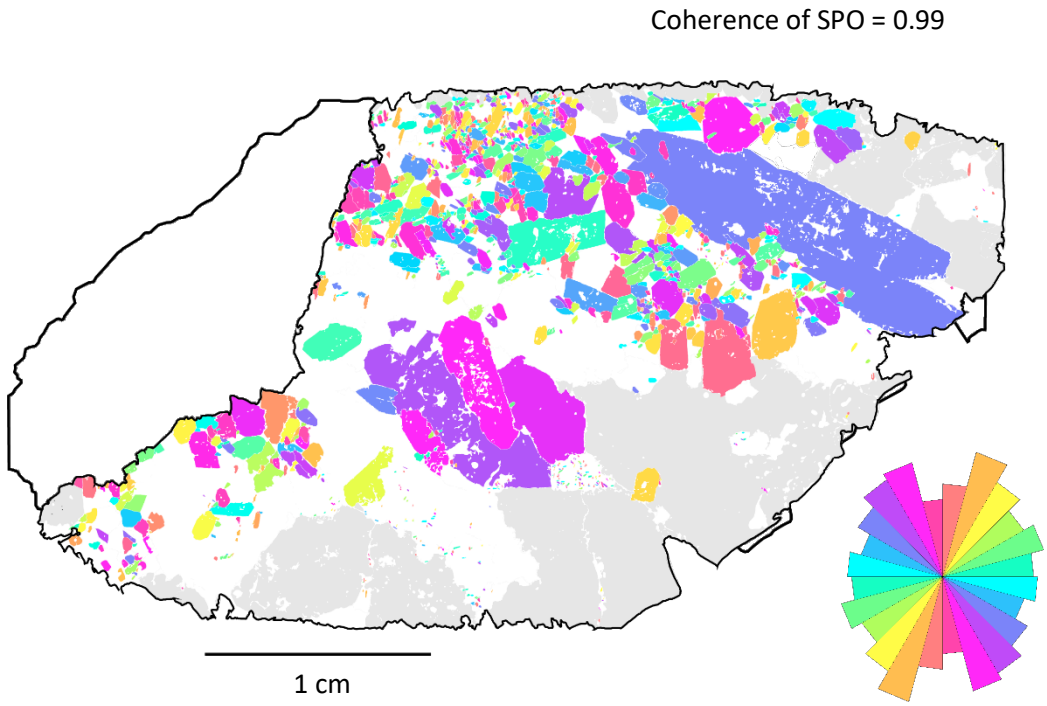

Figure C.15 – Visualisation of shape preferred orientation for clinopyroxene crystals in sample M2 B. Because the xenoliths are ex-situ they are unorientated, meaning that they have no significant direction.

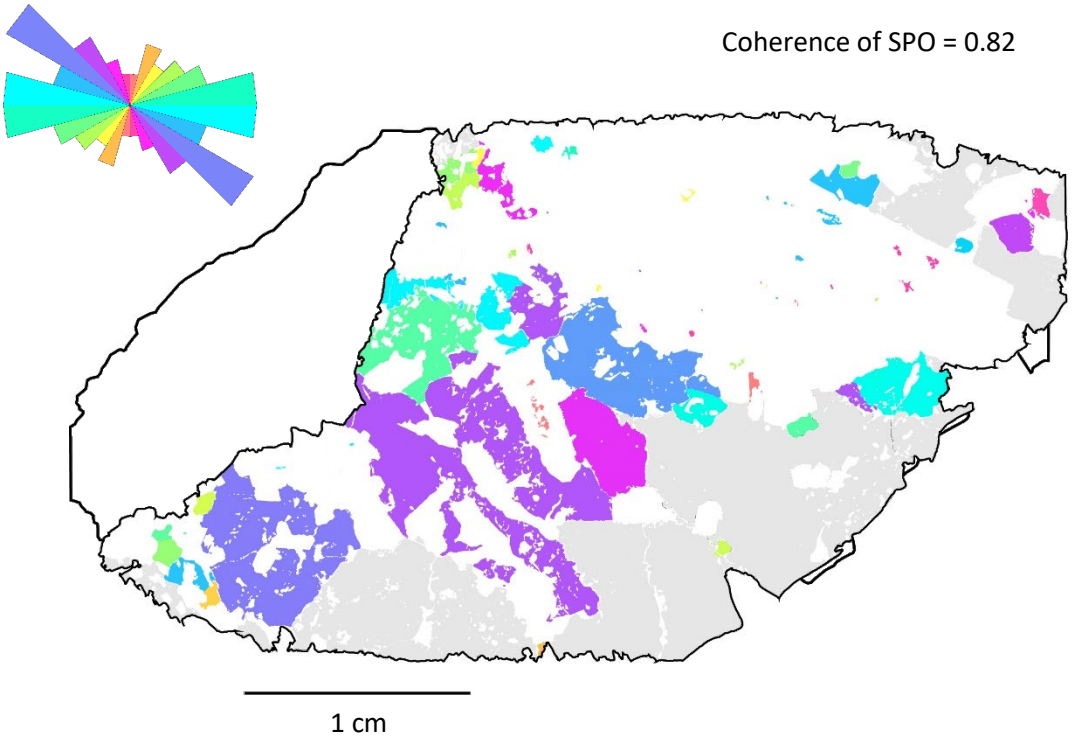

Figure C.16 – Visualisation of shape preferred orientation for hornblende crystals in sample M2 B. Because the xenoliths are ex-situ they are unorientated, meaning that they have no significant direction.

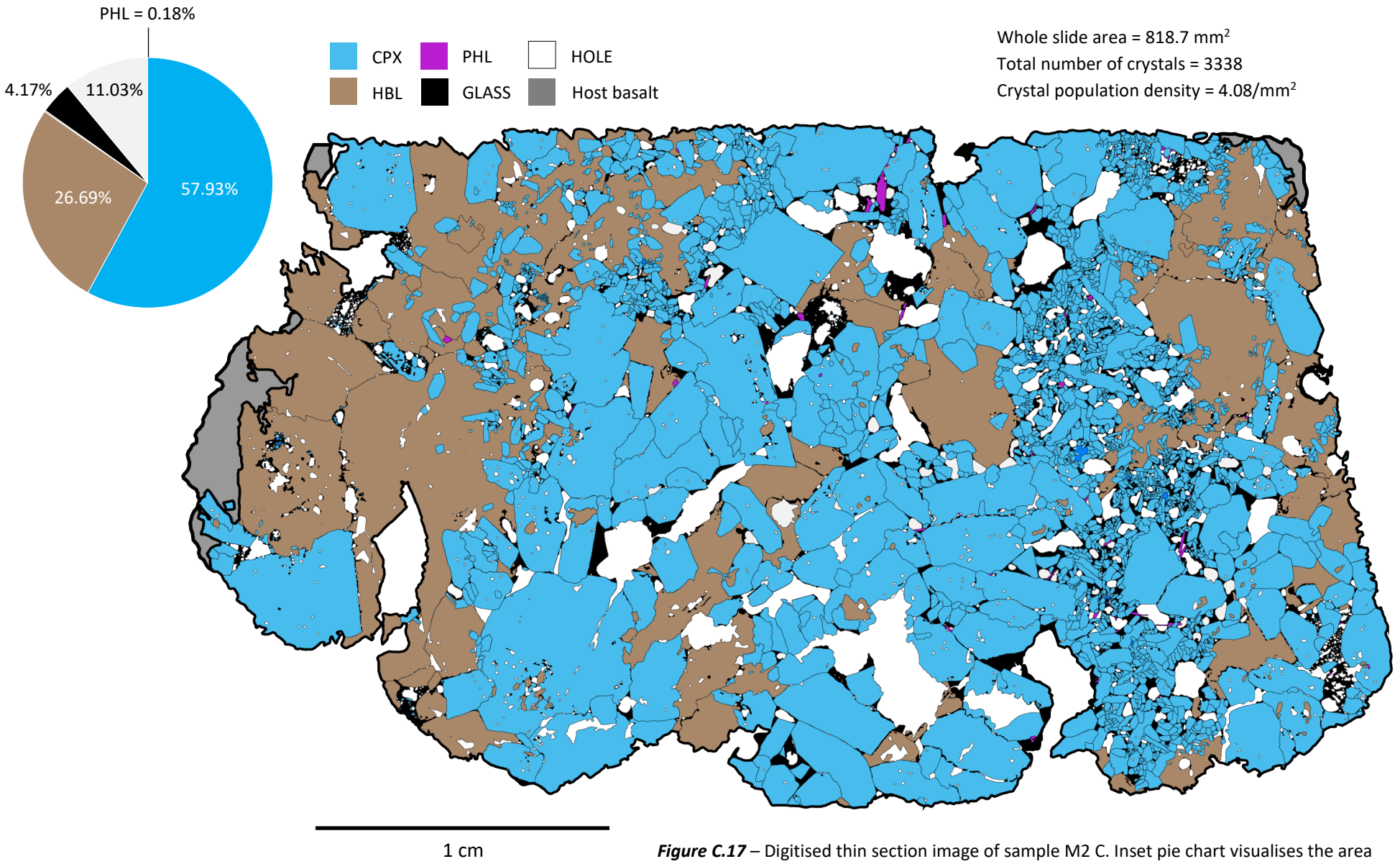

Figure C.17 – Digitised thin section image of sample M2 C. Inset pie chart visualises the area fraction of sample components.

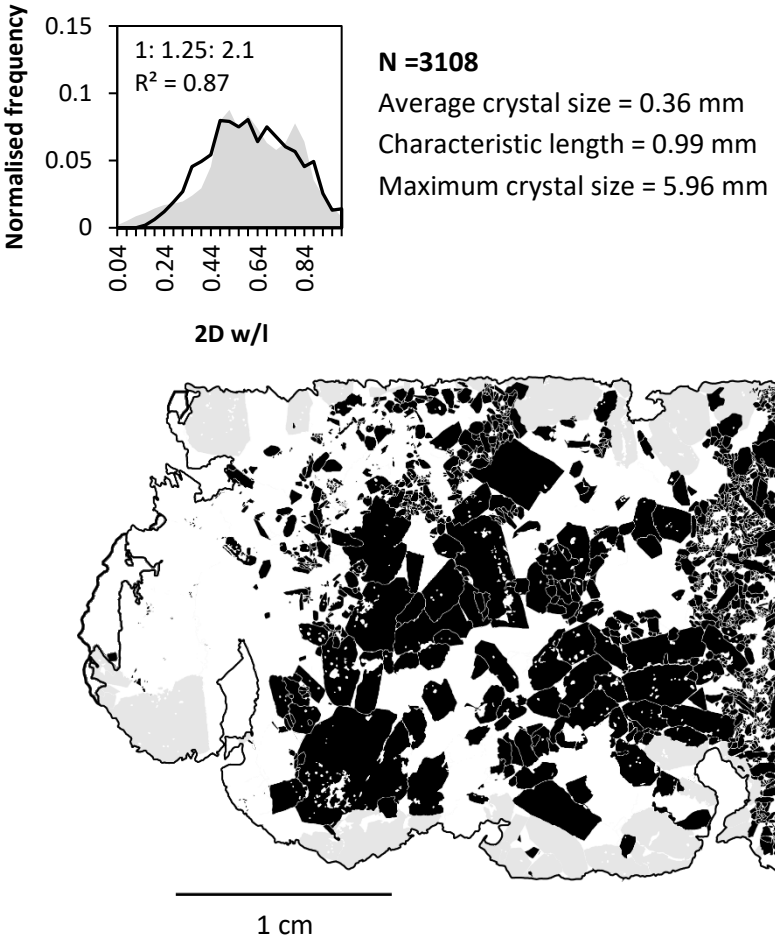

Figure C.18 – Binarised image used to calculate clinopyroxene CSDs in sample M2 C. Grey crystals indicate those truncated by the boundary of the thin section and thus excluded from analysis. Inset histogram visualises the aspect ratio distribution of the measured population (black line), against that of the best fitting shape estimate (grey area).

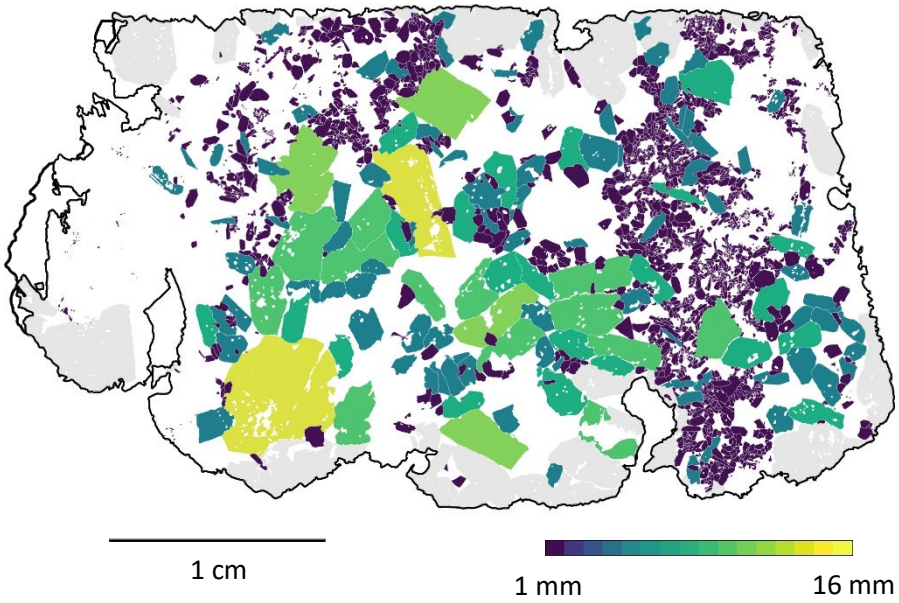

Figure C.19 – Visualisation of clinopyroxene crystal sizes in sample M2 C. Crystals are scaled according to their long axis length, measured by the two-dimensional best-fit ellipse. Grey crystals indicate truncated by the boundary of the thin section and thus excluded from analysis.

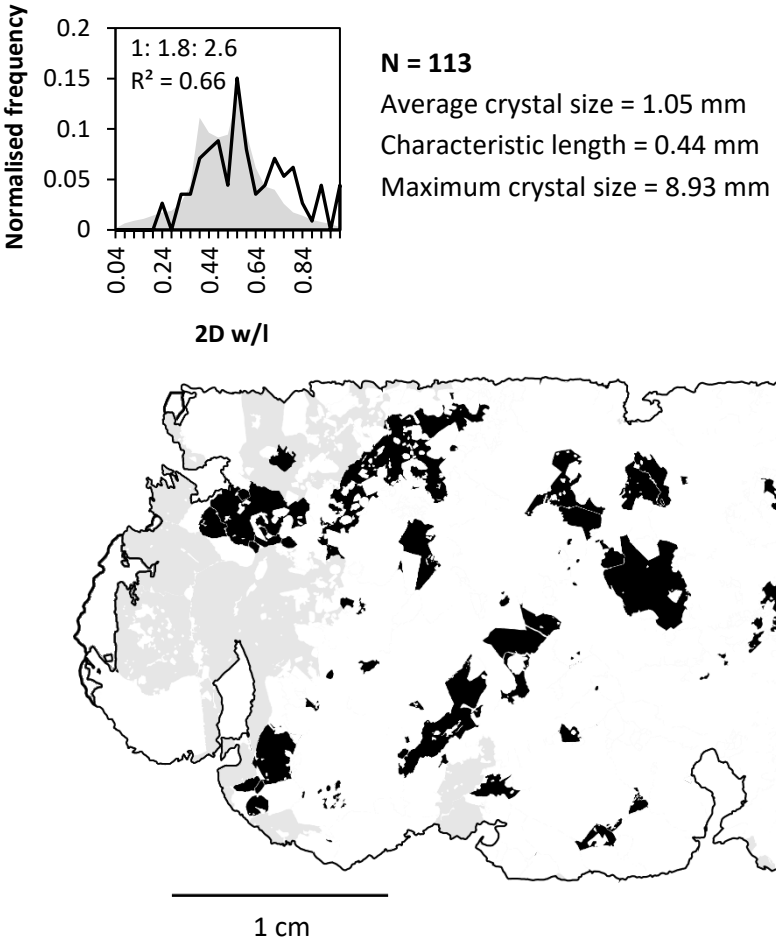

Figure C.20 – Binarised image used to calculate hornblende CSDs in sample M2 C. Grey crystals indicate those truncated by the boundary of the thin section and thus excluded from analysis. Inset histogram visualises the aspect ratio distribution of the measured population (black line), against that of the best fitting shape estimate (grey area).

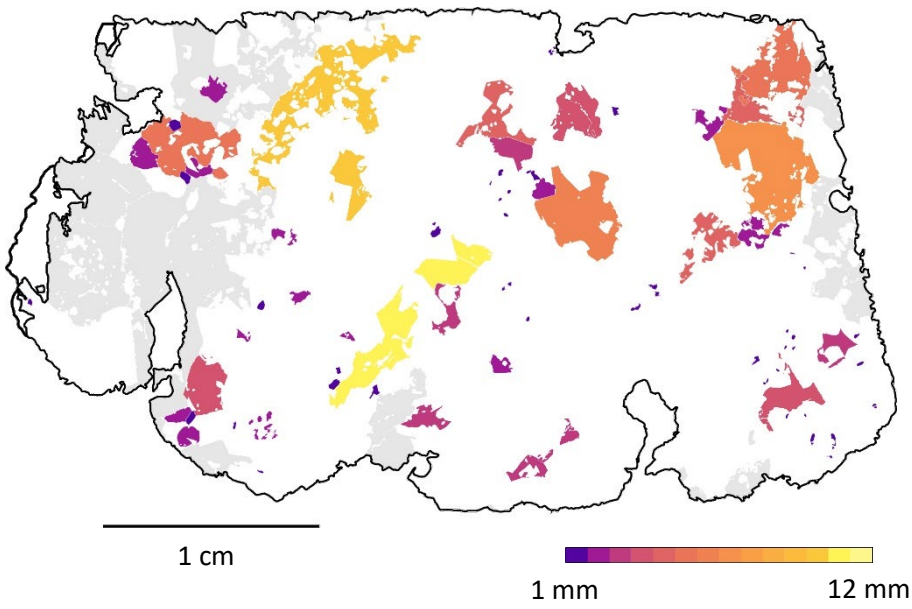

Figure C.21 – Visualisation of hornblende crystal sizes in sample M2 C. Crystals are scaled according to their long axis length, measured by the two-dimensional best-fit ellipse. Grey crystals indicate truncated by the boundary of the thin section and thus excluded from analysis.

	MNND	SDF
CPX	0.222	0.340
HBL	1.635	0.578

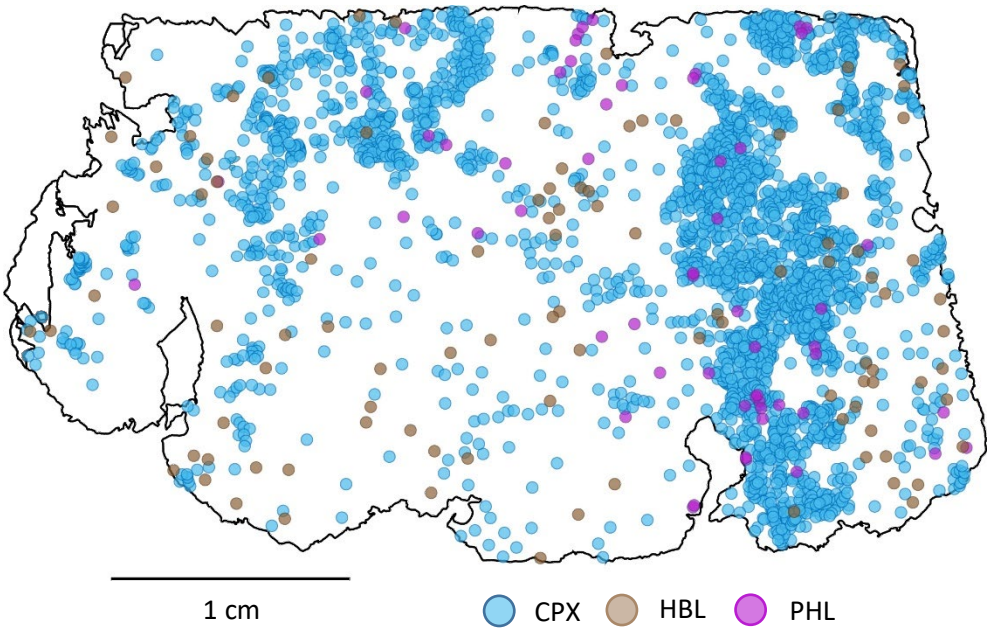

Figure C.22 – Coordinate points used to calculate nearest neighbour distances (in mm) for spatial distribution calculations in sample M2 C. Coordinates represent the weighted centre point of each identified crystal.

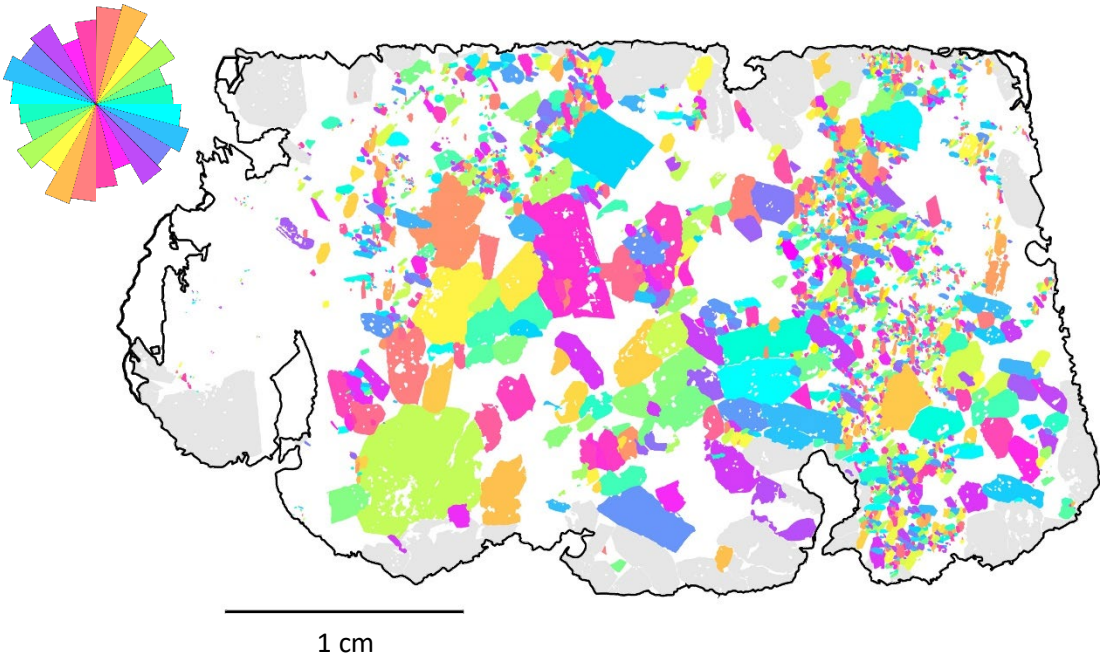

Figure C.23 – Visualisation of shape preferred orientation for clinopyroxene crystals in sample M2 C. Because the xenoliths are ex-situ they are unorientated, meaning that they have no significant direction.

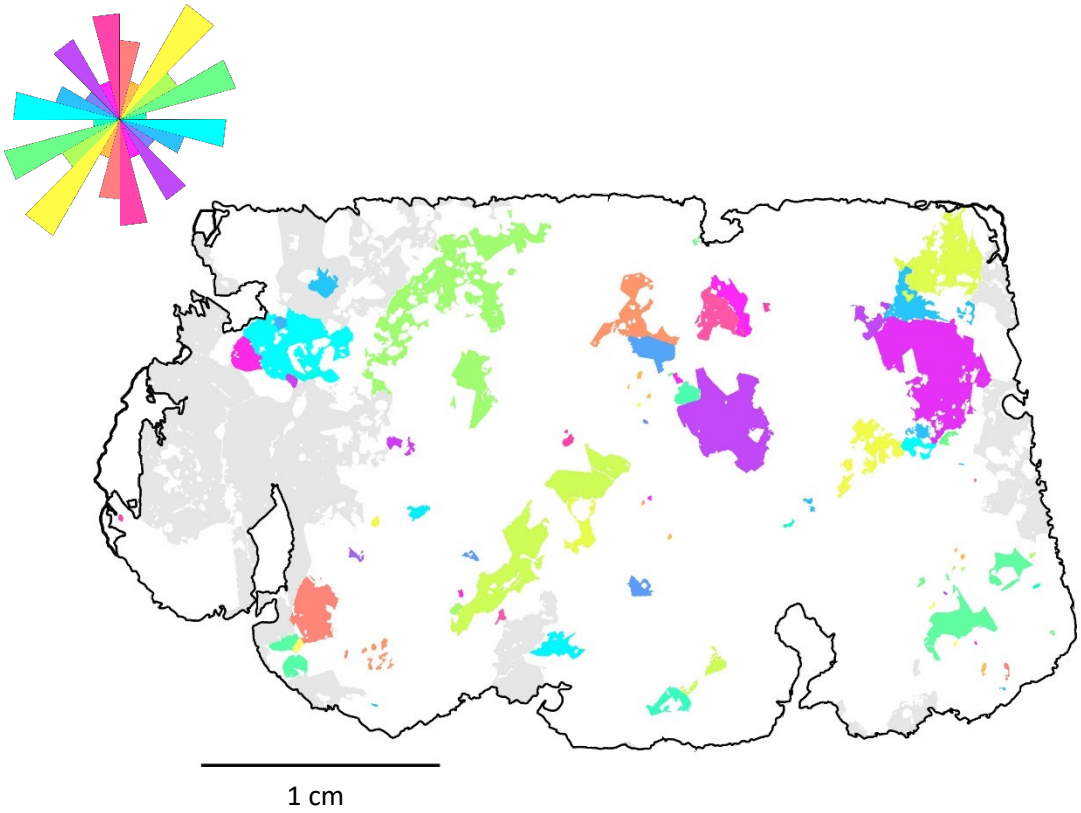

Figure C.24 – Visualisation of shape preferred orientation for hornblende crystals in sample M2 C. Because the xenoliths are ex-situ they are unorientated, meaning that they have no significant direction.

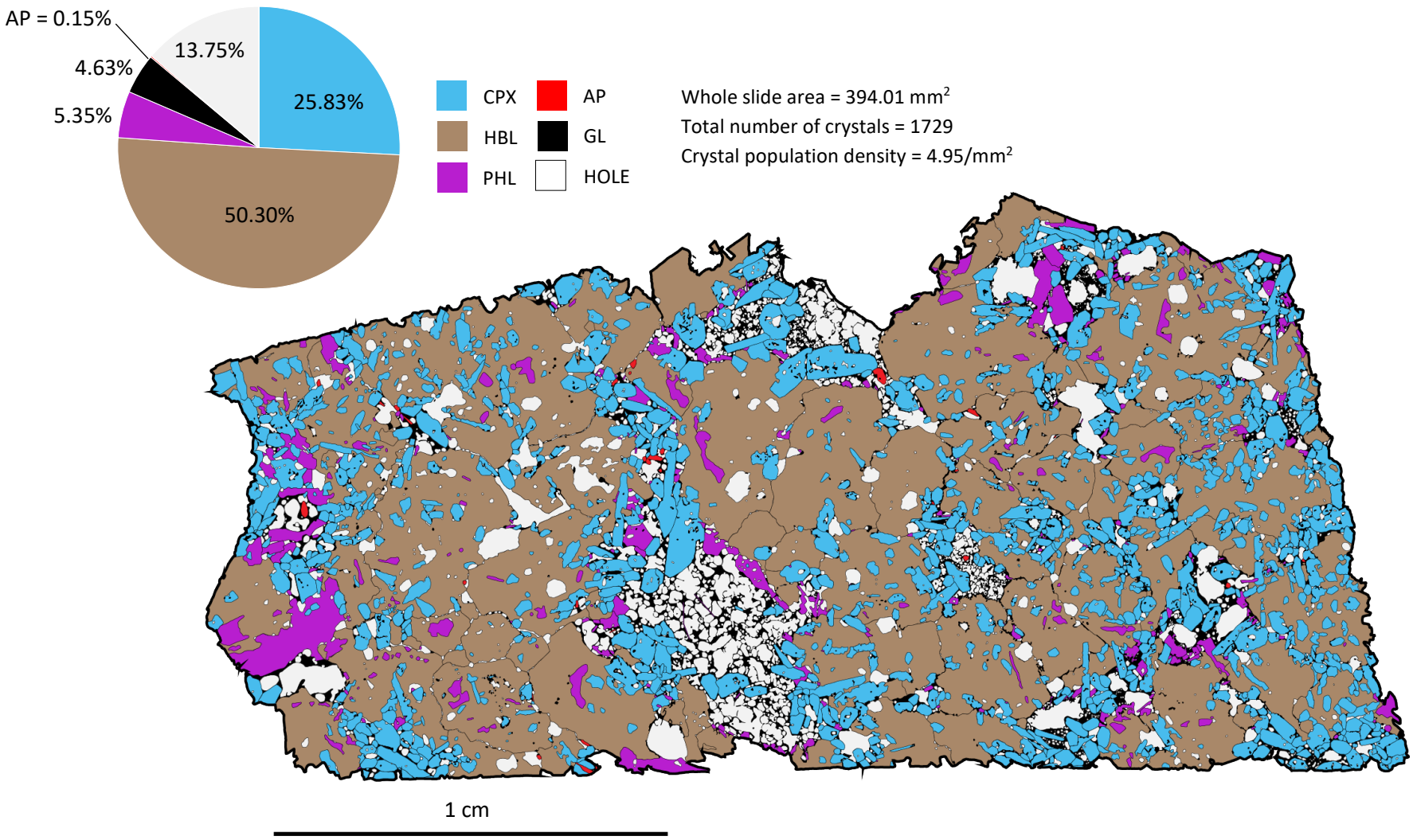

Figure C.25 – Digitised thin section image of sample M4 A. Inset pie chart visualises the area fraction of sample components.

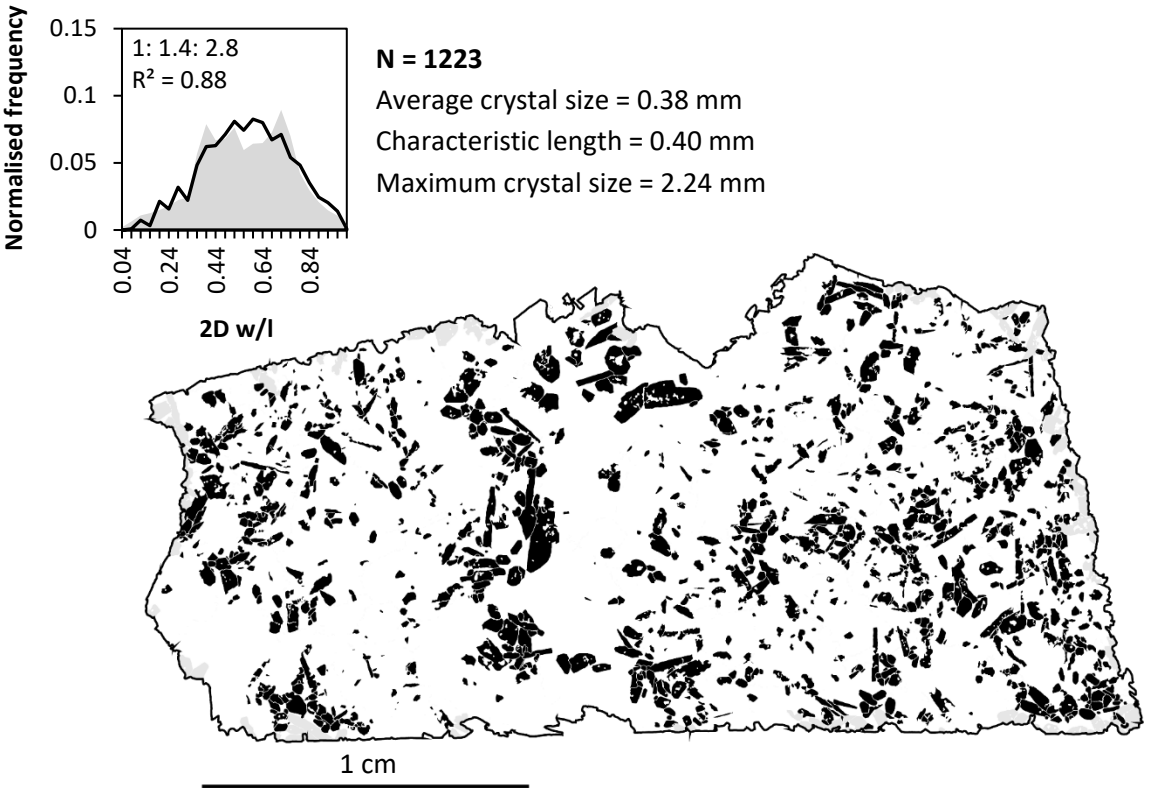

Figure C.26 – Binarised image used to calculate clinopyroxene CSDs in sample M4 A. Grey crystals indicate those truncated by the boundary of the thin section and thus excluded from analysis. Inset histogram visualises the aspect ratio distribution of the measured population (black line), against that of the best fitting shape estimate (grey area).

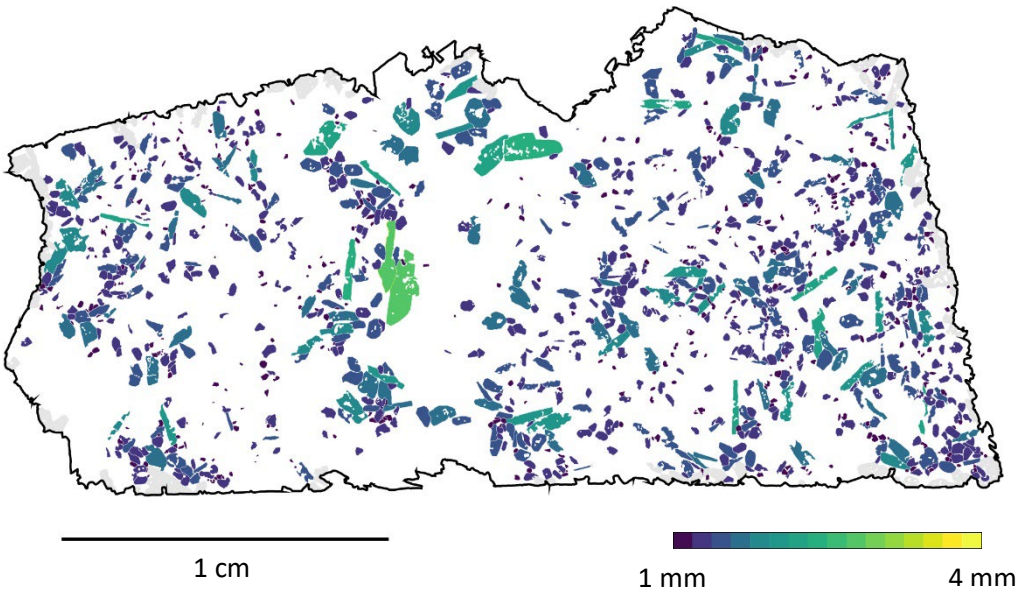

Figure C.27 – Visualisation of clinopyroxene crystal sizes in sample M4 A. Crystals are scaled according to their long axis length, measured by the two-dimensional best-fit ellipse. Grey crystals indicate truncated by the boundary of the thin section and thus excluded from analysis.

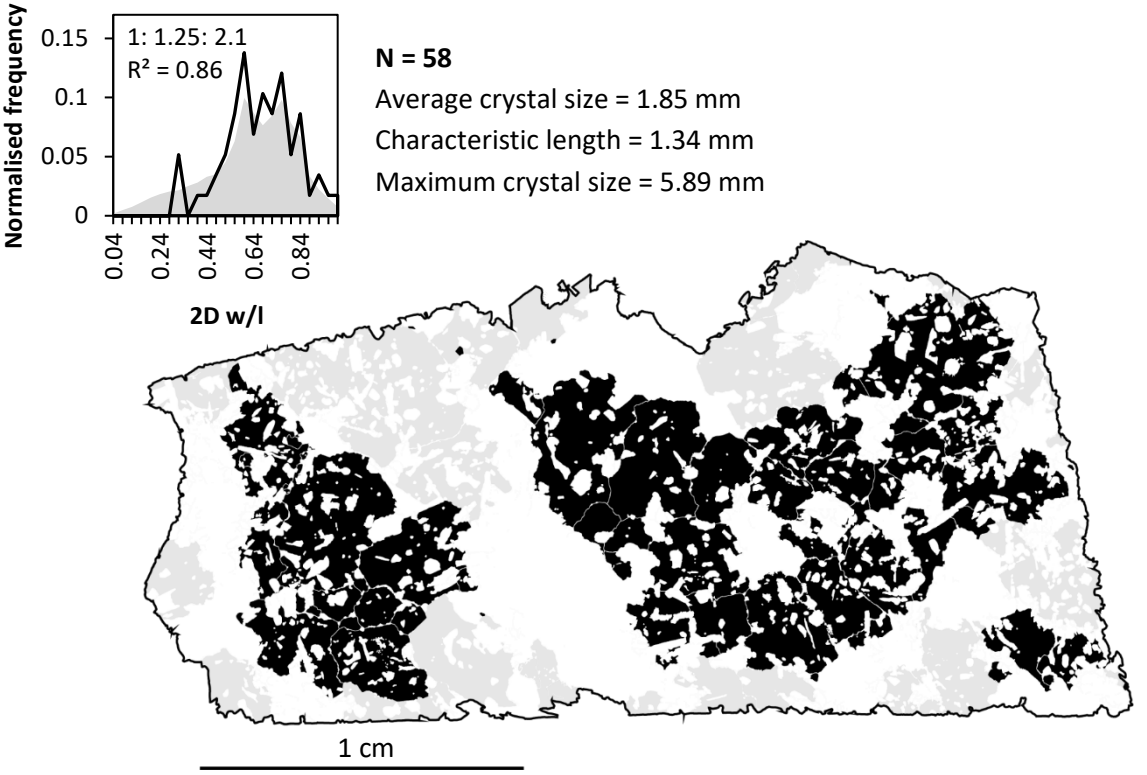

Figure C.28 – Binarised image used to calculate hornblende CSDs in sample M4 A. Grey crystals indicate those truncated by the boundary of the thin section and thus excluded from analysis. Inset histogram visualises the aspect ratio distribution of the measured population (black line), against that of the best fitting shape estimate (grey area).

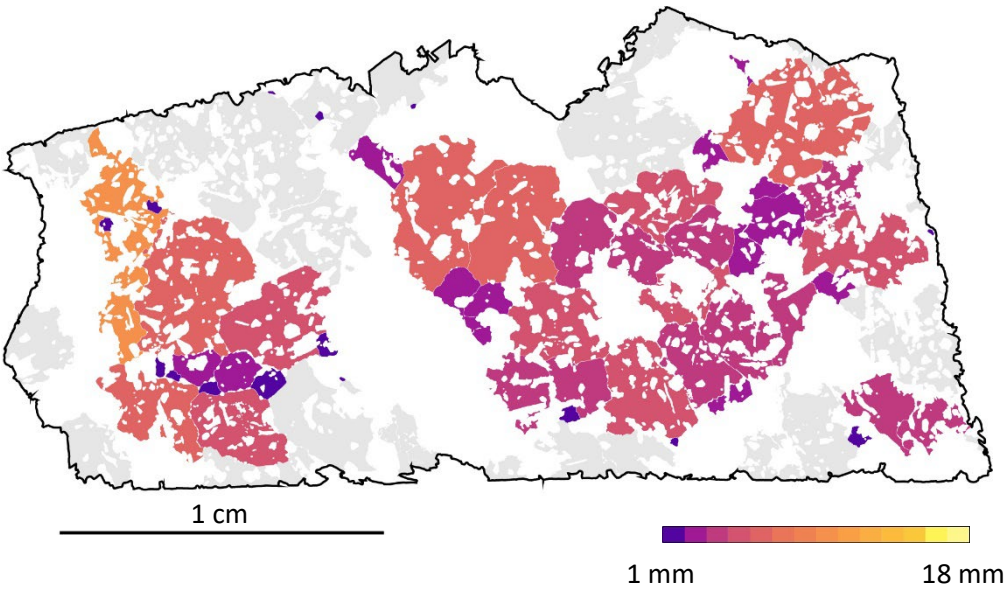

Figure C.29 – Visualisation of hornblende crystal sizes in sample M4 A. Crystals are scaled according to their long axis length, measured by the two-dimensional best-fit ellipse. Grey crystals indicate truncated by the boundary of the thin section and thus excluded from analysis.

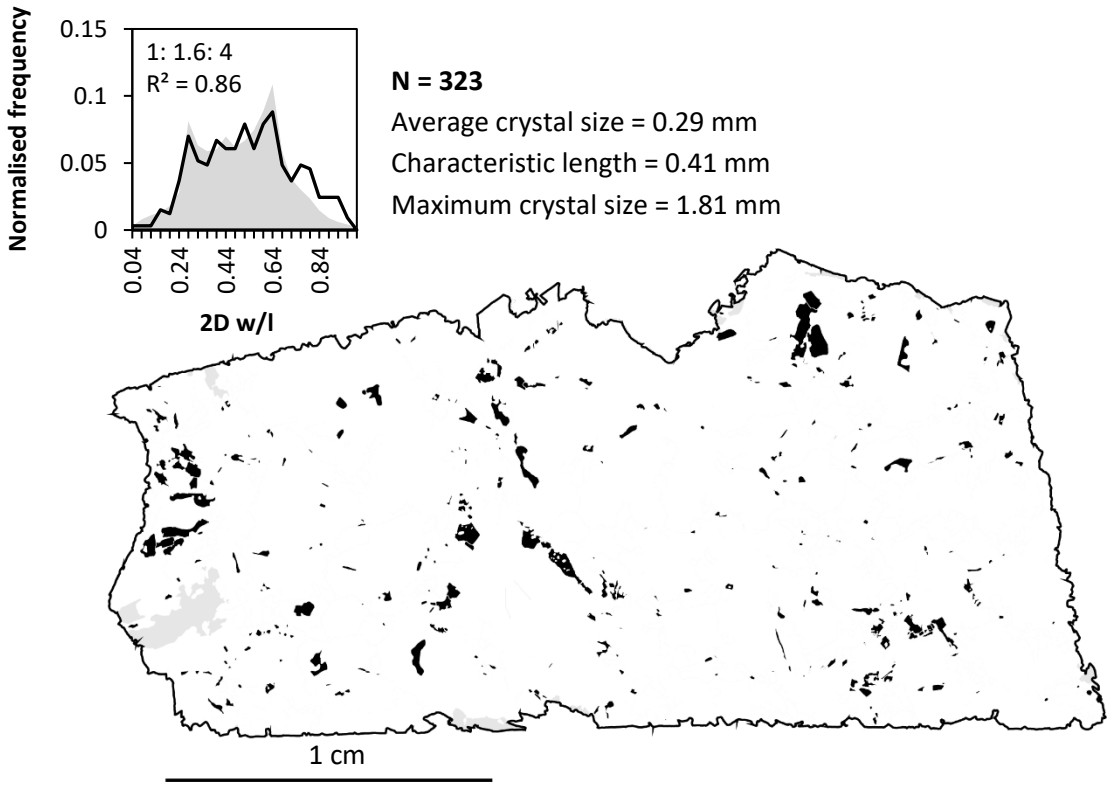

Figure C.30 – Binarised image used to calculate phlogopite CSDs in sample M4 A. Grey crystals indicate those truncated by the boundary of the thin section and thus excluded from analysis. Inset histogram visualises the aspect ratio distribution of the measured population (black line), against that of the best fitting shape estimate (grey area).

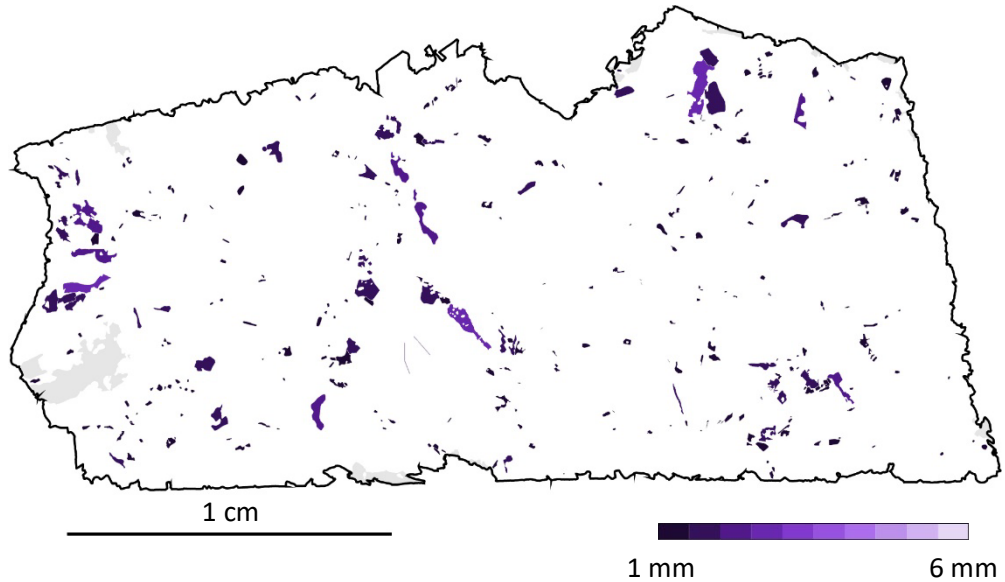

Figure C.31 – Visualisation of phlogopite crystal sizes in sample M4 A. Crystals are scaled according to their long axis length, measured by the two-dimensional best-fit ellipse. Grey crystals indicate truncated by the boundary of the thin section and thus excluded from analysis.

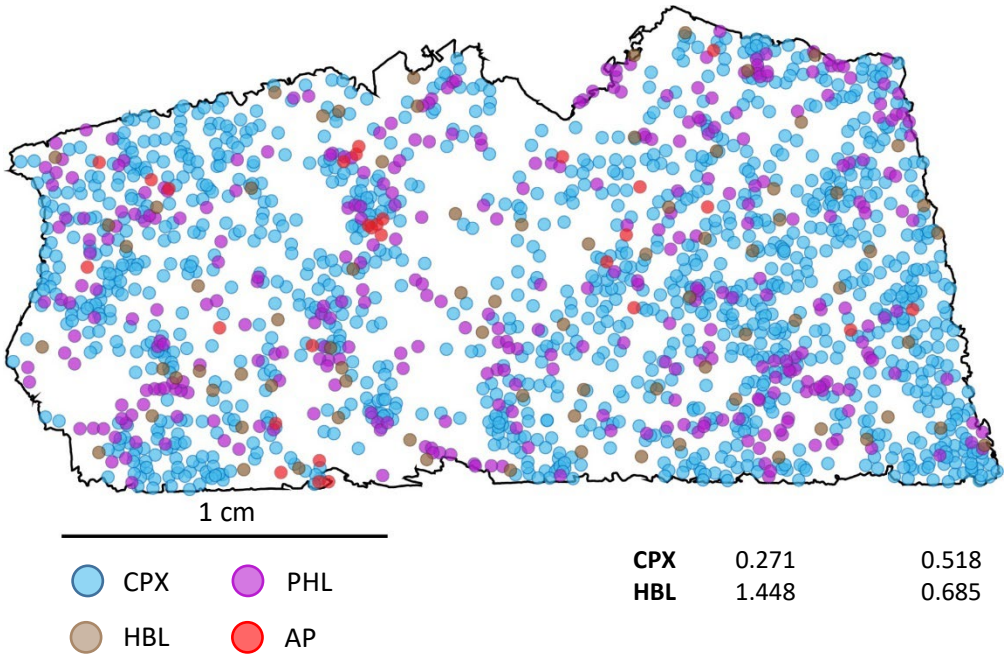

Figure C.32 – Coordinate points used to calculate nearest neighbour distances (in mm) for spatial distribution calculations in sample M4 A. Coordinates represent the weighted centre point of each identified crystal.

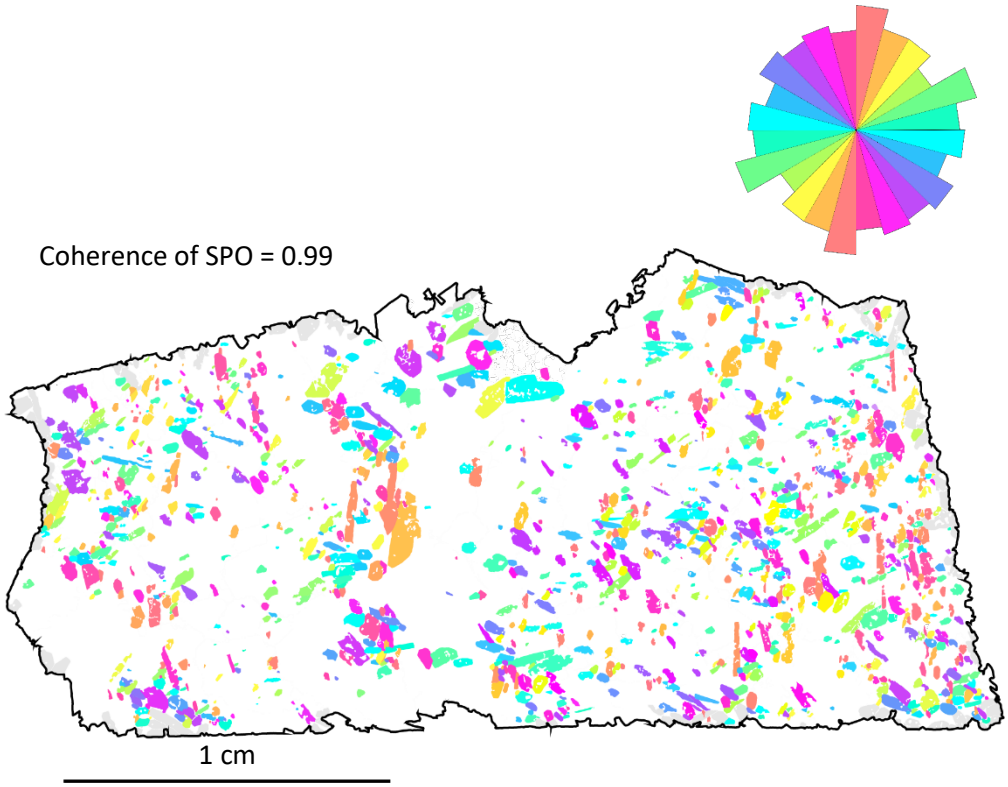

Figure C.33 – Visualisation of shape preferred orientation for clinopyroxene crystals in sample M4 A. Because the xenoliths are ex-situ they are unorientated, meaning that they have no significant direction.

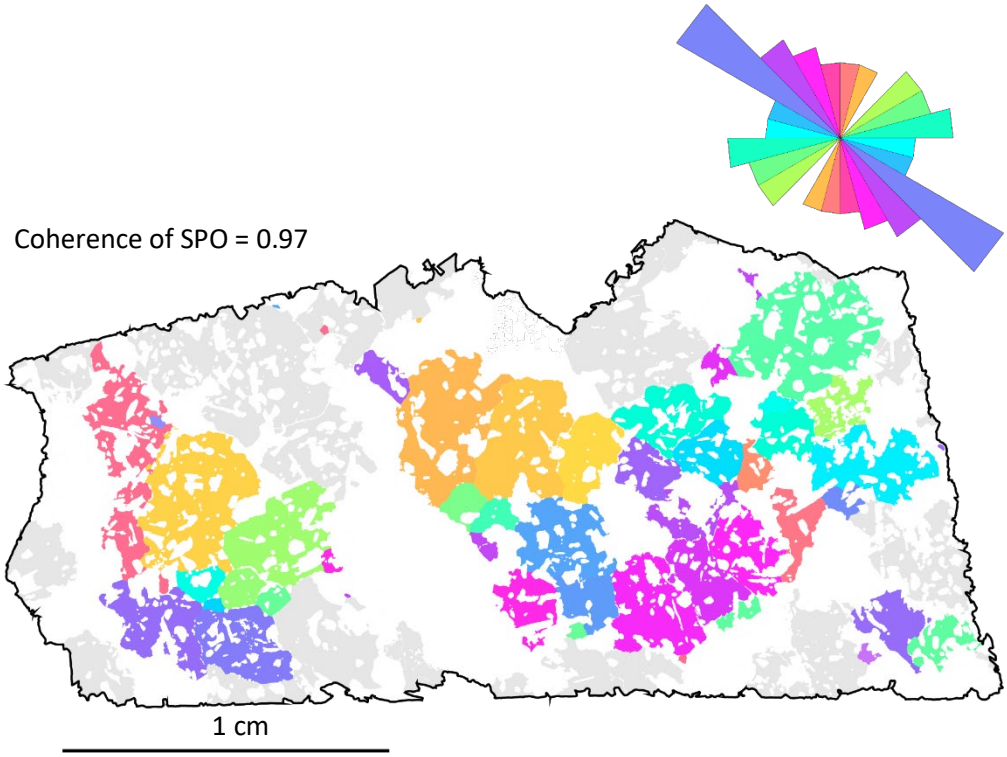

Figure C.34 – Visualisation of shape preferred orientation for hornblende crystals in sample M4 A. Because the xenoliths are ex-situ they are unorientated, meaning that they have no significant direction.

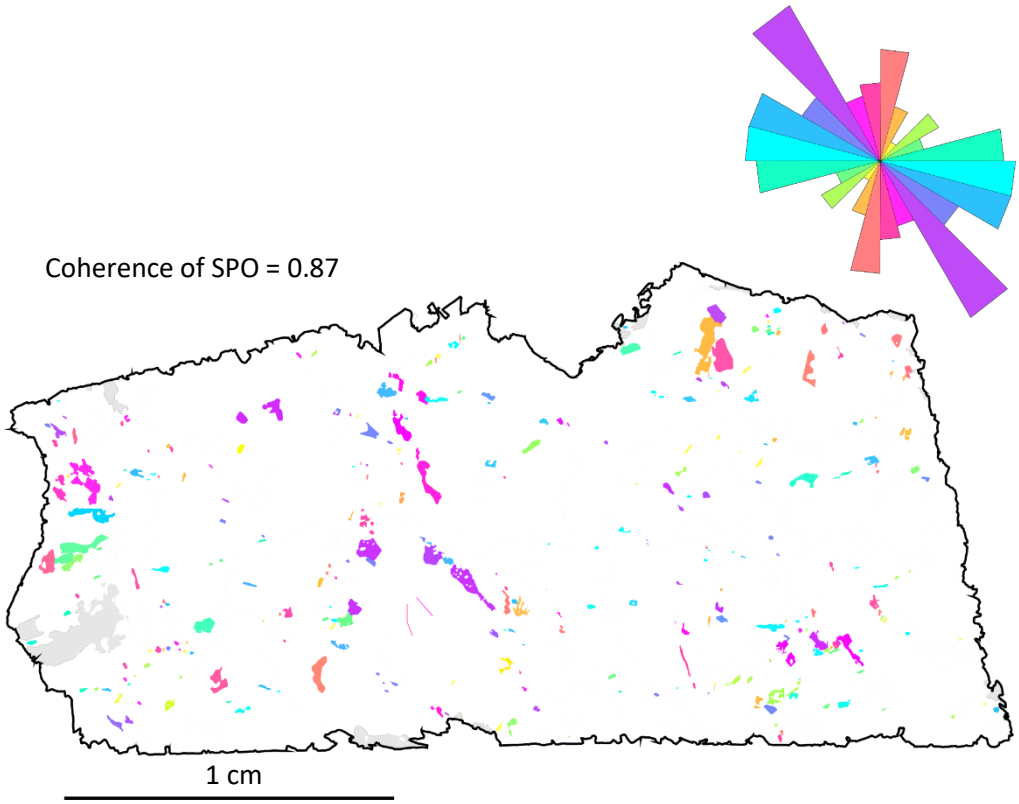

Figure C.35 – Visualisation of shape preferred orientation for phlogopite crystals in sample M4 A. Because the xenoliths are ex-situ they are unorientated, meaning that they have no significant direction.

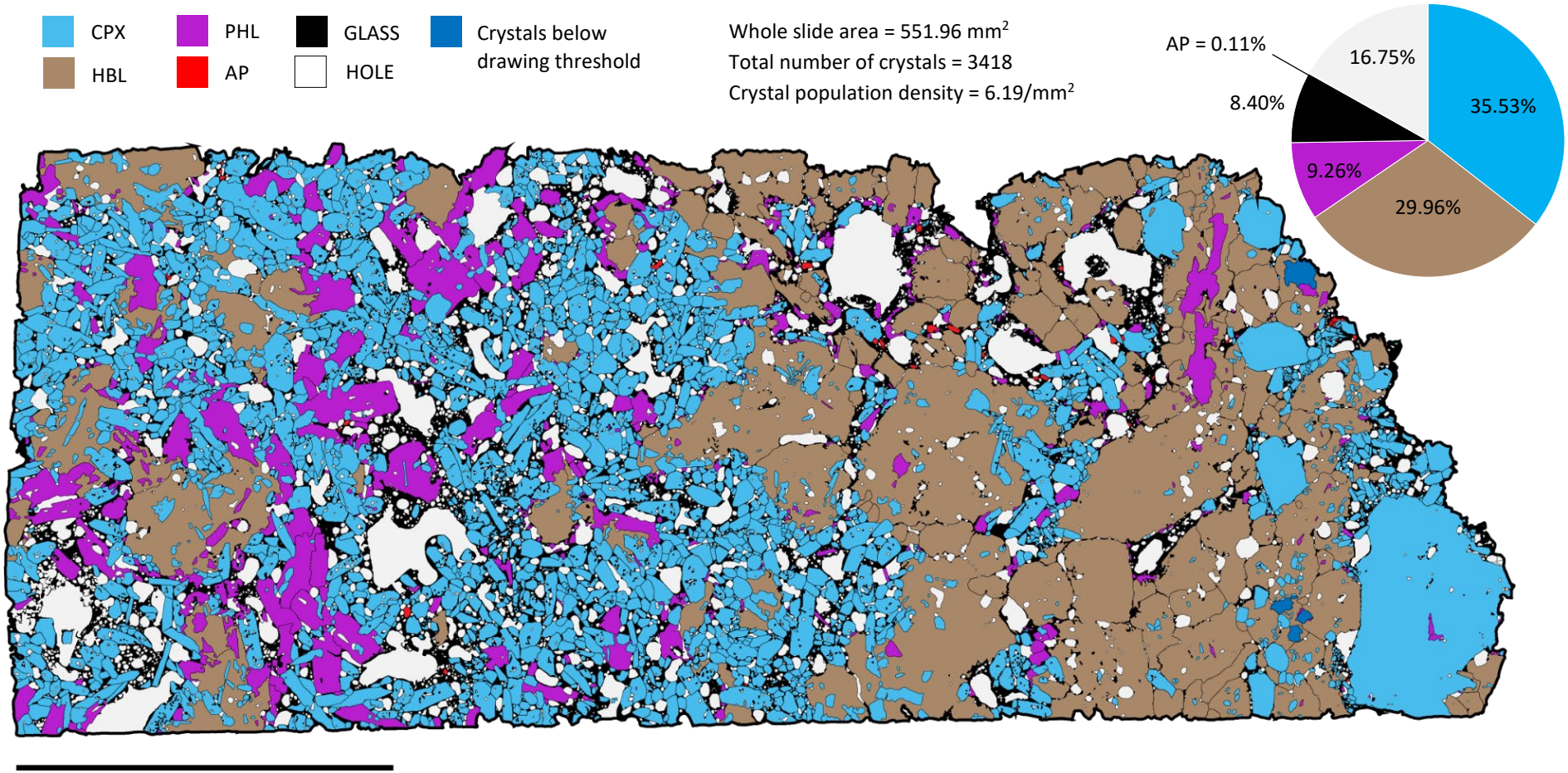

Figure C.36 – Digitised thin section image of sample M4 B. Inset pie chart visualises the area fraction of sample components.

N = 2359

Average crystal size = 0.38 mm

Characteristic length = 0.28 mm

Maximum crystal size = 2.82 mm

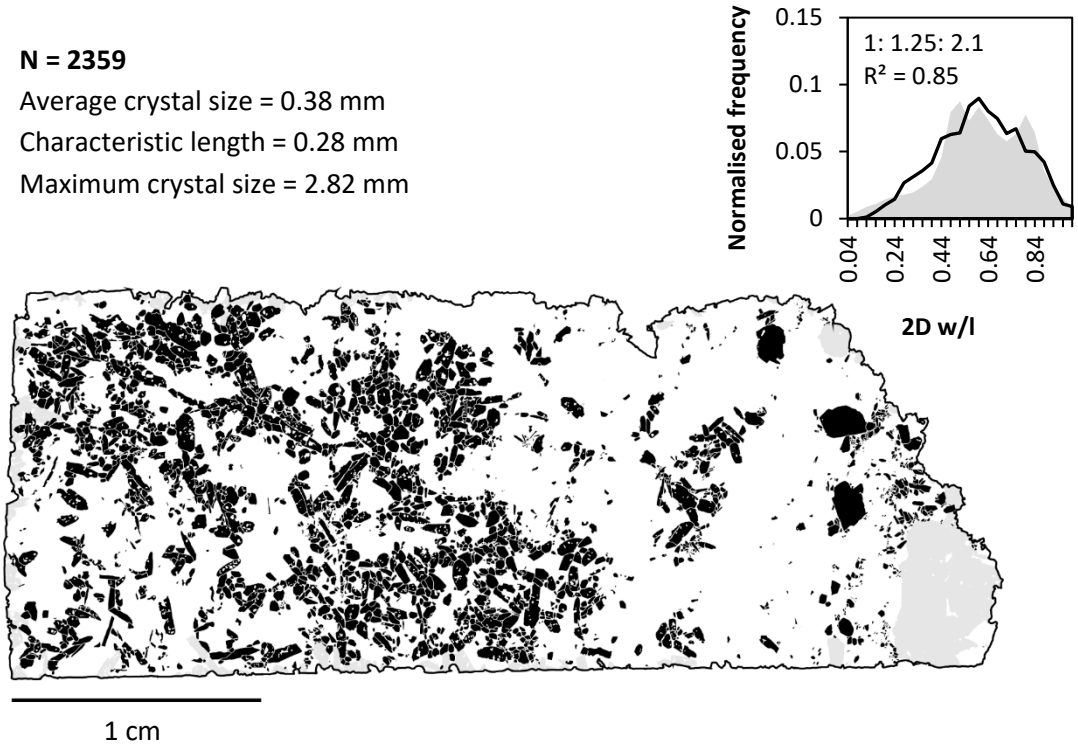

Figure C.37 – Binarised image used to calculate clinopyroxene CSDs in sample M4 B. Grey crystals indicate those truncated by the boundary of the thin section and thus excluded from analysis. Inset histogram visualises the aspect ratio distribution of the measured population (black line), against that of the best fitting shape estimate (grey area).

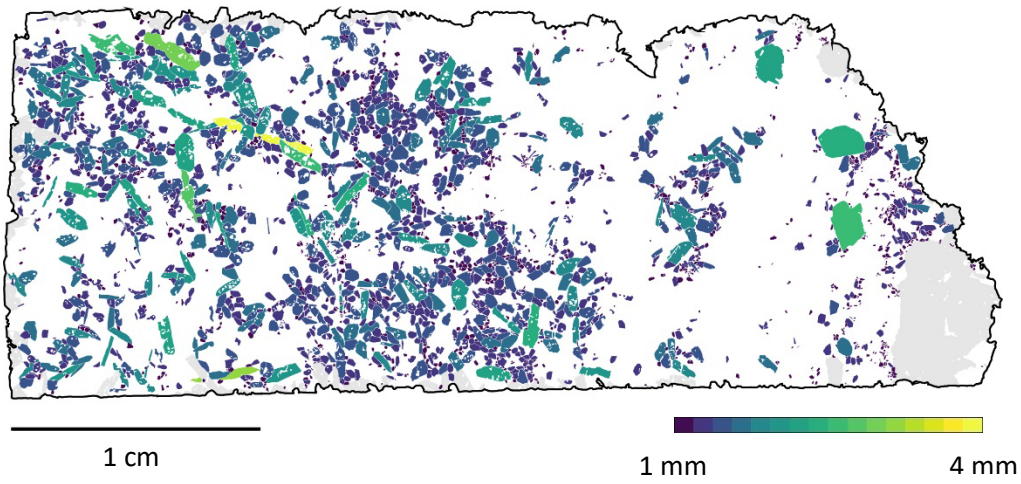

Figure C.38 – Visualisation of clinopyroxene crystal sizes in sample M4 B. Crystals are scaled according to their long axis length, measured by the two-dimensional best-fit ellipse. Grey crystals indicate truncated by the boundary of the thin section and thus excluded from analysis.

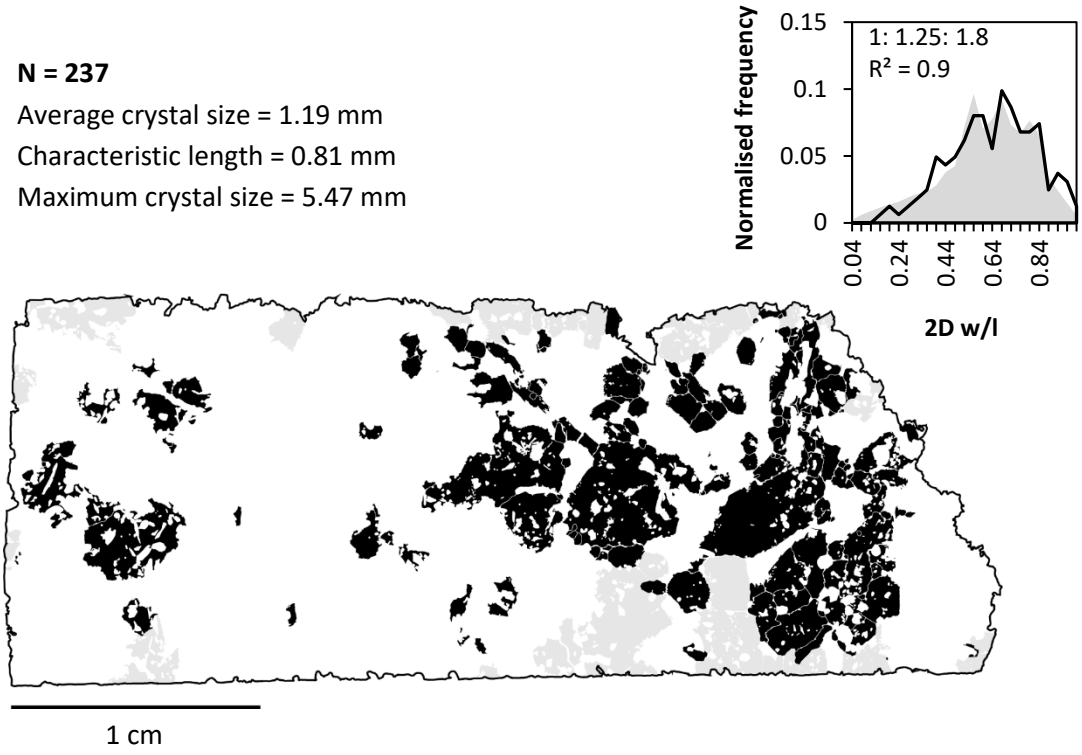

Figure C.39 – Binarised image used to calculate hornblende CSDs in sample M4 B. Grey crystals indicate those truncated by the boundary of the thin section and thus excluded from analysis. Inset histogram visualises the aspect ratio distribution of the measured population (black line), against that of the best fitting shape estimate (grey area).

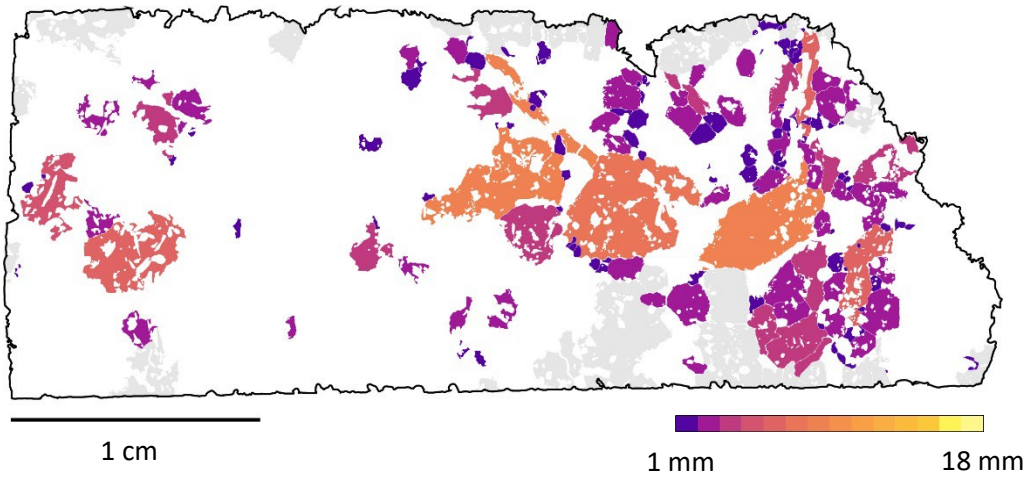

Figure C.40 – Visualisation of hornblende crystal sizes in sample M4 B. Crystals are scaled according to their long axis length, measured by the two-dimensional best-fit ellipse. Grey crystals indicate truncated by the boundary of the thin section and thus excluded from analysis.

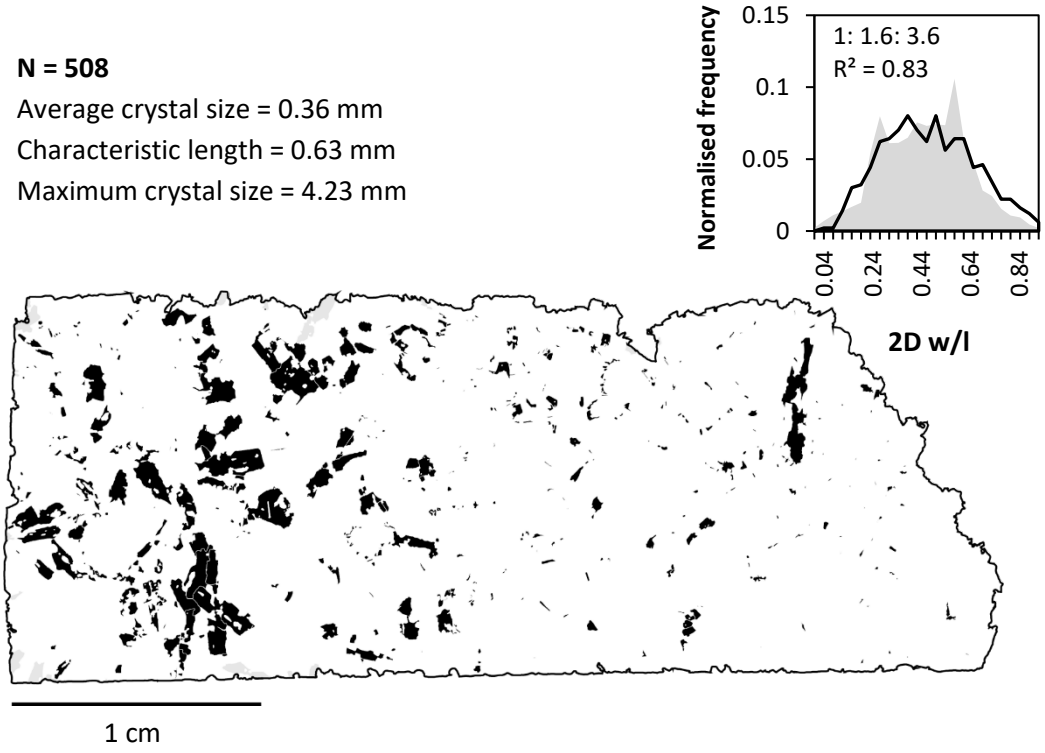

Figure C.41 – Binarised image used to calculate phlogopite CSDs in sample M4 B. Grey crystals indicate those truncated by the boundary of the thin section and thus excluded from analysis. Inset histogram visualises the aspect ratio distribution of the measured population (black line), against that of the best fitting shape estimate (grey area).

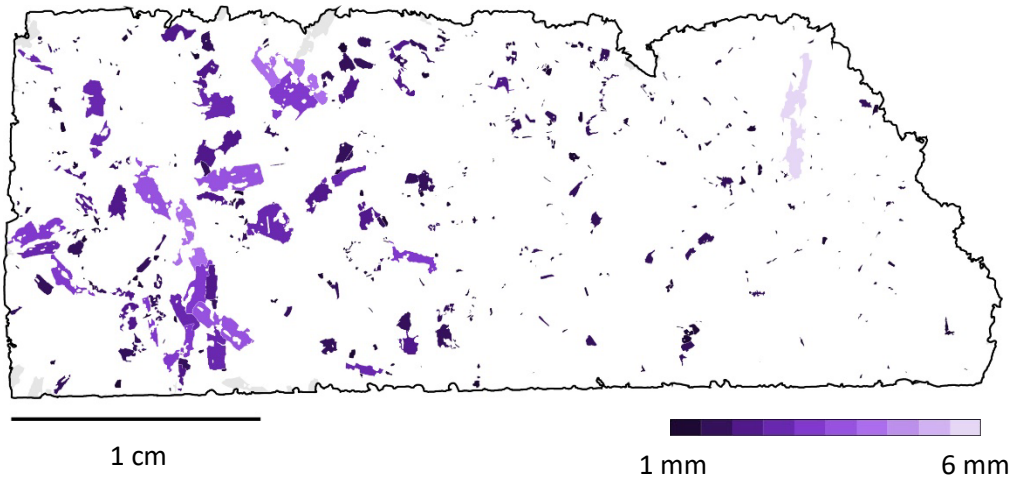

Figure C.42 – Visualisation of phlogopite crystal sizes in sample M4 B. Crystals are scaled according to their long axis length, measured by the two-dimensional best-fit ellipse. Grey crystals indicate truncated by the boundary of the thin section and thus excluded from analysis.

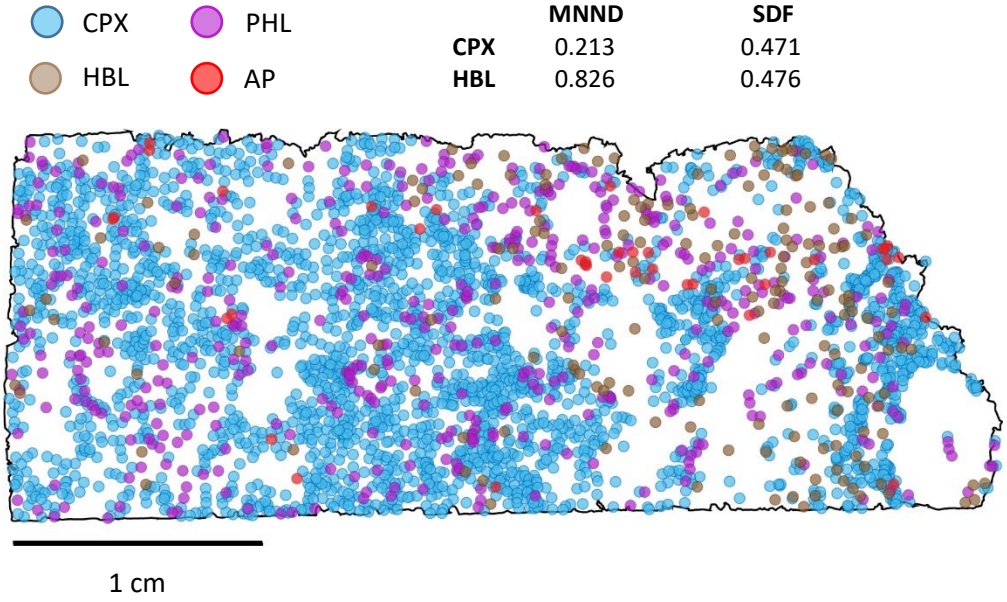

Figure C.43 – Coordinate points used to calculate nearest neighbour distances (in mm) for spatial distribution calculations in sample M4 B. Coordinates represent the weighted centre point of each identified crystal.

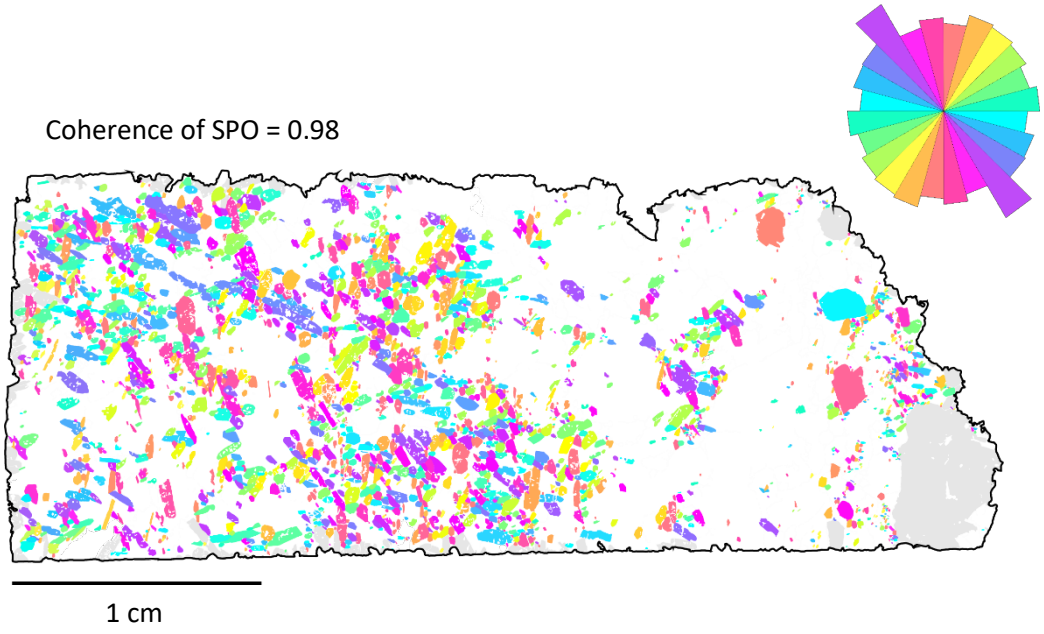

Figure C.44 – Visualisation of shape preferred orientation for clinopyroxene crystals in sample M4 B. Because the xenoliths are ex-situ they are unorientated, meaning that they have no significant direction.

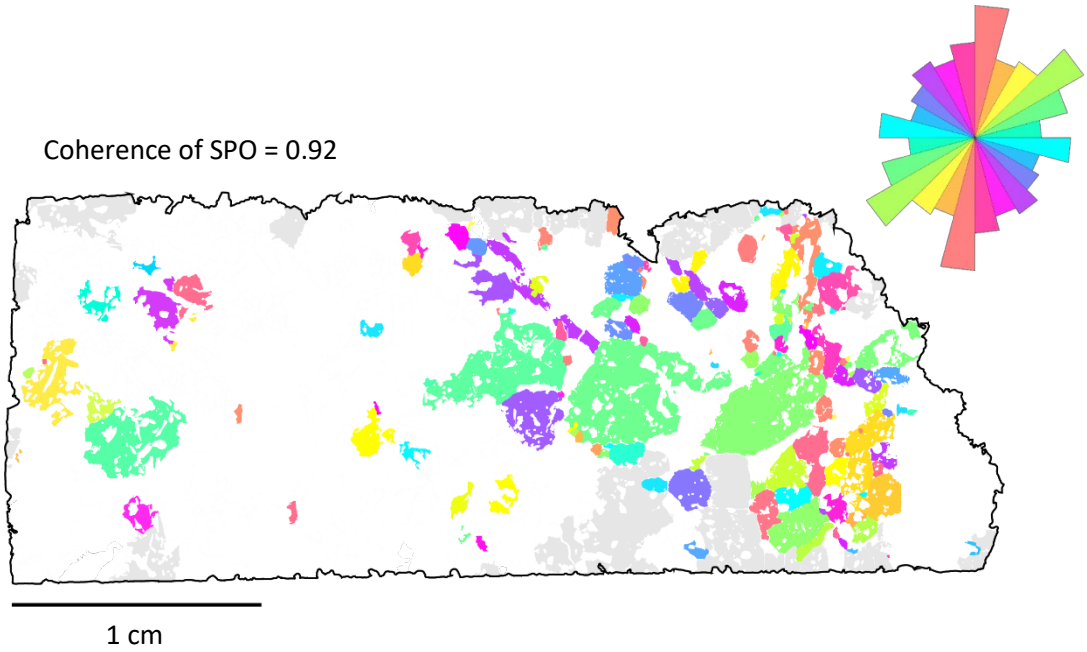

Figure C.45 – Visualisation of shape preferred orientation for hornblende crystals in sample M4 B. Because the xenoliths are ex-situ they are unorientated, meaning that they have no significant direction.

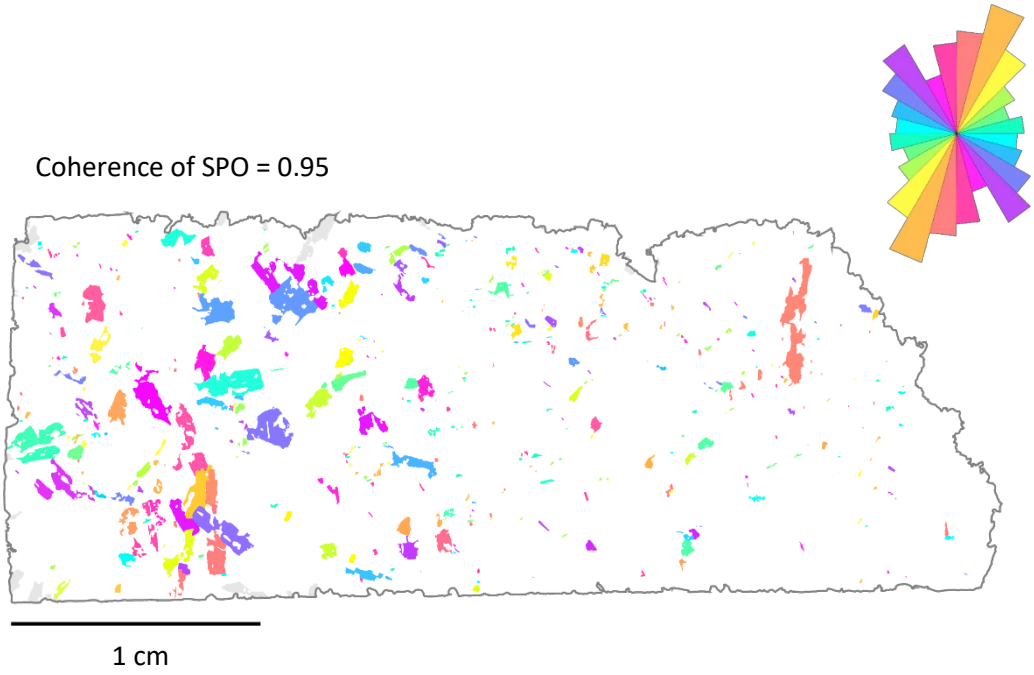

Figure C.46 – Visualisation of shape preferred orientation for phlogopite crystals in sample M4 B. Because the xenoliths are ex-situ they are unorientated, meaning that they have no significant direction.

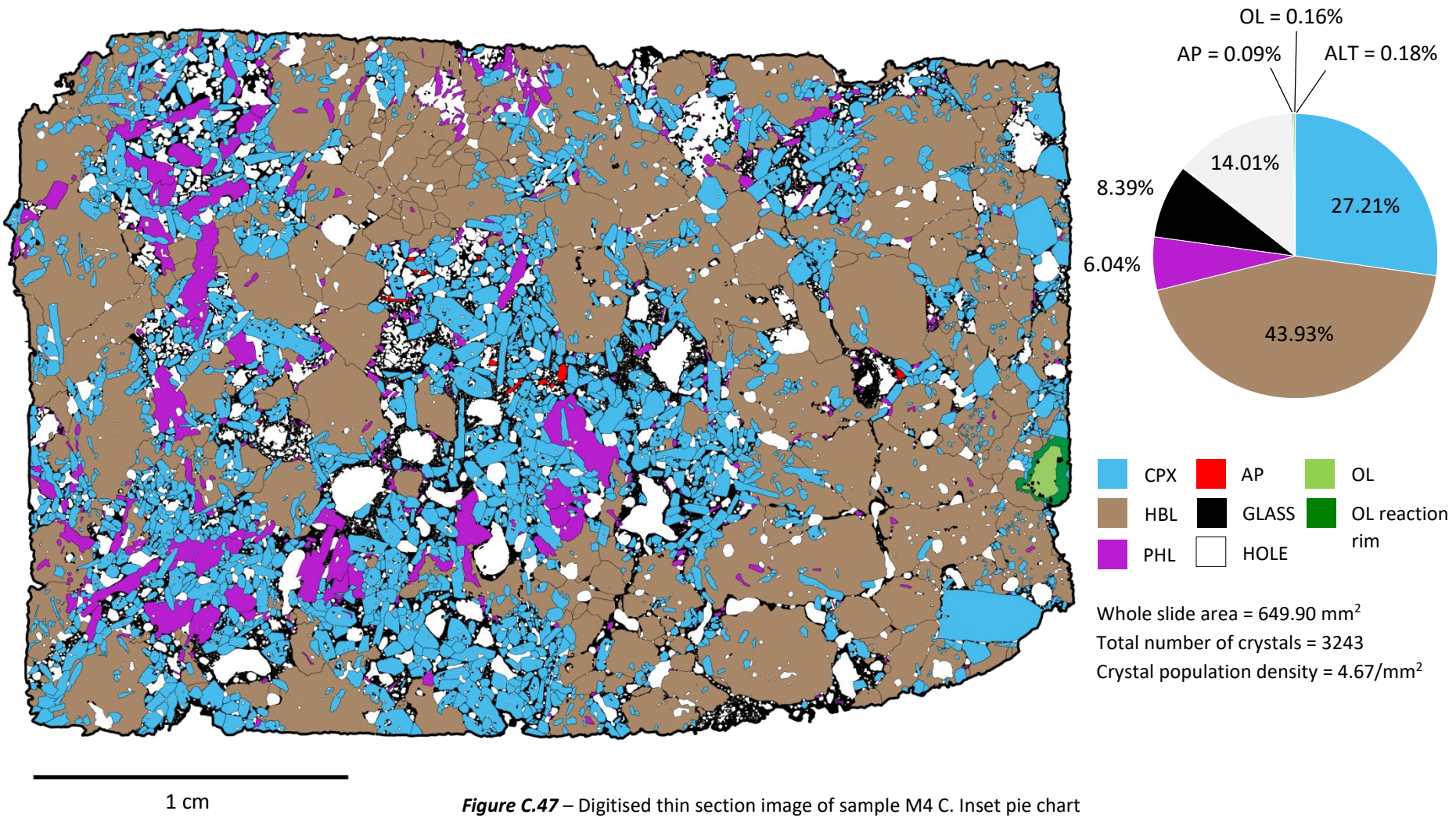

Figure C.47 – Digitised thin section image of sample M4 C. Inset pie chart visualises the area fraction of sample components.

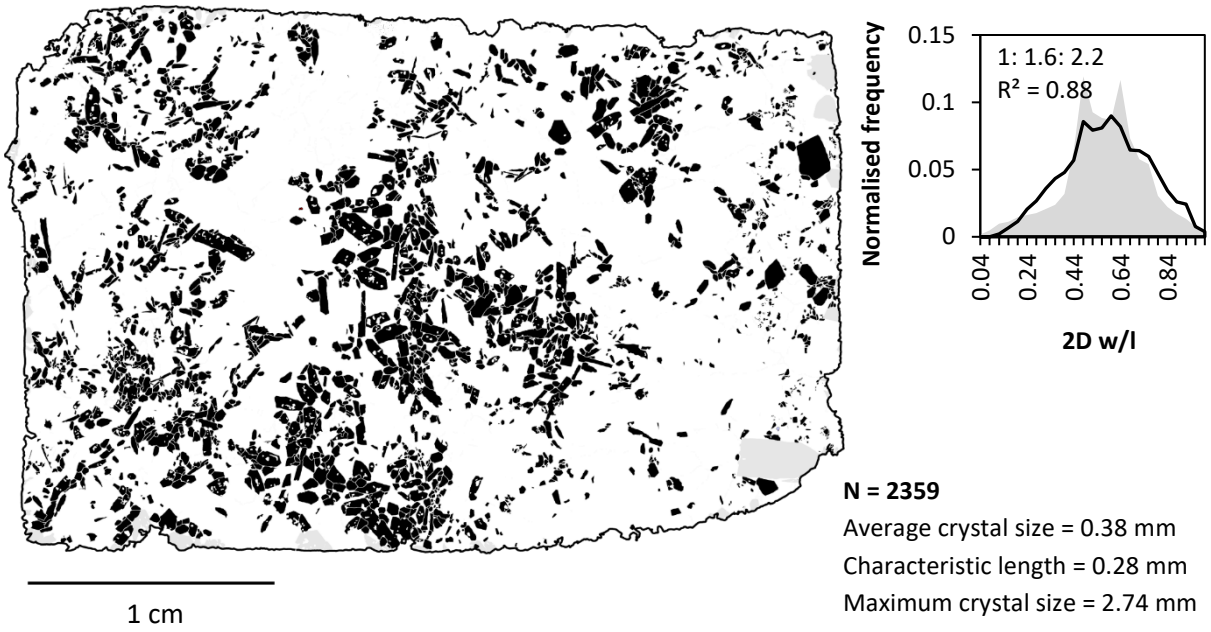

Figure C.48 – Binarised image used to calculate clinopyroxene CSDs in sample M4 C. Grey crystals indicate those truncated by the boundary of the thin section and thus excluded from analysis. Inset histogram visualises the aspect ratio distribution of the measured population (black line), against that of the best fitting shape estimate (grey area).

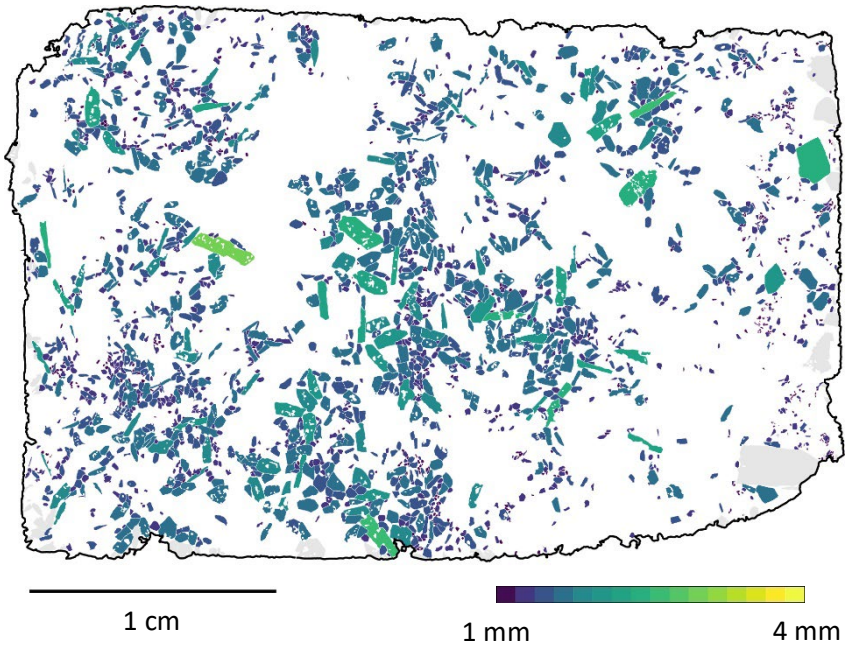

Figure C.49 – Visualisation of clinopyroxene crystal sizes in sample M4 C. Crystals are scaled according to their long axis length, measured by the two-dimensional best-fit ellipse. Grey crystals indicate truncated by the boundary of the thin section and thus excluded from analysis.

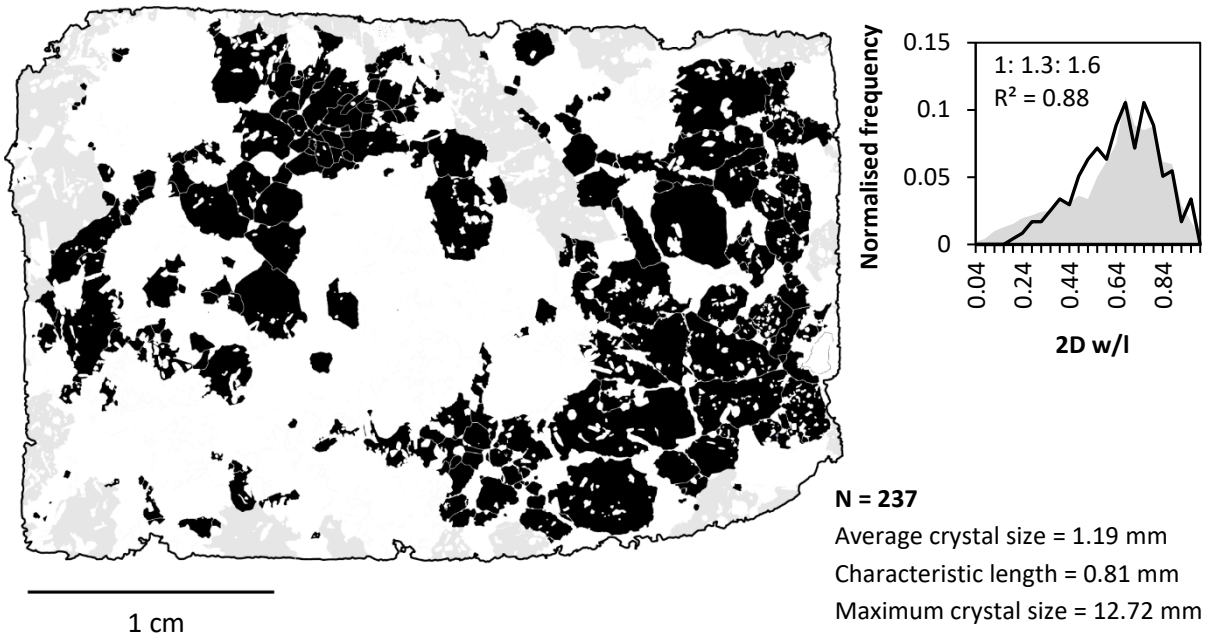

Figure C.50 – Binarised image used to calculate hornblende CSDs in sample M4 C. Grey crystals indicate those truncated by the boundary of the thin section and thus excluded from analysis. Inset histogram visualises the aspect ratio distribution of the measured population (black line), against that of the best fitting shape estimate (grey area).

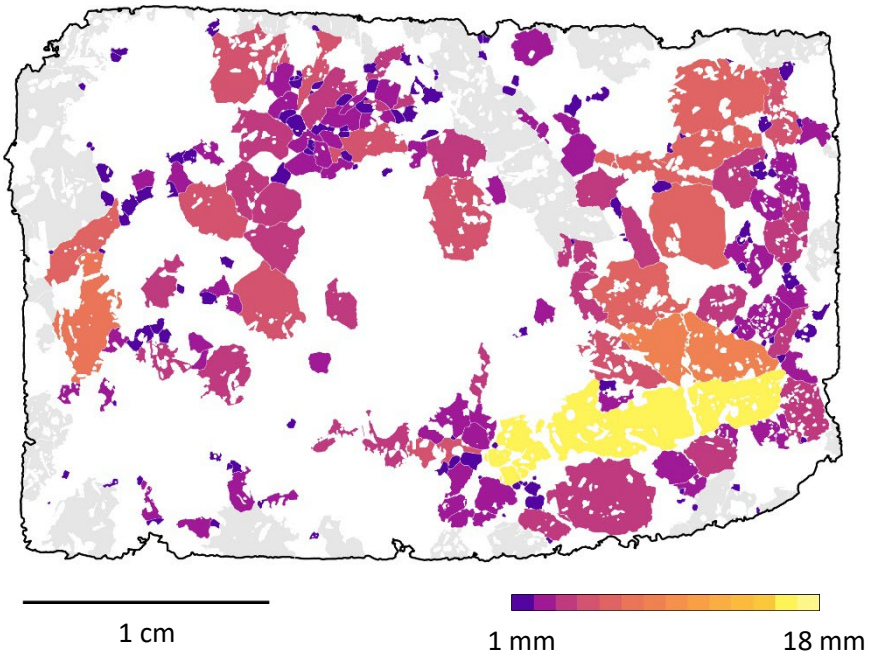

Figure C.51 – Visualisation of hornblende crystal sizes in sample M4 C. Crystals are scaled according to their long axis length, measured by the two-dimensional best-fit ellipse. Grey crystals indicate truncated by the boundary of the thin section and thus excluded from analysis.

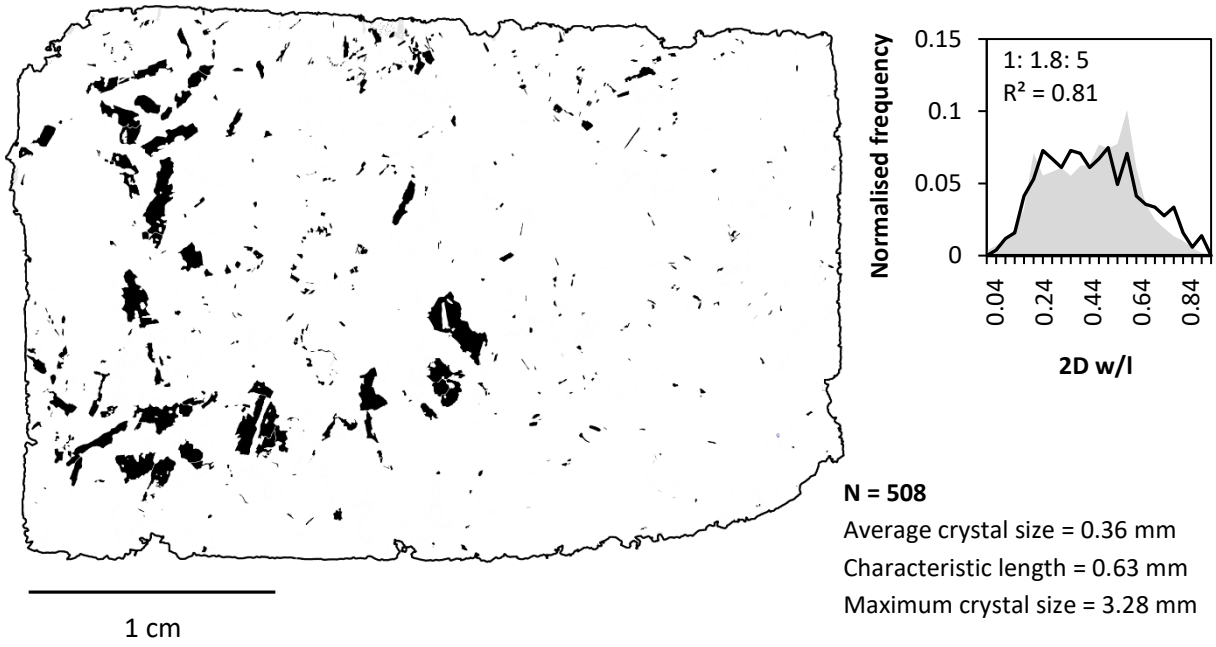

Figure C.52 – Binarised image used to calculate phlogopite CSDs in sample M4 C. Grey crystals indicate those truncated by the boundary of the thin section and thus excluded from analysis. Inset histogram visualises the aspect ratio distribution of the measured population (black line), against that of the best fitting shape estimate (grey area).

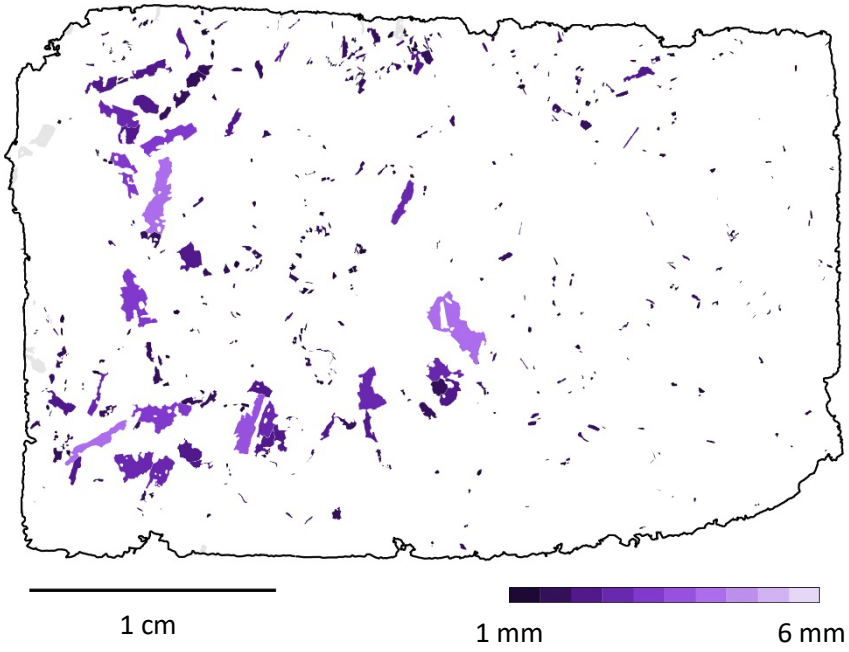

Figure C.53 – Visualisation of phlogopite crystal sizes in sample M4 C. Crystals are scaled according to their long axis length, measured by the two-dimensional best-fit ellipse. Grey crystals indicate truncated by the boundary of the thin section and thus excluded from analysis.

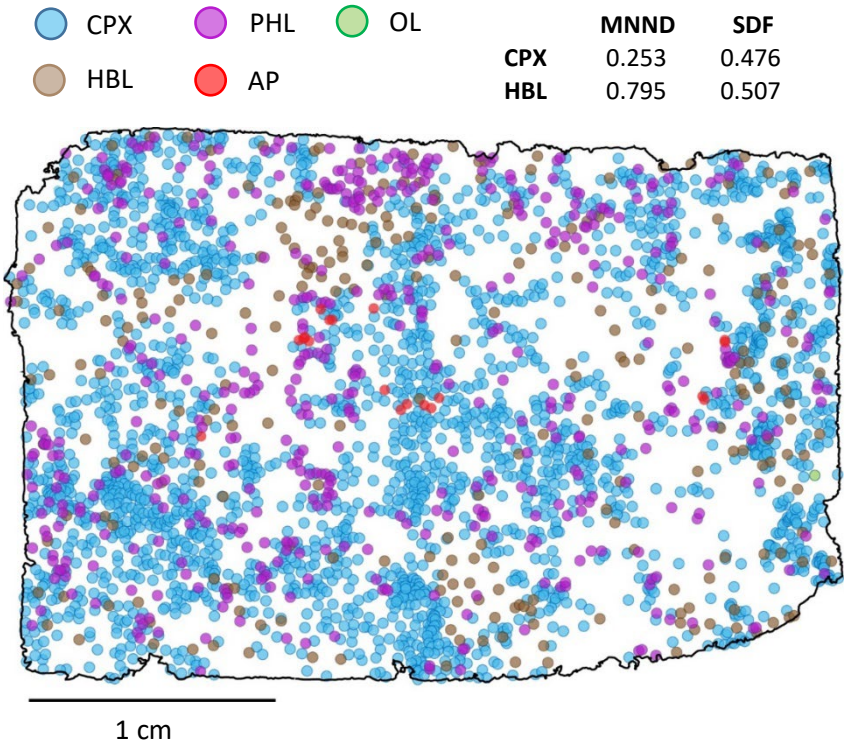

Figure C.54 – Coordinate points used to calculate nearest neighbour distances (in mm) for spatial distribution calculations in sample M4 C. Coordinates represent the weighted centre point of each identified crystal.

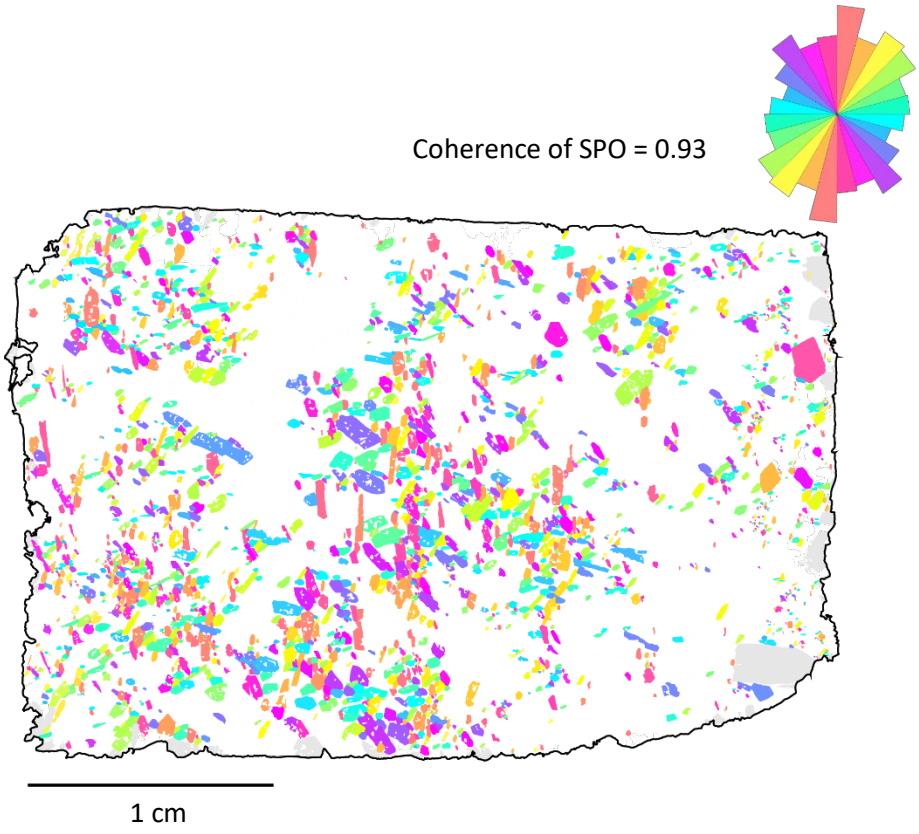

Figure C.55 – Visualisation of shape preferred orientation for clinopyroxene crystals in sample M4 C. Because the xenoliths are ex-situ they are unorientated, meaning that they have no significant direction.

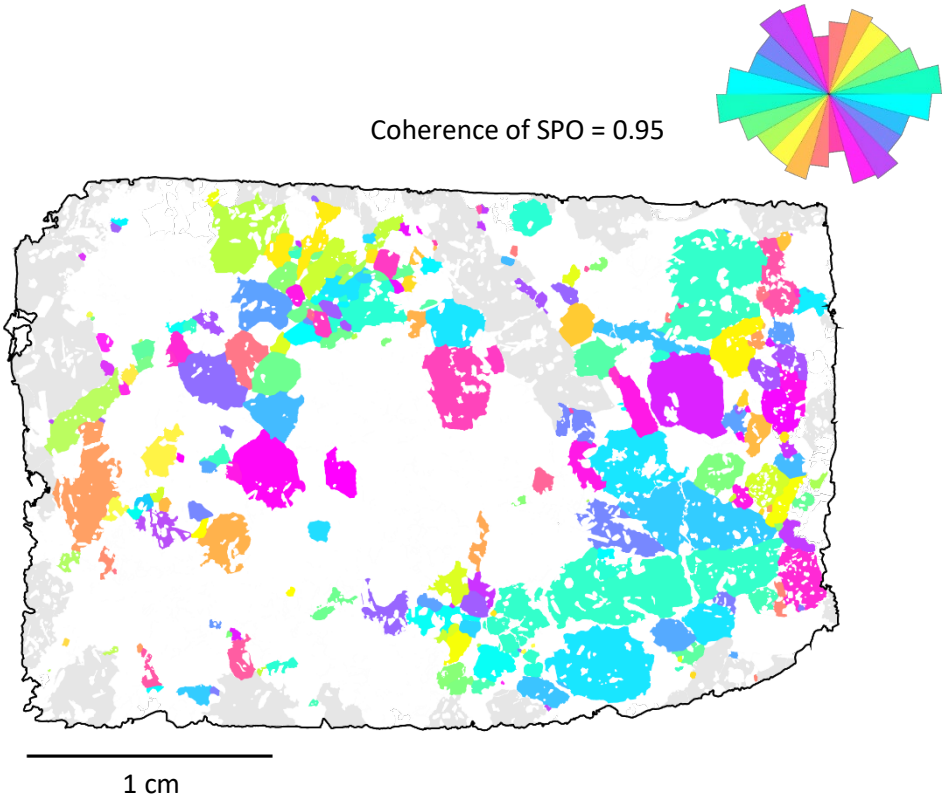

Figure C.56 – Visualisation of shape preferred orientation for hornblende crystals in sample M4 C. Because the xenoliths are ex-situ they are unorientated, meaning that they have no significant direction.

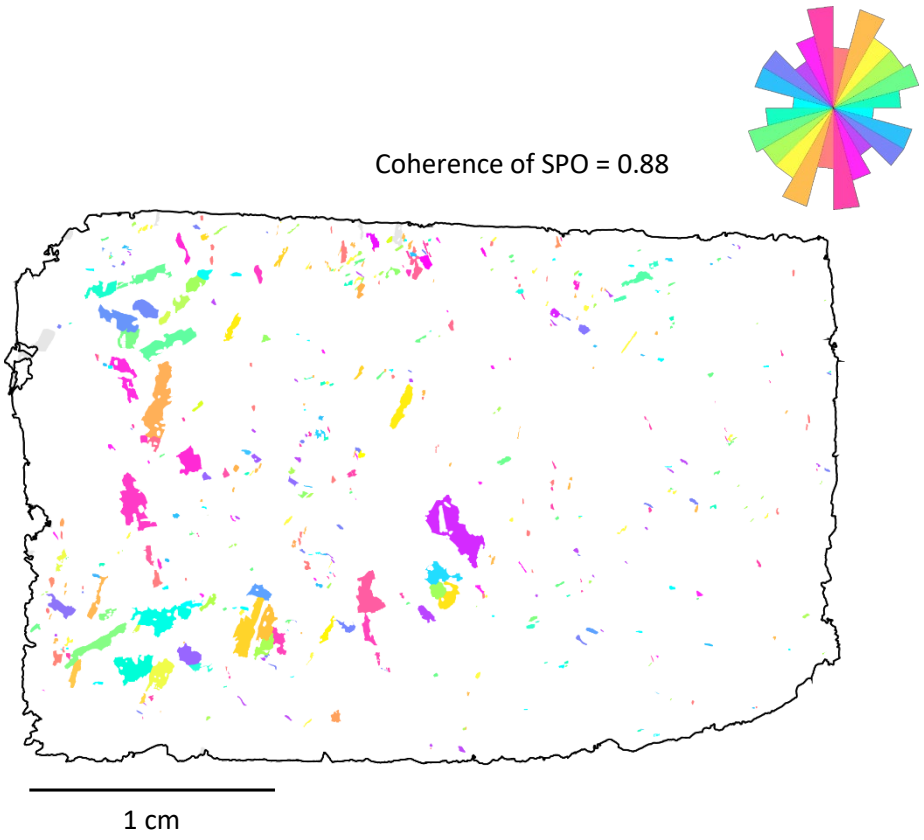

Figure C.57 – Visualisation of shape preferred orientation for phlogopite crystals in sample M4 C. Because the xenoliths are ex-situ they are unorientated, meaning that they have no significant direction.

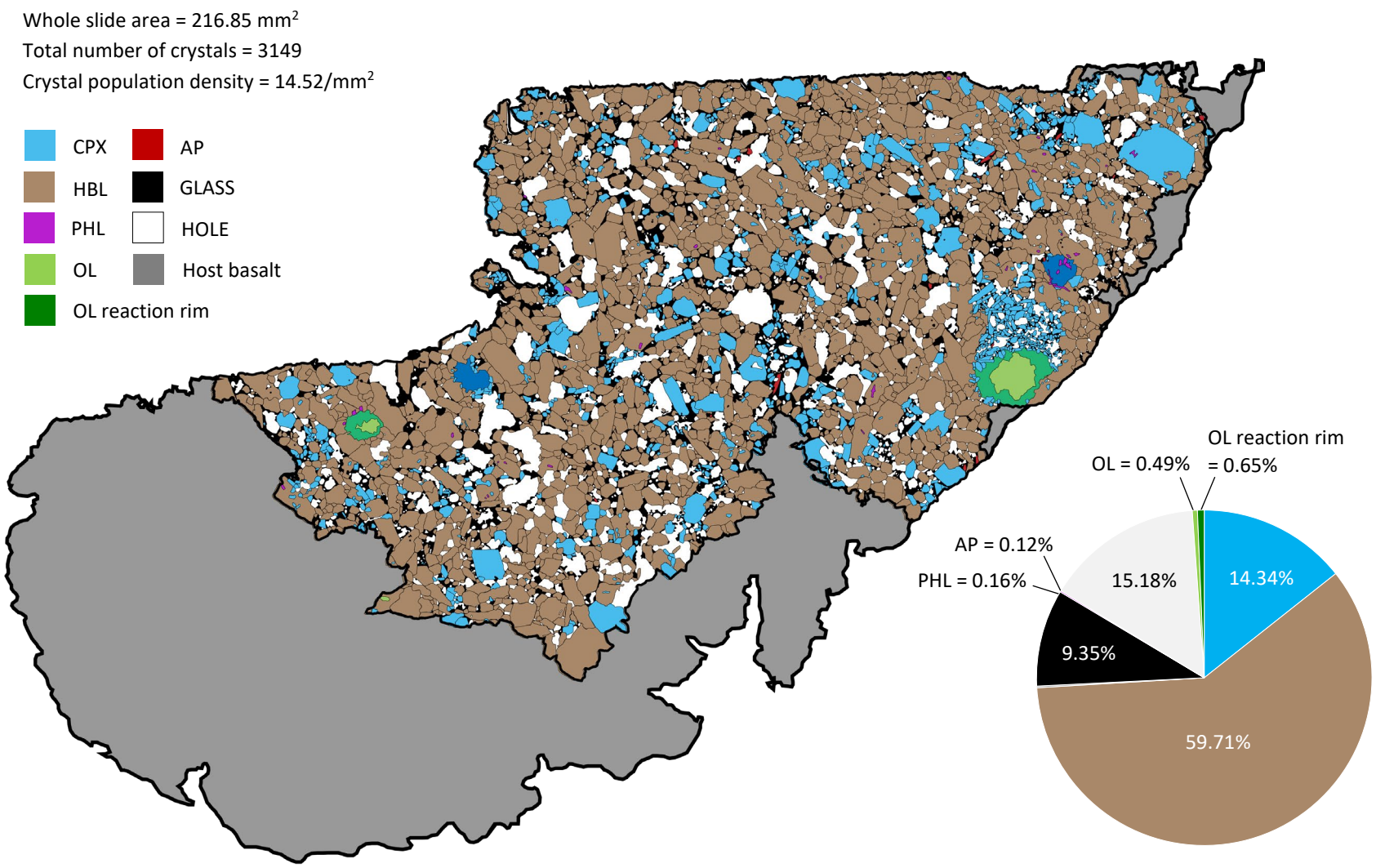

Figure C.58 – Digitised thin section image of sample M6 A. Inset pie chart visualises the area fraction of sample components.

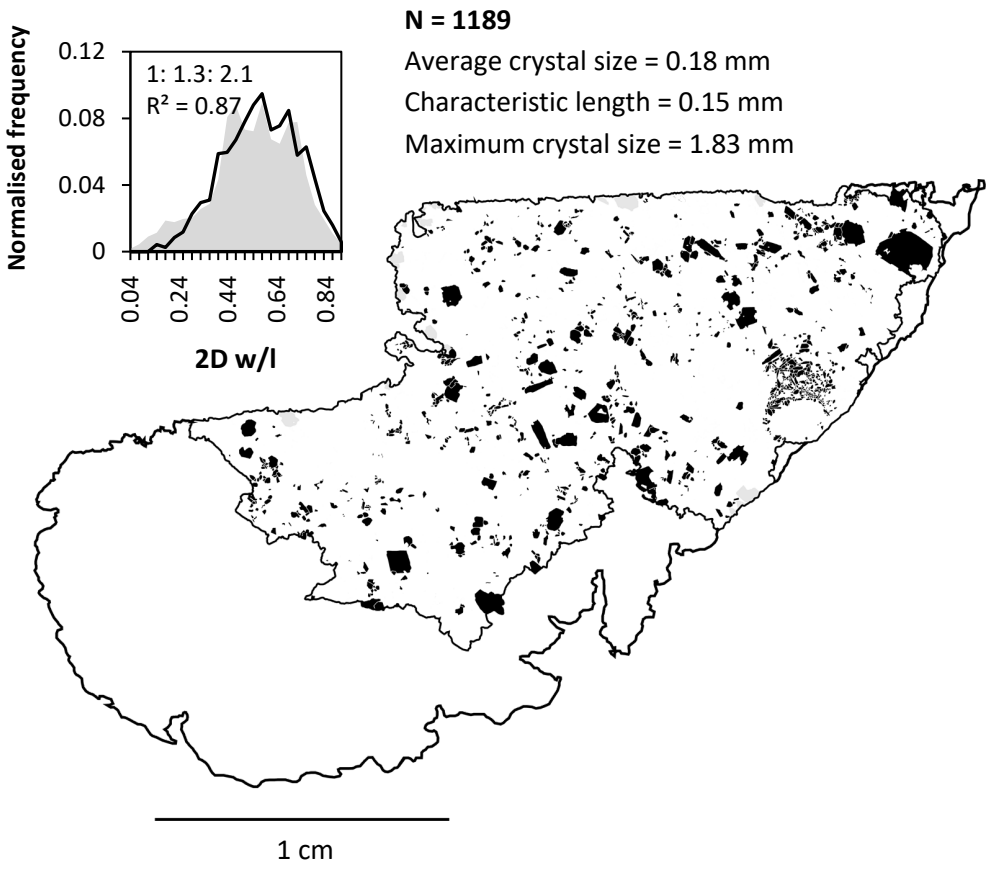

Figure C.59 – Binarised image used to calculate clinopyroxene CSDs in sample M6 A. Grey crystals indicate those truncated by the boundary of the thin section and thus excluded from analysis. Inset histogram visualises the aspect ratio distribution of the measured population (black line), against that of the best fitting shape estimate (grey area).

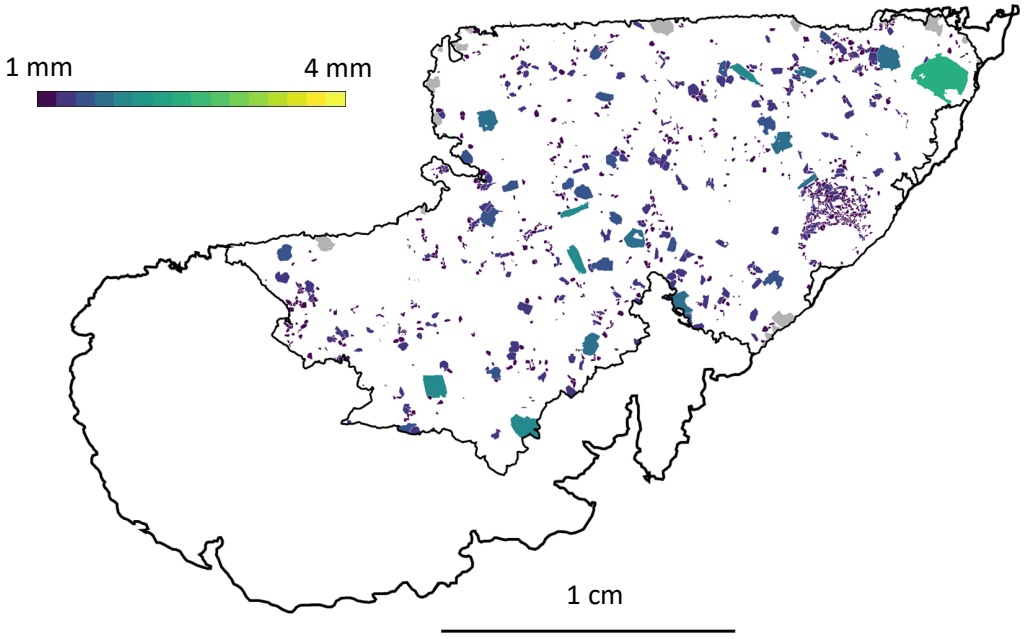

Figure C.60 – Visualisation of clinopyroxene crystal sizes in sample M6 A. Crystals are scaled according to their long axis length, measured by the two-dimensional best-fit ellipse. Grey crystals indicate truncated by the boundary of the thin section and thus excluded from analysis.

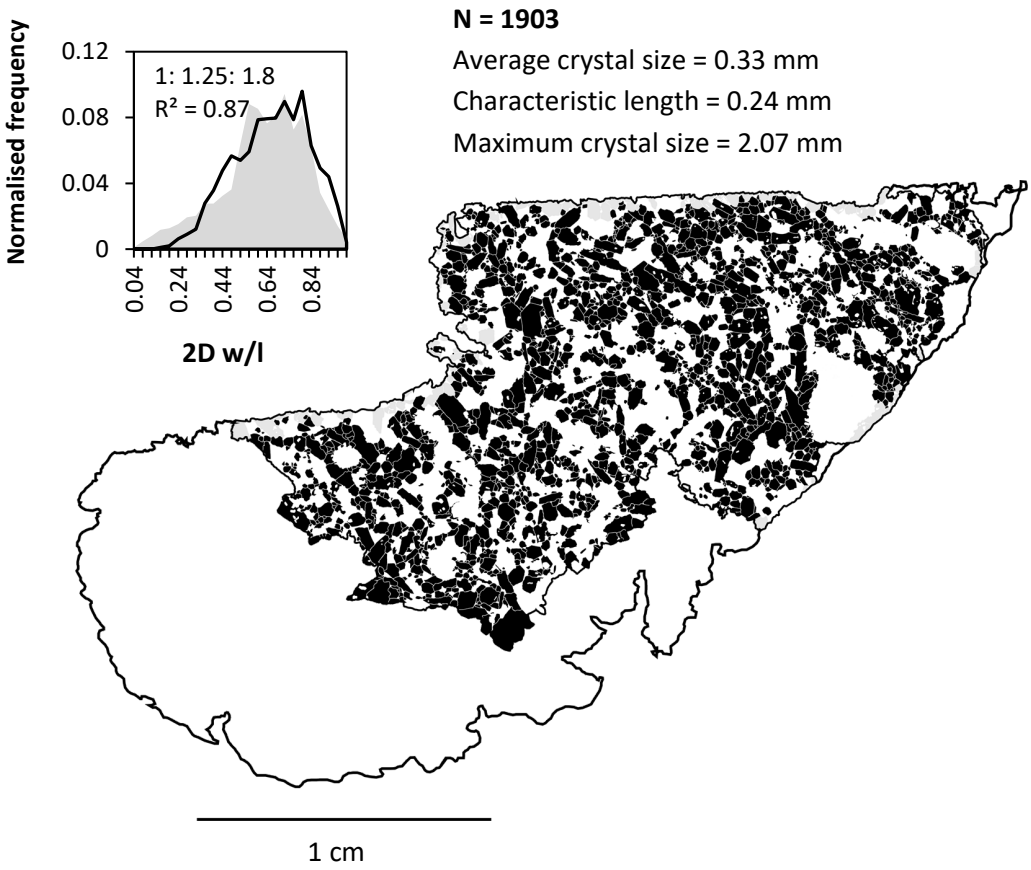

Figure C.61 – Binarised image used to calculate hornblende CSDs in sample M6 A. Grey crystals indicate those truncated by the boundary of the thin section and thus excluded from analysis. Inset histogram visualises the aspect ratio distribution of the measured population (black line), against that of the best fitting shape estimate (grey area).

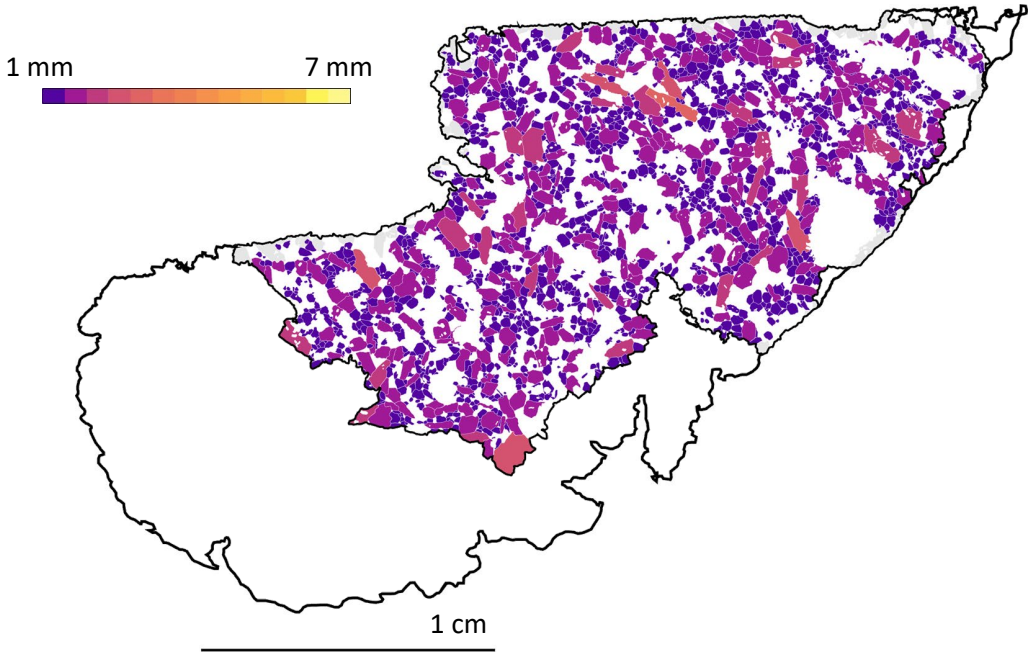

Figure C.62 – Visualisation of hornblende crystal sizes in sample M6 A. Crystals are scaled according to their long axis length, measured by the two-dimensional best-fit ellipse. Grey crystals indicate truncated by the boundary of the thin section and thus excluded from analysis.

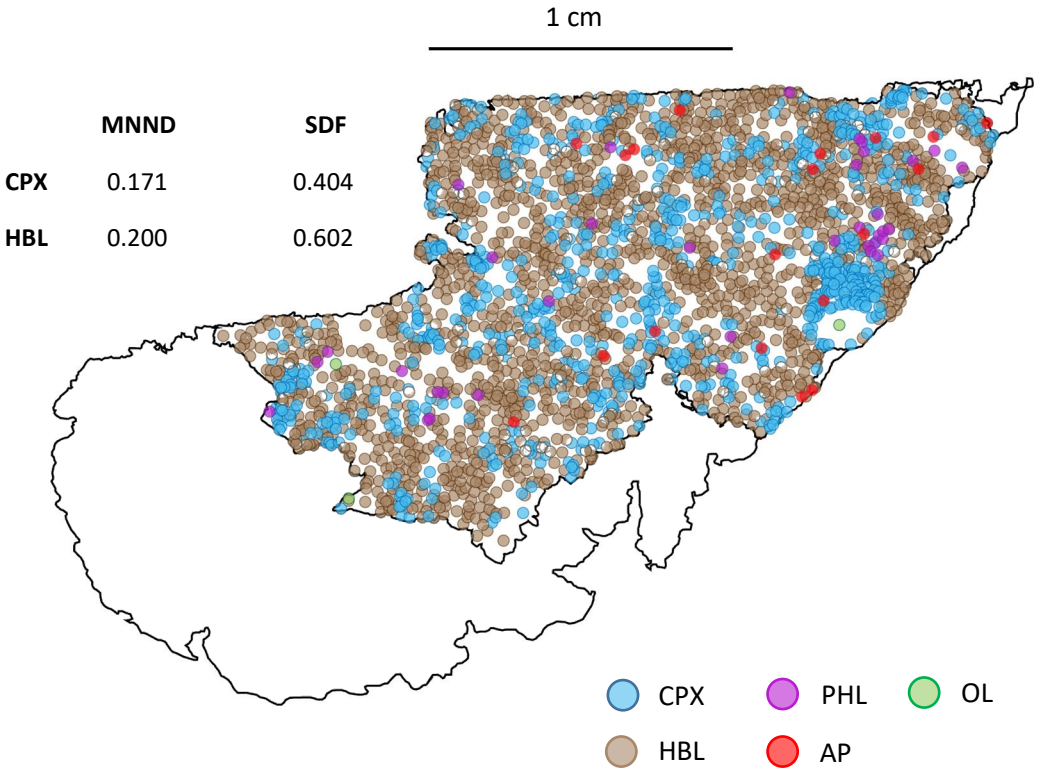

Figure C.63 – Coordinate points used to calculate nearest neighbour distances for spatial distribution calculations in sample M6 A. Coordinates represent the weighted centre point of each identified crystal.

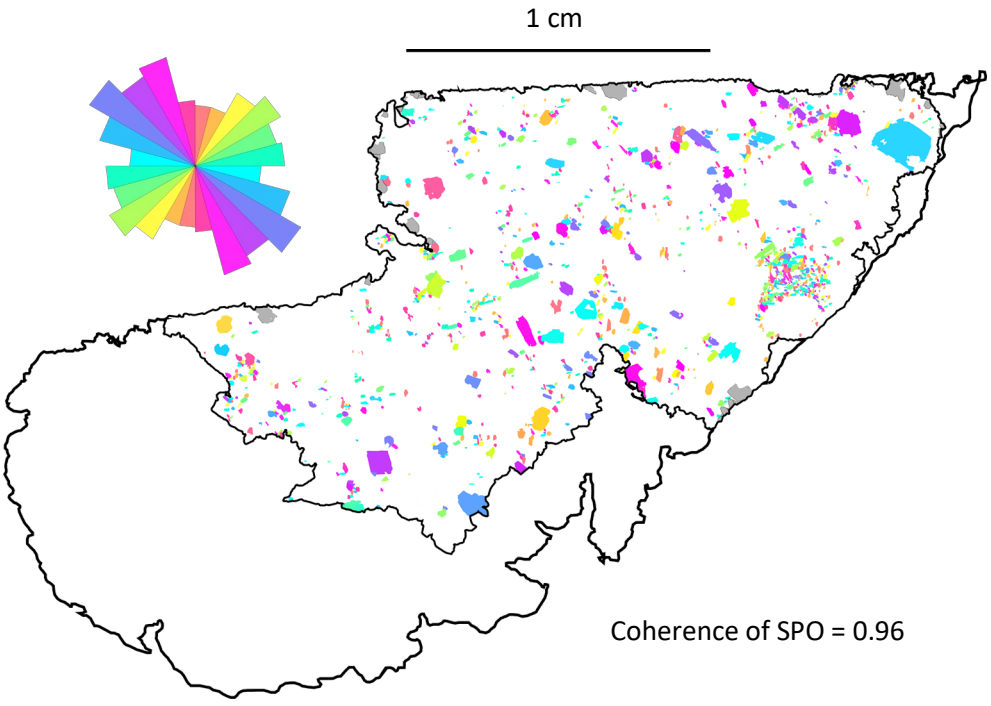

Figure C.64 – Visualisation of shape preferred orientation for clinopyroxene crystals in sample M6 A. Because the xenoliths are ex-situ they are unorientated, meaning that they have no significant direction.

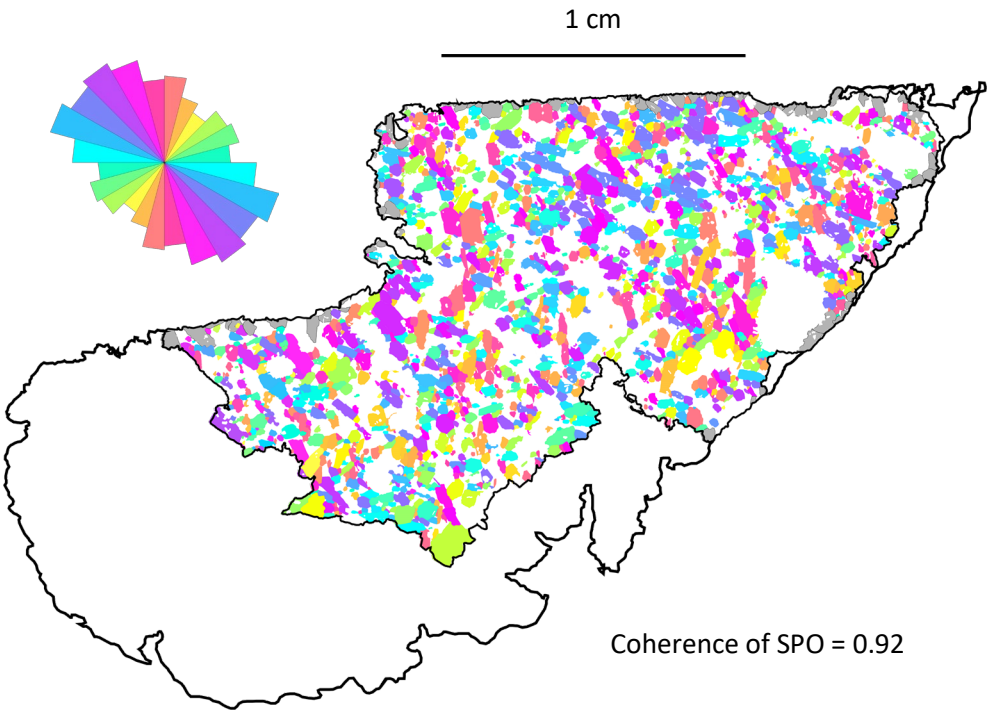

Figure C.65 – Visualisation of shape preferred orientation for hornblende crystals in sample M6 A. Because the xenoliths are ex-situ they are unorientated, meaning that they have no significant direction.

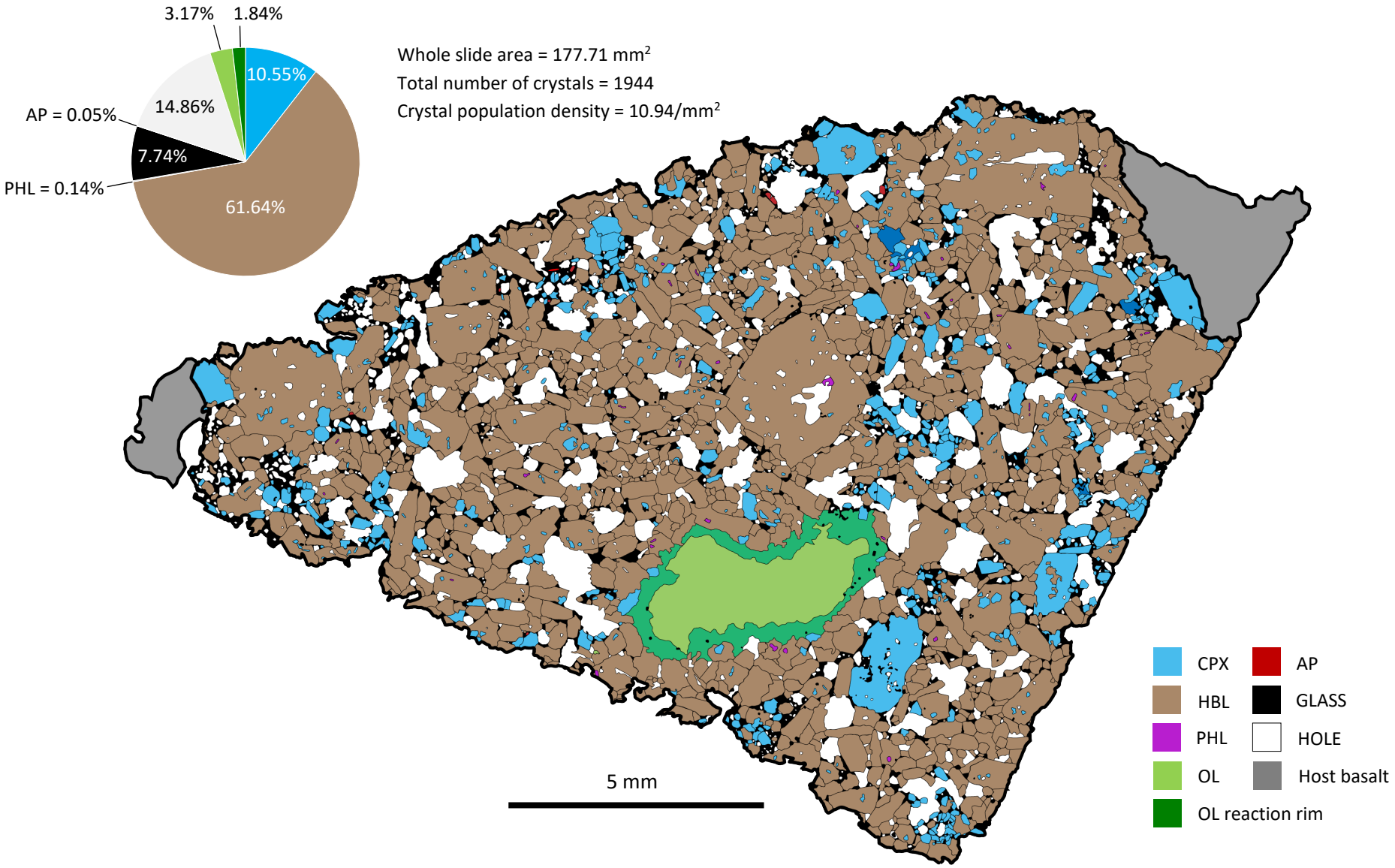

Figure C.66 – Digitised thin section image of sample M6 B. Inset pie chart visualises the area fraction of sample components.

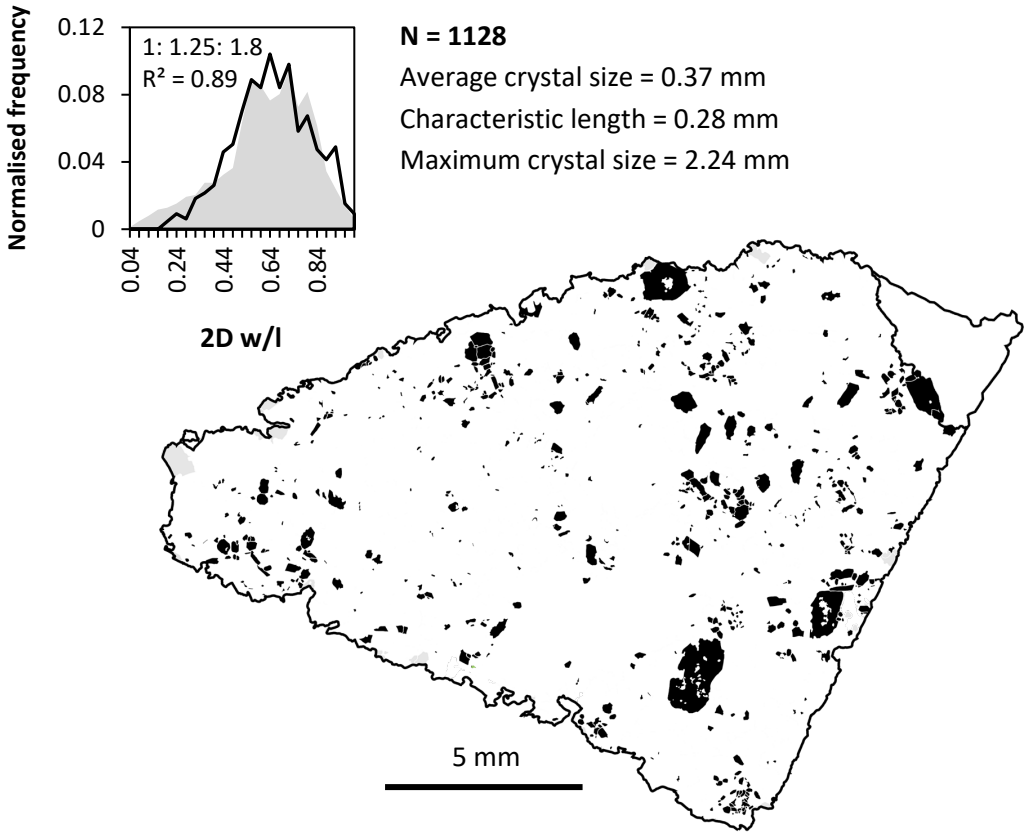

Figure C.67 – Binarised image used to calculate clinopyroxene CSDs in sample M6 B. Grey crystals indicate those truncated by the boundary of the thin section and thus excluded from analysis. Inset histogram visualises the aspect ratio distribution of the measured population (black line), against that of the best fitting shape estimate (grey area).

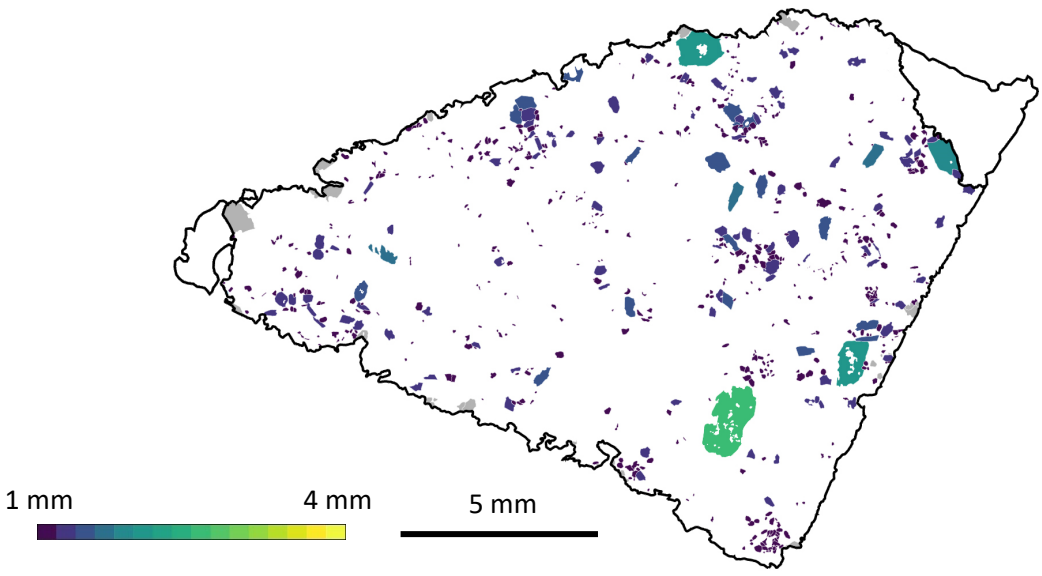

Figure C.68 – Visualisation of clinopyroxene crystal sizes in sample M6 B. Crystals are scaled according to their long axis length, measured by the two-dimensional best-fit ellipse. Grey crystals indicate truncated by the boundary of the thin section and thus excluded from analysis.

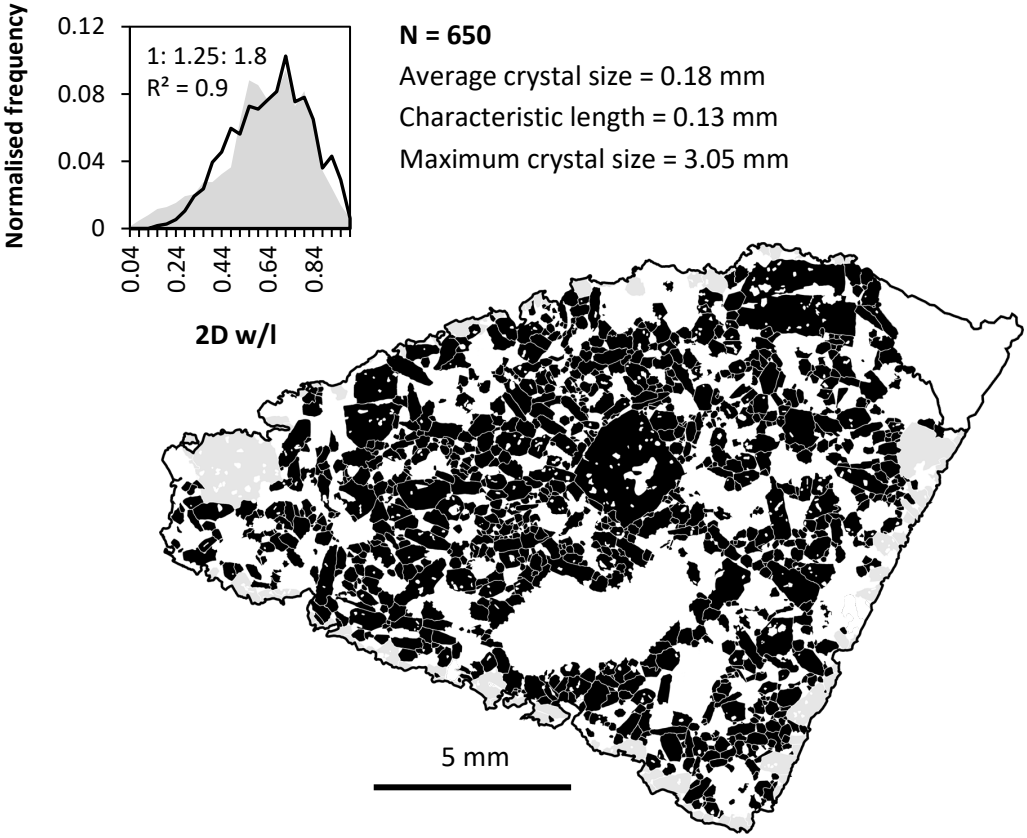

Figure C.69 – Binarised image used to calculate hornblende CSDs in sample M6 B. Grey crystals indicate those truncated by the boundary of the thin section and thus excluded from analysis. Inset histogram visualises the aspect ratio distribution of the measured population (black line), against that of the best fitting shape estimate (grey area).

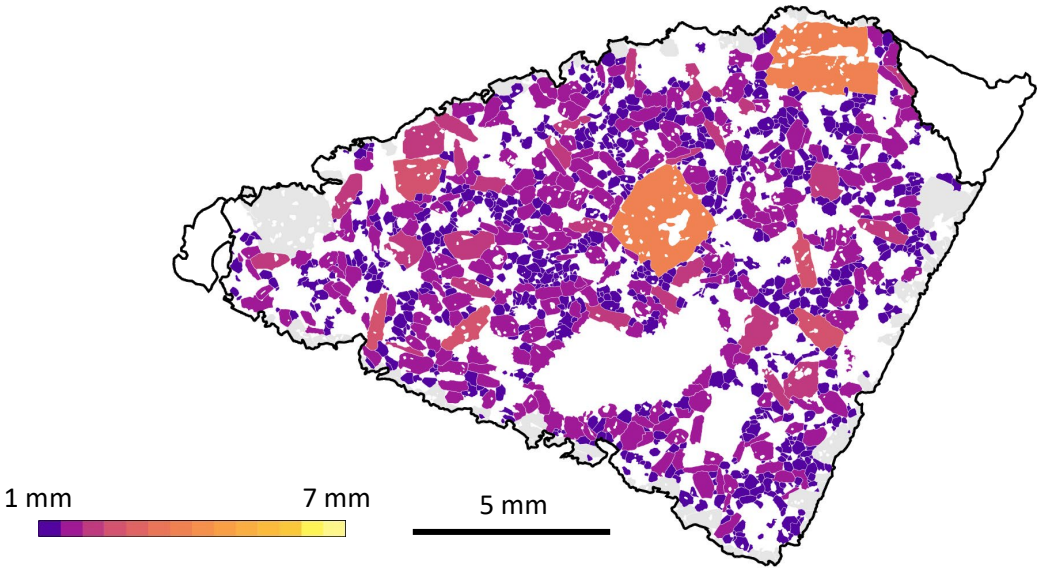

Figure C.70 – Visualisation of hornblende crystal sizes in sample M6 B. Crystals are scaled according to their long axis length, measured by the two-dimensional best-fit ellipse. Grey crystals indicate truncated by the boundary of the thin section and thus excluded from analysis.

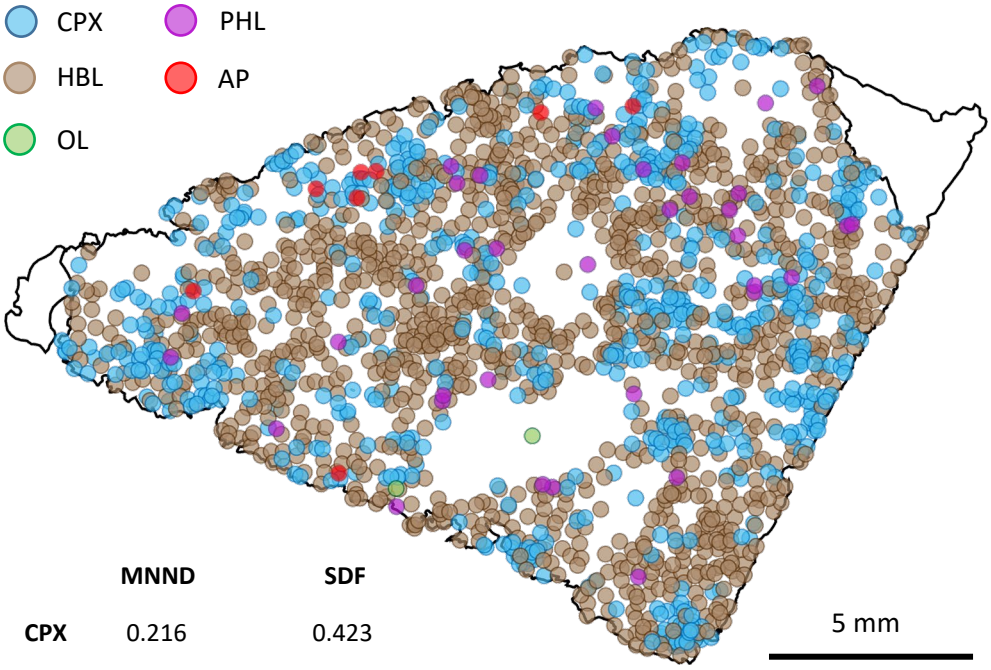

	MNND	SDF
CPX	0.216	0.423
HBL	0.221	0.583

Figure C.71 – Coordinate points used to calculate nearest neighbour distances for spatial distribution calculations in sample M6 B. Coordinates represent the weighted centre point of each identified crystal.

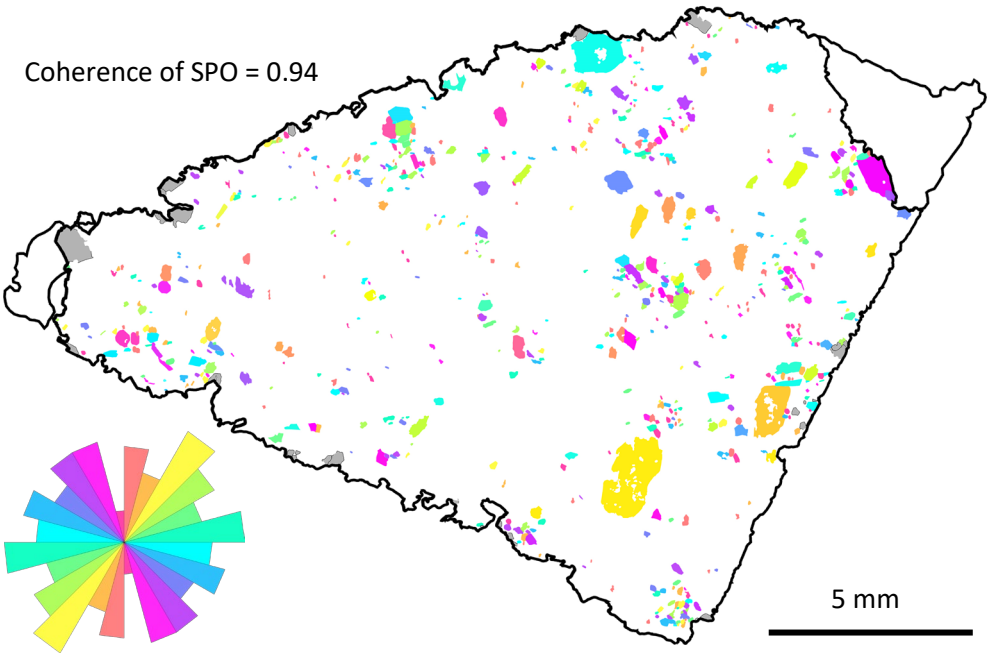

Figure C.72 – Visualisation of shape preferred orientation for clinopyroxene crystals in sample M6 B. Because the xenoliths are ex-situ they are unorientated, meaning that they have no significant direction.

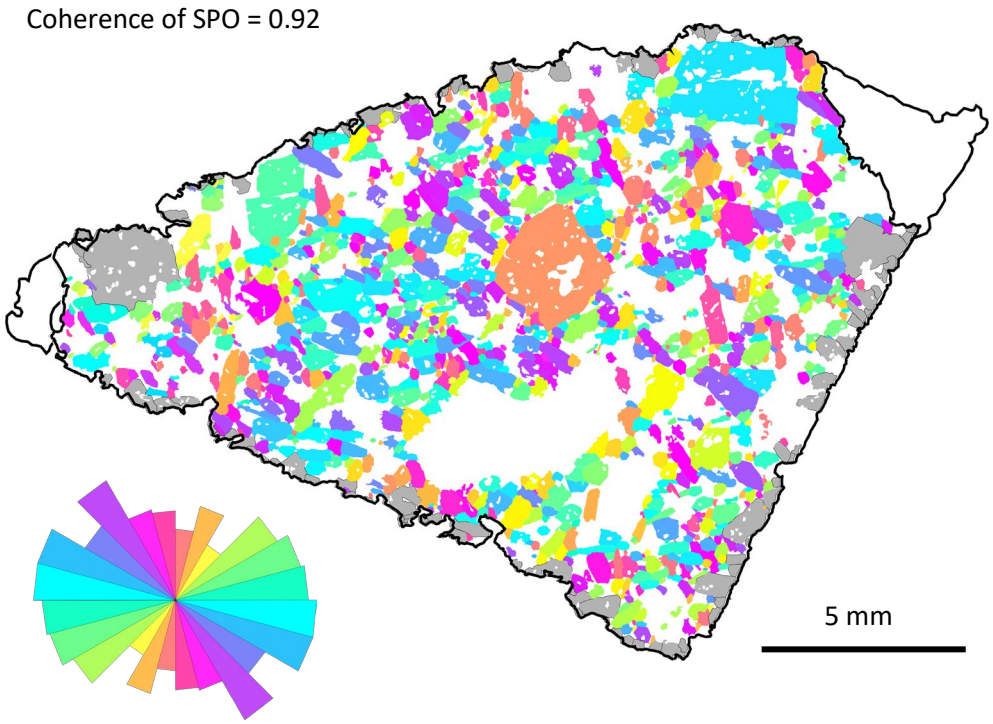

Figure XC.73– Visualisation of shape preferred orientation for hornblende crystals in sample M6 B. Because the xenoliths are ex-situ they are unorientated, meaning that they have no significant direction.

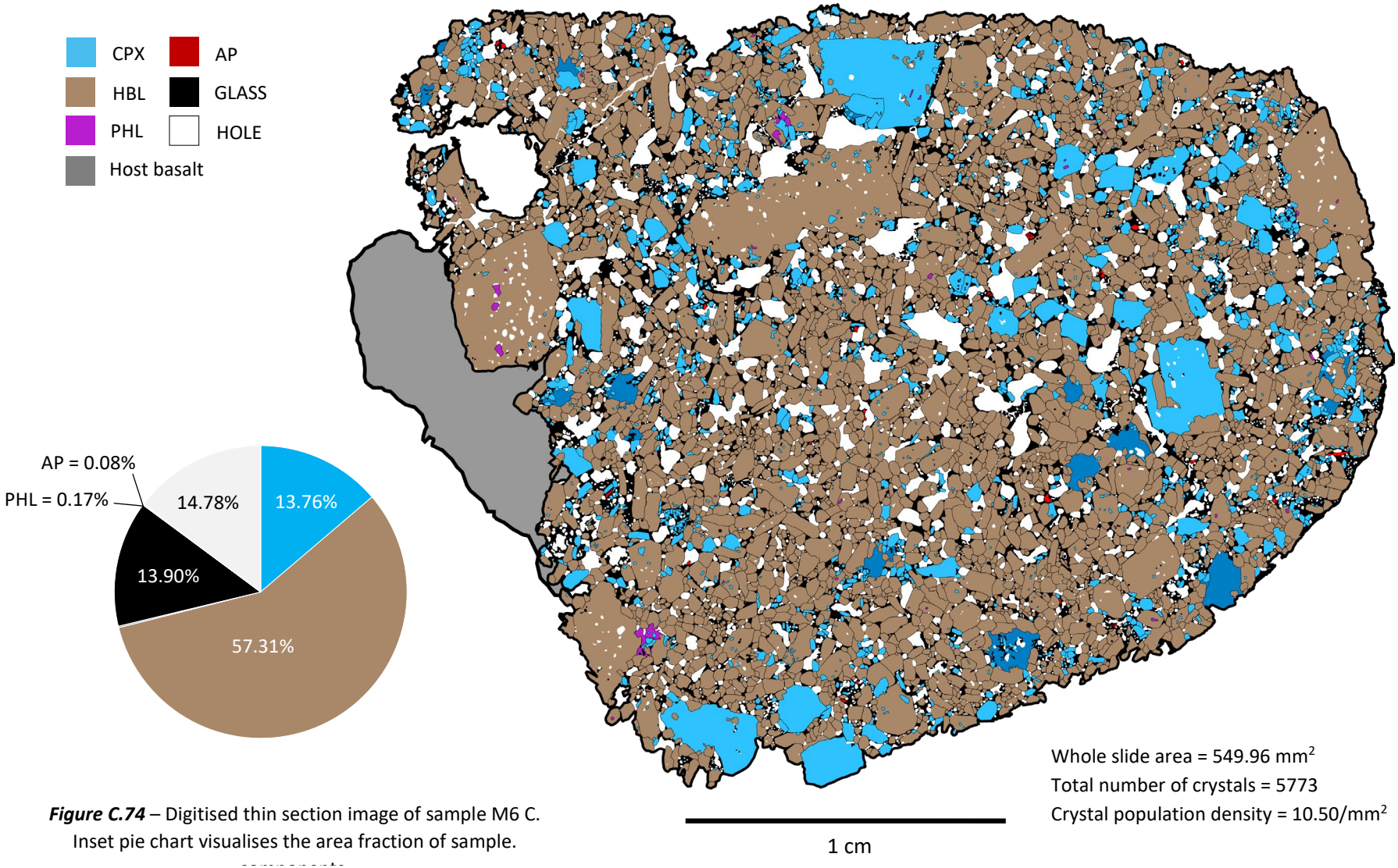

Figure C.74 – Digitised thin section image of sample M6 C. Inset pie chart visualises the area fraction of sample. components.

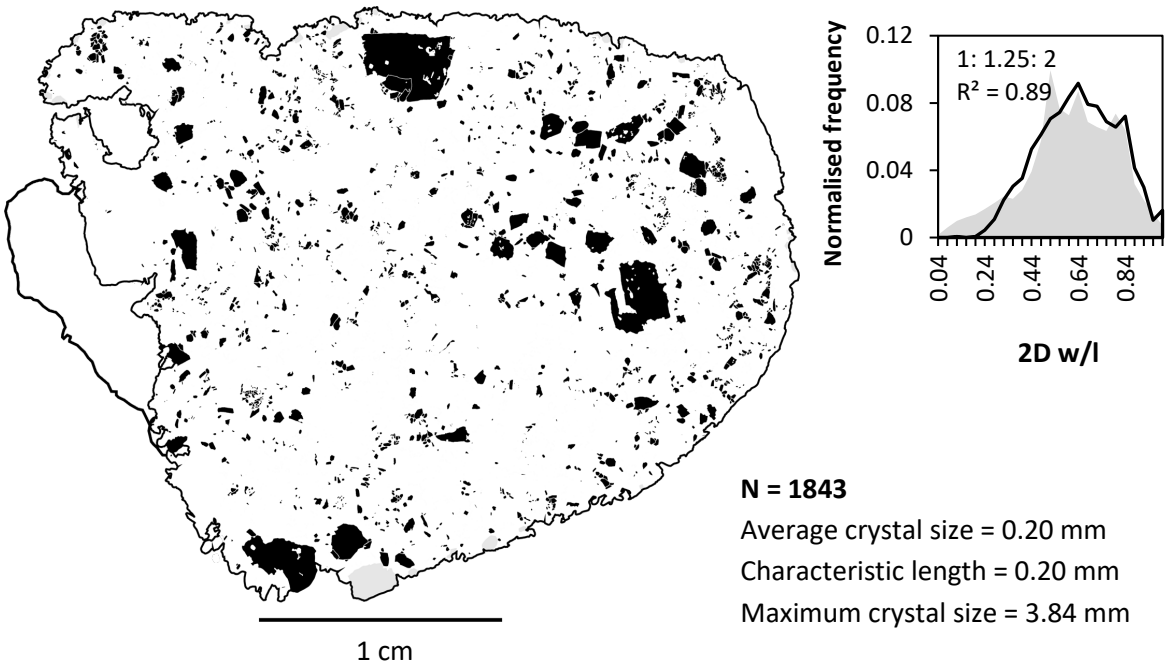

Figure C.75 – Binarised image used to calculate clinopyroxene CSDs in sample M6 C. Grey crystals indicate those truncated by the boundary of the thin section and thus excluded from analysis. Inset histogram visualises the aspect ratio distribution of the measured population (black line), against that of the best fitting shape estimate (grey area).

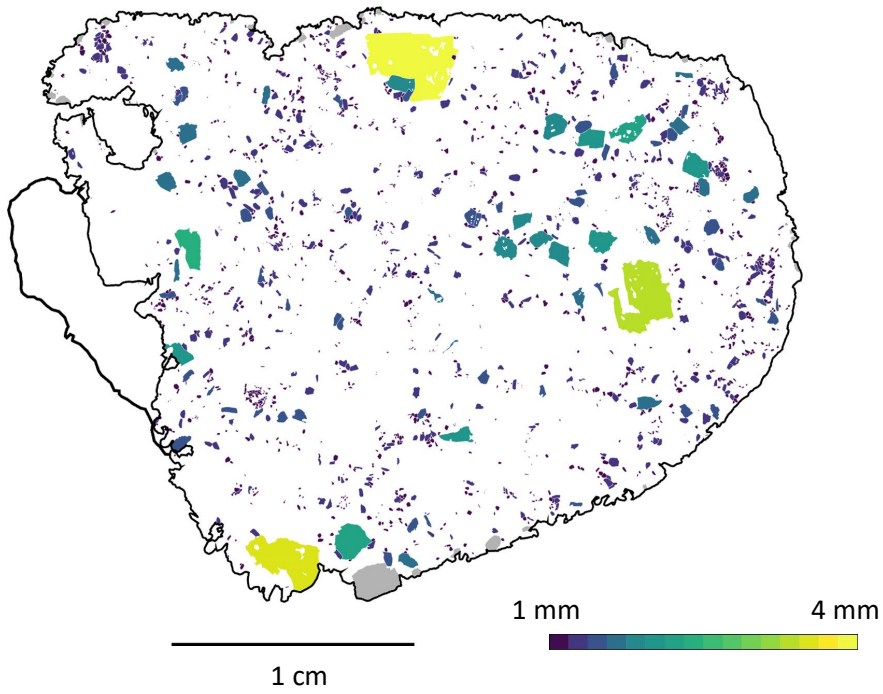

Figure C.76– Visualisation of clinopyroxene crystal sizes in sample M6 C. Crystals are scaled according to their long axis length, measured by the two-dimensional best-fit ellipse. Grey crystals indicate truncated by the boundary of the thin section and thus excluded from analysis.

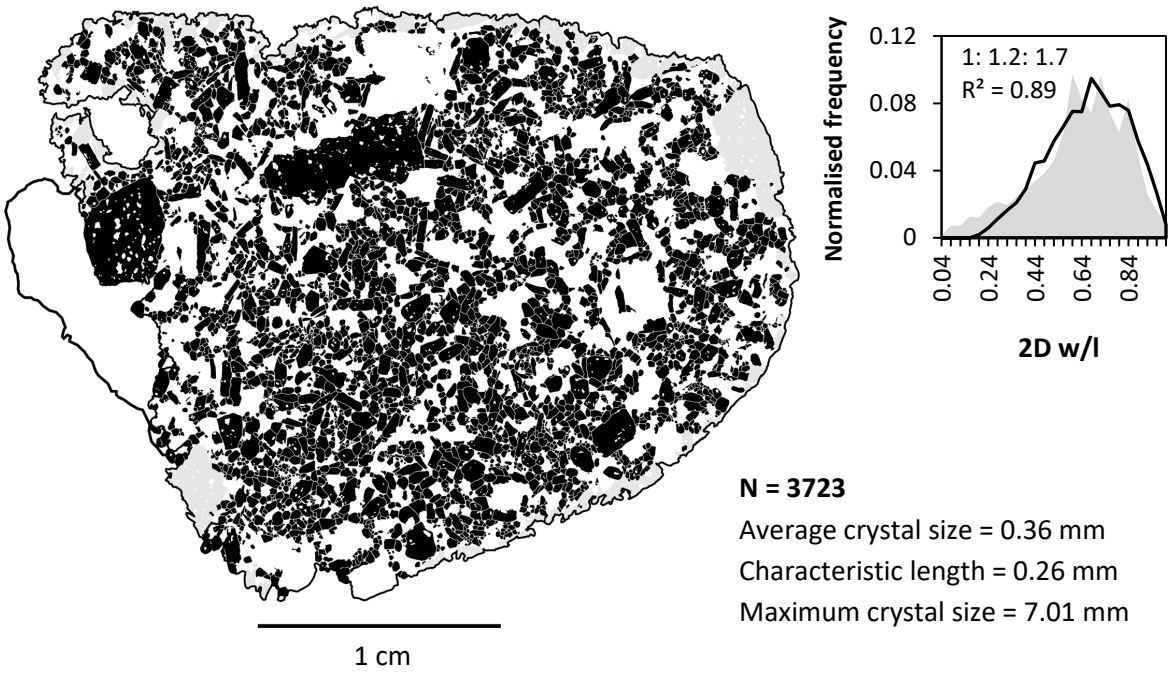

Figure C.77 – Binarised image used to calculate hornblende CSDs in sample M6 C. Grey crystals indicate those truncated by the boundary of the thin section and thus excluded from analysis. Inset histogram visualises the aspect ratio distribution of the measured population (black line), against that of the best fitting shape estimate (grey area).

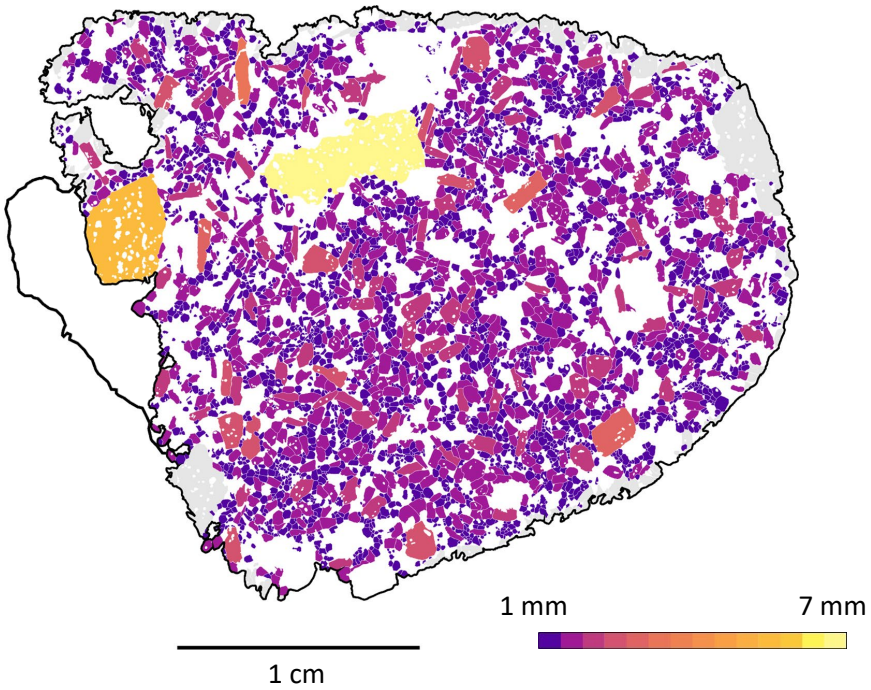

Figure C.78 – Visualisation of hornblende crystal sizes in sample M6 C. Crystals are scaled according to their long axis length, measured by the two-dimensional best-fit ellipse. Grey crystals indicate truncated by the boundary of the thin section and thus excluded from analysis.

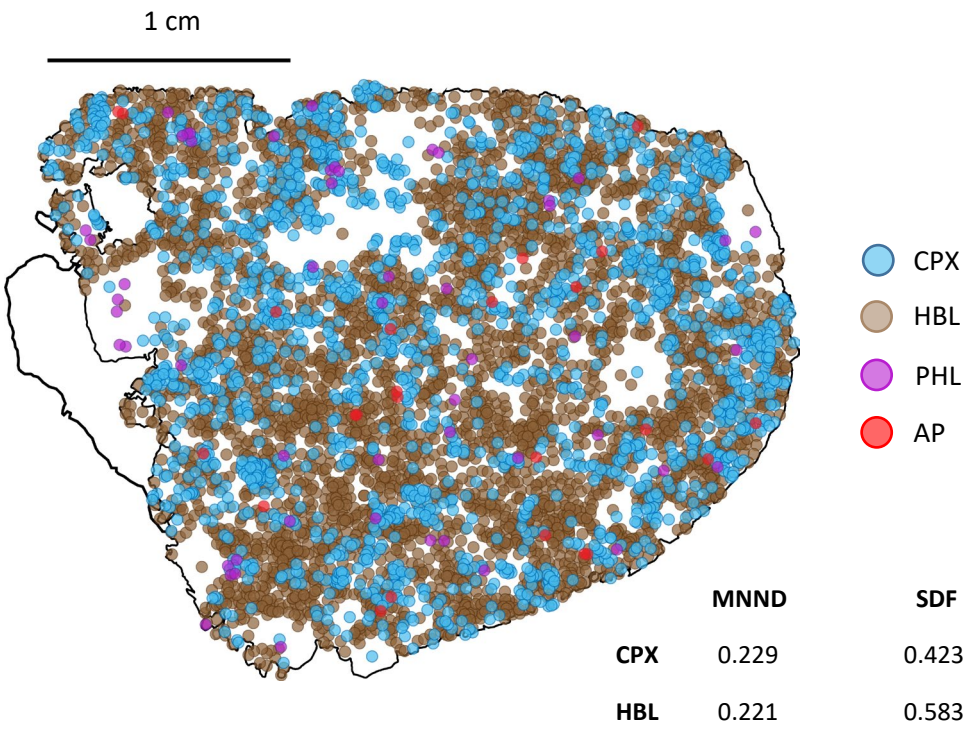

	MNND	SDF
CPX	0.229	0.423
HBL	0.221	0.583

Figure C.79 – Coordinate points used to calculate nearest neighbour distances for spatial distribution calculations in sample M6 C. Coordinates represent the weighted centre point of each identified crystal.

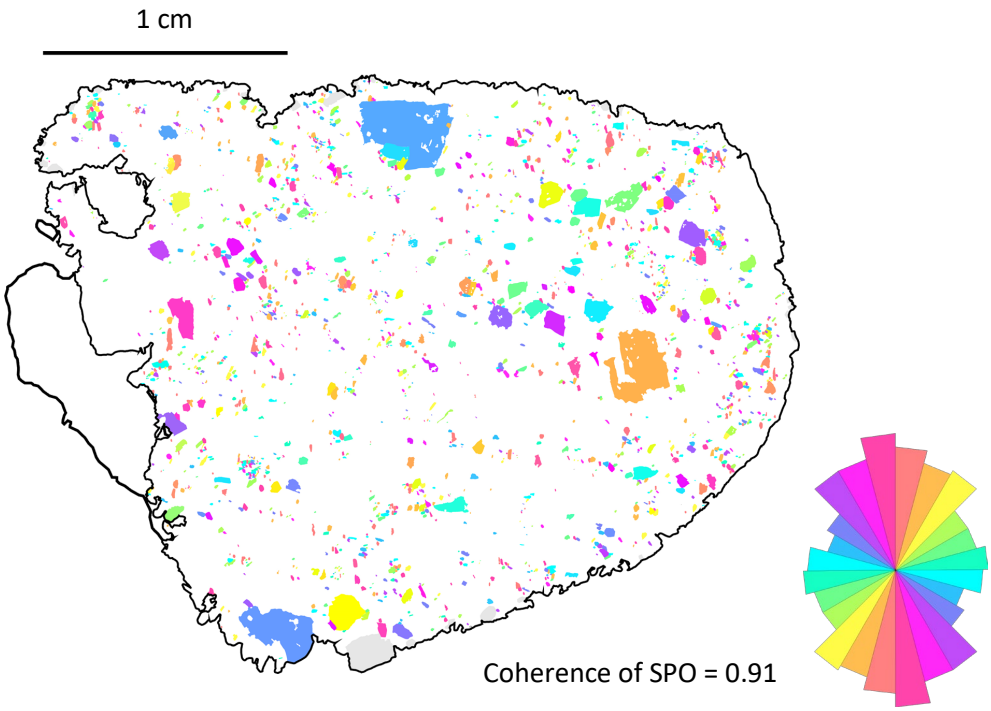

Figure C.80 – Visualisation of shape preferred orientation for clinopyroxene crystals in sample M6 C. Because the xenoliths are ex-situ they are unorientated, meaning that they have no significant direction.

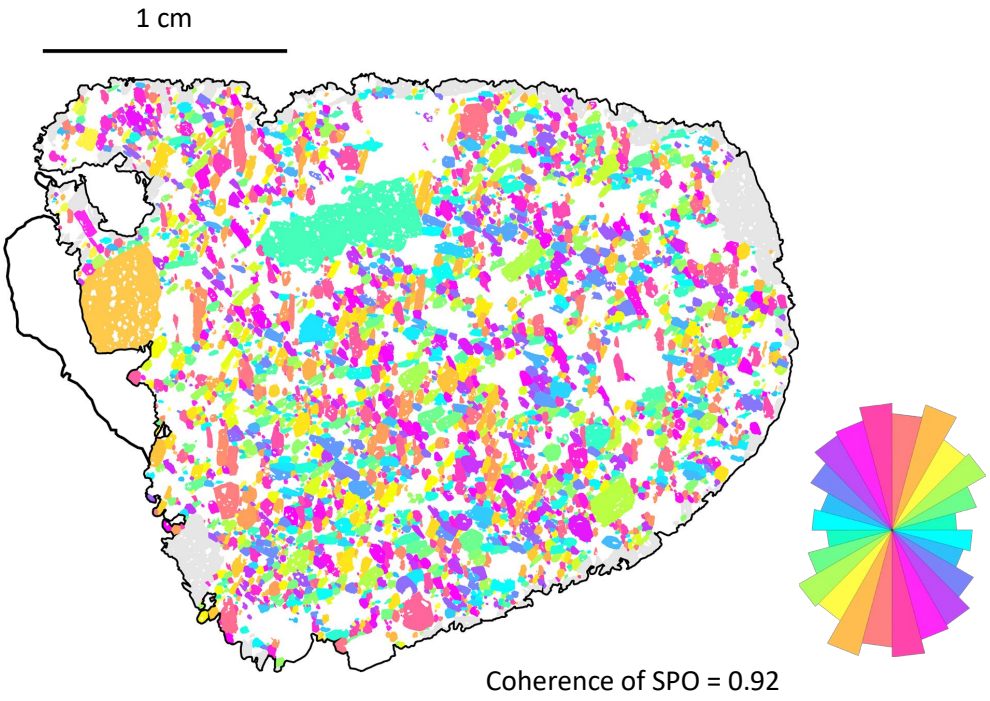

Figure XC.81– Visualisation of shape preferred orientation for hornblende crystals in sample M6 C. Because the xenoliths are ex-situ they are unorientated, meaning that they have no significant direction.

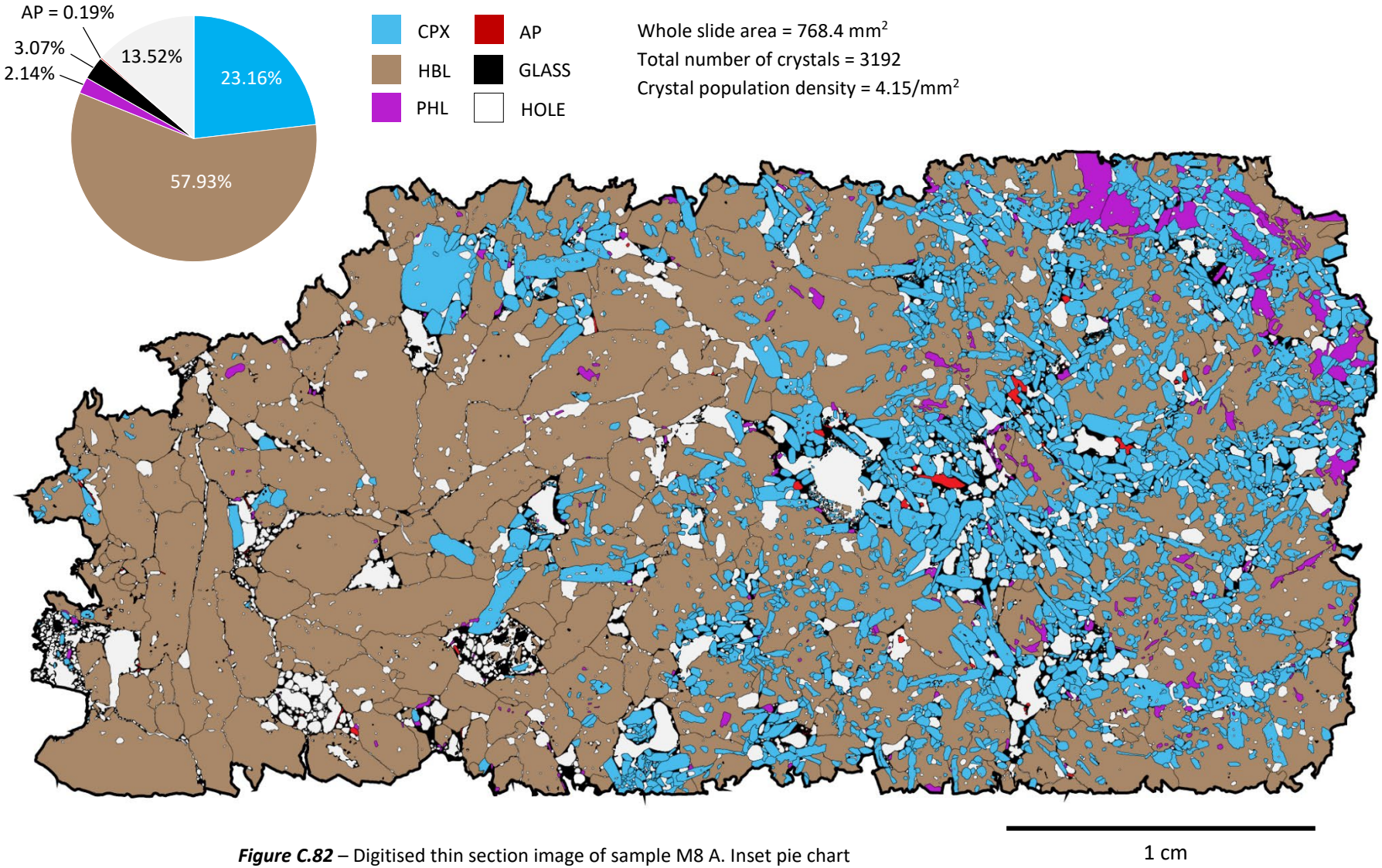

Figure C.82 – Digitised thin section image of sample M8 A. Inset pie chart visualises the area fraction of sample components.

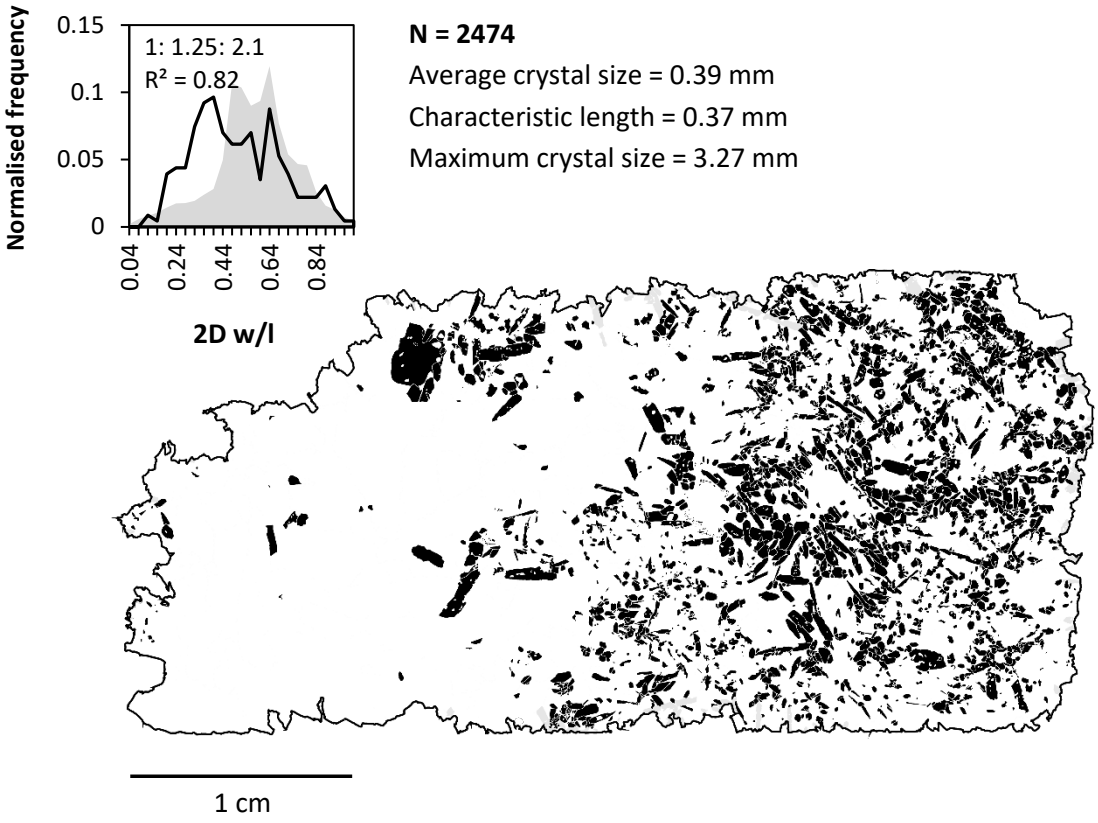

Figure C.83 – Binarised image used to calculate clinopyroxene CSDs in sample M8 A. Grey crystals indicate those truncated by the boundary of the thin section and thus excluded from analysis. Inset histogram visualises the aspect ratio distribution of the measured population (black line), against that of the best fitting shape estimate (grey area).

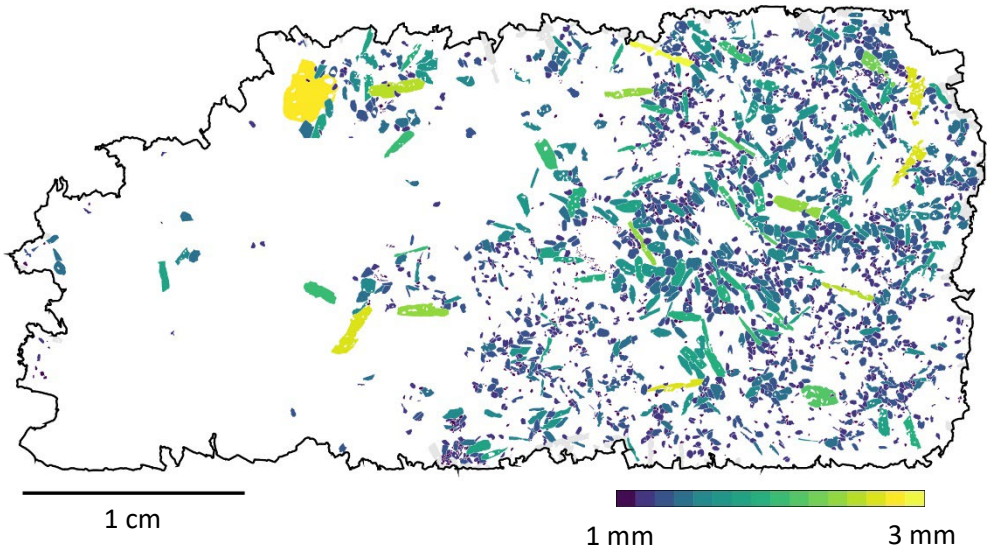

Figure C.84 – Visualisation of clinopyroxene crystal sizes in sample M8 A. Crystals are scaled according to their long axis length, measured by the two-dimensional best-fit ellipse. Grey crystals indicate truncated by the boundary of the thin section and thus excluded from analysis.

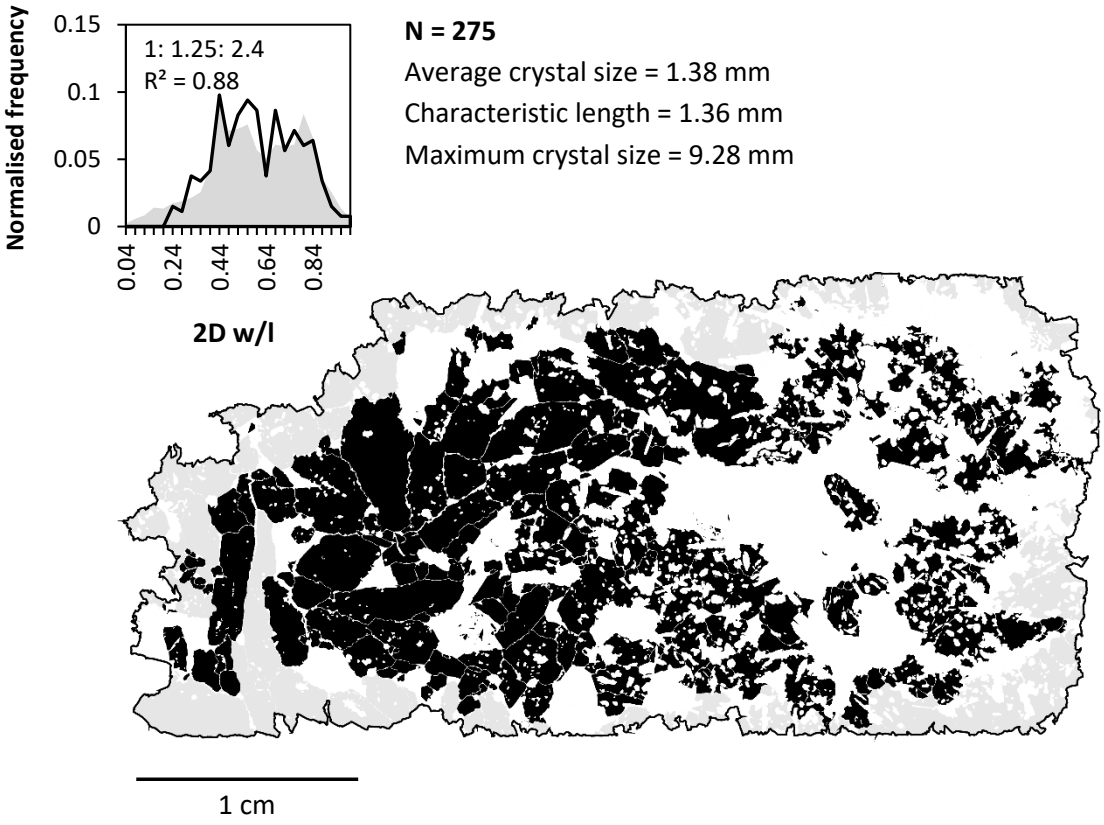

Figure C.85 – Binarised image used to calculate hornblende CSDs in sample M8 A. Grey crystals indicate those truncated by the boundary of the thin section and thus excluded from analysis. Inset histogram visualises the aspect ratio distribution of the measured population (black line), against that of the best fitting shape estimate (grey area).

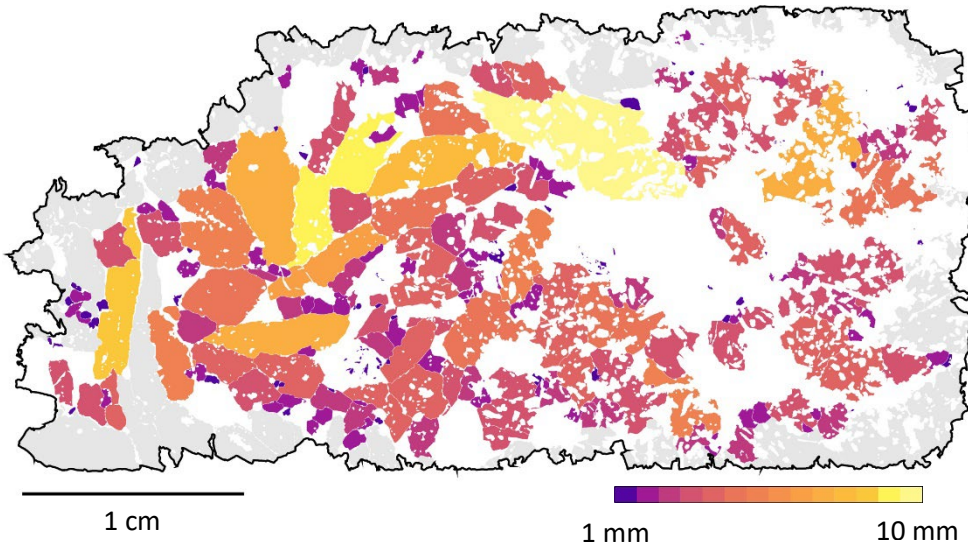

Figure C.86 – Visualisation of hornblende crystal sizes in sample M8 A. Crystals are scaled according to their long axis length, measured by the two-dimensional best-fit ellipse. Grey crystals indicate truncated by the boundary of the thin section and thus excluded from analysis.

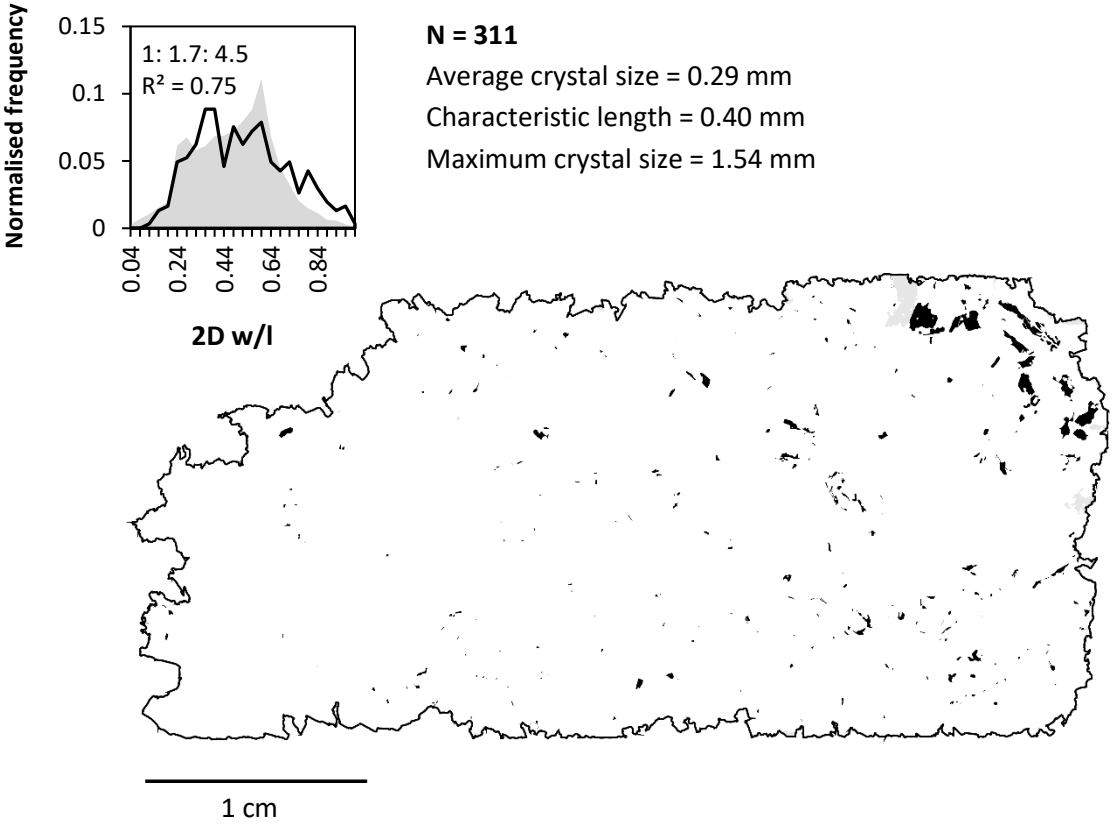

Figure C.87 – Binarised image used to calculate phlogopite CSDs in sample M8 A. Grey crystals indicate those truncated by the boundary of the thin section and thus excluded from analysis. Inset histogram visualises the aspect ratio distribution of the measured population (black line), against that of the best fitting shape estimate (grey area).

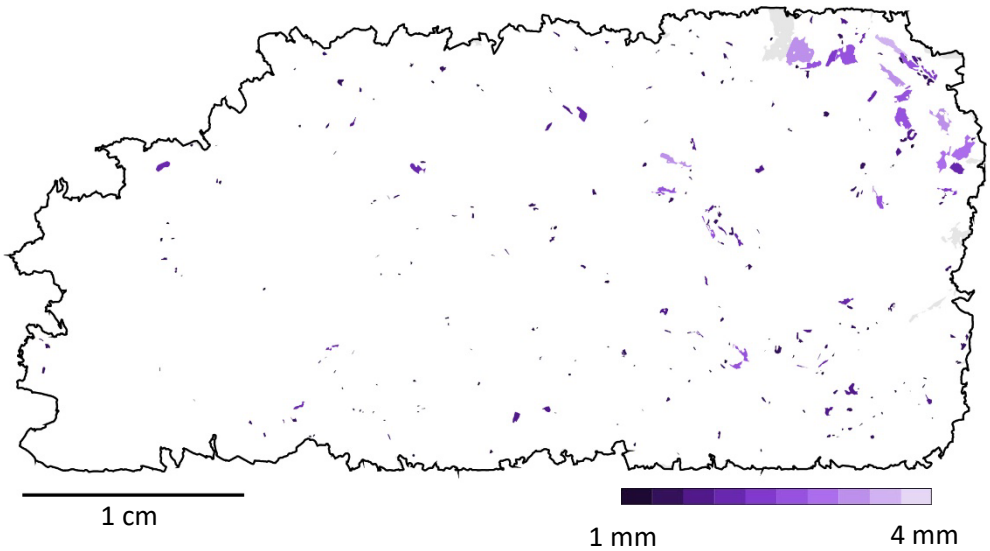

Figure C.88 – Visualisation of phlogopite crystal sizes in sample M8 A. Crystals are scaled according to their long axis length, measured by the two-dimensional best-fit ellipse. Grey crystals indicate truncated by the boundary of the thin section and thus excluded from analysis.

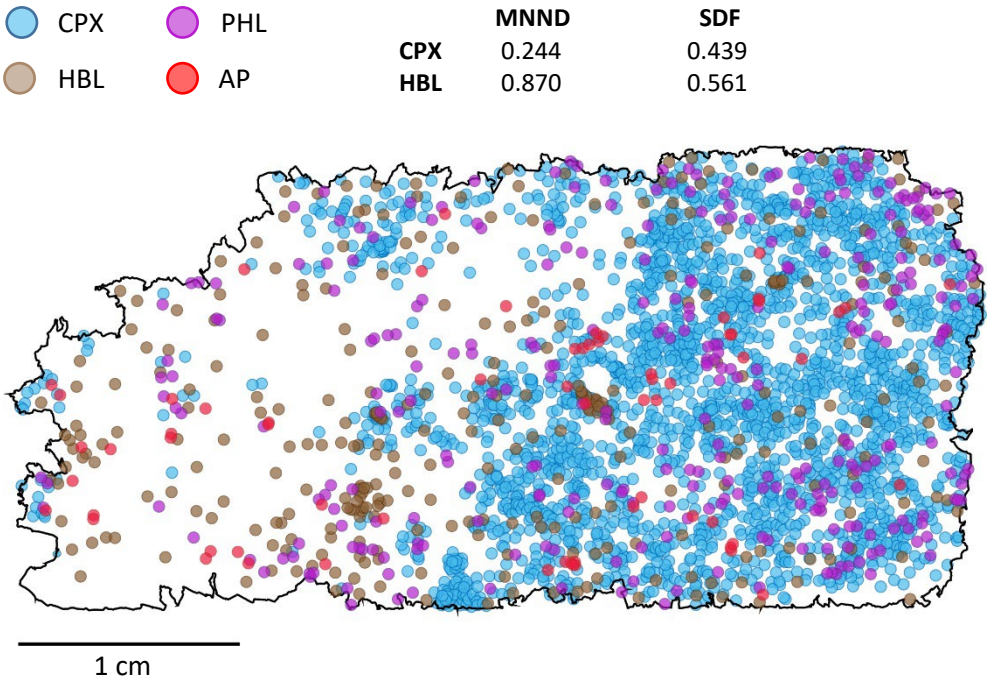

Figure C.89 – Coordinate points used to calculate nearest neighbour distances (in mm) for spatial distribution calculations in sample M8 A. Coordinates represent the weighted centre point of each identified crystal.

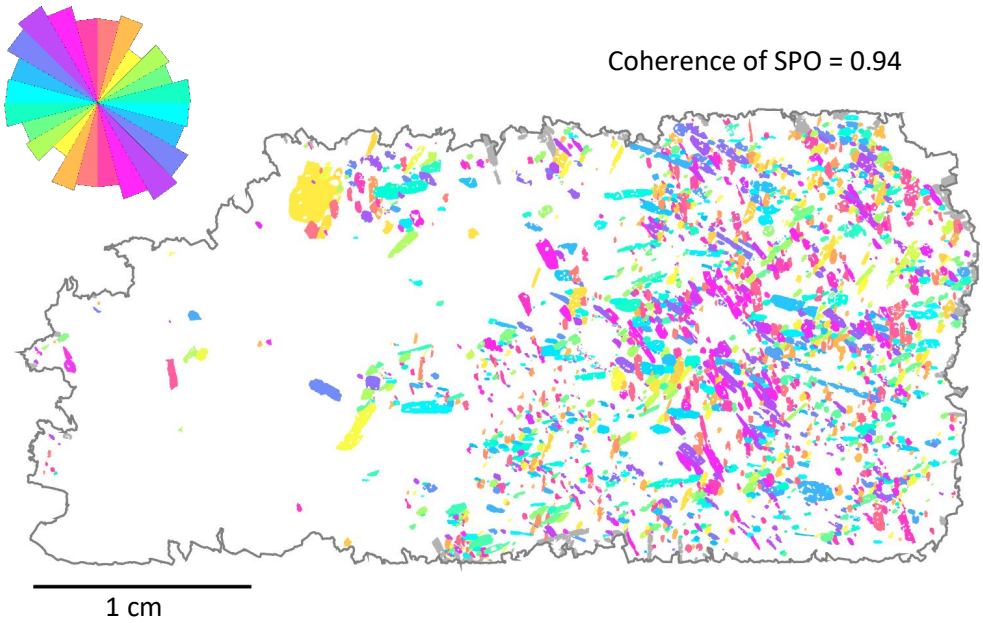

Figure C.90 – Visualisation of shape preferred orientation for clinopyroxene crystals in sample M8 A. Because the xenoliths are ex-situ they are unorientated, meaning that they have no significant direction.

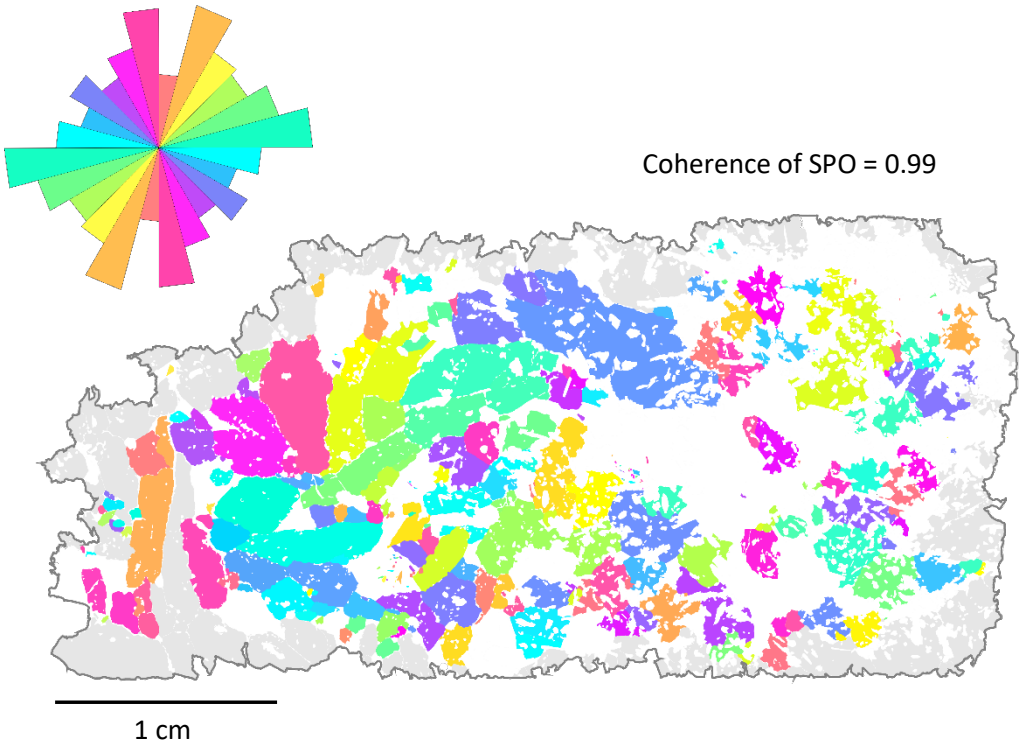

Figure C.91 – Visualisation of shape preferred orientation for hornblende crystals in sample M8 A. Because the xenoliths are ex-situ they are unorientated, meaning that they have no significant direction.

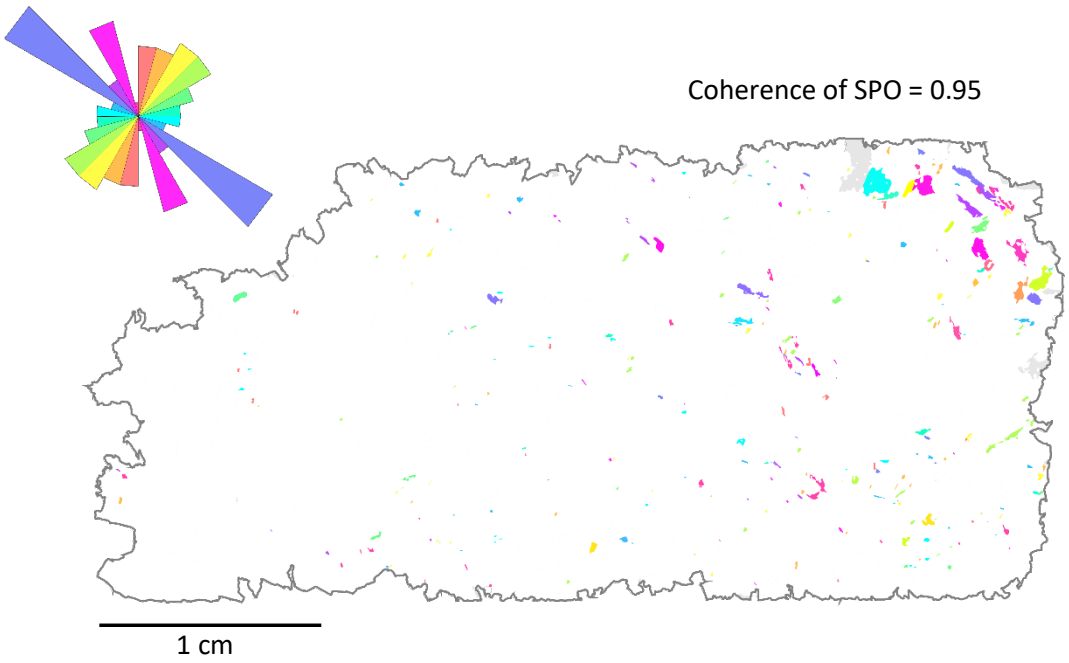

Figure C.92 – Visualisation of shape preferred orientation for phlogopite crystals in sample M8 A. Because the xenoliths are ex-situ they are unorientated, meaning that they have no significant direction.

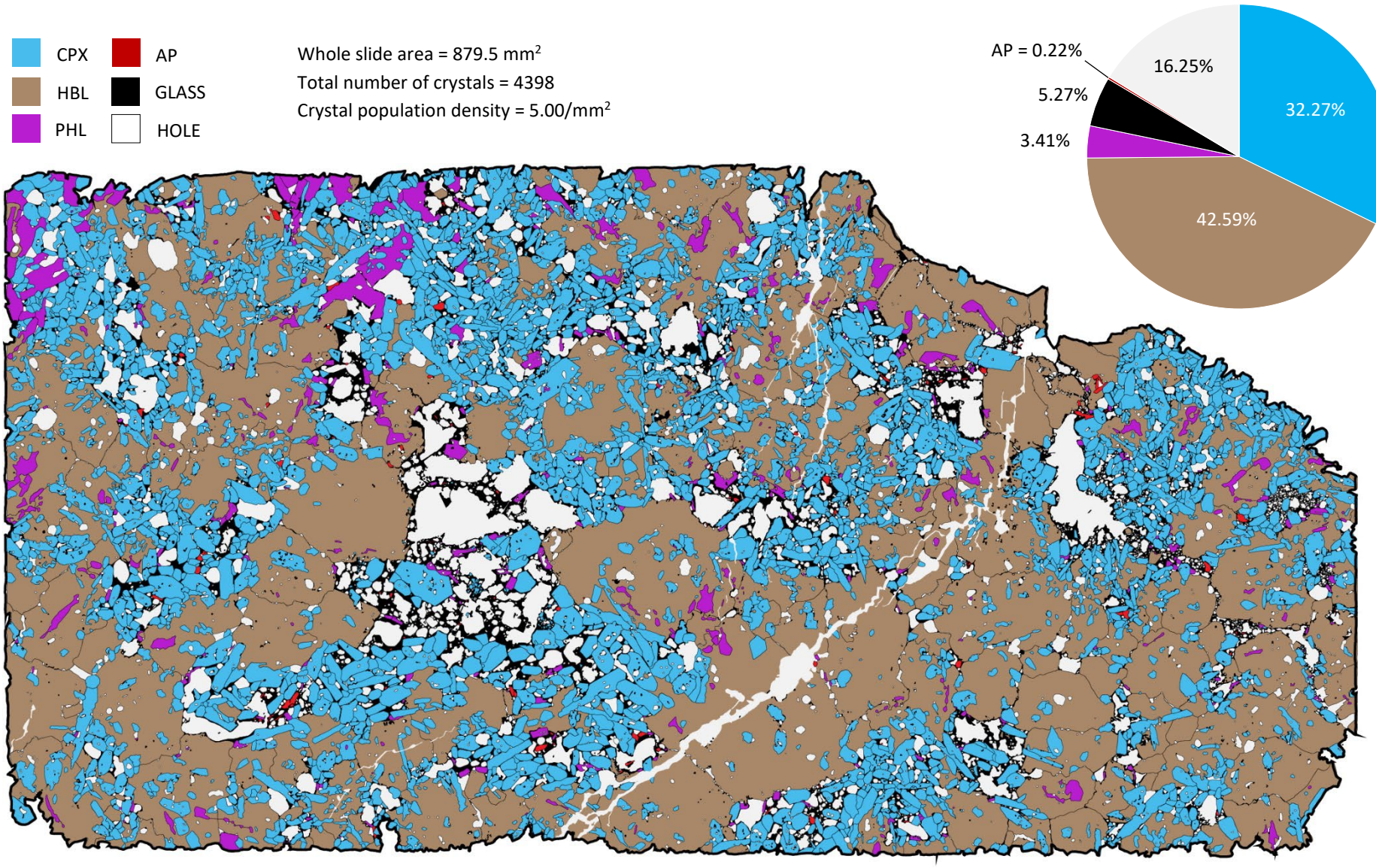

Figure C.93 – Digitised thin section image of sample M8 B. Inset pie chart visualises the area fraction of sample components.

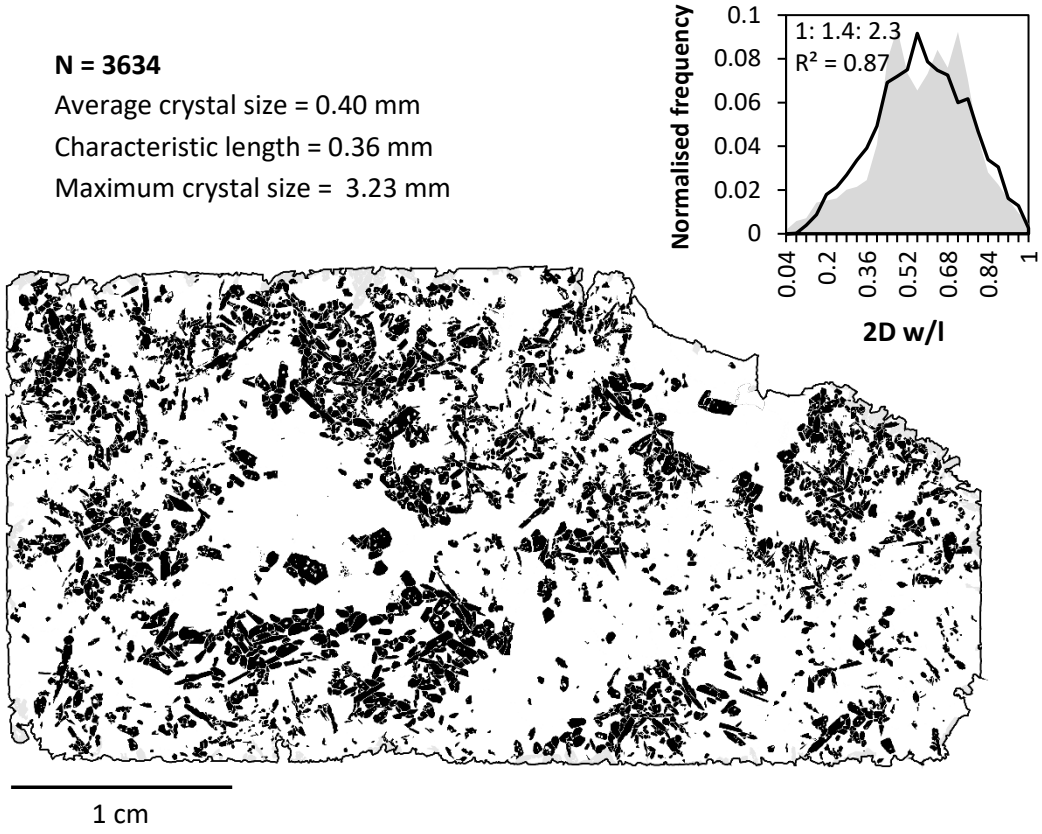

Figure C.94 – Binarised image used to calculate clinopyroxene CSDs in sample M8 B. Grey crystals indicate those truncated by the boundary of the thin section and thus excluded from analysis. Inset histogram visualises the aspect ratio distribution of the measured population (black line), against that of the best fitting shape estimate (grey area).

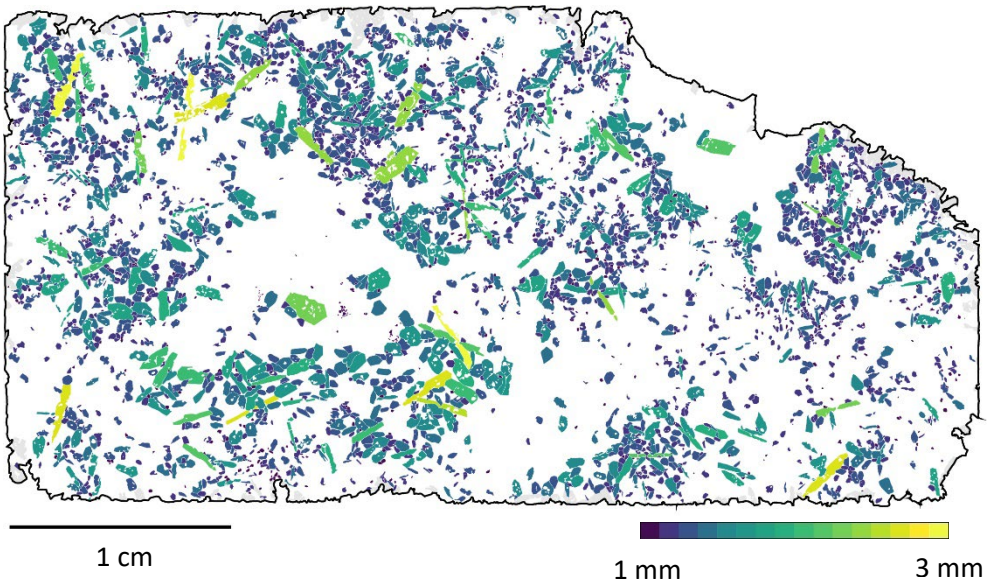

Figure C.95 – Visualisation of clinopyroxene crystal sizes in sample M8 B. Crystals are scaled according to their long axis length, measured by the two-dimensional best-fit ellipse. Grey crystals indicate truncated by the boundary of the thin section and thus excluded from analysis.

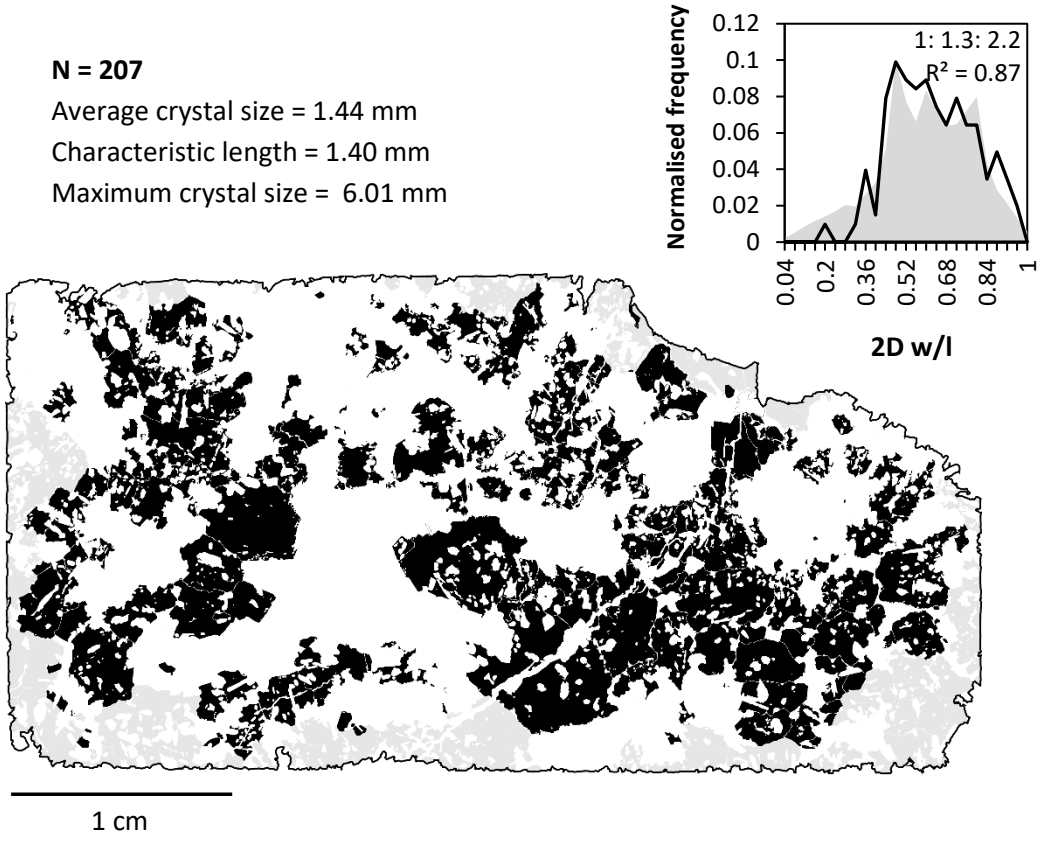

Figure C.96 – Binarised image used to calculate hornblende CSDs in sample M8 B. Grey crystals indicate those truncated by the boundary of the thin section and thus excluded from analysis. Inset histogram visualises the aspect ratio distribution of the measured population (black line), against that of the best fitting shape estimate (grey area).

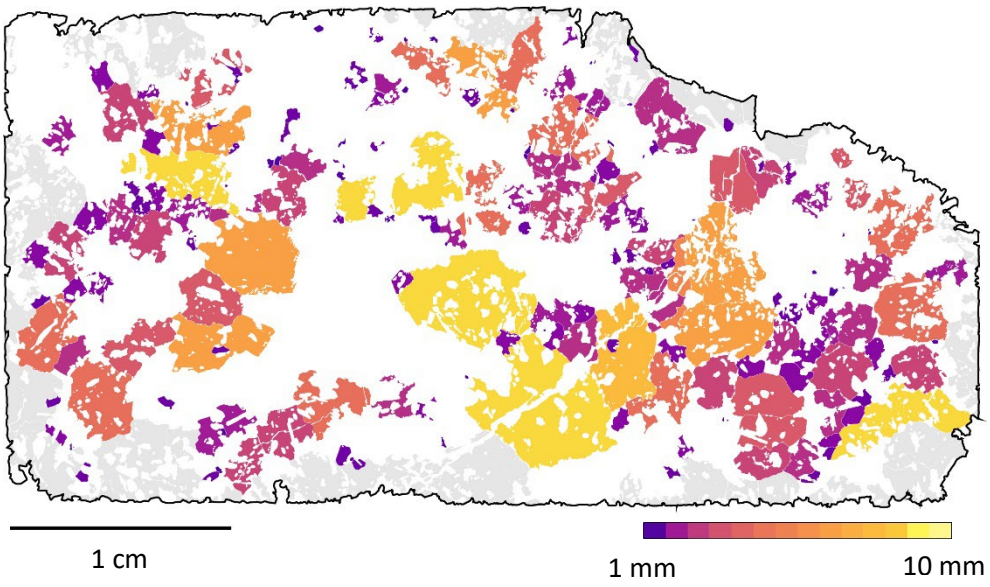

Figure C.97 – Visualisation of hornblende crystal sizes in sample M8 B. Crystals are scaled according to their long axis length, measured by the two-dimensional best-fit ellipse. Grey crystals indicate truncated by the boundary of the thin section and thus excluded from analysis.

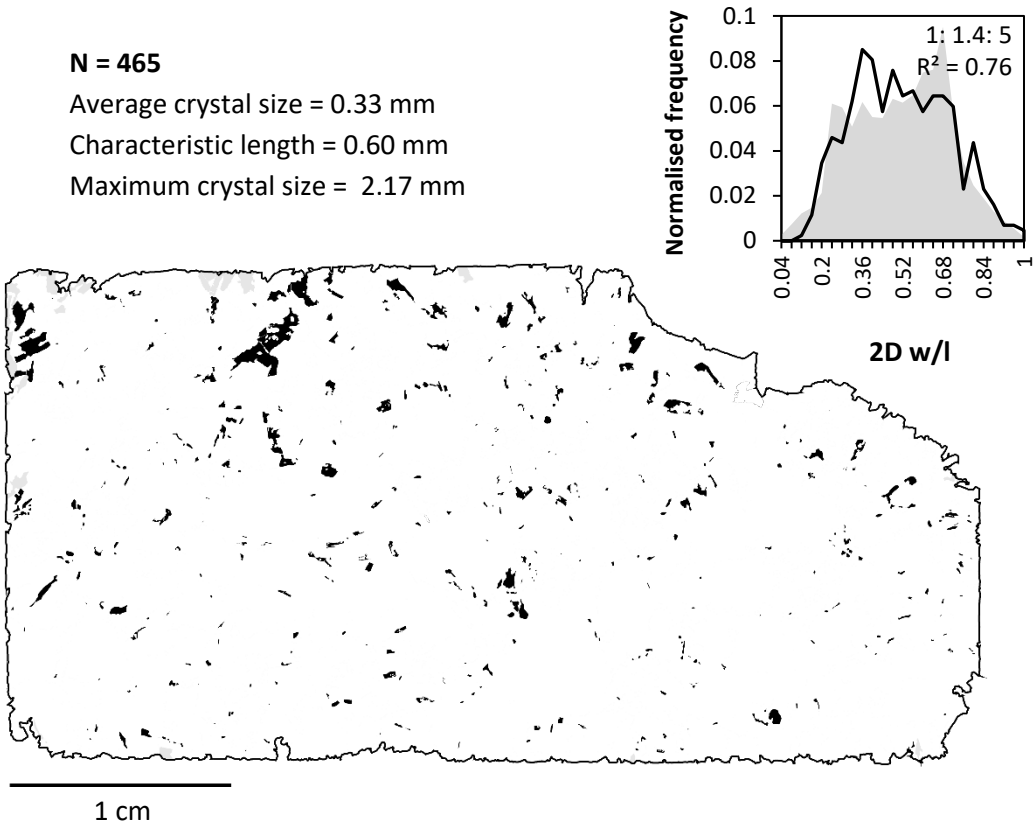

Figure C.98 – Binarised image used to calculate phlogopite CSDs in sample M8 B. Grey crystals indicate those truncated by the boundary of the thin section and thus excluded from analysis. Inset histogram visualises the aspect ratio distribution of the measured population (black line), against that of the best fitting shape estimate (grey area).

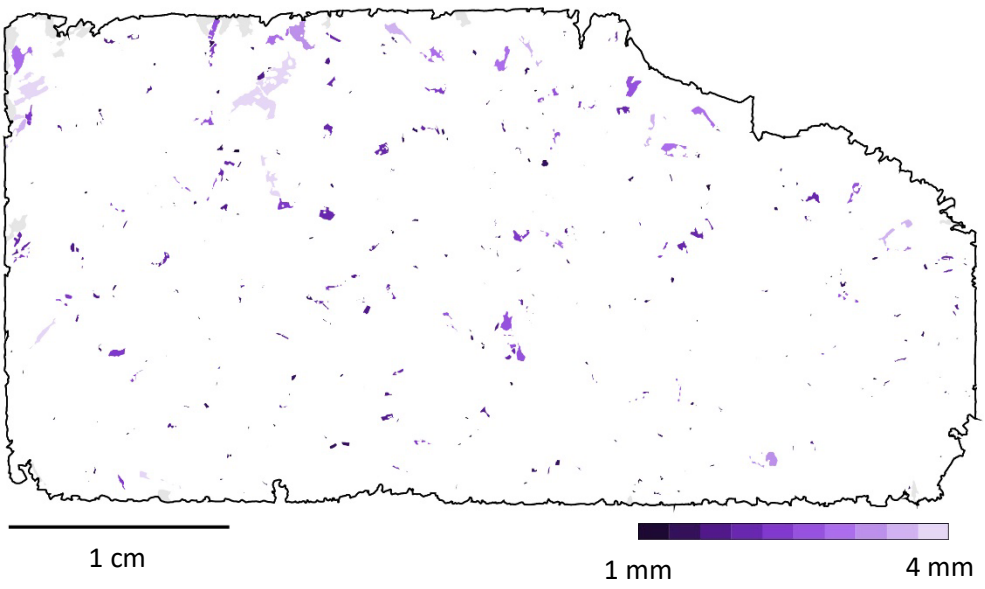

Figure C.99 – Visualisation of phlogopite crystal sizes in sample M8 B. Crystals are scaled according to their long axis length, measured by the two-dimensional best-fit ellipse. Grey crystals indicate truncated by the boundary of the thin section and thus excluded from analysis.

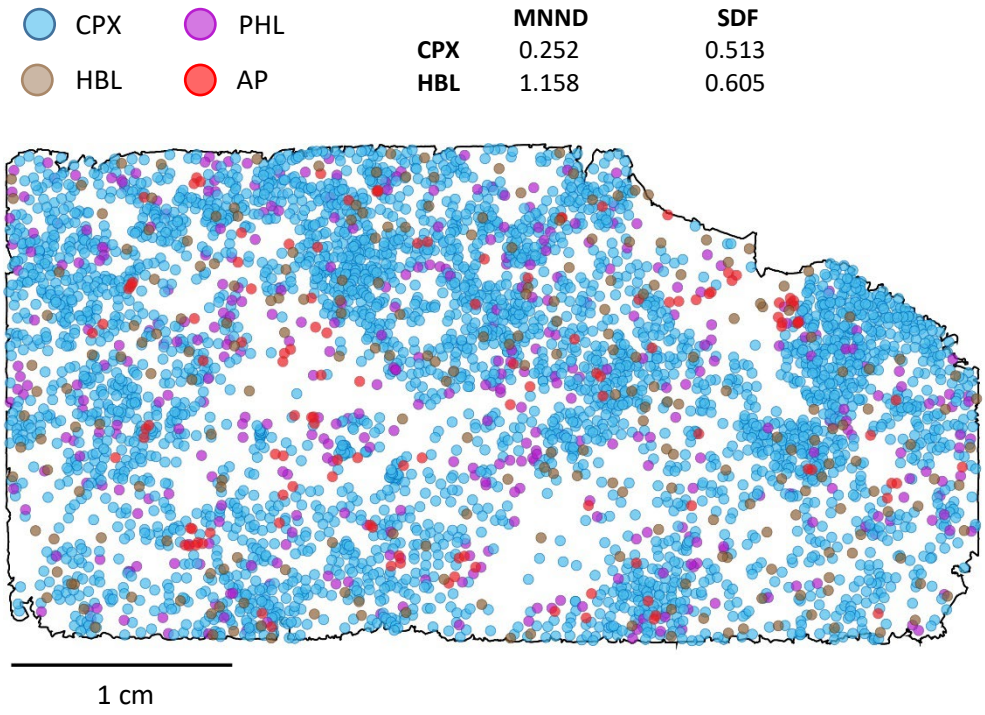

Figure C.100 – Coordinate points used to calculate nearest neighbour distances (in mm) for spatial distribution calculations in sample M8 B. Coordinates represent the weighted centre point of each identified crystal.

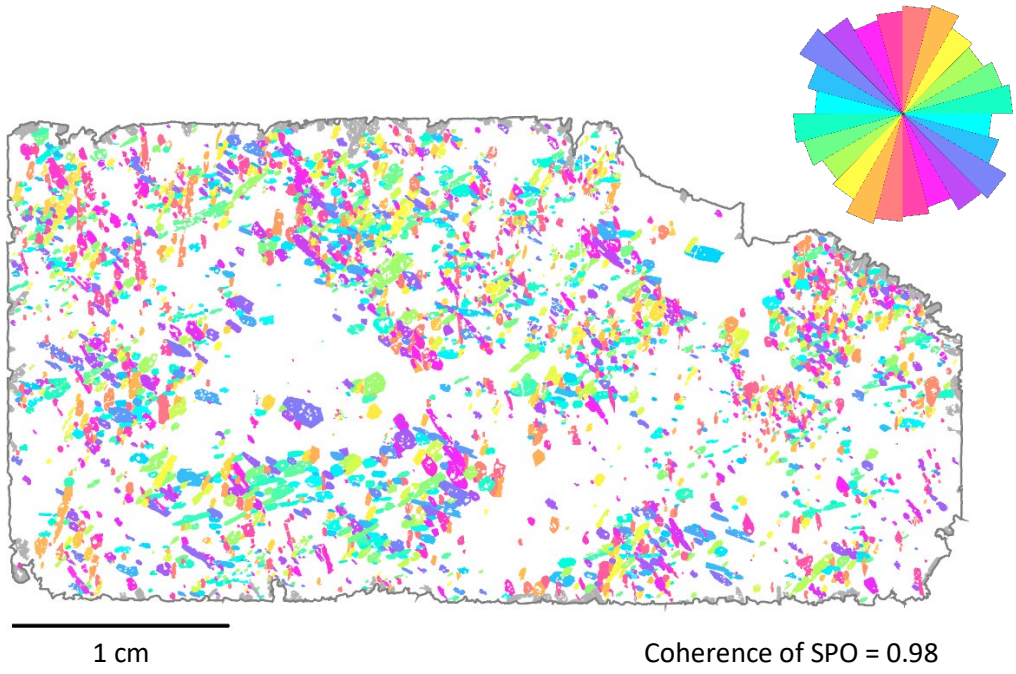

Figure C.101 – Visualisation of shape preferred orientation for clinopyroxene crystals in sample M8 B. Because the xenoliths are ex-situ they are unorientated, meaning that they have no significant direction.

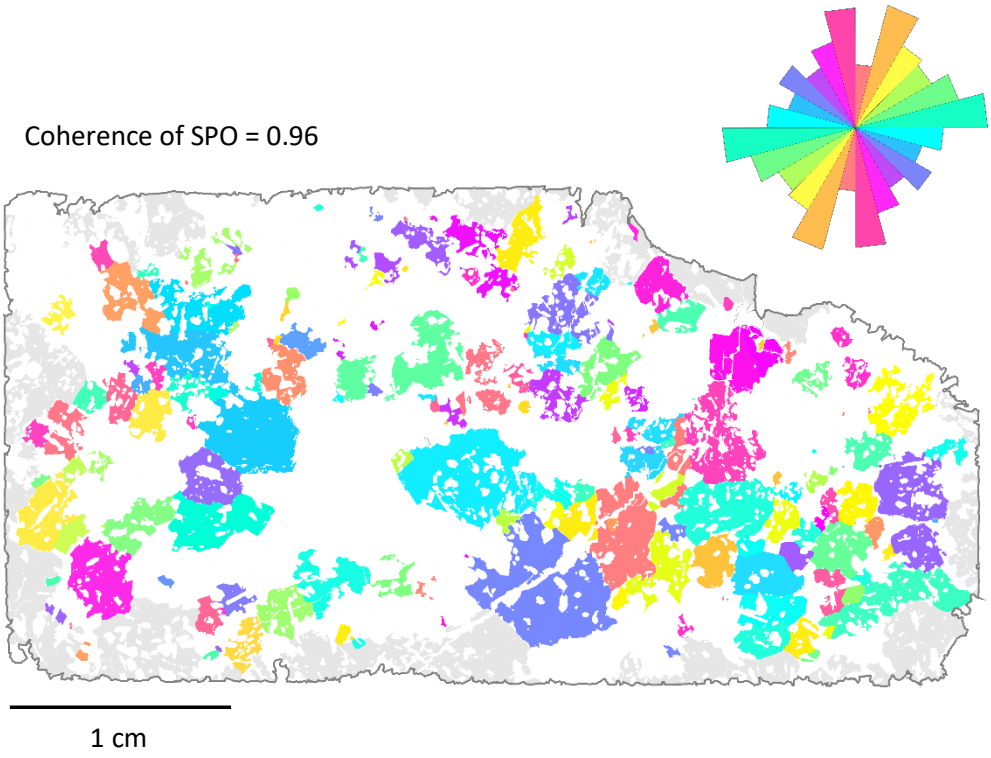

Figure C.102 – Visualisation of shape preferred orientation for hornblende crystals in sample M8 B. Because the xenoliths are ex-situ they are unorientated, meaning that they have no significant direction.

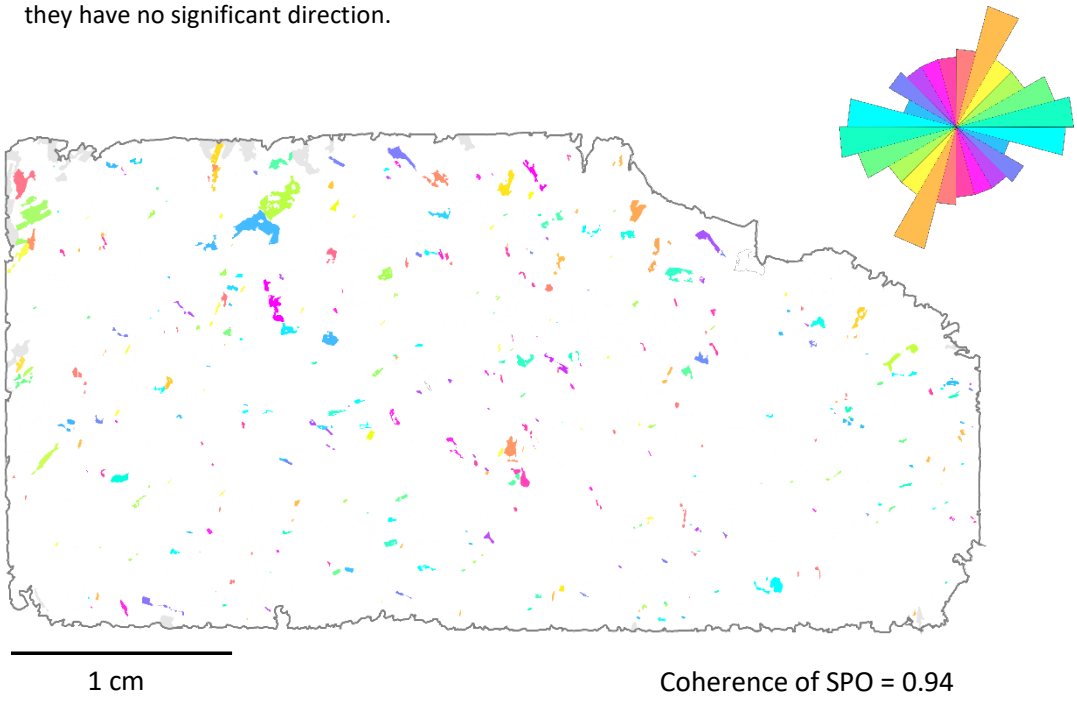

Figure C.103 – Visualisation of shape preferred orientation for phlogopite crystals in sample M8 B. Because the xenoliths are ex-situ they are unorientated, meaning that they have no significant direction.

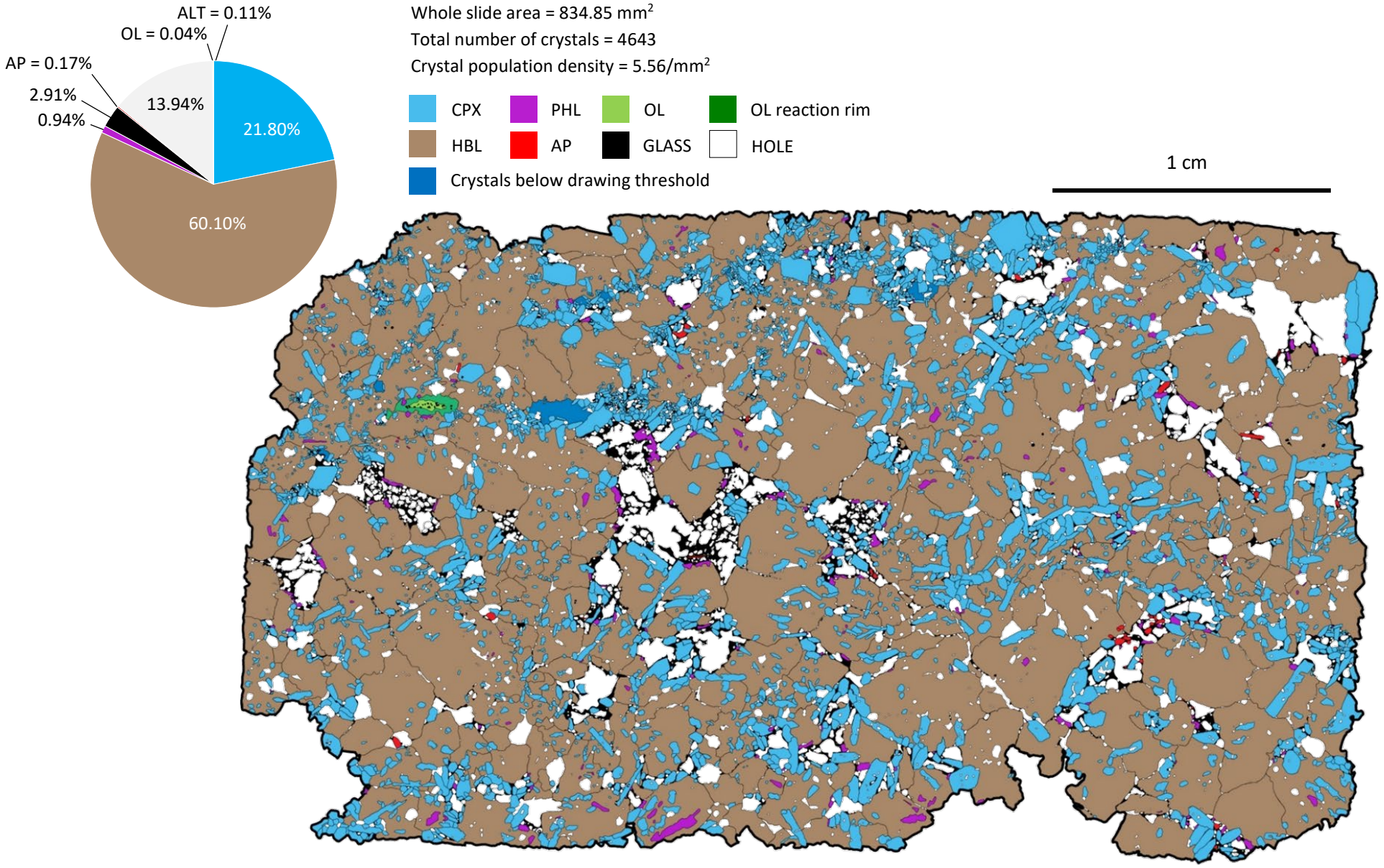

Figure C.104 – Digitised thin section image of sample M8 C. Inset pie chart visualises the area fraction of sample components.

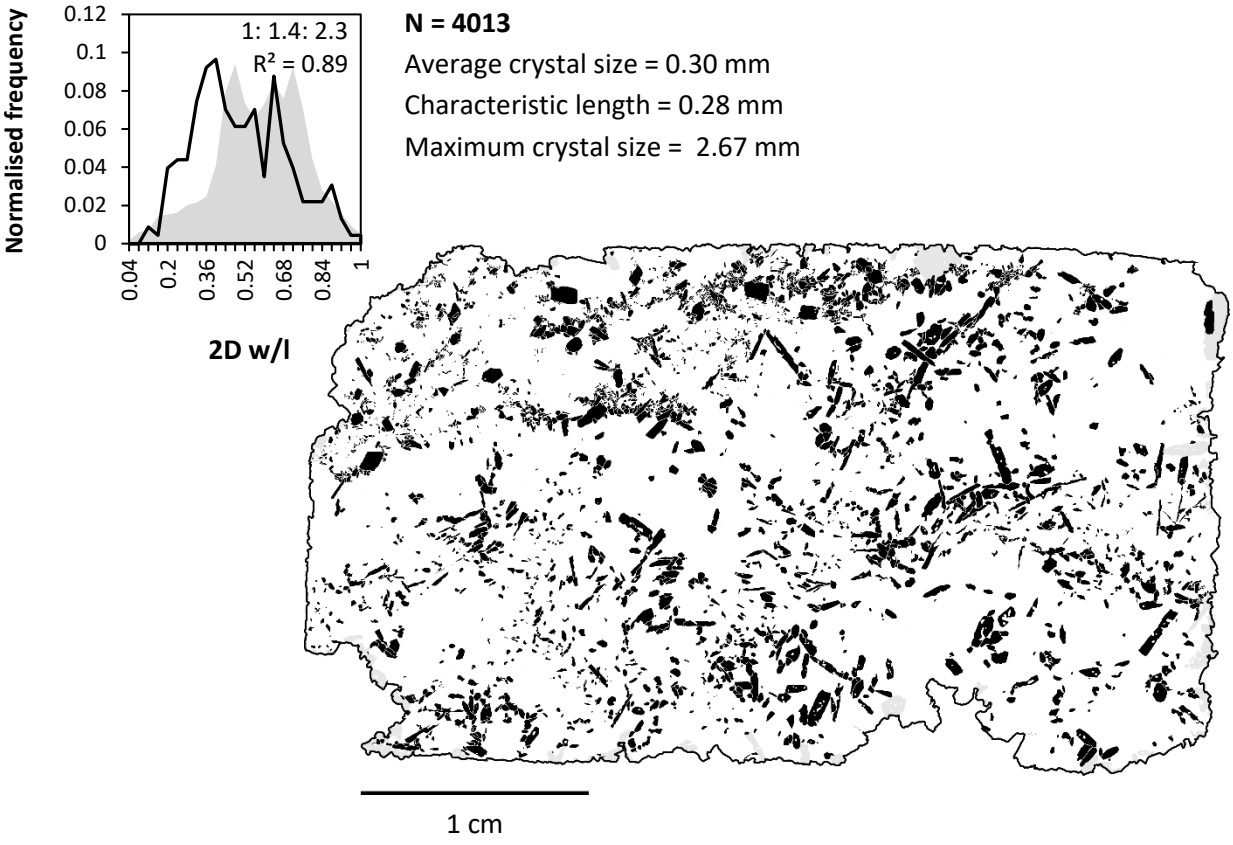

Figure C.105 – Binarised image used to calculate clinopyroxene CSDs in sample M8 C. Grey crystals indicate those truncated by the boundary of the thin section and thus excluded from analysis. Inset histogram visualises the aspect ratio distribution of the measured population (black line), against that of the best fitting shape estimate (grey area).

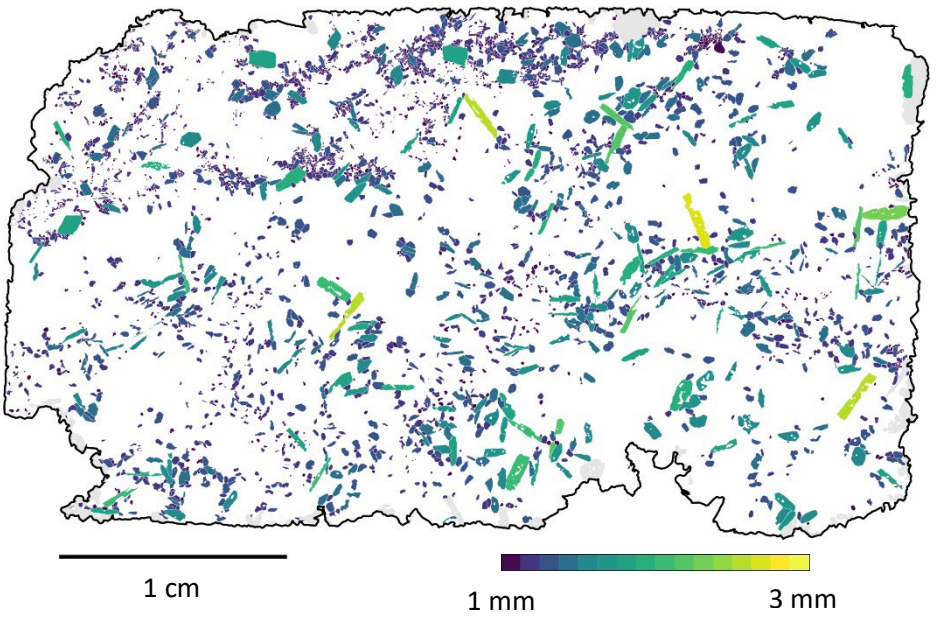

Figure C.106 – Visualisation of clinopyroxene crystal sizes in sample M8 C. Crystals are scaled according to their long axis length, measured by the two-dimensional best-fit ellipse. Grey crystals indicate truncated by the boundary of the thin section and thus excluded from analysis.

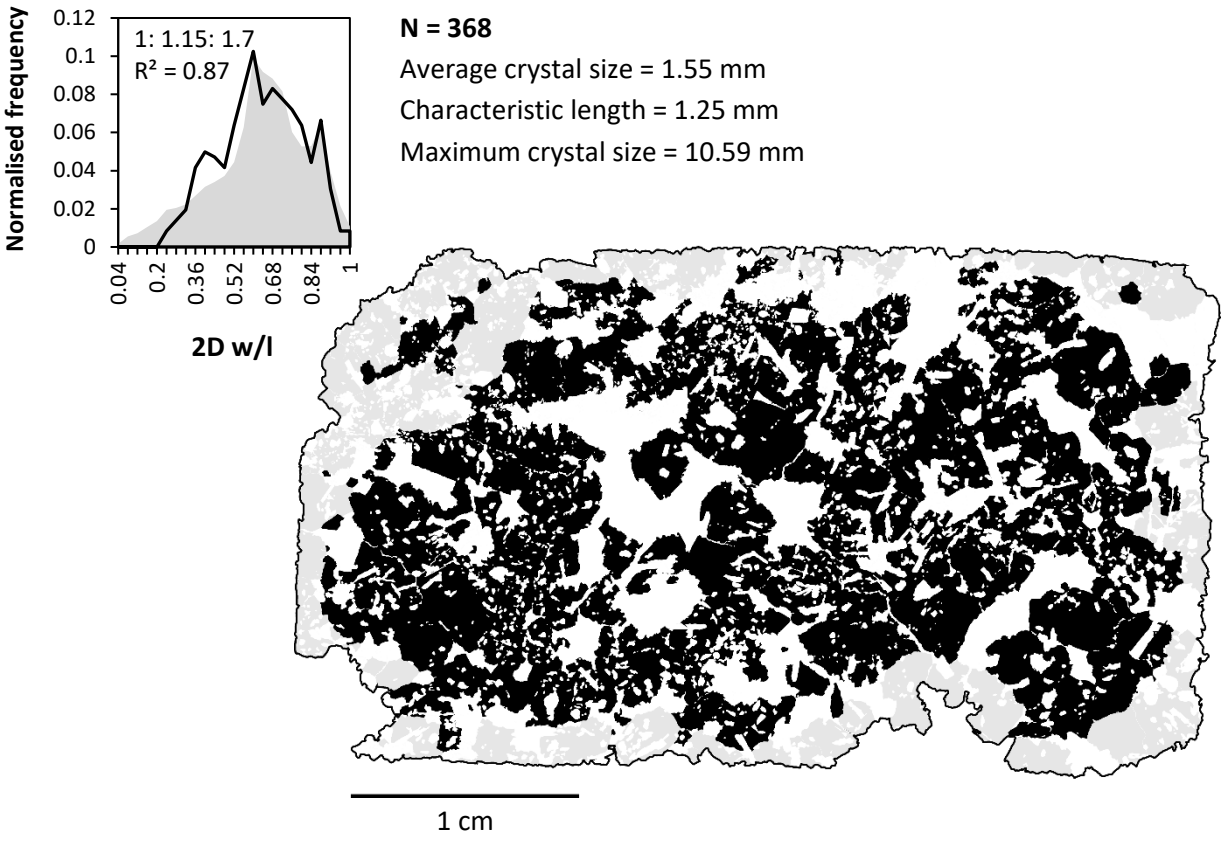

Figure C.107 – Binarised image used to calculate hornblende CSDs in sample M8 C. Grey crystals indicate those truncated by the boundary of the thin section and thus excluded from analysis. Inset histogram visualises the aspect ratio distribution of the measured population (black line), against that of the best fitting shape estimate (grey area).

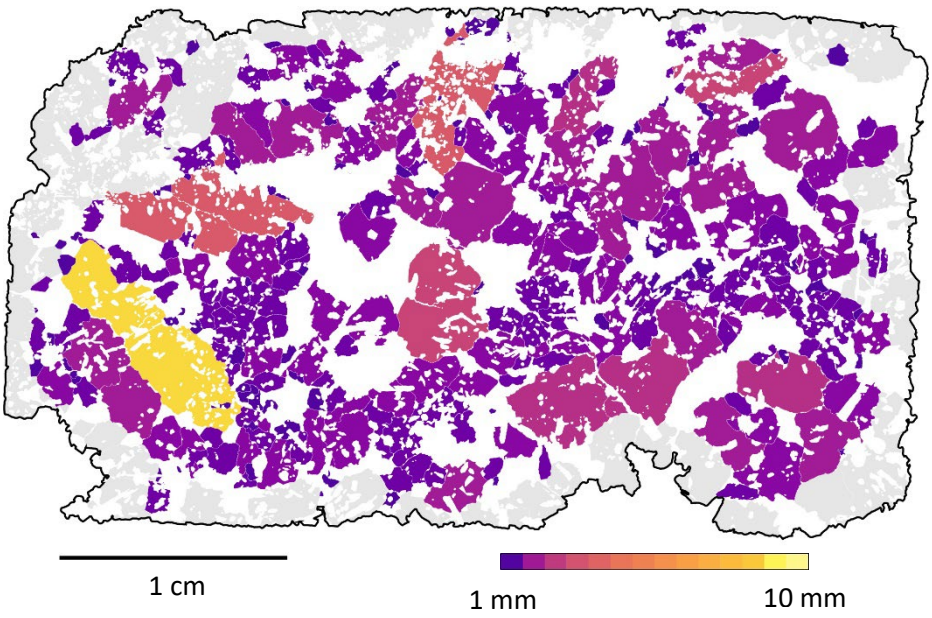

Figure C.108 – Visualisation of hornblende crystal sizes in sample M8 C. Crystals are scaled according to their long axis length, measured by the two-dimensional best-fit ellipse. Grey crystals indicate truncated by the boundary of the thin section and thus excluded from analysis.

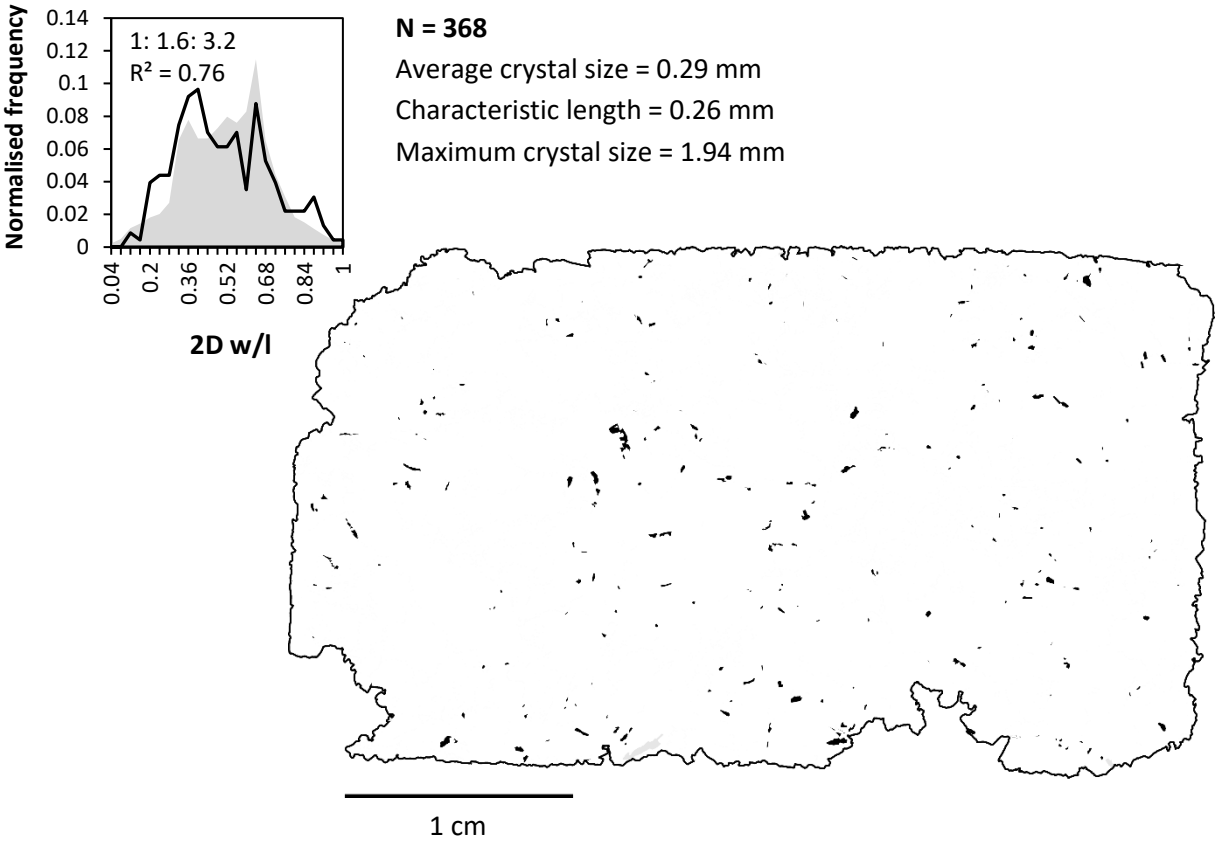

Figure C.109 – Binarised image used to calculate phlogopite CSDs in sample M8 C. Grey crystals indicate those truncated by the boundary of the thin section and thus excluded from analysis. Inset histogram visualises the aspect ratio distribution of the measured population (black line), against that of the best fitting shape estimate (grey area).

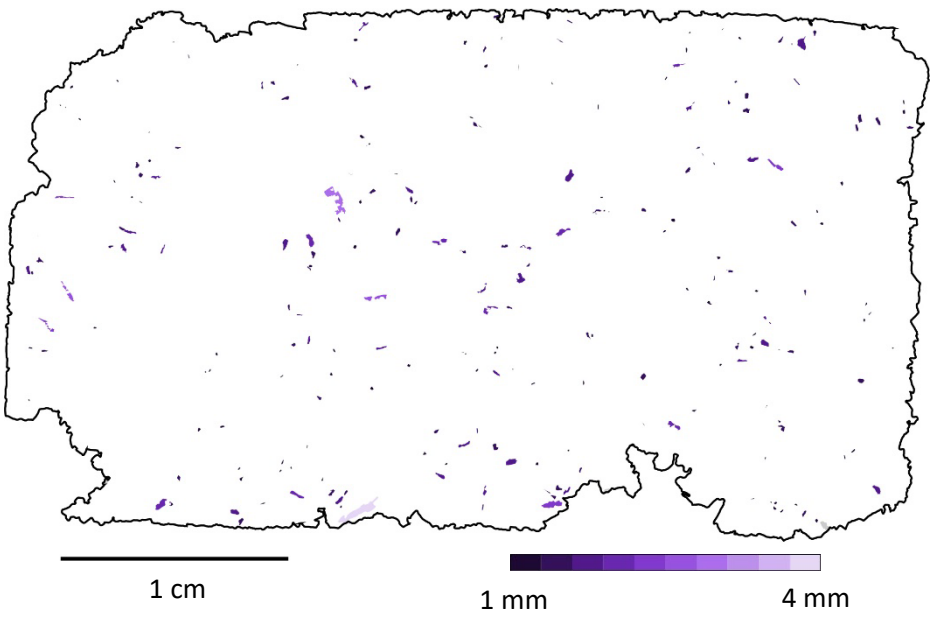

Figure C.110 – Visualisation of phlogopite crystal sizes in sample M8 C. Crystals are scaled according to their long axis length, measured by the two-dimensional best-fit ellipse. Grey crystals indicate truncated by the boundary of the thin section and thus excluded from analysis.

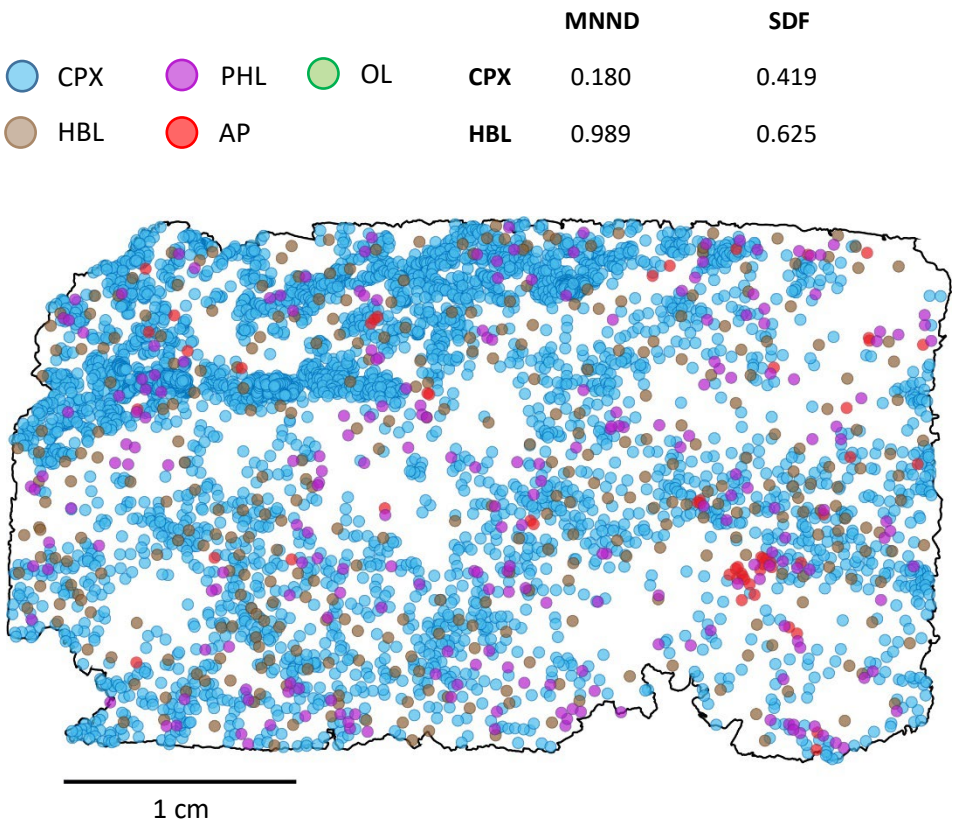

Figure C.111 – Coordinate points used to calculate nearest neighbour distances (in mm) for spatial distribution calculations in sample M8 C. Coordinates represent the weighted centre point of each identified crystal.

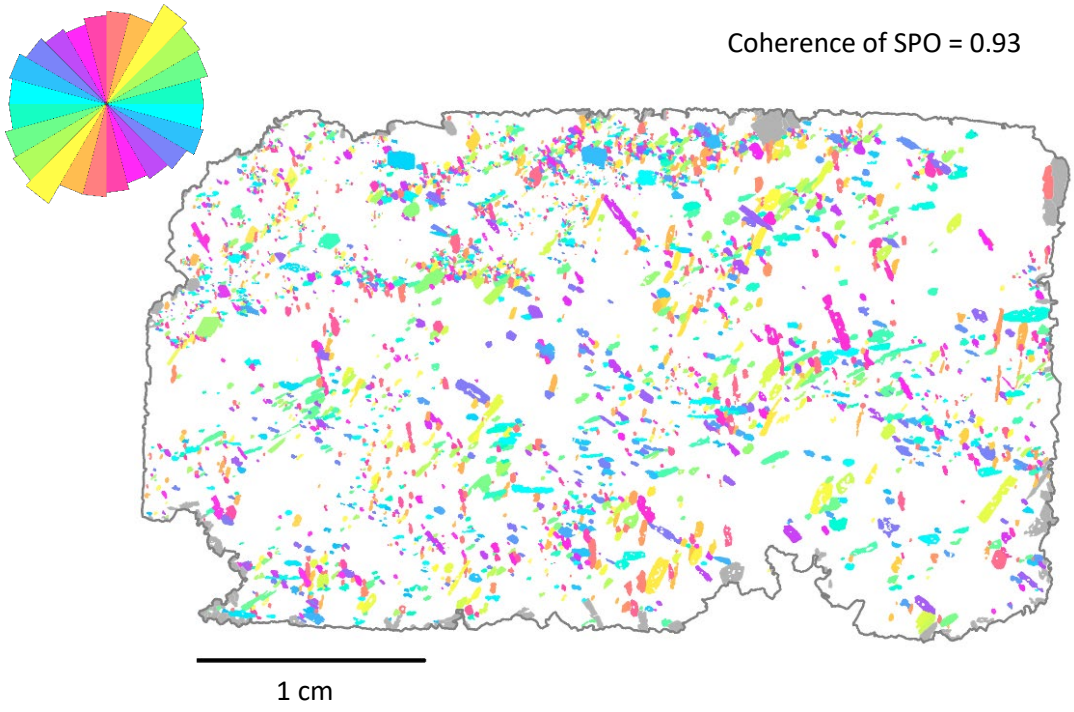

Figure C.112 – Visualisation of shape preferred orientation for clinopyroxene crystals in sample M8 C. Because the xenoliths are ex-situ they are unorientated, meaning that they have no significant direction.

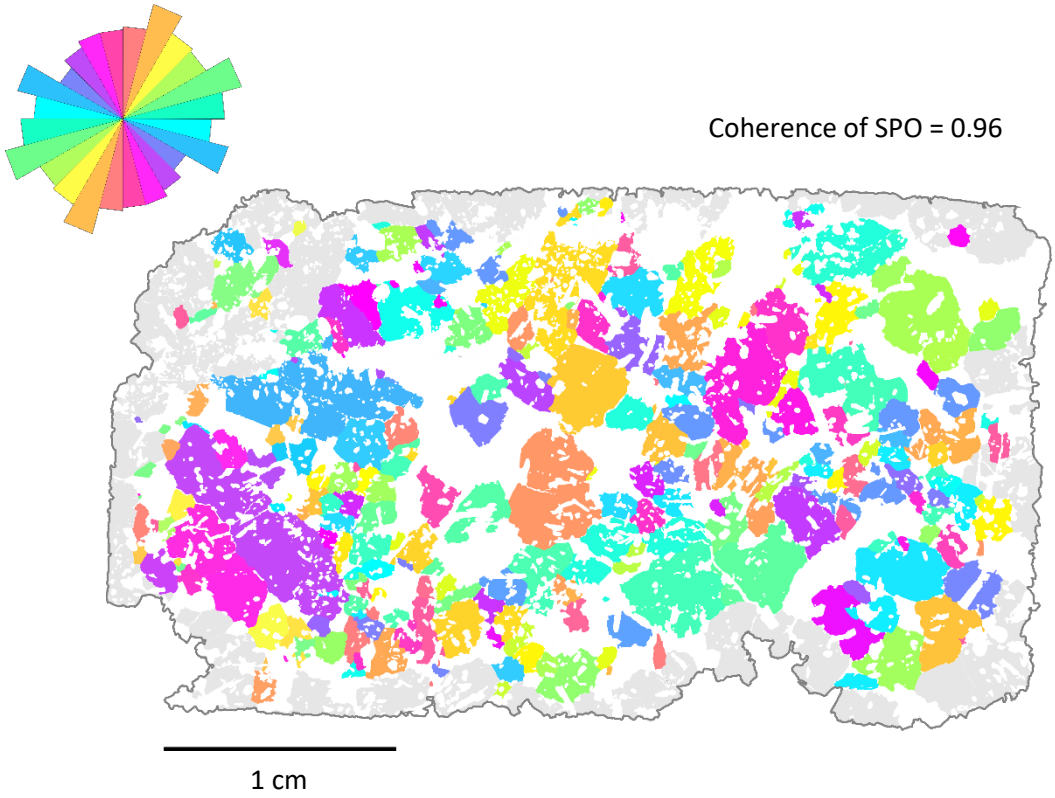

Figure C.113 – Visualisation of shape preferred orientation for hornblende crystals in sample M8 C. Because the xenoliths are ex-situ they are unorientated, meaning that they have no significant direction.

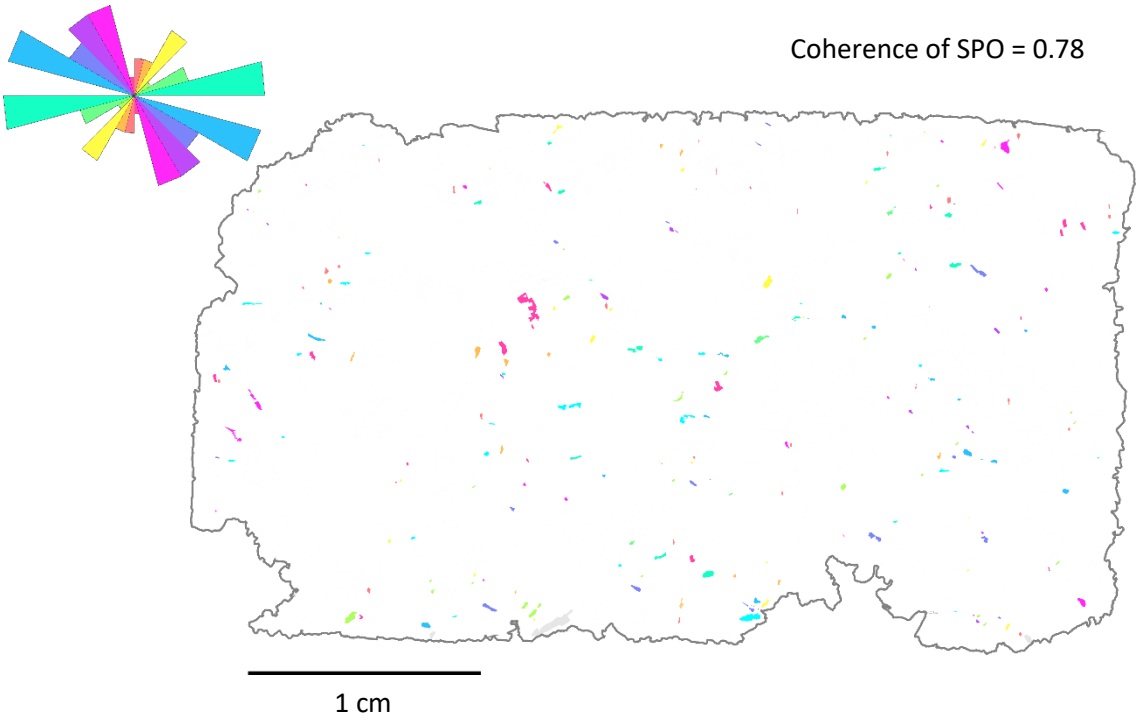

Figure C.114 – Visualisation of shape preferred orientation for phlogopite crystals in sample M8 C. Because the xenoliths are ex-situ they are unorientated, meaning that they have no significant direction.